Vincenzo Parenti-Castelli
Werner Schiehlen
Editors

International Centre
for Mechanical Sciences

ROMANSY 18
Robot Design, Dynamics and Control

CISM Courses and Lectures, vol. 524

SpringerWienNewYork

SpringerWienNewYork

CISM COURSES AND LECTURES

The series presents lecture notes, monographs, edited works and proceedings in the field of Mechanics, Engineering, Computer Science and Applied Mathematics.
Purpose of the series is to make known in the international scientific and technical community results obtained in some of the activities organized by CISM, the International Centre for Mechanical Sciences.

INTERNATIONAL CENTRE FOR MECHANICAL SCIENCES

COURSES AND LECTURES - No. 524

ROMANSY 18
ROBOT DESIGN, DYNAMICS AND CONTROL

PROCEEDINGS OF THE EIGHTEENTH
CISM-IFToMM SYMPOSIUM

EDITED BY

VINCENZO PARENTI CASTELLI
UNIVERSITY OF BOLOGNA, ITALY

WERNER SCHIEHLEN
UNIVERSITY OF STUTTGART, GERMANY

SpringerWienNewYork

This volume contains 291 illustrations

Printed in Italy
SPIN 80016144

All contributions have been typeset by the authors.

ISBN 978-3-7091-0276-3 SpringerWienNewYork

PREFACE

The First CISM-IFToMM Symposium on Theory and Practice of Robots and Manipulators was held on September 5-8, 1973, in Udine, Italy, not long after IFToMM had been founded in 1969. The first ROMANSY, or Ro.Man.Sy., as the Symposium used to be referred to, marks the beginning of a long-lasting partnership between two international institutions, CISM, the Centre International des Sciences Mécaniques and IFToMM, the International Federation for the Promotion of Mechanism and Machine Science.

As the 18th Symposium returned to Udine, Ro.Man.Sy 2010 continued to preserve this tradition, by encouraging papers that are of a broad interest to the participants and by providing an environment and setting for meaningful technical and personal interactions among the delegates. In particular, the conference solicited papers providing a vision of the evolution of the robotics disciplines and indicating new directions in which these disciplines are foreseen to develop. Paper topics include, but are not limited to:

1. *robot design and robot modules/components;*
2. *service, education, medical, space, welfare and rescue robots;*
3. *humanoid robots, bio-robotics, multi-robot, embodied multi-agent systems;*
4. *challenges in control, modeling, kinematical and dynamical analysis of robotic systems;*
5. *innovations in sensor systems for robots and perception;*
6. *recent advances in robotics.*

The 18th ROMANSY took place July 5-8, 2010 in Udine, Italy and was enriched with three keynote lectures presented by Makoto Kaneko from Japan, Jorge Angeles from Canada and Andres Kecskeméthy from Germany, who discussed new trends in applications and methodology. During the conference banquet a ceremony was arranged for the two recipients of the IFToMM Award of Merit 2010, Alberto Rovetta from Italy and Atsuo Takanishi from Japan, with a speech about IFToMM honors and awards, the presentation of each recipient by their nominators, the delivery of IFToMM honors and awards to recipients, and a short speech by each recipient.

The following scientists served on the Steering Committee of Ro.Man.Sy. 2010:

- *P. Bidaud (Laboratoire de Robotique de Paris, France)*
- *M. Ceccarelli (University of Cassino, Italy)*
- *I-Ming Chen (Chair of TC Robotics, Nanyang Technological University, Singapore)*
- *B. Heimann (Leibniz Universität Hannover, Germany)*
- *O. Khatib (Stanford University, USA)*
- *E. Martin (Canadian Space Agency, Canada)*
- *W. Schiehlen (CISM Representative, University of Stuttgart, Germany)*
- *A. Takanishi (Waseda University, Japan)*
- *T. Zielinska (Warsaw University of Technology, Poland)*

The Steering Committee reviewed together with the Symposium Co-Chairmen the 62 submitted papers and accepted 54 contributed papers from 19 countries. In this volume three keynote papers and the contributed papers are published after some revision.

The participants enjoyed the stimulating environment at CISM and the great service of the CISM staff. In particular, Mrs. Paola Agnola did an excellent job starting already in 2007 with the proposal for hosting Ro.Man.Sy. 2010, and continuing with the service for the co-chairmen and all the participants up to the closing of the Symposium. Thanks are also due to the printing office of CISM and Springer-Verlag Vienna for the efficient cooperation in publishing this proceedings volume.

Vincenzo Parenti Castelli, University of Bologna
Werner Schiehlen, University of Stuttgart

CONTENTS

CHAPTER III

Humanoid Robots, Bio-Robotics, Multi-Robot, Multi-Agent Systems

CHAPTER IV

Control, Modelling and Analysis of Robotic Systems

CHAPTER V

Innovations in Sensor Systems for Robots and Perception

CHAPTER VI

Recent Advances in Robotics

Keynote Lectures

Where Future Robots should Go and should not Go

Makoto Kaneko* and Mitsuru Higashimori*

* Department of Mechanical Engineering, Graduate School of Engineering, Osaka University, Japan

Abstract Where future robots should go and should not go and what is an adequate style of collaboration between human and robots? These questions are really interesting for discussing the future direction of robot, especially from the design point of view. While it is really hard to find a general answer for these questions, we try to provide our answers, particularly focusing on manipulation area, by reviewing our former works and exploring a success example of robot business. Our eventual message is that we should cut the function of "manipulation of object within hand" as an end-effector and focus on a hand with single purpose rather than universal hand.

1 Introduction

While many industrial robots are working in factories, robot businesses in other fields except industrial area are not so popular. In research level, a number of robots have been designed and developed in various fields so far all over the world. However, most of them have been fade away or will be so in the future. It is really hard either to send robots to a market or to keep continuously selling robots in market. People are easily tired in playing and enjoying with robots if they are toys or entertainment robots. In order to keep selling or increasing market continuously, there is a necessary condition where the robot is definitely necessary for human or human receives a serious damage without the robot. Of course, there is a category of weaker level, such as "convenient" instead of "definitely necessary". Home robots are categorized into the level of "convenient". As for home robots, people are expecting them to work outside of house as well as inside of house, instead of human. In this case, house wives will make decision whether they should buy or not, by considering the balance between the investment and the acquired convenience. At this point, we have to be careful for the reliability

(a) (b)

Figure 1. Juggling and manipulating a pencil.

of home robot, while this issue is not taken into consideration seriously. Suppose a home robot with the success rate of 99%. This success rate is quite high in research level. Now, suppose that a family with four members is taking meals for breakfast, lunch and dinner, and they utilize three dishes for each meal. As a result, the family utilizes 36 dishes per day. If the home robot with the success rate of 99% is supposed to make clean dishes after each meal, it will break one dish every three days. House wives will never buy such a robot. Even human are dropping a glass perhaps once a year. In order to keep reliability as human do, we have to design a home robot with the success rate of 99.99%, while it seems to be very hard for current robots to keep such a high reliability. We believe that this is a hurdle for home robots to clear.

On the other hand, if a robot is categorized into "definitely necessary", people will buy it, even though the price of robots is so expensive. This case does not happen for home robots but may happen for medical robots where human will either get a serious damage or eventually die without an assistance of such a robot. The robot which is definitely necessary will be never fade away, as X-ray based examination will be never in medical area. At the same time, such a robot includes essential functions while other robots do not. By exploring such functions, we can figure out a future robot to be definitely necessary and a robot design to avoid failure in practical application. This paper first discusses what is the special skill for human and what is the special one for robots. Also, how human and

robots are essentially different from each other? To discuss these issues, we have to know the current state-of-the-art of robot technology from the viewpoint of manipulation. We particularly pick up both dexterity and speed in manipulation based on our former works, M. Kaneko and Tsuji (1997, 2000a); M. Higashimori and Kaneko (2005a,b); M. Kaneko and Tsuji (2000b); M. Kaneko and Ishikawa (2003); M. Higashimori and Ishikawa (2005); M. Higashimori and Kaneko (2007, 2009c,a,b). By comparing these functions for human and robot, we show that human are good at dexterous manipulation, while robots are not. On the other hand, robots are good at speed, power, repeatability, accuracy, and so forth, while human are not in relative sense. Through these reviews, we discuss how we should collaborate with robots, and what skill we should expect and not expect for robots. As a successful example, we introduce a medical robot, da-Vinci developed by Intuitive Surgical Ltd. This company is doing a really good business recently from the viewpoint of stock market, which means that the robot should include something important function. What functions do they include and cut intentionally? Through exploring these questions, we eventually reach answers that we are looking for.

This paper is organized as follows; In Section 2, we consider special skills for both human and robot. Based on this consideration, we propose a collaboration style between human and robot in Section 3. In Section 4, we introduce an example of robot with success story. By analyzing the key function of this robot, we show a direction of future robots in Section V before concluding remarks in Section 5.

2 The Special Skill for Human and Robot

Two examples of highly skillful manipulation done by human are shown in Fig. 1, where (a) and (b) are juggling and manipulation of a pencil by hands, respectively. Perhaps, each person should have practiced for many years to get the skill. Through learning process, human have the potential capability for increasing manipulation skill gradually. There are three key parts to support human dexterity. The first part is finger tip where there are a numerous number of tactile sensing organs Bolanowski and Verrillo (1982); Bolanowski and Zwislocki (1984); Verrillo (1962). While there are four tactile receptors, such as Ruffini ending, Merkel cell, Meissner corpuscle, and Pacinian corpuscle in finger tip, it is well known that each mechanoreceptor is activated with different frequency and contributes to enhancing the touch sensitivity depending upon frequency. For example, Ruffini and Merkel are responsible for low frequency, such as less than 10 [Hz]. Meissner corpuscle and Pacinian corpuscle are responsible for the frequency between 10

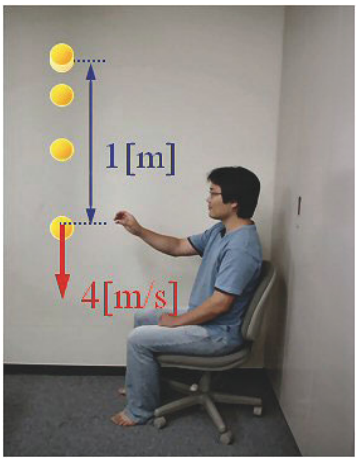

Figure 2. Catching a ball.

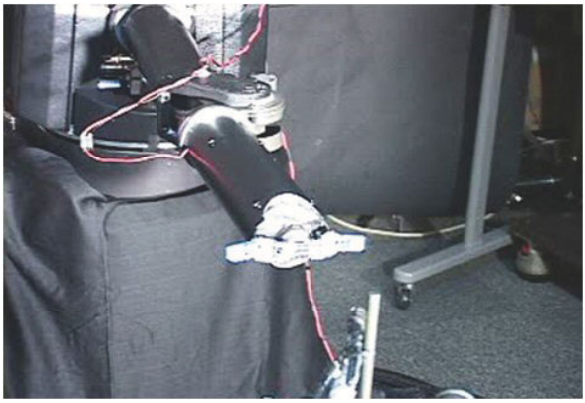

Figure 3. The 100G capturing robot.

through 50 [Hz] and more than 50 [Hz], respectively. They can detect not only pressure but also velocity and acceleration. We believe that these receptors are greatly support the dexterity of manipulation by human. The second part is our powerful brain having the function of learning and keeping data based on experience. Based on the information coming from fingertip tactile organs and on data base, our brain sends a command message to muscle quickly. The third part is our flexible and powerful muscle. The

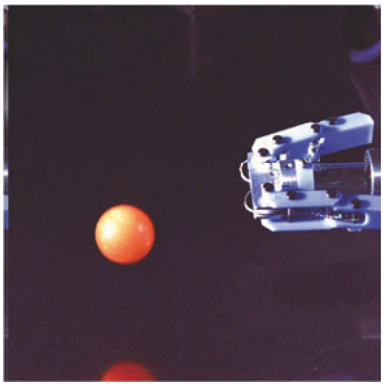

Figure 4. A few mmseconds before the hand captures a ball.

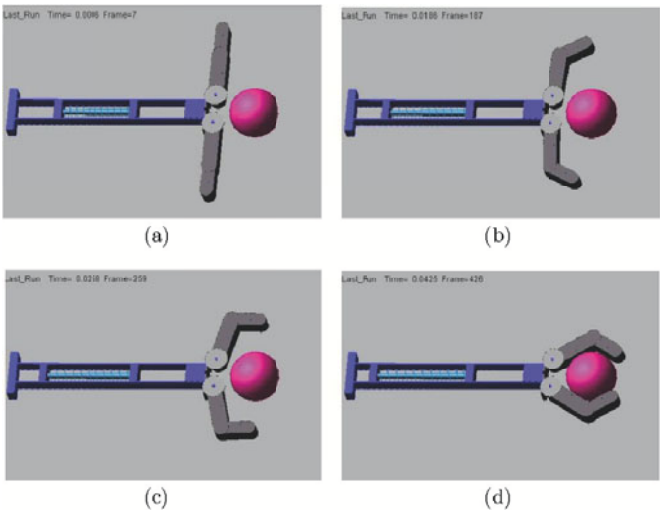

Figure 5. Simulation results for capturing an object.

muscles actuating each finger joint are distributed around the fore arm and produce the grasping force with more than 50 [kg]. Compliance is an essential key word for supporting dexterous manipulation. Furthermore, we should not forget that each finger tip has two compliance components; one is passive compliance coming from skin inherent compliance, where we can not change intentionally and the other is active compliance coming from

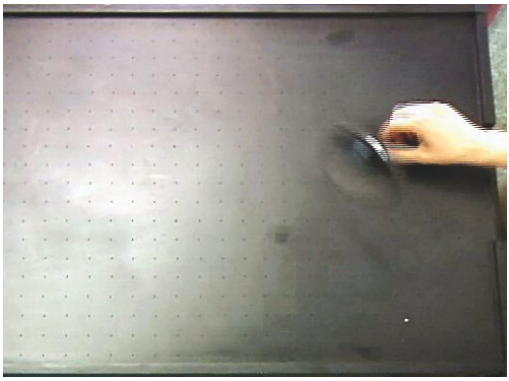

Figure 6. A subject is capturing a moving object.

muscle, by which we can control finger tip compliance intentionally. On the other hand, now let us observe the dexterous motion done by robots. We would note that while there have been a number of multifingered robot hands developed so far M. Kaneko and Tsuji (1997)–M. Kaneko and Tsuji (2000), the dexterity of robots is too behind that of human. Even with DLR hands DLR; workshop, which is probably one of the most sophisticated robot hands in the world, they are not as dexterous as human hand. The main reason why the dexterity of robot hands is so behind of human perhaps comes from their hard mechanism, lumped actuators, and sensors with low resolutions. While manipulation theories have been very much advanced with beautiful mathematics K. Harada and Tsuji (2000); M. Svinin and Tsuji (1999), the advancement of hardware has been too behind them. Successful hands are limited to uni-purpose ones, such as grippers which are familiar as an end-effector often utilized in industry.

While robots are too behind human in terms of dexterity, they have various fields where robots exceed human capability, such as speed, power, accuracy and so forth. We have done a couple of experiments for examining whether human can generate the motion for an object moving with a high speed. Fig. 2 is the first example where a subject is catching a ball dropped from 1 [m] height In this experiment, we ask a subject not to look up the object but to look forward naturally. We further ask the subject to take a catching action when the ball is within his viewing area in natural posture. For this experiment, no one could not catch the ball successfully, even through the ball passes through just the center of hand being in ready for catching. It takes 0.2 through 0.4 [sec] until finger motions start, while

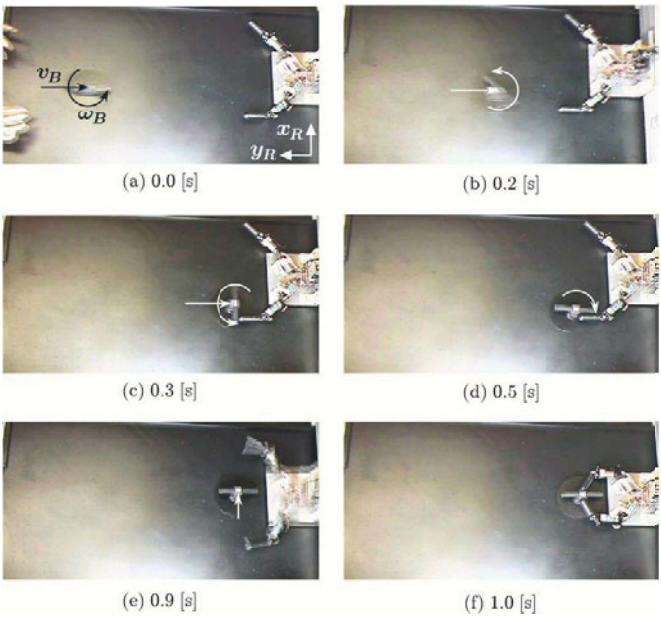

Figure 7. Two-fingered hand captures an object by 2-step strategy.

the speed of object results in roughly 4 [m/s] when the ball reaches at the position of hand. This means that the ball moves 80 though 160 [cm] at the capturing point. Therefore, it is essentially impossible for human to capture the ball without feed-forward action. To challenge this test by robot, we developed the 100G capturing robot M. Kaneko and Ishikawa (2003); M. Higashimori and Ishikawa (2005) where G denotes the gravitational acceleration. Fig. 3 shows the experimental result where the robot is successfully capturing a ball with an assistance of a high speed vision system developed by Ishikawa and Ishii T. Komuro and Yoshida (2003); Ishii and Ishikawa (1999); Numata and Tajima (2004); K. Tajima and Ishii (2004). Fig. 4 shows a snap shot where the scene is just a few milliseconds before catching a ball by the hand with one degree of freedom and Fig. 5 shows simulation results where the 100G robot hand is capturing an object. As far as the motion speed is concerned, the 100G robot has exceeded human capability. Due to this high acceleration, human can not see what is actually happening during mechanical adjustment. Due to this high speed, we can not adjust for the best wiring without an assistance of high speed camera. Fig. 6 shows another experiment where a subject is catching an object with

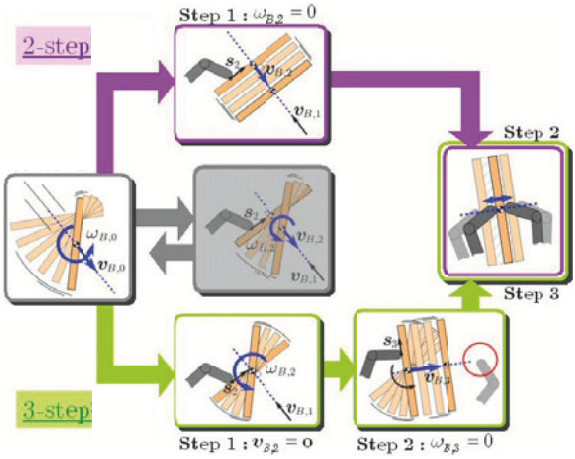

Figure 8. 2-step and 3-step strategies.

both rotational and translational velocities, where the object is moving on an air hockey table whose friction is drastically reduced by air flow. Since the recognition speed of human eye is roughly 15 [frames/sec], the subject can not clearly see the capturing point by his naked eye. To challenge this experiment by robot, we developed the two-fingered robot hand equipped with a high speed actuator for each joint. Under the assumption that both collision and friction coefficients are known in advance, this robot can completely stop either the rotational or translational motion of object at the initial collision with an assistance of a high speed vision, where the vision is always chasing the object and sending both position and orientation of object to the robot controller. We also showed that this robot can capture an object successfully after one or two collisions as shown in Fig. 7, while human can not do M. Higashimori and Kaneko (2007). For example, in two-step capturing strategy, the object results in a translational motion with constant posture to be easily captured by the robot as shown in Fig. 8 where three-step capturing strategy is illustrated as well. In this sense, this robot also exceeds human capability. Fig. 9 shows a further example, where a pizza master is manipulating a pizza dexterously by utilizing a tool composed of just a simple plate and a rod. An interesting observation is that he can manipulate a pizza rotationally as well as translation ally, by utilizing both friction and acceleration forces with a proper combination. By getting a hint from this observation, we figure out a robot system as shown in Fig. 10 where a humanoid robot is manipulating a plate, just like

Figure 9. Manipulating a pizza by a master.

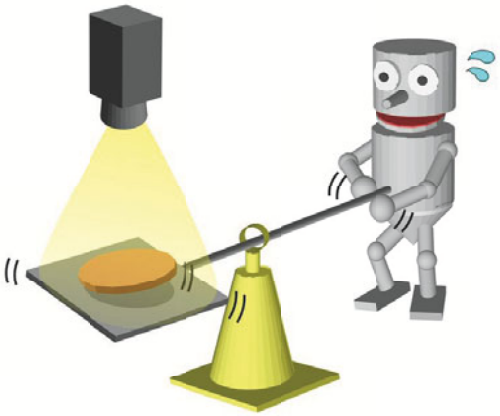

Figure 10. An example of pizza manipulation robot.

a pizza master. However, this approach will not work well, since a dexterity which is not good at for robots is requested. To cope with this issue, we have developed a robot with two-degrees of freedom M. Higashimori and Kaneko (2009c) instead of a humanoid robot. By combining a high speed vision, we have achieved various experiments, such as rotational as well as translational motions of object on the table. Also, we have done manipulation of the object from the starting point to the goal setting on the table. This

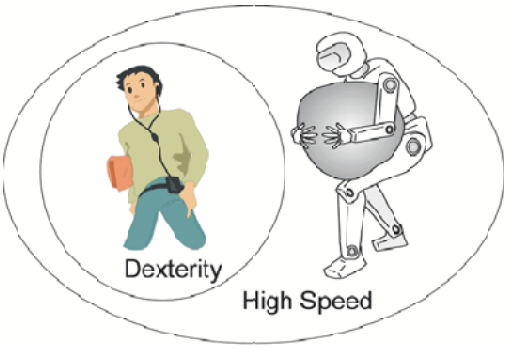

Figure 11. A possible style of collaboration between a robot and human.

robot can achieve the manipulation task less than just 10 [sec], while human can not do it even with more than 1 [min]. In such a scene, this robot also exceeds human capability. In our recent work M. Higashimori and Kaneko (2009a,b), we have shown that the pizza robot can rotate a compliant object just like a pizza before cooking even faster than a rigid one. These three examples suggest that by combining both high speed actuators and a high speed vision system, as far as speed is concerned, robots have already exceeded human capability. Therefore, we are now in a state where robots are too much behind human in dexterity and advanced more than human in speed. In collaboration between robots and human, we should consider this fact.

3 A Collaboration Style between Robots and Human

Many researchers have shown a collaboration style where both human and a robot achieve an equal task. This is based on the idea that we expect an equal skill for both human and robots, which is a big mistake at the starting point. As explained in the previous section, there are different special skills for human and robots, respectively. Human is good at dexterity whose skill is even more than the current robots. On the other hand, robots are good at a simple task with high speed. As for a collaboration style between robots and human, we should take these special skills into consideration. Fig. 11 explains a possible collaboration style where we expect dexterous motions for human and high speed simple motion for robots, respectively. We believe that this is a reasonable collaboration style between them. Now, let us consider an example of this style. Suppose that a medical doctor is

operating a patient under minimum invasive surgery. He should be good at in dexterity by his long term training. On the other hand, however, human have a limitation of recognition speed of human eye. It is well known that the limitation is roughly 30 [ms] in the maximum. This limitation can not been overcome by practice, while your skill for dexterity gradually increases by continuous practice and learning. Now, suppose that a medical doctor cut a blood pipe just by accident. At the next moment, the blood will spread over the area where he is looking. Since this happens very quickly, his eye can not follow and eventually lose where the accident part is. Here, we suppose that the medical system is equipped with a robot with high speed vision and always watching the motion area of forceps. At the moment he cut a blood pipe, the robot takes action for stopping the flow of blood based on the information of the high speed vision. This is a good style for the collaboration, in a sense that the robot is compensating for the function where human is lacking.

4 A Success Example in Robot Business

While an entertainment can be one of business fields of robotics, it is fade away quickly when people are tired with the robot. Robot history has proved that this is true. Is there any success example in robot business except industrial robots? While there have been a number of robots designed and developed so far, we do not know many examples where the company is doing a good business continuously through robot. da Vinci developed by Intuitive Surgical Co. Ltd. Vinci (a,b) is probably one of very rare examples where the company is doing a really good business as far as we check the increase of the price of stock during the last five years. While the price is $2.5 million/robot, they have sold out more than 1500 robots all over the world. Why this robot is so popular? Why hospitals are buying this robot? Through exploring these questions, we try to find the answer for the question given in the title of paper. I believe that da Vinci will be never fade away, because this robot is so useful for human. For example, more than 70% operation of prostate cancer in US are currently done by this robot. The operation of prosthetic cancer needs dexterous manipulating motion behind the bundle of nerve system. So far, it has been really hard for a surgeon to insert a forceps manually and cut a tumor without giving any damage to the bundle of nerve system around the cancer area. With the reacheability to the back side of the bundle of nerve system, da Vince successfully showed its unique function all over the world. Now, let us discuss the design policy of da Vinci. Fig. 12 shows an overview of da Vinci system where a surgeon remotely controls the robot based on the visual

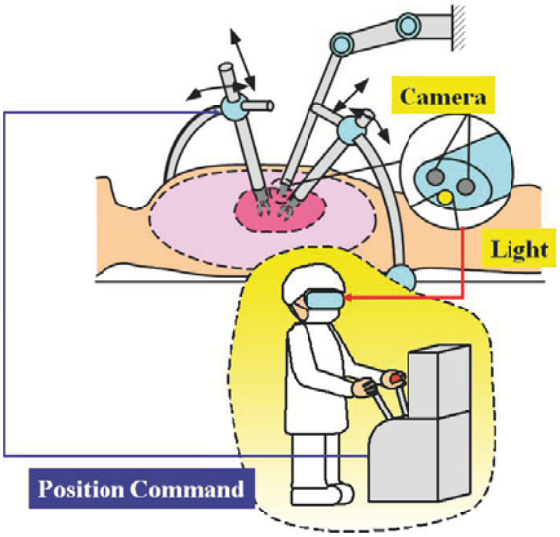

Figure 12. An example of medical robot system.

information obtained through 3D stereo image. Fig. 13 shows two possible end-effectors available for medical robots, where (a) and (b) are a gripper type hand and a multi-jointed hand, respectively. The biggest attractive function for multi-jointed hand is the potential capability of manipulation of object within the hand, while this function has never been practically utilized in either industry or medical field. In manipulation of object within a hand, robots are too behind human, as discussed in Section II. The designers in Intuitive Surgical cut this function from da Vinci and adopted a simple gripper type hand, as shown in Fig. 13(a). Nevertheless, it looks that da Vinci is achieving dexterous and skilful manipulation by using two arms. The key is that each gripper simply grasps the object, such as a needle, a thread, or internal organ, and a surgeon produces a gripper level coordination control through a master arm. The dexterous motions are, therefore, produced by the degrees of freedom of arm instead of finger. Once again, we should note that the dexterity of da Vinci is not produced by the finger motions but by the arm motions, together with master motion produced remotely by the surgeon. As far as we carefully examine da Vinci, their approach is quite naturally accepted in terms of the collaboration between human and robot. Also, we would completely agree with their decision for cutting the function of multi-jointed finger.

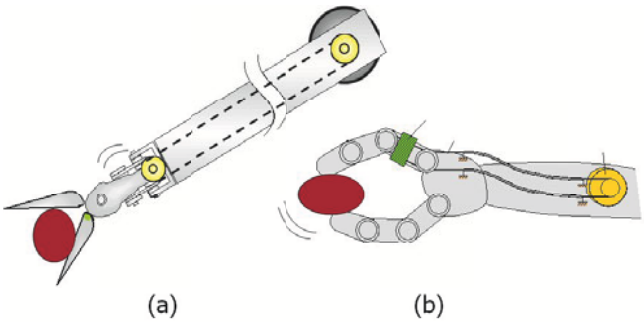

Figure 13. Two types of hand for medical application.

5 Where Future Robots should Go and should not Go

da Vinci is sending us a couple of important messages on future direction of robot. While so many innovative mechanisms are, of course, implemented into the robot, such as a wire driven gripper, an easily detachable hand according to wire damage during operation, and so forth, we believe that one of the best decision in design is to cut the choice of multi-jointed fingers and to produce dexterous motions by multiple arm coordination control by surgeons. The success of da Vince implicitly sends us a message that for robot design, we should not include a function of manipulation of object within the hand by utilizing multi-jointed robotic fingers, if we try to keep a high success rate in practical use, such as medical and even for industrial applications. Also, da Vince eventually succeeded in finding the task where only this robot can successfully remove a tissue of prostate cancer without giving any damage to human body.

6 Concluding Remarks

We have discussed the direction of future robots from the viewpoints of manipulation. Human hand is a universal tool for manipulating a knife, a spoon, a folk, a pencil, and many others. With this similarity, people are expecting that multifingered robotic hands will be available as a universal end-effector for future robots. But it is actually too difficult to design and develop a multifingered robot hand available with a reasonable reliability in a practical environment. We explained the difficulty of dexterous manipulation by comparing the difference between robots and human. Especially, the difficulty of manipulation of object within the hand comes from that

we are allowed to use a set of pushing forces only. The smooth and quick motion of object is also blocked by many physics, such as, slipping, rolling, and instability due to a large pushing force on object. The success story of da Vinci is sending a message toward a practical solution. Instead of designing a complicated hand system, we should design a hand as simple as possible. We believe that it is important to rearrange the manufacturing line, so that a single purpose hand may work in it with firm reliability.

Imitating living things is a well known approach for designing a robot. But we have to be careful that both artificial machines and living things are far different from each other, in terms of actuator, sensor, and even mechanism. Human fingers have continuously evolved through the process in using various tools for long long periods since making appearance, and eventually became a universal one. We should not expect such a universal hand for an artificial one. Over 30 years have passed already since many projects on multi-fingered robotic hand have been launched. At least, the research results on multifingered robotic hands so far have supported our messages without any counterexample. We are now in a state where we should send many robots working in various environments. In concluding, we would note once again that we should not devote our power in designing a human finger-like universal hand for a future robot hand, if we would see a robot system capable of working practically. We are more than happy if this article is helpful for researchers wishing to design a hand in the future.

Finally, this work is partially supported by NSF-JST joint research program on Contact Interface Modeling and Stiffness-based Biomedical Diagnosis with Sensing Technology Towards a Better Quality of Life.

Bibliography

S.J. Bolanowski and R.T. Verrillo. Temperature and criterion effects in a somatosensory subsystem: A neurophysiological and psychophysical study. In *Journal of Neurophysiology*, volume 48, pages 836–855, 1982.

S.J. Bolanowski and J.J. Zwislocki. Intensity and frequency characteristics of pacinian corpuscles. i. action potentials. In *Journal of Neurophysiology*, volume 51, pages 793–811, 1984.

DLR. http://www.dlr.de/rm/en/desktopdefault.aspx/tabid-3802/.

I. Ishii and M. Ishikawa. High speed target tracking algorithm for 1 ms visual feedback system. In *J. Robotics Soc. Japan 17*, pages 39–45, 1999.

M. Kaneko K. Harada and T. Tsuji. Rolling based manipulation for multiple object. In *IEEE Transactions on Robotics and Automation*, volume 16, pages 457–468, 2000.

A. Numata K. Tajima and I. Ishii. Development of a high-resolution, high-speed vision system using cmos image sensor technology enhanced by

intelligent pixel selection technique. In *Optics East 2004*, volume 5603, pages 215–224, 2004.

A. Namiki M. Higashimori, M. Kaneko and M. Ishikawa. Design of the 100g capturing robot based on dynamic preshaping. In *The International Journal of Robotics Research*, volume 24, pages 743–753, 2005.

I. Ishii M. Higashimori, M. Kimura and M. Kaneko. Dynamic capturing strategy for a 2-d stick-shaped object based on friction independent collision. In *IEEE Transactions on Robotics*, volume 23, pages 541–552, 2007.

Y. Omoto M. Higashimori and M. Kaneko. Non-grasp manipulation of deformable object by using pizza handling mechanism. In *Proc. of the IEEE Int. Conf. on Robotics and Automation*, pages 120–125, 2009a.

Y. Omoto M. Higashimori and M. Kaneko. Experimental approach on deformable object manipulation inspired by the handling of a pizza peel. In *Proc. of 9th Int. IFAC Symp. on Robot Control*, pages 511–516, 2009b.

Y. Omoto M. Higashimori, K. Utsumi and M. Kaneko. Dynamic manipulation inspired by the handling of a pizza peel. In *IEEE Transactions on Robotics*, volume 25, pages 829–838, 2009c.

N. Thaiprasert M. Kaneko and T. Tsuji. Experimental approach on enveloping grasp for column objects. In *5th International Symposium on Experimental Robotics*, pages 17–27, 1997.

R. Takenaka A. Namiki M. Kaneko, M. Higashimori and M. Ishikawa. The 100g capturing robot –too fast to see–. In *IEEE/ASME Trans. on Mechatronics*, volume 8, pages 37–44, 2003.

T. Shirai M. Kaneko and T. Tsuji. Scale-dependent grasp. In *IEEE Transactions on Systems, Man, and Cybernetics-Part B: Cybernetics*, volume 30, pages 806–816, 2000.

M. Kaneko M. Svinin and T. Tsuji. Internal forces and stability in multifinger grasps. In *IFAC Journal Control Engineering Practice*, volume 7, pages 413–422, 1999.

A. Numata and K. Tajima. Development of a mega-pixel and millisecond vision system using intelligent pixel selection. In *TExCRA2004*, pages 9–10, 2004.

M. Ishikawa T. Komuro, I. Ishii and A. Yoshida. A digital vision chip specialized for high-speed target tracking. In *IEEE Trans. Electron. Devices 50*, pages 191–199, 2003.

R.T. Verrillo. Investigation of some parameters of the cutaneous threshold for vibration. In *The Journal of the Acoustical Society of America*, volume 34, pages 1768–1773, 1962.

Da Vinci. http://www.youtube.com/watch?v=jsc1lbkwrdy. a.

Da Vinci. http://jp.redkaraoke.com/songs/no-future-in-the-past/116466/video. b.

workshop. http://www.laas.fr/ifipwg/workshops&meetings/49/workshop/13 albu-schaeffer.pdf.

Robust Drives for Parallel Robots

Jorge Angeles
Department of Mechanical Engineering, McGill University, Montreal, Canada
angeles@cim.mcgill.ca

Abstract Parallel robots are known to offer light, highly agile structures, particularly suited for assembly and machining tasks. By the same token, parallel robots pose unique challenges to the robot designer, in that a compromise must be found among the various requirements: large workspace with respect to footprint; high stiffness; high natural frequencies; high mobility; and low cost, among others. Most parallel robots are designed with as many limbs as degrees of freedom (dof), which increases their footprint and limits their dextrous workspace—that region of the workspace where the moving platform can undergo a full rotation. An alternative to these designs is a reduced number of limbs, lower than their dof, but this calls for limbs driven by two or more motors. The challenge here is to drive two axes in a serial array with two motors mounted on the base platform. This mode of driving has not received due attention from the robot-design community, but is worth exploring. Proposed in this paper is a *quasispherical* linkage intended to drive the tilt axis of one of the two limbs of a four-dof parallel robot, currently under development. The linkage is termed quasispherical in that it is nominally designed as a spherical four-bar linkage, but spherical linkages impose extremely tight tolerances to make them assemblable. A common alternative to tight tolerances is an increase in the degree of freedom of the linkage, upon replacing the passive revolutes by orientable pinned-joints, which are kinematically equivalent to spherical joints, thereby increasing unnecessarily the mobility of the linkage. This compromises the linkage stiffness, a major concern for effective actuation. As an alternative, a linkage of the RCCC type is proposed here, where R and C stand for revolute and cylindrical joints. However, cylindrical joints are not that common as machine elements, besides being demanding in terms of tolerances, while offering low stiffness. A realization of the C joint is proposed here by means of a serial array of a R and a screw joint, labeled H.

1 Introduction

SCARA (Selective-compliance Assembly Robot Arm) systems were developed in the eighties with the purpose of providing the manufacturing industry with agile robots capable of fast pick-and-place operations of flat workpieces, as those appearing in the consumer electronics industry (Makino and Furuya, 1980). In the late nineties, these robots had reached their physical limits, with cycle times reported by Adept Technology Inc. of 50 ms for an industry-adopted test cycle (Gauthier et al., 2008). Higher speeds would be possible only with larger motors, but these would impose correspondingly higher loads on their downstream counterparts. The obvious alternative was parallel SCARA systems. This is how several parallel architectures for the production of motions proper of SCARA were developed—e.g., (Company et al., 2001; Angeles and Morozov, 2006). Company et al.'s patent is currently marketed by Adept Technology Inc. under the trademark *Quattro*. This robot entails four limbs, each driven by one base-mounted direct-drive motor, the design challenge being how to allow the moving platform (MP) to undergo rotations about a vertical axis of at least 180°, as required by the manufacturing industry. The solution proposed by the designers of Quattro entails an ingenious mechanism composed of linkages and gears that does the job, at the expense of a large number of moving parts. The robot architectures patented by Angeles and Morozov (2006), termed *Schönflies Motion Generators* (SMGs), entail either four or two limbs. The McGill SMG motivating the work reported here is an instance of the latter, with two limbs, each driven by two identical motors mounted on the base platform (Morozov and Angeles, 2007).

A design challenge posed by the McGill SMG lies in the need to drive two axes in a serial array by means of two motors mounted on the same base platform. Of these two axes, one is vertical, producing the *pan motion* of the plate carrying the upper parallelogram of each limb, the other horizontal, producing the *tilt* motion of the parallelogram itself. The drive of each limb comprises a planetary gear train, as depicted in Fig. 1, whose sun and ring gears are driven by means of two identical motors, at angular velocities ω_S and ω_R, respectively. The output angular velocities of the train are the angular velocities of the planets and the planet-carrier, the latter being the pan angular velocity of the drive. The tilt angular velocity is to be taken from the *relative* (vertical) angular velocities of the planets with respect to their carrier, and hence, a conversion from an angular velocity about a vertical axis to one about a horizontal axis, preferably with a ratio of 1:1, is required. This design problem is the motivation behind the linkage proposed here. However, this problem arises also in the driving of a six-

dof parallel robot designed with three limbs, as opposed to six, which is the common design known as Stewart-Gough platform (Merlet, 2006). In a three-limb design, each limb has to be driven with a two-dof actuator, its two motors preferably a) mounted on the base platform and b) subject to identical loads. An obvious mode of driving in this case is also a pan-tilt mechanism, similar to that introduced here.

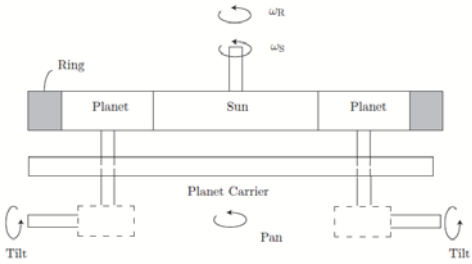

Figure 1. The two-dof limb-drive of the McGill SMG: a planetary gear train

The paper focuses on the synthesis of the transmission from planet axes to tilt axis, which is henceforth termed the *tilt-generator*.

2 Alternative Designs of the Tilt Generator

Four alternative design solutions were considered for the tilt-generator: 1) a bevel-gear train with input and output axes at right angles; 2) a double universal joint; 3) a five-link mechanism; and 4) a spherical four-bar linkage.

Alternative 1 appeared attractive because of the readily available, off-the-shelf, *right-angle gearboxes* (RAG) and their low cost. The McGill SMG prototype was built with these transmissions. As the planetary train of each drive unit comprises two planets, two RAG were installed per drive, which would distribute uniformly the load on all connected elements. Backlash in the bevel gears was expected to be reduced by the presence of actuation redundancy. As it turned out, however, after assembly, the RAG backlash was still too high, of about 4°. This backlash led to large vertical displacements of the MP, of about 300 mm, with all four motors blocked. An in-depth study was then conducted to find the best alternative out of the remaining three in the above list.

Work currently underway by the same design team[1] on the development

[1]The team in charge of developing the McGill SMG

of a theoretical framework for engineering design at the conceptual stage—i.e., in the absence of a parametric mathematical model—was applied to select the best design alternative. The framework is based on the concept of *complexity* (Khan et al., 2007; Caro et al., 2010). A complexity analysis of the three alternatives of interest, in fact, called for a revision of the paradigm proposed by Khan et al. in 2007. The details of the complexity evaluation of the three alternatives are available in (Khan and Angeles, 2010). The result was that, while the spherical four-bar linkage is unable to produce *exactly* a 1:1 constant velocity ratio between input and output axes, it is the simplest solution from a kinematic viewpoint. The ripple in the velocity ratio can be readily taken into account by means of kinematic control, which calls for the online inversion of a posture-dependent 2×2 Jacobian matrix mapping the two-dimensional array of input velocities—ω_S, ω_R—into its counterpart array of output velocities—ω_{pan}, ω_{tilt}

3 The Tilt-generating Spherical Linkage

A spherical four-bar linkage, with input and output axes at right angles, is depicted in Fig. 2, to illustrate the notation used in the paper. An *approximate function-generation* synthesis approach was adopted (Liu and Angeles, 1992), with m prescribed pairs of input-output angles, to determine the unknown linkage dimensions α_2, α_3 and α_4 of Fig. 2, as $\alpha_1 = 90^\circ$ is given from the layout of the input and output axes. Moreover, given the *symmetry of the functional requirement*, a *symmetric linkage* was assumed at the outset, with $\alpha_4 = \alpha_2$. The problem was then formulated using a set of dimensionless linkage parameters $k_1, \ldots, k_4$ similar to those proposed by Freudenstein (1955) for planar linkages, namely,

$$k_1 \equiv \frac{\lambda_1\lambda_2\lambda_4 - \lambda_3}{\mu_2\mu_4},\ k_2 = \frac{\lambda_4\mu_1}{\mu_4},\ k_3 = \lambda_1,\ k_4 = \frac{\lambda_2\mu_1}{\mu_2} \equiv \frac{\lambda_4\mu_1}{\mu_4} = k_2 \qquad (1)$$

where $\lambda_i \equiv \cos\alpha_i$, $\mu_i \equiv \sin\alpha_i$. With this formulation, the synthesis problem leads to an overdetermined system of $m > 4$ linear equations in the four parameters k_i, derived from the input-output function

$$F(\psi, \phi) \equiv k_1 + k_2\cos\psi + k_3\cos\psi\cos\phi - k_4\cos\phi + \sin\psi\sin\phi = 0 \qquad (2)$$

Furthermore, in view of the prescribed value of α_1 and the symmetry assumption, $k_3 = 0$ and $k_4 = k_2$, the number of unknowns thus reducing to only two, k_1 and k_2. Additionally, the zeros of the input and output dials were assumed to be placed at undetermined values of α and β, respectively.

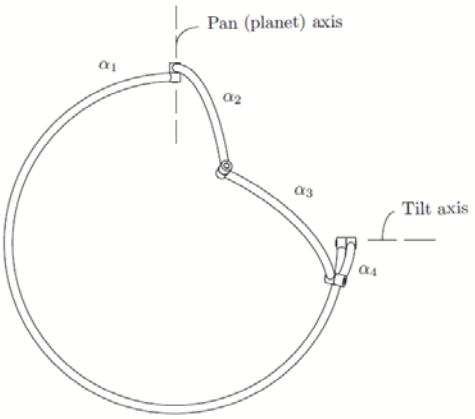

Figure 2. A spherical four-bar linkage with input and output axes at right angles

The m prescribed input-output values were thus defined in intervals $[\alpha - \pi/3,\ \alpha + \pi/3]$ and $[\beta - \pi/3,\ \beta + \pi/3]$, according to the relation

$$\phi = \alpha - \beta + \psi \tag{3}$$

A total of $m = 21$ points, evenly distributed over the given intervals, were defined, which thus led to a system of 21 linear equations in the two unknowns k_1 and k_2, with α and β as parameters. The least-square approximation of the given system of equations, for given values of α and β, was calculated over a grid in the α-β plane. The rms value of the *structural error*[2] (Tinubu and Gupta, 1984) s_{rms} was evaluated over the points of the grid, thereby obtaining a set of discrete values of the function $s_{\text{rms}}(\alpha, \beta)$. The minimum value of this function was obtained by inspection: minimum occurred at $\alpha_{\text{opt}} = 146°$, $\beta_{\text{opt}} = 34°$, which yielded $(s_{\text{rms}})_{\text{min}} = 1.66°$. For our purposes, this value is quite acceptable, as any deviation from the 1:1 ratio between input and output will be taken care of by means of online 2×2 Jacobian inversion. The structural-error distribution is plotted in Fig. 3.

The foregoing optimum values led to a linkage with the parameter values and dimensions recorded in Table 1. Because of space limitations, a rendering of this linkage is not included here. Instead, its quasispherical counterpart is included in Section 5.

[2]The structural error of a linkage is the difference between the output value *generated* by the synthesized linkage and the *prescribed* output value at the same input value.

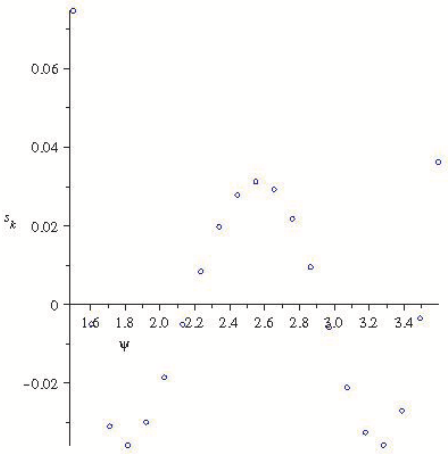

Figure 3. Structural error s_k at kth data point over the prescribed range of motion

i	1	2	3	4
k_i	1.2245	0.90890	0.0000	0.90890
α_i	90.000°	47.731°	132.11°	47.731°

Table 1. Optimum values of linkage parameters and dimensions

One more performance index, besides compliance with the function-generation task, that should be monitored, is the *transmission angle*, which measures the percentage of transmitted torque that goes into actually driving the output joint, vs. the percentage that produces internal wrenches—concurrent force and moment—that put extra load on the bearings and on the link structures (Chiang, 1988). Machine designers recommend to keep this angle between 45° and 135° in planar linkages. For spherical linkages there are no guidelines, but the main idea is to keep the transmission angle close to 90°. As a performance index in this regard, the *transmission defect* δ was proposed (Gosselin and Angeles, 1989), which is defined as the rms value of $\cos\mu$ over the range of motion of the input joint that is of interest for the task at hand. We thus have that the range of values of δ is $0 < \delta < 1$. The optimum linkage reported above has a $\delta = 0.4536$, which is fairly acceptable. This value corresponds to $\mu = 63°$.

4 The Kinematics of the Two-dof Drive

The two-dof drive involves two mechanisms, the epicyclic gear train and the spherical four-bar linkage, its Jacobian, mapping input rates into output rates, thus involving features of the two. If these rates are cast in the two-dimensional arrays $\boldsymbol{\omega}_i$ and $\boldsymbol{\omega}_o$, respectively, then the foregoing relation takes the form

$$\boldsymbol{\omega}_o = \boldsymbol{J}\boldsymbol{\omega}_i \tag{4}$$

where

$$\boldsymbol{\omega}_i = \begin{bmatrix} \omega_R \\ \omega_S \end{bmatrix}, \ \boldsymbol{\omega}_o = \begin{bmatrix} \omega_{\text{pan}} \\ \omega_{\text{tilt}} \end{bmatrix}, \ \boldsymbol{J} = \begin{bmatrix} \dfrac{1}{1+m} & \dfrac{m}{1+m} \\ \dfrac{\nu}{1-m} & \dfrac{-\nu m}{1-m} \end{bmatrix} \tag{5}$$

ν denoting the *input-output velocity ratio* of the four-bar linkage, namely,

$$\nu \equiv \phi'(\psi) = -\frac{\partial F/\partial \psi}{\partial F/\partial \phi} = \frac{k_2 \sin\psi + k_3 \sin\psi\cos\phi - \cos\psi\sin\phi}{-k_3\cos\psi\sin\phi + k_4\sin\phi + \sin\psi\cos\phi} \tag{6}$$

in which the partial derivatives are those of function $F(\psi, \phi)$ introduced in eq.(2). Thus, $\omega_{\text{tilt}} = \dot{\phi}$, while $\dot{\psi} = \omega_P - \omega_C$, with ω_P and ω_C denoting the angular velocities of the planets and the planet-carrier, respectively.

It is apparent from eq.(6) that ν, and hence, $\boldsymbol{J}$, is *posture*-dependent[3], as $\nu = \nu(\psi)$. Hence, the inverse Jacobian, needed for the kinematic control of the parallel robot at hand, cannot be computed off-line. Given the simple form of the Jacobian, however, a closed-form expression for its inverse is possible, namely,

$$\boldsymbol{J}^{-1}(\psi) = \frac{\nu}{1-m}\begin{bmatrix} \dfrac{\nu}{1-m} & \dfrac{m}{1+m} \\ \dfrac{\nu}{1-m} & \dfrac{-\nu m}{1-m} \end{bmatrix} \tag{7}$$

thereby completing the kinematics of the two-dof drive.

5 The Tilt-generating Quasispherical Linkage

The realization of the linkage synthesized in Section 3 is highly demanding in terms of accurate machining and assembly, given that a spherical linkage is an overconstrained mechanical system. Indeed, unless the axes of the four R pairs intersect, the linkage cannot be assembled. Expert designers have

[3] The posture of a mechanical system is the layout, or configuration, adopted by the system when its kinematic pairs undergo relative motion.

coped with this demand by replacing the passive revolute pairs by their *orientable* counterparts, which are kinematically equivalent to S joints. If every S pair is regarded as the serial array of three R pairs of intersecting axes, then the closed chain that originally comprised four joints now has $3 \times 3 + 1 = 10$ R joints. As a single-dof closed kinematic chain needs only seven R pairs to be movable (Hartenberg and Denavit, 1964), the new closed chain has an excess of three joints, which reduces substantially its stiffness. An alternative to this solution is to add the necessary and sufficient number of joints, which can be done by replacing the three passive R pairs by C pairs. If each of the latter is regarded as the serial array of a R and a prismatic (P) pair, then the new closed chain ends up with exactly seven pairs. This solution was implemented verbatim, i.e., with custom-made C pairs as such, in a previous system developed in the same laboratory (Bidault et al., 2001), given that these joints are not readily available in all sizes off-the-shelf. These joints, however, entail a large backlash that mars the system performance.

An alternative realization of the C pair was sought, that would be simpler than that tried above. Using the same complexity analysis mentioned above (Khan and Angeles, 2010), it was found that a HR serial array would yield a C pair with a lower complexity, and hence, we surmise, with a smaller backlash. The result is, then, a seven-joint linkage of the RHRHRHR type, and hence, isostatic. The linkage thus resulting is displayed in Fig. 4. In this figure, it can be appreciated that the four linkage axes are not concurrent at one single point. This makes the drive fault-tolerant, and hence, robust.

Any backlash brought about by this linkage is to be compensated for with redundant actuation: the epicyclic train was designed with three planets, to allow for various alternative driving mechanisms; two of these will be used to drive the same tilt axis of a parallelogram linkage. With this mode of actuation, the load will be evenly distributed between the two planets and on two teeth of the sun and the ring gears, as opposed to only one of each.

6 Conclusions

An innovative fault-tolerant, robust linkage for tilt generation from a vertical shaft was proposed in this paper. The linkage is termed quasispherical because it is designed using a nominal four-bar spherical linkage. The tight tolerances required by spherical linkages, as imposed by the required concurrency of its four axes at one common point, the center of the sphere, are relaxed by replacing the three passive R joints by a RH concatenation. This solution is attractive because all elements needed are readily available as off-the-shelf components, in various sizes and characteristics—from low-cost to

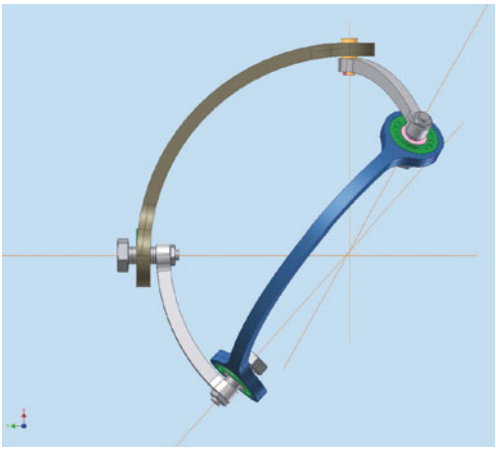

Figure 4. A quasispherical four-bar linkage for tilt-generation with a vertical shaft as input

high-precision.

7 Acknowledgements

The work reported here was supported mainly by Canada's Natural Sciences and Engineering Research Council (NSERC) via an Idea-to-Innovation grant that allowed the production of a first prototype of the McGill SMG, as well as a Discovery Grant and a Design Engineering Chair. The support of McGill University through a James McGill Professorship is dutifully acknowledged, as it allowed the author to lay the foundations of a theoretical framework for engineering design using complexity measures.

Bibliography

Angeles, J. and Morozov, A. (2006). *Four-degree-of-freedom Parallel Manipulator for Producing Schönflies Motions*, Patent No. US 7,127,962, Oct. 31st.

Bidault, F., Teng, C.P. and Angeles, J. (2001). "Structural optimization of a spherical parallel manipulator using a two-level approach," *Proc. ASME 2001 Design Engineering Technical Conferences*, Pittsburgh, PA, Sept. 9–12, CD-ROM DETC 2001/DAC-21030.

Caro, S., Khan, W.A., Pasini, D. and Angeles, J. (2010). The rule-based conceptual design of the architecture of serial Schönflies-motion generators. *Mechanism and Machine Theory*, Vol. 45, No. 2, pp. 251–260.

Chiang, C.H. (1988). *Kinematics of Spherical Mechanisms*, Cambridge University Press, Cambridge.

Company, O., Pierrot, F., Shibukawa, T. and Morita, K. (2001). *Four-Degree-of-Freedom Parallel Robot*, Patent No. EP1084802, March 21st.

Freudenstein, F. (1955). Approximate synthesis of four-bar linkages. *Trans. ASME*, Vol. 77, pp. 853–861.

Gauthier, J.-F., Angeles, J., Nokleby, S. and Morozov, A. (2008). Optimization of a test trajectory for SCARA Systems. In Lenarčič, J. and Wenger, P. (editors), *Advances in Robot Kinematics. Analysis and Design*, Springer, Dordrecht, pp. 225–234.

Gosselin, C. and Angeles, J. (1989). Optimization of planar and spherical function generators as minimum-defect linkages. *Mechanism and Machine Theory*, Vol. 24, No. 4, pp 293–307.

Hartenberg, R.S. and Denavit, J. (1964). *Kinematic Synthesis of Linkages*, McGraw-Hill Book Company, New York.

Khan, W.A., Caro, S., Angeles, J. and Pasini, D. (2007). A formulation of complexity-based rules for the preliminary design stage of robotic architectures. *Proc. Int. Conf. Engineering Design, ICED '07*, Paris, August 28–31.

Khan, W.A. and Angeles, J. (2010). *Novel Paradigm for the Qualitative Synthesis of Simple Kinematic Chains Based on Complexity Measures*, Department of Mechanical Engineering and Centre for Intelligent Machines Technical Report TR-2010-01, McGill University, Montreal. Available at http://www.cim.mcgill.ca/ rmsl/Index/index.htm

Liu, Z. and Angeles, J. (1992). Least-square optimization of planar and spherical four-bar function generators under mobility constraints. *ASME J. Mechanical Design*, Vol. 114, pp. 569–573.

Makino, H. and Furuya, N. (1980). Selective compliance assembly robot arm. *Proc. First Int. Conf. Assembly Automation*, March, Brighton.

Merlet, J.-P. (2006). *Parallel Robots*, Second Edition, Springer, Dordrecht.

Morozov, A. and Angeles, J. (2007). "The mechanical design of a novel Schönflies-motion generator," *Robotics and Computer-Integrated Manufacturing*, Vol. 23, pp. 82–93.

Tinubu, S.O. and Gupta, K.C. (1984). Optimal synthesis of function generators without the branch defect. *ASME, J. Mech., Transmissions, and Auto. in Design*, Vol. 106, pp. 348–354.

Minimal-Form Multibody Dynamics for Embedded Multidisciplinary Applications

KECSKEMÉTHY Andrés
Chair of Mechanics and Robotics, University Duisburg-Essen,
Lotharstraße 1, 47057 Duisburg, Germany
e-mail: andres.kecskemethy@uni-due.de
web page: http://www.uni-due.de/lmr

Abstract Multibody dynamics is a largely explored field in which several successful methodologies and commercial codes coexist. Recently, there is ongoing research in developing efficient, easily embeddable codes that can be used as kernels for multidisciplinary applications. This is triggered by the quest to apply methods developed for robotic systems to systems featuring more complex kinematics. This paper describes two approaches for producing easily embeddable and efficient multibody code based on a minimal-form formulation: an object-oriented approach based on the kinetostatic transmission properties, and a symbolical approach based on regarding kinematical loops as transmission elements. The concepts are illustrated by application examples from industry and research.

1 Introduction

Multibody modelling and simulation is a rich and classical area of research since many years. Starting at early concepts (Nikravesh and Haug, 1982, Schiehlen, 1984, Orlandea, 1987, Rulka, 1990), it has developed to a well-established discipline with major commercial software packages available. Nevertheless, there is still ongoing research in the modelling of kinematics and dynamics of multibody system which is aimed at producing efficient, easily embeddable code (Fanghella et al., 2003, Khan et al., 2005, Lot and Lio, 2004, Brüls et al., 2006, McPhee and Redmond, 2006, Bauchau, 2009, From et al., 2010).

This paper describes some developments performed at the Chair for Mechanics and Robotics of the University of Duisburg-Essen in the area of generation of object-oriented and closed-form solutions for the dynamical equations for multibody systems in minimal form

$$\mathbf{M}(\underline{q})\ddot{\underline{q}} + \underline{b}(\underline{q}, \dot{\underline{q}}) = \underline{Q}(\underline{q}, \dot{\underline{q}}, t) \tag{1}$$

where $\underline{q} = [q_1 \ldots, q_f]^{\mathrm{T}}$ are the independent generalized coordinates, M is the $f \times f$ mass matrix, $\underline{b}$ is the $f \times 1$ vector for generalized Coriolis, gyroscopic and centrifugal forces, $\underline{Q}$ is the $f \times 1$ vector of generalized forces, and f is the degree of freedom of the system. Although such equations can not always be produced for general multibody systems, and a more general approach is the use of Lagrange multipliers, for many actual applications closed-form solutions exist. For such applications, minimal-form formulations prove to be significantly more efficient than the Lagrange multiplier approach, and thus tools for their automated generation can contribute to better formulations and save substantial time of development. The paper briefly describes in the next two sections two main approaches — object-oriented modelling and symbolical equation generation — for this purpose and illustrates in Section 4 the concepts by some applications.

2 Object-Oriented Modelling

The idea of object-oriented programming consists in identifying real-world objects and the processing required by those objects, and then creating simulations of those objects, their processes, and the required communications between the objects (Sebesta, 1989). This paradigm has led to substantial improvements in software design, allowing the application engineer to think in terms of intuitive and familiar notions and reducing substantially the effort to maintain and extend a piece of code. Based on the client-server

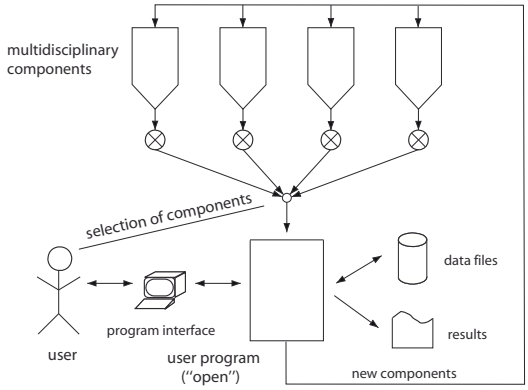

Figure 1. Basic concept for embeddable multibody code.

model (Wirfs-Brock and Wilkerson, 1989), it is possible to define embeddable code that can be mixed with other disciplines such that a user can

assemble a problem-specific simulation environment on a case-by-case basis (Fig. 1). This includes numerical algorithms, sensor data acquisition, graphical rendering, interfacing with external devices, and others. In this way, application-specific interfaces can be readily designed which are fast and efficient and at the same time intuitive to the user.

In order to realize the client-server model, one needs to define the mechanical interactions at an abstract level which is independent of the particular internal algorithms used to compute this behaviour. Such an intrinsic view is obtained by regarding a mechanical component as an abstract entity called "kinetostatic transmission element" which maps motion and forces between a set of 'input' state objects and a set 'output' state objects (Fig. 2). Here, input and output state objects can be spatial reference frames and/or scalar variables, including associated velocities, accelerations and generalized forces (Kecskeméthy and Hiller, 1994).

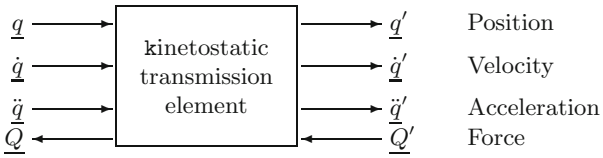

Figure 2. The concept of the kinetostatic transmission element.

The operation of *motion transmission* consists of the three sub-operations

$$\left.\begin{array}{lrcl} \underline{\text{position:}} & \underline{q}' & = & \underline{\varphi}(\underline{q}) \\ \underline{\text{velocity:}} & \dot{\underline{q}}' & = & \mathbf{J}_\varphi\, \dot{\underline{q}} \\ \underline{\text{acceleration:}} & \ddot{\underline{q}}' & = & \mathbf{J}_\varphi\, \ddot{\underline{q}} + \dot{\mathbf{J}}_\varphi\, \dot{\underline{q}} \end{array}\right\} , \tag{2}$$

where $\mathbf{J}_\varphi = \partial\underline{\varphi}/\partial\underline{q}$ represents the $m \times n$ *Jacobian* of the transmission element for n inputs and m outputs. Furthermore, a force-transmission mapping can be defined by assuming that the transmission element neither generates nor consumes power, i.e., that it is *ideal*. By equating virtual work at input and output, one obtains the *force transmission* function

$$\underline{\text{force:}} \qquad \underline{Q} \;=\; \mathbf{J}_\varphi^{\mathrm{T}}\, \underline{Q}' \quad . \tag{3}$$

which maps forces at the output to forces at the input via the transposed Jacobian.

A general-purpose C++ library termed MOBILE has been implemented which allows also to incorporate impact and limit events (Kecskeméthy,

2003). Here, all relevant computations arising in multibody dynamics are embodied by corresponding individual kinetostatic transmission elements, allowing one to access the transmission functions of a particular component without necessarily knowing which object is actually carrying out these functions. The library includes objects for elastic beams, constraint formulations, closed-loop solutions (both explicit and iterative), inverse dynamics, direct dynamics, optimization, etc. Basically, this corresponds to a view of dynamics as differential-geometric mappings between metric-endowed manifolds expressing coordinates at different modelling levels (rigid-body motion, joint variables, generalized coordinates, constraint measurements) and including metric and force pull-back transformations between them (Kecskeméthy, 1994). By the object-oriented approach, the library can be easily extended, as was done for example to incorporate interval analysis in kinematics and dynamics of closed-loop systems (Auer et al., 2008).

3 Symbolical Code Generation

Another approach for producing embeddable multibody code is to generate symbolical solutions. For simple systems like a pendulum or a planar four-bar mechanism, it is evident that a closed-form solution is the most efficient option, which is why in applications such solutions are always hand-coded after formulating them with pencil and paper and then inserted in the overall model. For more complex mechanisms, however, erroneously it has been assumed that closed-form solutions are not possible or too cumbersome to obtain and that thus iterative solutions must be used. However, by regarding the individual kinematical loops as transmission elements termed "kinematical transformers", it is possible to decompose general multiloop system in a series of interconnected kinematical transformers. In the cases where the individual loops allow for a closed-form solution and the interconnection of the kinematical loops allows for a recursive solution flow too, the complete kinematics can be solved in closed form, leading to an iterative-free formulation (Kecskeméthy et al., 1997).

The concepts discussed above have been implemented in a package called SYMKIN based on the symbolic processing language Mathematica (Fig. 3). The package is fully automated and includes, for spatial and/or planar systems, (1) detection of smallest loops by graph-theoretic methods, (2) generation of closed-form solutions in single-loop mechanisms where possible (Kecskeméthy and Hiller, 1992), (3) identification of the optimal solution flow in order to recognize recursively solvable systems, (4) generation of relative and absolute kinematics at position, velocity and accelration level, (5) generation of force transmission, and (6) generation of the equations

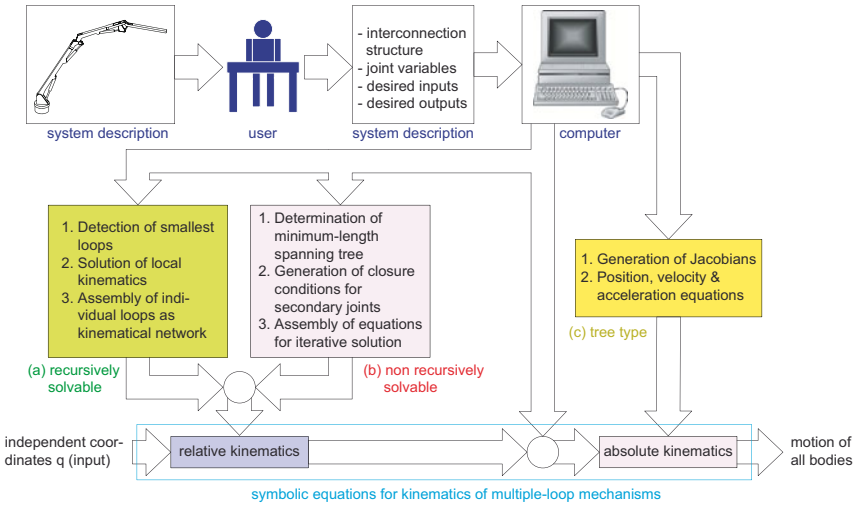

Figure 3. The symbolical equation generation package SYMKIN.

of motion in minimal form. The user just needs to define the kinematical structure of the system and which quantities are of interest. The system automatically recognizes planar subsystems and reduces the computations correspondingly. As the equations are coded by internal variables and elementary kinematical operations, it is easy to export the code to any other language such as C++, graphical processing units, assembler code for micro controllers, etc. by an appropriate back end.

4 Application Examples

In this section, the previous notions are briefly illustrated by some applications. As a first example, consider the design of industrial roller coasters. Here, the aim is to establish a spatial track such that a number of conditions (e.g. geometry of ground and premises, acceleration and force constraints, dimensioning of lifts, drives and brakes, block times, etc.) are fulfilled. Such roller coasters can have quite large tracks (up to 400m) with several figures, so that their design and manufacturing is costly. As the evaluation of the design criteria involves a complete dynamic simulation over the whole track, automatic optimization of the whole track from scratch is not possible. Hence the designer must be able to edit the track (translation and rotation) in terms of experience, and to combine this with automated optimization, without spoiling already polished segments. Moreover, rolling friction, air resistance and spatial moments of inertia parameters have to

be modelled and validated in order to obtain realistic motion predictions. Finally, the program should produce automatically the manufacturing instructions for the bending machine of the track.

Figure 4. Example of an industrial roller coaster track.

In order to solve this problem, a "spline joint" was designed offering position, velocity, acceleration and force transmission for a slider along a curved path (Fig. 5). As the orientation information is also relevant and

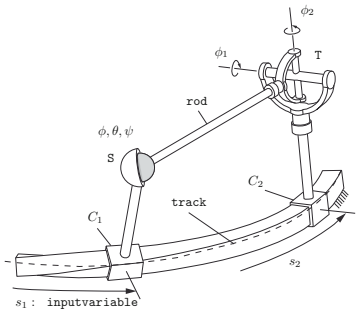

Figure 5. The concept of a spline joint and its use in kinematical loops.

one needs the second time derivative of the rotation for the dynamics, a spline of order five was chosen (Tändl et al., 2007). The spline was globally smoothed using the library of Dierckx (1993). By wrapping the code of the

spline joint as a kinetostatic transmission element, the spline joint could be used as a simple joint, i.e., it was possible to use several spline joints in a loop and to resolve one spline joint as a function of the other. By this it is easy to model trains of roller coaster cars on the track. The overall design environment allows for automatic optimization and local editing. One can choose and mix spline joints of three different parametrizations for key frame computations: Frenet, Darboux and Bishop. It is also possible to make copies of the spline objects and to link them together in master-slave mode. By this one can edit the heart line and the three circular rails are generated automatically. With this environment, the design cycle could be reduced from six months to about two weeks, as has been now verified by several industrial roller coasters. It is obvious that the implementation of such an application-specific environment would not have been possible using monolithic multibody . Moreover, the designed objects for spline joints can now be used for general spatial path planning of robots and machines.

The use of closed-form solutions is illustrated for two examples shown in Fig. 6. The one to the left is the main rotor control mechanism for the

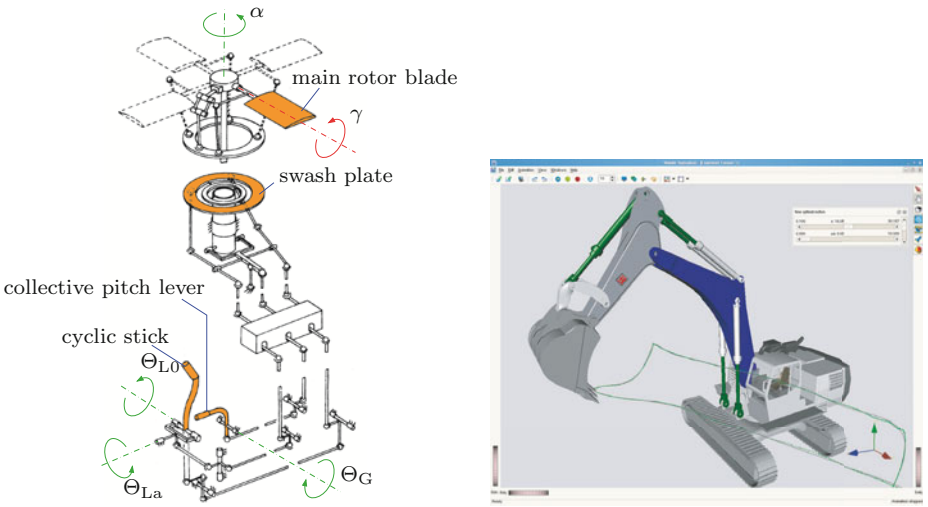

a) rotor contro mechanism b) mining excavator

Figure 6. Examples for systems with complex kinematics.

helicopter BO105, the one at the right is a mining excavator (Geu Flores et al., 2007). Both systems have only four degrees of freedom, but several bodies and joints. Both kinematics can be solved in closed-form. The excavator system has the property that the complete subsystem of the arm

is planar, while the points move in three dimensions. For both systems, the closed-form kinematics were generated automatically with SYMKIN.

	MOBILE (numerical)	SYMKIN (iterative)	SYMKIN (closed-form)
main rotor	1.00	4.45	31.12
excavator	1.00		8.22

Table 1. Relative computational times for the examples of Fig. 6.

Table 1 shows the relative efficiency of a numerical model in MOBILE, a symbolical iterative model in SYMKIN, and a symbolical closed-form model in SYMKIN for the main rotor mechanism, and the first and last model for the excavator model. One clearly sees that closed-form solutions substantially reduce the computational time. Hereby, it should be noted that the numerical MOBILE code is already faster than numerical Lagrange-multiplier codes (Xia and Kecskeméthy, 2010). By the reduced model, it is possible to easily apply concepts from robotics to the excavator, such as manipulability, path planning, force workspace, etc.

5 Conclusions and Acknowledgements

The paper describes two frameworks for producing embeddable minimal-form multibody code for multidisciplinary applications. The object-oriented framework allows one to combine mechanical elements with other disciplines and to rapidly design application-specific simulation and design environments. The symbolical approach allows one to produce highly-efficient code that can be used e.g. for controllers or within an optimization loop. Both frameworks have the advantage that methods derived for robotics can be easily extended to more complex structures, as the models are automatically generated and their use is as simple as the models of classical robotics. Although not all mechanical structures allow for a formulation in minimal form, this case is very common for actual designs and thus is of interest. The extension of the approaches to Lagrange multipliers and the corresponding numerical solution schemes for differential-algebraic equations is straightforward. Also, the object-library has been extended to biomechanics where it is being coupled with MRI measurements, 3D rendering and computerized diagnosis tools (Ambrosio and Kecskeméthy, 2007, Raab et al., 2009).

The results presented in this paper have been developed in a large working group over the past years. The author wishes to particularly thank Francisco Geu, Dr. Thorsten Krupp, Dr. Martin Schneider, Dr. Martin Tändl and Ms Shuxian Xia for their valuable contributions in this setting.

Bibliography

J. Ambrosio and A. Kecskeméthy. Multibody dynamics of biomechanical models for human motion via optimization. In Juan Carlos Garcia Orden, José M. Goicolea, and Javier Cuadrado, editors, *Computational Methods in Applied Sciences*. Springer Netherlands, 2007.

E. Auer, A. Rauh, E.P. Hofer, and W. Luther. Validated modeling of mechanical systems with smartmobile: Improvement of performance by valencia-ivp. In *Reliable Implementation of Real Number Algorithms: Theory and Practice*. Springer Netherlands, 2008.

O. Bauchau. Parallel computation approaches for flexible multibody dynamics simulations. *Journal of the Franklin Institute*, 347:53–68, 2009.

O. Brüls, P. Duysinx, and J.-C. Golinval. A model reduction method for the control of rigid mechanisms. *Multibody System Dynamics*, 15:213–227, 2006.

Paul Dierckx. *Curve and Surface Fitting with Splines*. Clarendon Press, Oxford, 1993.

P. Fanghella, C. Galletti, and G. Torre. An explicit independent-coordinate formulation for the equations of motion of flexible multibodynext term systems. *Mechanism and Machine Theory*, 38:417–437, 2003.

P.J. From, V. Duindam, K.Y. Pettersen, J.T. Gravdahl, and S. Sastry. Singularity-free dynamic equations of vehiclemanipulator systems. *Simulation Modelling Practice and Theory*, 18:712–731, 2010.

F. Geu Flores, A. Kecskeméthy, and A. Pöttker. Workspace analysis and maximal force calculation of a face-shovel excavator using kinematical transformers. In *CD Proceedings of the 12th World Congress in Mechanism and Machine Science*, Besançon, France, June 18–21 2007.

A. Kecskeméthy. An object-oriented differential-geometric approach to spatial mechanism dynamics. In *23th ASME Mechanisms Conference*, pages 369–374, Minneapolis, September 11–14 1994.

A. Kecskeméthy. *MOBILE 1.3 User's Guide and Reference Manual*. University of Duisburg-Essen, 2003.

A. Kecskeméthy and M. Hiller. Automatic closed-form kinematics-solutions for recursive single-loop chains. In *Proc. of the 22nd Biennal ASME-Mechanisms Conference, Scottsdale (USA)*, volume DE-Vol. 47, pages 387–393, September 13–16, 1992.

A. Kecskeméthy and M. Hiller. An object-oriented approach for an effective formulation of multibody dynamics. *Computer Methods in Applied Mechanics and Engineering*, 115:287–314, 1994.

A. Kecskeméthy, T. Krupp, and M. Hiller. Symbolic processing of multiloop mechanism dynamics using closed-form kinematics solutions. *Multibody System Dynamics*, 1(1):23–45, 1997.

W.A. Khan, V.N. Krovi, S.K. Saha, and J. Angeles. Modular and recursive kinematics and dynamics for parallel manipulators. *Multibody System Dynamics*, 14:419–455, 2005.

R. Lot and M. Da Lio. A symbolic approach for automatic generation of the equations of motion of multibody systems. *Multibody System Dynamics*, 12:147–172, 2004.

J. McPhee and S.M. Redmond. Modelling multibody systems with indirect coordinates. *Computer Methods in Applied Mechanics and Engineering*, 195:6942–6957, 2006.

P.E. Nikravesh and E.J. Haug. Generalized coordinate partitioning for analysis of mechanical systems with nonholonomic constraints. ASME-Paper No. 82-DET-94, 1982.

N. Orlandea. ADAMS (Theory and applications). In A.D. DePater and H.B. Pacejka, editors, *Proc. 3rd Seminar on Advanced Vehicle Systems Dynamics (Amalfi, Mai 1986)*, pages 121–166, 1987.

D. Raab, T. Stark, N.E. Erol, F. Löer, and A. Kecskeméthy. An integrated simulation environment for human gait analysis and evaluation. *Materialwissenschaft und Werkstofftechnik - Materials Science and Engineering Technology*, 40:43–53, January 2009.

Wolfgang Rulka. SIMPACK — A computer program for simulation of large-motion multibody systems. In Werner Schiehlen, editor, *Multibody Systems Handbook*, pages 265–284. Springer-Verlag, Berlin, Heidelberg, New York, 1990.

W. Schiehlen. Dynamics of complex multibody systems. *SM Archives*, 9: 159–195, 1984.

Robert W. Sebesta. *Concepts of Programming Languages*. Benjamin/Cummings Publishing Company, 1989.

M. Tändl, A. Kecskeméthy, and M. Schneider. A design environment for industrial roller coasters. In *CD Proceedings of the ECCOMAS Thematic Conference on Advances in Computational Multibody Dynamics*, Milano, Italy, June 25–28 2007.

R. Wirfs-Brock and B. Wilkerson. Object-oriented design: A responsibility-driven approach. In *OOPSLA '89 Proceedings*, pages 71–75, October 1989.

S. Xia and A. Kecskeméthy. Comparison of computational efficiency of closed-loop mechanisms dynamics using automated closed-form solution and ADAMS. In *Proceedings of the GAMM-Conference*, Karlsruhe, Germany, March 22-26 2010. To be published.

Chapter I

Novel Robot Design and Robot Modules/Components

Constructive Redesign of a Modular Metamorphic Microgripper

Luca Bruzzone, Giorgio Bozzini

Department of Mechanics and Design of Machines (DIMEC),
University of Genova, Genova, Italy
E-mail: {bruzzone, bozzini}@dimec.unige.it

Abstract. The paper presents the constructive re-design of a modular microgripper equipped with metamorphic fingertips. The experimental tests on the first prototype of the microgripper has shown that the adoption of the metamorphic fingertips permits to increase remarkably the grasping efficiency; nevertheless, the tests have highlighted some operative drawbacks. The proposed constructive re-design is oriented to increase the reliability and to make easier the tuning and maintenance operations.

1 Introduction

One of the most important paradigms of the present industrial scenario is miniaturisation. The market size of miniaturized products is constantly growing, due to the market expansion towards Developing Countries. Miniaturization can be achieved by means of the so-called mechatronic approach, that is the strict integration between mechanical, electrical and electronic components.

The outlay of the assembly phases represents a large share of the overall production cost for a wide variety of microsystems, in particular in case of small batches (Koelemeijer Chollet et al., 2003).

For all of these reasons, the design of flexible, effective and reliable micromanipulation devices is an important issue in robotics research; for example, significant application fields are: assembly of micromechanisms (Zubir and Shirinzadeh, 2008; Koelemeijer Chollet et al., 2002; Yesin and Nelson, 2005); assembly of micro electro-mechanical systems (MEMS) (Wang et al., 2008; Donald et al., 2008; Dechev et al., 2004; Nelson et al., 1998; Yang et al., 2003); manipulation of objects for microscopy observation (Bergander et al., 2000).

Industrial microassembly systems are generally composed of a gripper and a machine for the positioning of the gripper within the workspace. As regards microgrippers, there are several techniques that can be used for payload grasping: mechanical, cryogenic, vacuum, magnetic; mechanical grasping is usually adopted in case of complex products because it is more general-purpose.

Mechanical microgrippers can be divided into two categories:

- *microtweezers,* characterized by two opposing flat tips, with central gripping point;
- *special-purpose mechanical microgrippers*, designed to grasp specific micro-objects by means of specially shaped tips.

To simplify the production cycle and consequently to shorten the cycle time, it is evidently useful to adopt general-purpose microgrippers to grasp different components; nevertheless, sometimes non-negligible assembly forces are required and the adoption of special-purpose grippers is necessary. A possible solution to combine operative flexibility and grasping effectiveness is the development of metamorphic fingertips. In the following of the paper the design and the experimental tests on the proposed microgripper, MorphoGrip, will be discussed; then, on the basis of the tests on the preliminary prototype, a partial redesign is proposed to improve the mechanical reliability and to simplify the tuning and maintenance operations.

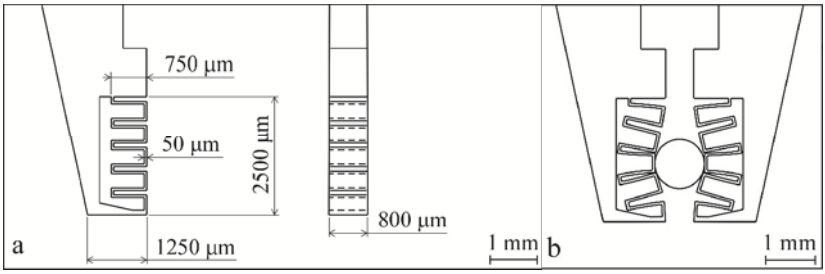

Figure 1. Design of the metamorphic fingertip (a); grasping of a 1 mm cylinder (b)

2 The MorphoGrip Architecture

The starting point of the design is the definition of the reference applications; we have considered the manipulation of cylindrical parts with diameter ranging from 0.5 to 2 mm, in presence of assembly forces up to 0.3 N; however, we tried to obtain a microgripper capable of grasping also payloads with different shapes. On these specifications, we have developed metamorphic fingertips characterized by a highly deformable contact zone. The fingertip plate (Figure 1a) is obtained by electro-discharge machining (EDM) from a Nitinol sheet; the adopted Nitinol alloy has superelastic behaviour with minimum residual strain (Young modulus 75 GPa, tensile strain up to 20% at 20°C). A thin protrusion with square wave shape enhances the contact compliance; the shape of this protrusion has been refined by means of FEM analysis to obtain a good compromise between high flexibility and structural resistance. Adopting the final protrusion design, the contact zone

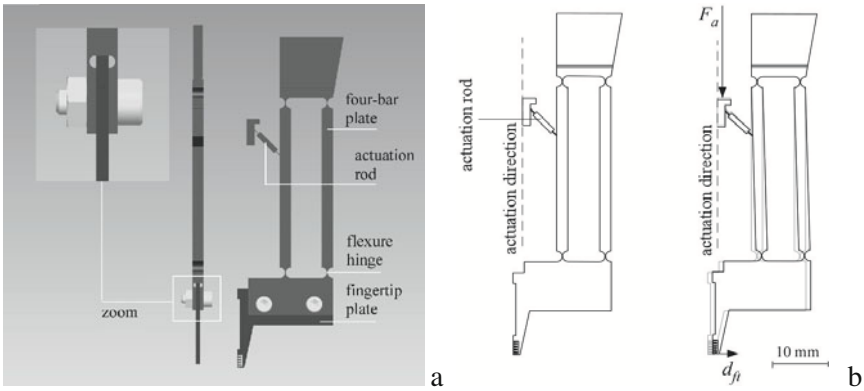

Figure 2. Architecture of the finger module (a); finger actuation (b)

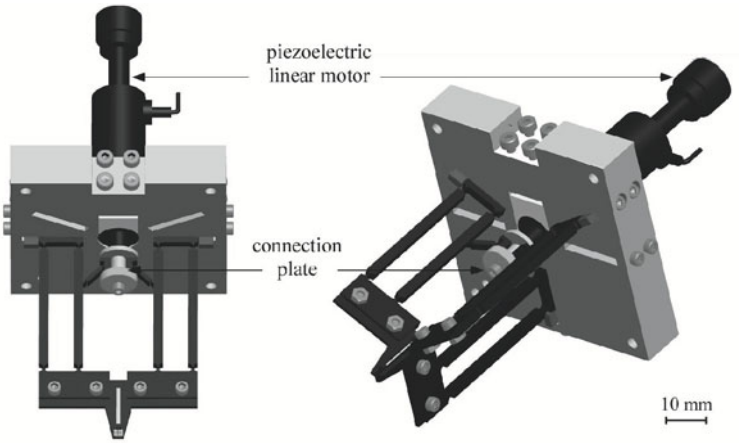

Figure 3. Off-line reconfigurability of the modular gripper

maximum deformation is of 60 μm while grasping a cylinder with 1 mm radius in presence of a closing force of 0.16 N (Bruzzone and Bozzini, 2007).

The fingertip plate is carried by the finger module shown in Figure 2; it is based on a flexible four-bar mechanism (Figure 2b); it is realized in Nitinol alloy, with 2 mm thickness. The fingertip plate is connected to the four-bar plate by a slot and bolts, to tune their relative position. The actuation of the four-bar plate is performed by means of an actuation rod (Figure 2a) pushed along the actuation direction (Figure 2b) by a piezoelectric actuator. The actuator opens the gripper, whereas the closing force is provided by the elastic return force of the four-bar flexure joints; the closing force can be tuned by regulating the position of the fingertip plate in the slot.

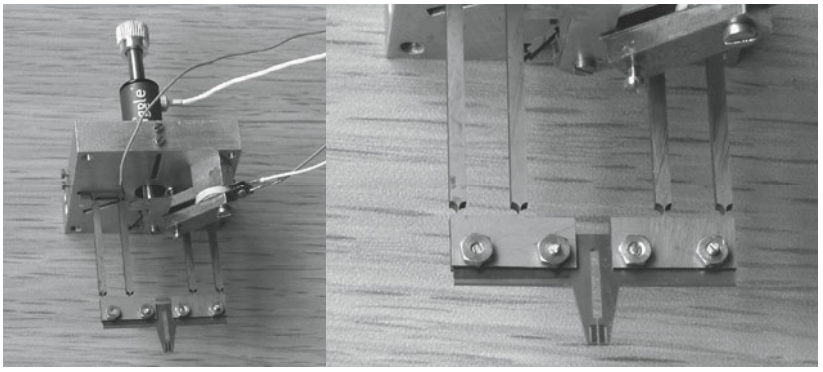

Figure 4. The MorphoGrip prototype

In the proposed gripper, the finger modules can be arranged in two different ways (*off-line reconfigurability):* a general-purpose two-fingered configuration (Figure 3, left), or a three-fingered configuration (Figure 3, right), with three fingers placed at 120°, to grasp components with axial symmetry.

3 Experimental Results

A first prototype of the MorphoGrip has been built (Bruzzone and Bozzini, 2008) (Figure 4) and an experimental campaign has been carried out. The gripper was mounted on a static layout to compare the grasping performance of the metamorphic fingertips with respect to standard non-metamorphic fingertips, characterized by the same geometry, material and surface finishing but without deformable square wave contact zone. The tests were performed using cylindrical payloads with diameters between 1 and 2 mm. In this test layout the linear actuator is vertical, and a vertical force F_g is applied to the payload by means of a wire connected to a small vessel, filling slowly the vessel with liquid (Bruzzone and Bozzini, 2009).

Some numerical results are summarized in Table 1. In this table: the closing force F_c (ranging from 0.1 to 0.25 N) is the force exerted on both sides of the payload by the fingertips; $F_{g,nm}$ is the force F_g that is necessary to wrest the cylinder from the non-metamorphic gripper; the *initial slipping force* $F_{g,slip}$ is the force F_g that is necessary to start the slipping of the cylinder in case of metamorphic gripper; the *maximum grasping force* $F_{g,max}$ is the force F_g that is necessary to wrest the cylinder from the metamorphic gripper.

The tests show that: 1) the grasping release with non-metamorphic fingertips is sudden when F_g reaches the value $F_{g,nm}$; 2) with metamorphic fingertips the grasping stability is higher, and the release gradual: when the traction force reaches the value $F_{g,slip}$ the payload starts to move; a further increment of F_g to

$F_{g,max}$ is necessary to have the complete release of the grasping; 3) $F_{g,slip}$ is much greater than $F_{g,nm}$.

A detailed comparison of metamorphic and non-metamorphic fingertips in different operative conditions is discussed in (Bruzzone and Bozzini, 2009).

Table 1. Experimental comparison of metamorphic and non-metamorphic fingertips.

payload type	F_c [N]	$F_{g,nm}/F_c$	$F_{g,slip}/F_c$	$F_{g,max}/F_c$
steel cylinder with 1 mm diameter	0.10	0.53	1.40	1.84
	0.15	0.38	1.03	1.50
	0.20	0.24	0.78	1.33
	0.25	0.20	0.69	1.14
steel cylinder with 2 mm diameter	0.10	0.93	1.68	2.12
	0.15	0.66	1.20	1.70
	0.20	0.47	0.98	1.44
	0.25	0.38	0.86	1.32

4 Constructive Re-Design of the Finger Module

The experimental results confirm the effectiveness of the design of the metamorphic fingertips. On the contrary, the tests have highlighted some operative drawbacks of the four-bar plate: 1) the alignment of the fingertip is critical: the four-bar plates are connected to the gripper base by means of slots and lateral bolts (Figure 3); small errors in the machining of these slots cause non-negligible misalignments of the fingertips; these misalignments can be corrected only by placing thin sheets in the slots; 2) the flexure hinges of the four bar plate, and in particular the ones of the actuation rod, are frail and have to be handled very carefully; moreover, a damage in one flexure hinge requires the expensive substitution of the whole four-bar plate.

In order to solve these problems the finger modules have been re-designed as shown in Figure 5, maintaining the same operating principle. The four flexure hinges have been replaced by thin sheets of superelastic alloy with 1.5 mm thickness (Figure 5, a), connected by bolts; these flexure sheets are endowed with slots (Figure 5, b) to tune the joint lengths. The actuation rods have been replaced by a more robust flexible element (Figure 5, c). The four-bar links (Figure 5, d,e,f) are realized in steel. A screw (Figure 5, g) has been added to tune more precisely the position of the fingertip plate in its slot and consequently the elastic preload.

The advantages of this re-design are the following: 1) the alignment of the fingertips can be easily tuned by means of the slots of the flexure sheets; 2) the break of a single flexure joint does not require the substitution of the whole finger module; 3) the elastic return force of the four-bar can be tuned by regulating the

lengths of the flexure joints l_j (Figure 5) in a range between 5.5 and 8.5 mm; 4) the module construction is less expensive (lower amount of superelastic alloy).

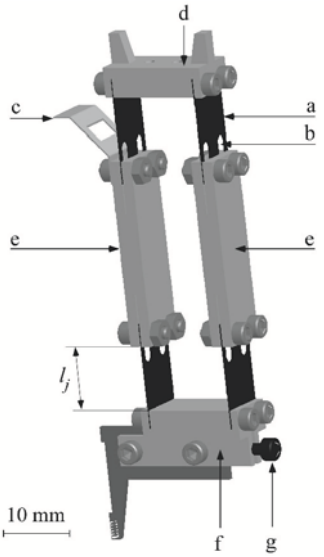

Figure 5. Second version of the finger module

The structural features of the first and second versions of the finger module have been compared by means of FEM analysis. Let us define: the *functional stiffness* $k_f = F_a / d_{ft}$, where F_a and d_{ft} are the actuation force and the corresponding translation of the end of the fingertip (Figure 2b); the *lateral stiffness* $k_l = F_l / d_{ft,l}$, where F_l is a lateral force applied to the end of the fingertip (perpendicular to the four-bar plane) and $d_{ft,l}$ is the corresponding lateral displacement of the end of the fingertip; the *torsional stiffness* $k_t = M_t / \theta_t$, where M_t is a moment applied to the lower surface of the link *f* with direction parallel to the actuation direction and θ_t is the corresponding rotation of the same link.

In the estimation of these stiffness values, the model boundary conditions are: upper link of the four-bar fully constrained, upper end of the actuation rod constrained to translate along the actuation direction (Figure 2b). The results of the FEM simulations are collected in Table 2. Figure 6 shows the deformed shapes in the three load cases for the re-designed finger module (l_j = 8.5 mm).

While the functional stiffness has to be compatible with the maximum actuation force and the required closing force, high values of lateral and torsional stiffness allow a more precise grasping, without unwanted deformations. In the second version the functional stiffness is variable in a range between 0.525 N/mm (l_j = 8.5 mm) and 1.083 N/mm (l_j = 5.5 mm). This allows a wider regulation of the

closing force: in the first version, on the contrary, it can be tuned only by moving the fingertip plates in their slots.

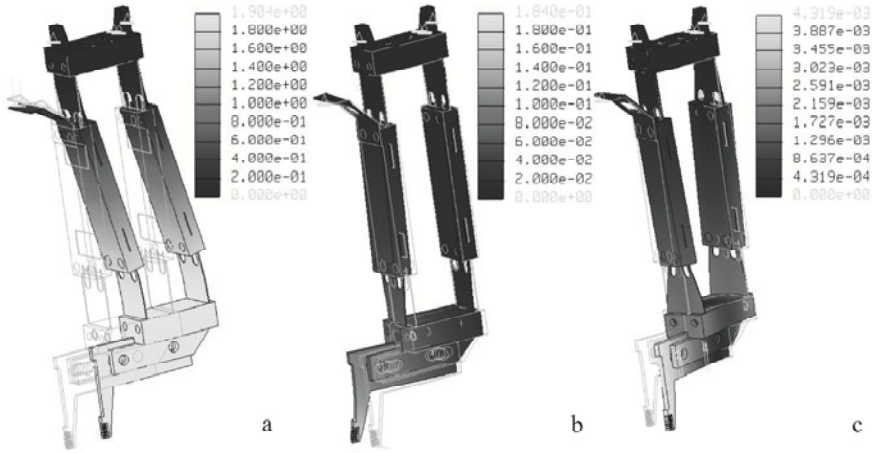

Figure 6. Displacements in mm (l_j = 8.5 mm); load cases corresponding to: functional stiffness, F_a = 1 N (a); lateral stiffness, F_l = 1 N (b); torsional stiffness, M_t = 1 Nmm (c).

Table 2. Functional, lateral and torsional stiffness of the different finger modules.

Finger module	k_f [N/mm]	k_l [N/mm]	k_t [Nmm/rad]
first version	0.823	2.083	820.5
second version (l_j =8.5 mm)	0.525	5.434	3097.3
second version (l_j =5.5 mm)	1.083	8.696	6730.8

The increments in the values of lateral and torsional stiffness mean that the structural quality is better even if the flexure hinges (characterized by lumped section restriction) are replaced with flexure sheets (with distributed elasticity).

5 Conclusions

MorphoGrip is a modular and reconfigurable microgripper designed to increase the level of operative flexibility with respect to the state-of-the-art. The experiments on the first prototype has shown that the adoption of the metamorphic fingertips allows to remarkably increase the strength and the stability of the grasping; nevertheless, the tests have highlighted some practical drawbacks. The second version is characterized by an easier tuning of the alignment of the fingertips, by an easier and more flexible regulation of the closing force and by lower costs of realization and maintenance. In the next future the second prototype will be realized; it can be

considered as a pre-production development stage of a general-purpose industrial microgripper.

References

Bergander, A., Breguet, J.M., Schmitt, C., and Clavel R. (2000). Micropositioners for Microscopy Applications based on the Stick-Slip Effect. In *Proceedings of the IEEE Intl. Symposium on Micromechatronics and Human Science (MHS 2000)*, Nagoya, Japan, October 22-25, 2000, 213-216.

Bruzzone, L., and Bozzini, G. (2007). Design of electro-discharge machined flexible fingertips for microassembly. In *Proceedings XVIII Congresso Associazione Italiana di Meccanica Teorica e Applicata (AIMETA 2007)*, Brescia, Italy, September 11-14, 2007, CD.

Bruzzone, L., and Bozzini, G. (2008). MorphoGrip: metamorphic gripper for miniaturized assembly. In *Proceedings of the RAAD 2008, 17th International Workshop on Robotics in Alpe-Adria-Danube Region*, Ancona, Italy, September 15-17, 2008, CD.

Bruzzone, L., and Bozzini, G. (2009). A flexible joints microassembly robot with metamorphic gripper. Accepted for publication on Assembly Automation.

Dechev, N., Cleghorn, W.L., and Mills, J.K. (2004). Microassembly of 3D Microstructures Using a Compliant, Passive Microgripper. *IEEE Journal of Microelectromechanical Systems* 2(13):176-189.

Donald, B.R., Levey, C.G., and Paprotny I. (2008). Planar Microassembly by Parallel Actuation of MEMS Microrobots. *IEEE Journal of Microelectromechanical Systems* 4(17):789-808.

Koelemeijer Chollet, S., Moll, B., Bourgeois, F., Wulliens, C. Benmayor, L., and Jacot, J. (2002). A Flexible Microassembly Cell for Small and Medium Sized Batches. In *Proceedings of the Intl. Symposium on Robotics (ISR02),* Stockholm, Sweden, October 7-11, 2002, CD.

Koelemeijer Chollet, S., Bourgeois, F., and Jacot, J. (2003). Economical Justification of Flexible Microassembly Cells. In *Proceedings of the 5th IEEE Intl. Symposium on Assembly and Task Planning*, Besancon, France, July 10-11, 2003, 48-53.

Nelson, B., Zhou, Y., and Vikramaditya, B. (1998). Sensor-based microassembly of hybrid MEMS devices. *IEEE Control Systems Magazine* 6(18):35-45.

Wang, L., Mills, J.K., and Cleghorn, W.L. (2008). Automatic Microassembly Using Visual Servo Control. *IEEE Tran. on Electronics Packaging Manufacturing* 4(31):316-325.

Yang, G., Gaines, J.A., and Nelson, B.J. (2003). A Supervisory Wafer-Level 3D Microassembly System for Hybrid MEMS Fabrication. *Journal of Intelligent and Robotic Systems* 1(37): 43–68.

Yesin, K.B., and Nelson, B.J. (2005). A CAD model based tracking system for visually guided microassembly. *Robotica,* 4(23):409–418.

Zubir, M.N.M., and Shirinzadeh, B. (2008). Development of a Compliant-Based Microgripper for Microassembly. In *Proc. IEEE/ASME Intl. Conf. on Mechtronic and Embedded Systems and Applications (MESA 2008)*, Beijing, China, Oct. 12-15, 2008, 522–527.

A One-Motor Full-Mobility 6-PUS Manipulator

Patrick Grosch(°), Raffaele Di Gregorio(°°), Federico Thomas(°)*

(°)Institut de Robòtica i Informàtica Industrial (CSIC-UPC), Barcelona, Spain
(°°)Department of Engineering – University of Ferrara, Ferrara, Italy

Abstract. This paper presents the feasibility study of an under-actuated parallel manipulator with 6-PUS topology, destined to handle work-tables in CNC machine tools. The proposed device exploits the fact that, in such an application, the path between the initial and final poses of the mobile platform is not assigned to reduce the number of actuators to only one.

1 Introduction

The need of making an object move along an assigned path arises only in a limited number of applications. In most cases, the only initial and final poses of the object are assigned, whereas the path between them must just satisfy weak constraints (e.g., obstacle avoidance, preventing interferences among machine components, etc.) which leave the choice of the path practically free. Such a freedom can be exploited during design to simplify the machine architecture.

Work-tables of machine tools usually either perform simple translations or just lock the workpiece during cutting. Thus every time the workpiece has to be reoriented or, in general, repositioned with respect to the spindle axis either manual operations or external devices must intervene. Repositioning workpieces is a manipulation task that involves small six-dimensional workspaces, good positioning precision and high stiffness in the final configuration; it does not impose any constraint to the path between the initial and final poses.

Parallel manipulators can satisfy the requirements on positioning precision and stiffness; moreover, they are specially suitable for applications that involve small workspaces. Therefore, they are natural candidates to move the work-table during workpiece repositioning.

* This work was supported by the Spanish Ministry of Science and Innovation, by the contribution of Regione Emilia Romagna (District Councillorship for Productive Assets, Economic Development, Telematic Plan), PRRIITT misura 3.4 azione A, to InterMech (Division Acoustics and Vibrations - LAV), and by UNIFE funds.

How to exploit the free path for reducing the complexity of a manipulator destined to move the work-table during repositioning is an open problem.

This paper proposes an under-actuated parallel manipulator that, by exploiting the free path, is able to control the mobile platform pose in a six-dimensional workspace by using only one motor. Section 2 describes the manipulator architecture and illustrates its operation. Section 3 addresses the kinetostatic analysis of the machine and gives conditions the path must satisfy to keep the mobile platform pose controllable during motion. Eventually, the conclusions are drawn in section 4.

2 Manipulator Architecture and Operation

Parallel manipulators (PMs) with topology 6-PUS[1] feature a mobile platform connected to a fixed base through six in-parallel kinematic chains (legs) of type PUS. Their architectures vary according to the relative disposition of the prismatic-pair sliding directions, the platform geometry, and the six fixed distances (leg lengths) between universal-joint center and spherical-pair center of each leg. By changing these geometric parameters, a number of 6-PUS PMs have been proposed in the literature (see Merlet (2006, chap. 2) for Refs.). Boye and Pritschow (2005) named them linapods. Honegger *et al.* (1997) proposed the Hexaglide that has six parallel and coplanar guides. Moreover, some of the proposed architectures (Bernier *et al.* 1995; Pritschow *et al.* 2002) exhibit coincident guides for couples of prismatic pairs, and, in particular, Nabla 6, proposed by Bernier *et al.* (1995), has three coplanar guides each carrying two sliders. The actuation of each prismatic pair is independent of the other actuations in all the linapods proposed in the literature.

Figure 1 shows the proposed linapod. On the base, a single motor, through a transmission, actuates, one at a time, two racks that are constrained to slide along two mutually orthogonal guides forming a cross-shaped path. The transmission is able to actuate one or the other rack by using two clutches that also act as brakes for the non-actuated rack. The racks carry suitably shaped hooks which can firmly lock revolute-pair housings (the cubes attached to the racks in Fig. 1). In these revolute-pair housings, legs' universal joints insert one pin of their cross link so that the resulting revolute pair has the axis perpendicular to the plane of the guides. In so doing, all the universal joints have the other revolute-pair axis parallel to the plane of the guides, and their centers are constrained to lie on T paths that are all parallel to the plane of the guides. The universal-joint centers slide on these T paths when the racks are moved.

On the mobile platform, the housing of the spherical pairs, which join the leg endings to the platform, are embedded in the platform.

[1] P, U, and S stand for prismatic pair, universal joint, and spherical pair, respectively; whereas, the underscoring indicates that the corresponding joint is actuated.

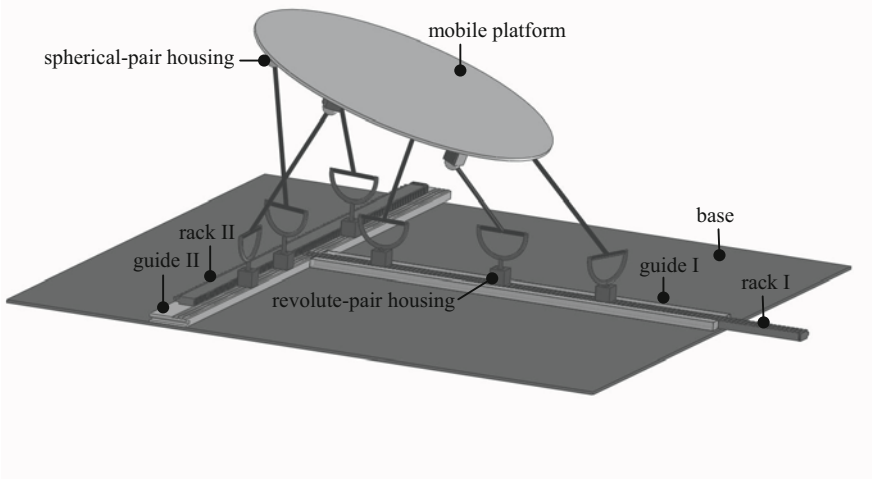

(a)

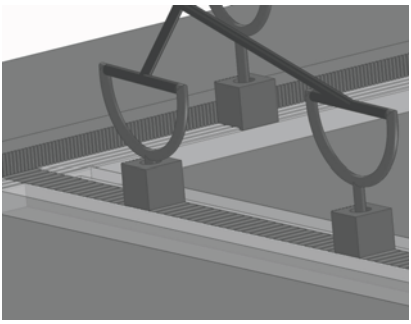

(b)

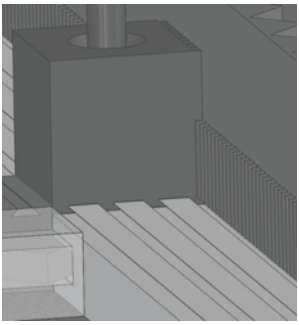

(c)

Figure 1. Under-actuated 6-PUS: (a) 3D CAD model, (b) detail of the racks, the guides, and some of the revolute-pair housings, (c) revolute-pair housing at the intersection between the two racks.

The hooking between rack and revolute-pair housing is managed by a purely mechanical device carried either on the revolute-pair housing or on the guides. This hooking device and the hooks on the racks are conceived so that the following functional requirements are satisfied:

(i) if the revolute-pair housing is in contact with only one rack, the hooking device must provide a constraint that, combined with the constraint of rack's hooks, firmly holds the housing fixed to the rack;

(ii) if the revolute-pair housing is in contact with both racks (i.e., at the intersection of the T path), the hooking device must not provide any constraint, whereas the hooks of both racks must provide the constraints necessary to hold the housing;

(iii) if the revolute-pair housing is at the intersection of the T path and one rack starts moving, the hooks of the moving rack must be able to tow the housing, whereas the hooks of the other rack must not forbid this towing and must be so shaped that, during the housing motion, make the hooking device intervene to provide its constraint.

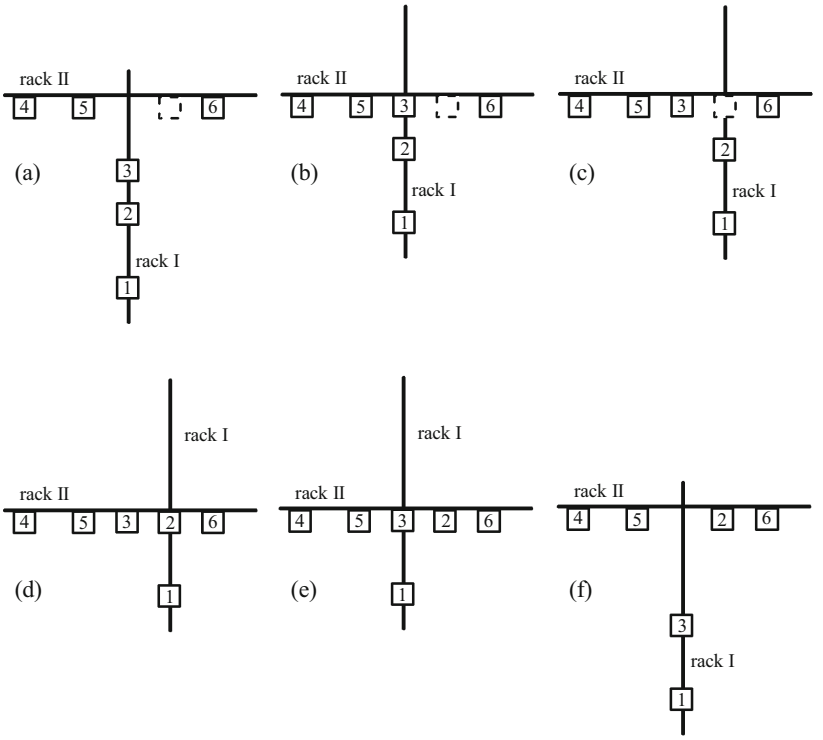

Figure 2. Sequence of rack motions (the numbered boxes represent the revolute-pair housings): (a) initial configuration, (b) rack I was moved to make housing 3 touch rack II, (c) rack II was moved to make the dotted box centered on rack I, (d) rack I was moved to make housing 2 touch rack II, (e) rack II was moved back to its initial position, (f) final configuration obtained by moving back rack I to its initial position.

Many hooking devices and complementary hooks for the racks can be easily devised to satisfy the above technical requirements. For instance, in Fig. 1, the hooks of rack I are dovetail joints parallel to rack II, whereas the hooks of rack II are frontal teeth with rectangular cross section; moreover, the hooking device is constituted of two lateral stops fixed to guide I, and of dovetail joints, identical to the ones of rack I, fixed to guide II (see Figs. 1(b) and 1(c)). The many design alternatives for these equipments will not be discussed here, for the sake of conciseness.

By exploiting the above-reported properties of hooking device and racks' hooks the positions of the universal-joint centers on the T paths can be about freely changed. In fact, if, for instance, housing 2, on rack I, (Fig. 2(a)) must be moved to the dotted position on rack II and housing 3 must be moved to the actual position of housing 2, the sequence of operations shown in Fig. 2 can be implemented.

In general, many different rack-motion sequences lead to the same final configuration, and the number of operations to implement may decrease when the number of housing permutations increases.

3 Kinetostatics and Constraints on the Path

The inverse position analysis (IPA) that, for this linapod, means the determination of the housing positions on the racks for an assigned platform pose (position and orientation) must be solved every time the platform is repositioned. This determination is straightforward once the positions of the universal-joint centers have been computed. The assigned relative pose between base and platform involves that the six T paths (one per leg), the universal-joint centers must lie on, have assigned poses with respect to the spherical-pair centers embedded in the platform. Thus, for each leg, the determination of the universal-joint center's position reduces itself to compute the intersection points between the T path the universal-joint center must lie on and a sphere, with center at the spherical-pair center and radius equal to the leg length. This geometric problem has at most four solutions: the two sets of intersections between the sphere and the two sides of the T. At most four solutions for each leg yields at most 4^6 (i.e., 4096) leg arrangements compatible with an assigned platform pose. Such a high number of IPA solutions is mainly theoretical. In fact, many line-sphere intersections will fall out of the line segments actually occupied by the T-path's sides. Moreover, other solutions will be excluded by the fact that two or more housings cannot be located on the same position, and that, on each rack, the hooks' sequence has a fixed pitch, which implies that the distance between couples of housings positioned on the same rack can only be multiples of the hooks' pitch. Eventually, all the leg arrangements that give a singular configuration (see below) must be excluded.

The direct position analysis (DPA) of the proposed linapod consists in the determination of the platform poses compatible with an assigned disposition of the

revolute-pair housings on the two racks. If the positions of the revolute-pair housings are assigned, the positions of the universal-joint centers will be assigned, too. Thus this problem reduces itself to the determination of the assembly modes of the 6-US structure (i.e., two rigid bodies connected by six in-parallel US legs), which was broadly treated in the last two decades in connection with the DPA solution of the general Stewart platform (see Merlet (2006) for Refs.). The result of these studies is that the 6-US structure can have at most forty assembly modes which can be even analytically determined (Husty, 1996; Innocenti, 2001).

The singularities of the forward instantaneous kinematics are, for this linapod, the configurations where the platform can perform instantaneous motions even though the racks are locked (i.e., they are uncertainty configurations of the 6-US structure). At a singularity of this type, the platform pose is not controllable, and the internal loads of one or more links of the legs are not able to equilibrate the external loads applied on the platform. Thus, they must be identified during design and avoided during operation. The uncertainty configurations of the 6-US structure have been studied by many authors, and, in the literature, both geometric and analytic conditions to identify them have been provided (see, for instance, Merlet (1989), McCarthy (2000), St-Onge and Gosselin (2000), Di Gregorio (2002)). The actual implementation of the proposed linapod requires that all this literature be exploited to correctly design and control it. In this paper, for the sake of brevity, the authors will only give the justification of some design choices due to the need of avoiding uncertainty configurations.

From a static point of view, in 6-US structures, an uncertainty configuration occurs when the six forces applied to the platform through the spherical pairs are not able to equilibrate any system of external loads. The fact that these forces are aligned with the leg axes[2] allowed the geometric classification of the singular configurations through particular arrangements of the six leg axes (McCarthy, 2000). All these singular arrangements satisfy at least one out of the following three geometric conditions: (a) the six axes either intersect or are parallel to a line, (b) the six axes are all parallel to a plane, and (c) the six axes are tangent to coaxial helices with the same pitch.

For the linapod under study, the possibility of locating all the revolute-pair housings on one rack would greatly improve the path planning algorithms (see below). Therefore, making this housing arrangement non-singular is important. Once all the housings are located on the same rack all the universal-joint centers lie on the same plane. And, in order to avoid the geometric conditions (a) and (b), the universal-joint centers must not be located at the same height on the rack (i.e., the T paths must not coincide); whereas the spherical-pair centers must be suitably dis-

[2] In a US leg, the leg axis is the line passing through the centers of the universal joint and of the spherical pair.

tributed on the platform. The manufacturing conditions that allow condition (c) to be avoided are much more difficult to be visualized and a careful numerical check is necessary. It is worth noting that the leg arrangements with all the housings on the same rack geometrically coincide with the Hexaglide architecture (Honegger *et al.*, 1997), and the results obtained for the Hexaglide can also be usefully exploited.

A path-planning algorithm for the proposed linapod has to take into account all the above-reported kinetostatic considerations. In addition, it needs the implementation of a motion strategy for choosing the sequence of rack motions able to move from the initial platform pose to the final one. Each step of this sequence finishes with a particular arrangement (state) of the revolute-pair housings on the racks that is reached when both the racks are at rest and the actuation is about to be switched from one rack to the other. Thus, a path-planning algorithm has to determine the states' sequence by respecting the rule that the transition from one state to the successive one must be possible by moving only one rack. For instance, the motion described in Fig. 2 is characterized by six states and five transitions. Two different paths that have the same initial and final housing arrangements can be compared on the basis of the number of intermediate states, and, of course, the lower is the number the better is the path.

The sequence that moves only one housing from any position to any other without changing the positions of the other housings, in the final state, can be easily automated. Thus, a simple path-planning algorithm could reduce itself to implement six separate sequences each of which brings only one housing from its initial to its final position and, in the final state, does not change the positions of the housings already brought to their final positions. Such a motion strategy employs a great number of intermediate states. For instance, it is easy to realize that, in Fig. 2, the motion of the only housing 2 without changing the position of housing 3 would have required nine states, whereas the strategy reported in Fig 2 uses only six states to move both housings 2 and 3 to their final positions.

A much better motion strategy can be obtained by finding a state (parking state) from which any other state can be reached through a reduced number of intermediate states. The state with all the housings located on rack II and no housing at the rack intersection could be a parking state. In fact, from this parking state, a housing can be put on rack I, at any position, with a sequence involving only two intermediate states, whereas only four intermediate states are required to change the position of a housing on rack II. A path-planning algorithm based on this parking state, first, has to implement the sequences that bring all the housings on rack II (note that the only housings located on rack I in the initial state are involved in this phase); then, it has to move all the housings from the parking positions to their final positions.

4 Conclusions

The feasibility study of an under-actuated parallel manipulator with 6-PUS topology, destined to handle work-tables in CNC machine tools, has been presented. The proposed device exploits the fact that, in such an application, the path between the initial and final poses of the mobile platform is not assigned to reduce the number of actuators to only one. For the proposed manipulator, all the hardware critical points have been addressed. Its kinematic and static characteristics have been discussed, and the availability of the solutions to all the problems involved in its design and control has been verified. Two motion strategies that can be used in the path-planning algorithms have been proposed.

A formalization of the allowed rearrangements using group theory will probably provide a deeper insight into this path planning problem (Joyner, 2002). This is certainly a point that deserves further attention

References

Bernier, D., Castelain, J.-M., and Li, X. (1995). A new parallel structure with six degrees of freedom. In *Proceedings of the 9th World Congress on the Theory of Machines and Mechanisms*, Milan (Italy), 8 - 12.

Boye, T., and Pritschow, G. (2005). New transformation and analysis of a N-DOF LINAPOD with six struts for higher accuracy. *Robotica* 23: 555-560.

Di Gregorio, R. (2002). Singularity-locus expression of a class of parallel mechanisms. *Robotica* 20: 323-328.

Honegger, M., Codourey, A., and Burdet, E. (1997). Adaptive control of the Hexaglide a 6 dof parallel manipulator. In *Proc. of the 1997 IEEE Int. Conf. on Robotics and Automation*, Albuquerque, 543-548.

Husty, M.L. (1996). An algorithm for solving the direct kinematics of the Stewart-Gough platform. *Mechanism and Machine Theory* 31(4): 365-380.

Innocenti, C. (2001). Forward kinematics in polynomial form of the general Stewart platform. *Journal of Mechanical Design* 123(2): 254-260.

McCarthy, J.M. (2000). *Geometric Design of Linkages*. Springer-Verlag, New York, chapter 12: 272-283.

Merlet, J.-P. (1989). Singular configurations of parallel manipulators and Grassmann geometry. *Int. J. of Robotics Research* 8(5): 45-56.

Merlet, J.-P. (2006). *Parallel Robots.* Dordrecht, The Netherlands: Springer, 2nd edition.

Pritschow, G., Eppler, C., and Lehner, W.-D. (2002). Highly dynamic drives for parallel kinematic machines with constant arm length. In *Proc. 1st Int. Colloq., Collaborative Res. Center*, Vol. 562, Braunschweig, Germany, 199–211.

St-Onge, B.M., and Gosselin, C.M. (2000). Singularity analysis and representation of the general Gough-Stewart platform. *Int. J. of Robotics Research* 19(3): 271-288.

Joyner, D. (2002). *Adventures in Group Theory. Rubik's cube, Merlin's machine and other mathematical toys*. The Johns Hopkins University Press, Baltimore (USA).

Dynamic Hybrid Position/Force Control for Parallel Robot Manipulators

Wenbin Deng, Hyuk-Jin Lee and Jeh-Won Lee

Dept. of Mechanical Engineering, Yeungnam University, Gyeongsan, Korea

Abstract It is necessary to control both the position of a manipulator and the force when a robot manipulator interacts with the environment. In this paper, a simple compliant motion control algorithm for parallel robot manipulators is presented. Based on the concept of hybrid position/force control scheme, the task space is split into position controlled and force controlled subspaces. We designed two controllers for position and force control to track the desired position trajectories and force in operational space. Experimental results obtained from a two degree of freedom parallel robot show and verify the effectiveness of the control method.

1 Introduction

Force control has been known to be one of the complicated control methods for robotic manipulator interacting with other objects. Specially, the desired force should be maintained while following the desired trajectories when the robot contact with the environment. So it is necessary to control both force and motion when a robot manipulator interacts with the environment. At the same time, force control of robot manipulators has been studied by many researchers (see Whitney, 1977, Khatib, 1985, Li et al., 2009 and so on). Although the demand of applying a force control technique is increasing, many problems still remain to be solved.

Recently, parallel robot manipulators are being more and more used in industry. A parallel robot typically consists of a moving platform which is connected to a fixed base by several kinematic chains, also called “limbs” or “legs”. Typically, every limb is controlled by one actuator and all the actuators can be mounted at or near the fixed base. Comparing with a traditional serial manipulator that is constituted of rigid-body links and joints connected in series, a parallel robot manipulator has a more rigid structure and better payload-carrying ability. So it is more suitable for situations in high precision, stiffness, velocity, and heavy load-carrying suggested by Merlet (2001).

In this paper, we adopt hybrid position/force control scheme because most machining tasks require precise positional control in some directions and force control in others. Based on the dynamics of parallel manipulators, two controllers were designed to achieve the desired force and position.

2 Dynamic Modeling of Parallel Manipulator

The equation of motion for the constrained parallel robotic manipulator, considering the contact force and the constraints, is given (Tsai, 1999) in joint space as follows:

$$M(q)\ddot{q} + h(q,\dot{q})\dot{q} + G(q) = u - J^{-T}(q)F_e \tag{1}$$

where:
q , $\dot{q}$, $\ddot{q}$ denotes the joint angle, velocity, acceleration of the manipulator;
M(q) is the robot inertia matrix which is symmetric and positive;
$h(q,\dot{q})$ contains the Centrifugal terms and Coriolis terms;
G(q) is the gravity matrix;
u denotes the joint input control torques;
F_e is the interaction forces associated with the constraints;
J(q) is the Jacobian matrix of parallel manipulator.

It is well known that when the end-effector contacts the environment, a task space coordinate system defined with reference to the environment is convenient for the study of contact motion. In the absence of friction, the dynamic equation of a parallel manipulator can be expressed by Lagrangian approach in the task space as

$$M(X)\ddot{X} + h(X,\dot{X}) = F - F_e \tag{2}$$

where: $M(X) = J^T M(q)J$, $h(X,\dot{X}) = J^T h(q)J - J^T M(q)J\dot{J}J$, $F = J^T u$.

It is easy to see that the control *F* should be chosen according to

$$F = F_e + M(X)\ddot{X} + h(X,\dot{X}) \tag{3}$$

The generalized input force *F* is related to the input torque *u* by Jacobian matrix.

$$u = J^{-T}(q)F \tag{4}$$

3 Hybrid Position/Force Control Method

Precise control of manipulators in the face of uncertainties and variations in their environments is a prerequisite to feasible application of robot manipulators to complex handling and assembly problems. A pure position control of a manipulator is severely limit in a manufacturing environment where uncertainties are significant and sophisticated tasks such as polishing, deburring, grinding etc.. The necessity of force control along with position control was recognized and proposed by Raibert et al. in 1981. But it did not take into account the manipulator dynamics rigorously. Yoshikawa (1987) presented the dynamic hybrid control approach which is based on the dynamic equation of the robot manipulators and a description of the end effector constraints. However, he took dynamics of serial manipulator into consid-

eration and adopted a SCARA robot for the application to test the control scheme. We adopted and developed this method for the parallel robots in this paper.

To implement the hybrid position/force scheme, we design both a position control law along force constrained directions and a force control law along position constrained directions through the use of so-called selection matrices. Such an overall control scheme is shown in Figure 1. The inner loop control law consists of an inverse dynamics control computed in task space.

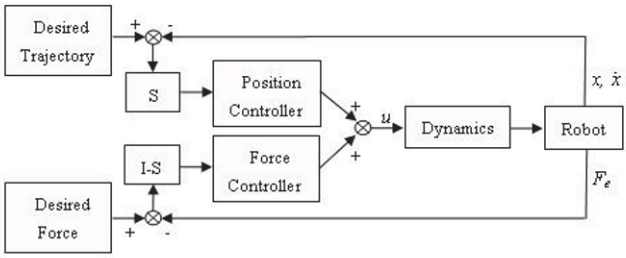

Figure 1. Hybrid control architecture.

The selection matrix S is diagonal with ones and zeros shown in Figure 1, which is used to decide that each DOF is uniquely specified as being either position controlled or force controlled.

We derive the control law as follows. Considering the dynamics of a parallel robot as equation (2) and the hybrid position/force control scheme in Figure 1, we define the control force as

$$F = M(X)SA_X + h(X, \dot{X}) + (I - S)A_f \tag{5}$$

where A_X and A_f are the outer loop control inputs for position control and force control respectively. The selection matrix S is diagonal with ones and zeros on the diagonal. When a one is present in S, position control is in effect. Otherwise, for force control, a zero is present.

Substituting equation (5) into (2) yields

$$M(X)(\ddot{X} - SA_X) + [F_e - (I - S)A_f] = 0 \tag{6}$$

Since we desire to control position, we would like to use a servo-control law for A_X discussed by Satya et al. (1995), and we add an integral term to the control law to eliminate steady-state error. Hence

$$A_X = \ddot{\rho}_d + K_d(\dot{\rho}_d - \dot{\rho}) + K_{Pp}(\rho_d - \rho) + K_{Pi}\int(\rho_d - \rho) \tag{7}$$

where K_d is the derivative gain, K_{Pp} is the proportional gain and K_{Pi} is the integral gain. and K_d, K_{Pp} and K_{Pi} are constant diagonal matrices, ρ_d is the desired position.

And we use a PI controller to achieve force tracking.

$$A_f = K_{Fp}(f_d - f) + K_{Fi}\int_0^t (f_d(u) - f(u))du \tag{8}$$

where K_{Fp}, K_{Fi} are constant diagonal matrices, f_d is the desired force.

Now we can simultaneously track motion and force by choosing

$$A_X = \left[a_{Xi}\right],\ A_f = \left[a_{fi}\right] \tag{9}$$

where

$$\begin{cases} a_{Xi} = \ddot{\rho}_{di} + K_{di}(\dot{\rho}_{di} - \dot{\rho}_i) + K_{Ppi}(\rho_{di} - \rho_i) + K_{Pii}\int(\rho_{di} - \rho_i) \\ a_{fi} = K_{Fpi}(f_{di} - f_i) + K_{Fii}\int_0^t (f_{di}(u) - f_i(u))du \end{cases} \tag{10}$$

$a_{fi} = 0$ if i belongs to the position controlled subspace; else i belongs to the force controlled subspace.

Base on the above discussion, we can get the block diagram of the hybrid control scheme as Figure 2.

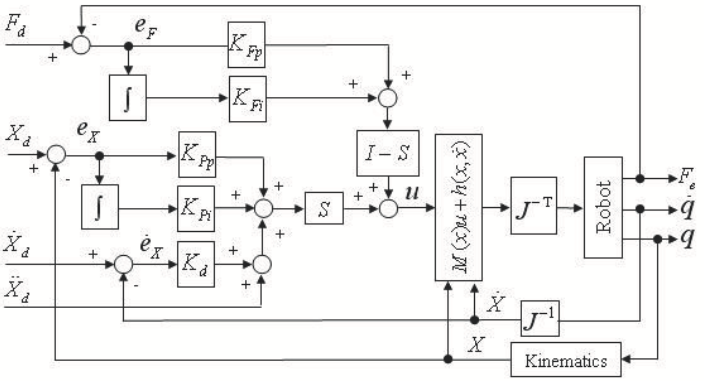

Figure 2. The control block scheme of the proposed hybrid control method.

4 Experiments

In this section, the proposed control method is applied to a new five-bar parallel manipulator and experimental results are presented.

4.1 Experimental Setup

The robot used in this experiment is shown in Figure 3. This manipulator has two degrees of freedom as illustrated in the schematic diagram of Figure 4. Two AC servo motors (FMA- CN04A-AB00) are attached to the joint A of link AE and C of link CG respectively. Motor rotations are measured by means of two incremental encoders with 2000 pulses/rev resolution. Velocity is estimated through numerical differentiator. An ATI GammaSI-130-10 force/torque sensor with a resolution of 0.05N is mounted at the end-effector. A low-pass second order filter is used to process the signal from force/torque sensor. The contact is achieved by a bearing whose purpose is to reduce tangential friction force which may arise from contact with the environment.

Communication with the manipulator is provided by a data acquisition card (Quanser Q8 H.I.L Control Board) mounted in PCI slot of a personal computer and terminal board.

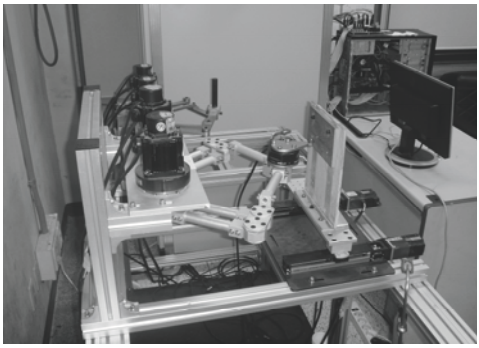

Figure 3. The experimental setup.

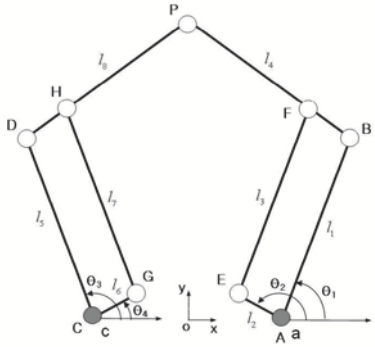

Figure 4. The schematic diagram.

The system software core is WinCon, real-time Windows XP application. It allows running code generated from a Simulink diagram in real-time on the same PC. Acquisition and control were performed with sampling time of 0.001 s.

Chung et al. (2001) investigated the kinematic analysis and performance of this parallel robot. We can get the Jacobian matrix and kinematic equations of the parallel manipulator from it.

The dynamic model of this manipulator can be described by equation (1) as explained in section 2. The parameters of the robot can be detailed as

$$M(q)=\begin{bmatrix} m_{11} & m_{12} & 0 & 0 \\ m_{21} & m_{22} & 0 & 0 \\ 0 & 0 & m_{33} & m_{34} \\ 0 & 0 & m_{43} & m_{44} \end{bmatrix},\ h(q,\dot{q})=\begin{bmatrix} 0 & h_{12} & 0 & 0 \\ h_{21} & 0 & 0 & 0 \\ 0 & 0 & 0 & h_{34} \\ 0 & 0 & h_{43} & 0 \end{bmatrix},\ u=\begin{bmatrix} 0 \\ u_2 \\ 0 \\ u_4 \end{bmatrix} \quad (11)$$

where

$m_{11}=m_1 l_{c1}^{\ 2}+m_3 l_{c3}^{\ 2}+m_4 l_1^{\ 2}+I_1+I_3$, $m_{12}=m_{21}=(m_3 l_2 l_{c3}+m_4 l_1 l_{c4})\cos(\theta_2-\theta_1)$,
$m_{22}=m_2 l_{c2}^{\ 2}+m_3 l_2^{\ 2}+m_4 l_{c4}^{\ 2}+I_2+I_4$, $m_{33}=m_5 l_{c5}^{\ 2}+m_7 l_{c7}^{\ 2}+m_8 l_5^{\ 2}+I_5+I_7$,
$m_{34}=m_{43}=(m_7 l_6 l_{c7}+m_8 l_5 l_{c8})\cos(\theta_4-\theta_3)$, $m_{44}=m_6 l_{c6}^{\ 2}+m_7 l_6^{\ 2}+m_8 l_{c8}^{\ 2}+I_6+I_8$,
$h_{12}=-(m_3 l_2 l_{c3}+m_4 l_1 l_{c4})\sin(\theta_2-\theta_1)\dot{\theta}_2$, $h_{21}=(m_3 l_2 l_{c3}+m_4 l_1 l_{c4})\sin(\theta_2-\theta_1)\dot{\theta}_1$,
$h_{34}=-(m_7 l_6 l_{c7}+m_8 l_5 l_{c8})\sin(\theta_4-\theta_3)\dot{\theta}_4$, $h_{43}=(m_7 l_6 l_{c7}+m_8 l_5 l_{c8})\sin(\theta_4-\theta_3)\dot{\theta}_3$.

θ_i denotes the joint angle; m_i, l_i and l_{ci} denote the mass, the length and the distance from the previous joint to the center of mass of link i respectively; I_i denotes the moment of inertia of link i about an axis coming out of the page, passing through the center of mass of link i.

4.2 Approaching and Contacting a Stiff Wall

The first experiment is to test the performance of the robot with the proposed control method when the end-effector approaches and contacts a stiff environment. A wooden wall was used as the environment object.

For the 2-DOF manipulator, the selection matrix was S=diag(1,0). Along the position controlled direction, $\ddot{X}_d=0$, $\dot{X}_d=0$, $X_d=X_0$, X_0 is the initial position. For the force controlled direction, the desired force was 20N. The end-effector was controlled to approach and contact the wooden wall along the normal. Figure 5 is the force response. We can see that the system remains stable after the collision from it. Figure 6 shows the position response of the end-effector.

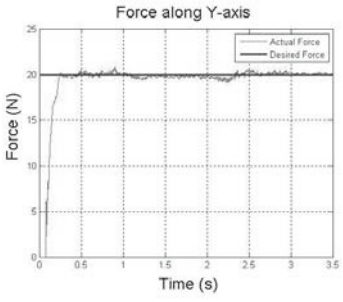

Figure 5. Force response.

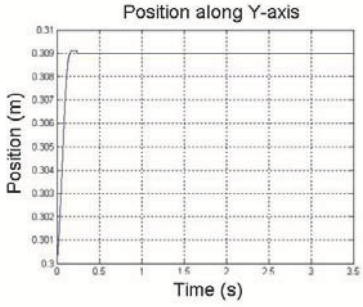

Figure 6. Position response.

Approaching objects is an important phase of automatic tasks with robots. This experiment shows that the proposed control method is competent to control the manipulator to approach and contact the stiff environment. And the distance between the end-effector and the object surface can be totally unknown.

4.3 Trajectory Tracking in Unconstrained Environment

A trapezoidal velocity profile is assigned in Y-axis, which imposes the resulting trajectory formed by a linear segment connected by two parabolic segments to the initial and final positions. The position of the start and end points of the trajectory is (0, 0.2) and (0, 0.3) respectively. The selection matrix was S=diag(1,1), both directions were position controlled. The end-effector moved along the trajectory in 10 seconds. Figure 7 shows position error of the end-effector.

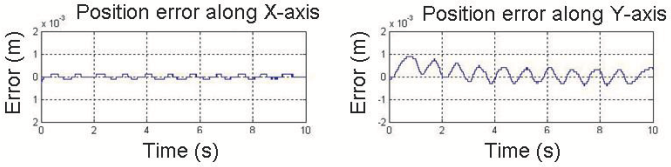

Figure 7. Position error of the end-effector.

From Figures 7, we can see that the manipulator can follow the desired trajectories within small error during the whole tracking process.

4.4 Trajectory Tracking in Constrained Environment

The last experiment is designed to demonstrate the effective control of force and position in a constrained environment. The selection matrix also was S=diag(1,0). The X-axis was position controlled, and the Y-axis was force controlled. The position trajectory of the end-effector along X direction is illustrated in Figure 8. The external force along Y direction shown in Figure 9 was applied to the end-effector.

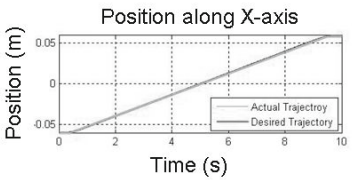

Figure 8. Position of the end-effector.

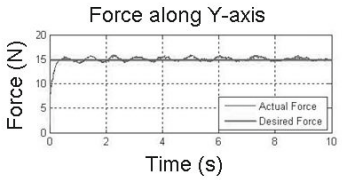

Figure 9. Force of the end-effector.

From Figures 8-9, we can see that the hybrid position/force control method has the ability to control the position and force in the constrained environment. All the experimental results show that the proposed dynamics based hybrid control strategy can control the parallel manipulator working in both the unconstrained environment and the constrained environment.

5 Conclusions

Parallel robot manipulators are beginning to play an important role in industry, especially in process of assembly, grinding, deburring and so on. They need position/force control in unconstraint and constraint environment at different time. Based on the task of position/force control, we designed two controllers for position control and force control respectively. This work shows satisfactory performance when such control techniques were implemented on a two degree of freedom parallel robot. Several experiments have been done to test the control scheme. The results have confined the effectiveness of the proposed control approach.

Bibliography

D. E. Whitney. Force feedback control of manipulator fine motions. *Trans. ASME, J. DSMC*, vol. 99, 91–97, June 1977.

K. J. Salisbury. Active stiffness control of a manipulator in Cartesian coordinates. *In Proc. 19th IEEE Conf. Decision and Control*, 95–100, Nov. 1980.

O. Khatib. The operational space formulation in the analysis, design, and control of robot manipulators. *In Proc. 3rd Znt. Symp. Robotics Research*, 103–110, Oct. 1985.

M. Callegari, M. C. Palpacelli, M. Principi. Dynamics modelling and control of the 3-RCC translational platform. *Mechatronics*, vol. 16, 589–605, 2006.

Y. M. Li, Q. S. Xu. Dynamic modeling and robust control of a 3-PRC translational parallel kinematic machine. *Robotics and Computer-Integr. Manuf.*, vol. 25, 630–640, 2009.

J. P. Merlet. A generic trajectory verifier for the motion planning of parallel robots. *Trans. of the ASME, J. of Mech. Design*, vol. 123, no. 4, 510–515, Des. 2001.

L. W. Tsai. Robot Analysis: The Mechanics of Serial and Parallel Manipulators. New York: John Wiley & Sons, Inc., 1999.

M. H. Raibert and J. J. Craig. Hybrid Position/Force Control of Manipulators. *ASME J. of Dynamic System, Measurement and Control*, Vol. 102, 126–133, 1981.

T. Yoshikawa. Dynamic hybrid position/force control of robot manipulators-description of hand constraints and calculation of joint driving force. *IEEE J. of Robotics and Automation*, Vol. RA-3, No. 5, 386–392, Oct. 1987.

S. M. Satya and M.W. Spong. Hybrid control of a planar 3-Dof parallel manipulator for machining operations", *Trans. of the NAMRI/SME*, Vol. 23; 273–280, 1995.

Y. H. Chung and J. W. Lee. SenSation: A new translational 2 DOF haptic device with parallel mechanism. *Trans. on Control, Autom., and Syst. Eng.*, Vol. 3, 217–222, 2001.

Decoupled Parallel Manipulator with Universal Joints and Additional Constraints

Leonid Tyves[1], Victor Glazunov[1], Pavel Danilin[1], Nguyen Minh Thanh[2]

[1]Mechanical Engineering Research Institute of RAS, Moscow, Russia
[2]HoChiMinh City University of Transport, HoChiMinh City, Vietnam

Abstract. Decoupled parallel manipulator with three parallel kinematic chains is considered. Each kinematic chain contains two universal joints with additional constraints. The synthesis of this manipulator is carried out by means of screw groups. This approach allows avoiding completed equations by synthesis and singularity analysis of mechanisms.

1 Introduction

It is well-known that the closed-loops of parallel manipulators cause high stiffness and payload capacity (Merlet, 2000, Cecarelli, 2004, Kong and Gosselin, 2007). However, due to the coupling between kinematic chains, control of the motions of the moving platform (end-effector) becomes complicated. There exist different solutions of this problem. One of them is to arrange for coincidence of centers of the spherical kinematic pairs of three identical kinematic chains S-P-S of the Gough-Stewart platform (Koliskor, 1986, Innocenti and Parenti-Castelli, 1991). Another solution corresponds to the special architecture of the U-P-U kinematic chains of a 6 degrees of freedom (6-DOF) parallel manipulator in which three U-joints mounted on the moving platform are designed as a spherical mechanism (Mianovski, 2007).

Another approach to a solution of this problem is applicable for a parallel manipulator with reduced degrees of freedom. For example, the well known Delta robot consists of three R-R-P-R kinematic chains causing translation motions of the moving platform and of one R-U-P-U kinematic chain, causing rotation about the vertical axis (Clavel, 1990). This robot corresponds to Schoenflies motions besides, in this robot, three translation motions and one rotation motion are decoupled. Another well known robot with Shoenflies motions of the platform is PAMINSA (Arakelyan et al., 2005). In this manipulator one vertical motion is decoupled from planar motions.

Note that the translation kinematic pairs can be represented as planar four-bar parallelograms (Mianovski, 2007, Clavel, 1990, Gogu, 2009). By this approach

numerous families of decoupled and translation parallel mechanisms are obtained.

A 6-DOF manipulator with decoupled translation and rotation motions and with linear and rotating actuators is synthesized by means of geometrical constraints (Yan Jin et al., 2007). This manipulator consists of three kinematic R-P-P-P-R-R chains.

In this paper, we use the approach to synthesis of decoupled parallel manipulators based on closed screw groups (Dimentberg, 1965) that include all the screw products of the main members of these groups. Similar screw groups are considered from different viewpoints (Sugimoto, 1990, Herve, 1991, Angeles, 2004, Glazunov, 1995). In this article a new decoupled 6-DOF parallel manipulator is proposed which consists of three kinematic R-P-P-P-R-R chains where two P-pairs correspond to two U-joints with additional constraints. Structural design is discussed with details but no performance characteristics are outlined.

With regard to the determination of the singularity the Jacobian matrices can be applied (Gosselin and Angeles, 1990). Using this approach one needs to differentiate equations expressing the constraints. In this paper we use the screw groups approach to describe singularities which allows avoidance of mathematical equations.

2 The kinematic chains with universal joints and additional constraints and 4-DOF mechanisms

Let us consider a kinematic chain with two universal joints (Figure 1, a). These U-joints can be represented by four rotation kinematic pairs. In particular, the Plücker coordinates of the unit screws $\boldsymbol{E_1}$, $\boldsymbol{E_2}$, $\boldsymbol{E_3}$, $\boldsymbol{E_4}$ of the R-pairs can be expressed as $\boldsymbol{E_1}$ *(1, 0, 0, 0, 0, 0),* $\boldsymbol{E_2}$ *(0, 1, 0, 0, 0, 0),* $\boldsymbol{E_3}$ *(1, 0, 0, 0,* e^o_{3y}, e^o_{3z}*),* $\boldsymbol{E_4}$ *(0, 1, 0,* e^o_{4x}, *0,* e^o_{4z}*).* This chain can transfer rotations from the input axis to the output axis. These axes are drown vertical.

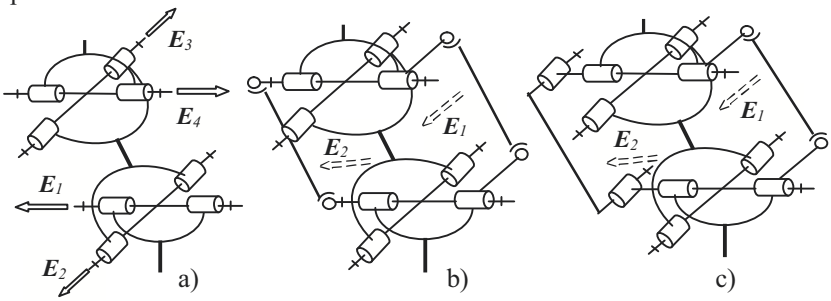

Figure 1. The kinematic chains with universal joints and additional constraints.

In order to retain the constant orientation of the output axis relating to the input axis two additional constraints can be mounted between the U-joints (Figure 1, b, c). One of these constraints can be mounted by R-pairs (Figure 1, c). The kinematic chain with additional constraints can be represented by two P-pairs. The Plücker coordinates of the unit screws $\boldsymbol{E_1}$, $\boldsymbol{E_2}$ of the P-pairs can be expressed as $\boldsymbol{E_1}$ $(0, 0, 0, e^o_{1x}, e^o_{1y}, e^o_{1z})$, $\boldsymbol{E_2}$ $(0, 0, 0, e^o_{2x}, e^o_{2y}, e^o_{2z})$. The axes of the P-pairs are perpendicular each to another and to the link connecting the U-joints. This chain transfers rotations from the input axis to the output axis and retain orientation of the output axis.

Now let us consider a parallel mechanism of Schoenflies motions (Figure 2, a).

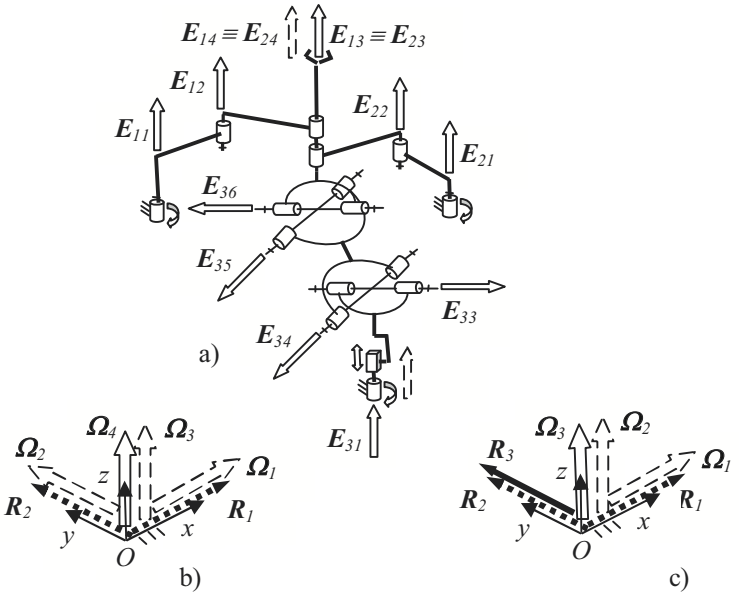

Figure 2. The Schoenflies motion parallel mechanism.

The first and the second kinematic chains consist of one actuated rotation pair (rotating actuator) situated on the base, two rotation kinematic pairs and one prismatic kinematic pair (the axes of all the pairs of these two chains are parallel). The third kinematic chain consists of one actuated rotation pair (rotating actuator) situated on the base, one actuated prismatic pair (linear actuator) (the axes of rotating and linear actuators coincide) and two U-joints represented as two rotation kinematic pairs. The unit screws of the axes of these kinematic pairs can be represented by coordinates: $\boldsymbol{E_{11}}$ $(0, 0, 1, e^o_{11x}, e^o_{11y}, 0)$, $\boldsymbol{E_{12}}$ $(0, 0, 1, e^o_{12x}, e^o_{12y}, 0)$,

$\boldsymbol{E_{13}}$ (0, 0, 1, e^{o}_{13x}, e^{o}_{13y}, 0), $\boldsymbol{E_{14}}$ (0, 0, 0, 0, 0, 1), $\boldsymbol{E_{21}}$ (0, 0, 1, e^{o}_{21x}, e^{o}_{21y}, 0), $\boldsymbol{E_{22}}$ (0, 0, 1, e^{o}_{22x}, e^{o}_{22y}, 0), $\boldsymbol{E_{23}}$ (0, 0, 1, e^{o}_{23x}, e^{o}_{23y}, 0), $\boldsymbol{E_{24}}$ (0, 0, 0, 0, 0, 1), $\boldsymbol{E_{31}}$ (0, 0, 1, e^{o}_{31x}, e^{o}_{31y}, 0), $\boldsymbol{E_{32}}$ (0, 0, 0, 0, 0, 1), $\boldsymbol{E_{33}}$(e_{33x}, e_{33y}, 0, e^{o}_{33x}, e^{o}_{33y}, e^{o}_{33z}), $\boldsymbol{E_{34}}$(e_{34x}, e_{34y}, 0, e^{o}_{34x}, e^{o}_{34y}, e^{o}_{34z}), $\boldsymbol{E_{35}}$(e_{35x}, e_{35y}, 0, e^{o}_{35x}, e^{o}_{35y}, e^{o}_{35z}), $\boldsymbol{E_{36}}$ (e_{36x}, e_{36y}, 0, e^{o}_{36x}, e^{o}_{36y}, e^{o}_{36z}).

The screws $\boldsymbol{E_{14}}$, $\boldsymbol{E_{24}}$, $\boldsymbol{E_{32}}$, are of infinite pitch. All other screws are of zero pitch. The first and the second kinematic chains impose the same constraints corresponding to four-member closed screw group, so that one can insert other similar chains between the base and platform and the degree of freedom will remain equal to four. The third kinematic chain does not impose any constraints. The wrenches of the constraints have coordinates (Figure 2, b): $\boldsymbol{R_1}$ (0, 0, 0, 1, 0, 0), $\boldsymbol{R_2}$ (0, 0, 0, 0, 1, 0). All the twists of motions of the platform can be represented by the twists reciprocal to the wrenches of the constraints (Figure 2, b): $\boldsymbol{\Omega_1}$ (0, 0, 0, 1, 0, 0), $\boldsymbol{\Omega_2}$ (0, 0, 0, 0, 1, 0), $\boldsymbol{\Omega_3}$ (0, 0, 0, 0, 0, 1), $\boldsymbol{\Omega_4}$ (0, 0, 1, 0, 0, 0).

In this mechanism singularities corresponding to loss of one degree of freedom exist if four screws $\boldsymbol{E_{i1}}$, $\boldsymbol{E_{i2}}$, $\boldsymbol{E_{i3}}$ and $\boldsymbol{E_{i4}}$ ($i = 1, 2$) or if six screws $\boldsymbol{E_{31}}$, $\boldsymbol{E_{32}}$, $\boldsymbol{E_{33}}$, $\boldsymbol{E_{34}}$, $\boldsymbol{E_{35}}$ and $\boldsymbol{E_{36}}$ are linearly dependent. It is possible if three axes $\boldsymbol{E_{i1}}$, $\boldsymbol{E_{i2}}$, $\boldsymbol{E_{i3}}$ ($i = 1, 2$) are situated on the same plane or if the link connecting the U-joints in the third chain is horizontal. In particular if the axes $\boldsymbol{E_{11}}$, $\boldsymbol{E_{12}}$, $\boldsymbol{E_{13}}$ are situated on the plane parallel to the *y* axis then there exist three wrenches (Figure 2, c) of constraints imposed by the kinematic chains: $\boldsymbol{R_1}$ (0, 0, 0, 1, 0, 0), $\boldsymbol{R_2}$(0, 0, 0, 0, 1, 0) and $\boldsymbol{R_3}$ (0, 1, 0, 0, 0, 0) and only three twists of motion of the platform reciprocal to these wrenches $\boldsymbol{\Omega_1}$ (0, 0, 0, 1, 0, 0), $\boldsymbol{\Omega_2}$ (0, 0, 0, 0, 0, 1) and $\boldsymbol{\Omega_3}$ (0, 0, 1, 0, 0, 0). This mechanism is particularly decoupled. The rotating actuator drives the orientation of the end-effector. The linear actuators drive the position of the end-effector.

Now let us consider a parallel mechanism of Schoenflies motions containing one kinematic chain with two universal joints and additional constraints (Figure 3, a). The first and the second kinematic chains consist of one actuated prismatic pair, one spherical pair and two rotation pairs with intersecting axes. The third kinematic chain consists of one actuated rotation pair, one actuated prismatic pair and two U-joints represented as two rotation kinematic pairs. The unit screws of the axes of these kinematic pairs can be represented by coordinates: $\boldsymbol{E_{11}}$ (0, 0, 0, 1, 0, 0), $\boldsymbol{E_{12}}$ (1, 0, 0, 0, e^{o}_{12y}, e^{o}_{12z}), $\boldsymbol{E_{13}}$ (0, 1, 0, e^{o}_{13x}, 0, e^{o}_{13z}), $\boldsymbol{E_{14}}$ (0, 0, 1, e^{o}_{14x}, e^{o}_{14y}, 0), $\boldsymbol{E_{15}}$(e_{15x}, e_{15y}, 0, e^{o}_{15x}, e^{o}_{15y}, e^{o}_{15z}), $\boldsymbol{E_{16}}$ (0, 0, 1, e^{o}_{16x}, e^{o}_{16y}, 0), $\boldsymbol{E_{21}}$ (0, 0, 0, 0, 1 , 0), $\boldsymbol{E_{22}}$ (1, 0, 0, 0, e^{o}_{22y}, e^{o}_{22z}), $\boldsymbol{E_{23}}$ (0, 1, 0, e^{o}_{23x}, 0, e^{o}_{23z}), $\boldsymbol{E_{24}}$ (0, 0, 1, e^{o}_{24x}, e^{o}_{24y}, 0), $\boldsymbol{E_{25}}$(e_{25x}, e_{25y}, 0, e^{o}_{25x}, e^{o}_{25y}, e^{o}_{25z}), $\boldsymbol{E_{26}}$ (0, 0, 1, e^{o}_{26x}, e^{o}_{26y}, 0), $\boldsymbol{E_{31}}$ (0, 0, 1, e^{o}_{31x}, e^{o}_{31y}, 0), $\boldsymbol{E_{32}}$ (0, 0, 0, 0, 0, 1), $\boldsymbol{E_{33}}$ (0, 0, 0, e^{o}_{33x}, e^{o}_{33y}, e^{o}_{33z}), $\boldsymbol{E_{34}}$ (0, 0, 0, e^{o}_{34x}, e^{o}_{34y}, e^{o}_{34z}). The screws $\boldsymbol{E_{12}}$, $\boldsymbol{E_{13}}$, $\boldsymbol{E_{14}}$, $\boldsymbol{E_{15}}$, $\boldsymbol{E_{16}}$, $\boldsymbol{E_{21}}$, $\boldsymbol{E_{22}}$, $\boldsymbol{E_{23}}$, $\boldsymbol{E_{24}}$, $\boldsymbol{E_{25}}$, $\boldsymbol{E_{26}}$, $\boldsymbol{E_{31}}$ are of zero pitch. All other screws are of infinite pitch. The first and the second kinematic chains do not impose any constraints. The third kinematic chain imposes two constraints corresponding to four-member closed screw group. The

wrenches of the constraints have coordinates (Figure 3, b): $\boldsymbol{R_1}$ *(0, 0, 0, 1, 0, 0),* $\boldsymbol{R_2}$ *(0, 0, 0, 0, 1, 0).* All the twists of motions of the platform can be represented by the twists reciprocal to the wrenches of the constraints (Figure 3, b): $\boldsymbol{\Omega_1}$ *(0, 0, 0, 1, 0, 0),* $\boldsymbol{\Omega_2}$ *(0, 0, 0, 0, 1, 0),* $\boldsymbol{\Omega_3}$ *(0, 0, 0, 0, 0, 1),* $\boldsymbol{\Omega_4}$ *(0, 0, 1, 0, 0, 0).* The twists $\boldsymbol{\Omega_1}$, $\boldsymbol{\Omega_2}$ and $\boldsymbol{\Omega_3}$ are of infinite pitch, the twist $\boldsymbol{\Omega_4}$ is of zero pitch.

In this mechanism singularities corresponding to loss of one degree of freedom exist if six screws $\boldsymbol{E_{i1}}$, $\boldsymbol{E_{i2}}$, $\boldsymbol{E_{i3}}$, $\boldsymbol{E_{i4}}$, $\boldsymbol{E_{i5}}$ and $\boldsymbol{E_{i6}}$ *(i = 1, 2)* or if four screws $\boldsymbol{E_{31}}$, $\boldsymbol{E_{32}}$, $\boldsymbol{E_{33}}$, and $\boldsymbol{E_{34}}$ are linearly dependent. It is possible if one of the axes of the links connecting the axes $\boldsymbol{E_{i4}}$ and $\boldsymbol{E_{i5}}$ *(i = 1, 2)* is perpendicular to the axis $\boldsymbol{E_{i1}}$ or if the axis of the link connecting the U-joints of the third chain is perpendicular to $\boldsymbol{E_{32}}$.

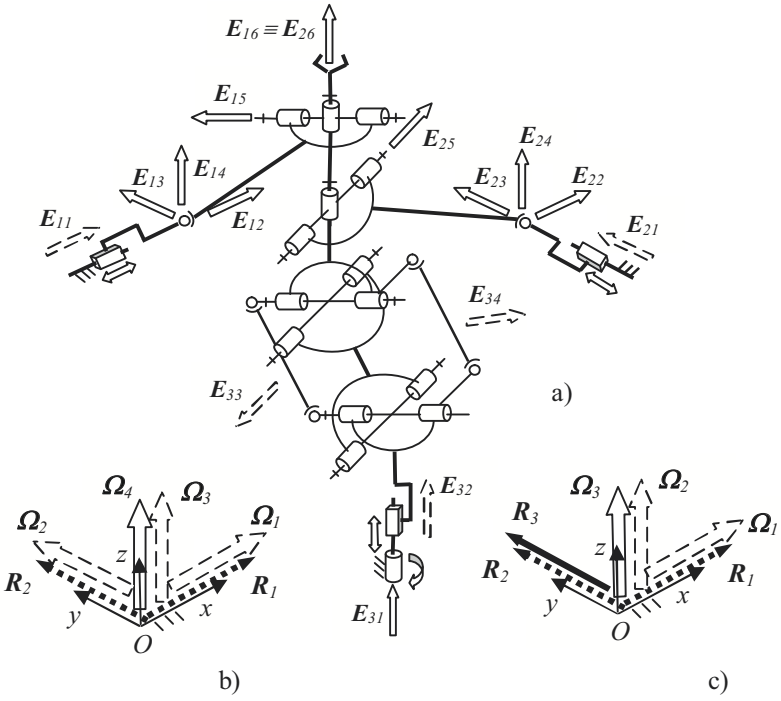

Figure 3. The Schoenflies motion mechanism with U-joints and additional constraints.

In particular if the axis of the link connecting the U-joints of the third chain is parallel to the *y* axis then there exist three wrenches (Figure 3, c) of constraints imposed by the kinematic chains: $\boldsymbol{R_1}$ *(0, 0, 0, 1, 0, 0),* $\boldsymbol{R_2}$*(0, 0, 0, 0, 1, 0)* and $\boldsymbol{R_3}$ *(0, 1, 0, 0, 0, 0)* and only three twists of motion of the platform reciprocal to these wrenches $\boldsymbol{\Omega_1}$ *(0, 0, 0, 1, 0, 0),* $\boldsymbol{\Omega_2}$ *(0, 0, 0, 0, 0, 1)* and $\boldsymbol{\Omega_3}$ *(0, 0, 1, 0, 0, 0).*

3 The design of 6-DOF decoupled parallel mechanism

In this section, let us consider a 6-DOF decoupled parallel mechanism 3 R-P-P-P-R-R (Figure 4, a). Each kinematic chain consists of one rotating actuator situated on the base, one linear actuator, two prismatic kinematic pairs represented as two U-joints with additional constraints and two passive rotation pairs.

The axes of all the passive rotation pairs intersect in the same point O which is the origin of the coordinate system. This point O is movable but the directions of the coordinate axes are constant. The unit screws of the axes of kinematic pairs have coordinates: $\boldsymbol{E_{11}}$ (1, 0, 0, 0, 0, 0), $\boldsymbol{E_{12}}$ (0, 0, 0, 1, 0, 0), $\boldsymbol{E_{13}}$ (0, 0, 0, e^o_{13x}, e^o_{13y}, e^o_{13z}), $\boldsymbol{E_{14}}$ (0, 0, 0, e^o_{14x}, e^o_{14y}, e^o_{14z}), $\boldsymbol{E_{15}}$ (e_{15x}, e_{15y}, e_{15z}, 0, 0, 0), $\boldsymbol{E_{16}}$ (e_{16x}, e_{16y}, e_{16z}, 0, 0, 0), $\boldsymbol{E_{21}}$ (0, 1, 0, 0, 0, 0), $\boldsymbol{E_{22}}$ (0, 0, 0, 0, 1, 0), $\boldsymbol{E_{23}}$ (0, 0, 0, e^o_{23x}, e^o_{23y}, e^o_{23z}), $\boldsymbol{E_{24}}$ (0, 0, 0, e^o_{24x}, e^o_{24y}, e^o_{24z}), $\boldsymbol{E_{25}}$ (e_{25x}, e_{25y}, e_{25z}, 0, 0, 0), $\boldsymbol{E_{26}}$ (e_{26x}, e_{26y}, e_{26z}, 0, 0, 0), $\boldsymbol{E_{31}}$ (0, 0, 1, 0, 0, 0), $\boldsymbol{E_{32}}$ (0, 0, 0, 0, 0, 1), $\boldsymbol{E_{33}}$(0, 0, 0, e^o_{33x}, e^o_{33y}, e^o_{33z}), $\boldsymbol{E_{34}}$ (0, 0, 0, e^o_{34x}, e^o_{34y}, e^o_{34z}), $\boldsymbol{E_{35}}$ (e_{35x}, e_{35y}, e_{35z}, 0, 0, 0), $\boldsymbol{E_{36}}$ (e_{36x}, e_{36y}, e_{36z}, 0, 0, 0). The screws $\boldsymbol{E_{i1}}$, $\boldsymbol{E_{i5}}$, $\boldsymbol{E_{i6}}$ are of zero pitch, the screws $\boldsymbol{E_{i2}}$, $\boldsymbol{E_{i3}}$, $\boldsymbol{E_{i4}}$ are of infinite pitch (i = 1, 2, 3).

All six twists of motions of the platform can be represented as: $\boldsymbol{\Omega_1}$ (1, 0, 0, 0, 0, 0), $\boldsymbol{\Omega_2}$ (0, 1, 0, 0, 0, 0), $\boldsymbol{\Omega_3}$ (0, 0, 1, 0, 0, 0), $\boldsymbol{\Omega_4}$ (0, 0, 0, 1, 0, 0), $\boldsymbol{\Omega_5}$ (0, 0, 0, 0, 1, 0), $\boldsymbol{\Omega_6}$ (0, 0, 0, 0, 0, 1). If rotating actuators are fixed then the linear actuators drive translation motions of the end-effector. By this the kinematic pairs corresponding to the screws $\boldsymbol{E_{i2}}$, $\boldsymbol{E_{i3}}$, $\boldsymbol{E_{i4}}$ are used. If linear actuators are fixed then the rotating actuators drive orientation motions of the end-effector. By this the kinematic pairs $\boldsymbol{E_{i1}}$, $\boldsymbol{E_{i5}}$, $\boldsymbol{E_{i6}}$ are used and rotations are transferred by the U-joints.

In considered mechanism (Figure 4, a) singularities expressed by loss of one or more degrees of freedom exist if any six screws $\boldsymbol{E_{i1}}$, $\boldsymbol{E_{i2}}$, $\boldsymbol{E_{i3}}$, $\boldsymbol{E_{i4}}$, $\boldsymbol{E_{i5}}$, $\boldsymbol{E_{i6}}$ (i = 1, 2, 3) are linearly dependent. It is possible if at least one of the axes of the links connecting the U-joints is perpendicular to the axis $\boldsymbol{E_{i2}}$. In particular if the axis of the link connecting the U-joints of the third chain is parallel to the y axis then there exists one wrench of the constraint imposed by this kinematic chain: $\boldsymbol{R}$ (0, 1, 0, 0, 0, 0) and only five twists of motion of the platform reciprocal to this wrench $\boldsymbol{\Omega_1}$ (1, 0, 0, 0, 0, 0), $\boldsymbol{\Omega_2}$ (0, 0, 1, 0, 0, 0), $\boldsymbol{\Omega_3}$ (0, 0, 1, 0, 0, 0), $\boldsymbol{\Omega_4}$ (0, 0, 0, 1, 0, 0) and $\boldsymbol{\Omega_5}$ (0, 0, 0, 0, 1, 0). If the unit screws $\boldsymbol{E_{11}}$ (1, 0, 0, 0, 0, 0), $\boldsymbol{E_{15}}$ (e_{15x}, e_{15y}, e_{15z}, 0, 0, 0), $\boldsymbol{E_{16}}$ (e_{16x}, e_{16y}, e_{16z}, 0, 0, 0) are coplanar then there exists one wrench of the constraint imposed by the first kinematic chain: $\boldsymbol{R}$ (0, 0, 0, 0, r^o_y, r^o_z) and only five twists of motion of the platform reciprocal to this wrench $\boldsymbol{\Omega_1}$ (1, 0, 0, 0, 0, 0), $\boldsymbol{\Omega_2}$ (ω_{2x}, ω_{2y}, ω_{2z}, 0, 0, 0), $\boldsymbol{\Omega_3}$ (0, 0, 0, 1, 0, 0), $\boldsymbol{\Omega_4}$ (0, 0, 0, 0, 1, 0), $\boldsymbol{\Omega_5}$ (0, 0, 0, 0, 0, 1). The wrench $\boldsymbol{R}$ is of infinite pitch, it is perpendicular to the axes $\boldsymbol{E_{11}}$, $\boldsymbol{E_{15}}$, $\boldsymbol{E_{16}}$.

If the actuators are fixed then the wrenches of the constraints have coordinates (Figure 4, b): $\boldsymbol{R_{11}}$ (r_{11x}, r_{11y}, r_{11z}, 0, 0, 0), $\boldsymbol{R_{12}}$ (0, 0, 0, r^o_{12x}, r^o_{12y}, r^o_{12z}), $\boldsymbol{R_{21}}$ (r_{21x}, r_{21y}, r_{21z}, 0, 0, 0), $\boldsymbol{R_{22}}$ (0, 0, 0, r^o_{22x}, r^o_{22y}, r^o_{22z}), $\boldsymbol{R_{31}}$ (r_{31x}, r_{31y}, r_{31z}, 0, 0, 0), $\boldsymbol{R_{32}}$ (0,

0, 0, r^{o}_{32x}, r^{o}_{32y}, r^{o}_{32z}). The wrenches $\boldsymbol{R_{i1}}$ and $\boldsymbol{R_{i2}}$ are imposed by the *i*-th kinematic chain. The wrenches $\boldsymbol{R_{i1}}$ are of zero pitch, the wrenches $\boldsymbol{R_{i2}}$ are of infinite pitch (*i = 1, 2, 3*). The wrenches $\boldsymbol{R_{i1}}$ are perpendicular to the links connecting the U-joints, the wrenches $\boldsymbol{R_{i2}}$ are perpendicular to the screws $\boldsymbol{E_{i5}}$ and $\boldsymbol{E_{i6}}$.

Singularities corresponding to non-controlled infinitesimal motion of the moving platform exist if the wrenches $\boldsymbol{R_{11}}$, $\boldsymbol{R_{12}}$, $\boldsymbol{R_{21}}$, $\boldsymbol{R_{22}}$, $\boldsymbol{R_{31}}$, $\boldsymbol{R_{32}}$ are linearly dependent. It is possible if the wrenches $\boldsymbol{R_{11}}$, $\boldsymbol{R_{21}}$, $\boldsymbol{R_{31}}$ or $\boldsymbol{R_{12}}$, $\boldsymbol{R_{22}}$, $\boldsymbol{R_{32}}$ are coplanar. In particular if the wrenches $\boldsymbol{R_{12}}$, $\boldsymbol{R_{22}}$, $\boldsymbol{R_{32}}$ are coplanar (Figure 4, c) then the twist $\boldsymbol{\Omega}$ (ω_x, ω_y, ω_z, *0, 0, 0)* exists which is perpendicular to the axes of the wrenches $\boldsymbol{R_{12}}$, $\boldsymbol{R_{22}}$, $\boldsymbol{R_{32}}$ and reciprocal to $\boldsymbol{R_{11}}$, $\boldsymbol{R_{12}}$, $\boldsymbol{R_{21}}$, $\boldsymbol{R_{22}}$, $\boldsymbol{R_{31}}$, $\boldsymbol{R_{32}}$.

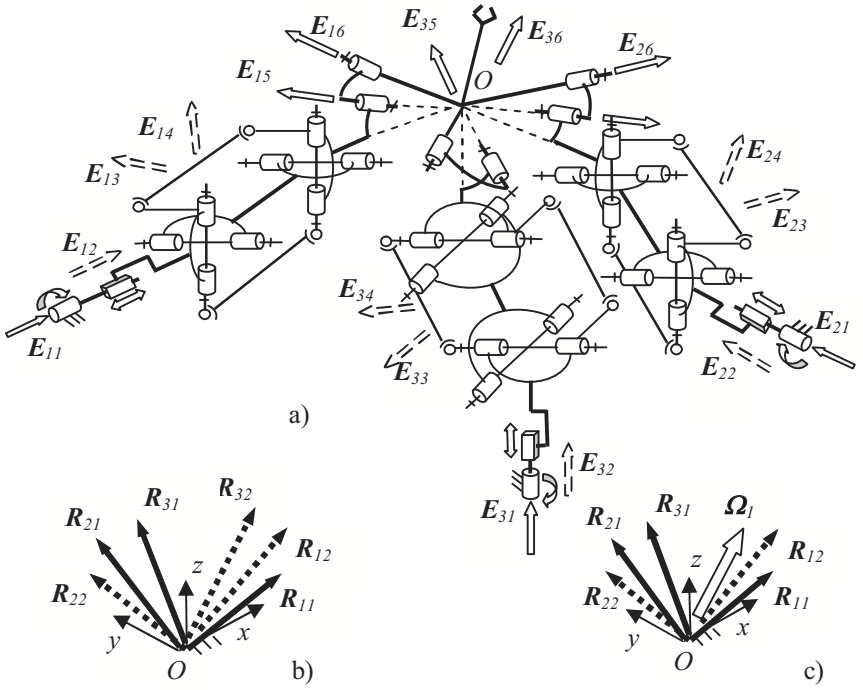

Figure 4. The 6-DOF decoupled parallel mechanism.

In this mechanism, also singularities exist corresponding both to loss of one degree of freedom and to non-controlled infinitesimal motion of the platform. The corresponding conditions are represented above. This mechanism is decoupled. The rotating actuators drive the orientation of the end-effector, the linear actuators drive the position of the end-effector.

4 Conclusion

In this article, new decoupled parallel manipulator consisting of three parallel kinematic chains containing U-joints with additional constraints is represented. The synthesis and the singularity analysis is carried out by using of Plücker coordinates of twists and wrenches corresponding to the kinematic chains. The application of closed screw groups allows obtaining all the twists of the platform and the wrenches of the constraints without any equations.

References

Merlet, J.-P. (2000). *Parallel Robots*. Kluwer Academic Publishers.

Ceccarelli, M. (2004). *Fundamentals of Mechanics of Robotic Manipulations.* Kluwer Academic Publishers.

Kong, X., Gosselin, C. (2007). *Type Synthesis of Parallel Mechanisms.* Springer.

Koliskor, A. (1986). The *l*-coordinate approach to the industrial robot design. In *V IFAC / IFIP / IMACS / IFORS Symposium*, Suzdal, URSS, April 22-25: 108-115.

Innocenti, C., Parenti-Castelli, V. (1991). Direct kinematics of the 6-4 fully parallel manipulator with position and orientation uncoupled. In *European Robotics and Intelligent Systems Conf.*, Corfou, June 23-28.

Mianovski, K. (2007). Singularity analysis of parallel manipulator POLMAN 3×2 with six degrees of freedm. In *12th IFToMM World Congress*, Besançon (France), June 18-21.

Clavel, R. (1987). Device for Displacing and Positioning an Element in Space. In *Patent WO 87/03528*.

Arakelian, V., Guegan, S., Briot, S. (2005). Static and Dynamic Analysis of the PAMINSA. In *ASME 2005. International Design Engineering Technical Conferences & Computers and Information in Engineering Conference.* Long Beach. CA, USA: 24-28.

Gogu, G. (2009). *Structural Synthesis of Parallel Robots, Part 2: Translational Topologies with Two and Three Degrees of Freedom,* Springer, Dordrecht.

Yan Jin, I-Ming Chen, Guilin Yang. (2007). Structure Synthesis of 6-DOF 3-3 Decoupled Parallel Manipulators. In *12th IFToMM World Congress*, Besançon, June 18-21.

Dimentberg, F. (1965). *The Screw Calculus and its Applications in Mechanics.* Nauka. (Eng. trans.: AD680993, Clearinghouse for Federal Tech. and Sc. Inf., Virginia).

Sugimoto, K. (1990). Existence Criteria for Overconstrained Mechanisms: An Extension of Motor Algebra. In *Tr. ASME, J. of Mech. Design,* 3: 295-298.

Herve, J. (1991). The Lie group of rigid body displacements, a fundamental tool for mechanism design. In *Mechanism and Machine theory,* 34: 719-730.

Angeles, J. (2004). The Qualitative Synthesis of Parallel Manipulators. In *Journal of Mechanical Design,* 126: 617-624.

Glazunov, V. (1995). Principles of the construction and analysis of spatial parallel structure mechanisms. In *Jour. of Mach. Manuf. and Reliab.,* Aller. Press Inc. 1: 10-15.

Gosselin, C., and Angeles, J. (1990). Singularity Analysis of Closed Loop Kinematic Chains. In *IEEE Trans. on Robotics and Automation*, 6(3): 281-290.

Positio: A 4R Serial Manipulator Having a Surface of Isotropic Positioning

Khaled Akrout and Luc Baron*
Ecole Polytechnique de Montreal
Montreal, QC, Canada
(Khaled.Akrout, Luc.Baron)@polymtl.ca

Abstract A new 4-revolute serial manipulator having a non-trivial path of positioning isotropy is introduced. As opposed to only isolated isotropic postures, the operational point of the end-effector can move on the surface of a sphere, while maintaining an isotropic posture. Moreover, the orientation ability of this manipulator is very close to isotropy, since its condition number is $\sqrt{2}$ on this surface.

1 Introduction

This paper introduces a new 4-revolute (4R) serial manipulator having a non-trivial path of positioning isotropy. A manipulator is said *isotropic* if its Jacobian matrix can reach isotropic values—i.e. the minimum condition numLucber of unity—at least at a single posture within its workspace (Salisbury and Craig, 1982). The design of manipulators able to reach isotropy is of particular interest because they exhibit their best kinematic performances in such postures, namely *isotropic postures* (Chablat and Angeles, 2000). Consequently, many research works have been conducted toward finding architectures capable to reach isotropy and their corresponding isotropic postures. When the concept of isotropy is applied to serial manipulators, two basic properties have been pointed out in the literature. First, the isotropy is not affected by Luca rotation of the first joint, and hence, a point P of the end-effector (EE) can undergo a *trivial path*—i.e. a circle—, while being at the same isotropic posture (Salisbury and Craig, 1982). Second, the isotropy of an orienting serial chain is not affected by a rotation of the last joint (Angeles, 2003).

For positioning tasks, a 2R, a 3R and a 4R planar serial manipulators have, respectively, 2, 2 and 4 isotropic postures along a trivial path (Angeles,

*The authors acknowledge the financial support of NSERC under grant RGPIN-203618.

1992; Chablat and Angeles, 2000). A 4R spatial serial manipulator has also isotropic postures along a trivial path (Angeles, 1992). For orienting tasks, a 3R, 4R and 5R spherical serial manipulators have isotropic postures along a trivial pathLuc (Chablat and Angeles, 2003; Baron and Wang, 2008). Recently, a 6R spherical serial manipulator has been proposed by Akrout and Baron (2009), for which the EE can undergo a non-trivial path—any EE orientation—, while being at the same isotropic posture. In fact, this manipulator is obtained from the serial composition of two isotropic 3R orienting manipulators. The non-trivial path comes from the trivial path of the first joint together with the trivial path of the intermediate joints of the two sub-chains, i.e., joints 3 and 4.

For both positioning and orienting tasks, it is required to render dimensionless the jacobian matrix by dividing both sides of the veLuclocity equation of point P by a *characteristic length* of the manipulator. This length is defined as the one minimizing the condition number of the dimensionless jacobian (Angeles, 1992). Resorting to this characteristic length, the nR planar serial isotropic manipulators have isotropic postures along a trivial path (Angeles, 1992). Similarly, the 6R spatial serial manipulator, called *diestro*, has also isotropic postures along a trivial path (F. Ranjbaran and Gonzalez-Palacios, 1995).

In this paper, a new 4R spatial serial manipulator is proposed, for which a point P of the EE can undergo a *non-trivial path*—the surface of a sphere—, while being at the same isotropic posture. This manipulator is obtained from the serial composition of an isotropic 3R orienting manipulators followed by an isotropic 2R planar manipulator with a shared intermediate revolute joint, thus resulting in a 4R spatial serial manipulator with isotropic positioning.

2 Kinematic Model

The Denavit-Hartenberg (DH) parameters of the new 4R serial manipulator, named *positio* (meaning position in *latin*), is listed in Table 1 and depicted in Figure 1. The angular velocity of the end-effector (EE), namely $\boldsymbol{\omega}$, is given as

$$\boldsymbol{\omega} = \mathbf{A}\dot{\boldsymbol{\theta}}, \quad \dot{\boldsymbol{\theta}} \equiv [\dot{\theta}_1 \ \dot{\theta}_2 \ \dot{\theta}_3 \ \dot{\theta}_4]^T, \tag{1}$$

in terms of the 3×4 *orienting Jacobian matrix* $\mathbf{A}$ defined as

$$\mathbf{A} \equiv [\mathbf{e}_1 \ \mathbf{e}_2 \ \mathbf{e}_3 \ \mathbf{e}_4], \tag{2}$$

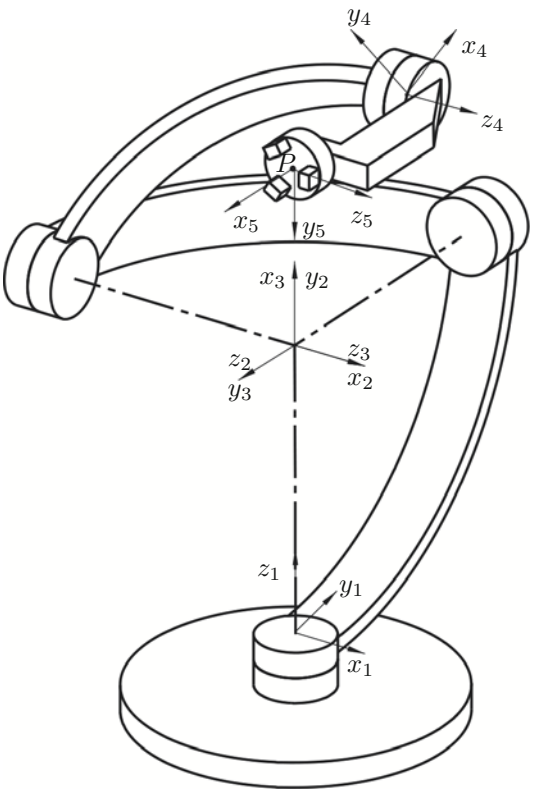

Figure 1. Positio: a new 4R serial manipulator with isotropic positioning

with

$$\mathbf{e}_1 = \begin{bmatrix} 0 \\ 0 \\ 1 \end{bmatrix}, \quad \mathbf{e}_2 = \begin{bmatrix} s_1 \\ -c_1 \\ 0 \end{bmatrix}, \quad \mathbf{e}_3 = \mathbf{e}_4 = \begin{bmatrix} c_1 s_2 \\ s_1 s_2 \\ -c_2 \end{bmatrix} \tag{3}$$

and

$$s_i \equiv \sin\theta_i, \;\; c_i \equiv \cos\theta_i. \tag{4}$$

Moreover, the velocity vector of point P of the EE, namely $\dot{\mathbf{p}}$, is given as

$$\dot{\mathbf{p}} = \mathbf{B}\dot{\boldsymbol{\theta}}, \quad \dot{\mathbf{p}} \equiv [\dot{x}\ \dot{y}\ \dot{z}]^T, \tag{5}$$

in terms of the 3×4 *positioning Jacobian matrix* $\mathbf{B}$ defined as

$$\mathbf{B} \equiv [\mathbf{e}_1 \times \mathbf{r}_1\ \mathbf{e}_2 \times \mathbf{r}_2\ \mathbf{e}_3 \times \mathbf{r}_3\ \mathbf{e}_4 \times \mathbf{r}_4] \tag{6}$$

with $\mathbf{r}_i$ being the position of P relative to the origin of frame F_i expressed in the base frame (Angeles, 2003, see Chap. 4). Because of the lack of spaces, the $\mathbf{r}_i$ of *positio* are not provided here, but can be readily obtained from the DH parameters.

Table 1. DH parameters of *positio* of an arbitrary size l

i	θ_i	a_i	b_i	α_i
1	θ_1	0	l	$\frac{\pi}{2}$
2	θ_2	0	0	$\frac{\pi}{2}$
3	θ_3	l	0	0
4	θ_4	$l\frac{\sqrt{2}}{2}$	0	0

3 Isotropic Conditions and Associated Surface

A $m \times n$ rectangular Jacobian matrix $\mathbf{M}$ is isotropic if (Angeles, 1992):

$$\mathbf{M}\mathbf{M}^T = \sigma^2 \mathbf{1}_{m\times m} \quad m \leq n \tag{7}$$

$$\mathbf{M}^T\mathbf{M} = \sigma^2 \mathbf{1}_{n\times n} \quad m \geq n \tag{8}$$

for which the condition number is unity.

3.1 Positioning Tasks

For a positioning task, *positio* has an isotropic positioning Jacobian matrix $\mathbf{B}$ such that

$$\mathbf{B}\mathbf{B}^T = \sigma^2 \mathbf{1}_{3\times 3}. \tag{9}$$

if

$$\theta_2 = \pm\frac{\pi}{2}, \quad \theta_4 = \pm\frac{3\pi}{4}, \quad \forall\theta_1, \theta_3. \tag{10}$$

Under the isotropic conditions of eq.(10), matrix $\mathbf{B}$ takes the form

$$\mathbf{B} = \frac{1}{2}l \begin{bmatrix} c_1\phi_3 & c_1\psi_3 & -s_1\psi_3 & -s_1\phi_3 \\ s_1\phi_3 & s_1\psi_3 & c_1\psi_3 & c_1\phi_3 \\ 0 & 0 & -\phi_3 & \psi_3 \end{bmatrix} \tag{11}$$

with $\phi_3 \equiv (s_3 + c_3)$ and $\psi_3 \equiv (s_3 - c_3)$. Substituting eq.(11) into eq.(9), the isotropic conditions are readily verified with $\sigma^2 = \frac{1}{2}$. As shown in Figure 2, *positio* is not only able to reach isotropic values along a trivial path but point P is also able to undergo a non0-trivial path—the surface of a sphere of radius $\frac{l}{2}$—. The manipulator is more likely to maintain a good

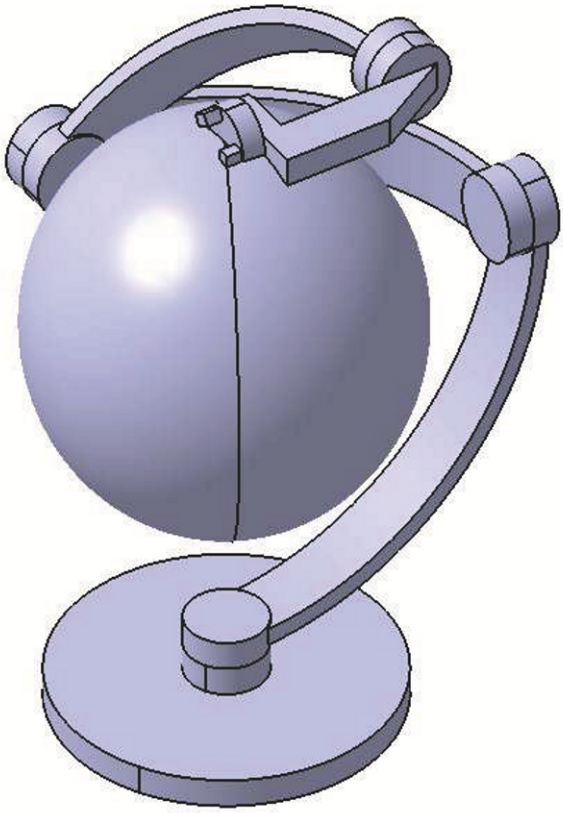

Figure 2. Surface of isotropic position of P with $\theta_2 = \frac{\pi}{2}$ and $\theta_4 = \frac{3\pi}{4}$

condition number, when P undergo an arbitrary trajectory in the vicinity of this surface. Obviously, when $\theta_4 = \pm\pi$ and $\theta_4 = 0$, matrix $\mathbf{B}$ becomes rank-deficient, which correspond to the limits of the reachable workspace of P, as shown in Figures 3 and 4.

3.2 Orienting Tasks

For an orienting task, *positio* has an orienting Jacobian matrix $\mathbf{A}$ such that

$$\mathbf{A}\mathbf{A}^T \approx \sigma^2 \mathbf{1}_{3\times 3}, \tag{12}$$

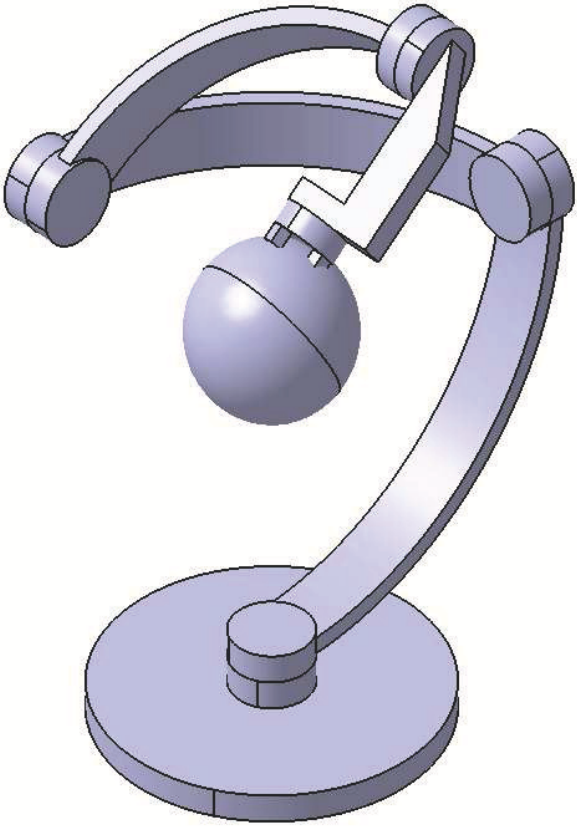

Figure 3. Surface of position singularities of P with $\theta_4 = \pi$

which never reach isotropic values for the isotropic conditions of eq.(10). In general, matrix $\mathbf{A}$ takes the form

$$\mathbf{A} = \begin{bmatrix} 0 & s_1 & c_1 s_2 & c_1 s_2 \\ 0 & -c_1 & s_1 s_2 & s_1 s_2 \\ 1 & 0 & -c_2 & -c_2 \end{bmatrix}. \tag{13}$$

Apparently, matrix $\mathbf{A}$ is independent of both θ_3 and θ_4. Upon substituting eq.(10) into (13), the conditioning of $\mathbf{A}$ is very close to isotropy, i.e.,

$$cond(\mathbf{A}) = \sqrt{2}, \quad \forall \theta_1, \theta_3, \theta_4. \tag{14}$$

As expected, the isotropy of the manipulator is independent of θ_1, .

3.3 Positioning and Orienting Tasks

For this kind of tasks, a *dimensionless* Jacobian matrix, namely $\mathbf{J}$, is required, which use a characteristic length L in order to normalize matrix $\mathbf{B}$, i.e.,

$$\mathbf{J} = \begin{bmatrix} \mathbf{A} \\ \frac{1}{L}\mathbf{B} \end{bmatrix}, \quad L = \frac{l}{2} \tag{15}$$

where $L = \frac{l}{2}$ is the characteristic length that minimize $cond(\mathbf{J})$. Upon substituting eq.(15) and (10) into (8), we obtain

$$\mathbf{J}^T\mathbf{J} \approx \sigma^2 \mathbf{1}_{4\times 4}, \tag{16}$$

which never reach isotropic values for the conditions of eq.(10). However, the condition number is

$$cond(\mathbf{J}) = 2, \quad \forall \theta_1, \theta_3. \tag{17}$$

Again here, point P can undergo any position onto the isotropic sphere, while having a constant conditioning of $\mathbf{J}$ of 2, a rather interesting behavior.

4 Conclusions

A new isotropic design of a 4R serial manipulator has been proposed for positioning tasks. The manipulator is able to reach positioning isotropy for any positions of its operational point P over the surface of a sphere. To the knowledge of the authors, *positio* is the first nR serial manipulator, aimed for positioning tasks, that exhibit such a *non-trivial isotropic path*. We recall that a trivial isotropic path is obtained by a rotation θ_1 from an isotropic posture. For orienting tasks, the conditioning is maintained at a constant value of $\sqrt{2}$ over the same isotropic surface, while for both positioning and orienting tasks, the conditioning is maintained to a value of only 2.

Bibliography

K. Akrout and L. Baron. Manipulateur 6r sphérique isotrope pour toute orientation de son effecteur. *Transactions of the Canadian Society for Mechanical Engineering*, 33(4):679–688, 2009.

J. Angeles. *Fundamentals of Robotic Mechanical Systems*. Springer-Verlag, 2003.

J. Angeles. The design of isotropic manipulator architectures in the presence of redundancies. *Int. J. of Robotic Research*, 11:96–201, 1992.

K. Akrout L. Baron and X. Wang. Existence d'une infinité non dénombrable de positions isotropes pour les manipulateurs 5r sphériques, *Besançon, France. The tenth IFToMM World Congress*, 2008.

D. Chablat and J. Angeles. On isotropic sets of points in the plane: application to the design of robot architectures. In *Advances in Robot Kinematic*, pages 73–82, 2000.

D. Chablat and J. Angeles. The computation of all 4r serial spherical wrists with an isotropic architecture. *J. of Mechanical Design*, 125:275–280, 2003.

J. Angeles F. Ranjbaran and M.A. Gonzalez-Palacios. The mechanical design of a seven-axes manipulator with kinematic isotropy. *Int. J. of Intelligent and Robot Systems*, 14:21–41, 1995.

J. K. Salisbury and J. J. Craig. Articulated hands: Force control and kinematic issues. *Int. J. of Robotic Research*, 1:4–17, 1982.

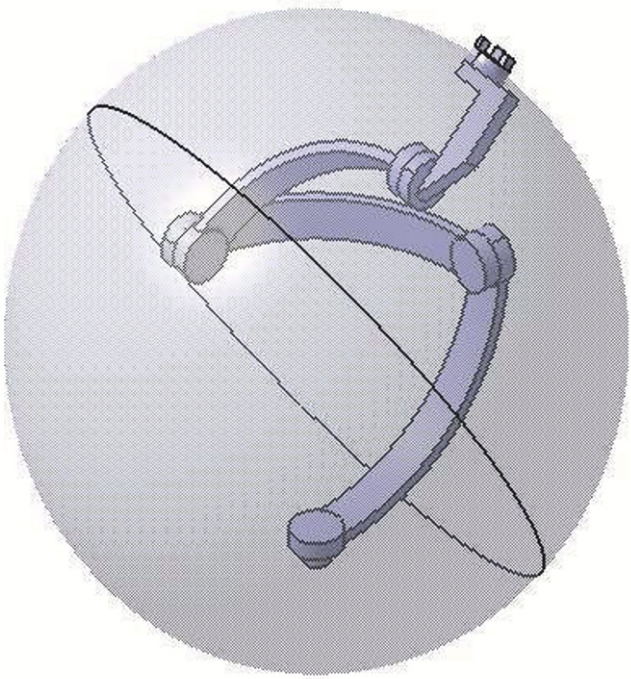

Figure 4. Surface of position singularities of P with $\theta_4 = 0$

Joint space and workspace analysis of a two-DOF closed-chain manipulator

Damien Chablat
Institut de Recherche en Communications et Cybernétique de Nantes,
UMR CBRS 6597, 1 rue de la Noë, Nantes, France
damien.chablat@irccyn.ec-nantes.fr

Abstract: The aim of this paper is to compute of the generalized aspects, i.e. the maximal singularity-free domains in the Cartesian product of the joint space and workspace, for a planar parallel mechanism in using quadtree model and interval analysis based method. The parallel mechanisms can admit several solutions to the inverses and the direct kinematic models. These singular configurations divide the joint space and the workspace in several not connected domains. To compute this domains, the quadtree model can be made by using a discretization of the space. Unfortunately, with this method, some singular configurations cannot be detected as a single point in the joint space. The interval analysis based method allow us to assure that all the singularities are found and to reduce the computing times. This approach is tested on a simple planar parallel mechanism with two degrees of freedom.

1 INTRODUCTION

The kinematic design of parallel mechanism has drawn the interest of several researchers. The workspace is usually considered as a relevant design criterion [1, 2, 3]. Parallel singularities [4] occur in the workspace where the moving platform cannot resist any effort. They are very undesirable and generally eliminated by design. Serial singularities [5] occur if the mechanism admit several solutions to the inverse kinematic model. To cope with the existence of multiple inverse kinematic solutions in *serial* manipulators, the notion of aspects was introduced in [6]. The aspects equal the maximal singularity-free domains in the joint space. For usual industrial serial manipulators, the aspects were found to be the maximal sets in the joint space where there is only one inverse kinematic solution.

A definition of the notion of aspect was given by [4] for parallel manipulators with only one inverse kinematic solution and was extended by [5] for parallel manipulators with several solutions to the inverse and direct kinematic problem. These aspects were defined as the maximal singularity-free domains in the Cartesian product of the joint space and the workspace. To compute the aspects, we can

used discretization methods. However, we cannot find any singularity in particular if the singularity is a point. Interval based analysis method was implemented by [7, 8] in ALIAS to compute the workspace of parallel mechanism. However, the result is a set of boxes in which is not easy to separate the maximum singularity free regions of the workspace and the computational times is difficult to estimate.

This article introduces an algorithm based on the tree-like structure and the interval analysis based method which takes the advantages of the interval analysis based method and the simplicity of tree-like structures.

2 ALGORITHM

The aim of this section is to define an algorithm able to compute either the joint space or the workspace of parallel mechanism. This is done using the structure of a quadtree model and the interval based method. This algorithm will be illustrated by a planar parallel mechanism in section 3 but can easily be extended to mechanism with three degrees of freedom in using octree model. Unlike numerical computing methods, such a method allows to prove formally that there is no singular configuration in the final result.

2.1 Definition of the quadtree/octree model

The tree-like structure, called in this paper, quadtree or octree, are a hierarchical data structure based on a recursive subdivision of space [9]. It is particularly useful for representing complex $2-D$ or $3-D$ shapes, and is suitable for Boolean operations like union, difference and intersection. Since the quadtree/octree structure has an implicit adjacency graph, arcwise-connectivity analysis can be naturally achieved. The quadtree/octree model of a space $\mathcal{S}$ leads to a representation with cubes of various sizes. Basically, the smallest cubes lie near the boundary of the shape and their size determines the accuracy of the quadtree/octree representation. Quadtree/octrees have been used in several robotic applications [4], [10], [11].

The main advantages of the octree model are (i) very compact file (only B (Black), W (White) and G (Gray) letter) and (ii) accelerates display speed facilities by differentiating model into lower levels of resolution while being rotated and higher resolution while an orientation is temporarily set. Conversely, the computational times can be high due to the discretization. If we test only the center of each cube, some singularities can exist and are not detected. This feature is true even if we increase the level of resolution. The accuracy of the model is directly defined by the depth of the quadtree and the size of the initial box. For a quadtree model with a depth d and a initial box of lengths b, the accuracy is $b/2^d$.

2.2 Notion of aspect for fully parallel manipulators

We recall here briefly the definition of the generalized octree defined in [5]:

Definition 1. The generalized aspects $\mathbf{A}_{ij}$ are defined as the maximal sets in $W \cdot Q$ so that $\mathbf{A}_{ij} \subset W \cdot Q$, $\mathbf{A}_{ij}$ is connected, and $\mathbf{A}_{ij} = \{(\mathbf{X}, \mathbf{q}) \in Mf_i \setminus det(\mathbf{A}) \neq 0\}$

In other words, the generalized aspects $\mathbf{A}_{ij}$ are the maximal singularity-free domains of the Cartesian product of the reachable workspace with the reachable

joint space.

Definition 2. The projection of the generalized aspects in the workspace yields the parallel aspects $\mathbf{WA}_{ij}$ so that $\mathbf{WA}_{ij} \subset W$, and $\mathbf{WA}_{ij}$ is connected.

The parallel aspects are the maximal singularity-free domains in the workspace for one given working mode.

Definition 3. The projection of the generalized aspects in the joint space yields the serial aspects $\mathbf{QA}_{ij}$ so that $\mathbf{QA}_{ij} \subset Q$, and $\mathbf{QA}_{ij}$ is connected.

The serial aspects are the maximal singularity-free domains in the joint space for one given working mode.

The aim of this paper is to compute separately the parallel and serial aspects thanks to the properties of the quadtree models.

2.3 Introduction to ALIAS library

An algorithm for the definition of the joint space and workspace of parallel mechanism is described in the following sections. This algorithm uses the `ALIAS` library [7], which is a C++ library of algorithms based on interval analysis. These algorithms deal with systems of equations and inequalities of which expressions are an arbitrary combination of the most classical mathematical functions (algebraic terms, sine, cosine, log etc..) and of which coefficients are real numbers or, in some cases, intervals. Unfortunately, this library is not connected to the octree model and generates large data file to describe by a set of boxes the solution of the problem. Thus, the operations between the set of boxes is more difficult if we compare to the boolean operations that we can made with the octree models.

2.4 A first basic tool: Box verification

Our purpose is to determine the quadtree model associated with the joint space or the workspace, that we will call only the space $\mathcal{C}$. For a given box B defined by two intervals, we note *valid box* if it is included in $\mathcal{C}$ and *invalid box* otherwise. For that purpose we need to design first a procedure, called $\mathcal{M}(B)$, that takes as input a box B and returns:

- 1: if every point in B is valid,
- -1: if no point in B is valid,
- 0: if neither of the other two conditions could be verified.

To check if one point is valid, we can used several approaches. For example, in the Cartesian space, we have to compute the inverse kinematic model to test if at least one solution exists, which defines the workspace. Thus, for each solution, we can define completely the mechanism for each working mode and compute the determinant of the parallel Jacobian matrix [5]. This procedure is able to define the non-singular domains but their are not necessary connected. However, with a quadtree model, it is easy to perform a connectivity analysis to separate the quadtree model in connected domains. This is a main advantage of the tree-like structures in comparison with the method implemented in the `ALIAS` library. Some

additional constraints can be to define dexterous domains in using a kinetostatic index as in [8].

The problem is now to implement an inverse and direct kinematic model able to take as input a box B and to return, if the box is valid, a box S which contains the solutions of the problem.

2.5 A second basic tool: Quadtree model definition

The definition of a quadtree is made recursively by calling several times the same procedure, call $\mathcal{Q}(B, d, P)$, that takes as input a box B, the local depth d in the tree and a pointer P on the data structure which contains the quadtree model.

- If $\mathcal{M}(B)$ returns -1, it is the end of the recursive search.
- If $\mathcal{M}(B)$ returns 1, a black node is created in the current depth.
- If $\mathcal{M}(B)$ returns 0, if the local depth is smallest than the maximal depth of the quadtree, we divide the box B into four new boxes B_1, B_2, B_3 and B_4, and we call

$$\mathcal{Q}(B_1, d+1, P) \quad \mathcal{Q}(B_2, d+1, P) \quad \mathcal{Q}(B_3, d+1, P) \quad \mathcal{Q}(B_4, d+1, P)$$

When $\mathcal{M}(B)$ returns -1, we can also create a another quadtree model, called *complementary space* in which we save the box B where at least one constraint is not valid. With this knowledge, we can compute the quadtree model with a higher definition without retesting the valid and non valid boxes. An example of this result will be given in the following section.

3 MECHANISM UNDER STUDY

For more legibility, a planar manipulator is used as illustrative example in this paper. This is a five-bar, revolute (R)-closed-loop linkage, as displayed in figure 1. The actuated joint variables are θ_1 and θ_2, while the Output values are the (x, y) coordinates of the revolute center P. The displacement of the passive joints will always be assumed unlimited in this study. Lengths L_0, L_1, L_2, L_3, and L_4 define the geometry of this manipulator entirely.

Two sets of dimensions are used to illustrate the algorithm. The first one, called $\mathcal{M}_1$, is defined in [5] and its dimensions are $L_0 = 9$, $L_1 = 8$, $L_2 = 5$, $L_3 = 5$ and $L_4 = 8$, in certain units of length that we need not to specify. And, the second one, called $\mathcal{M}_2$, is defined in [12] and its dimensions are $L_0 = 2.55$, $L_1 = 2.3$, $L_2 = 2.3$, $L_3 = 2.3$ and $L_4 = 2.3$.

3.1 Kinematic Relations

The velocity $\dot{\mathbf{p}}$ of point P, of position vector $\mathbf{p}$, can be obtained in two different forms, depending on the direction in which the loop is traversed, namely,

$$\dot{\mathbf{p}} = \dot{\mathbf{b_1}} + \dot{\theta}_3 \mathbf{E}(\mathbf{p} - \mathbf{b_1}) \quad \dot{\mathbf{p}} = \dot{\mathbf{b_2}} + \dot{\theta}_4 \mathbf{E}(\mathbf{p} - \mathbf{b_2}) \tag{1}$$

with matrix $\mathbf{E}$ defined as $\mathbf{E} = \begin{bmatrix} 0 & -1 \\ 1 & 0 \end{bmatrix}$ and $\mathbf{b}_1$ and $\mathbf{b}_2$ denoting the position vectors, in the frame indicated in figure 1 of points B_1 and B_2, respectively.

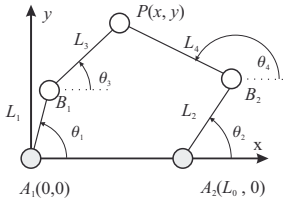

Figure 1: A two-dof closed-chain manipulator

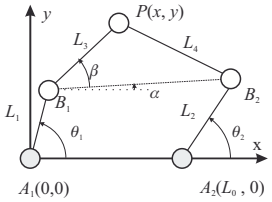

Figure 2: The angle α and β used to solve the DKP

Furthermore, note that $\dot{\mathbf{c}}$ and $\dot{\mathbf{d}}$ are given by

$$\dot{\mathbf{b_1}} = \dot{\theta}_1 \mathbf{E}(\mathbf{b}_1 - \mathbf{a}_2), \quad \dot{\mathbf{b_2}} = \dot{\theta}_2 \mathbf{E}(\mathbf{b}_2 - \mathbf{a}_2)$$

Two Jacobian matrix, $\mathbf{A}$ and $\mathbf{B}$, permit to study the serial and parallel singular configurations [4],

$$\mathbf{A} = \begin{bmatrix} (\mathbf{p} - \mathbf{b_1})^T \\ (\mathbf{p} - \mathbf{b_2})^T \end{bmatrix}, \ \mathbf{B} = \begin{bmatrix} L_1 L_2 \sin(\theta_3 - \theta_1) & 0 \\ 0 & L_3 L_4 \sin(\theta_4 - \theta_2) \end{bmatrix} = \begin{bmatrix} B_{11} & 0 \\ 0 & B_{22} \end{bmatrix} \quad (2)$$

Two assembly modes can be defined with the sign of $\det(\mathbf{A})$. To characterize the assembly mode, we can only compute $(\mathbf{p} - \mathbf{b_1}) \times (\mathbf{p} - \mathbf{b_2})$.

The parallel singular configurations are located at the boundary of the joint space. Such singularities occur whenever B_1, P and B_2 are aligned. In such configurations, the manipulator cannot resist an effort in the orthogonal direction of B_1B_2. Besides, when B_1 and B_2 coincide, the position of P is no longer controllable since P can rotate freely around B_1 even if the actuated joints are locked. This singularity cannot be find by the discretization of the workspace but is detected by the interval analysis based method.

3.2 Direct kinematic problem

For planar mechanism, the computation of the direct kinematic problem (DKP) is very simple. However, if we want to return the good information to the function $\mathcal{C}$, we have to distinguish more cases. If there is no joint limits, they are zero or two solutions for the DKP.

The procedure takes as input a box B defined by two intervals $\tilde{\theta_1} = [\underline{\theta_1}, \overline{\theta_1}]$ and $\tilde{\theta_2} = [\underline{\theta_2}, \overline{\theta_2}]$, the actuated joint variables. In this example, the values of the length are defined as a float but can be also defined by a interval to represent the tolerances of manufacturing.

The algorithm can be described by the following steps:

- Compute the position of $\tilde{\mathbf{b}_1}$ and $\tilde{\mathbf{b}_2}$ which is the location of B_1 and B_2 respectively.
- Compute the distance $\tilde{L}$ between B_1 and B_2:
  - $[\underline{L}, \overline{L}] = ||\tilde{\mathbf{b}_1} - \tilde{\mathbf{b}_2}||$

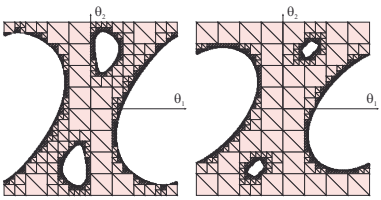

Figure 3: Joint space of $\mathcal{M}_1$ and $\mathcal{M}_2$

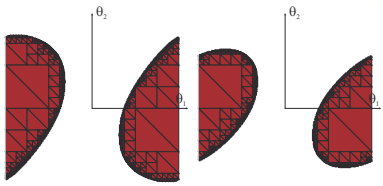

Figure 4: The complementary joint space of $\mathcal{M}_1$ and $\mathcal{M}_2$

  - If $\underline{L} > L_3 + L_4$ then the mechanism can be assembly and the function return -1.
  - If $\underline{L} = 0$ then the mechanism can be in a singular configuration.
- Compute the angle α and β of the triangle (B_1, B_2, P) (Figure 2).
  - $C(\alpha) = \sqrt{(\tilde{L}^2 + L_3^2 - L_4^2)/(2L_3\tilde{L})}$.
  - $\beta = \arctan\left(\frac{B_{2y}-B_{1y}}{B_{2x}-B_{1x}}\right)$
  - If ($\underline{C(\alpha)} \geq -1$ and $C(\alpha) \leq 1$) then $\alpha = \arccos(C(\alpha))$.
- Compute the two solutions P_1 and P_2 of point P:
  - $P_{1x} = B_{1x} + L_3\cos(\alpha + \beta)$
  - $P_{1y} = B_{1y} + L_3\sin(\alpha + \beta)$
  - $P_{2x} = B_{1x} + L_3\cos(\alpha - \beta)$
  - $P_{2y} = B_{1y} + L_3\sin(\alpha - \beta)$.

To perform this procedure, all the trigonometric function come from the `ALIAS` library and accept as input an interval and return an interval. For each step, we have to check that the argument are not out of range.

For the two mechanism under study, we can plot with this function the joint space (Figure 3). The results are equivalent to the solution computed in [5] and [12]. However, conversely to a discretization method, we can detect the parallel singularity where B_1 and B_2 coincide. Normally, it is a point but with the interval analysis method, the algorithm cannot define valid boxec where det($\mathbf{A}$) is equal to zero. The set of box where at least one constraint is not valid is called the complementary joint space, figure 4.

3.3 Selection of the assembly mode

For a parallel mechanism with only two solutions to the direct kinematic problem, the assembly mode is characterize by the sign of det($\mathbf{A}$). To simplify, we can only compute

$$\tilde{\mathbf{t}} = (\tilde{\mathbf{b}_1} - \tilde{\mathbf{p}}) \times (\tilde{\mathbf{b}_2} - \tilde{\mathbf{p}}) \tag{3}$$

and to test if $\tilde{\mathbf{t}_z}$ is positive or negative.

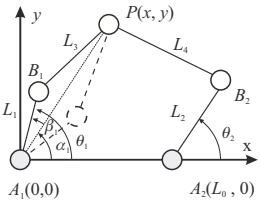

Figure 5: The angle α and β used to solve the IKP

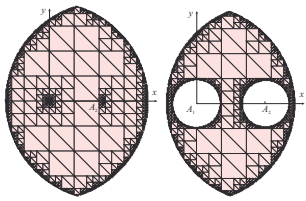

Figure 6: Workspace of $\mathcal{M}_1$ and $\mathcal{M}_2$

3.4 Inverse kinematic problem

For the mechanism under study, there are four solutions for the inverse kinematic problem (IKP), two solutions for each leg. The procedure takes as input a box B defined by to two intervals $\tilde{x} = [\underline{x}, \overline{y}]$ and $\tilde{y} = [\underline{y}, \overline{y}]$, the position of $\tilde{P}$.

The algorithm can be described by the following steps:

- Compute the distance $\tilde{M_1}$ between A_1 and P, and $\tilde{M_2}$ between A_2 and $\tilde{P}$.
- If ($\underline{M_1} > L_1 + L_3$ or $\underline{M_2} > L_2 + L_4$) then P is outside the workspace and the function returns -1.
- If ($\overline{M_1} < ||L_1 - L_3||$ or $\overline{M_2} < ||L_2 - L_4||$) then P is located in a hole of the workspace and the function returns -1.
- If ($\underline{M_1} > 0$) and ($\underline{M_2} > 0$) and ($\underline{M_1} > ||L_1 - L3||$) and ($\underline{M_2} > ||L_2 - L4||$) and ($\overline{M_1} < L_1 + L_3$) and ($\overline{M_2} < L_2 + L_4$) then compute the angles $\beta_1 = \widehat{B_1 A_1 P}$ and $\beta_2 = \widehat{B_2 A_2 P}$ noted in Figure 5:
  - $\tilde{C}(\beta_1) = \frac{L_1^2 + \tilde{M}_1^2 - L_3^2}{2\tilde{M}_1 L_1}$ $\quad \tilde{C}(\beta_2) = \frac{L_2^2 + \tilde{M}_2^2 - L_4^2}{2\tilde{M}_2 L_2}$
  - If ($||\tilde{C}(\beta_1)|| \leq 1$) and ($||\tilde{C}(\beta_2)|| \leq 1$) then
    - $\alpha_1 = \arctan(P_y/P_x)$ $\quad \alpha_2 = \arctan(P_y/(C_2 - P_x))$
    - $\beta_1 = \arccos(\tilde{C}(\beta_1))$ $\quad \beta_2 = \arccos(\tilde{C}(\beta_2))$
    - $\alpha_{11} = \alpha_1 + \beta_1$ $\quad \alpha_{12} = \alpha_1 - \beta_1$ $\quad \alpha_{21} = \pi - \alpha_2 + \beta_2$ $\quad \alpha_{22} = \pi - \alpha_2 - \beta_2$
    - Returns 1;
  - Else, returns 0;

For the two mechanism under study, we can plot with this function the joint space (Figure 6). For the mechanism $\mathcal{M}_\in$, there is a hole in A_1 and A_2 which is only a point. On the picture, we can only notice that there exists a sub-division of the space because there are small boxes. The size of the hole is equal to the size of the smallest box.

3.5 Selection of the working mode

For a parallel mechanism with only four solutions to the inverse kinematic problem, the working mode is characterized by the sign of B_{11} and B_{22}. This can

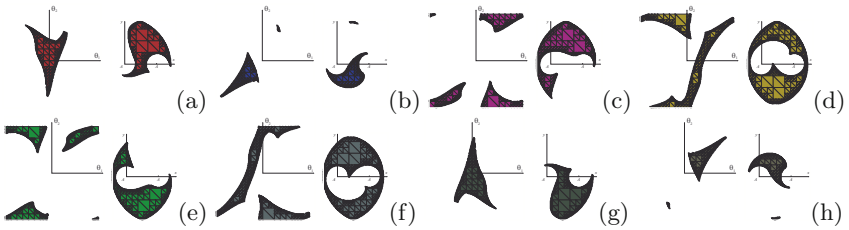

Figure 7: Aspects of $\mathcal{M}_1$

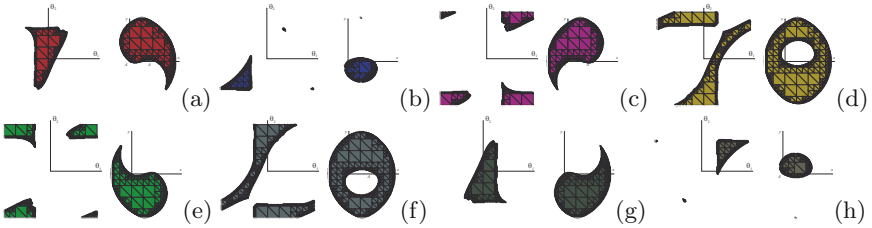

Figure 8: Aspects of $\mathcal{M}_2$

be done simply

$$\tilde{\mathbf{u}} = (\tilde{\mathbf{b}_1} - \tilde{\mathbf{a}_1}) \times (\tilde{\mathbf{p}} - \tilde{\mathbf{b}_1}) \quad \tilde{\mathbf{v}} = (\tilde{\mathbf{b}_2} - \tilde{\mathbf{a}_2}) \times (\tilde{\mathbf{p}} - \tilde{\mathbf{b}_2}) \tag{4}$$

and to test the sign of $\tilde{\mathbf{u}_z}$ or $\tilde{\mathbf{v}_z}$.

3.6 Computation of the generalized aspects

The number of aspects is the same for the both mechanisms. We can compute separately the serial and parallel aspects for all the working modes. For a give sign of $\det(\mathbf{A})$, B_{11} and B_{22}, we have define a quadtree model. To obtain the generalized aspects, a connectivity analysis is made to separate the connected regions. We need to test only one point in the workspace and its projection on the joint space to associate a serial aspect to its parallel aspect counterpart.

The study of the joint space allow us to know if a trajectory between two generalized aspects exists by passing through a serial singularity. Figures 9 and 10 permit us to conclude that, for $\mathcal{M}_1$ and $\mathcal{M}_2$, no trajectory exists in which we change only one time the working modes, between the aspects 1 and 4 and between the aspects 2, 3 and 5.

3.7 Comparison between classical quadtree computation and the new algorithm

The aim of this section is to compare the number of times where the inverse or direct kinematic function is called to build the quadtree for the both mechanisms and for several depths of the tree which is equivalent to the accuracy of the model. For the joint space, the initial box B is defined by two intervals equal to $[-\pi, \pi]$ and for the workspace, the initial box B is defined by two intervals equal to $[-(L_1 + L_3), (L_1 + L_3)]$.

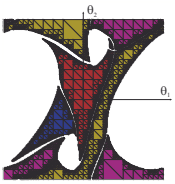

Figure 9: The serial aspects of $\mathcal{M}_1$ for $\det(\mathbf{A}) > 0$

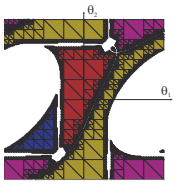

Figure 10: The serial aspects of $\mathcal{M}_2$ for $\det(\mathbf{A}) > 0$

Table 1: Comparison between classical quadtree computation and the new algorithm to compute the joint space and the workspace

Joint space	Depth #	5	6	7	8	9	10
	$\mathcal{M}_1$	99%	73%	40%	22%	13 %	9 %
	$\mathcal{M}_2$	111%	83%	40%	18%	8 %	4 %
Workspace	Depth #	5	6	7	8	9	10
	$\mathcal{M}_1$	72%	45%	25%	13%	7 %	3 %
	$\mathcal{M}_2$	65%	37%	19%	10%	5 %	2 %

With the discretization method, the number of times where the inverse or direct kinematic problem is used is $n_{discretization} = 2^{2d}$ with d is the depth of the tree. We call $n_{quadtree}$ the number of times where where the inverse or direct kinematic problem is used to build the quadtree model. To compare the computing cost between the both method, we define the following criteria:

$$\mathcal{K} = n_{quadtree}/n_{discretization} \tag{5}$$

Table 1 compares the computing times for the joint space and the workspace for the mechanisms $\mathcal{M}_1$ and $\mathcal{M}_2$. When the depth of the quadtree is small, there is no advantage to used the interval analysis based method. But, when the depth increase, the advantages can be very important. For example, to compute the workspace of $\mathcal{M}_1$ with $d = 10$, we call 36893 times the IKP while the discretization method calls $2^{20} = 1048576$ times the IKP.

4 CONCLUSIONS AND FUTURE WORKS

In this paper, we have presented an algorithm able to compute the joint space and workspace of parallel mechanism by using the octree model and the interval based method. We have the maximum singularity regions, called *aspects*, for two planar mechanisms and we have compared the number of times where the inverse and direct kinematic problem is called according to the accuracy used. Thanks to the use of the interval analysis based method, the result is guaranteed for all the depth used, i.e. we are sure to detect all the singular configurations. The quadtree model can be saved in text file and its size is very small. Plugin exist now to visualize the model in a 3D viewer in Web pages (as www.octree.com).

Future works will be made to define as interval the lengths of the legs and to find the influence of the manufacturing error on the joint space and workspace.

5 ACKNOWLEDGMENTS

This work was supported partly by the French Research Agency A.N.R. (Agence Nationale pour la Recherche).

REFERENCES

[1] Merlet, J-P., "Workspace-0riented Methodology for Designing a Parallel Manipulator," Proc. IEEE Int. Conf. on Robotics and Automation, pp. 3726–3731, 1996.

[2] Clavel, R., "DELTA, a Fast Robot with Parallel Geometry," Proc. 18th Int. Symposium of Industrial Robots, pp. 91–100, 1988.

[3] Gosselin, C. and Angeles, J., "A Global Performance Index for the Kinematic Optimization of Robotic Manipulators," Journal of Mechanical Design, vol. 113, pp. 220–226, 1991.

[4] Wenger Ph., and Chablat D., "Definition Sets for the Direct Kinematics of Parallel Manipulators," Proc.8th International Conference in Advanced Robotics, pp. 859–864, 1997.

[5] Chablat D., and Wenger Ph., "Working Modes and Aspects in Fully-Parallel Manipulator," Proc. IEEE International Conference on Robotics and Automation, pp. 1964–1969, May 1998.

[6] Borrel, P., "A study of manipulator inverse kinematic solutions with application to trajectory planning and workspace determination," Proc. IEEE International Conference on Robotic And Automation, pp. 1180–1185, 1986.

[7] Merlet, J-P., "ALIAS: an interval analysis based library for solving and analyzing system of equations," Pro. Séminaire Systèmes et équations algébriques, SEA, June, pp. 1964–1969, 2000.

[8] Chablat D., Wenger P., Majou F., and Merlet J.P., "An Interval Analysis Based Study for the Design and the Comparison of 3-DOF Parallel Kinematic Machine", International Journal of Robotics Research, pp. 615–624, vol. 23(6), June 2004.

[9] Meagher, D., "Geometric Modelling using Octree Encoding", Technical Report IPL-TR-81-005, Image Processing Laboratory, Rensselaer Polytechnic Institute, Troy, 1981, New York 12181.

[10] Faverjon B., "Obstacle avoidance using an octree in the configuration space of a manipulator", Proc. IEEE International Conference on Robotics And Autaumation, pp. 504–510, 1984.

[11] Garcia G., Wenger P., Chedmail P., "Computing moveability areas of a robot among obstacles using octrees", Proc. International Conference on Advanced Robotics, Columbus, Ohio, USA, June 1989.

[12] Figielski, A., Bonev, I.A., and Bigras, P., "Towards Development of a 2-DOF Planar Parallel Robot with Optimal Workspace Use", IEEE International Conference on Systems, Man, and Cybernetics (SMC 2007), Montréal, QC, Canada, 7–10 October 2007.

Identification of Base Parameters for Large-scale Kinematic Chains Based on Physical Consistency Approximation by Polyhedral Convex Cones

Ko Ayusawa[†] *, and Yoshihiko Nakamura[†]

[†] Department of Mechano-Informatics, The University of Tokyo, Tokyo, Japan

Abstract In this paper, we propose the identification method to realize physical consistency and computational stability. As inertial parameters of each link are represented with a finite number of mass points, the physical conditions can be approximated by linear inequalities. The evaluation function is also designed to control the exactness of identification results and the stability of computation.

1 Introduction

For the study of physical ability performed by humanoid robots and humans, it is required to understand the dynamics of their multibody systems. In the field of robotics, the identification technique using the feature found in the equations of motion is developed(Mayeda et al. (1984); Atkeson et al. (1986)), which identifies the unknown inertial parameters, such as mass, center of mass, and inertia of each link. The classical identification problem can be solved with a least squares method. Nevertheless, the obtained result is not necessarily physically consistent(Yoshida and Khalil (2000)). Mata et al. (2005) proposed the method considering physical consistency, and also tested it on the 6-axis industrial manipulator. This method solves the quadratic programming with the non-linear inequality constraints which come from the condition of positive definiteness of the parameters.

For application to legged systems, there exist the following problems when using the method developed for manipulators. First above all, the number of degrees of freedom (DOF) of the system is large, which requires

*This research is supported by Category S of Grant-in-Aid for Scientific Research(20220001), Japan Society for the Promotion of Science, and supported by IRT Foundation to Support Man and Aging Societyh under Special Coordination Funds for Promoting Science and Technology from MEXT.

large-scale non-linear optimization. And it is difficult to generate the exciting motion because of the kinematics and dynamics complexity of the systems, resulting ill condition problem of optimization. Thus, converged solution is difficult to be obtained by the usual method mentioned above.

In this paper, we propose the identification method to realize physical consistency and computational stability for large-scale systems like legged systems. Inertial parameters of each link are represented with a finite number of mass points. Then the positive definiteness of the parameters can be replaced with linear inequalities, which always satisfy the original conditions, and the performance of approximation can be enhanced as the number of mass points increase. We also design the evaluation function to control the exactness of identification results and the computational stability.

2 Identification methods developed for manipulators

The equations of motion of multibody systems can be written in a linear form with respect to the dynamic parameters. The equations of the robot, composed of N rigid bodies and that has N_J DOF, is given by Eq.(1).

$$\boldsymbol{Y}\boldsymbol{\phi} = \boldsymbol{\tau} + \sum_{k=1}^{N_c} \boldsymbol{J}_k{}^T \boldsymbol{f}_k^{ext} \tag{1}$$

Where, $\boldsymbol{\phi} \in \boldsymbol{R}^{10N}$ is the vector of constant inertial parameters, $\boldsymbol{Y} \in \boldsymbol{R}^{N_J \times 10N}$ is the regressor matrix or regressor, $\boldsymbol{\tau} \in \boldsymbol{R}^{N_J}$ is the vector of joint torques, N_c is the number of contact points with the environment, $\boldsymbol{f}_k^{ext} \in \boldsymbol{R}^6$ is the vector of external forces exerted to the system at contact k, $\boldsymbol{J}_k \in \boldsymbol{R}^{N_J \times 6}$ is the basic Jacobian matrix of the position at contact k and of the orientation of the contact link with respect to generalized coordinates.

Only the minimal set of inertial parameters that describes the dynamics of the system can be identified. This minimal set is called base parameters. It is computed symbolically or numerically from the inertial parameters $\boldsymbol{\phi}$ by eliminating those that have no influence on the model and regrouping some according to the kinematics of the system(Khalil and Bennis (1995)). The minimal identification model given by Eq.(2) is thus obtained.

$$\boldsymbol{Y}_B\boldsymbol{\phi}_B \;\; = \;\; \boldsymbol{f} \tag{2}$$

Where, N_B is the number of the base parameters, $\boldsymbol{Y}_B \in \boldsymbol{R}^{N_j \times N_B}$ is called the regressor matrix for the base parameters, and $\boldsymbol{f} \in \boldsymbol{R}^{N_j}$ is equal to the right-hand side of Eq.(1). $\boldsymbol{\phi}_B \in \boldsymbol{R}^{N_B}$ is the vector of the base parameters, and it is a liner combination $\boldsymbol{\phi}_B = \boldsymbol{Z}\boldsymbol{\phi}$, using the composition matrix $\boldsymbol{Z} \in \boldsymbol{R}^{N_B \times 10n}$ which can be computed from the structure of a robot.

For the identification process, we have to compute $\boldsymbol{Y}_B$ and $\boldsymbol{f}$ at every sampling time, measuring generalized coordinates, joint torques, and external forces acted on a robot. Then we arrange T sampled regressors and forces of Eq.(2) at $t = t_1, t_2 \cdots t_T$ lengthwise, and compose the large regressor matrix $\boldsymbol{Y}_{all}$ and the large vector of forces $\boldsymbol{F}_{all}$ as bellow.

$$\boldsymbol{Y}_{Ball}\boldsymbol{\phi}_B(\triangleq \left[{\boldsymbol{Y}_{B,t_1}}^T \cdots {\boldsymbol{Y}_{B,t_T}}^T \right]^T \boldsymbol{\phi}_B) = \boldsymbol{f}_{all}(\triangleq \left[{\boldsymbol{f}_{t_1}}^T \cdots {\boldsymbol{f}_{t_T}}^T \right]^T) \quad (3)$$

After sampling, the parameter $\boldsymbol{\phi}_B$ in Eq.(3) is solved by the least squares method (LSM). Nevertheless, the obtained result is not necessarily physically consistent because of measurement noise and modeling error. Physical consistency means that the inertial matrix of each link j $(1 \leq j \leq N)$ must be positive definite(Yoshida and Khalil (2000)).

$$m_j > 0, \quad \boldsymbol{I}_{Cj} > 0 \quad (4)$$

Where, $\boldsymbol{I}_{Cj}(= \boldsymbol{I}_j - m_j[\boldsymbol{s}_j\times][\boldsymbol{s}_j\times]^T)$ is the inertia matrix around center of mass $\boldsymbol{s}_j$ expressed in the frame attached to link j. Mata et al. (2005) proposed a identification method to solves the quadratic programming (QP) with the nonlinear inequality constraints Eq.(4), and also tested it on the 6-axis industrial manipulator. The solution satisfies Eq.(4) and minimizes the following evaluation function.

$$f(\boldsymbol{\phi}) = \lambda_\tau |\boldsymbol{Y}_{all}\boldsymbol{\phi} - \boldsymbol{f}_{all}|^2 + \lambda_\tau |\boldsymbol{Z}\boldsymbol{\phi} - \widehat{\boldsymbol{\phi}}_B|^2 \quad (5)$$

Where, $\boldsymbol{Y}_{all} \triangleq \boldsymbol{Y}_{Ball}\boldsymbol{Z}$, and $\widehat{\boldsymbol{\phi}}_B \triangleq \boldsymbol{Y}_{Ball}^{\#}\boldsymbol{F}_{all}$ is the solution of LSM.

3 Identification for legged systems considering physical consistency and computational stability

QP with the evaluation function Eq.(5) and the nonlinear inequality constraints Eq.(4) can be also applied for legged systems. However, the following problems exist, which make it difficult to obtain the converged solution.

- First above all, the number of DOF of legged systems is generally large, which require large-scale non-linear optimizations.
- As there exist no links fixed to the environment, it is difficult to separate motion planning for identification from control stability. This dynamics constraint leads to decrease the performance of persistent exciting trajectories(Gautier and Khalil (1992)).
- The characteristics of every joint such as joint velocity and range of motion are significantly different, which causes gaps of identification performance among parameters.

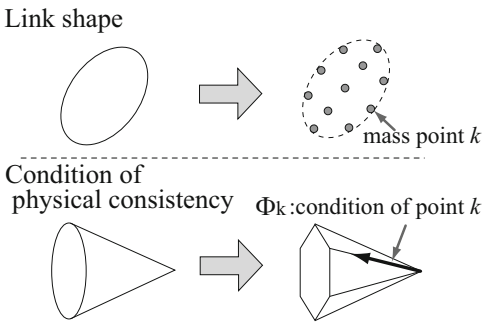

Figure 1. A link object is approximated by a finite number of mass points. It leads that the physical condition represented by a convex cone in the space of inertial parameters is approximated by a polyhedral convex cone.

In this paper, we approximate both Eq.(4) and Eq.(5) to improve the computational stability under those problems.

First, we place a finite number of mass points in the convex hull of the link object as shown in Figure 1, in order to replace Eq.(4) with linear inequalities. $S_{\phi_j}(\subset \boldsymbol{R}^{10})$ is the set of inertial parameters $\boldsymbol{\phi}_j \in \boldsymbol{R}^{10}$ of the link j satisfying Eq.(4). S_{ϕ_j} is clearly a convex set, and $\forall a > 0$, $(a\boldsymbol{\phi}_j) \in S_{\phi_j}$ is verified, thus S_{ϕ_j} is an open set within a convex cone. And we define the function $\boldsymbol{\Phi}(m, \boldsymbol{s}, \boldsymbol{I}) \in \boldsymbol{R}^{10}$ to compose the vector of inertial parameters.

$$\boldsymbol{\Phi}(m, \boldsymbol{s}, \boldsymbol{I}) \triangleq \left[m\, ms_x\, ms_y\, ms_z\, I_{xx}\, I_{yy}\, I_{zz}\, I_{yz}\, I_{zx}\, I_{xy} \right]^T \tag{6}$$

Here, we approximate the parameters $\boldsymbol{\phi}_j \triangleq \boldsymbol{\Phi}(m_j, \boldsymbol{s}_j, \boldsymbol{I}_j)$ of the link j using $N_{\rho,j}$ mass points as follow.

$$\boldsymbol{\phi}_j = \boldsymbol{P}_j \boldsymbol{\rho}_j \ \left(\triangleq \sum_{k=1}^{N_{\rho,j}} \boldsymbol{\Phi}(1,\ {}^j\boldsymbol{r}_k,\ [{}^j\boldsymbol{r}_k\times][{}^j\boldsymbol{r}_k\times]^T)\rho_{j,k} \right) \tag{7}$$

Where, $\rho_{j,k}$ is the mass of the point $k(1 \leq k \leq N_{\rho,j})$, $\boldsymbol{\rho}_j \triangleq [\ \rho_{j,1}\ \cdots\ \rho_{j,N_{\rho,j}}\ ]^T \in \boldsymbol{R}^{N_{\rho,j}}$, ${}^j\boldsymbol{r}_k \in \boldsymbol{R}^3$ is the position with respect to the origin of the frame attached to link j, and $\boldsymbol{P}_j \in \boldsymbol{R}^{10\times N_{\rho,j}}$ is the matrix to compose $\boldsymbol{\phi}_j$ of $\boldsymbol{\rho}_j$. Hence, $\boldsymbol{\phi}$ is represented using all $N_\rho (= \sum_j N_{\rho,j})$ mass points as follow.

$$\boldsymbol{\phi} = \boldsymbol{P}\boldsymbol{\rho} \ \left(\triangleq \mathrm{diag}(\boldsymbol{P}_1, \cdots, \boldsymbol{P}_N) \left[\rho_{j,1} \cdots \rho_{j,N} \right]^T \right) \tag{8}$$

Where, $\boldsymbol{P} \in \boldsymbol{R}^{10N\times N_\rho}$ is the matrix with $\boldsymbol{P}_j$ on the j-th diagonal submatrix. If $\boldsymbol{P}_j$ is a full row rank matrix, then $\boldsymbol{P}$ is also full row rank, and

there exists $\boldsymbol{\rho}$ to realize any $\boldsymbol{\phi}$. Thus, mass points have to be located to make each $\boldsymbol{P}_j$ full row rank. Then, Eq.(4) can be approximated as $\boldsymbol{\rho} > \boldsymbol{0}$.

As we mentioned, Eq.(4) means the open set within a convex cone as Figure 1. On the other hand, the inertial matrix of the parameters $\rho_k \boldsymbol{\Phi}_k$ consist only of the mass point k is semi-positive definite, thus $\rho_k > 0$ means a ridge line of the convex cone as Figure 1. It means that $\boldsymbol{\rho} > \boldsymbol{0}$ approximates the convex cone by the polyhedral convex cone. Thus, if $\boldsymbol{\rho} > \boldsymbol{0}$ is verified, then Eq.(4) is verified, and Eq.(4) will be well approximated if the number of mass points increases. And the centers of mass satisfying $\boldsymbol{\rho} > \boldsymbol{0}$ always exist in the convex hull of the mass points, i.e. the link object. The optimization strategy to approximate nonlinear inequality constraints represented as a convex cone by a polyhedral convex cone is often adopted in other fields of robotics, for example in grasp analysis (Kerr and Roth (1986)).

Next, we deal with the following evaluation function instead of Eq.(4).

$$g(\boldsymbol{\rho}) = (\boldsymbol{Y}_{all}\boldsymbol{P}\boldsymbol{\rho} - \boldsymbol{f}_{all})^T \boldsymbol{W}_f (\boldsymbol{Y}_{all}\boldsymbol{P}\boldsymbol{\rho} - \boldsymbol{f}_{all}) + \boldsymbol{\rho}^T \boldsymbol{W}_\rho \boldsymbol{\rho} \quad (\boldsymbol{\rho} > \boldsymbol{0}) \tag{9}$$

Where, $\boldsymbol{W}_f \in \boldsymbol{R}^{N_j T \times N_j T}$ and $\boldsymbol{W}_\rho \in \boldsymbol{R}^{N_\rho \times N_\rho}$ are the weight matrices, and (semi-)positive definite. The solutions from LSM satisfy the first term of Eq.(9). However, the Hessian matrix of the usual evaluation function is always semi-positive definite as following reasons. Standard inertial parameters $\boldsymbol{\phi}$ (and of course $\boldsymbol{\rho}$) cannot be structurally identified as mentioned in the section 2. Moreover, the poor motion trajectories cause the ill condition that the rank of $\boldsymbol{Y}_{Ball}$ is nearly equal to zero and identification performance of some parameters declines significantly. Thus, the second term of Eq.(9) is added to evaluate. This term makes the Hessian matrix of the evaluation function a positive definite matrix, and prevents from those ill conditions.

The evaluation function Eq.(5) is the generalized notation which includes both the evaluation of LSM and QP using Eq.(5). If $\boldsymbol{W}_f = \lambda_\tau \boldsymbol{E}_{N_j T} + \lambda_\phi \boldsymbol{Y}_{Ball}{}^{\#T} \boldsymbol{Y}_{Ball}{}^{\#}$ and $\boldsymbol{W}_\rho = \boldsymbol{O}$, then Eq.(9) is equal to Eq.(5). Thus we can control both the exactness of the solution obtained from LSM and the stability of computation, choosing the weight matrices $\boldsymbol{W}_f$ and $\boldsymbol{W}_\rho$. This problem establishment uses an analogy from inverse kinematics solution with singularity robustness shown by Nakamura and Hanafusa (1986).

4 Experimental results

In this section, we show identification results of the humanoid robot shown in Figure 2 using the proposed method. This robot has 38 DOF as Table 1, however, the fingers were not used and maintained in a constant position during experiments, resulting in the use of 32 DOF. We use the identification model for legged systems(Ayusawa et al. (2009)). Its feature is to make use

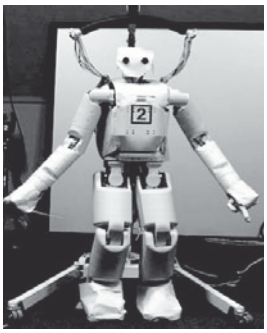

Figure 2. The IRT project humanoid robot.

Table 1. The joint specification and the mounted sensors of the humanoid.

Number of joint	3 (neck) 1 (waist) 7 (each leg) 7 (each arm) 3 (each hand)
Sensors	gyro/acceleration sensor (in the upper body link) 6-axis force sensors (in both feet) encorders (in each joint)

Table 2. Standard inertial parameters of 6 links estimated from the proposed method. (L1:upper trunk, L2: lower trunk, L3:left upper leg, L4:left foot, L5:right upper arm, L6:right hand)

Link	m	s_x^{BB}	s_y^{BB}	s_z^{BB}	I_{cxx}	I_{cyy}	I_{czz}	I_{cxy}	I_{cyz}	I_{czx}
L1	5.05	0.09	0.04	0.70	0.26	0.19	0.16	0.03	0.00	0.00
L2	4.06	0.03	0.56	-0.03	0.07	0.04	0.08	0.01	0.00	0.00
L3	2.53	0.12	0.13	-0.30	0.08	0.06	0.06	-0.03	0.01	0.01
L4	1.07	0.05	-0.12	-0.48	0.02	0.01	0.01	0.00	0.00	0.00
L5	1.59	0.15	0.34	0.32	0.01	0.01	0.01	0.00	0.00	0.00
L6	1.07	0.00	-0.06	-0.40	0.02	0.01	0.02	0.00	0.00	0.00

of only the six equations of motion of the base-link, and thus making the joint-torque measurement unnecessary. And we generated several types of walking motions and upper body motions to be used for identification.

The bounding box (BB) of each link object is treated as the convex hull, and we put $27(=3^3)$ equally-spaced points in BB. The matrix $\boldsymbol{W}_f$ is equivalent to the weight matrix of LSM. Thus, we used the weight matrix which minimizes variances of the estimated errors of input forces. And we choose $\boldsymbol{W}_\rho = 0.001\boldsymbol{E}_{N_{\rho,j}}$ to prevent from the ill condition of the optimization.

The standard inertial parameters estimated from the proposed method are given in Table 2. Table 2 shows the mass m[kg], the center of mass s_i^{BB} from the center of BB which is normalized by the size of BB, and the inertias I_{cij}[kg-m^2] (around the center of mass) of some links. All the results satisfy the physical conditions of Eq.(4), and the centers of mass also exist in BB because all the elements of s_i^{BB} are within ± 1. On the other hand, we could not obtain the converged solution from the QP with Eq.(4) and Eq.(5), and the results obtained from standard LSM using the same weight matrix $\boldsymbol{W}_f$ are not physically consistent. Hence, the proposed

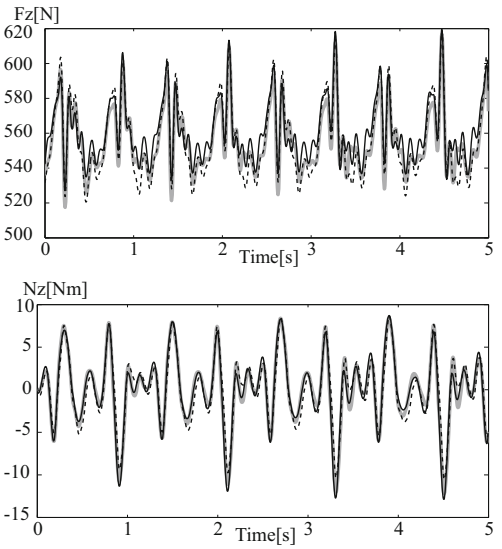

Figure 3. Cross validation figures of the external forces (F_Z and N_Z). The black thin lines show the measured external forces $\boldsymbol{F}$. The gray thick lines mean the estimated ones $\widehat{\boldsymbol{F}}_{LS}$ from LSM. The black dashed thin lines are the estimated ones $\widehat{\boldsymbol{F}}$ of the proposed method.

method shows both physical consistency and computational stability. It should be paid attention that the obtained values of Table 2 themselves are meaningless, because only base parameters can be identified from the dynamics model. Thus, they have meanings when the base parameters are composed of them, and the base parameters show physical consistency if the standard parameters of Table 2 are physically consistency.

Figure 3 shows the comparison of the total external forces acted on the base-link in the walking motion that is not used during the identification procedure. The black thin lines show the external forces $\boldsymbol{F}$ measured by force sensors, the gray thick lines mean the estimated ones $\widehat{\boldsymbol{F}}_{LS}$ from LSM, and the black dashed thin lines are the estimated ones $\widehat{\boldsymbol{F}}$ of the proposed method. As seen from the figures, the proposed method slightly reduces the accuracy with respect to LSM.

5 Conclusion

In this paper, the identification method for large-scale systems like legged system considering physical consistency and computational stability has

been proposed. Inertial parameters of each link are represented with a finite number of mass points, which can replace the physical conditions with linear inequalities. The performance of approximation can be enhanced as mass points increase, and the physical conditions concerning centers of mass can be also considered. The bounds of centers of mass can give physical consistency of standard inertial parameters, even though only base parameters are obtained in usual identification. We also design the evaluation function to control the exactness of identification results and the stability of computation. The method has been tested on a humanoid robot. The optimization has been performed successfully, and all the results show the physical consistency. The results are compared to ones obtained from LSM, and the proposed method slightly reduce the accuracy with respect to LSM.

Bibliography

C.G. Atkeson, C.H. An, and J.M. Hollerbach. Estimation of inertial parameters of manipulator loads and links. *Int. J. of Robotic Research*, 5(3): 101–119, 1986.

K. Ayusawa, G. Venture, and Y. Nakamura. Symbolic identifiability of legged mechanism using base-link dynamics. In *IFAC Symposium on System Identification*, pages 693–698, 2009.

M. Gautier and W. Khalil. Exciting trajectories for the identification of base inertial parameters of robots. *Int. J. of Robotics Research*, 11(4): 363–375, 1992.

J. Kerr and B. Roth. Analysis of multifingered hands. *Int. J. of Robotics Research*, 4(4):3–17, 1986.

W. Khalil and F. Bennis. Symbolic calculation of the base inertial parameters of closed-loop robots. *Int. J. of Robotics Research*, 14(2):112–128, 1995.

V. Mata, F. Benimeli, N. Farhat, and A. Valera. Dynamic parameter identification in industrial robots considering physical feasibility. *Int. J. of Advanced Robotics*, 19(1):101–119, 2005.

H. Mayeda, K. Osuka, and A. Kanagawa. A new identification method for serial manipulator arms. In *Pre. IFAC 9th World Congress*, pages 74–79, 1984.

Y. Nakamura and H. Hanafusa. Inverse kinematic solutions with singularity robustness for robot manipulator control. *ASME J. of Dynamic Systems, Measurement, and Control*, 108(4):163–171, 1986.

K. Yoshida and W. Khalil. Verification of the positive definiteness of the inertial matrix of manipulators using base inertial parameters. *Int. J. of Robotics Research*, 19(5):498–510, 2000.

Modeling Effects on Free Vibration of a Two-Link Flexible Manipulator

Carmelo di Castri[†] and Arcangelo Messina[†]

[†] Dipartimento di Ingegneria dell'Innovazione, Università del Salento, Lecce, Italia

Abstract In this article, the frequency characteristics of a two-link flexible manipulator in an arbitrary position are investigated by using two analytical models. In particular, two formulations based on Euler-Bernoulli beam theory are herein used to derive analytical modal data for different slenderness ratios of robotic manipulators. The comparison between the results stresses that, except for extremely flexible manipulators, appreciable discrepancies can occur; these latter can be attributed to axial vibrations which, are neglected in one model, but are instead introduced in the other as proposed by the present authors. A finite element analysis validates this latter model thus making the authors confident on the ability of the model to provide more accurate results for a larger class of robotic manipulators.

1 Introduction

During recent decades, increasing demand for precise high speed operation has made flexible manipulators attractive and great attention has been dedicated to the modeling and vibration control of such structures, mainly in the area of space and industrial robots with flexible links. Many researchers have tried to develop dynamic models that describe the motion of flexible manipulators by taking into account the effects of links flexibility in order to have an explicit, complete and accurate dynamic model (see, *e.g.*, Tomei and Tornambè, 1989; De Luca and Siciliano, 1991; Chen, 2001). Their dynamic formulations of the flexible multibody system (based on Euler-Bernoulli beam theory) led to infinite-dimensional models described by a set of partial differential equations that could not be solved analytically; then, approximate techniques were used to change these partial differential equations to a set of ordinary differential equations in order to obtain a finite-dimensional system that can easily be solved numerically.

Milford and Asokanthan (1999) derived the exact partial differential equations governing the system modes of a two-link flexible manipulator within the framework of the Euler-Bernoulli beam theory; they used an exact boundary conditions formulation and showed that eigenfrequencies and eigenfunctions are a strong function of manipulator configuration. Here, based on the assumptions by Di Castri et al. (2009),

an exact model to determine modal data (*i.e.* natural frequencies and mode shapes) of a two-link manipulator based on Euler-Bernoulli beam theory is presented; in this work, the configuration-dependent differential eigenvalue problem is derived by also taking the axial dynamics into account. It is highlighted how the inclusion of the axial influence is not computationally expensive as also stressed by Di Castri et al. (2009); however, in this latter paper, a complete validation of the axial influence was not provided neither with respect to a frequency range on modal data nor within the frame of occurring configurations of robotic manipulators.

In this paper, a comparison between the above mentioned two formulations is presented; it is herein shown how the results predicted by the two models can become very different when the slenderness ratio of the structure changes and these discrepancies can be attributed to the axial deformation effect, which is absent in Milford and Asokanthan (1999). The comparison is done firstly through simulations carried out for an extremely flexible two-link manipulator and subsequently for different values of the slenderness ratio. Natural frequencies are reported for different nominal configurations of the manipulator, chosen as significant cases. Finally, results of a finite element package are presented and are found to be in excellent agreement with those of the model here introduced.

2 Manipulator models

The two-link manipulator model is illustrated in Figure 1 in its undeformed shape. It consists of two homogeneous, isotropic and elastic links with constant cross section S_i and linear mass density μ_i (i=1,2), with each link having length L_i and flexural rigidity E_iI_i. The flexible robot has a shoulder joint variable θ_1 and an elbow joint variable θ_2. Robot motion and vibration modes are planar with gravity being neglected. Mass M_i and inertia J_i take account for the presence of joint actuators, whereas M_P and J_P are referred to a possible payload handled by the manipulator end effector. Moreover, in order to express elastic deformations, two local reference frames (X_1,Y_1) and (X_2,Y_2) are defined, which are respectively attached to the shoulder and elbow hub as shown in Figure 1. X_1 and X_2 axes coincide with the undeformed neutral axes, which fully characterize the spatial shapes of the links. Henceforth, let us denote with "M model" the formulation presented by Milford and Asokanthan (1999), and with "D model" the one presented here.

Both models present modal analysis of the two-link manipulator, based on small perturbation about a nominal configuration; in order to derive configuration-dependent modal data, rigid body motions of the system are prevented by blocking both joints. The main difference between analytical formulations is whether or not the axial deformations are considered in the system dynamic description. In particular, M model neglects longitudinal dynamics of the links, whereas D model takes into account the axial and transverse dynamics; this leads to consider, according to the exact model,

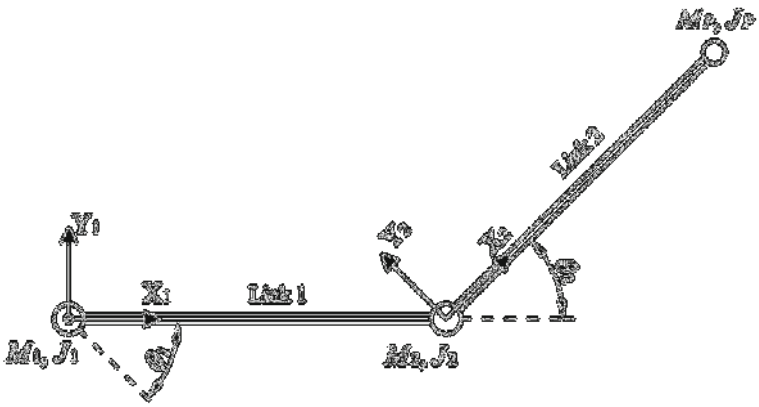

Figure 1. Two-link flexible manipulator.

different arrangements of the local reference frames to represent the deformed shape of the manipulator.

Firstly, referring to Figure 2, since the boundary-value problem does not depend on joint variable θ_1, a simplifying cantilever boundary condition is considered in the shoulder section O_1 for both models. In order to represent the *i*th mode shape of the manipulator, M model moves the local frame (X_2,Y_2) along X_2 by a measure equal to the rigid displacement that the second link undergoes along that direction because of the bending of the first link. For this reason, the position of the local frame (X_2,Y_2) changes according to the represented mode shape.

Moreover, if we consider the system at rest and a point of the *i*th link (i=1,2) which has coordinates $(x_i,0)$ in the reference system (X_i, Y_i), being x_i the distance from O_i measured on the neutral axis, its position after deformation will be $(x_i, v_i(x_i,t))$, where $v_i(x_i,t)$ is the field variable associated with the transverse displacement. Conversely, D model always represents all the mode shapes in the same coordinate systems, which are those initially associated with the undeformed shape of the system (Figure 2). In this case, the above considered point $(x_i,0)$ is located, in its actual state, by the position $(x_i+u_i(x_i,t), v_i(x_i,t))$, being $u_i(x_i,t)$ the axial displacement.

According to the Euler-Bernoulli beam theory, M model requires the following two partial differential equations (PDEs) to describe the transverse motion of the links:

$$E_i I_i \frac{\partial^4 v_i(x_i,t)}{\partial x_i^4} + \mu_i \frac{\partial^2 v_i(x_i,t)}{\partial t^2} = 0, \quad i=1,2 \tag{1}$$

In addition to the PDEs in (1), D model introduces the following PDEs for the axial dynamics of the links:

$$E_i S_i \frac{\partial^2 u_i(x_i,t)}{\partial x_i^2} - \mu_i \frac{\partial^2 u_i(x_i,t)}{\partial t^2} = 0, \quad i=1,2 \tag{2}$$

In spite of the possible simplicity of equation (2), it is here shown that the relevant results can introduce appreciable variations with respect to its absence when coupling phenomena are involved through the boundary conditions.

Now, choosing a value for θ_2 (denoted by θ_{20}) and using boundary conditions, it is possible to obtain the corresponding differential eigenvalue problem for each model, associated with the nominal configuration θ_{20}; such a problem is expressed in compact form as

$$\mathbf{A}(\omega)\mathbf{x} = \mathbf{0} \tag{3}$$

where $\mathbf{A}(\omega)$ is the characteristic matrix of the manipulator, with ω natural frequency, and $\mathbf{x}$ is the vector of modal coefficients that characterize the axial eigenfunction $U_i(x_i)$ and the transverse eigenfunction $V_i(x_i)$, i=1,2. The appendix explicitly illustrates the relevant analytical quantities for the model here introduced.

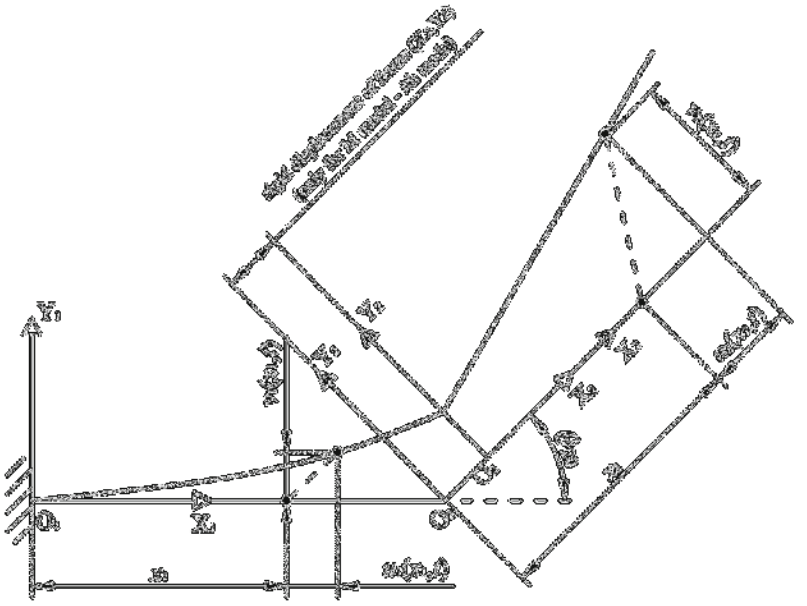

Figure 2. Displacement functions for deformed shape.

We observe that $\mathbf{A}(\omega)$ and $\mathbf{x}$ are quite different for both models (*e.g.* see Milford and Asokanthan (1999 pp.198-199) compared to the appendix); in fact, the characteristic matrix for M model is a square matrix of order 8 and $\mathbf{x}$ is 8×1, since boundary conditions for this model have been formulated from relations for transverse displacement, slope, bending moment and shear force, which are related to eight modal constants. D model is instead based on a 12×12 characteristic matrix with a modal vector $\mathbf{x}$ having 12 components, since, in addition to the aforementioned physical quantity, contributions due to axial displacements and axial forces have been taken into account in the boundary sections. To this end, we stress that even if PDEs for axial and transverse vibrations are always uncoupled, this uncoupling also depends on the boundary conditions; indeed, D model, with its axial-transverse formulation, couples the two vibratory behaviours through boundary conditions.

3 Simulations and discussion

To demonstrate the effects of the modeling strategies described in the previous section, simulation results are presented in this section. The basic structural model adopted is the extremely flexible two-link manipulator used by Milford and Asokanthan (1999) to experimentally validate their analytical predictions. In order to derive modal data through both exact models, M model and D model are implemented in MATLAB® R2007a and a contextual finite element analysis is also carried out by using ABAQUS 6.6, with each link divided into fifty-five Euler-Bernoulli beam elements.

Among all the possible choices, natural frequencies are calculated for three nominal configurations of the manipulator, which correspond to $\theta_{20} = -30°$, $\theta_{20} = 0°$ and $\theta_{20} = 45°$; for each configuration, a slenderness-dependent analysis is carried out. More precisely, a thickness factor t_f is introduced and modal data are derived for the assigned configuration when t_f is equal to 1, 25 and 50, so that thicknesses equal to $t_f \cdot h_i$ (i=1,2) are respectively considered for each case (where h_i is the original thickness value of the experimental manipulator originally used by Milford and Asokanthan (1999)). We observe that by varying t_f from 1 to 50, local slenderness ratios range approximately between 3000 and 60; this considerable variation is chosen in order to allow a better investigation of the modeling effects on frequency characteristics (see also the mode shape change of Figure 3) of the two-link flexible manipulator if thicker links than those used by Milford and Asokanthan (1999) were considered. In fact, h_i is really a small quantity (0.6 mm) whilst larger values can easily be encountered when treating with flexible manipulators.

Table 1. Natural frequencies [Hz] for $\theta_{20} = -30°$.

	$t_f = 1$			$t_f = 25$			$t_f = 50$		
Mode	M model	D model	e%	M model	D model	e%	M model	D model	e%
1	0.2051	0.2051	0.00	11.253	11.253	0.00	23.454	23.454	0.00
2	0.8898	0.8898	0.00	57.199	57.189	0.02	121.88	121.79	0.07
3	4.8716	4.8716	0.00	188.34	188.26	0.04	390.49	389.87	0.16
4	9.0299	9.0299	0.00	336.89	335.95	0.28	699.08	687.48	1.7
5	14.478	14.478	0.00	594.38	592.59	0.3	1243.3	1204.0	3.3
6	20.610	20.610	0.00	854.83	844.05	1.3	1771.6	1439.4	23
7	36.366	36.366	0.00	1187.7	1162.3	2.2	2525.4	1902.9	33
8	36.749	36.749	0.00	1546.4	1396.0	11	3302.6	2576.1	28
9	62.809	62.809	0.00	1967.6	1621.9	21	4196.4	3314.0	27
10	70.890	70.890	0.00	2341.4	2004.1	17	5125.3	3692.1	39

Table 1 reports the first ten natural frequencies calculated through M model and D model when θ_{20} is equal to –30°. The occurring natural frequency changes are calculated as

$$e_j\% = \frac{\text{M model} - \text{D model}}{\text{D model}} \cdot 100, \quad j = 1 \ldots 10 \tag{4}$$

Finite elements results are reported in Table 2 and correspond to results obtained after having submitted the relevant FE-analysis to a relevant convergence test (55 elements for each beam). As it can be observed from tables 1 and 2, both models agree with each other and with the finite element analysis only for t_f =1, *i.e.* when an extremely high flexibility is taken into account. In this case, the assumption made by M model, which neglects the axial deformations, is validated and the model can be used to obtain accurate data. However, as t_f increases, the above agreement ceases and appreciable discrepancies occur, up to 21% and 39% for t_f equal to 25 and 50 respectively. Since finite element results fully agree with D model, we can state that this latter represents a more reliable way of deriving modal data, whereas M model becomes appreciably inaccurate; moreover, it can be expected that this inaccuracy is intended to grow for larger values of t_f; however, in these latter cases the possibility of adopting a higher order model (uniform o higher order shear deformable theories) should also to be taken into account. Figure 4 again presents the same comparison between exact models by a graphical representation of the frequency changes occurred for $\theta_{20} = 0°$ and for $\theta_{20} = 45°$. It is observed that in the second case (on the right of the figure), the same considerations of the previous comparison in Table 1 can be deduced;

in particular, for t_f=50, the error is again over 30%. Finite element analysis agrees again with D model . The only case for which M model and D model give the same results, for any thickness, is when θ_{20} = 0° (on the left of the figure); it can be explained by observing that, in this condition, axial and transverse vibrations are uncoupled, and the manipulator behaves like a cantilever beam.

Table 2. Finite element results [Hz] for θ_{20} = –30° (ABAQUS 6.6, B23 element).

Mode	t_f = 1	t_f = 25	t_f = 50
1	0.2051	11.253	23.454
2	0.8898	57.189	121.79
3	4.8716	188.26	389.87
4	9.0299	335.95	687.48
5	14.478	592.59	1204.0
6	20.610	844.05	1439.4
7	36.366	1162.3	1902.9
8	36.749	1396.0	2576.1
9	62.809	1621.9	3314.0
10	70.890	2004.1	3692.1

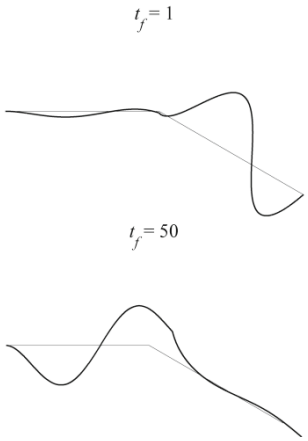

Figura 3. Analytical modes (D model: 20.610, 1439.4 Hz).

4 Concluding remarks

In this paper, two analytical models for investigating the modal analysis of a two-link flexible manipulator have been compared and the model here proposed has been numerically validated too. The two analytical descriptions differ for a different treatment of both the axial dynamics of the links and the local system of coordinates. Exact modal data have been derived through both formulations for different geometrical configurations of a manipulator having links modeled as Euler-Bernoulli beams. For each chosen configuration, the influence of the structural slenderness ratio on the predicted results by the two analytical models has been evaluated through a simulation study. Natural frequencies and data plots have been reported in detail. It has been shown that, except for extreme flexibility conditions (tenths of millimeter thicknesses), substantial discrepancies can arise between both models. A finite element analysis has validated all the results obtained through the analytical axial-transverse model here introduced.

References

Chen, W. (2001). Dynamic modeling of multi-link flexible robotic manipulators. *Computers and Structures* 79:183-195.

De Luca, A., and Siciliano, B. (1991). Closed form dynamic model of planar multilink lightweight robots. *IEEE Transactions on Systems, Man, and Cybernetics*, July-August 1991, vol. 21, no. 4, 826-839.

Di Castri, C., Messina, A., and Reina, G. (2009). Modal Analysis of a Two Link Flexible Manipulator. *Proceedings of the RAAD 2009 18TH International Workshop of Robotics in Alpe-Adria-Danube Region*, Brasov, Romania, May 2009.

Milford, R. I., and Asokanthan, S. F. (1999). Configuration dependent eigenfrequencies for a two-link flexible manipulator: experimental verification. *Journal of Sound and Vibration* 222:191-207.

Simulia (2006). ABAQUS Version 6.6 HTML Documentation.

The MathWorks™ (2007). MATLAB® Online Documentation.

Tomei, P., and Tornambè, A. (1988). Approximate modeling of robots having elastic links. *IEEE Transactions on Systems, Man, and Cybernetics*, September-October 1988, vol. 18, no. 5, 831-840.

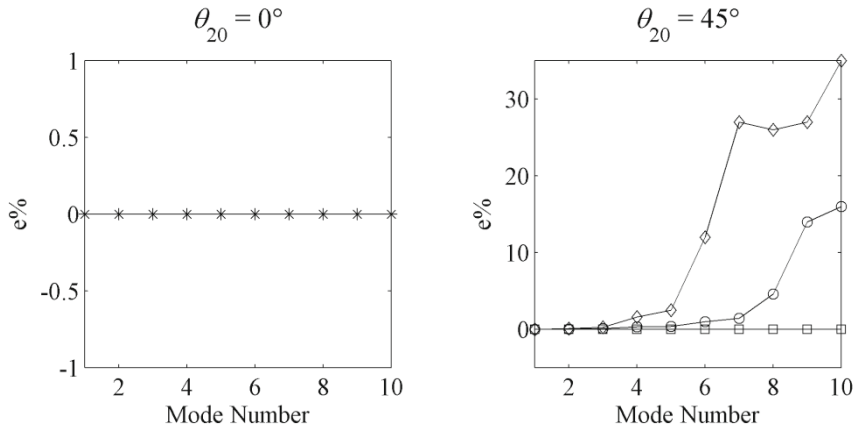

Figure 4. Natural frequency changes. * t_f =(1,25,50); □ t_f =1; ○ t_f =25; ◊ t_f =50.

Appendix: mathematical formulation of the two-link manipulator with axial dynamics (D model)

Abbreviations: $s(\cdot)=\sin(\cdot)$; $c(\cdot)=\cos(\cdot)$; $sh(\cdot)=\sinh(\cdot)$; $ch(\cdot)=\cosh(\cdot)$

Eigenfunctions (i=1,2): transverse $V_i(x_i)=C_{i1}s(\alpha_i x_i)+C_{i2}c(\alpha_i x_i)+C_{i3}sh(\alpha_i x_i)+C_{i4}ch(\alpha_i x_i)$; axial $U_i(x_i)=C_{i5}c(\omega x_i/c_i)+C_{i6}s(\omega x_i/c_i)$

Parameters: $\alpha_i=[\mu_i\omega^2/(E_iI_i)]^{1/4}$; $c_i=(E_iS_i/\mu_i)^{1/2}$ Vector of modal coefficients $\mathbf{x}=[C_{11}\ C_{12}\ C_{13}\ C_{14}\ C_{15}\ C_{16}\ C_{21}\ C_{22}\ C_{23}\ C_{24}\ C_{25}\ C_{26}]^T$

Characteristic matrix $\mathbf{A}(\omega)=\begin{pmatrix}[\mathbf{A}_{O_1}(\omega)]_{3x12}\\ [\mathbf{A}_{O_2}(\omega)]_{6x12}\\ [\mathbf{A}_P(\omega)]_{3x12}\end{pmatrix}$ where: $\mathbf{A}_{O_1}(\omega)=\begin{pmatrix}0&1&0&1&0&0\\1&0&1&0&0&0\\0&0&0&0&1&0\end{pmatrix}\ [\mathbf{0}]_{3x6}$

$$\mathbf{A}_{O_2}(\omega)=\begin{pmatrix}
-\alpha_1 s(\alpha_1L_1) & \alpha_1 c(\alpha_1L_1) & \alpha_1 sh(\alpha_1L_1) & \alpha_1 ch(\alpha_1L_1) & 0 & 0 & 0 & -\alpha_2 & 0 & -\alpha_2 & 0 & 0\\
c(\alpha_1L_1)s(\theta_2) & s(\alpha_1L_1)s(\theta_2) & ch(\alpha_1L_1)s(\theta_2) & sh(\alpha_1L_1)s(\theta_2) & c(\omega/c_1L_1)c(\theta_2) & s(\omega/c_1L_1)c(\theta_2) & 0 & 0 & 0 & 0 & -1 & 0\\
c(\alpha_1L_1)c(\theta_2) & s(\alpha_1L_1)c(\theta_2) & ch(\alpha_1L_1)c(\theta_2) & sh(\alpha_1L_1)c(\theta_2) & -c(\omega/c_1L_1)s(\theta_2) & -s(\omega/c_1L_1)s(\theta_2) & -1 & 0 & -1 & 0 & 0 & 0\\
\begin{matrix}-E_1I_1\alpha_1^2c(\alpha_1L_1)\\ +\omega^2J_2\alpha_1s(\alpha_1L_1)\end{matrix} & \begin{matrix}-E_1I_1\alpha_1^2s(\alpha_1L_1)\\ -\omega^2J_2\alpha_1c(\alpha_1L_1)\end{matrix} & \begin{matrix}E_1I_1\alpha_1^2ch(\alpha_1L_1)\\ -\omega^2J_2\alpha_1sh(\alpha_1L_1)\end{matrix} & \begin{matrix}E_1I_1\alpha_1^2sh(\alpha_1L_1)\\ -\omega^2J_2\alpha_1ch(\alpha_1L_1)\end{matrix} & 0 & 0 & E_2I_2\alpha_2^2 & 0 & -E_2I_2\alpha_2^2 & 0 & 0 & 0\\
\begin{matrix}-E_1I_1\alpha_1^3s(\alpha_1L_1)\\ -\omega^2M_2\alpha_1c(\alpha_1L_1)\end{matrix} & \begin{matrix}E_1I_1\alpha_1^3c(\alpha_1L_1)\\ -\omega^2M_2\alpha_1s(\alpha_1L_1)\end{matrix} & \begin{matrix}-E_1I_1\alpha_1^3sh(\alpha_1L_1)\\ -\omega^2M_2\alpha_1ch(\alpha_1L_1)\end{matrix} & \begin{matrix}-E_1I_1\alpha_1^3ch(\alpha_1L_1)\\ -\omega^2M_2\alpha_1sh(\alpha_1L_1)\end{matrix} & 0 & 0 & 0 & \begin{matrix}-E_2I_2\alpha_2^3\cdot\\ c(\theta_2)\end{matrix} & 0 & \begin{matrix}E_2I_2\alpha_2^3\cdot\\ c(\theta_2)\end{matrix} & 0 & \begin{matrix}-E_2S_2(\omega/c_2)\cdot\\ s(\theta_2)\end{matrix}\\
0 & 0 & 0 & 0 & \begin{matrix}-E_1S_1(\omega/c_1)s(\omega/c_1L_1)\\ -\omega^2M_2c(\omega/c_1L_1)\end{matrix} & \begin{matrix}E_1S_1(\omega/c_1)c(\omega/c_1L_1)\\ -\omega^2M_2s(\omega/c_1L_1)\end{matrix} & 0 & \begin{matrix}E_2I_2\alpha_2^3\cdot\\ s(\theta_2)\end{matrix} & 0 & \begin{matrix}-E_2I_2\alpha_2^3\\ \ \end{matrix} & 0 & \begin{matrix}-E_2S_2(\omega/c_2)\cdot\\ c(\theta_2)\end{matrix}
\end{pmatrix}$$

$$\mathbf{A}_P(\omega)=\begin{pmatrix}
 & \begin{matrix}-E_2I_2\alpha_2^2c(\alpha_2L_2)\\ +\omega^2J_P\alpha_2s(\alpha_2L_2)\end{matrix} & \begin{matrix}-E_2I_2\alpha_2^2s(\alpha_2L_2)\\ -\omega^2J_P\alpha_2c(\alpha_2L_2)\end{matrix} & \begin{matrix}E_2I_2\alpha_2^2ch(\alpha_2L_2)\\ -\omega^2J_P\alpha_2sh(\alpha_2L_2)\end{matrix} & \begin{matrix}E_2I_2\alpha_2^2sh(\alpha_2L_2)\\ -\omega^2J_P\alpha_2ch(\alpha_2L_2)\end{matrix} & 0 & 0\\
[\mathbf{0}]_{3x6} & \begin{matrix}-E_2I_2\alpha_2^3s(\alpha_2L_2)\\ -\omega^2M_P\alpha_2c(\alpha_2L_2)\end{matrix} & \begin{matrix}E_2I_2\alpha_2^3c(\alpha_2L_2)\\ -\omega^2M_P\alpha_2s(\alpha_2L_2)\end{matrix} & \begin{matrix}-E_2I_2\alpha_2^3sh(\alpha_2L_2)\\ -\omega^2M_P\alpha_2ch(\alpha_2L_2)\end{matrix} & \begin{matrix}-E_2I_2\alpha_2^3ch(\alpha_2L_2)\\ -\omega^2M_P\alpha_2sh(\alpha_2L_2)\end{matrix} & 0 & 0\\
 & 0 & 0 & 0 & 0 & \begin{matrix}-E_2S_2(\omega/c_2)s(\omega/c_2L_2)\\ -\omega^2M_Pc(\omega/c_2L_2)\end{matrix} & \begin{matrix}E_2S_2(\omega/c_2)c(\omega/c_2L_2)\\ -\omega^2M_Ps(\omega/c_2L_2)\end{matrix}
\end{pmatrix}$$

Chatter Suppression in Sliding Mode Control: Strategies and Tuning Methods

Michael D O'Toole, Kaddour Bouazza-Marouf, and David Kerr
Wolfson School, Loughborough University, Loughborough, UK

Abstract. Sliding mode control is a highly robust technique for control of systems with bounded uncertainty. In practice however, sliding mode controllers induce chatter in the system, degrading the system's performance and damaging its physical components. In this paper, sliding mode controllers for chatter suppression are investigated. Harmonic linearization functions are presented for each of the sliding mode controllers, and are used to obtain estimations of the chattering amplitude and decay-rate of the closed-loop system. The aim is to assist in the tuning of chatter suppression sliding mode controllers to meet a desired system performance specification.

1. Introduction

Sliding mode control uses a relay in the feedback loop to drive a state-trajectory towards a 'sliding surface' and maintain it on this surface for all time. The sliding surface is designed so that, while the state-trajectory is in contact, the system exhibits desired dynamic properties and is invariant to matched uncertainty.

The design of classical sliding mode controllers requires the relative degree of the system with respect to the output switching variable (or sliding variable) be equal to one [1]. In practice however, un-modeled parasitic dynamics in the actuators and sensors raise the relative degree of the system. If the relative degree is greater than three, then the relay in the feedback loop causes self-sustaining oscillations (limit-cycles) in the system output, which degrade the system's performance and can damage its physical components. This phenomenon is referred to as chattering. The problem of chatter in sliding mode control is well-studied [2, 3], and several chatter suppression sliding mode controllers have been proposed. The aim of this paper is to explore the affect on system behavior of using these chatter suppression controllers, in order to more effectively tune the controllers to meet a prescribed system performance. The following notation is used throughout this paper: A single-input single-output system, with 1^{st} order parasitic dynamics on the actuator channel and each of the sensor channels, is expressed as

$$\begin{bmatrix} \dot{z} \\ \mu_s \dot{x} \\ \mu_A \dot{\tilde{u}} \end{bmatrix} = \begin{bmatrix} A & 0 & B \\ I_2 & -I_2 & 0 \\ 0 & 0 & -1 \end{bmatrix} \begin{bmatrix} z \\ x \\ \tilde{u} \end{bmatrix} + \begin{bmatrix} 0 \\ 0 \\ 1 \end{bmatrix} u \ , \ \sigma = S \begin{bmatrix} z \\ x \\ \tilde{u} \end{bmatrix} \tag{1}$$

where $z \in R^n$ is the plant state-variable, $x \in R^n$ the sensor state variable, $\tilde{u} \in R^1$ is the actuator state variable, and $\sigma \in R^1$ the output sliding variable. μ_s, μ_A are the time-constants of the parasitic dynamics, $A \in R^{n \times n}, B \in R^n$ are the plant matrices, and $S \in R^{2n+1}$ is the output distribution matrix, which describes the sliding surface.

2. Chatter Suppression Strategies

2.1 Continuous Approximation Strategies

Chattering can be suppressed by smoothing the discontinuity present in the closed-loop by replacing the hard-relay with a continuous approximation. The smoother the approximation, the more the resultant chatter is attenuated, until chattering is no-longer an equilibrium solution, and the system converges with the sliding plane. Further smoothing has the effect of damping the system, reducing the number of diminishing oscillations before convergence. The trade-off for this advantage is that finite-time convergence with the sliding-plane cannot be guaranteed; rather the trajectory will converge within some small neighborhood about the sliding-plane, resulting in a steady-state error. The second disadvantage is the loss of invariance to matched uncertainty. The use of a hard relay in the feedback loop ensures the full influence of the controller is deployed when the trajectory departs from the sliding surface, regardless of the size of the perturbation. A continuous approximation on the other hand, deploys a control effort proportional to the deviation from the sliding surface, and thus, small perturbations are tolerated.

The three most commonly used continuous approximation control laws are the boundary layer method, the sigmoid function method, and the power-law method. These functions are described below:

1) The *boundary layer method* [4] replaces the discontinuous relay function with a saturation relay function. Within a bounded region, chosen by design, the sliding mode controller becomes a continuous high-gain linear controller. The controller has the following form

$$u(\sigma, t) = -\rho . sat\left(\frac{\sigma(t)}{\delta} \right), \quad sat(\xi) = \begin{cases} \xi & if |\xi| < 1 \\ \text{sgn}(\xi) & otherwise \end{cases} \tag{2}$$

where δ is the boundary-limit about the switching surface.

2) The *sigmoid function method* has been used in both SISO and MIMO sliding mode controllers [1, 5, 6]. It has the form

$$u(\sigma,t) = -\rho \frac{\sigma(t)}{\|\sigma(t)\| + \delta} \tag{3}$$

where $\delta > 0$ is a small design constant that smoothes the discontinuity.

3) The *power-law method* [1, 7] smoothes the relay by raising the switching function to a power δ where $0 \le \delta < 1$. This is coupled with a signum function to reflect the result across into the negative plane. The controller has the form

$$u(\sigma,t) = -\rho \|\sigma(t)\|^{\delta} \operatorname{sgn} \sigma(t) \tag{4}$$

2.2 Higher Order Sliding Modes

The classical sliding mode controller assumes the system has relative degree one with respect to the switching variable $\sigma(t)$. Higher order sliding mode controllers allow this condition to be relaxed. For simplicity, the proceeding discussion will be reserved to sliding mode controllers designed for systems with relative degree 2. By convention, these controllers are referred to as 2-sliding mode controllers. Controllers for sliding mode systems with higher relative degrees have also been developed [8].

The *twisting controller* [9, 10] was an early evolution of 2-sliding mode control and has subsequently proved very popular with control practitioners. This can partly be attributed to the relative simplicity of its design. The twisting controller has the form

$$u = -\left(r_1 \operatorname{sgn}(\sigma(t)) + r_2 \operatorname{sgn}(\dot{\sigma}(t))\right) \tag{5}$$

where r_1 and r_2 are design parameters that satisfy $r_1 > r_2$.

The *generalized sub-optimal controller* [2, 11] uses the extremal value of the switching variable, i.e. the maximum and minimum values of the switching variable, as an adaptive term within its structure. Unlike the other 2-sliding mode controllers, no intermediate differentiator is required to derive $\dot{\sigma}(t)$. This results in a simpler algorithm with less input noise. The controller has the form

$$u = -r_1 \operatorname{sgn}(\sigma(t) - r_2 \sigma_M) \tag{6}$$

where σ_M is the last extremal value of the sliding variable, and r_1, r_2 are design variables.

3. Performance Estimation

3.1 Stability

The open-loop system in equation (1) can redefined as the n^{th} derivative of the output variable (sliding variable), i.e.

$$\sigma^{(n)}(t) = h(x,t) + g(x,t)u(\sigma,t) \tag{7}$$

where $h(x,t)$ and $g(x,t)$ are unknown smooth functions that can be determined from input-output relations, i.e. $h(x,t)$ is the n^{th} derivative when $u = 0$, and $g(x,t) = (\partial / \partial u)\sigma^{(n)}(t)$. Both functions are assumed to be bounded by the constants $K_m, K_M, C > 0$ such that

$$0 < K_m \le \frac{\partial}{\partial u}\sigma^{(n)}(t) \le K_M \qquad \left|\sigma^{(n)}(t)\right|_{u=0} \le C$$

From these bounds, a differential inclusion is derived to obtain stability conditions for the sliding mode controllers. The conditions are given in table 1.

Table .1. Stability conditions for sliding mode controllers.

Controller	Stability Condition
Saturation	$\rho > C / K_m$
Sigmoid function	$\rho > C\left(1 + \delta / \sigma(t)\right) / K_m$
Power-law	$\rho > C / \left(K_m \lvert\sigma(t)\rvert^{\delta}\right)$
Twisting Controller	$(r_1 + r_2)K_m - C > K_M(r_1 - r_2) + C$ $(r_1 - r_2)K_m > C, \quad 0 < r_2 < r_1$
Generalized Sub-optimal controller	$r_1 > C / K_m, \qquad r_2 > \frac{2C + (1-\beta)K_M r_1}{(1+\beta)K_m r_2}$

3.2 Harmonic linearization

The decay-rate and chattering amplitude of a sliding mode controlled system can be estimated using the harmonic linearization of the controller. The accuracy of the linearization is dependent on the open-loop system having a frequency response equivalent to a low-pass filter. Otherwise the omission of higher order terms in the Fourier approximation contributes considerable error. The characteristic equation of the system in equation (1) is expressed as

$$A(p)\sigma(t) + B(p)F(\sigma(t), \dot{\sigma}(t)) = 0 \tag{8}$$

where p is the laplace variable (for the linear components of the characteristic equation), and $F(\sigma(t), p\sigma(t))$ the nonlinear controller. Assume that the state-trajectory of the sliding variable $\sigma(t)$ can be satisfactorily approximated by a first order solution

$$\sigma(t) = a(t)\sin\theta(t)$$

$$\frac{da}{dt} = a\zeta(t)\,,\ \frac{d\theta(t)}{dt} = \omega(t) \tag{9}$$

where are $\zeta(t)$ and $\omega(t)$ are analogous to (but not the same as) damping ratio and damped frequency in second-order linear systems theory. It follows that

$$\begin{aligned}\sigma(t) &= a(t)\sin\theta(t)\\ \dot{\sigma}(t) &= a\left[\zeta(t)\sin\theta(t) + \omega(t)\cos\theta(t)\right]\end{aligned} \tag{10}$$

Thus, the first harmonic linearization of the nonlinear function is [12]

$$\begin{aligned}F(\sigma(t), \dot{\sigma}(t)) &= N(a, \zeta, \omega)\sigma(t) = \frac{1}{a}\left[P(a, \zeta, \omega) + jQ(a, \zeta, \omega)\right]\sigma(t)\\ P &= \frac{1}{\pi}\int_0^{2\pi} F\left[a\sin\theta(t), a\left(\omega\cos\theta(t) + \zeta(t)\sin\theta(t)\right)\right]\sin\theta(t)d\theta\\ Q &= \frac{1}{\pi}\int_0^{2\pi} F\left[a\sin\theta(t), a\left(\omega\cos\theta(t) + \zeta(t)\sin\theta(t)\right)\right]\cos\theta(t)d\theta\end{aligned} \tag{11}$$

The harmonic linearization, in combination with the characteristic equation, is used to derive an amplitude dependent function of the damping ratio $\zeta(a)$. The time for the system to settle from an initial oscillation a_0 amplitude to a final amplitude a_k is given by

$$t_s = \int_{a_0}^{a_k} \frac{1}{a\zeta(a)}da \tag{12}$$

which is obtained from equation (8). Alternatively by setting $\zeta = 0$, equation (7) is rearranged to give an expression to find chattering frequency and amplitude

$$G(j\omega) = \frac{B(j\omega)}{A(j\omega)} = -\frac{1}{N(a,0,\omega)} \tag{13}$$

where $G(j\omega)$ is the open-loop frequency response. Equation (13) is the describing function method, which is used to graphically find limit-cycle solutions in

nonlinear systems using Nyquist plots [13]. A stable limit-cycle occurs at a point of intersection between the open-loop frequency response of the system $G(j\omega)$ and the negative reciprocal of the harmonic linearization. The amplitude a and the frequency ω at the intersection are the amplitude and frequency of the chatter.

The harmonic linearization of each of the controllers is given in table 2. The term a is the chatter amplitude, and $\Gamma(\cdot)$ is the gamma function.

Table .2. Harmonic Linearization of sliding mode controllers.

Controller	Describing Function
Standard SMC	$N(a) = 4\rho / \pi a$
Saturation function	$N(a) = \frac{2\rho}{\pi\delta}\left\{\frac{\delta}{a}\sqrt{1-(\delta/a)^2} + \sin^{-1}(\delta/a)\right\}$
Sigmoid function	$N(a) = \frac{2\rho}{\pi a}\left(2 - \frac{\delta}{a}\pi\right) + \frac{4\rho(\delta/a)^2}{\pi a\sqrt{(\delta/a)^2-1}}\left(\frac{\pi}{2} - \tan^{-1}\left(\frac{1}{\sqrt{(\delta/a)^2-1}}\right)\right)$
Power-law [7]	$N(a) = 2\rho a^{\delta-1}\Gamma\left(\frac{\delta}{2}+1\right)/\sqrt{\pi}\Gamma\left(\frac{\delta}{2}+1.5\right)$
Twisting controller	$N(a,\zeta,\omega) = \frac{4}{\pi a}\left(r_1 - \frac{r_2}{\sqrt{1+(-\omega/\zeta)^2}} - j\frac{r_2\omega}{\zeta\sqrt{1+(-\omega/\zeta)^2}}\right)$
Generalized Sub-optimal controller	$N(a,\zeta,\omega) = \frac{4r_1}{\pi a}\left(\sqrt{1-(r_2 e^{-\zeta\pi/(\omega\sqrt{2})})^2} + j(r_2 e^{-\zeta\pi/(\omega\sqrt{2})})\right)$

4. Example

Introducing a second order plant with fast-acting first order sensor and actuator dynamics

$$\begin{bmatrix}\dot{z}\\ \ddot{z}\end{bmatrix} = \begin{bmatrix}0 & 1\\ -15 & -5\end{bmatrix}\begin{bmatrix}z\\ \dot{z}\end{bmatrix} + \begin{bmatrix}0\\ 3\end{bmatrix}\tilde{u}\,, \quad \begin{aligned}\mu_S\dot{x} &= 0.03\dot{x} = -x + z,\\ \mu_S\ddot{x} &= 0.03\ddot{x} = -\dot{x} + \dot{z}\\ \mu_A\dot{\tilde{u}} &= 0.01\dot{\tilde{u}} = -\tilde{u} + u\end{aligned} \tag{14}$$

A switching function is defined using the nominal plant (ignoring the sensor and actuator dynamics) with the procedure outlined in Edwards and Spurgeon (1998) [1]. The switching function is given as

$$\sigma = 10x + \dot{x} \tag{15}$$

A set of tuning parameters for each of the sliding mode control parameters are chosen to conservatively satisfy the stability conditions in table 1 for a range of uncertainty. The procedure in section 3.2 is followed for each of the controllers to predict chatter amplitude and settling time. The chattering amplitude is ascertained from the Nyquist plot using the graphical method described. Settling time is found by using a genetic algorithm to find ω and ζ at discrete points of a, and then numerical integration to find a solution to equation (11). The predicted values are compared with a simulation, implemented using the Simulink environment (Mathworks Inc, USA). The results are shown in table 3. For each controller, the method outlined in section 3.2 is able to closely predict the chatter and settling time of the simulated system.

Table .3. Harmonic Linearization of sliding mode controllers.

Controller	Controller Parameters	Predicted Chattering Amplitude	Actual Chattering Amplitude	Predicted Settling Time†	Actual Settling Time
Standard SMC	$\rho = 10$	0.3613	0.380	0.29 (a_F =0.4)	0.26
Saturation function	$\rho = 10$ $\delta = 0.25$	0.320	0.323	0.41 (a_F =0.35)	0.31
Sigmoid function	$\rho = 10$ $\delta = 0.05$	0.290	0.298	0.29 (a_F =0.35)	0.25
Power-law	$\rho = 10$ $\delta = 0.2$	0.261	0.270	0.24 (a_F =0.35)	0.22
Twisting controller	$r_1 = 10$ $r_2 = 3$	0.174	0.188	0.13 (a_F =0.3)	0.15
Generalized Sub-optimal controller	$r_1 = 10$ $r_2 = 0.3$	0.161	0.172	0.17 (a_F =0.2)	0.15

† settling time is from $\sigma(0) = 1$ to $\sigma(t_s) = a_F$ (included in table)

5. Conclusion

Chatter suppression is an important area of research that aims to make sliding mode controllers practical in real systems. The source of chatter is the existence of fast-acting parasitic dynamics that inevitably exist in any real system, but are often ignored for simplicity. Recently, several variant sliding mode controllers have been suggested that can suppress chatter. It is important to know how these controllers affect the system in order to optimally tune them to meet a desired performance specification. In this paper, the problem of performance estimation of some

popular chatter-suppression algorithms is addressed. All parasitic dynamics at the sensor and actuator side of the plant are modeled as fast-acting first order systems. A harmonic linearization of each of the controllers is proposed, and is used in a procedure to estimate chattering amplitude and settling time for a specific choice of tuning parameters. The procedure is intuitive, simple to implement, and relatively accurate, provided that the system is equivalent to a low-pass filter. The main contribution is to create a resource for control practitioners to design chatter-suppressing sliding mode controllers for practical systems that meet a prescribed performance criteria.

References

[1] C. Edwards and S. K. Spurgeon, "Sliding mode control: theory and applications," London: Taylor & Francis, 1998.

[2] I. Boiko, L. Fridman, A. Pisano, and E. Usai, "Analysis of chattering in systems with second-order sliding modes," *IEEE Transactions on Automatic Control,* vol. 52, pp. 2085-2102, 2007.

[3] H. Lee and V. I. Utkin, "Chattering suppression methods in sliding mode control systems," *Annual Reviews in Control,* vol. 31, pp. 179-188, 2007.

[4] J. J. Slotine and S. S. Sastry, "Tracking control of non-Linear systems using sliding surfaces, with application to robot manipulators," *International Journal of Control,* vol. 38, pp. 465-492, 1983.

[5] J. A. Burton and A. S. I. Zinober, "Continuous approximation of variable structure control," *International Journal of Systems Science,* vol. 17, pp. 875-885, 1986.

[6] G. Ambrosino, G. Celentano, and F. Garofalo, "Variable structure model-reference adaptive-control systems," *International Journal of Control,* vol. 39, pp. 1339-1349, 1984.

[7] I. Boiko and L. Fridman, "Analysis of chattering in continuous sliding-mode controllers," *IEEE Transactions on Automatic Control,* vol. 50, pp. 1442-1446, 2005.

[8] A. Levant, "Higher-order sliding modes, differentiation and output-feedback control," *International Journal of Control,* vol. 76, pp. 924-941, 2003.

[9] A. Levant, "Sliding order and sliding accuracy in sliding mode control," *International Journal of Control,* vol. 58, pp. 1247-1263, 1993.

[10] I. Boiko, L. Fridman, and M. L. Castellanos, "Analysis of second-order sliding-mode algorithms in the frequency domain," *IEEE Transactions on Automatic Control,* vol. 49, pp. 946-950, 2004.

[11] G. Bartolini, A. Pisano, E. Punta, and E. Usai, "A survey of applications of second-order sliding mode control to mechanical systems," *International Journal of Control,* vol. 76, pp. 875-892, 2003.

[12] Z. Vukic, "Nonlinear control systems," New York: Dekker, 2003.

[13] J. J. Slotine and W. Li, "Applied nonlinear control," Englewood Cliffs N.J.: Prentice Hall, 1991.

On Solving the Forward Kinematics of the 6-6 General Parallel Manipulator with an Efficient Evolutionary Algorithm

Luc Rolland [*‡] and Rohitash Chandra[†‡]

[*] Department of Mechanical Engineering Middle East Technical University, Northern Cyprus Campus' Guzelyurt, TRNC

[†] Department of Computer Science Victoria University Wellington, New Zealand

Abstract The G3-PCX genetic algorithm is compared with hybrid meta-heuristic approaches for solving the forward kinematics problem of the 6-6 general parallel manipulator. The G3-PCX shows improvements in terms of accuracy, response time and reliability. Several experiments confirm solving the given problem in less than 1 second. It also reports all the 16 unique real solutions which are verified by an exact algebraic method. This opens the way to simulation and certification applications.

1 Introduction

Solving the parallel manipulator forward kinematics problem (FKP) with genetic algorithms (GA) was initially achieved on the 3-RPR manipulators where they were shown slower than Newton-Raphson's method (Boudreau and Turkkan, 1995). However, Newtons method can be plagued by Jacobian inversion failure, problematic convergence and numeric instabilities. Later, the Gough platform (SSM) FKP was solved with GAs, (Omran et al., 2008a), and the general 6-6 hexapod FKP was first solved with GAs by (Rolland and Chandra, 2009) where the pivot mutation operator was introduced. Using Wright's heuristic crossover and non-uniform mutation, several solutions could be found. Combination of GAs with simulated annealing improved performance, (R. Chandra and Rolland, 2009).

The main contribution of this paper is the application of an efficient evolutionary algorithm (G3-PCX) in solving completetly the FKP of the general 6-6 parallel manipulator to an acceptable precision. The selected FKP has 16 distinct real solutions confirmed by an exact algebraic method, (Rolland, 2007).

The paper is organised as follows: In Section 2, the FKP formulation is reviewed and the equation system conversion into an optimisation problem is studied. Section 3 gives a brief overview of developments in genetic algorithms. Section 4 presents the experiments, the results and their analysis. Section 5 concludes the paper and suggests directions for future research.

2 The Forward Kinematics Problem Formulation

This article studies the 6-6 parallel manipulator FKP, Figure 1, and which is defined as: *g*iven the joint positions, find the generalised coordinates of the manipulator end-effector.

The mechanical configuration parameters are, OA_O, the base joint coordinates in O (the base reference frame), and CB_C, the mobile platform joint coordinates in C (the mobile platform reference frame). The kinematics model variables are the actuator coordinates l_i and end-effector coordinates $\overline{X}$, the end-effector position and orientation.

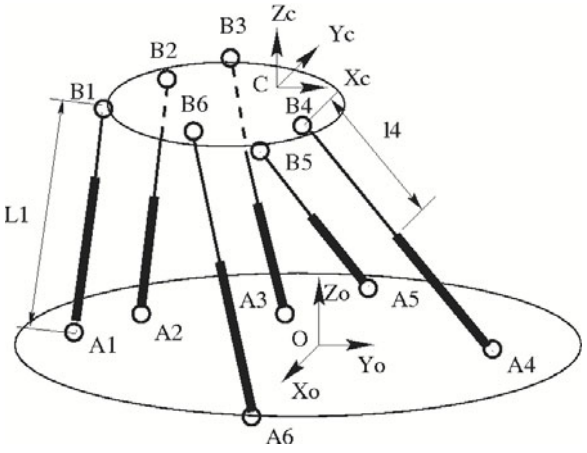

Figure 1. The 6-6 parallel manipulator

Vectorial Formulation of the Basic Kinematics Model

Containing as many equations as variables, vectorial formulation constructs an equation system as a closed vector cycle between the following points: A_i, B_i, O and C. The distance between A_i and B_i is set to l_i.

The mobile platform is positioned by 3 distinct points selected as the 3 joint centres B_1, B_2, B_3, (Rolland, 2005). The 9 variables are set as : $\overline{OB_i}_{|_O} = [x_i, y_i, z_i]$ for $i = 1 \ldots 3$. One reference frame b_1 is precisely located on B_1. The unit vectors u_1, u_2 and u_3 represent the new non-Cartesian frame axes, defined by:

$$u_1 = \frac{\overline{CB_1CB_2}_{|_O}}{||\overline{CB_1CB_2}_{|_O}||},\ u_2 = \frac{\overline{CB_1CB_3}_{|_O}}{||\overline{CB_1CB_3}_{|_O}||},\ u_3 = u_1 \wedge u_2 \tag{1}$$

Any platform point M can be expressed as $\overline{B_1M} = a_M u_1 + b_M u_2 + c_M u_3$ where a_M, b_M, c_M are constants in terms of these 3 points. Hence, in the case of the Inverse kinematics problem (IKP), the constants are noted $a_{B_i}, b_{B_i}, c_{B_i}$, $i = i \ldots 6$ and can explicitly be deduced from CB_C by solving the following linear system of equations :

$$\overline{B_1B_i}_{|R_{b_1}} = a_{B_i} u_1 + b_{B_i} u_2 + c_{B_i} u_3\ ,\ i = 1 \ldots 6. \tag{2}$$

where a_{B_i}, b_{B_i} and c_{B_i} are parameters only depending of platform geometry. Using the relations in Equation(2), the distance constraint equations $l_i^2 = ||\overline{A_iB_i}_O||^2$, $i = 1 \ldots 6$ can be expressed. Therefore, for $i = 1 \ldots 6$, the IKP is obtained by isolating the l_i actuator variables in the six following equations:

$$l_i^2 = (x_i - OA_{ix})^2 + (y_i - OA_{iy})^2 + (z_i - OA_{iz})^2\ ,\ i = 1 \ldots 3 \tag{3}$$

$$l_i^2 = ||\overline{B_i}_{|_{b_1}} - \overline{OA_i}_{|_O}||^2\ ,\ i = 4 \ldots 6 \tag{4}$$

The IKP comprises the first 6 equations in terms of 3 point variables : $x_1, y_1, z_1, x_2, y_2, z_2, x_3, y_3, z_3$, (4).

The meta-heuristic techniques need one objective function to be minimised thereby requiring conversion of the non-linear equation problem into an optimisation one where the IKP is integrated into one single objective function ($f$itness function) representing the total error on each kinematics chain lengths. Let lg_i be the length of kinematics chain i and $H_i = l_i^2$ from Equation (4), the fitness function is set to : $\sum_{i=1}^{6}(sqrt(H_i) - lg_i)^2$ containing the 6 kinematics chain length objectives. Preliminary tests with GAs led to several solutions which were NOT in correspondence with the exact proven ones, (Rolland and Chandra, 2009). This function is then augmented by the 3 constant distances between the 3 distinct platform points : B_1, B_2 and B_3:

$$\begin{aligned} G_1 &= ||\overline{B_2B_1}_C||^2 - (x_2 - x_1)^2 + (y_2 - y_1)^2 + (z_2 - z_1)^2 \\ G_2 &= ||\overline{B_3B_1}_C||^2 - (x_3 - x_1)^2 + (y_3 - y_1)^2 + (z_3 - z_1)^2 \\ G_3 &= ||\overline{B_3B_2}_C||^2 - (x_3 - x_2)^2 + (y_3 - y_2)^2 + (z_3 - z_2)^2 \end{aligned} \tag{5}$$

The final fitness function includes the 9 single objectives obtained from the 6 kinematics chain lengths and 3 platform distance constraints :

$$\sum_{k=1}^{3}(sort(H_k) - kg_k)^2 + \sum_{n=1}^{3}(G_n)^2 \tag{6}$$

3 Solving with genetic algorithms

Real coded genetic algorithms (RCGA) are coding with real numbers, maintaining precision, requiring smaller solutions and reducing the computation time. A number of possible random solutions (chromosomes or individuals) constitute the initial population. Each chromosome is evaluated according to its *f*itness. Two or more solutions (*p*arents) are selected from the population to produce new solutions (*o*ffsprings) by applying operators like *selection, crossover* and *mutation*. Offsprings are added to the population while the least fit members are removed. The selected common 3 genetic operators are :

Selection operator: It ensures that the fittest chromosome qualities survive in future generations. Some common selection strategies are rank selection, roulette wheel selection and the elitist strategy.

Crossover operator: It exchanges genetic material from selected parents. Some common crossover operators are flat crossover, simple crossover, arithmetic crossover, blend crossover, linear breeder crossover and Wright's heuristic crossover.

Mutation operator: It provides random diversity in the population. Some common mutation operators are random uniform mutation and Michalewicz non-uniform mutation. In uniform mutation, a random number in the range of $[a, b]$ is added to a selected gene where a and b are the highest and lowest values in the chromosome, respectively. In non-uniform mutation, the strength of mutation is decreased with generation number increase.

3.1 Hybridization of genetic algorithms

Hybrid meta-heuristic and Memetic algorithms refer to algorithms where two or more heuristic search techniques are combined providing intensification and diversification, respectively, at different points during the search process. Memetic algorithms combine population based evolutionary algorithms with local search approaches in-order to provide an improved solution with faster global convergence. The local search provides for intensification while retaining the diversification through the population during the search process.

The implemented Hybrid GA-SA approach combines both algorithms in parallel where the GA uses the SA for a predefined number of iterations during the search process after the crossover operation, (R. Chandra and Rolland, 2009). In this approach, the SA replaces the mutation operator.

3.2 G3-PCX genetic algorithm

The generalized generation gap (G3) with parent-centric crossover (PCX) operator, (K. Deb and Joshi, 2002), differs from standard genetic algorithms in terms of selection and offspring creation. The population is randomly initialised and evaluated similarly to standard GAs. Then, a small subpopulation is made of a few chosen parents and children. At each generation, only the subpopulation is evaluated where the best individual is retained. The new children become part of the main population.

The parent centric crossover operator is used for creating an offspring based on the orthogonal distance between parents. The *female* parent points to the search areas and the *male* parent is used to determine the search extent. The offsprings extract values from intervals associated with the female and male neighbourhood using probability distribution, with range depending on the distance between male and female parent genes. The parent-centric crossover operator assigns more probability to create an offspring near the female.

The G3-PCX algorithm amendments led to a mutation operator retaining diversity and being self-adaptive, (Jason et al., 2007). Further amendments have been done by introducing a female and male differentiation process which selects the population male and female individuals, (Garcia-Martinez et al., 2008b).

4 Results and Analysis

4.1 Configuration for the FKP of 6-6 general Parallel Manipulator

The proposed FKP example of a typical 6-6 hexapod has the configuration shown on Table 1 where the fixed base and mobile platform joint coordinates, OA_O, CB_C are given. The actuator variables are set to $l_i = 1250, i = 1, \ldots, 6$.

4.2 Experimental Set-up

The implemented G3-PCX algorithm performance is compared with the simulated annealing one and the genetic algorithm one hybrided with simulated annealing. The G3-PCX algorithm uses 2 offsrpings, 2 parents and a

Table 1. Parallel manipulator configuration table

Joint Coordinates	Respective Values
$OA_1(x)$ $OA_1(y)$ $OA_1(z)$	464.141 389.512 -178.804
$OA_2(x)$ $OA_2(y)$ $OA_2(z)$	569.471 207.131 -178.791
$OA_3(x)$ $OA_3(y)$ $OA_3(z)$	529.050 -597.151 -178.741
$CB_1(x)$ $CB_1(y)$ $CB_1(z)$	68.410 393.588 236.459
$CB_2(x)$ $CB_2(y)$ $CB_2(z)$	375.094 -137.623 236.456
$CB_3(x)$ $CB_3(y)$ $CB_3(z)$	306.664 -256.012 236.461

Table 2. An evaluation of the best method for the FKP

Algo	Pop	NFE	Fitness	CPU
SA	–	709300 ± 149900	0.004 ± 0.0006	3.19 ± 0.66
Hyb	40	–	0.006 ± 0.0003	56.39 ± 4.66
G3	100	247091 ± 2815	3.60E-18 ± 3.07E-18	1.50 ± 0.09
G3	150	151790 ± 4904	2.75E-19 ± 2.13E-19	1.18 ± 0.05
G3	200	132851 ± 5174	3.09E-20 ± 1.91E-20	0.73 ± 0.03
G3	250	116164 ± 3951	1.44E-20 ± 4.02E-21	0.95 ± 0.05
G3	300	117438 ± 1918	1.94E-20 ± 1.32E-20	1.03 ± 0.05

population size of either 100, 150, 200, 250 or 300. The initial solutions are selected in the range $[-1000, 1000]$ deliberately chosen large to provide the GA with a greater search space. For each trials, a total of 100 experiments with different initial positions were done. The search process is terminated when the algorithm reaches either the maximum training time or the fitness value of 1E-20. An experimental run was considered successful when the algorithm terminated by obtaining an error of 1E-20. The experiments were performed on an IBM compatible PC with 1.74 GHz dual core processors with Linux as the operating system.

4.3 Results

The results obtained with simulated annealing (SA), Hybrid GA-SA (Hyb) and G3-PCX (G3) are compiled in Table 4 showing population size (Pop), number of function evaluations (NFE) for 100 experimental runs (the mean and 95 percent confidence interval), the fitness, CPU response time in seconds and success rate. The optimisation performance is given by the

Table 3. FKP Unique Solutions

No.	x_1, y_1, z_1	x_2, y_2, z_2
1	-68.3187, 917.379, 821.976	-375.049, 430.181, 610.328
2	185.472, -539.987, -966.61	761.004, -518.48, -1177.66
3	-125.675, -427.508, -918.336	-432.246, 103.767, -919.18
4	67.7181, -616.597, 449.881	373.604, -363.006, 917.177
5	-68.1685, 917.387, -1178.05	-374.843, 430.066, -966.607
6	-127.172, 506.525, 917.082	-499.754, 367.052, 450.21
7	185.446, -539.781, 610.843	761.051, -518.405, 821.702
8	-68.3917, -394.265, -993.816	-375.024, 136.976, -994.343
9	-125.705, -427.868, 561.915	-431.976, 103.579, 563.519
10	-68.2931, -394.147, 637.993	-375.098, 136.994, 638.259
11	68.116, -616.726, -805.925	374.52, -363.503, -1273.08
12	112.655, 417.050, 1021.28	420.437, -113.526, 1021.04
13	112.496, 418.835, -1377.19	419.065, -112.442, -1377.16
14	-127.162, 505.756, -1273.17	-499.804, 366.797, -806.191
15	68.204, 392.804, -1363.68	375.287, -138.177, -1363.68
16	68.3473, 392.975, 1007.72	375.18, -138.15, 1007.67

number of function evaluations and the CPU time. The SA success rate reduces to 52 % compared with others which all reach 100 %.

4.4 Discussion

Hybrid GA-SA and SA can solve the FKP problem but only the G3-PCX algorithm obtained all 16 solution shown in Table 3. The SA performed better in terms of response time but its success rate is lower. The G3-PCX has outperformed the two other methods in terms of response times, success rates and fitness. The different population sizes influenced the overall performance of the algorithm. Population size of 200 leads to better response times being as low as 0.73 s. It is important to do trial experiments to determine the optimal population size.

5 Conclusion

The use of the parent-centric crossover operator with the generalized generation gap in the G3-PCX algorithm has shown to be effective in completely solving the forward kinematics of the 6-6 general parallel manipulator. The

method provided all distinct real solutions to an acceptable accuracy level with adequate response times.

Future work should aim at reducing the response times in order to allow for path planning and trajectory pursuit simulation.

Bibliography

R. Boudreau and N. Turkkan. Solving the forward kinematics of parallel manipulators with a genetic algorithmn. *Journal of Robotics Systems*, 13(2):111–125, 1995.

A. Omran et al. Genetic algorithm based optimal control for a 6-dof non redundant stewart manipulator. *Intern. Journal of Mechanical Systems Science and Engineering*, 2(2):73–79, 2008a.

C. Garcia-Martinez et al. Global and local real-coded genetic algorithms based on parent-centric crossover operators. *European Journal of Operational Research*, 185(3):1088 – 1113, 2008b.

T. Jason et al. Harnessing mutational diversity at multiple levels for improving optimization accuracy in g3-pcx. In IEEE Congress on Evolutionary Computation, *Singapore, 2528 September 2007*

K. Deb, A. Anand and D. Joshi. A computationally efficient evolutionary algorithm for real-parameter optimization. *Evolutionary Computation*, 10(4):371–395, 2002.

K. Hyunchul, N. Koichi and G. Mitsuo. A method for maintenance scheduling using ga combined with SA. *Comput. Ind. Eng.*, 27(1-4):477–480, 1994.

R. Chandra, M. Frean and L. Rolland. A hybrid meta-heuristic paradigm for solving the forward kinematics of 6-6 general parallel manipulator. In 8th IEEE Intern. Symposium on Computational Intelligence in Robotics and Automation (CIRA 2009), *Daejeon, Korea, 15-18 December 2009*

L. Rolland. Certified solving of the forward kinematics problem with an exact method for the general parallel manipulator. *Advanced Robotics*, 19(9):995–1025, 2005.

L. Rolland. Synthesis of the forward kinematics problem algebraic modeling for the general parallel manipulator: displacement-based equations. *Advanced Robotics*, 21(9):1071–1092, 2007.

L. Rolland and R. Chandra. Forward kinematics of the 6-6 general parallel manipulator using real coded genetic algorithms. In IEEE/ASME Conference on Advanced Intelligent Mechatronics (AIM 2009), *Singapore, 14-17 July 2009.*

Determination of Mobility in a Kinematic Chain by Properly Using the Jacobian Matrix.

Alejandro Tadeo, Gerardo Pérez, José M. Rico, and J. Jesús Cervantes*
* Division de Ingenierías, Campus Irapuato-Salamanca.
Universidad de Guanajuato, México.

Abstract This contribution presents a new and simple method for the determination of the mobility of kinematic chains whose mobility can not be determined by analyzing intersections of subalgebras of the Lie algebra, $se(3)$, of the Euclidean group, $SE(3)$. Previous approaches have to analyze the kinematic chain constraints or wrench space to obtain these results. In this contribution, it is shown that properly analyzing the kinematic chain Jacobian matrix, the mobility of the kinematic chain can be obtained within the realm of screw twists without resorting to wrenches or constraints.

1 Introduction.

The determination of the mobility of kinematic chains is still, after two centuries of history, an active area of research with still unanswered questions. The authors and his coworkers, Rico and Ravani (2003) and Rico *et al* (2003), had proposed two basic ideas

1. The mobility of kinematic chains can be treated either using group theory applied to the Euclidean group, $SE(3)$, or the Lie algebra, $se(3)$, of the Euclidean group, which is isomorphic to classical screw theory. Moreover, their use is interchangeable.

2. Since mobility is naturally related to "twist" screws, the mobility of kinematic chains may be completely determined using *properly* the Jacobian matrix of the kinematic chain without resorting to wrench or constraint screws.

There are plenty of contributions that employ wrench screws to determine the degree of constraint of a kinematic chain. Some provide incorrect results, Huang and Ge (2006), while others, Kong and Gosselin (2004, 2007), produce the correct results in a two step process; first determining the instantaneous degree of constraint and later proving that this degree remain unchanged under finite displacements of the kinematic chain.

The unfinished goal of an intended research program is to determine, at once, both the instantaneous and finite mobility by *properly* using the Jacobian matrix of any kinematic chain in a non-singular configuration. As indicated in the abstract, this contribution is a step toward this goal.

2 Representations of the Euclidean Group.

The representation of algebraic groups and Lie groups is an important tool in mathematics research see, for example, Selig (2005). In particular, the different representations of the Euclidean group, $SE(3)$, provide important insight on the behavior of kinematic chains.

Definition 1: Representation of a group over the general and real linear of order n**,** $GL(n)$. Let G be a group and let $GL(n)$ be the general and real linear group of order n; i.e. $GL(n)$ is the group formed by all non-singular or invertible real matrices or order n, together with the operation of multiplication. A representation of the group G is a group isomorphism, denoted ρ, such that

$$\rho : G \longrightarrow \rho(G) \leq GL(n)$$

Since the mapping is a group isomorphism, it preserves the group operation and taking of inverses. In addition, the image of an arbitrary $g \in G$ under a representation ρ is a real non-singular, or invertible, matrix of order n.

The most common representation of the Euclidean group, $SE(3)$, an important example of a Lie group, is the 4×4 homogeneous matrix representation. There a Euclidean displacement, an element of the Euclidean group, is represented by a matrix of the form

$$\mathbf{M} = \begin{bmatrix} \mathbf{Q} & \vec{t} \\ \vec{0} & 1 \end{bmatrix}, \tag{1}$$

where $\vec{t} \in \Re^3$, and $\mathbf{Q}$ is a proper orthogonal matrix of order 3 known as the **rotation matrix** that satisfies the following properties

$$\mathbf{Q}\mathbf{Q}^T = \mathbf{I}_3 = \mathbf{Q}^T\mathbf{Q} \qquad \text{and} \qquad |\mathbf{Q}| = 1. \tag{2}$$

This representation of the Euclidean group acts over the points of the physical space. In contrast, the **adjoint representation** acts over the lines of the physical space, and it is useful in determining the invariant properties of the subspaces of the Lie algebra, $se(3)$, of the Euclidean group, $SE(3)$.

The Plücker's coordinates of a line L, see Selig (2005), are given by

$$\vec{L} = \begin{bmatrix} \hat{u} \\ \vec{r} \times \hat{u} \end{bmatrix} = \begin{bmatrix} \hat{p} \\ \vec{q} \end{bmatrix} \qquad \text{where} \quad \hat{p} = \hat{u} \quad \text{and} \quad \vec{q} = \vec{r} \times \hat{u}. \tag{3}$$

Here $\hat{u}$ is a unit vector along the direction of the line and $\vec{r}$ is the position vector of a point along the line with respect to the chosen coordinate system.

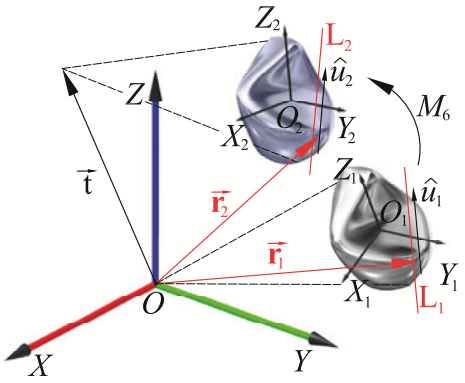

Figure 1. Geometrical Interpretation of the Adjoint Representation.

Selig (2005) also shows, pp. 54-57, that the Plücker's coordinates of the image, $\vec{L}\,'$, of the original line $\vec{L}$, when a rigid body undergoes the Euclidean displacement represented by the 4×4 homogeneous matrix $\mathbf{M}$, see equation (1), is given by

$$\vec{L}\,' = \begin{bmatrix} \hat{u}\,' \\ \vec{r}\,' \times \hat{u}\,' \end{bmatrix} = \begin{bmatrix} \mathbf{Q} & \mathbf{0} \\ \mathbf{TQ} & \mathbf{Q} \end{bmatrix} \begin{bmatrix} \hat{u} \\ \vec{r} \times \hat{u} \end{bmatrix} = M_6 \begin{bmatrix} \hat{p} \\ \vec{q} \end{bmatrix} = M_6\, \vec{L}. \qquad (4)$$

where $\mathbf{T}$ is the skewsymmetric matrix, obtained from the vector $\vec{t}$, by

$$\mathbf{T} = \begin{bmatrix} 0 & -t_z & t_y \\ t_z & 0 & -t_x \\ -t_y & t_x & 0 \end{bmatrix}. \qquad (5)$$

Therefore, the matrix $\mathbf{M}_6$

$$\mathbf{M}_6 = \begin{bmatrix} \mathbf{Q} & \mathbf{0} \\ \mathbf{TQ} & \mathbf{Q} \end{bmatrix} \qquad (6)$$

is a representation of the Euclidean group known as the *adjoint representation* of the Euclidean group. As any other representation of the Euclidean group, the adjoint representation satisfies the properties indicated here.

3 The Lie Product and the Adjoint Representation.

It is shown, Murray *et al* (1994) pp. 29-51, that the rotation matrix $\mathbf{Q}$ representing a rotation of an angle θ around an axis given by a unit vector

$\hat{e} = (e_x, e_y, e_z)$ is represented by

$$\mathbf{Q} = \begin{bmatrix} C\,\theta + (1 - C\,\theta)\,{e_x}^2 & (1 - C\,\theta)\,e_x\,e_y - S\,\theta e_z & (1 - C\,\theta)\,e_x\,e_z + S\,\theta\,e_y \\ (1 - C\,\theta)\,e_x\,e_y + S\,\theta\,e_z & C\,\theta + (1 - C\,\theta)\,{e_y}^2 & (1 - C\,\theta)\,e_y\,e_z - S\,\theta\,e_x \\ (1 - C\,\theta)\,e_x\,e_z - S\,\theta\,e_y & (1 - C\,\theta)\,e_y\,e_z + S\,\theta\,e_x & C\,\theta + (1 - C\,\theta)\,{e_z}^2 \end{bmatrix}.$$

Moreover, its time derivative, evaluated at time $t = 0$, is given by

$$\left.\frac{d\mathbf{Q}(t)}{dt}\right|_{t=0} = \begin{bmatrix} 0 & -\omega e_{z0} & \omega e_{y0} \\ \omega e_{z0} & 0 & -\omega e_{x0} \\ -\omega e_{y0} & \omega e_{x0} & 0 \end{bmatrix} = \omega \begin{bmatrix} 0 & -e_{z0} & e_{y0} \\ e_{z0} & 0 & -e_{x0} \\ -e_{y0} & e_{x0} & 0 \end{bmatrix}$$

where, $\theta(0) = 0°$, $\hat{e}(0) = (e_{x0}, e_{y0}, e_{z0})$, and $\dot{\theta} = \omega$. In addition $\mathbf{Q}(0) = \mathbf{I}_3$.

In a similar way, the skewsymmetric matrix $\mathbf{T}$, which represents the translation of the origin, and its time derivative, evaluated at time $t = 0$ are respectively given by

$$\mathbf{T} = \begin{bmatrix} 0 & -t_z(t) & t_y(t) \\ t_z(t) & 0 & -t_x(t) \\ -t_y(t) & t_x(t) & 0 \end{bmatrix} \quad \text{and} \quad \left.\frac{d\mathbf{T}}{dt}\right|_{t=0} = \begin{bmatrix} 0 & -\dot{t}_z(0) & \dot{t}_y(0) \\ \dot{t}_z(0) & 0 & -\dot{t}_x(0) \\ -\dot{t}_y(0) & \dot{t}_x(0) & 0 \end{bmatrix}$$

where $\vec{v}_O(0) = (\dot{t}_x(0), \dot{t}_y(0), \dot{t}_z(0))$ represents the velocity of the origin at time $t = 0$. In addition $\mathbf{T}(0) = \mathbf{0}_3$.

The action of the adjoint representation of a Euclidean displacement represented by equation (6) over a constant screw $\$_2 \in se(3)$, is given by

$$\$_2' = \begin{bmatrix} \hat{u}_2' \\ \vec{r}_2\,' \times \hat{u}_2' \end{bmatrix} = \begin{bmatrix} \mathbf{Q} & \mathbf{0} \\ \mathbf{TQ} & \mathbf{Q} \end{bmatrix} \begin{bmatrix} \hat{u}_2 \\ \vec{r}_2 \times \hat{u}_2 \end{bmatrix} = \begin{bmatrix} \mathbf{Q} & \mathbf{0} \\ \mathbf{TQ} & \mathbf{Q} \end{bmatrix} \$_2 \qquad (7)$$

Thus, the derivative with respect to time, of this action, is given by

$$\left.\frac{d\hat{u}_2'}{dt}\right|_{t=0} = \left.\frac{d\mathbf{Q}}{dt}\right|_{t=0} \hat{u}_2 = \omega \begin{bmatrix} 0 & -e_{z0} & e_{y0} \\ e_{z0} & 0 & -e_{x0} \\ -e_{y0} & e_{x0} & 0 \end{bmatrix} \hat{u}_2 = \omega(\hat{u}_1 \times \hat{u}_2) \qquad (8)$$

where, one defines $\hat{u}_1 = (e_{x0}, e_{y0}, e_{z0})$. Similarly, it can be proved that

$$\left.\frac{d\,(\vec{r}_2\,' \times \hat{u}_2')}{dt}\right|_{t=0} = \omega(\vec{r}_1 \times \hat{u}_1 + h\hat{u}_1) \times \hat{u}_2 + \omega\hat{u}_1 \times (\vec{r}_2 \times \hat{u}_2) \qquad (9)$$

Combining these results, it follows that

$$\left.\frac{d}{dt}\begin{bmatrix} \hat{u}_2' \\ \vec{r}_2 \times \hat{u}_2' \end{bmatrix}\right|_{t=0} = \omega \left[\begin{bmatrix} \hat{u}_1 \\ \vec{r}_1 \times \hat{u}_1 + h\hat{u}_1 \end{bmatrix}, \begin{bmatrix} \hat{u}_2 \\ \vec{r}_2 \times \hat{u}_2 \end{bmatrix}\right] = \omega\,[\$_1, \$_2] \qquad (10)$$

This result proves that the Lie product is the derivative of the action of the adjoint representation over the screws of the physical space.

4 Serially Connected Kinematic Chains.

In this section, some properties of serially connected chains are presented.

Definition 2: Serially Connected Kinematic Chain. Two kinematic chains are serially connected if the end effector of the first kinematic chain is rigidly connected to the fixed link of the second kinematic chain.

Definition 3: Mechanical Generator of a Subalgebra of the Lie Algebra $se(3)$**.** A mechanical generator of a subalgebra $se(3)$ is a kinematic chain –a set of links connected by kinematic pairs– such that the end effector of a kinematic chain can have, with respect to the fixed link, any arbitrary velocity state contained in the subalgebra. A similar definition applies to a mechanical generator of a subgroup of the Euclidean group, $SE(3)$, see Hervé (1978).

In Rico *et al* (2008), it was proven that if a kinematic chain is obtained by serially connecting the mechanical generators of two subgroups of the Euclidean group, $SE(3)$, the serially connected chain, also referred to as the mechanical representation of the composition of two subgroups, does not necessarily generates a subgroup of the Euclidean group, but it always generates a subset of the Euclidean group that possesses finite mobility; i.e. the kinematic chain remains movable under finite displacements of the kinematic pairs.

Here, the equivalent result employing the Lie algebra, $se(3)$, of the Euclidean group, $SE(3)$ will be presented. This result provides support to the claims that: *Properly applying only local information the mobility of kinematic chains can be correctly determined and the group theory and the Lie algebra mobility approaches are interchangeable.*

Proposition 4. Consider a kinematic chain obtained by serially connecting the mechanical generators of two subalgebras of the Lie algebra, $se(3)$, then the serially connected chain, also referred to as the mechanical representation of the sum of the two subalgebras, Rico *et al* (2003), does not necessarily generates a subalgebra of the Lie algebra of the Euclidean group, but it always generates a subspace of the Lie algebra, $se(3)$. Nevertheless, if the serially connected chains are not, initially, in a singular configuration, then the dimension of the generated subspace remains unchanged throughout any finite motion of the kinematic chain, that does not lead into a singular configuration.

Proof: The adjoint representation of the first subalgebra is a nonsingular or invertible linear mapping. Therefore the action of this representation over the screws that represent the sum of the subalgebras does not change the dimension of the subspace generated by the subalgebras.

Corollary 5. Since the statement of proposition 4, does not have any

restriction about the order of the serially connected chains, it follows that the properties of proposition 4 are valid regardless the order in which the chains are serially connected. Hence, a closed kinematic chain formed by two subalgebras with non-zero intersection will be always movable.

Finally, some examples of the application of the arguments introduced in this contribution are presented.

Example 1. Consider the kinematic chain shown in figure 2, this chain has been derived from the Sarrus' linkage. However, the revolute pair in D is not parallel to those in E and F.

The Jacobian matrix associated with the kinematic chain is given by

$$\mathbf{J} = \begin{bmatrix} 1 & 1 & 1 & 1/2\sqrt{2} & 0 & 0 \\ 0 & 0 & 0 & 0 & 0 & 0 \\ 0 & 0 & 0 & 1/2\sqrt{2} & 1 & 1 \\ 0 & 0 & 0 & 1 & 1/2\sqrt{2} & 0 \\ 1/2\sqrt{2} & \sqrt{2} & 1/2\sqrt{2} & 0 & -1/2\sqrt{2} & 0 \\ 0 & -1/2\sqrt{2} & -\sqrt{2} & -1 & 0 & 0 \end{bmatrix}$$

where, the columns of the Jacobian matrix correspond respectively to the

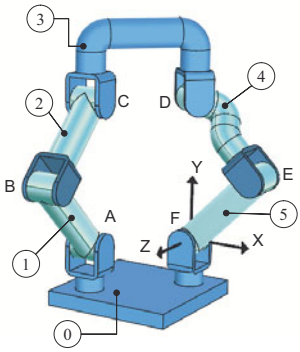

Figure 2. A Kinematic Chain Derived From the Sarrus' Linkage.

revolutes located in points A, through F. It is easy to see that the first three columns generate the three-dimensional subalgebra of planar displacements perpendicular to the X axis. The remaining revolutes generate, each one, a one dimensional subalgebra of revolute displacements. If the closed kinematic chain is made open by cutting the base link in two, the serial chain contains four subalgebras. Acccording with proposition 4, the finite displacements of the first three revolutes that generate the planar displacements subalgebra made no impact over the mobility of the kinematic chain.

One needs to consider only the following Lie products $[\$_4, \$_5]$, $[\$_4, \$_6]$ and

$$[\$_4, \$_5] = [0, -1/2\sqrt{2}, 0, 1/2, -1/2, -1/2] \qquad [\$_4, \$_6] = [0, -1/2\sqrt{2}, 0, 0, -1, 0]$$

The new Jacobian matrix obtained by substituting in the first case, $\$_5$ by $[\$_4, \$_5]$ and in the second case $\$_6$ by $[\$_4, \$_6]$ have both rank equal to 6, and the mobility of the kinematic chain is 0. The remaining Lie product

$$[\$_5, \$_6] = [0, 0, 0, 1/2\sqrt{2}, 1/2\sqrt{2}, 0]$$

does not change the rank of the corresponding Jacobian matrix.

Examples 2 and 3. Both kinematic chains shown in figure 3 contain a plane subalgebra followed by a cylindrical subalgebra and a revolute subalgebra. However, while in the chain shown on the left, the revolute pair is parallel to the cylindrical pair, in the chain on the left is not parallel to the cylindrical pair but its direction is contained in the plane formed by the unit vectors of the remaining revolute pairs and the cylindrical pair

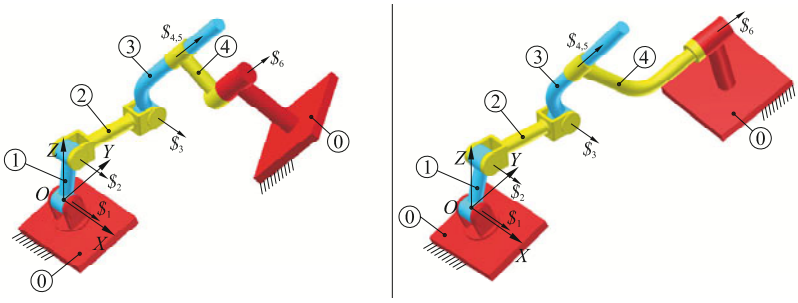

Figure 3. Two Kinematic Chains with Two Common Subalgebras.

The Jacobian matrix associated with the chain on the left of figure 3 is given by

$$J = \begin{bmatrix} 1 & 1 & 1 & 1/3\sqrt{3} & 0 & 1/3\sqrt{3} \\ 0 & 0 & 0 & 1/3\sqrt{3} & 0 & 1/3\sqrt{3} \\ 0 & 0 & 0 & 1/3\sqrt{3} & 0 & 1/3\sqrt{3} \\ 0 & 0 & 0 & \frac{42061}{30000}\sqrt{3} & 1/3\sqrt{3} & \frac{75551}{50000}\sqrt{3} \\ 0 & 3/2\sqrt{3} & \frac{6057}{100000} & \frac{286057}{300000}\sqrt{3} & 1/3\sqrt{3} & -\frac{48311}{150000}\sqrt{3} \\ 0 & -3/2 & -\frac{31333}{5000} & -\frac{706667}{300000}\sqrt{3} & 1/3\sqrt{3} & -\frac{89171}{75000}\sqrt{3} \end{bmatrix}.$$

Its rank is 5. Thus, according with proposition 4, one needs to consider only the Lie products

$$[\$_4, \$_5] = \left[0, 0, 0, \frac{366331}{150000}, -\frac{317287}{300000}, -\frac{3323}{2400}\right] \quad \text{and} \quad [\$_4, \$_6] = [0, 0, 0, 0, 0, 0]$$

The new Jacobian matrix obtained by substituting in the first case, $\$_6$ by $[\$_4, \$_6]$ and in the second case $\$_6$ by $[\$_5, \$_6]$ have both rank equal to 5. The conclusion is that the kinematic chain has mobility 1.

For the kinematic chain on the right of figure 3, its Jacobian matrix is obtained by substituting its sixth column by a screw, $\$_6$, see equation (7), where

$$\hat{u}_6 = \left[\sqrt{\frac{3+\sqrt{3}}{6}}, \frac{1}{\sqrt{6+2\sqrt{3}}}, \frac{1}{\sqrt{6+2\sqrt{3}}}\right] \text{ and } \vec{r}_6 = \left[\frac{421057}{50000}, \frac{774787}{100000}, \frac{26301}{50000}\right]$$

The rank of this new Jacobian matrix is 5. Thus, according with proposition 4, one needs to consider only the Lie products $[\$_4, \$_6]$ and $[\$_5, \$_6]$. It is easily shown that the new Jacobian matrix obtained by substituting $\$_6$ by $[\$_4, \$_6]$ has rank equal to 6. The conclusion is that the kinematic chain has mobility 0 and it is a structure. The remaining Lie product $[\$_5, \$_6]$ does not change the rank of the corresponding Jacobian matrix.

5 Conclusions.

The contribution has shown a new method of determining the mobility of kinematic chains using *properly* the information of the Jacobian matrix of the kinematic chain in a non-singular configuration.

Bibliography

Huang, Z. and Ge Q. J. *A Simple Method for Mobility Analysis Using Reciprocal Screws*, ASME 2006 IDETC September 10-13, 2006, Philadelphia, Pennsylvania, USA. DETC2006-99677.

Hervé, J.M., *Analyse Structurelle des Mécanismes par Groupe des Déplacements*, Mechanism and Machine Theory, Vol. 13, pp. 437–450, 1978.

Kong, X. and Gosselin, C. M. *Type synthesis of 3-DOF spherical parallel manipulators based on screw theory*, ASME Journal of Mechanical Design, Vol. 126, pages 101–108, 2004.

Kong, X. and Gosselin, C. M. *Type Synthesis of Parallel Mechanisms*, Berlin: Springer Verlag, 2007.

Murray, R. M., Li, Z. and Sastry, S. S. *A Mathematical Introduction to Robotic Manipulation*, Boca Raton: CRC Press, 1994.

Rico, J. M. and Ravani, B. *On Mobility Analysis of Linkages Using Group Theory*, ASME Journal of Mechanical Design, Vol. 125, pages 70–80, 2003.

Rico, J. M., Gallardo J. and Ravani, B. *Lie Algebra and the Mobility of Kinematic Chains*, Journal of Robotic Systems, Vol. 20, pages 477–499, 2003.

Rico, J. M., Cervantes, J. J., Tadeo, A., Pérez G. I. and J. Rocha, J. *New Considerations on the Theory of Type Synthesis of Fully Parallel Platforms*, ASME Journal of Mechanical Design, Vol. 130, 112302, 2008.

Selig, J. M. *Geometrical Foundations of Robotics, 2nd. Ed.*, New York: Springer Verlag, 2005.

Micro Hinges and their Application to Micro Robot Mechanisms

Mikio Horie[1]

[1] Precision and Intelligence Laboratory, Tokyo Institute of Technology, Japan,
mahorie@pi.titech.ac.jp

Abstract. In the present paper, two kinds of manipulators are shown and their characteristics are discussed. Their manipulators are as follows, (1) a micromanipulator with elastic hinges made by FAB(Fast Atom Beam) machine, and (2) a molding pantograph mechanism with large-deflective hinges, which is used as one component mechanism of a palmtop surface mount system using at the one room factory. In the case of the micromanipulator with elastic hinges, its micromanipulator's relationship between input and output displacements in the experiments are coincident with theoretical results. In the case of the molding pantograph mechanism with large-deflective hinges whose materials are polypropylene, it was confirmed that the hinge in the mechanism had not fractured even if more than one million repeatable motion of the mechanism in the mechanism's fatigue test. Moreover, in order to have a long life hinge, the fatigue process toward the fracture of the hinge specimen was clarified in experiments by hinge-specimen's fatigue test.

1. Introduction

In the case of micromechanisms, micromachines, MEMS, micro systems, instead of bearings at joints, the flexural hinges, large-deflective elastic hinges, and large-deflective hinges are used to avoid of friction effects at the bearing . Mechanisms with elastic elements, that is, flexural hinges, have been researched and developed in the world. For example, Kota, S.(1999) proposed a compliant mechanism which has single-piece flexible structures that deliver the desired motion by undergoing an elastic deformation, and Müglitz, J. and Schönherr, J.(1999) suggested a miniaturized planar mechanism for guiding a surgical instrument whose joints are designed as thin compliant segments acting like bending beams, that is, large-deflective elastic hinges, while the joints of this pantograph mechanism are large-deflective hinges whose aspect ratio of thickness to length is nearly 1 to reduce the displacement error by Mikio Horie et. al.(2001).

In the present paper, the feature of them and differences among them are explained, and their applications are introduced. The flexural hinge has not a large angular displacement. Therefore, the flexural hinges are used to have a large and precision output displacement by use of a lot of hinges and an enlargement mechanism. On the other hand, a large-deflective elastic hinge is used to obtain a large angular displacement described in Chapter 2. Moreover, a new concept, that is, a large-deflective hinges are used to obtain a large angular displacement and to have a precision output, because of a hinge center small motion described in Chapter 3. Then, the characteristics of the micromechanisms with large-deflective hinges which has a long life, are discussed in Chapter s 4 and 5.

2. Micro Motion Convert Mechanism made by FAB Machine

Figure 1 shows a FAB(Fast Atom Beam) manufacturing machine. Figure 2 shows the manufacturing view by use of the mask and the FAB. A PRRR Mechanism, which consists of revolute pairs (R) and prismatic pairs (P), is shown in Fig. 3. In this mechanism, the Y-direction displacement of the central revolute pairs (R) is taken as the output when an X-direction displacement is given to the prismatic pairs (P) as the input. A micro motion convert mechanism based on the PRRR Mechanism is shown in Fig. 4. The micro motion convert mechanism consists of micro order hinges, which are substituted for the revolute pairs in the PRRR mechanism, and links.

A micro motion convert mechanism was manufactured with polyimide for the structural material based on the manufacturing process of the micro motion convert mechanism as shown in Fig.5, and aluminum for the mask by semiconductor micromachining technology including FAB etching, which is shown in Fig. 6 (a) and (b). In Fig. 6 (b), the hinges of Type B are made in the same

Figure 1. Fast Atom Beam(FAB) manufacturing machine

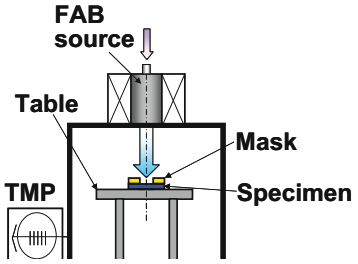

Figure 2. Manufacturing view by use of mask and FAB

Micro Hinges and their Application to Micro Robot Mechanisms

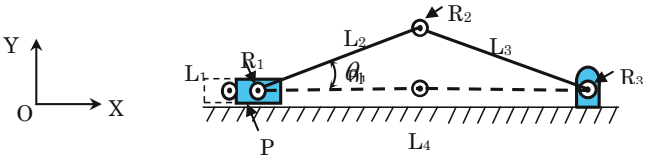

Figure 3. PRRR mechanism (R :Revolute pairs, P :Prismatic pairs)

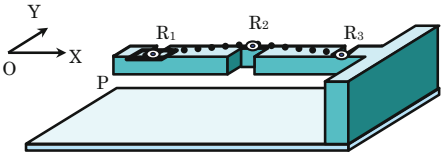

Figure 4. Micro motion convert mechanism

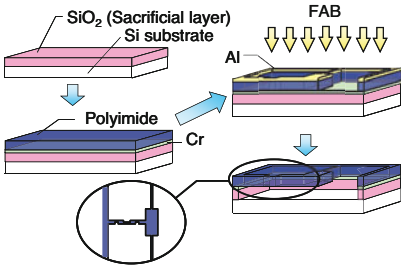

Figure 5. Manufacturing process of the micro motion convert mechanism

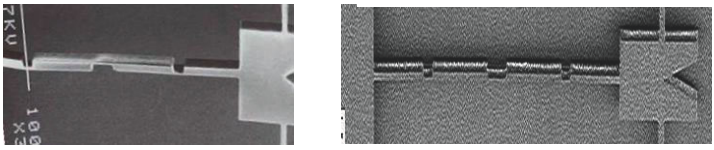

(a) Type A (b) Type B

Figure 6. Manufactured micro motion convert mechanisms

one way manufacturing direction. Figures 7 (a) and (b) show the dimensions of the micro motion convert mechanisms Type A and Type B, respectively.

Using the experimental apparatus, the input and output displacement characteristics of the micro motion convert mechanism were examined. In the results, the Type B has not the determined motion direction because of the same manufactured direction of the hinge. Figure 8 shows the relationship among output displacements *Y*out, θ_1, θ_2 and input displacement *X*in of the Type A. In this experiment, when the X-direction displacement was given to the mechanism as the input, Y-direction displacement of the central hinge and the angles between the each rigid body part of the mechanism(link parts) were taken as the output. Through the use of a micromanipulator operated with the joystick, the tip of the needle was made to scrape the rigid body and move parallel to the mechanism so that it would produce the same effect with prismatic pairs, creating the mechanism to undergo a displacement. Also, when the X value or input displacement increased, it was taken as forward while when X value

decreased, it was taken as backward. The images of the process were grabbed and analyzed to measure the output displacement as well as the output angles relative to the input displacement. Output values relative to each input displacement, X, were presented in graphical forms: Figure 9 shows the output displacement, Y. The output angles θ_1 and θ_2, for X are obtained similarly. In the results, the input-output displacement relationship is investigated experimentally.

3. Palmtop Surface Mount System for Micro Devices by Use of a Pantograph Mechanism with Large-Deflective Hinges

When we opened the cellular phone case, we can look a lot of micro devices on the electric circuit board. In the case of conventional surface mount systems to make the electric circuit board with micro devices, the size is very large, for example, 2m(width)× 4m(length)× 2m(height). In this chapter, a new palmtop surface mount system which consists of groups of manipulators that have been

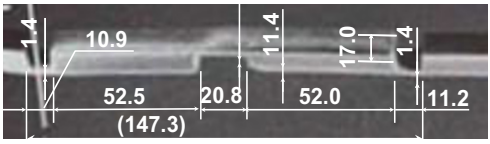

(a) Type A

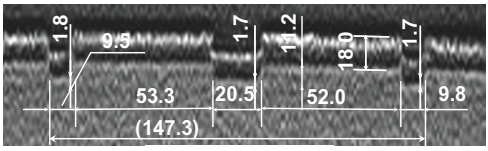

(b) Type B

Figure 7. Dimensions of the micro motion convert mechanisms [Unit: μm]

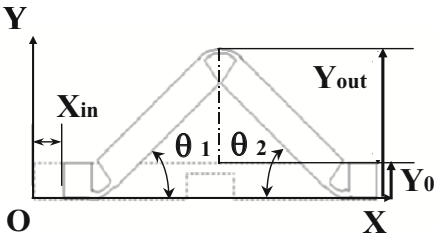

Figure 8. Relationship among output Y_{out}, θ_1, θ_2 and input X_{in} of Type A

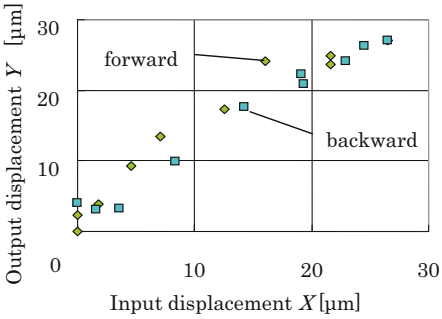

Figure 9. Output displacement Y

Micro Hinges and their Application to Micro Robot Mechanisms

minimized by an molding pantograph mechanism with hinges and links is proposed as shown in Figs. 10 and 11 by Mikio Horie et. al.(2001). Figure 10 shows the proposed new palmtop surface mount system. Figure 11 shows the molding pantograph mechanism with large-deflective hinges and links. The pantograph mechanism has linear input actuators in the experimental apparatus. The mechanism material is the Polypropylene. The hinge length of the pantograph mechanism used in the experiment was determined to be 200 μm, with the thickness being 180 μm. The width is 5 mm because of the section of the link 5*5mm. We confirmed that the mechanism has not fractured even if more than one million repeatable motion of the mechanism in the fatigue test shown by Mikio Horie et. al.(2006).

4. Fatigue Tests of an Molding Pantograph Mechanism with Large Deflective Hinges

Large deflective hinges are known to be able to obtain large angular displacements by producing larger deformations on the materials than the elastic regions. Therefore, when they are used as hinge parts of a pantograph mechanism, it is thought that there might be some possibility that the materials could be destroyed by fatigue under the condition that repeated use creates large deformations. Consequently, these results led to conducting the fatigue test of the model- devised pantograph mechanism using the apparatus. The experimental apparatus consists of three parts: the vibrator based on the slider crank mechanism, the laser displacement sensors, and the oscilloscope. The test is conducted as follows: Using a vibrator, the sinusoidal displacement input at 7.5mm vibration is given to the input part (Point A in Fig. 11) in the horizontal direction of a pantograph mechanism, and then the displacements of input-output ending points are measured by a laser displacement sensor. The relation between the input vibratory frequencies and the repeatable numbers until hinge parts has fractured is determined after the molding pantographs using hinges of different thickness lengths have been examined. The hinge thickness, the vibration frequency, the number of cycles, and failed hinge parts of the molding pantograph mechanisms in each conducted experiment, are shown in Table 1. A hyphen mark in Table 1 shows that a pantograph mechanism does not fracture even after one million-time repetition. The A, B, C, etc. in Table 1 mean a hinge name in Fig. 11.

5. Experimental Method of the Fatigue Test of One Hinge Model

Two kinds of hinge specimens used in a fatigue test were manufactured by injection molding, whose shape and dimensions(Length*Thickness*Width) are

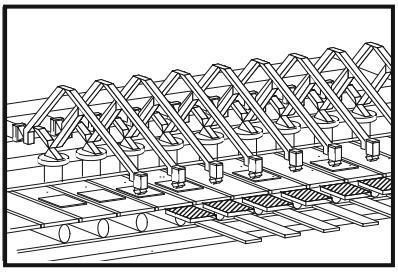

Figure 10. A new palmtop surface mount system composed of parallel arrangement pantograph mechanisms

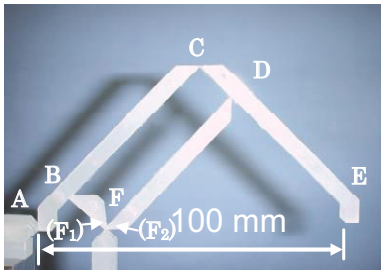

Figure 11. A pantograph mechanism with large-deflective hinges and links (Material: Polypropylene)

respectively 0.2mm*0.2mm*5mm and 0.2mm*0.5mm*5mm.

The material of the specimens is a widely used thermoplastic resin such as polypropylene(PP), polyethylene(PE), polyamide(PA) and polystyrene(PS). Regarding polypropylene(PP), Type A[PP(A)] and Type B[PP(B)] are used and are made by a different company with same materials.

A fatigue test was conducted on hinge specimens using the test apparatus. A cyclic bending load with ±45° angular displacement, and a sinusoidal cyclic tensile-compressive load were applied on the specimens. Cyclic frequency of 10Hz was applied on hinges 200μm thick, while 20Hz was applied on hinges 500μm thick. The results are shown in Fig. 12. The horizontal axis represents the number of cycles when hinges were broken while the vertical axis represents cyclic tensile compressive load by the fatigue test apparatus. The results show that hinges 500μm thick are more durable than hinges 200μm thick. This is

Table 1 Results of the fatigue test

Group	I					II			
Exp. No.	1	2	3	4	5	6	7	8	9
Hinge thickness [μm]	60	90	90	90	100	110	110	115	120
Input frequency [Hz]	19.4	15	15	20	22.2	5	20	18	15
Number of cycles	100	-	153900	3140	100	-	3900	30600	-
Failed hinge	D	-	C, D	B,C,D	F_2, D	-	C, D	D	-

Group	II				III			
Exp. No.	10	11	12	13	14	15	16	17
Hinge thickness [μm]	125	125	130	135	150	165	225	260
Input frequency [Hz]	17	20	26	20	26.8	17	10	20
Number of cycles	-	6040	100	8600	100	-	-	-
Failed hinge	-	F_2, D	F_2, D	A	F_2, D	-	-	-

Micro Hinges and their Application to Micro Robot Mechanisms

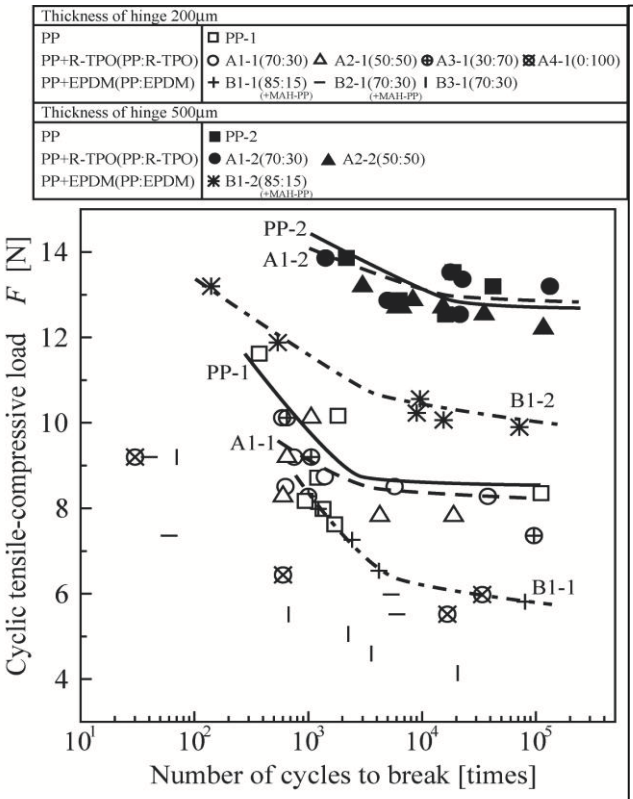

Attention:
(1) Polypropylene(PP),
(2) Polymerization blend PP (A1~A4) which we call PP+R-TPO, that is, the thermoplastic elastomer to which PP monomer and ethylene are polymerized by multistep,
(3) Machine blend PP(B1~B3) called PP+EPDM that PP and Ethylene Propylene-Diene Monomer(EPDM) were mechanically mixed using a mixer, and
(4) Another machine blend PP(B1~B3) (+MAH-PP) that we mixed maleic anhydride modified PP(MAH-PP) with the above (3) machine blend PP.

Figure 12. Results of fatigue test

because stress by the tensile-compressive load gets smaller as the cross section of hinge gets larger. However, the number of cycles of tensile-compressive load stayed at about one and a half times as many when the cross section of the hinge was two and a half times as large. It is conceivable that damages by bending load got severer as hinges were thicker. It was also confirmed that PP was the most durable among 8 kinds of specimens with 200μm-thick hinge and 4 kinds of specimens with 500μm-thick hinge, while PP was as durable as A1 regarding 500μm-thick hinges. A1 which is one of the name of specimen has the bending ratio PP: Elastomer = 70: 30(R-TPO) and bending ratio of Mah-PP = 0 %. It is because 200μm-thick hinges with elastomer, such as A1, got significantly longer and buckling in the hinge part became prominent during the test. This had an adverse effect on hinge durability.

It was also found that the durability of hinges with a thickness of 200μm or 500μm became less durable as the proportion of elastomer blended in the material became

larger. But the result could be reversed when hinges are made thicker and the fatigue damage by bending load got severer. Moreover, it was found that Machine Blend PP was far less durable than Polymerized Blend PP.

6. Conclusions

The characteristics of the two kinds of micro-manipulators with large-deflective elastic hinges and large-deflective hinges are discussed, and the following conclusions are obtained.

(1) A micro motion convert mechanism was manufactured with polyimide for the structural material based on the FAB(Fast Atom Beam) manufacturing process.

(2) A molding pantograph mechanism consisting of large deflective hinges with 200 μm of the length,180 μm of the thickness an 5 mm of the width did not fracture in displacement input fatigue tests on the mechanism even after repeatedly used one million times.

(3) This study performed cyclic-bending tests with a static tensile load on hinges made from polypropylene, polyethylene, polyamide, as well as polystyrene, and ascertained that polypropylene, and polyamide hinges have a relatively high fatigue resistance among them. Regarding the polypropylene hinge, the relationship between the tensile strength and the normal logarithm of the number of bending cycles to fracture was displayed in a straight line.

(4) From the results of a fatigue test on the hinge specimens in the chapter 5, it was found that hinges 500μm thick were more durable than 200μm thick specimens, and that Machine Blend PP was less durable compared to Polymerized Blend PP.

References

Kota, S., Design of compliant mechanisms with applications to MEMS and smart structures, *Proceedings of the 10th World Congress on the Theory of Machines and Mechanisms*, Oulu, Finland, 20 to 24, June 1999, Vol.7, pp. 2722-2728.

Müglitz, J. and Schönherr, J., Miniaturized mechanism - joint design, modeling, example, *Proceedings of the 10th World Congress on the Theory of Machines and Mechanisms,* Oulu, Finland, 20 to 24, June 1999, Vol.2, pp. 848-855.

Horie, M., Uchida, T., and Kamiya, D.(2001), A Pantograph Mechanism with Large-deflective Hinges for Miniature Surface Mount Systems, *ROMANSY 13-THEORY AND PRACTICE OF ROBOTS AND MANIPULATORS*, ISBN 3-211-83333-1,Springer-Verlag Wien New York, 93-102.

Horie M., Okabe Y., Yamamoto M., and Kamiya D.(2006), Durability of Large-Deflective Hinges made of Blend Polypropylene used for Molded Pantograph Mechanisms, *ROMANSY 16-ROBOT DESIGN, DYNAMICS, AND CONTROL*, ISBN 3-211-36064-6, Springer-Verlag Wien New York, 355-362.

Parallel RPR-||-RPR Manipulator Generating 2-DOF Translation along One-Sheet Revolute Hyperboloid

Chung-Ching Lee
Professor, Dept. Tool & Die-Making Engineering,
National Kaohsiung University of Applied Sciences,
415 Chien Kung Road, Kaohsiung, 80782, Taiwan R.O.C.
E-mail:cclee@cc.kuas.edu.tw

Jacques M. Hervé
Honor Professor, Ecole Centrale Paris,
Grande Voie des Vignes,
F-92295, Chatenay-Malabry, France
E-mail: jacques.herve07@orange.fr

Abstract. Based on the theorem that any subset of translations is normal or invariant by conjugation in the group of a spatial 3-DoF translation, a novel type of parallel manipulator RPR-||-RPR generating 2-DoF translation along a revolute hyperboloid of one sheet is synthesized. A special type of plane symmetric RPRP Delassus mechanism, which has two noncontiguous parallel revolute axes and two prismatic pairs bilaterally symmetric with respect to the plane containing the revolute axes, is further derived as being a special case of the previous manipulator with coincident R axes.

Keywords: Group conjugation, 2-DoF translation, revolute hyperboloid of one sheet, parallel manipulator, doubly ruled surface, Delassus linkages

1. Introduction

Parallel generation of 3-degree-of-freedom (3-DoF) translation has been attractive to researchers for a long time [Clavel, 1987; Hervé, 1991; Wenger and Chablat, 2000; Gao et al., 2002; Kong and Gosselin, 2002; Angeles, 2004, Lee and Hervé, 2006, 2007, 2009a]. However, a parallel manipulator generating 2-DoF translation along a surface that is neither a plane nor a sphere is still a novel topic in robot kinematics. In [Hervé, 2009], a useful theorem derived from the group-algebraic properties of the 6-dimensional (6D) set of displacements is stated: any subset of translations is invariant by conjugation (or normal) in the

commutative (or Abelian) Lie 3D group $\mathcal{T}$ of 3-DoF translations. By application of the foregoing theorem, any 2-DoF translation along a surface that may be, for instance, a revolute hyperboloid of one sheet is normal in the group $\mathcal{T}$. Through this theorem, a novel parallel manipulator generating 2-DoF translation along a revolute hyperboloid is synthesized. Under a special geometric arrangement, a new derivation of a particular Delassus paradoxical mechanism, which is a plane symmetric RPRP chain, is also obtained.

The first step is to introduce a single-closed-loop chain with an end effector moving by translation along the surface of a revolute hyperboloid of one sheet with respect to a fixed frame. This chain can be considered to be the parallel arrangement of a PPP generator of the group $\mathcal{T}$ with a RPR open chain with parallel revolute axes. Hereinafter, P and R are the usual notations of a prismatic pair and a revolute pair respectively and the underline indicates the parallelism of R axes. The RPR chain generates a special 3D submanifold of a 4D group $\mathcal{X}$ of Schoenflies motions. An explicit vector calculation is done for verification. The second step is the addition of another single closed-loop RPR-||-PPP chain, which is conjugate or congruent by translation to the first RPR-||-PPP chain. As for the third step, the rigid connection of the two end-effectors and the removal of the superfluous PPP subchains are made. From the plane symmetry of the hyperboloid, a novel manipulator architecture is derived. Finally, we also attain a plane symmetric RPRP mechanism with 1-DoF finite paradoxical mobility, which is a special Delassus four-bar linkage.

2. Single-Closed Loop Chains with 2-DoFs

The parallel arrangement of a PPP generator of the group $\mathcal{T}$ with a RPR open chain having two parallel R axes produces a single-closed-loop RPR-||-PPP chain, which is depicted in Figure 1 where (**i**, **j**, **k**) indicates an orthonormal vector base. The points A and B are assumed to be located on the R axes, which are both parallel to **k**. $\mathcal{R}(A, \mathbf{k})$ and $\mathcal{T}(\mathbf{s})$ denote the 1D group of rotational motions of axis (A, **k**) and the 1D group of rectilinear translations parallel to **s**, respectively. Such a chain embodies $\mathcal{R}(A, \mathbf{k})\mathcal{T}(\mathbf{s})\mathcal{R}(B, \mathbf{k}) \cap \mathcal{T}(\mathbf{j})\mathcal{T}(\mathbf{i})\mathcal{T}(\mathbf{k})$ and is movable with two DoFs as being a trivial chain associated to the 4D Schoenflies group $\mathcal{X}(\mathbf{k})$ [Lee and Hervé, 2009b]. In a 2-DoF translation, any point of the translating body moves on a surface that is a 2D submanifold of the 3D Euclidean affine space. In RPR-||-PPP manipulator, let M be any point belonging to the moving end-effector. One limb is the RPR chain. The other limb is a PPP generator of $\mathcal{T}$. The 3D group $\mathcal{T}$ is the set of point transformations

$$M \longrightarrow M' = M + a_1\mathbf{i} + b_1\mathbf{j} + c_1\mathbf{k} \quad (1)$$

which is also expressed by (**MM'**)= $a_1\mathbf{i}+b_1\mathbf{j}+c_1\mathbf{k}$ where (**MM'**) denotes the free vector obtained from the points M and M'. The parameters a_1, b_1 and c_1 are the scalar values of the rectilinear translations produced by the P pairs from a given home configuration of the PPP chain.

In Figure 1, the RPR limb is such as (**AN**) is perpendicular to (**NB**), which is parallel to the unit vector **s**; (**AN**)=$r\mathbf{i}$, (**NB**)=$b\mathbf{s}$, **s**=$\sin\alpha\,\mathbf{j}+\cos\alpha\mathbf{k}$ where the angle α is a given constant. To facilitate a clear understanting, the point position B does not coincide with N and b is not zero in the figure. Because displacements or rigid-body motions are the body-position changes, the geometric description of an initial home configuration of a mechanism shown in Figure 2 is a datum that is necessary for the characterization of all relative displacements. For simple calculation, at the home configuration, the position B_0 of the end-effector point B is assumed to coincide with N. Hence, $B_0=N(\neq B)$ in the following. Moreover, the position of M is M_0 at the home configuration, as shown in Figure 2. The set of feasible displacements generated by the RPR limb can be attained by a sequence of three 1-DoF motions. In the first stage, the second R moves with an angle φ around the axis (B_0, **k**) while the first R and the P keep their home postures (θ=0 and b=0); M_0 becomes M_i , which is expressed by

$$M \longrightarrow M_i = B_0 + \exp(\varphi\mathbf{k}\times)(\mathbf{B}_0\mathbf{M}_0) \text{ or } (\mathbf{B}_0\mathbf{M}_i) = \exp(\varphi\mathbf{k}\times)(\mathbf{B}_0\mathbf{M}_0) \quad (2)$$

In the second stage, the second R is locked (angle φ keeps its value), the first R keeps its home position (θ=0) and the P provides a translation parallel to **s** , with an amplitude b. Then, the point M_i becomes M_i'

$$M_i \longrightarrow M_i' = M_i + b\,\mathbf{s} \quad (3)$$

With ($\mathbf{B}_0\mathbf{M}'_i$)=$b\mathbf{s}$+exp($\varphi\mathbf{k}\times$)($\mathbf{B}_0\mathbf{M}_0$) and ($\mathbf{NM}'_i$)=$b\mathbf{s}$+exp($\varphi\mathbf{k}\times$)($\mathbf{B}_0\mathbf{M}_0$) because of the choice $B_0=N$, we have

$$(\mathbf{NM}'_i)=b\sin\alpha\,\mathbf{j}+b\cos\alpha\mathbf{k}+\exp(\varphi\mathbf{k}\times)(\mathbf{NM}_0) \quad (4)$$

In the third stage, the second R and P are locked and the parameters φ and b keep their values. The first R moves with angle θ around the fixed axis (A, **k**) and M_i' is transformed into M',

$$M_i' \longrightarrow M' = A + \exp(\theta\mathbf{k}\times)(\mathbf{AM}_i') \text{ or } (\mathbf{AM}') = \exp(\theta\mathbf{k}\times)(\mathbf{AM}_i') \quad (5)$$

Using ($\mathbf{AM}_i'$)=(**AN**)+($\mathbf{NM}_i'$)= $r\mathbf{i}+b\sin\alpha\,\mathbf{j}+b\cos\alpha\,\mathbf{k}$+exp($\varphi\mathbf{k}\times$)($\mathbf{B}_0\mathbf{M}_0$) yields

$$(\mathbf{AM}')= =b\cos\alpha\mathbf{k}+\exp(\theta\mathbf{k}\times)(r\mathbf{i}+b\sin\alpha\,\mathbf{j})+\exp[(\theta+\varphi)\mathbf{k}\times](\mathbf{B}_0\mathbf{M}_0) \quad (6)$$

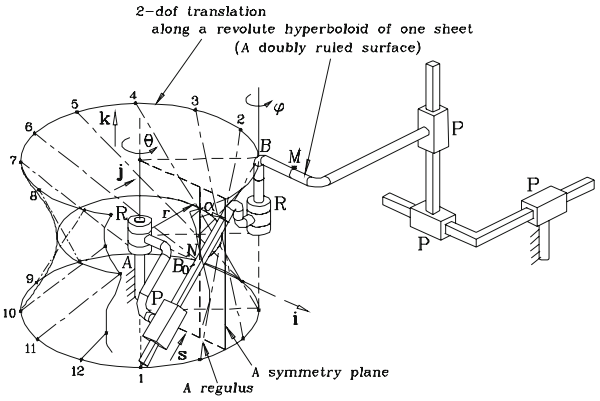

Figure 1. RPR-||-PPP generator of 2-DoF translation along a one-sheet hyperboloid: general configuration

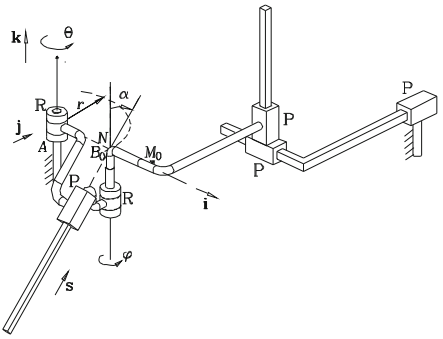

Figure 2. RPR-||-PPP generator of 2-DoF translation along a one-sheet hyperboloid: initial posture of parametrization.

Notice that $\exp(\theta\mathbf{k}\times)(r\mathbf{i})=r(\cos\theta\,\mathbf{i}+\sin\theta\,\mathbf{j})$ and $\exp(\theta\mathbf{k}\times)(b\,\sin\alpha\,\mathbf{j})=b\,\sin\alpha\,(-\sin\theta\mathbf{i}+\cos\theta\mathbf{j}\,)$ and we have

$$(\mathbf{AM}')=b\cos\alpha\mathbf{k}+(r\cos\theta-b\sin\alpha\sin\theta)\mathbf{i}+(r\sin\theta+b\sin\alpha\cos\theta)\mathbf{j}+\exp[(\theta+\varphi)\mathbf{k}\times](\mathbf{B}_0\mathbf{M}_0) \quad (7)$$

This is an explicit expression of the product of transformations $R(A, \mathbf{k};\theta)T(\mathbf{s};b)R(B, \mathbf{k};\varphi)$ belonging to the set product $\mathcal{R}(A, \mathbf{k})\mathcal{T}(\mathbf{s})\mathcal{R}(B, \mathbf{k})$. In the RPR-||-PPP parallel mechanism, for any point M, the feasible displacements of the moving platform have to satisfy Eq.(7) and have to be a translation, which is achieved for $\varphi=-\theta$. As a matter of fact, by translation, (**BM**) must keep unchanged, that is, $(\mathbf{B}'\mathbf{M}')=(\mathbf{B}_0\mathbf{M}_0)$. Then, Eq.(7) becomes

$$(\mathbf{AM}')= b\cos\alpha\mathbf{k}+[r(\cos\theta-1)-b\sin\alpha\sin\theta]\mathbf{i}+(r\sin\theta+b\sin\alpha\cos\theta)\mathbf{j}+(\mathbf{AM}_0) \quad (8)$$

It is straightforward to verify that the end-effector point B that coincides with B_0 at the home configuration moves on the ruled hyperboloid with the axis (A, $\mathbf{k}$), which has the parametric representation

$$(\mathbf{AB}')= r(\cos\theta\,\mathbf{i}+\sin\theta\,\mathbf{j})+b[\sin\alpha(-\sin\theta\,\mathbf{i}+\cos\theta\,\mathbf{j})+\cos\alpha]\mathbf{k} =(\mathbf{AN}_\theta)+b\mathbf{s}_\theta \quad (9)$$

where N_θ and $\mathbf{s}_\theta$ are respectively the transformation of N and $\mathbf{s}$ through a rotation of angle θ around the axis (A, $\mathbf{k}$). Because of the end-effector translation, any point moves also on a ruled hyperboloid, which is congruent by translation with the orbit of B. In other words, the end-effector moves by a 2-DoF translation along a surface of revolute hyperboloid of one sheet. This hyperboloid is a doubly ruled surface resulting obviously from its plane symmetry.

3. Parallel Manipulator Generating 2-DoF Translation along a Ruled Hyperboloid

Two 2-DoF translation manipulators that are congruent by any given translation produce the same translational motion of their end effector [Hervé, 2009]. In the two congruent manipulators, two end-effectors move with the same motion and consequently can be rigidly connected. Then, more than two congruent limbs can connect the fixed base with the end effector.

In Figure 3, two RPR-||-PPP mechanisms produce the same ruled-hyperboloid translation. That way, rigidly connecting the two end effectors and removing the PPP subchains lead to a parallel generator RPR-||-RPR of 2-DoF translation (2D submanifold of the group $\mathcal{T}$) along a hyperboloid of one sheet, as in Figure 4. This surface has a special property: it is doubly ruled and symmetric with respect to any plane containing its axis of revolution. In addition, based on this property, the double generation of the 2-DoF translation along a revolute hyperboloid of one sheet is derived and a new type of RPR-||-RPR parallel chain is synthesized as depicted in Figure 5.

4. Derivation of Delassus RPRP Paradoxical Chain

The end-effector motion in the previous manipulator is 2-DoF translation along a revolute hyperboloid of one sheet. The foregoing surface is doubly ruled, which leads to not only a non-obvious parallel generator of 2-DoF translation but also a new demonstration of the Delassus plane symmetric RPRP mechanism. In

Figure 6, actually, each of the two Rs is made up of two coaxial Rs, which are equivalent to one R when ignoring the internal self rotation of the intermediate body. This special geometric case is obtained when the distance *d* between the parallel R axes of the translating end-effector is equal to zero. Then the distance between the parallel R axes of the fixed base, which is also equal to *d*, becomes zero. In fact, *d* is the amplitude of the translation used in section 3 to introduce two conjugate RPR limbs.

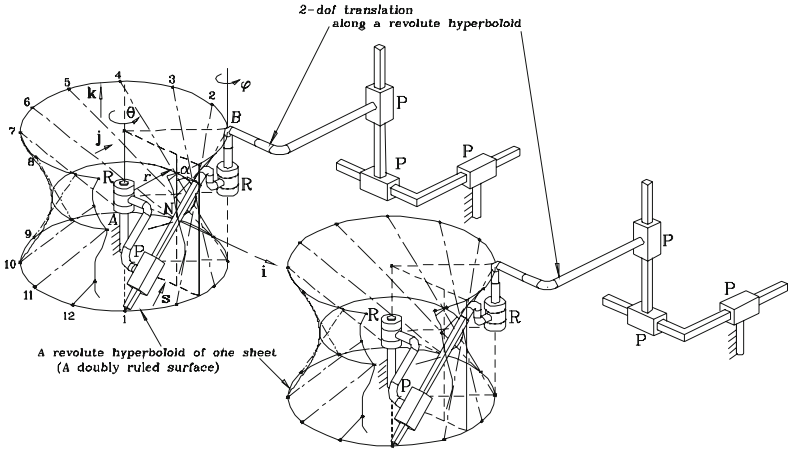

Figure 3. Two mechanisms generating the same 2-DoF translation

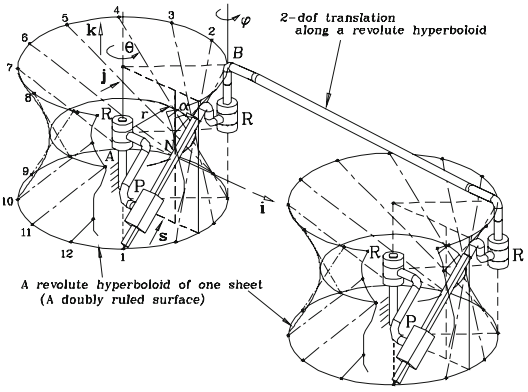

Figure 4. An RPR-||-RPR parallel generator of 2-DoF translation along a one-sheet hyperboloid

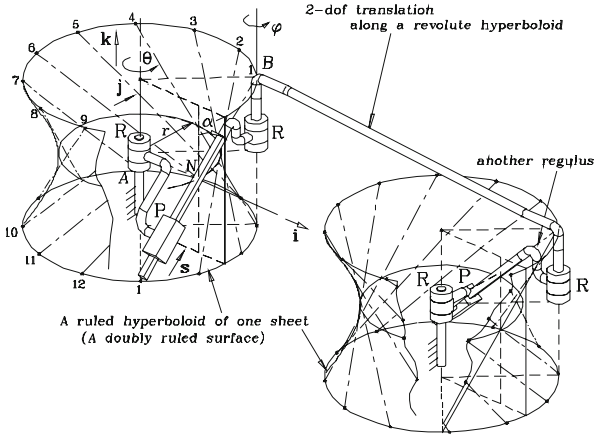

Figure 5. Another RPR-||-RPR manipulator of 2-DoF hyperboloidal translation

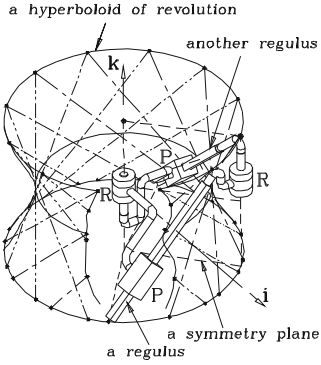

Figure 6. A plane symmetric RPRP Delassus chain

5. Conclusion

A novel parallel RPR-||-RPR manipulator generating 2-DoF translation along the surface of a hyperboloid of one sheeet is synthesized via the invariance by conjugation of any submanifold of translations in the commutative (or Abelian) Lie group $\mathcal{T}$. In addition, a special case of plane symmetric Delassus mechanism, namely the RPRP paradoxical mechanism with 1-DoF finite mobility is introduced through the double generation of the surface by the rotation of a straight line together with an adequate geometric arrangement of the RPR-||-RPR

parallel mechanism. The simulation of the proposed manipulators has been verified by computer animation software. The new mechanism becomes a RR-||-RR hinged parallelogram when one P is locked and therefore it has the singular posture of the flattened parallelogram. In despite of its singularity, the hinged parallelogram has many practical applications. In further work, the mechanisms revealed here will be extended to mechanisms with screw pairs and will lead to a new derivation of the general Delassus paradoxical HPHP four-bar linkage. Last but not least, generators of 2-DoF translation can be employed as composite joints in the synthesis of robotic manipulators and further generalize the hinged parallelogram, which generates translation with only one degree of freedom. This is also the motivation of our work.

Acknowledgements

The authors are very thankful to the National Science Council for supporting the research under grant NSC 98-2221-E-151-019.

References

Angeles, J. (2004), The qualitative synthesis of parallel manipulators, ASME J. Mech. Des., 126: 617-624.

Clavel, R. (1987), Dispositif pour le déplacement et le positionnement d'un éléments dans l'espace, Swiss patent n° 672089A5, 1985; international patent (PCT) n° WO 87/03538.

Gao, F., Li, W., Zhao, X., Jin, Z. and Zhao, H. (2002), New kinematic structures for 2-, 3-, 4-, and 5-DOF parallel manipulator designs, Mech. Mach. Theory, 37:1395-1411.

Hervé, J. M. and Sparacino, F. (1991), Structural synthesis of parallel robots generating spatial translation, Proc. 5th IEEE Int. Conf. Adva. Rob., Pisa, Italy, 808-813.

Hervé, J. M. (2009), Conjugation in the displacement group and mobility in mechanisms, Trans. Canadian Society for Mechanical Engineering, 33: 3-14.

Kong, X.-W. and Gosselin, C. (2002), Kinematics and singularity analysis of a novel type of 3-CRR 3-DOF translational parallel manipulator, Int. J. Robot. Res. 21:791-798.

Lee, C.-C. and Hervé, J. M. (2006), Translational parallel manipulators with doubly planar limbs, Mech. Mach. Theory, 41: 433-455.

Lee, C.-C. and Hervé, J. M. (2009a), On some applications of primitive Schoenflies-motion generators, Mech. Mach. Theory, 44:2153-2163.

Lee, C.-C. and Hervé, J. M. (2009b), Type synthesis of primitive Schoenflies-motion generators, Mech. Mach. Theory, 44:1980-1997.

Lee, C.-C. and Hervé, J. M. (2007), Cartesian parallel manipulators with pseudoplanar limbs", ASME J. Mech. Des., 129:1256-1264.

Wenger, P. and Chablat, D. (2000), Kinematic anlaysis of a new parallel machine tool:The orthoglide, Advances in Robot Kinematics, J. Lenarcic and M. M. Stanisic eds., Kluwer Academic Publisher, Dordrecht, 305-314.

A Study on the Effects of Cable Mass and Elasticity in Cable-Based Parallel Manipulators

Erika Ottaviano and Gianni Castelli

LARM: Lab. of Robotics and Mechatronics, DiMSAT, University of Cassino, Italy

Abstract. This paper presents numerical and experimental results for an analysis of the effects of cable's mass and elasticity in cable-based parallel manipulators. It will be shown, through numerical simulation and experimental results, that effects of these characteristics cannot be always neglected, because they affect the pose capability of the end-effector. A planar 2 cable point-mass manipulator is considered as a case of study. The model and results can be further extended to all classes of cable-based manipulators, such as under or fully constrained types.

1 Introduction

Cable-based manipulators belong to the class of parallel robots in which the fixed frame and platform are connected by several cables, which can be exerted or retracted by suitable actuation system. A cable-based manipulator has better characteristics than a classical parallel robot as reported in (Verhoeven, 2004).
Although cable manipulators have a rather long history of industrial applications, many of their fundamental problems regarding the kinematics, dynamics, and control were addressed by researchers only in the recent years. The stiffness problem has been studied by (Verhoeven et al., 1998). To investigate the vibration effects some researchers modeled cables as linear springs (Behzadipour and Khajepour, 2006) or nonlinear springs (Kawamura et al., 2000). However, all of them assumed that a cable has axial flexibility only (i.e., ignoring the transversal flexibility), which was taken into account by (Diao and Ma, 2009). The cable's mass is usually neglected in the modeling phase, considering the end-effector mass only. The effect of cable mass has been considered in few cases only, for which large manipulation operations are considered (Bouchard and Gosselin, 2006; Riehl et al., 2009). In this paper it will be shown that the key point for the choice of an appropriate model deals with the ratio between end-effector and cable masses or, more generally, between the end-effector wrenches and cables' tensions. In particular, it will be shown that axial and transversal flexibility of a cable affect the position capability of the end-effector (Castelli, 2010). Cables with no negligible mass will tend to sag under their own weight and deviation from ideal mass less cable model can be significant and cannot be ignored when an accurate modeling is required.

2 Cable Modeling for Cable-Based Manipulators

In the following 4 different models of a cable will be considered for the analysis of cable-based manipulators: mass less inextensible cable, mass less cable with elasticity, cable with continuous mass and elasticity, and lumped mass cable with elasticity. In most of cases cables are modeled as mass less and inextensible. Some authors take into account cable's elasticity only, but for some applications cable mass should be considered also to have an accurate model. Cable mass should be taken into account in general when cable sagging effects cannot be neglected.

2.1 Mass Less Inextensible Cable Model

A model for the Kinematic analysis can be based on the assumption of mass less inextensible cables, with the hypothesis that they are always in tension and can thus be treated as line segments representing bilateral constraints. Therefore, the IK consists in computing the norm of the vector $\boldsymbol{l}_{\mathrm{i}}$ connecting each cable attachment point, to the ending point of the cable attached to the mobile platform. In order to check the cables forces distribution, Statics or Dynamics analyses can be performed.

2.2 Elastic Mass Less Cable Model

Cables can be supposed to be mass less, therefore, deformation due to gravity can be neglected. According to this model, cables behave as linear springs and their elasticity coefficient can be evaluated as function of the cable section area A, the Young Modulus E, and the cable length l. Therefore, the cable tension F_{i} can be evaluated as function of the elasticity coefficient k_i and cable longitudinal deformation Δl_i. The passive stiffness (Verhoeven, 2004) describes the reaction of a mechanical system by small perturbation. For many practical applications, due to high elasticity of real cables (especially using plastic materials) the stiffness may be low in some regions of the workspace. This can affect the precision of the overall system, requiring appropriate control strategies or a suitable design.

2.3 Continuous Cable Model with Mass and Elasticity

In a static or quasi-static application in gravitational field cables can be assumed to have homogeneous properties and negligible flexural stiffness. In the following cables are considered elastic, and cable's attachment points are assumed as fixed. Let us consider the unstrained length of the cable given by l_0, and the force applied to the end of the cable given by $\boldsymbol{F}$, both of them are assumed as known. Figure 1a) shows the model of a sag cable under the gravity effect. Main parameters are ρ, E, A, and Δl, which represent the unstrained linear density, the elastic modulus, the

unstrained cross-sectional area, and the strain of the cable, respectively. Each point of the cable can be represented by Cartesian coordinates (x, z) and path variable denoted by s. The variable s represents the strained length of the cable segment as measured from the attachment point of the cable to the current point. A model has been used (Irvine, 1981; Kozac et al. 2006) to compute the static displacement of a cable and thus, its derivation will not be presented here. Coordinate of each cable point (x, z) can be defined by its curvilinear abscissa s as

$$z(s) = \frac{F_z s}{EA} + \frac{\rho_0 g}{EA}\left(\frac{s^2}{2} - l_0 s\right) + \frac{\sqrt{F_x^2 + \left(F_z + \rho_0 g\left(s - l_0\right)\right)^2} - \sqrt{F_x^2 + \left(F_z - \rho_0 g l_0\right)^2}}{\rho_0 g}$$

$$x(s) = \frac{F_x s}{EA} + \frac{\left|F_x\right|}{\rho_0 g} + \left[\sinh^{-1}\left(\frac{F_z + \rho_0 g\left(s - l_0\right)}{F_x}\right) - \sinh^{-1}\left(\frac{F_z - \rho_0 g l_0}{F_x}\right)\right] \qquad (1)$$

Equations (1) describe the profile of an elastic cable under the action of gravity and forces at its free end. In these equations, the axial elasticity can easily be identified. An experimental validation of the above-mentioned model is given in (Kozac et al. 2006). Although the analysis provides a continuous model, it can be used for static applications only (Riehl et al., 2009).

2.4 Lumped Mass and Elastic Cable Model

Each cable can be modeled as lumped masses connected in series by mass less springs, as shown in Fig. 1b). Therefore, considering a cable, it will be composed by N lumped masses m_i, and N+1 linear springs connecting the adjacent masses with elasticity coefficient k_i. In this context, it has been assumed that all the m_i masses are equal, as well as the k_i. The sum of the m_i masses equals to the total cable mass, and k_i is equal to (N+1)k, in which k is the overall cable elasticity.

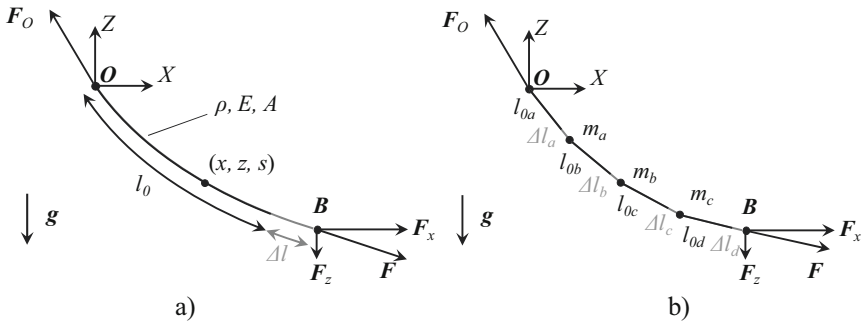

Figure 1. A cable with mass and elasticity: a) continuous model; b) lumped mass model.

3 Case of Study: Planar 2 Cables Point-Mass Robot

In the following the above-mentioned cable models have been used to evaluate the effects of elasticity and cable mass for end-effector positioning for a planar 2 cables point-mass manipulator. In particular, the mass less inextensible cable, elastic cable and cable with mass and elasticity have been modeled in ADAMS environment for simulation purposes. Moreover, the latter one shown in Fig.2b) has been compared with the continuous cable model. Simulations and experimental tests have been carried out by varying the end-effector mass leaving the cables' nominal lengths and, consequently, their masses unchanged.

Let us consider a planar point mass cable-suspended robot shown in Fig. 2a). A fixed reference frame *OXY* is considered and attachment points are denoted as A_1 and A_2. According to the mass less inextensible cable model cables lengths can be readily computed as (for i = 1, 2)

$$l_{\mathrm{i}}(\boldsymbol{x}_{\mathrm{G}}) = \left\| \boldsymbol{A}_{\mathrm{i}} - \boldsymbol{x}_{\mathrm{G}} \right\| = \sqrt{\left(A_{\mathrm{ix}} - x\right)^2 + \left(\mathrm{A}_{\mathrm{iz}} - z\right)^2} \; ; \; \theta_{\mathrm{i}}(\boldsymbol{x}_{\mathrm{G}}) = \tan^{-1}\left(\frac{A_{\mathrm{iz}} - z}{A_{\mathrm{ix}} - x}\right) \quad (2)$$

where $\boldsymbol{x}_{\mathrm{G}} = [x, z]^{\mathrm{T}}$ are the coordinates of center of gravity of the end-effector expressed in the fixed frame and l_{i} and θ_{i} are respectively the length and angle for the *i*-th cable. Vectors $\boldsymbol{F}_{\mathrm{i}}$ and $\boldsymbol{F}_{\mathrm{G}}$ respectively identify the tension in the *i*-th cable and weight force of the end-effector under the gravity action. According to Fig. 2a) the static equilibrium can be expressed as

$$F_1\cos(\theta_1) - F_2\cos(\theta_2) = 0 \; ; \qquad F_1\sin(\theta_1) + F_2\sin(\theta_2) = m_{\mathrm{ee}}g \quad (3)$$

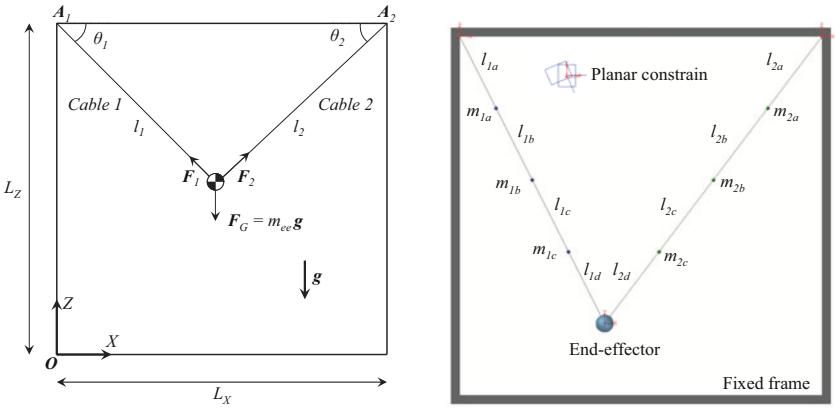

a) b)

Figure 2. A scheme for a planar 2 cables point-mass manipulator: a) with mass less cables; b) ADAMS model with cables' mass and elasticity.

3.1 Simulation Results

According to the scheme of Fig. 2a), parameters (expressed in mm) are: $L_X = 2000.0$, $L_Z = 2000.0$, l_1=1788.85, l_2=2000.0, the initial pose is x=800.0 and y=400.0. Cables have a nominal diameter of 0.8 mm, Young's modulus of 200 GPa, linear density of 0.003 kg/m and breaking load of 543 N.

The first simulation deals with the mass less inextensible cable model, therefore it has been assumed $k_1 = k_2 = \infty$ N/m; $m_1 = m_2 = 0$ kg. A second simulation is related to a model with mass less elastic cables, and cables are modeled as linear springs with k_1= 5.619E+005 N/m and k_2= 5.026E+005 N/m with $m_1 = m_2 = 0$ kg. Third simulation deals with a model considering cables with mass and elasticity. Each cable has been modeled by lumped masses and linear springs, according to the scheme shown in Fig. 2b) such as: $m_{ia} = m_{ib} = m_{ic} = m_a/3$; and lengths $l_{ia} = l_{1ib} = l_{ic} = l_{id} = l_i/4$. Cable elasticity is $k_{ia} = k_{ib} = k_{ic} = k_{id} = 4k_i$ with $k_i = EA_i/l_i$. Cables masses are m_1= 6.45 g; m_2= 7.21 g. Simulations have been carried out in ADAMS environment by varying the end-effector mass from 13.66 g (which represents the overall cables mass m_{tot} for the given configuration) to 79.56 kg, which is 700 times m_{tot} (Castelli, 2010).

Figure 3 shows the effect of end-effector mass over cable mass on the end-effector positioning capability. Figure 4 shows a comparison between the lumped and continuous mass cable's models. Results for the latter one are obtained by Eqs.(1). Figures 3a) and 3b) show respectively horizontal and vertical end-effector displacements, when the second and third models are considered. These two models give different displacements up to a threshold value for the ratio between end-effector and cables' masses, that in this case is equal to 100. Over this value the two models have the same behaviour, and cable mass can be neglected.

Therefore, the end-effector positioning capability depends on the ratio between end-effector and cables' masses. In particular, for low ratios the cable's sagging is quite relevant and determines a large deviation in end-effector positioning.

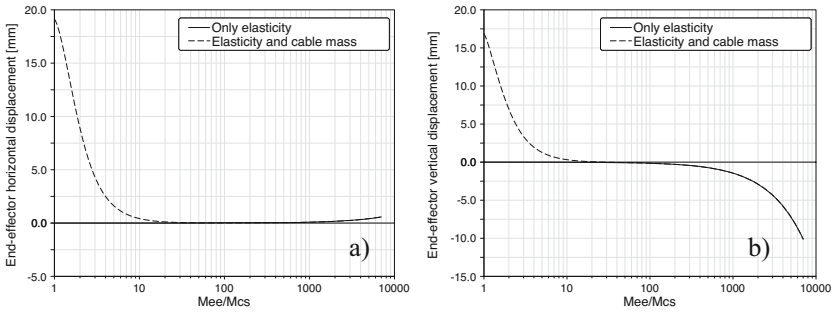

Figure 3. Comparison among the proposed cables models for the end-effector position: a) horizontal displacement; b) vertical displacement.

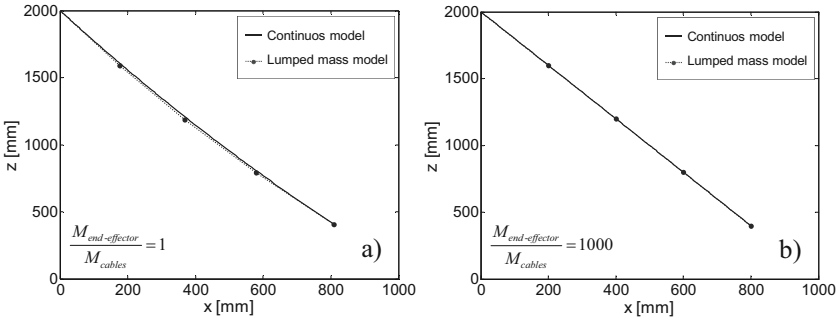

Figure 4. A comparison between lumped and continuous mass cable's models: a) low end-effector and cables masses ratio; b) high end-effector and cables masses ratio.

For the lumped mass model it has been chosen to use 3 masses, this value provides an optimal compromise between computational complexity and accuracy of the model (Castelli, 2010). A simulation test shown in Fig.4 has been carried out to compare results for the lumped and continuous mass models.

3.2 Experimental Characterization

A validation of numerical simulations has been carried out by considering a planar 2 cables point-mass manipulator. For the prototype under-study, according to the scheme of Fig. 2a) the pose is x=629.45 and y=1153.65. Plastic cables were chosen, with average nominal diameter of 4 mm and linear density of 10.94 g/m. The Young's modulus was determined experimentally by means of a stress-strain test on a test-piece of the cable and it was set equal to 50 MPa, neglecting the nonlinear relationship between stress and deformation of the cable.

During the tests 5 different masses have been used as end-effector, while the total mass of cables was always equal to 29.88 g. Table I shows values of the lengths of the cables and end-effector coordinates collected for the 5 tests. Measurements of the manipulator's configurations were performed by using an algorithm based on Image Processing and implemented in MATLAB environment (Castelli, 2010). Figure 5 shows the phases of the implemented program.

In Table I deformation rates ε_1 and ε_2 are reported for the 2 cables and deviations of the end-effector coordinates Δx and Δz with respect to the initial conditions. As expected, according to numerical results in previous Section, by increasing the mass of the end-effector a greater axial deformation of the cable will occur because of its elasticity together with lower longitudinal strain due to the mass of cables. It is worth noting that deviations of the end-effector position from the initial configuration are due to both elasticity of the cables (on a priority basis for tests M_4 and M_5) and mass of cables (on a priority basis for tests M_1, M_2 and M_3). Indeed, tests M_1 and M_2 show

significant vertical deviations of the end-effector along Z^+ direction due to the mass of cables, while the vertical deviation of the end-effector along the Z^- direction is due to the elongation of the cables. The ADAMS model in Fig. 2b) has been used for a comparative analysis (Castelli, 2010). As for experimental tests, during the simulation the end-effector weight was increased continuously from the value of 98.1 mN (10 g) to a value of 49.05 N (5 kg), while nominal cables lengths were kept constant. Figure 6 shows a comparison for end-effector position during the experimental tests and numerical simulation. The maximum deviation between experimental and numerical values do not exceed the 8% of the average of the cables' lengths.

Table I. Experimental results for the tests varying the end-effector masses.

test	mass [g]	l_1 [mm]	l_2 [mm]	ε_1 [%]	ε_2 [%]	x [mm]	Δx [mm]	z [mm]	Δz [mm]
M_1	53.26	1052.1	1690.9	0.10	0.47	672.2	42.7	1227.3	74.6
M_2	101.34	1054.8	1695.4	0.36	0.74	667.6	38.1	1219.5	66.8
M_3	676.47	1080.6	1721.6	2.81	2.29	651.4	21.9	1170.6	17.9
M_4	1305.40	1109.8	1777.2	5.55	5.60	630.7	1.2	1110.7	-41.9
M_5	3048.30	1117.6	1779.8	6.28	5.75	625.9	-3.5	1107.6	-45.1

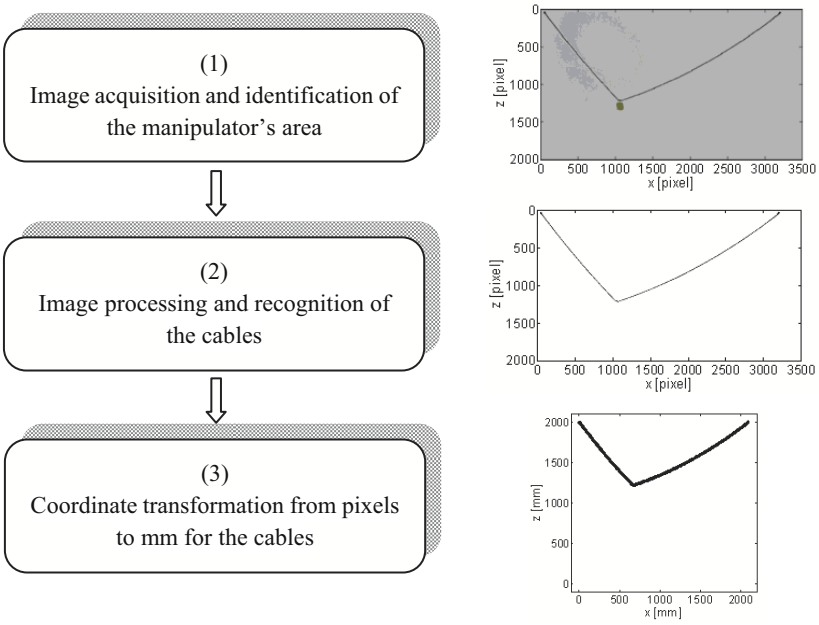

Figure 5. The 3 phases of the Matlab program based on Image Processing.

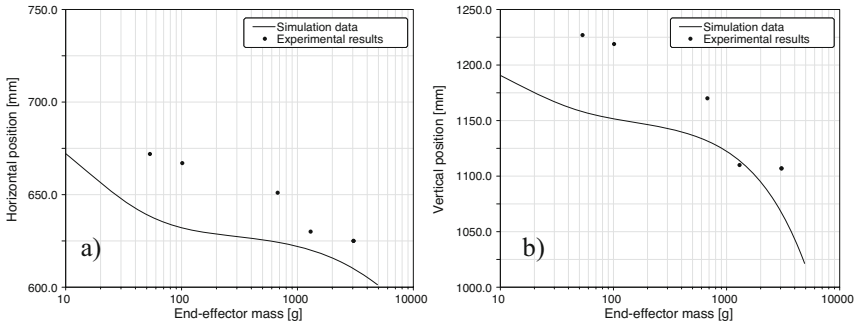

Figure 6. Comparison between the end-effector position obtained by experimental tests and numerical simulation: a) *x* coordinate, b) *z* coordinate.

Conclusions

In this paper modeling and experimental results are presented for the analysis of the effects of cable's mass and elasticity. It has been shown that they affect pose capability of cable-based parallel manipulators. These effects must be analyzed through the ratio of end-effector and cables masses. Observing the results it is evident that the possibility to neglect the cables' masses is related to the end-effector and cables and do not depend by the manipulator dimensions. Further extension of this work is related to vibration and dynamic problems considering the cables' masses.

Bibliography

Behzadipour, S., Khajepour, A. (2006). Stiffness of Cable-Based Parallel Manipulators with Application to Stability Analysis. *Jnl. Mech. Des.* **128**(1), 303–310.

Bouchard, S. Gosselin, C. M. (2006). Kinematic Sensitivity of a Very Large Cable-Driven Parallel Mechanism", *ASME DETC '06*, Philadelphia, paper n. DETC2006-99222.

Castelli. G. (2010). Analysis, Modeling and Experimentation of Cable-Based Manipulators. *PhD thesis, University of Cassino*.

Diao. X. and Ma. O. (2009). Vibration Analysis of Cable-Driven Parallel Manipulators. *Multibody System Dyamics.* **21**, 347–360.

Irvine, H. (1981). Cable Structures. *Cambridge, MA: MIT Press*.

Kawamura, S., Kino, H., Won, C. (2000). High-Speed Manipulation by Using a Parallel Wire-Driven Robots. *Robotica*, **18**, 13–21.

Kozak, K., Zhou, Q., Wang, J. (2006). Static Analysis of Cable-Driven Manipulators with Non-Negligible Cable Mass. *IEEE Trans. on Robotics*, **22** (3), 425-433.

Riehl, N., Gouttefarde, M., Krut, S., Baradat, C., Pierrot, F., (2009). Effects on Non-Negligible Cable Mass on the Behavior of Large Workspace Cable-Driven Parallel Mechanism. *IEEE Int. Conf. Robotics and Autom.*, Kobe, pp. 2193-2198.

Verhoeven, R. (2004). Analysis of the Workspace of Tendon-Based Stewart Platforms. *PhD thesis, University of Duisburg-Essen.*

Chapter II

Service, Education, Medical, Space, Welfare and Rescue Robots

Motion Planning of the Trident Snake Robot: An Endogenous Configuration Space Approach

Janusz Jakubiak ‡, Krzysztof Tchoń‡ and Mariusz Janiak‡

‡ Institute of Computer Engineering, Control and Robotics, Wrocław University of Technology, Wrocław, Poland

Abstract We address the motion planning problem of the trident snake robot. The problem is solved with the help of the imbalanced Jacobian inverse kinematics algorithm dedicated to nonholonomic systems with constraints. Performance of the algorithm is illustrated with computer simulations.

1 Introduction

The trident snake robot is a sort of research platform for studying nonholonomic locomotion. The robot consists of a triangular root block and three articulated branches. Each branch includes a number of links connected by actuated rotational joints. At its center each link is supported by a passive wheel that rolls without lateral slip. The design of this robot, a model of its kinematics, and selected control strategies have been presented in Ishikawa (2004). More advanced analysis of the locomotion principles and control algorithms of the robot as well as results of physical experiments are reported in Ishikawa et al. (2006, 2010). An application of the transverse functions approach to the control of the trident snake robot can be found in Ishikawa et al. (2009).

In this paper we address the problem of motion planning of the trident snake robot using the endogenous configuration space approach, Tchoń and Jakubiak (2003). Various control system representations of the robot are introduced, and a constrained motion planning problem addressed, respecting the constraints on the robot joint variables. The problem has been solved by the imbalanced Jacobian algorithm, Janiak (2009). The performance of the motion planning algorithm is illustrated by computer simulations for 1-link and 2-link robots.

The paper is composed as follows. Section 2 contains the problem formulation. The motion planning algorithm is introduced in section 3. Computer simulations are presented in 4. Section 5 concludes the paper.

2 Problem Formulation

We shall study the kinematics of a trident snake robot equipped with l-link branches. For simplicity, it is assumed that the edges of the root triangle, and the distances between the joints and the wheels are equal to 1. The joint variables of the robot will be grouped in triples $\phi_i = (\phi_{1i}, \phi_{2i}, \phi_{3i})$, $i = 1, \ldots, l$, and denoted as $\phi = (\phi_1, \ldots, \phi_l) \in R^{3l}$. The position and orientation of the root block is described as $w = (x, y, \theta) \in SE(2)$. The 2-link robot has been shown in the figure 1. As has been shown in Ishikawa

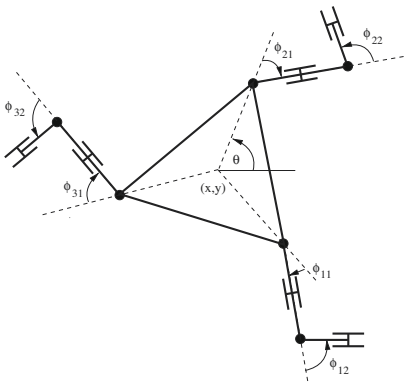

Figure 1. 2-link trident snake robot.

(2004); Ishikawa et al. (2006, 2010), the motion of the trident snake robot is subject to $3l$ nonholonomic constraints in the Pfaffian form

$$P(\phi, \theta)\dot{w} - Q(\phi)\dot{\phi} = 0, \tag{1}$$

for $P(\phi, \theta) = \left[P_1^T(\phi, \theta), \ldots, P_i^T(\phi, \theta), \ldots, P_l^T(\phi, \theta)\right]^T$ and $Q(\phi) = [Q_{ij}(\phi)]$. The matrices $P_i(\phi, \theta)$ and $Q_{ij}(\phi)$, $i, j = 1, \ldots, l$ have dimensions 3×3.

The constraints (1) provide a representation of the robot kinematics in the form of a driftless control system

$$\begin{pmatrix} \dot{w} \\ \dot{\phi} \end{pmatrix} = \begin{bmatrix} G(\phi, \theta) \\ H(\phi, \theta) \end{bmatrix} u, \tag{2}$$

where blocks of $H(\phi, \theta) = \left[H_1^T(\phi, \theta), \ldots, H_k^T(\phi, \theta), \ldots, H_l^T(\phi, \theta)\right]^T$ as well as $G(\phi, \theta)$ are 3×3 matrices. The variable $u \in R^3$ denotes a control vector of the trident snake robot. In order to define the vector fields appearing in (2), we need to solve a system of matrix equations

$$P(\phi, \theta)G(\phi, \theta) - Q(\phi)H(\phi, \theta) = 0 \tag{3}$$

that is tantamount to

$$P_i(\phi,\theta)G(\phi,\theta) = \sum_{j=1}^{l} Q_{ij}(\phi)H_j(\phi,\theta) \tag{4}$$

for $i = 1,\ldots,l$. Depending on the physical meaning of the control vector u, there exist $l+1$ possibilities of solving this system. First, let us assume that the root block velocities are directly controlled. If this is the case, we set $G(\phi,\theta) = I_3$, the unity matrix, and compute from (3) $H(\phi,\theta) = Q^{-1}(\phi)P(\phi,\theta)$. By Ishikawa (2004), the matrix $H(\phi,\theta)$ is invertible, so the resulting representation (2) always exists. Alternatively, suppose that the control vector has the interpretation of the kth joint velocities of each branch, i.e. $u = \dot{\phi}_k$. Consequently, we choose $H_k(\phi,\theta) = I_3$ and obtain from (4) the following equation for $G(\phi,\theta)$ and the matrices $H_i(\phi,\theta)$, $i \neq k$,

$$\begin{bmatrix} P_1(\phi,\theta) & -Q_{11}(\phi) & \ldots & -Q_{1l}(\phi) \\ P_2(\phi,\theta) & -Q_{21}(\phi) & \ldots & -Q_{2l}(\phi) \\ \vdots & & & \vdots \\ P_l(\phi,\theta) & -Q_{l1}(\phi) & \ldots & -Q_{ll}(\phi,\theta) \end{bmatrix} \begin{bmatrix} G(\phi,\theta) \\ H_1(\phi,\theta) \\ \vdots \\ H_l(\phi,\theta) \end{bmatrix} = \begin{bmatrix} Q_{1k}(\phi) \\ Q_{2k}(\phi) \\ \vdots \\ Q_{lk}(\phi) \end{bmatrix}. \tag{5}$$

The corresponding representation of kinematics (2) is well defined provided that the $3l \times 3l$ matrix on the left hand side of (5) is invertible.

Relying on Ishikawa (2004), below we shall provide explicit formulas for the system (2) representing the kinematics of the trident snake robot for $l = 1$ and $l = 2$. If $l = 1$, we deduce that $P(\phi,\theta) = A(\phi)R^T(Z,\theta)$, $R(Z,\theta)$ denoting the rotation matrix around Z-axis by the angle θ, and

$$A(\phi) = \begin{bmatrix} \sin(\phi_{11}+\alpha_1) & -\cos(\phi_{11}+\alpha_1) & -1-\cos\phi_{11} \\ \sin(\phi_{21}+\alpha_2) & -\cos(\phi_{21}+\alpha_2) & -1-\cos\phi_{21} \\ \sin(\phi_{31}+\alpha_3) & -\cos(\phi_{31}+\alpha_3) & -1-\cos\phi_{31} \end{bmatrix},$$

where the angles $\alpha_1 = -\frac{2\pi}{3}$, $\alpha_2 = 0$, and $\alpha_3 = \frac{2\pi}{3}$. Furthermore, since $Q(\phi) = I_3$, we arrive at two representations of the kinematics of the trident snake robot:

$$\begin{pmatrix} \dot{w} \\ \dot{\phi} \end{pmatrix} = \begin{bmatrix} I_3 \\ P(\phi,\theta) \end{bmatrix} u, \tag{6}$$

controlled directly by the velocities of the root block, and the representation

$$\begin{pmatrix} \dot{w} \\ \dot{\phi} \end{pmatrix} = \begin{bmatrix} P^{-1}(\phi,\theta) \\ I_3 \end{bmatrix} u, \tag{7}$$

where the control input includes the branch joint velocities. It has been noticed in Ishikawa (2004) that the matrix $A(\phi)$, so also $P(\phi,\theta)$ remains

invertible as long as all the joint angles lie in the range $\pm\frac{\pi}{3}$, therefore the representation (7) is well defined locally. Obviously, wherever defined, these representations are feedback equivalent. For the case of $l = 2$, it follows from Ishikawa (2004) that

$$P(\phi,\theta) = \begin{bmatrix} P_1(\phi,\theta) \\ P_2(\phi,\theta) \end{bmatrix},$$

where $P_1(\phi,\theta) = A(\phi)R^T(Z,\theta)$, and $P_2(\phi,\theta) = B(\phi)R^T(Z,\theta)$, with

$$B(\phi) = \begin{bmatrix} \sin(\phi_{11}+\phi_{12}+\alpha_1) & -\cos(\phi_{11}+\phi_{12}+\alpha_1) & -1-\cos(\phi_{11}+\phi_{12})-2\cos\phi_{12} \\ \sin(\phi_{21}+\phi_{22}+\alpha_2) & -\cos(\phi_{21}+\phi_{22}+\alpha_2) & -1-\cos(\phi_{21}+\phi_{22})-2\cos\phi_{22} \\ \sin(\phi_{31}+\phi_{32}+\alpha_3) & -\cos(\phi_{31}+\phi_{32}+\alpha_3) & -1-\cos(\phi_{31}+\phi_{32})-2\cos\phi_{32} \end{bmatrix}.$$

The matrix $Q(\phi) = [Q_{ik}(\phi)]$, $i,k = 1,2$ has entires $Q_{11}(\phi) = Q_{22}(\phi) = I_3$, $Q_{12}(\phi) = 0$, $Q_{21}(\phi) = diag\{2\cos\phi_{12}+1, 2\cos\phi_{22}+1, 2\cos\phi_{32}+1\}$. In consequence, we obtain the following representations of the kinematics (2). The system

$$\begin{pmatrix} \dot{w} \\ \dot{\phi} \end{pmatrix} = \begin{bmatrix} I_3 \\ Q^{-1}(\phi)P(\phi,\theta) \end{bmatrix} u, \tag{8}$$

steered by the velocities of the root block, and two systems

$$\begin{pmatrix} \dot{w} \\ \dot{\phi}_1 \\ \dot{\phi}_2 \end{pmatrix} = \begin{bmatrix} G_1(\phi,\theta) \\ I_3 \\ H_2(\phi) \end{bmatrix} u, \qquad \begin{pmatrix} \dot{w} \\ \dot{\phi}_1 \\ \dot{\phi}_2 \end{pmatrix} = \begin{bmatrix} G_2(\phi,\theta) \\ H_1(\phi) \\ I_3 \end{bmatrix} u, \tag{9}$$

steered, respectively, by branch joint velocities $\dot{\phi}_1$ and $\dot{\phi}_2$, where

$$\begin{bmatrix} G_1(\phi,\theta) \\ H_2(\phi) \end{bmatrix} = \begin{bmatrix} P_1(\phi,\theta) & -Q_{12}(\phi) \\ P_2(\phi,\theta) & -Q_{22}(\phi) \end{bmatrix}^{-1} \begin{bmatrix} Q_{11}(\phi) \\ Q_{21}(\phi) \end{bmatrix} \quad \text{and}$$

$$\begin{bmatrix} G_2(\phi,\theta) \\ H_1(\phi) \end{bmatrix} = \begin{bmatrix} P_1(\phi,\theta) & -Q_{11}(\phi) \\ P_2(\phi,\theta) & -Q_{21}(\phi) \end{bmatrix}^{-1} \begin{bmatrix} Q_{12}(\phi) \\ Q_{22}(\phi) \end{bmatrix}.$$

Again, all three representations (8)-(9) are feedback equivalent within their common region of definition. It can be checked that the two systems (9) are well defined provided that $\det A(\Phi) \neq 0$ and $\det[B(\phi) - Q_{21}(\phi)A(\phi)] \neq 0$.

3 Motion Planning

All the representations of the kinematics of the trident snake robot derived in section 2 have the form of a driftless control system with outputs

$$\dot{q} = F(q)u, \quad y = k(q), \tag{10}$$

where $q = (\phi, w) \in R^n$, $n = 3l + 3$, collects robot coordinates, $y \in R^r$ refers to the task coordinates (often y is just a sub vector of q), and $u \in R^m$, $m = 3$, stands for the control vector. The control functions $u(\cdot) \in L^2_m[0, T]$ are assumed Lebesgue square integrable on a time interval $[0, T]$. Suppose that $q(t) = \varphi_{q_0,t}(u(\cdot))$ denotes the robot trajectory started from q_0. According to the endogenous configuration space approach Tchoń and Jakubiak (2003), the end point map $K_{q_0,T}(u(\cdot)) = k(q(T))$ of the system (10) is identified with the kinematics of the trident snake robot.

The following motion planning problem with state constraints will be addressed in the system (10): given $y_d \in R^r$, find a control function $u_d(t)$ such that $K_{q_0,T}(u_d(\cdot)) = y_d$, while certain robot coordinates remain bounded, $q_{k\,lb} \leq q_k(t) \leq q_{k\,ub}$. A solution of this problem proposed in this paper relies on the approach invented in Janiak (2009), that will be sketched below. First, to incorporate the state constraints, we use the plus function $(x)_+ = \max\{x, 0\}$, so that the inequality constraints for $q_k(t)$ are satisfied, when the functions $(q_k(t) - q_{k\,ub})_+$ and $(-q_k(t) + q_{k\,lb})_+$ vanish on $[0, T]$. Because the plus function is nonnegative, this means that the sum of integrals over $[0, T]$ of these functions vanish. The plus function will be approximated by a smooth function $(x)_+ \cong p(x, \alpha) = x + \frac{1}{\alpha}\ln(1 + \exp(-\alpha x))$, parameterized by $\alpha > 0$. Assume that the coordinates q_k, $j \leq k \leq s$ need to be bounded. To take this into account, we shall extend the control system (10) with state variables q_{n+k} by setting

$$\dot{q}_{n+k} = p(q_k - q_{k\,ub}, \alpha) + p(-q_k + q_{k\,lb}, \alpha), \qquad q_{n+k}(0) = 0, \quad j \leq k \leq s.$$

If we define the extended state $q_e = (q, q_{n+k}, j \leq k \leq s)$ and the extended output $y_e = (y, q_{n+k}, j \leq k \leq s)$ variables, then the extended system (10) becomes an affine control system with outputs, of the form

$$\dot{q}_e = f_e(q_e) + F_e(q_e)u, \;\; y_e = k_e(q_e), \tag{11}$$

where the extended vector fields

$$f_e(q_e) = \begin{pmatrix} 0 \\ p(q_j - q_{j\,ub}, \alpha) + p(-q_j + q_{j\,lb}, \alpha) \\ \vdots \\ p(q_s - q_{s\,ub}, \alpha) + p(-q_s + q_{s\,lb}, \alpha) \end{pmatrix}, \quad F_e(q_e) = \begin{bmatrix} F(q) \\ 0 \end{bmatrix},$$

and the extended output function $k_e(q_e) = (k(q), q_{n+j}, \ldots, q_{n+s})$. Obviously, the extended kinematics $K^e_{q_{e0},T}(u(\cdot)) = k_e(q_e(T))$, and $q_{e0} = (q_0, 0)$.

In the extended system the constrained motion planning problem is reformulated as follows: find a control $u_d(t)$ such that $K^e_{q_{e0},T}(u_d(\cdot)) = y_{ed}$,

where $y_{ed} = (y_d, 0)$. Since the re-formulated problem is unconstrained, it can be solved by a standard Jacobian inverse kinematics algorithm, Tchoń and Jakubiak (2003). However, to prevent the Jacobian algorithm from getting singular, the extended system is subject to a regularization, that calls for an inverse kinematics algorithm called imbalanced, Janiak (2009). The algorithm goes along the following lines. To each extended coordinate q_{n+k} of (11) we add a regularizing term $r(q_{rk}) = q_k^2$, obtaining a system

$$\dot{q}_e = f_r(q_e) + F_e(q_e)u, \;\; y_r = k_e(q_e), \tag{12}$$

where the drift vector field $f_r(q_e) = f_e(q_e) + \left(0, q_j^2, \ldots, q_s^2\right)^T$, and the desirable output $y_{rd} = \left(y_d, \int_0^T q_j^2(t)dt, \ldots, \int_0^T q_s^2(t)dt\right)$.

Let $K^r_{q_e,T}(u(\cdot)) = k_e(q(T))$ denote the kinematics of (12). Given a curve of control functions $u_\theta(\cdot)$, we compute the error

$$e_r(\theta) = K^r_{q_e,T}(u_\theta(\cdot)) - y_{rd}(\theta), \tag{13}$$

differentiate it, and request the error decreases with a rate $\gamma > 0$

$$\frac{de_r(\theta)}{d\theta} = J^r_{q_{e0},T}(u_\theta(\cdot))\frac{du_\theta(\cdot)}{d\theta} - \frac{dy_{rd}(\theta)}{d\theta} = -\gamma e_r(\theta), \tag{14}$$

where $J^r_{q_{e0},T}(u(\cdot))$ is the Jacobian of the regularized system. Recall that, given a control function $v(\cdot)$, the Jacobian $J^r_{q_{e0},T}(u(\cdot))v(\cdot) = C(T)\mathcal{J}(T)$, where $C(T) = \frac{\partial k_e(q_e(T)}{\partial q_e}$, while $\mathcal{J}(T)$ solves the differential equation

$$\frac{d}{dt}\mathcal{J}(t) = \mathcal{A}(t)\mathcal{J}(t) + \mathcal{B}(t)v(t)$$

with zero initial condition, and $\mathcal{A}(t) = \frac{\partial(f_r(q_e)+F_e(q_e)u(t))}{\partial q_e}$, $\mathcal{B}(t) = G(q_e(t))$.

Next, we skip from the middle part of (14) the term $\frac{dy_{rd}(\theta)}{d\theta}$, that yields a Ważewski-Davidenko equation

$$J^r_{q_{e0},T}(u_\theta(\cdot))\frac{du_\theta(\cdot)}{d\theta} = -\gamma e_r(\theta). \tag{15}$$

After applying a right Jacobian inverse $J^{\#r}_{q_{e0},T}(u(\cdot))$, (15) transforms into a dynamic system

$$\frac{du_\theta(\cdot)}{d\theta} = -\gamma J^{\#r}_{q_{e0},T}(u_\theta(\cdot))e_r(\theta). \tag{16}$$

underlying the imbalanced Jacobian inverse kinematics algorithm. The solution of the constrained inverse kinematic problem $u_d(t) = \lim_{\theta\to+\infty} u_\theta(t)$.

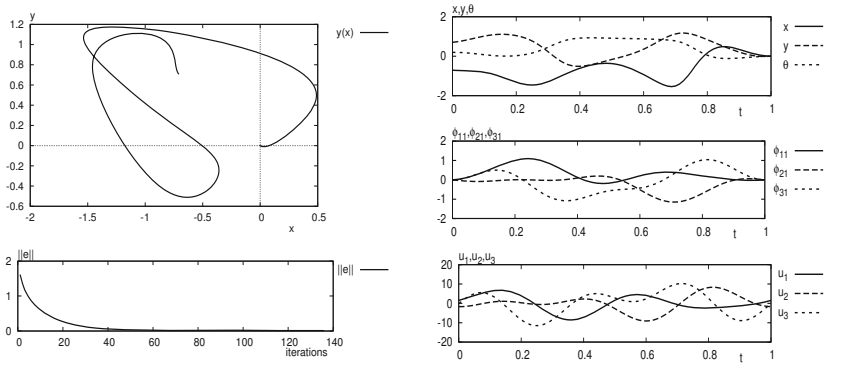

Figure 2. 1-link trident snake trajectories: joint control

4 Computer Simulations

In order to illustrate the performance of the motion planning algorithm, we have solved two motion planning problems for l = 1-link and l = 2-link trident snake robot whose kinematics models are described by (7) and (8). The constraints $|\phi_{il}| \leq \frac{\pi}{3}$, $i = 1, 2, 3$, have been imposed, and the desirable taskspace point $y_d = 0$. The controls have had the form $u_i(t) = \lambda_{i0} + \sum_{k=1}^{2l+1} \sin 2k\pi t + \cos 2k\pi t, \quad i = 1, 2, 3$. The imbalanced algorithm (16) has been applied involving the Jacobian pseudoinverse, Tchoń and Jakubiak (2003), with $\gamma = \frac{0.2}{l}$, and the plus function parameter $\alpha = 90$. The computations stop, when the taskspace error norm drops below 0.01.

In simulations for 1-link case, the initial robot configuration is equal to $q_0 = (-0.707107, 0.707107, 0.19635, 0, 0, 0)$, while initial control data $\lambda_0 = (0.5, 0.01, 0.01, 0, 0, 0, 0, -0.2, 0.01, 0.01, 0, 0, 0, 0, -0.3, 0.01, 0.01, 0, 0, 0, 0)$.

Simulations for 2-link case employed the initial robot configuration $q_0 = (-0.707107, 0.707107, 0.19635, 0, 0, 0, 0, 0, 0)$, and the initial $\lambda_{0ij} = 0.01$ except for $\lambda_{010} = 0.1$ and $\lambda_{020} = \lambda_{030} = -0.1$. Solutions of the motion planning problems: the root block position path, trajectories of robot variables, control functions, and the error are displayed in figures 2 and 3.

5 Conclusion

Using the imbalanced Jacobian inverse kinematics algorithm for nonholonomic systems we have solved the constrained motion planning for the single joint and a specific double joint trident snake robot. It turns out that, indeed, the trident snake creates a challenge for motion control algorithms.

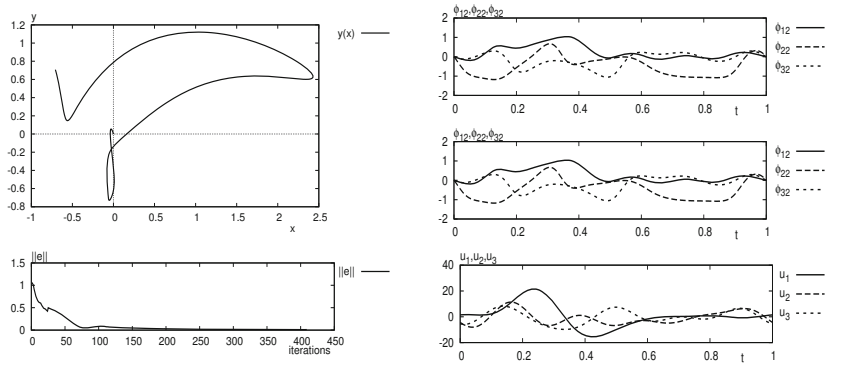

Figure 3. 2-link trident snake trajectories: root block control

Extension of the presented method accounting for more stringent motion constraints and longer branches of the robot will be a subject of future investigation.

6 Acknowledgment

This research has been supported by the Wrocław University of Technology.

Bibliography

M. Ishikawa. Trident snake robot: Locomotion analysis and control. In *Proceedings of the IFAC NOLCOS*, pages 1169–1174, 2004.

M. Ishikawa, Y. Minami, and T. Sugie. Development and control experiment of the trident snake robot. In *Proceedings of the 45th IEEE CDC*, pages 6450–6455, 2006.

M. Ishikawa, P. Morin, and C. Samson. Tracking control of the trident snake robot with the transverse function approach. In *Proceedings of the 48th IEEE CDC*, 2009.

M. Ishikawa, Y. Minati, and T. Sugie. Development and control experiment of the trident snake robot. *IEEE/ASME Trans. on Mechatronics*, 15: 9–16, 2010.

M. Janiak. *Jacobian inverse kinematics algorithms for mobile manipulators with constraints on state, control, and performance*. PhD thesis, Wrocław University of Technology, 2009.

K. Tchoń and J. Jakubiak. Endogenous configuration space approach to mobile manipulators: a derivation and performance assessment of Jacobian inverse kinematics algorithms. *Int. J. Control*, 76:1387–1419, 2003.

A Novel Stair-Climbing Wheelchair with Variable Configuration Four-Bar Linkage –Mechanism Design and Kinematics–

Yusuke Sugahara*, Naoaki Yonezawa* and Kazuhiro Kosuge*
* Department of Bioengineering and Robotics, Tohoku University, Sendai, Japan
E-mail: sugahara@irs.mech.tohoku.ac.jp

Abstract. This paper describes the mechanism of a novel multi-wheel stair climbing wheelchair. The necessity of the mobility aid technology for elderly and handicapped people which has "Minimally-invasiveness for historical environment" are described, and with this goal, a novel multi-wheel stair climbing wheelchair with variable configuration four-bar linkage is proposed. Its mechanical design, principle of operation and kinematics are mainly illustrated.

1 Introduction

Recently, to create a society where it is easy for elderly and disabled people to be self-reliant, the "barrier-free" concept has been disseminated, and the scope of activity of elderly and disabled wheelchair users has expanded. However, considering environments having cultural meanings such as historical buildings, cultural heritage and historic sites, from the viewpoint of the authenticity (Taylor, 2001) and historic value, it is undesirable to remove barrier easily by improvement of infrastructure such as installing elevators. Especially in Japan where most of historic buildings are wooden construction, it is difficult to attach such barrier-free facilities without damaging heritages, and today, in the multistoried historical buildings designated as a national treasure, it is impossible to enter for wheelchair users.

The final target of our research involves realizing smooth and hospitable locomotion of wheelchair users in the environments having cultural meanings such as Japanese historical wooden buildings and castle ruin, without tampering with the authentic style of the environment. It is in a manner development of mobility aid technology having "Minimally-invasiveness for historical environment". Especially in this research, the purpose is to develop a wheelchair to contribute independence locomotion ability to

wheelchair users in the historical environment, without tampering environment, doing only same damage as human walking to the environment, on the historically authentic pathway including stairs and uneven terrain.

There are studies on stair climbing machines as methodology of barrier-free. HELIOS-V (Uchida et al., 1999) has ability to climb stairs using special wheels, but it applies concentrated load on the edges of stairs which causes damage for wooden buildings. A stair climbing wheelchair (Yanagihara et al., 1999) is sophisticated, it is difficult to operate in narrow historical buildings because it is long from front to back and cannot turn during climbing. The electric wheelchair named "iBOT", capable of ascending and descending stairs and slopes (Independence Technology L.L.C., 2003) which applies high ground pressure because of its weight and the number of the landing wheels is difficult to be utilized in wooden buildings. It has also another demerit that the stability during climbing is not ensured. Stair Climbing Wheelchair (Miyagi et al., 1998) and Zero Carrier (Davies et al., 2009) having similar mechanism are also sophisticated stair climbing vehicles which can adopt various step heights and treads with wide support polygon. But they have too many DOFs and are difficult to run on uneven terrain because it is essentially impossible to use large wheel. CALMOS (Gonzalez et al., 2009), which has a four-bar based mechanism to climb stairs, is one of simple solutions, however, is also difficult to use large wheels. Top Chair (Top Chair SAS, 2003) which is a stair climbing wheelchair using crawler applies concentrated load on the edge of a stair.

In the Japanese historic buildings and sites, it is desirable to do only same damage as human walking to the environment. Therefore it is necessary to run and climb stairs with low ground pressure as much as human walking, and not to apply concentrated load on the edge of a stair. Furthermore, it is necessary to have an ability to turn during climbing in order to cope with curved stairs and to run on uneven terrain to travel historically authentic pathway. On the other hand, from the point of view of safety, it is necessary to ensure static stability anytime during climbing.

With this goal, authors propose a stair-climbing wheelchair with variable configuration four-bar linkage. In this paper, mechanical design, principle of operation and kinematics of this novel mechanism are illustrated.

2 Design and Principle of Operation

Figure 1 shows the outline of the developed wheelchair having variable configuration multi-wheel stair climbing mechanism "TBW-1". Its upper body is diverted commercially-available wheelchair, and the joint of the leg part is connected under the seating face. Leg part has active hip pitch joint and ankle pitch joint, and this ankle joint connects to right and left wheeled four-bar linkage module.

Structure of the wheeled four-bar linkage module is shown in Figure 1(b). This mechanism has four wheels at every vertex, and adjacent two joints are active joints. By driving these active joints, this mechanism can transform from Parallelogram mode (Figure 2(a)) to Straightness mode (Figure 2(b)). Since length of four links are equal, it can also transform to Dogleg mode (Figure 2(c)) by controlling joints appropriately.

Motion sequence to ascend and descend stairs is shown in Figure 3. As shown in figure, it basically ascends and descends stairs by repeating transformation between Parallelogram mode and Straightness mode. At least four wheels are landing all of the time through ascending and descending stairs, and this enables theoretically low ground contact pressure and wide support polygon. Here, stability can be ensured by controlling joints to

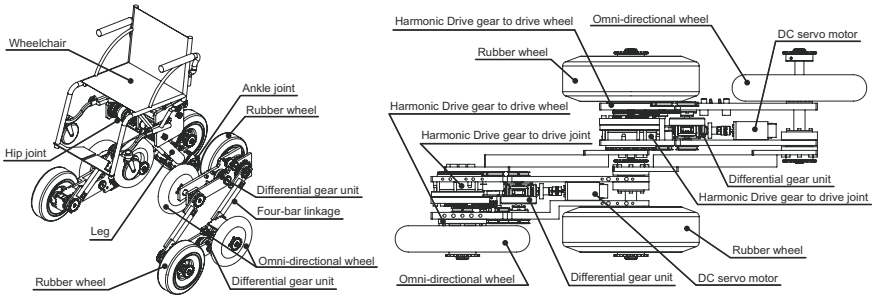

Figure 1. TBW-1 Matsushima. (a): Outline, (b): Four-bar linkage module.

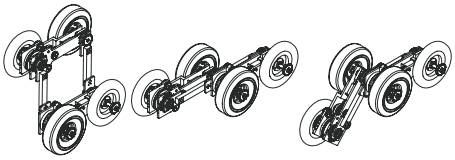

Figure 2. Transformation of the wheeled four-bar linkage module. (a): Parallelogram mode, (b): Straightness mode, (c): Dogleg mode.

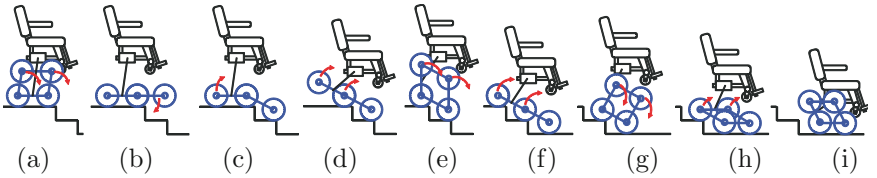

Figure 3. Motion sequence of descending stairs.

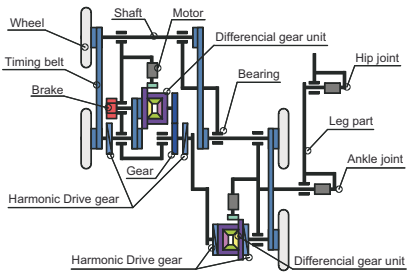

Figure 4. Structure of wheeled four-bar linkage mechanism.

maintain ZMP (Vukobratović et al., 1972) to locate near center of this support polygon. As shown in (c), described Dogleg mode is utilized at the beginning of descending and the end of ascending. In addition, half of the eight wheels are omni-directional wheel, and this enables to turn anytime whether on the stairs or on the road.

To drive this wheeled four-bar linkage mechanism, generally, three actuators are needed: one for driving wheels and two for driving its configuration. However in this study, reduction of actuator number has been tried by using coupled actuation (Hirose et al., 1989) of joints and wheels with two actuators. Figure 4 shows the structure of this mechanism. Motors are attached on the parallel two links, and output of each motor is distributed by differential gear unit to two motions: rotation of wheel and actuation of adjacent two active joints. Angles of joints are geometrically coupled, and angles of four wheels connected by timing belt are equal. Here, two output axes of only one differential gear unit are connected to wheel axis and joint axis via timing belt and spur gears respectively. Therefore, joints are actuated and the configuration of the four-bar linkage is varied when two motors rotate in same direction, and joints are fixed and wheels are driven when they rotate in opposite direction. Wheel axes and joint axes have Harmonic Drive gears, and this enables to choose appropriate reduction ratio for both of stair-climbing motion and running motion.

Because there are two postures in Dogleg mode, adjacent two active joints can drive its configuration in both postures. However, only one active joint must be rotate to vary its mode from Straightness to Dogleg, and it has an electromagnetic brake to fix wheel rotation in this situation.

3 Kinematics

In this chapter, kinematic relations between formation of the robot, wheel angles and actuator angles of the four-bar linkage mechanism are described.

A Cartesian coordinate system is determined as shown in Figure 5. The X and Y axes of world coordinate system $O-XYZ$ form a plane identical to

that of the floor. A waist coordinate system $O_W - X_W Y_W Z_W$ is established on the waist axis of the robot. With definition of the robot joint angles as shown in Figure 5, the relations between angles and velocities of the wheel angles and joint angles can be written as:

$$\phi_{w\_A} = \phi^*_{w\_A} + \theta_{hi} + \theta_{an} \qquad \phi_{w\_B} = \phi^*_{w\_B} + \theta_{hi} + \theta_{an} \tag{3.1}$$

$$\phi^*_{w\_B} = \phi^{**}_{w\_B} + \phi_{j\_A} + \phi_{j\_B} - \pi \qquad \omega^*_{w\_B} = \omega^{**}_{w\_B} + \omega_{j\_A} + \omega_{j\_B} \tag{3.2}$$

where, θ_{hi} and θ_{an} are the joint angles of hip and ankle joints, ϕ_{j_A}, ϕ_{j_B}, ω_{j_A} and ω_{j_B} are angles and velocities of joint A and B, ϕ_{w_A}, ϕ_{w_B} are angles of wheel A and B with respect to $O_W - X_W Y_W Z_W$, $\phi^*_{w\_A}$, $\phi^*_{w\_B}$, $\omega^*_{w\_A}$ and $\omega^*_{w\_B}$ are angles and velocities of wheel A and B with respect to the link DA, $\phi^{**}_{w\_B}, \omega^{**}_{w\_B}$ are angles and velocities of wheel B with respect to the link BC.

In general, differential gear has a characteristic on angular velocity as:

$$2\omega_{c\_A} = \omega_{out1\_A} + \omega_{out2\_A} \tag{3.3}$$

where $\omega_{c\_A}, \omega_{out1\_A}$ and ω_{out2_A} are the angular velocities of the carrier, output axes for the joint and the wheel of differential gear unit A. Same characteristic consists on differential gear unit B.

The relations between the angular velocities of motors and carriers can be written as:

$$\omega_{m\_A} = -\omega_{c\_A}\gamma_{bg} \qquad \omega_{m\_B} = \omega_{c\_B}\gamma_{bg} \tag{3.4}$$

where ω_{m_A} and ω_{m_B} are the angular velocities of the motor A and B, γ_{bg} is the gear ratio between motor and carrier.

Also, the relations between the angular velocities of joints, wheels and each output axes with respect to the link where differential gear unit is fixed can be written as:

$$\omega_{out1\_A} = -\gamma_{hj}\omega_{j\_A} \qquad \omega_{out2\_A} = -\gamma_{hw}\omega^*_{w\_A} \tag{3.5}$$

$$\omega_{out1\_B} = -\gamma_{hj}\gamma_{sg}\omega_{j\_B} \qquad \omega_{out2\_B} = -\gamma_{hw}\gamma_b\omega^{**}_{w\_B} \tag{3.6}$$

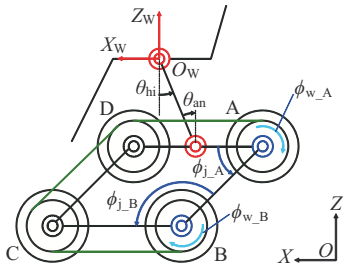

Figure 5. Kinematic model.

where γ_{hj} and γ_{hw} are gear ratio of Harmonic Drive gear for joint and wheel, γ_{b} and γ_{sg} are reduction ratio of the timing belt and spur gear of output axis.

From these, following relations are obtained.

$$2\omega_{\mathrm{m\_A}} = (\omega_{\mathrm{j\_A}}\gamma_{\mathrm{hj}} + \omega^{*}_{\mathrm{w\_A}}\gamma_{\mathrm{hw}})\gamma_{\mathrm{bg}} \quad 2\omega_{\mathrm{m\_B}} = -(\omega_{\mathrm{j\_B}}\gamma_{\mathrm{hj}}\gamma_{\mathrm{sg}} + \omega^{**}_{\mathrm{w\_B}}\gamma_{\mathrm{hw}}\gamma_{\mathrm{b}})\gamma_{\mathrm{bg}} \tag{3.7}$$

Here, by integrating Equation (3.7) with initial conditions as $\theta_{\mathrm{hi}} = \theta_{\mathrm{an}} = 0$, $\theta_{\mathrm{m\_A}} = \theta_{\mathrm{m\_B}} = 0$, $\phi_{\mathrm{j\_A}} = 0$, $\phi_{\mathrm{j\_B}} = \pi$, $\phi^{*}_{\mathrm{w\_A}} = \phi^{**}_{\mathrm{w\_B}} = 0$, relations between angles of joints, wheels and motors are obtained as follows:

$$\begin{aligned} 2\theta_{\mathrm{m\_A}} &= (\phi_{\mathrm{j\_A}}\gamma_{\mathrm{hj}} + \phi^{*}_{\mathrm{w\_A}}\gamma_{\mathrm{hw}})\gamma_{\mathrm{bg}} \\ 2\theta_{\mathrm{m\_B}} &= -\left((\phi_{\mathrm{j\_B}} - \pi)\gamma_{\mathrm{hj}}\gamma_{\mathrm{sg}} + \phi^{**}_{\mathrm{w\_B}}\gamma_{\mathrm{hw}}\gamma_{\mathrm{b}}\right)\gamma_{\mathrm{bg}} \end{aligned} \tag{3.8}$$

where $\theta_{\mathrm{m\_A}}$ and $\theta_{\mathrm{m\_B}}$ are the angles of motor A and B.

By transforming this to the waist coordinate system, following relations are obtained.

$$\begin{aligned} 2\theta_{\mathrm{mA}} &= (\phi_{\mathrm{jA}}\gamma_{\mathrm{hj}} + (\phi_{\mathrm{wA}} - \theta_{\mathrm{hi}} - \theta_{\mathrm{an}})\gamma_{\mathrm{hw}})\gamma_{\mathrm{bg}} \\ 2\theta_{\mathrm{mB}} &= -(\phi_{\mathrm{jB}} - \pi)\gamma_{\mathrm{hj}}\gamma_{\mathrm{sg}}\gamma_{\mathrm{bg}} - (\phi_{\mathrm{wB}} - \theta_{\mathrm{hi}} - \theta_{\mathrm{an}} - \phi_{\mathrm{jA}} - \phi_{\mathrm{jB}} + \pi)\gamma_{\mathrm{hw}}\gamma_{\mathrm{b}}\gamma_{\mathrm{bg}} \end{aligned} \tag{3.9}$$

Because the rotation angles of all wheels are synchronized with timing belt, following equation consists.

$$\phi_{\mathrm{w\_B}} = \phi_{\mathrm{w\_A}} \tag{3.10}$$

Furthermore, there are several different mechanical constraints according to its transformation modes shown in Figure 2.

In the Parallelogram mode, following consists.

$$\phi_{\mathrm{j\_A}} + \phi_{\mathrm{j\_B}} = \pi \tag{3.11}$$

In the Dogleg mode with bending joint A, following consists.

$$\phi_{\mathrm{j\_B}} = 0 \tag{3.12}$$

In the same mode with bending joint B, following consists.

$$\phi_{\mathrm{j\_A}} = 0 \tag{3.13}$$

In the Straightness mode as the singular point, constraint that the wheels cannot rotate with respect to the link by the brake can be added.

When the wheel B cannot rotate with respect to link BC, following consists from $\phi^{**}_{\mathrm{w\_B}} = 0$.

$$\phi_{\mathrm{w\_B}} = \phi_{\mathrm{j\_A}} + \phi_{\mathrm{j\_B}} + \theta_{\mathrm{hi}} + \theta_{\mathrm{an}} - \pi = \phi_{\mathrm{w\_A}} \tag{3.14}$$

On the other hand, when the wheel A cannot rotate with respect to link DA, following consists from $\phi^*_{\mathrm{w\_A}} = 0$.

$$\phi_{\mathrm{w\_A}} = \theta_{\mathrm{hi}} + \theta_{\mathrm{an}} \tag{3.15}$$

Inverse kinematics solutions in each transformation mode are shown below. Although not shown here because of space limitations, forward kinematics solutions can be solved by transforming following equations.

In Parallelogram mode, following inverse kinematics equations are obtained by Equation (3.9), (3.10) and (3.11).

$$\begin{aligned}\theta_{\mathrm{m\_A}} &= \frac{\gamma_{\mathrm{bg}}}{2}\left(\phi_{\mathrm{j\_A}}\gamma_{\mathrm{hj}} + (\phi_{\mathrm{w\_A}} - \theta_{\mathrm{hi}} - \theta_{\mathrm{an}})\gamma_{\mathrm{hw}}\right)\\ \theta_{\mathrm{m\_B}} &= \frac{\gamma_{\mathrm{bg}}}{2}\left(\phi_{\mathrm{j\_A}}\gamma_{\mathrm{hj}}\gamma_{\mathrm{sg}} - (\phi_{\mathrm{w\_A}} - \theta_{\mathrm{hi}} - \theta_{\mathrm{an}})\gamma_{\mathrm{hw}}\gamma_{\mathrm{b}}\right)\end{aligned} \tag{3.16}$$

In Dogleg mode with bending joint A, following equations are obtained from Equation (3.9), (3.10) and (3.12).

$$\begin{aligned}\theta_{\mathrm{m\_A}} &= \frac{\gamma_{\mathrm{bg}}}{2}\left(\phi_{\mathrm{j\_A}}\gamma_{\mathrm{hj}} + (\phi_{\mathrm{w\_A}} - \theta_{\mathrm{hi}} - \theta_{\mathrm{an}})\gamma_{\mathrm{hw}}\right)\\ \theta_{\mathrm{m\_B}} &= \frac{\gamma_{\mathrm{bg}}}{2}\left(\pi\gamma_{\mathrm{hj}}\gamma_{\mathrm{sg}} - (\phi_{\mathrm{w\_A}} - \theta_{\mathrm{hi}} - \theta_{\mathrm{an}} - \phi_{\mathrm{j\_A}} + \pi)\gamma_{\mathrm{hw}}\gamma_{\mathrm{b}}\right)\end{aligned} \tag{3.17}$$

In the same way, in this mode with bending joint B, following equations are obtained from Equation (3.9), (3.10) and (3.13).

$$\begin{aligned}\theta_{\mathrm{m\_A}} &= \frac{\gamma_{\mathrm{hw}}\gamma_{\mathrm{bg}}}{2}(\phi_{\mathrm{w\_A}} - \theta_{\mathrm{hi}} - \theta_{\mathrm{an}})\\ \theta_{\mathrm{m\_B}} &= -\frac{\gamma_{\mathrm{bg}}}{2}((\phi_{\mathrm{j\_B}} - \pi)\gamma_{\mathrm{hj}}\gamma_{\mathrm{sg}} + (\phi_{\mathrm{w\_A}} - \theta_{\mathrm{hi}} - \theta_{\mathrm{an}} - \phi_{\mathrm{j\_B}} + \pi)\gamma_{\mathrm{hw}}\gamma_{\mathrm{b}})\end{aligned} \tag{3.18}$$

By braking wheel A in Straightness mode, following equations are obtained from Equation (3.9), (3.10) and (3.14).

$$\begin{aligned}\theta_{\mathrm{m\_A}} &= \frac{\gamma_{\mathrm{bg}}}{2}((\phi_{\mathrm{w\_A}} - \phi_{\mathrm{j\_B}} - \theta_{\mathrm{hi}} - \theta_{\mathrm{an}} + \pi)\gamma_{\mathrm{hj}} + (\phi_{\mathrm{w\_A}} - \theta_{\mathrm{hi}} - \theta_{\mathrm{an}})\gamma_{\mathrm{hw}})\\ \theta_{\mathrm{m\_B}} &= -\frac{\gamma_{\mathrm{hj}}\gamma_{\mathrm{sg}}\gamma_{\mathrm{bg}}}{2}(\phi_{\mathrm{j\_B}} - \pi)\end{aligned} \tag{3.19}$$

In the same way, by braking wheel B, following equations are obtained from Equation (3.9), (3.10) and (3.15).

$$\begin{aligned}\theta_{\mathrm{m\_A}} &= \frac{\gamma_{\mathrm{hj}}\gamma_{\mathrm{bg}}}{2}\phi_{\mathrm{j\_A}}\\ \theta_{\mathrm{m\_B}} &= -\frac{\gamma_{\mathrm{bg}}}{2}\left((\phi_{\mathrm{j\_B}} - \pi)\gamma_{\mathrm{hj}}\gamma_{\mathrm{sg}} - (\phi_{\mathrm{j\_A}} + \phi_{\mathrm{j\_B}} - \pi)\gamma_{\mathrm{hw}}\gamma_{\mathrm{b}}\right)\end{aligned} \tag{3.20}$$

4 Conclusions and Future Work

In this paper, mobility aid technology for elderly and handicapped people which has "Minimally-invasiveness for historical environment" are described. With this goal, a novel multi-wheel stair climbing wheelchair with variable configuration four-bar linkage is proposed, and its mechanical design, principle of operation and kinematics are illustrated.

In the next report, its static characteristics, several experimental results and consideration will be reported. The studies on stabilization control method, evaluation of the invasiveness through experiments in the actual historical heritage environment and to clarify the problem for practical application are our future work.

Acknowledgment A part of this research was done as a sponsored research in Aoba Foundation for The Promotion of Engineering and supported partially by MEXT Grant-in-Aid for Young Scientists (B).

Bibliography

D. Davies et al. Continuous high-speed climbing control and leg mechanism for an eight-legged stair-climbing vehicle. *Proc. of the AIM2009*, pages 1606–1612, 2009.

A. Gonzalez et al. On the kinematic functionality of a four-bar based mechanism for guiding wheels in climbing steps and obstacles. *Mechanism and Machine Theory*, 44:1507–1523, 2009.

S. Hirose et al. Coupled drive of the multi-DOF robot. *Proc. of the ICRA 1989*, pages 1610–1616, 1989.

Independence Technology L.L.C. Independence iBOT 3000 mobility system, 2003. URL `http://www.independencenow.com/ibot/index.html`.

M. Miyagi et al. Development of stair climbing wheelchair with legs and wheel system (1st report). *J. of the JSPE*, 64(3):403–407, 1998. (in Japanese).

Top Chair SAS. The stair climbing wheelchair, 2003. URL `http://pagesperso-orange.fr/topchair/index_en.htm`.

J. P. Taylor. Authenticity and sincerity in tourism. *Annals of Tourism Res.*, 28(1):7–26, 2001.

Y. Uchida et al. Fundamental performance of 6 wheeled off-road vehicle "HELIOS-V". *Proc. of the ICRA 1999*, pages 2336–2341, 1999.

M. Vukobratović et al. On the stability of anthropomorphic system. *Mathematical Biosciences*, 15:1–37, 1972.

N. Yanagihara et al. Mechanicalanalysis of a stair-climbimg wheelchair using rotary cross arm with wheels. *Proc. of the 17th Annual Conf. of the RSJ*, 1999. (in Japanese).

Motion and Force measures on tortoises to design and control a biomimetic quadruped robot

Hadi EL DAOU*, Paul-Antoine LIBOUREL†, Sabine RENOUS†, Vincent BELS†, and Jean-Claude GUINOT*

* Universite Pierre et Marie Curie, Institut des Systemes Intelligents et de Robotique, 4 place Jussieu, 75252 Paris Cedex, France

† Museum National d'Histoire Naturelle, Rue Cuvier 57, 75231 Paris Cedex 5, France

Abstract This paper is concerned with locomotion systems modelling and control; in particular the locomotion of bio-mimetically inspired quadruped robots. Using observations and experimentations, we propose a virtual model of quadruped with no dorsal vertebrae, such as the case in the majority of legged mobile robots. This condition applies to the terrestrial tortoise and makes it a good example for bio-mimetic inspiration. Extensive experiments *in vivo* and *in vitro* are conducted to estimate the motion, the kinematics and the dynamic properties of two living subjects and a dead one. The experimental results are used to model, control and simulate the motion of a tortoise-like quadruped robot. The result is TATOR II, a successful example of robots mimicking the mechanical design and motion trajectories of animals; it is a linkage of 15 rigid bodies articulated by 22 degrees of freedom, it is built on the ADAMS-View platform and is shown to perform through animation with a motion controller. Analyses of the influence of the phase between legs on the robot speed are also presented. Conclusions and future Works are detailed.

1 Introduction

This study is achieved in the Institute of Intelligent Systems and Robotics (ISIR) with partnership with the UMR 7179 of the National Museum of Natural History in Paris. We expect that by studying the locomotion of living animals, we can find interesting parameters that could be used in mobile robotics and are invariant from specie to another. We also expect to create a model that helps to study the locomotion of current and extinct

species. Two animals are studied: the European hedgehog (J.Villanova, 2003), and the Hermann tortoise (B.Hennion, 2006). Two virtual models are built; a bi-dimensional model of the hedgehog and a 3D model of the Herman Tortoise called TATOR I. In this study, we will present a new and much precise methods for creating a bio-mimetic virtual quadruped robot inspired from terrestrial tortoises. This model is called TATOR II. The remaining of this paper is organized as follows: In section II we describe the experiments *in vivo* and *in vitro* performed on animals; in section III, we present the dynamic model TATOR II. Section IV highlights the contributions and the future perspectives. Figure 1 presents a basic summary of the study.

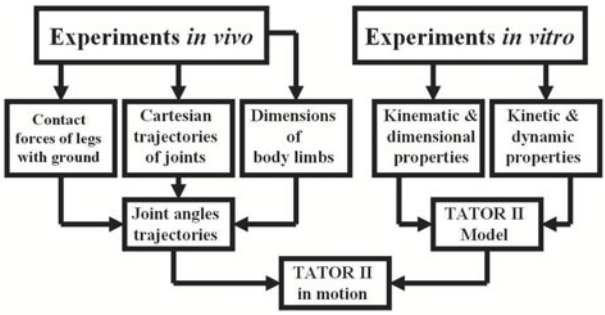

Figure 1. Basic summary of the study

2 Experiments on animals

We perform experiments on three adult tortoises. Two are alive (subject I and subject II) and the third (subject III) is dead for natural reasons (this subject has approximately the same inertial and dimensional properties of subject I). These experiments are divided into two categories: *in vivo* and *in vitro*. We use measures on subject III to create the virtual model TATOR II, while we use those on subject I to control it. We choose two different subjects to model and control TATOR II, because the dissection is forbidden on living subjects.

2.1 Experiments *in Vivo*

The experimental bench (Figure 2) used during these experiments is composed of: a video camera filming at 25 frames per second, an X-ray generator, a brightness amplifier, a digital camera filming at 50 frames per second and four piezoelectric force sensors mounted under four beams of

wood. All measures are synchronized and nine metallic markers are attached

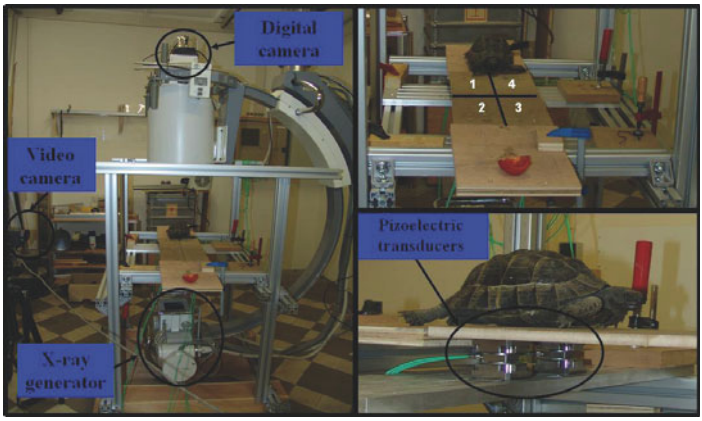

Figure 2. Experimental setup used to record the motion of studied subject in the dorsal and frontal plane and the contact forces of legs with the ground.

to subject I shell; these markers are used to measure the shell motion. Subject I in motion is filmed in the dorsal plane using cineradiography (Figure 3) and in the lateral plane using a video camera.

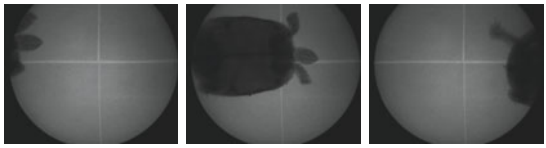

Figure 3. X-Rays video shoot of subject I in motion Top view

The used sensors measure only the three components of the contact force vector; we consider that the contacts are punctual. For economical reasons, we activate sensors 1, 2 and 3 (see Figure 2). Many trials are performed on subject I; in this paper we analyse the recording of sensor 3 for a given trial. However the logic is the same for sensor 1 and 2 outputs. The Figure 4 shows the recordings of sensor 3, three quantities are measured: the three components of the ground-reaction force on subject I right fore-limb, the sum of the three components of the ground-reaction force on subject I right limbs and the three coordinates of the ground reaction-force on subject I right hind-limb. From recording of sensor 3, we measure the ground-reaction forces on the right hind and fore limbs for more then a

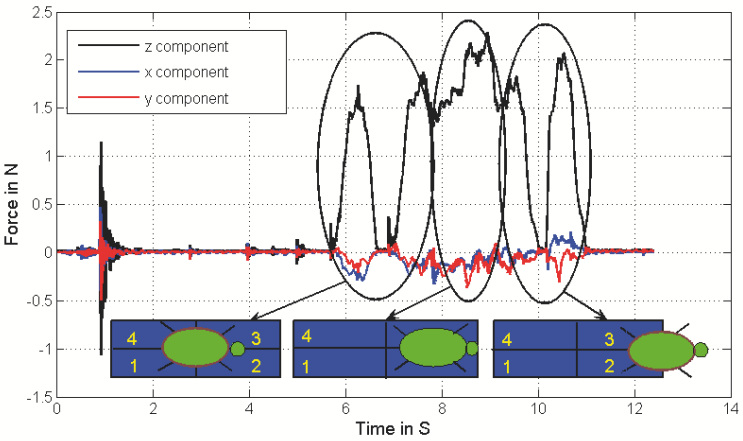

Figure 4. Recording of sensor 3 from a trial on subject I in motion.

locomotion cycle. We repeat the same analysis for the outputs of sensors 1 and 2. From these recordings we have measures of the ground-reaction forces on the left limbs for more then a locomotion cycle. In spite the use of three among four existing sensors, we have measures of the ground-reaction forces on each limb. The recording on subject I in motion shows that it uses its hind limbs to accelerate and the fore limbs to decelerate. This result is also observed when analysing ground-reaction forces on subject II limbs. An Important experimental result that should be investigated by performing experiments on more living specimens. Nevertheless, the x-ray films show that the shell-femur and the shell-scapula articulations are difficult to identify. An original method to solve this problem and to measure the length of internal limbs is detailed in ((DAOU, 2009)). The acquisition of the Cartesian coordinates of special points is done using a home made software developed using MATLAB.

2.2 Experiments *in Vitro*

These experiments are conducted on subject III to measure its inertial properties and to model its kinematics. We digitalize the shell, the markers, and the femur-shell and scapula-shell joints using a *Microscribe*. We dissect the tortoise and measure the weight of body limbs. We reconstruct the shell using Solidworks and we record its inertial properties. Due to the complex geometry and the small weight of other limbs, we can not apply

this approach to calculate the inertial properties of all limbs; the limbs are modelled using cylinders having the same weight and length (J.Villanova, 2003). The bones are digitalized using a special medical scanner. The kinematics of the tortoise is approximated by two kinds of joints: spherical and revolute (Figure 5). We use a mechanical method adapted to biology to define the axe of rotation of revolute joint between the bones i and i+1 (DAOU, 2009).

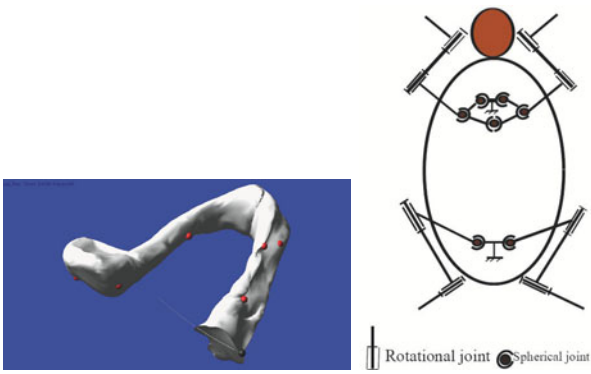

Figure 5. Reconstruted bones an markers; Functional diagram of the tortoise kinematics.

3 TATOR II Model

We use the collected data from the *in vitro* experiments to create a three-dimensional model of the tortoise. It is called TATOR II and built using the MSC ADAMS commercial software. It is a linkage of 15 rigid bodies articulated by 22 degree-of freedom; it imitates the mechanical design of subject III and it is controlled from experiments on subject I in motion. The model consists of the shell imported from Solidworks articulated to four legs. The friction and contact properties of the unilateral joint formed between the foot and the ground are modelled using the impact and coulomb friction modelling options in ADAMS. An experimental method is used to measure the static and dynamic coefficient of friction (B.Hennion and J-C.Guinot, 2005). Due to imprecision in Cartesian trajectories measures, a classical method to solve the inverse geometry problem is not possible. To solve this problem, we create two models of the left limbs using ADAMS platform (Figure 6). In both models the shell is created using the attached markers on subject I during the experiments *in vivo*.

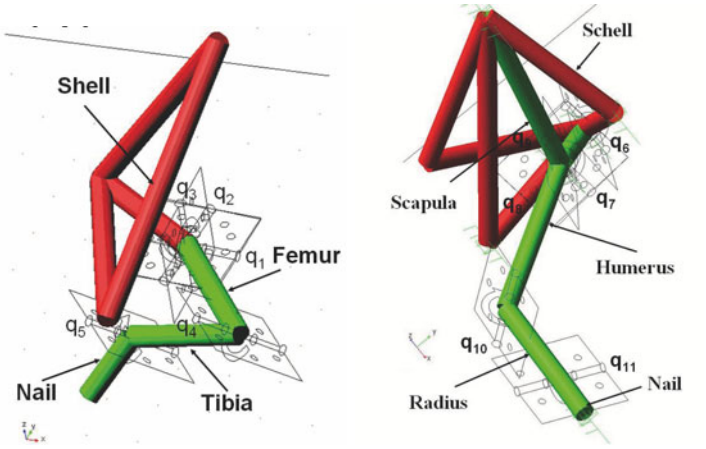

Figure 6. Models of the left limbs used to solve the inverse geometry problem;hind and fore limb.

We animate the markers, the intermediate bodies (black spheres in Figure 7) and the claw contact point with the ground using the Cartesian trajectories of particular anatomical points for a stance to stride movement of each limb measured during the experiments *in vivo*. We choose to use

Figure 7. Model of the left hind limb animated by the measured trajectories.

intermediate bodies because we can not track all measured Cartesians trajectories due to imprecision in measures. We record the joint angles and we interpolate it using Fourier series. We observe that two joint angles coordinate of the shell-scapula spherical joint articulation are related by a simple linear equation and the third joint angle q_8 is approximately constant (Figure 8). We use the interpolated joint angle to control TATOR II using a PD control law and we simulate its motion for the crawl posture(Figure 9). According to (R.M.ALEXANDER, 1984) and (S.RENOUS, 1994), the quadruped has eight gaits defined by the relative phase between the legs. We simulate the locomotion of TATOR II for these gaits and we record the distance travelled by the center of mass (Table 1).

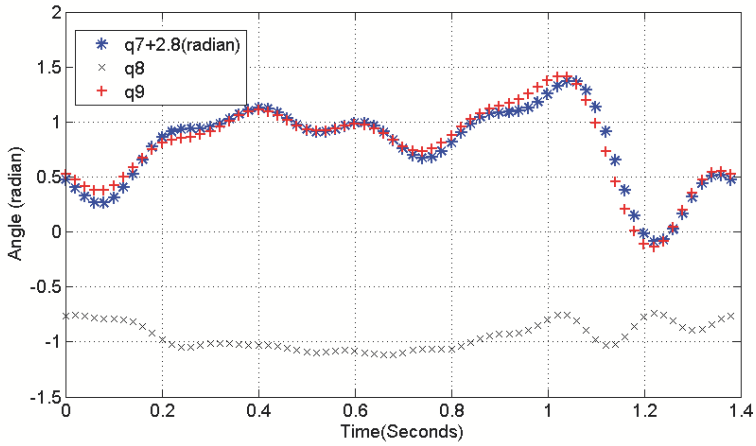

Figure 8. Joint angle q_8; Synergy between q_7 and q_9 two joint angles of the shell-scapula joint articulation

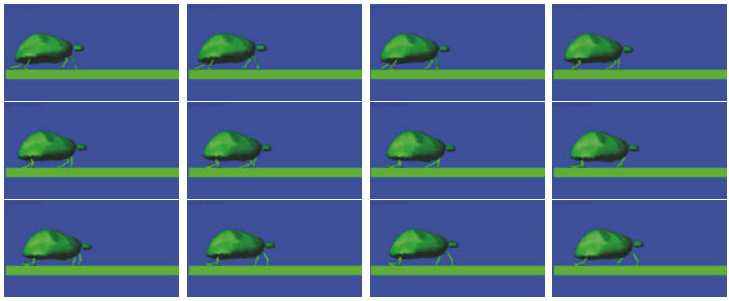

Figure 9. Sequence of a simulation video of TATOR II in crawl posture

Table 1. Distance travelled by the center of mass for the different gaits

Posture	Distance(mm)
crawl	45 mm
trot	62 mm
pace	50 mm
canter	63 mm
transverse gallop	51 mm
rotary gallop	58 mm
bound	43mm
pronk	8.2 mm

4 Conclusion

This paper presents new methods and protocols to create a virtual model of quadrupeds by performing experiments on real animals. Many contributions to the field of bio-mimetic and quadruped robot research are presented in particular:

- an approach to model the kinematics and estimate the motion of a physical terrestrial turtle;
- a new dynamic model of bio-mimetically inspired robot from real animal for simulation and Control;
- Significant experimental results on turtle locomotion and important new conclusions on gates and contact. In particular a synergy between joint angles and a resemblance in locomotion modes between the living subjects used during the experiments. In fact, during the experiences both subject use the hind limb to accelerate and the fore limb to create breaking forces. Experience on a larger number of specimens should be conducted to verify these results.
- A new experimental bench to measure the motion and the contact forces of moving tortoises.

Nevertheless, in this study we control our model by using a position control law; a future perspective is to control it using a hybrid force-position control law (J.Park and O.Khatib, Sept 2008) .

Bibliography

B.Hennion. *Une approche bio-inspiree de la locomotion quadrupede.* Universite Pierre et Marie CURIE, 2006.

J.Pill B.Hennion and J-C.Guinot. A biologically inspired model for quadruped locomotion. *8th Int. Conf on Climbing ad Walking Robots, United Kingdom*, 2005.

H.EL DAOU. *Une approche biomimetique pour la modelisation et la commande d'un quadrupede.* Universite Pierre et Marie CURIE, 2009.

J.Park and O.Khatib. Robot multiple contact control. *Robotica*, pages 667–677, Sept 2008.

J.Villanova. *Simulation dynamique de quadrupedes inspires d'animaux reels.* Universite Pierre et Marie CURIE, 2003.

R.M.ALEXANDER. The gaits of bipedal and quadrupedal animals. *International Journal of Robotics Research, 3(2)*, pages 49–59, 1984.

S.RENOUS. *Locomotion.* DUNOD, 1994.

Mechanism Design Improvements of the Airway Management Training System WKA-3

Y. Noh[a], K.Sato[a],A. Shimomura[a], M. Segawa[a] H. Ishii[b], J. Solis[bc], A. Takanishi[bc], K. Hatake[d]

[a] Graduate School of Advanced Science and Engineering, Waseda University, Tokyo, Japan
[b] Department of Modern Mechanical Engineering, Waseda University, Tokyo, Japan
[c] Department of Modern Mechanical Engineering and the Humanoid Robotics Institute (HRI), Waseda University, Tokyo, Japan
[d] Kyoto Kagaku Co. Ltd., Kyoto, Japan
E-mail: yohan@takanishi.mech.waseda.ac.jp

Abstract. This paper reports on the development of an Airway Management Training System. Airway management is a standard operation executed in emergency and operating rooms. However, medical accidents occur due to unskilled operations. In order to avoid accidents, medical doctors undergo to mannequin-based training. However, traditional training techniques do not provide quantitative information on the trainee's performance and are not capable to assess the trainee's performance based on the quantitative information. In this context, we proposed a novel airway management training system, dubbed WKA-3. This work presents both the electromechanical and the control sub-systems of the WKA-3. The results of preliminary experiments carried out by medical doctors to doctors to verify the training system are also provided.

1 Introduction

Airway management is a standard operation executed in emergency or operating rooms. However, medical accidents occur due to the unskilled operations. In order to avoid these accidents, medical doctors undergo to mannequin-based training (Satake et al. 1999). However, traditional training techniques *i)* fail to simulate the real conditions of the task, *ii)* do not provide quantitative information on trainee's performance and *iii)* do not assess the trainee's performance based on the collected quantitative information. In this context, using Robot Technology (RT), we would propose more efficient training system in the medical field. The advantage of using RT is that we could conceive advanced medical training systems designed to reproduce the conditions of the task and provide information of the task performance of the trainee.

In particular; in Solis et al., 2007, the concept of an active training system has been introduced based on robotic platforms. Such training system should fulfills at least three conditions: *i)* reproduce the real-world condition of the task, *ii)* provide objective assessments of the training progress, and *iii)* provide useful feedback to

trainees.

As a result; since 2004, we propose a *robotic patient* as a long-term project. The robotic patient is capable: to serve *i)* as an active training device and *ii)* as an advanced evaluation tool. In order to fulfill these two requirements, the robotic patient should *i)* be designed to emulate the human body (both anatomically and physiologically), *ii)* have sensors embedded into the simulator, *iii)* have actuators capable of reproducing the real conditions of the task, *iv)* provide feedback information to the trainee, and *v)* assess the trainee's performance objectively (Solis et al., 2007). For the purpose of these, we are proposing an innovative effective medical training system for the Airway management training.

In this paper, we propose the WKA-3, which provides quantitative information on the training progress and simulates the real conditions of the task. The WKA-3 features the same basic functionalities of the previous prototypes WKA-1R (Noh et al., 2008) and WKA-2 (Noh et al., 2009) but with improved performance both at the mechanical and at the control level. In this work, we present the electro-mechanical design and the control system of the WKA-3. The design of the WKA-3 is focused on integrating sensors and actuators into both the link drive mechanism and the wire drive mechanism. From a control point of view, the WKA-3 is capable to support both position control and *Virtual Compliance Control*. Finally, we provide the experimental results on the effectiveness of the WKA-3 using the feedback from medical doctors.

2 Design of the WKA-3

The WKA-3 consists of a standard medical mannequin integrated with sensors and actuators. The mannequin consists of six parts such head, neck, mandible, tongue, vocal cord and trachea, as reported in Figure 1. The WKA-3 features seven degrees of freedom (six active and one passive). Tongue and mandible actuation is achieved by three mechanisms integrated into the WKA-3, namely a link drive mechanism, wire drive mechanism and under-actuated mechanism. Both the wire drive mechanism and the under-actuated mechanism are driven by *Wire Drive Unit*. Airway management challenges, such as restricted mouth opening, restricted cervical range can be reproduced by synchronization of WKA-3 mandible and tongue motions. Force control strategies (based on torque and force sensor readouts) are adopted to reproduce the stiffness of the muscular system and to response to operator's forces. In order to register the quantitative information of operator's performance, several sensors were integrated in redesigned WKA components, such as incisor teeth, vocal cord and trachea.

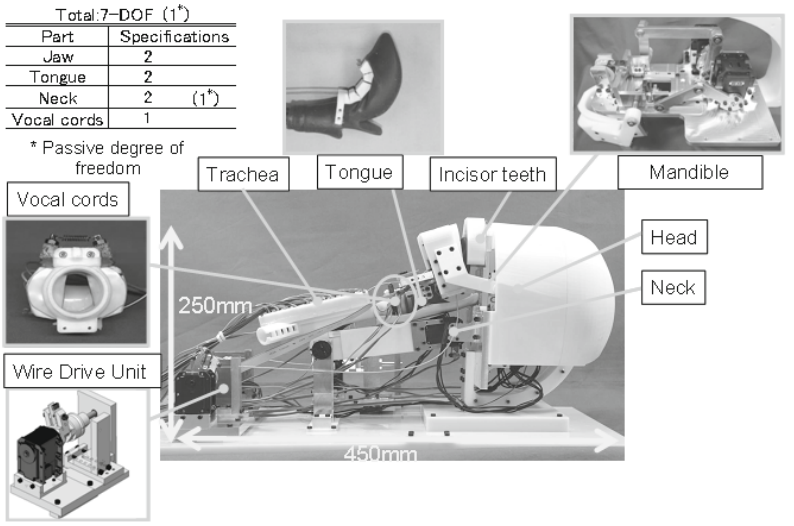

Figure 1. WKA-3 Waseda Kyotokagaku Airway management training system

2.1 Wire Drive Unit

To improve the efficiency of the torque transmission to the wire a novel design, named *Wire Drive Unit*, is proposed. The latter consists of a rotary stage, a force sensor, a wire tube and a pulley, as described in Fig. 1. The pulley and wire are connected through the wire tube, while the pulley and the rotary stage are assembled in order to measure the torque applied on the wire. These units can be controlled either via position or torque control.

2.2 Mandible

The mandible can be model via a 3-DOF (two rotational and one translational) system when simulating mouth opening motions (Ishihara et al., 1975). However, while performing the airway management, the motion can be simplified to a 2-DOF system. For this reason, we implemented a 2-DOF system (Figure 2), which represents the rotational motion (θ_{Jaw}) and the translational one ($d_{JawAxis}$). In order to control both rotational and translational motions of the mandible, we have attached a four-bar mechanism and crank mechanism to the actuators. For the $d_{JawAxis}$, both the four-bar and the crank mechanisms are driven. For the θ_{Jaw}, only the four-bar is driven. Upon solving the inverse kinematics, both θ_{JawRot} and $\theta_{JawTrans}$ angles can be computed, as shown in Eqs.1-4; θ_{JawRot} is the angle describing the rotation of the jaw; $\theta_{JawTrans}$ is the angle associated to the translation of the jaw. Force/torque sensors were embedded both in the four-bar and in the crank

mechanism.

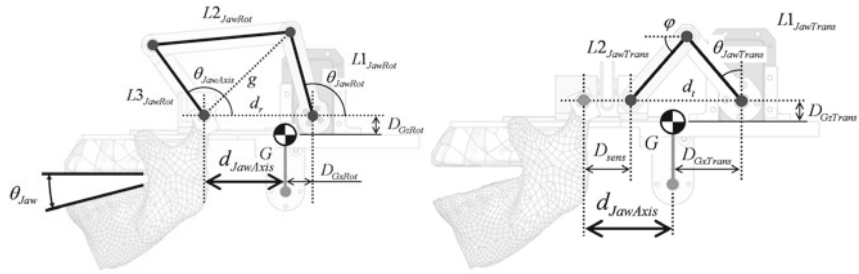

Figure 2. Operation of the mechanism of the mandible

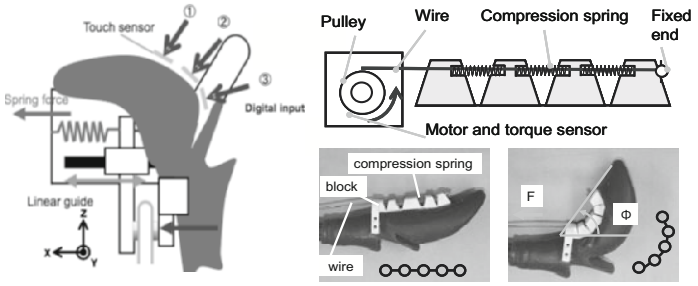

a) b)

Figure 3. Tongue mechanisms: a) linear guide mechanisms; b) under-actuated mechanism.

$$d_t = L1\sin\theta_{JawTrans} + \sqrt{L1^2\sin^2\theta_{JawTrans} - L1^2 + L2^2} \tag{1}$$

$$\theta_{JawTrans} = -\sin^{-1}((L2^2 - L1^2 - d_t^2)/(2\cdot L1\cdot d_t)) \tag{2}$$

$$g = \sqrt{d_r{}^2 + L3^2 - 2d_r\cdot L3\cdot\cos\theta_{JawAxis}} \tag{3}$$

$$\theta_{JawRot} = 180 - \cos^{-1}[\frac{d_r - L3\cos\theta_{JawAxis}}{g}] - \cos^{-1}[\frac{L1^2 + g^2 - L2^2}{2\cdot L1\cdot g}] \tag{4}$$

2.3 Tongue

We focused on two motions of the tongue, which are typical in airway management tasks. During unconsciousness, all the muscles are relaxed; as a result, the tongue falls down into the pharynx, thereby blocking the airway. This medical condition is named *tongue swallowing*. To treat this medical condition, the tongue needs to be lifted up in order to observe the vocal cords and insert a tube into the vocal cords to provide oxygen to the lungs. With reference to the tongue, we

simulate the translational motion and the shape change (Turkstra et al., 2007). This is achieved via a linear guide mechanism and an under-actuated mechanism. The linear guide mechanism, which consists of a linear guide, tensile spring and wires, reproduces the translational motion of the tongue (Figure 3). The under-actuated mechanism consists of blocks, wire, and compression spring. The foregoing blocks are disposed along an array. This array is in charge of changing the shape of tongue. The compression spring is responsible for restoring the original shape of the tongue upon applying tension via the wire. Each wire is connected to the *Wire Drive Unit*, thus allowing for position and force control.

3 Force and Position Control of the WKA-3

The muscular system is distributed over all the bones. When arms, legs and neck are moved, all the muscles associated with these elements undergo contraction or relaxation. In order to simulate the muscles, we implemented a virtual compliance control for the WKA-3. This control schemes adjusts the stiffness of the end-effector by modifying the v*irtual spring coefficient (K)* and the *virtual damper coefficient (C)*. The virtual compliance control is applied on each of the joints such as the neck, mandible, and tongue. A block diagram of the control system of the WKA-3 is shown in Fig. 4.

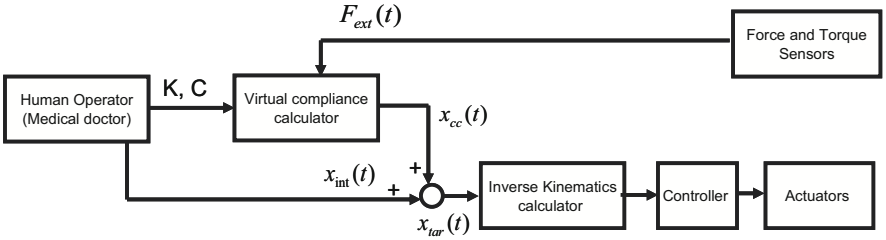

Figure 4. Block diagram of the control system of the WKA-3

The first step consists in selecting the patient's medical condition $x_{int}(t)$, such as restricted mouth opening, restricted cervical range, and shapes of the tongue. When this selection is made the WKA-3 reproduces the desired medical condition. As soon as an external force $F_{ext}(t)$ is applied on the mandible, the neck and the tongue, the WKA-3 computes the virtual compliance $x_{cc}(t)$ by adjusting *Virtual Spring Compliance Coefficient K* and *Virtual Damper Coefficient C* according to Eqs. 5-7. The controller compensates the virtual compliance so as to respect the selected medical condition. This attempts to simulate the stiffness of the actual muscles.

$$F_{ext}(t) = K \cdot x_{cc}(t) + C \cdot \dot{x}_{cc}(t) \tag{1}$$

$$\dot{x}_{cc}(t) = \frac{x_{cc}(t) + x_{cc}(t - \Delta T)}{\Delta T} \tag{2}$$

$$x_{cc}(t) = \left(K + \frac{C}{\Delta T} \right)^{-1} \left\{ F_{ext}(t) + \frac{C}{\Delta T} x_{cc}(t - \Delta T) \right\} \tag{3}$$

$$x_{tar}(t) = x_{cc}(t) + x_{\text{int}}(t) \tag{4}$$

4 Experimental results

Based on medical literature, we can define the distance between the minimum and maximum tongue-pharynx distance. Tongue swallowing condition feature a trivial distance 0 mm. Distance being different from zero and smaller than 20 mm is associated to a certain degree of the consciousness (Turkstra et al., 2007). Tongue swallowing condition can be reproduced using the WKA-3 as shown in Fig. 5a. *Protrusion* is the medical condition where the upper jaw protrudes from the mandible; the maximum value of the protrusion is 18.7 mm. *Retrusion* defines, instead, the mandible retruding from the upper jaw; the maximum value of the retrusion is 7.4 mm. The protrusion (retrusion) can be reproduced using the WKA-3 from a distance of 0 mm up to a distance of 22mm (-15mm), as shown in Fig. 5b.

On the other hand, several medical conditions, such as restricted cervical range, restricted mouth opening and responses to specific external forces can be reproduced by adjusting the virtual compliance coefficients, such as spring and damper characteristics. Restricted mouth opening takes place when the distance between the incisor teeth of the upper jaw and the mandible is less than 30-40 mm (American Society of Anesthesiologists, 2003). By setting the compliance coefficients to high (low), WKA-3 can reproduce normal (restricted) mouth opening, as it is shown in Figure 5c. WKA-3 can reproduce normal (restricted) cervical range (Greenland et al., 2008), by setting the compliance coefficients to high (low), as it is shown in Fig. 5d. Finally, the WKA-3 can also simulate the stiffness of the tongue by adjusting the compliance coefficients, as depicted in Fig. 5e.

Finally, in order to verify the WKA-3 system, the system was tested by medical doctors (MDs) and a survey was conducted aimed at gathering the feedback from the MDs. Eight MDs participated to the experiments. For each of the medical conditions reproduced by the WKA-3, MDs touched and operated the airway management system in order to make an assessment. The results are summarized in Fig. 6. According to the MDs, the reproduction of protrusion, retrusion, and restricted cervical range is acceptable. However, the tongue swallowing and the restricted mouth opening need major revisions.

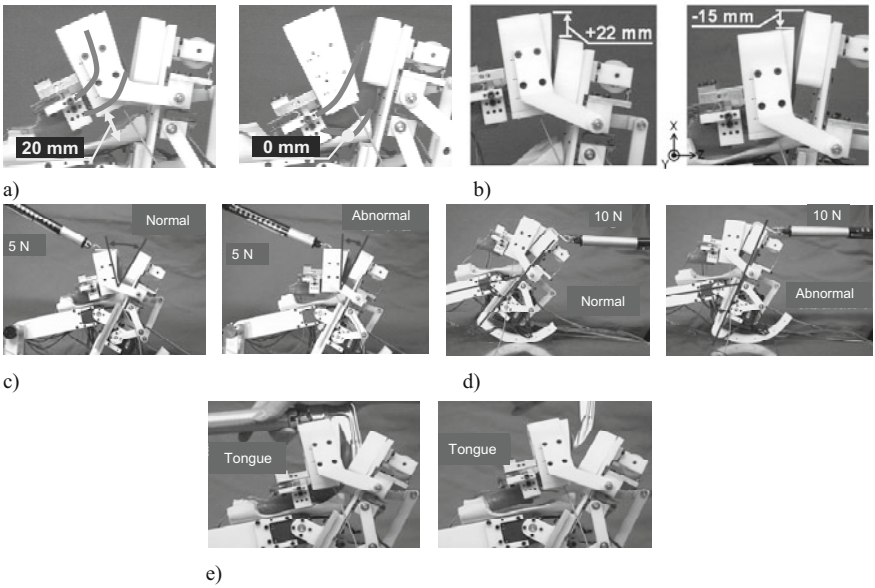

Figure 5. Airway-related medical conditions reproduced using the WKA-3: a) normal tongue position (left) tongue swallowing (right); b) protrusion (left) retrusion (right); c) normal mouth opening (left) restricted mouth opening (right); d) normal cervical range (left) restricted cervical range (right); e) tongue response to external forces applied by a laryngoscope.

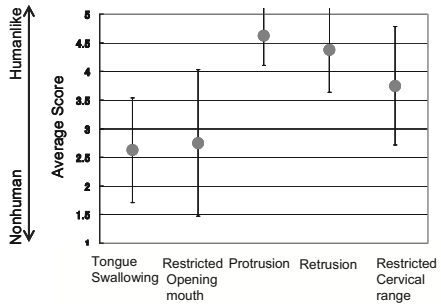

Figure 6. Results of medical doctor feedback on the WKA-3 system.

5 Conclusions & Future Work

In this paper, we have presented the detailed design of the Waseda-KyotoKagaku Airway No. 3 (WKA-3) system. The improvements with respect to previous designs are the easiness of maintenance, the mechanism compliance, and the

reduction of actuators. A set of experiments was conducted to assess the performance of the WKA-3. The *Virtual Compliance Control* was tested for each of the following test cases: normal mouth opening restricted mouth opening restricted cervical range and tongue lift-up. Finally, a survey, aimed at verifying the medical performance, was conducted among eight medical doctors.

As a future work, we will focus on additional experiments aimed at validating the *Virtual Compliance Control*. Moreover, the design mechanism to control the shape of the artificial tongue will be proposed.

Acknowledgment

The authors would like to express gratitude to G-COE Global Robot Academia, Waseda University. Finally, we would like to thank the doctors from the Department of Anesthesiology at the Tokyo Women's Medical University and the Otsuka Hospital for their valuable time.

Bibliography

Satake, J.(1999), Is it possible to prevent medical accidents? Practice of activity in the nursing care safety measure committee. Starting at analysis of near-miss cases, *in Japanese Journal of Nursing Administration, vol. 9(8), pp.599-602.*

Solis, J., Marcheshi, S., Frisoli, A., Avizzano, C.A., Bergamasco, M. (2007), Reactive Robots System: An active human/robot interaction for transferring skills from robot to unskilled persons, *Advanced Robotics Journal, vol. 21(3/4), pp. 267-291.*

Noh, Y., Segawa, M., Shimomura, A., Ishii, H., Solis, J., Hatake, K., Takanishi, A. (2008), Development of the Evaluation System for the Airway Management Training System WKA-1R, *in Proc. of Int. Conference on Biomedical Robotics and Biomechatronics, Tokyo, Japan, pp. 574-579.*

Noh, Y., Segawa, M., Shimomura, A., Ishii, H., Solis, J., Takanishi, A., Hatake, K. (2009), Development of the Airway Management Training System WKA-2 Designed to Reproduce Different Cases of Difficult Airway, in Proc. of Int. Conference on Robotics and Automation, Kobe, Japan, pp. 3833-3838.

Ishihara T, Hasegawa S, AI M. (1975), Mandibular Movement and Articulators (in Japanese). *Tokyo, Japan,. HYORON, p 103.*

Turkstra TP, Pelz DM, Shaikh AA, Craen RA. (2007), Cervical spine motion: a fluoroscopic comparison of Shikani Optical Stylet vs Macintosh laryngoscope, *Can J Anaesth. Jun;54(6):441-7.*

Greenland KB. (2008), The sniffing and extension-extension position: the need to develop the clinical relevance, *Anaesthesia; 63(9):1013-4.*

American Society of Anesthesiologists, Inc. Lippincott Williams & Wilkins, Inc. (2003), Management of the Difficult Airway Practice Guidelines for Management of the Difficult Airway- An Updated Report by the American Society of Anesthesiologists Task Force on Management of the Difficult Airway- *Anesthesiology; 98(5):1269–77*

Design for a Dual-Arm Space Robot

Hui Li, Qiang Huang, Que Dong, Chen Li, Yu He, Zhihong Jiang, Yue Li, Peng Lv, Lin Xie, Xiaopeng Chen, and Kejie Li*

Intelligent Robotics Institute, School of Mechatronical Engineering, Beijing Institute of Technology, Beijing, China

Abstract With the development of space technology, plenty of work for space assembly and maintenance should be carried out. However, these tasks are dangerous and high cost for astronauts. It is necessary to develop a space robot to complete these dangerous space operations. In this paper, we present a method of the design of dual-arm space robot, including the mechanism, integrative joint, vision system and vision-based climbing trajectory plan. Finally, the joint control performance experiment is provided.

1 Introduction

The environment outside of the space station is very dangerous, but with the increase of space activities, as well as the need for scientific research, astronauts will engage in more and more work outside the space station, and astronauts have to accomplish many fine extravehicular operations, while the ordinary manipulator-type robots are unable to meet this need. Therefore, a new kind of robot has to be developed.

Robonaut is a humanoid robot designed by the Robotic Systems Technology Branch at NASA's Johnson Space Center in a collaborative effort with DARPA (Bluethmann et al. (2003)). Robonaut can reduce the burden of extravehicular activity and planetary exploration on astronauts and also serve in rapid response capacities (Lovchik et al. (1999)).

We are developing a space climbing robot. The robot is composed of head, trunk, and two arms, and is expected to replace the astronauts to do

* his work was supported by Basic Scientific Research (Grand No. A2220080252), National Science Foundation for Distinguished Young Scholar under (60925014), "111 Project" (Grant No. B08043), and the National High Technology Research of China (863 Project) (Grant No.2009AA04Z207). Corresponding Author: Zhihong Jiang, Email: jiangzhihong@bit.edu.cn.

the extravehicular activity such as space station maintenance and construction. The space climbing robot equips with high-cohesion integrative joint which is specially designed for the space robot.

2 Description of Robot System

To conduct earthbound research on robotic applications for outer space environments, compensation for the gravitational field must be considered. Several schemes have been employed to compensate for the earth's gravity (White and Xu (1993)). The underwater experiment is the most widely used, but it is expensive, and sealing requirements for the robot is very high. Therefore, in our system, the dual-arm space robot is suspended by passive mechanism to simulate the weightless environment.

The experiment system of Dual-arm space robot is composed of dual-arm space robot, passive mechanism, climbing rods and support mechanism. The dual-arm space robot system is shown in Figure 1.

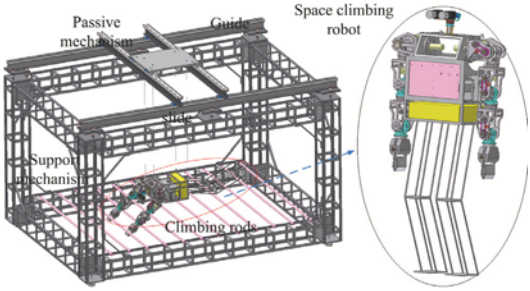

Figure 1. The dual-arm space robot system.

The position of the climbing rod can be calculated by the binocular stereo vision system. With the guidance of the vision system, the hand of robot can grab the climbing rod, the two hands of the robot alternately grab the climbing rod, and the robot moves about in the horizontal plane.

Till now the main control architectures used for robots can be summarized as centralized control architecture and distributed control architecture (Yu et al. (2007), Sakagami and Watanabe (1999)).The distributed control architecture is adopted in the control system for dual-arm space robot, the control system consists of industrial computer and joint-controller, and computer and joint controller are connected by CAN bus. RT-Linux is operating system of the industry computer to meet the real-time and deadline requirements.

Based on position of the climbing rod calculated by vision system, and the joint position of arm, the industrial PC plans the next time position of each joint on next moment, and transmitted the joint positions to the corresponding joint controllers by CAN bus, the joint controllers control all joints to reach their desired position, and realize the task of climbing. The control system of dual-arm space robot is shown in Figure 2.

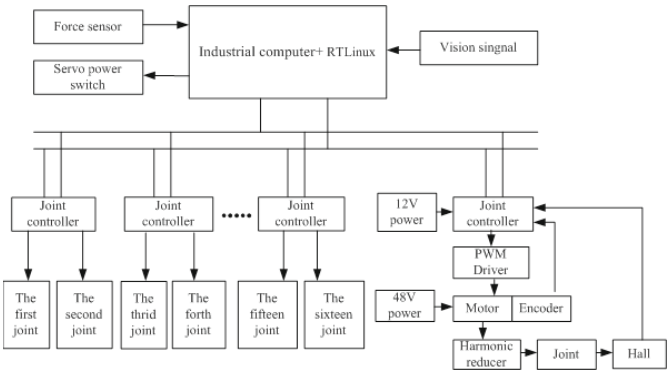

Figure 2. The control system of dual-arm space robot.

3 Mechanism of Dual-Arm Space Robot

Dual-arm space robot is composed of head, two arms and trunk. It has sixteen degrees of freedom. The head has two degrees of freedom, each arm has six degrees of freedom, and every hand has one degree of freedom.

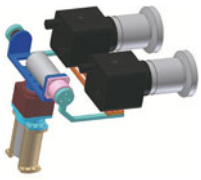

Figure 3. robot head.

Figure 4. robot arm.

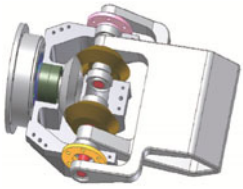

Figure 5. robot hand.

3.1 Mechanism of the Head

In order to ensure vision system can observe all the position, and accurately calculate any target in front of the robot, the head of dual-arm space

robot has two degrees of freedom. The transmission mode of head uses the combination of PMSM and harmonic reducer, which ensures the cameras can accurately move to desired position. The head is shown in Figure 3.

3.2 Mechanism of the Arm

In order to get enough dexterous workspace and reachable workspace, the arm of the robot has six degrees of freedom, which can guarantee the arm to reach the target in any pose in the dexterous workspace of the arm and to realize the climbing task. The axes of the dual-arm space robot arms joints are parallel or intersect at one point to ensure the robot arm has analytic inverse kinematic and simple trajectory planning. The arm is shown in Figure 4.

3.3 Mechanism of the Hand

In order to ensure the hand can grab the climbing rod firmly, and the hand is of low cost and easy to control, the robot hand has one degree of freedom, and the hand can open and close. The hand is shown in Figure 5.

3.4 Design of High-Cohesion Integrative Joint

In order to obtain large output torque, good heat dissipation performance, good speed control performance, and reliable position detection, a kind of integrative joint is designed for space robot. The integrative joint selects the permanent magnet synchronous motor and harmonic reducer as driving mode, and the resolver as position detection device.

In the design process, according to the integrative joint's performance requirement, all the components of the joint are synchronously planned and designed from a whole perspective; all the components achieve exactly match in structure and performance; the joint eliminates redundant installation surfaces and mechanical structures, so the joint realizes high-cohesion.

As shown in Figure 6, the integrative joint includes two shaft systems: joint shaft system and the motor shaft system, and the two shaft systems are installed on the same shaft. Driving joint, driven joint and joint bears compose the integrative joint shaft system. Joint shaft system is driven by harmonic reducer. Rigid wheel of harmonic reducer is installed at driving joint, flexible wheel of harmonic reducer is installed at driven joint. The stator of the permanent magnet synchronous motor is installed at driving joint. One stator of resolvers is installed at driving joint, and the other is installed at driven joint. Motor shaft system includes motor, motor shaft and motor bears. Motor rotor, the harmonic generator of the harmonic

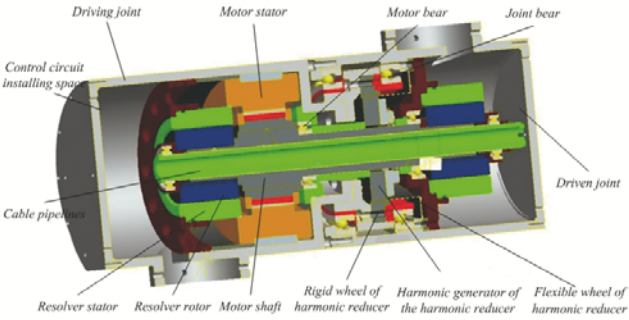

Figure 6. Mechanism of integrative joint.

reducer and the two rotors of the resolvers are all installed at motor shaft.

4 Vision-Based Climbing Plan

4.1 Vision Processing System

The three-dimensional measuring system of the robot includes binocular cameras and visual processing circuit. The structure of visual processing circuit is shown in Figure 7.

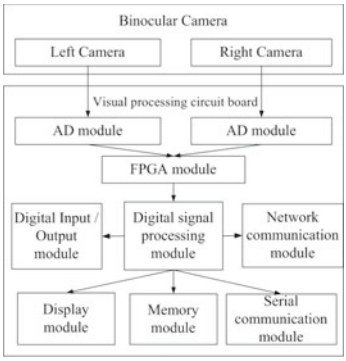

Figure 7. The structure of visual processing circuit.

The process that visual system gets the three-dimensional coordinates of the climbing rod is as follows.

1. The intrinsic parameters of camera can be obtained by the monocular calibration of the left camera and right camera. The extrinsic parameters

describing the relative position of two cameras can be obtained through the binocular calibration;

2. FPGA module filters the digital image;

3. According to the left and right camera matrix, by the three-dimensional measurement of binocular vision algorithms, the digital signal processing module obtains the image's feature points of the two images from the filtered digital image. The target's coordinate in the real world coordinate can be got from the optimal corresponding points of left and right images by the matching algorithm. Then the three-dimensional coordinate of the climbing rod is got.

4.2 Climbing Trajectory Plan

Climbing trajectory planning of the dual-arm space robot is divided into the following steps.

1. Robot arms stop at the initial position, the vision system calculates the position of climbing rod, and robot puts out the first hand to grab rod.

2. The first hand of robot grabs the climbing rod, and then this arm bends to make the robot move in horizontal plane.

3. The visual system calculates the position of the next climbing rod, and the second hand of robot puts out to grab the next climbing rod.

4. The first hand of robot opens and releases the climbing rod, and this arm returns to the initial position. The second arm bends to make the robot move in horizontal plane.

Dual-ram space robot is able to move in the horizontal plane by continuous implementing the cycle of the above four steps.

4.3 Force Control of Hand

Because vision system has error, only the position control can't guarantee the hand to grab the climbing rod firmly. Therefore, force control should be used for robot hand. In order to reduce the size and the cost of robot hands, force sensor is not installed on robot hand. Robot hand uses DC servo motor, the motor torque is expressed as

$$T = k_m i \tag{1}$$

Where i is the armature circuit current; T is the output torque of the motor; k_m is the motor torque constant.

From Eq.(1), we can control the motor torque T by controlling armature current i. The motor torque for firmly grabbing the climbing rod is T_e, according to Eq.(1), we can calculate the corresponding armature current i_e. A current limiting module is added in front of the current loop, the maxi-

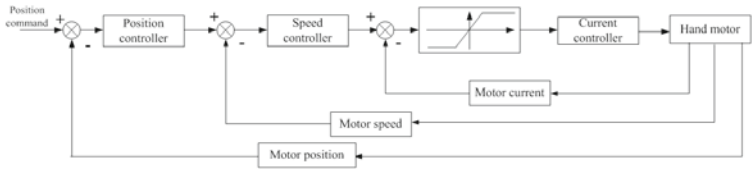

Figure 8. The control diagram of robot hand motor.

mum armature current of the motor is limited to i_e, and the corresponding maximum torque is limited to T_e. Therefore, the hand of the robot grabs the climbing rod firmly without force sensor. The control diagram of the robot hand motor is shown in Figure 8.

5 Experiment

The control system of integrative joint, as shown in Figure 9, is composed of control circuit, motor drive circuit and resolver decoding circuit.

Figure 9. Control and drive circuit of integrative joint.

We use PID control method to carry out the joint control performance experiment. The curves of reference and feedback were shown in Figure 10, and it can be seen the output trajectory of joint can accurately track the desired trajectory. The curve of tracking error was shown in Figure 11, and the steady-state tracking error is only about 0.01°.

6 Conclusion

This paper explores to design dual-arm space robot to replace the astronauts to do the extravehicular activity such as space station maintenance and construction. The main results are as follows: 1) we design a dual-arm

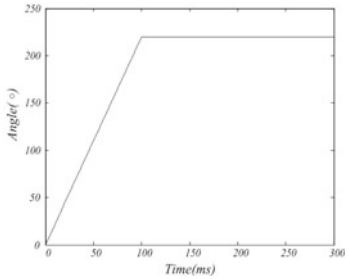

Figure 10. Output trajectory of the joint.

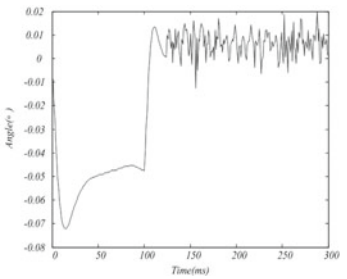

Figure 11. The position control error of the joint.

space robot system, and the robot can climb about in the horizontal plane. 2) We design an integrative joint which has large output torque, good heat dissipation performance, good speed control performance, and reliable position detection 3) We construct a vision system. By the vision system, the three-dimensional coordinate of the climbing rod can be got. 4) We present a vision-based climbing trajectory plan. 5) We do experiments on the control performance of integrative joint.

Bibliography

W. Bluethmann, R. Ambrose, R. Diftler, S. Askew, E. Huber, M. Goza, F. Rehnmark, C. Lovchik, and D.Magruder. Robonaut: A robot designed to work with humans in space. *Autonomous Robots*, 14:179–198, 2003.

C. Lovchik, H. Aldridge, and M. Diftler. Design of the nasa robonaut hand. In *Proceeding of ASME Dynamics and Control Division*, pages 813–830, 1999.

Y. Sakagami and R. Watanabe. The intelligent asimo: System overview and integration robots and system. In *IEEE/RSJ Int. Conf. on Intelligent Robots and System*, pages 813–830, 1999.

Gregory C. White and Yangsheng Xu. An active z gravity compensation system. In *Proceedings of the 1993 IEEE/RSJ International Conference on Intelligent Robots and Systems*, pages 1181–1187, 1993.

Zhangguo Yu, Qiang Huang, Jianxi Li, Wenmin Zhang, and Xuechao Chen. Distributed control system for a humanoid robot. In *proceedings of IEEE International Conference on Mechatronics and Automation*, pages 1166–1171, 2007.

Mechanical Design of a Novel Biped Climbing and Walking Robot

Giorgio Figliolini, Pierluigi Rea and Marco Conte

DiMSAT, University of Cassino, Italy

Abstract. The present paper deals with the mechanical design of a novel biped climbing and walking robot, which is provided of a 2 (3-RPS) leg mechanism with 6 d.o.f.s. and which makes use of suction-cups for climbing on flat and rigid vertical surfaces. The serial-parallel kinematic structure of each leg mechanism, along with the climbing and walking motions of the proposed biped robot, are analyzed.

1 Introduction

In the last years, the mechatronic design of a low-cost biped robot was carried out in Cassino and several prototypes of the EP-WAR (Electro-Pneumatic-Walking-Robot) were designed, built and tested since 1995, as reported in (Figliolini and Ceccarelli, 1997; 1999; 2004). In particular, the last prototype, named EP-WAR3, was provided of a binary pneumatic actuation in order to be controlled in on/off environment by a PLC (Programmable-Logic-Controller) and good performances were obtained to walk along a straight line, turn right and left, climb and descend stairs. The equilibrium of the EP-WAR prototypes was obtained by means of two suction-cups, which were installed on the underside of each foot. Later, the attention was focused on the gait analysis and mechanical design of six-legged walking robots, as shown in (Figliolini and Rea, 2007; Figliolini et al., 2009). Currently, the mechatronic design of a novel biped climbing and walking robot is in progress at the University of Cassino. Several prototypes of walking and climbing robots were designed, built and tested around the world, but only some of these have inspired the current research project. In fact, the most significant and pertinent prototypes are described in (Nishi, 1992; Hirose and Kawabe, 1998; Bahr et al., 1996; Minor and Mukherjee, 2003; Balaguer et al., 2005). In particular, referring to (Nishi, 1992; Hirose and Kawabe, 1998), a biped robot capable of moving on wall surfaces with irregular shapes and the quadruped robot NINJA, were developed in Japan at the Miyazaki University and Tokyo Institute of Technology, respectively. Similarly, a quadruped climbing robot for the aircraft maintenance, named ROSTAM, was developed at Wichita State University (U.S.A.), before to design a new light-weight biped robot, as reported in (Bahr et al., 1996). Two biped designs for miniature climbing robots were proposed in (Minor

and Mukherjee, 2003), as based on under-actuated kinematic structures. Finally, an interesting overview on the main features of non-conventional climbing robots mobility on complex 3D environments is reported in (Balaguer et al., 2005).
Therefore, at moment, our attention has been focused on the overall mechanical design of a novel biped climbing and walking robot, which is provided of a 2 (3-RPS) leg mechanism with 6 d.o.f.s. and which makes use of suction-cups for climbing on flat and rigid vertical surfaces. The type and dimensional synthesis of the serial-parallel kinematic structure of each leg mechanism, along with the climbing and walking motion analysis, are presented in this paper by referring to (Kim and Tsai, 2003; Mattiazzo et al., 2005; Lukanin, 2005; Di Gregorio and Parenti-Castelli, 2006) and as first step of the current research project.

2 The 2 (3-RPS) Leg Mechanism

The idea of the proposed 2 (3-RPS) leg mechanism comes from the design specifications, which are aimed to obtain wide workspace and good mobility, high rotation and stiffness, along with a good integration of the linear actuators in the overall kinematic structure. In particular, the foot is represented by the second moving platform of the serial-parallel kinematic structure, which can be rotated up to 90° with respect to the robot body, as required to climb vertical walls by starting from an horizontal walking. Referring to Fig.1, the proposed leg mechanism shows 6 d.o.f.s since composed by two modules of 3-RPS (Revolute-Prismatic-Spherical) parallel mechanisms, which are connected in series from the robot body to the foot. Each 3-RPS parallel mechanism shows 3 d.o.f.s of the moving platform with respect to the reference platform, *i.e.* one translation along the normal (*Z*-axis) to the reference platform and two rotations across the *X* and *Y* axes of the *O X Y Z* fixed frame. In particular, referring to the kinematic sketch of Fig. 1a, each 3-RPS parallel mechanism is composed by a moving platform, which is connected to the fixed platform through 3-RPS legs.

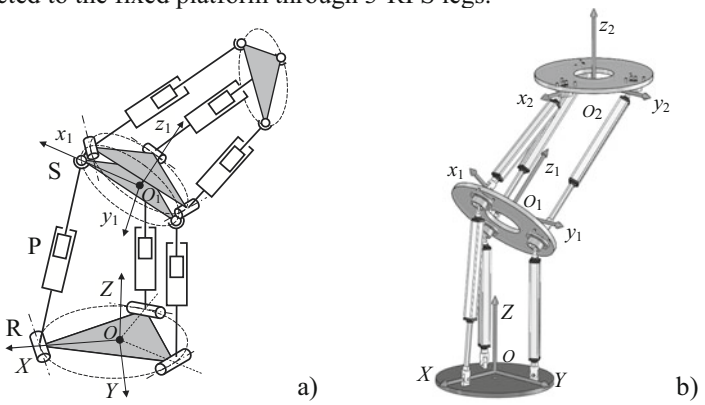

Figure 1. The proposed 2 (3-RPS) leg mechanism: a) kinematic sketch; b) 3D model.

Each of these legs is composed by a prismatic pair P, which is connected to the moving platform through a spherical joint S and to the fixed platform through a revolute joint R. These R and S joints are installed on the fixed and moving platforms at 120° among them in the order to allow only the radial rotation of each RPS leg. Figure 1b shows a 3-D view of the proposed leg mechanism, where the foot is parallel to the platform of the robot body.

Therefore, the proposed 2 (3-RPS) leg mechanism has been assembled in order to have the equilateral triangle among the three spherical joints S of the upper 3-RPS parallel mechanism in opposite position with respect to the antagonist leg mechanism. In particular, Figs. 2a and 2b show the leg mechanism configurations to perform the long and short steps, with step sizes p_1 and p_2, respectively. Figure 2c shows the starting configuration to climb a vertical wall, before to in stroke completely the left leg to perform the next climbing step, as shown in Fig. 2d.

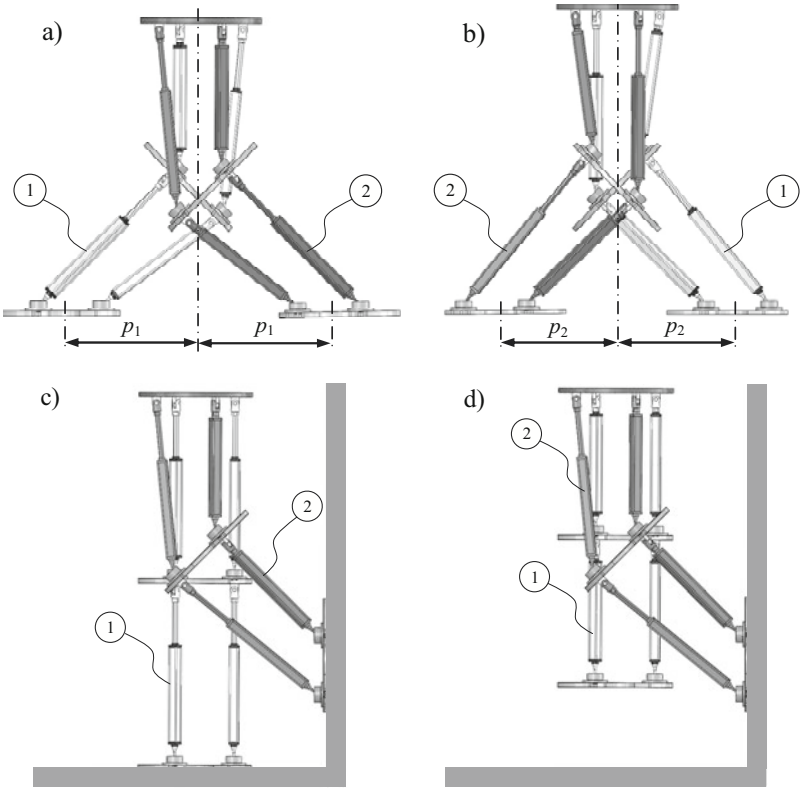

Figure 2. Starting configurations of both 2 (3-RPS) leg mechanisms (left and right legs are indicated with 1 and 2, respectively): a) long step with step size p_1; b) short step with step size p_2; c) vertical wall climbing; d) first configuration on the vertical wall.

3 The 3-RPS Parallel Mechanism: Kinematic Synthesis

The kinematic synthesis of one-module of the proposed 2 (3-RPS) leg mechanism has been formulated by referring to the kinematic sketches of Fig. 3, where Figs. 3a and 3b show the top and front views of one 3-RPS parallel mechanism for the maximum clockwise and counter-clockwise rotations, β_M and γ_M, respectively, of the moving platform (link *AB*).

Figure 3a shows the case for which the linear actuator that is represented through the link *CB*, moves outstroke to perform the maximum clockwise rotation β_M of the link *AB*. Similarly, Fig. 3b shows the case for which the two linear actuators that are represented through the link *DA*, move outstroke to perform the maximum counter-clockwise rotation γ_M of the link *AB*. The proposed algorithm has been formulated as function of the following design parameters, the side size *L* of the equilateral triangle made by the three R joints and the lenght l_0 of the fully instroke RPS leg, while α is equal to 60°. The input data are *L*, l_0 and α = 60°, while the main design specification is β_M = 45°. Thus, referring to Fig. 3a, one has

$$d = L\cos(\alpha/2) \ , \tag{1}$$

$$x_{B'} = d\left(1-\cos\beta_M\right) \quad \text{and} \quad y_{B'} = d\sin\beta_M \ , \tag{2}$$

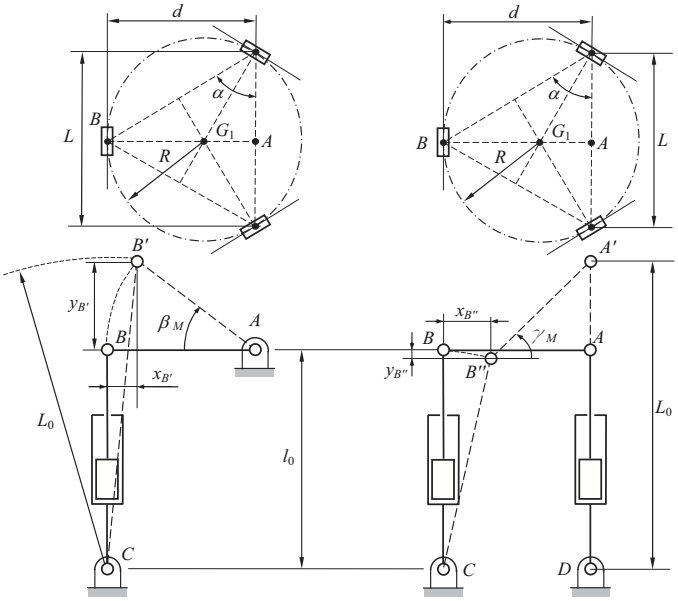

Figure 3. Kinematic sketches of one-module for two configurations: a) max clockwise rotation through β_M of *AB*; b) max counter-clockwise rotation through γ_M of *AB*.

which give

$$L_0 = \sqrt{x_{B'}{}^2 + \left(l_0 + y_{B'}\right)^2} \qquad \text{and} \qquad s = L_0 - l_0\,, \tag{3}$$

where s is the stroke of the linear actuator of link CB. Likewise, referring to Fig. 3b, one has

$$x_{B''} = d\left(1 - \cos\gamma_M\right) \qquad \text{and} \qquad y_{B''} = l_0 - L_0 + d\sin\gamma_M\,, \tag{4}$$

which give

$$l_0 = \sqrt{\left(l_0 - y_{B''}\right)^2 + x_{B''}^2}\,. \tag{5}$$

Thus, substituting the Eqs. (4) in Eq. (5) and developing, it yields

$$2L_0\sin\gamma_M + 2d^2\cos\gamma_M + l_0^2 - L_0^2 - 2d^2 = 0 \tag{6}$$

that for

$$\sin\gamma_M = \frac{2t}{1+t^2} \qquad \text{and} \qquad \cos\gamma_M = \frac{1-t^2}{1+t^2}\,, \tag{7}$$

gives the following second order algebraic equation

$$\left(L_0^2 - l_0^2 + 4d^2\right)t^2 - 4L_0 dt + L_0^2 - l_0^2 = 0\,. \tag{8}$$

Both solutions of Eq. (8) are given by

$$\gamma_{M_{1,2}} = 2\tan^{-1}t_{1,2} \quad \text{for} \quad t_{1,2} = \frac{2L_0 d \pm \sqrt{2l_0^2L_0^2 - l_0^4 - L_0^4 + 4d^2l_0^2}}{L_0^2 - l_0^2 + 4d^2}\,. \tag{9}$$

Thus, for L = 300 mm, l_0 = 545 mm, α = 60° and β_M = 45°, this algorithm gives : d = 259,81 mm, d_0 = 183,71 mm, L_0 = 732,67 mm, s = 187,67 mm and γ_M = 48,58°. Two configurations of a prototype with pnuematic actuation is shown in Fig. 4.

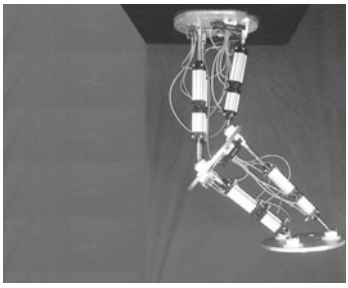

a)

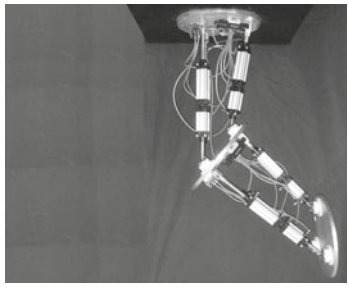

b)

Figure 4. Two configurations of a built prototype: a) fully ahead to perform a short step, as leg 1 of Fig.2b; b) fully ahead to perform a vertical wall climbing, as leg 2 of Figs.2c and 2d.

4 The 3-RPS Parallel Mechanism: Workspace Analysis

The workspace analysis for the 3-RPS parallel mechanism has been carried out by using a numerical procedure for the Forward Kinematics (FK), as proposed in (Lukanin, 2005) and then extended in (Figliolini et al., 2009). In particular, the Newton-Kantorovich Method has been applied in order to obtain a numerical solution for the FK and workspace analysis of the 3-RPS parallel mechanism. Referring to Fig. 5, a set of geometrical constraints can be expressed as $|A_1B_1| = |B_1C_1| = |C_1A_1| = \sqrt{3}\,R$ or in the Cartesian form as

$$\begin{cases} \left(X_{B1}-X_{A1}\right)^2+\left(Y_{B1}-Y_{A1}\right)^2+\left(Z_{B1}-Z_{A1}\right)^2=3R^2 \\ \left(X_{C1}-X_{B1}\right)^2+\left(Y_{C1}-Y_{B1}\right)^2+\left(Z_{C1}-Z_{B1}\right)^2=3R^2 \\ \left(X_{A1}-X_{C1}\right)^2+\left(Y_{A1}-Y_{C1}\right)^2+\left(Z_{A1}-Z_{C1}\right)^2=3R^2 \end{cases}, \tag{10}$$

where the Cartesian coordinates of the points A_1, B_1 and C_1 are given by

$$\begin{cases} X_{A1}=R-l_1\cos\alpha \\ Y_{A1}=0 \\ Z_{A1}=l_1\sin\alpha \end{cases}, \begin{cases} X_{B1}=-1/2\left(R-l_2\cos\beta\right) \\ Y_{B1}=-\sqrt{3}/2\left(R-l_2\cos\beta\right) \\ Z_{B1}=l_2\sin\beta \end{cases}, \begin{cases} X_{C1}=-1/2\left(R-l_3\cos\gamma\right) \\ Y_{C1}=\sqrt{3}/2\left(R-l_3\cos\gamma\right) \\ Z_{C1}=l_3\sin\gamma \end{cases}. \tag{11}$$

Thus, substituting these Cartesian coordinates into Eqs. (10), a system of three non-linear equations is obtained in the unknown α, β and γ for the input parameters l_1, l_2 and l_3, which can be expressed in compact form as

$$f_i\left(\alpha,\beta,\gamma\right)=0 \qquad \text{for} \qquad i=1,\,2,\,3. \tag{11}$$

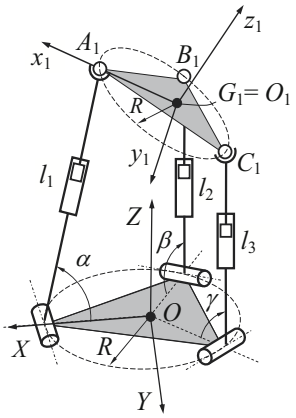

Figure 5. Kinematic sketch of the 3-RPS parallel mechanism.

This system of three non-linear equations has been solved numerically by using the Newton-Kantorovich Method, which is based on the linearization of each equation through the Taylor Series. In particular, a system of three linear equations has been obtained and solved by applying the common Cramer's determinant method, where the 3 x 3 matrix of the coefficients is given by the Jacobi matrix, which elements are obtained as partial derivatives of the functions f_i for $i = 1$, 2 and 3 of the Eqs. (11) with respect to α, β and γ.

This algorithm for the FK analysis of the 3-RPS parallel mechanism has been implemented in a MatLab code and the workspace of point G_1 of the moving platform has been obtained by varying the lengths l_1, l_2 and l_3 within the range of values to perform the maximum stroke s of Eq. (3). In fact, this stroke can give the maximum rotation $\beta_M = 45°$ (G_{1m} moves up to G_{A1}, G_{B1} or G_{C1}) or the maximum translation s (G_{1m} moves up to G_{1M}) of the moving platform, when only one (l_1, l_2 or l_3) or all three (l_1, l_2 and l_3) linear actuators are moved at end outstroke, respectively, as shown in the axonometric projections of Fig. 6.

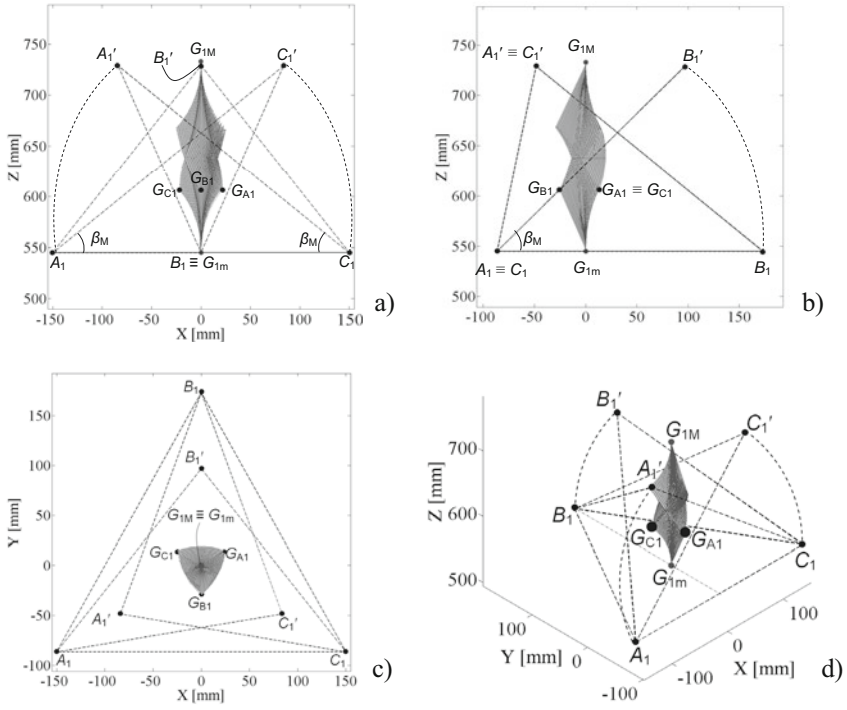

Figure 6. Workspace of the 3-RPS parallel mechanism: a) *X Z* front view; b) *Y Z* lateral view; c) *X Y* top view; d) *X Y Z* axonometric view.

Conclusions

The mechanical design of a novel biped climbing and walking robot with a 2 (3-RPS) leg mechanism has been described. In particular, the type synthesis of the leg mechanism along with the analysis of the climbing and walking motions, the dimensional synthesis and the workspace analysis of the 3-RPS parallel mechanism, have been carried out. Moreover, a first prototype of the 2 (3-RPS) leg mechanism with pneumatic actuation has been built and shown in the paper. The dimensional synthesis and the workspace analysis of the whole leg mechanism is in progress to formulate a general algorithm for the required walking and climbing performances.

Bibliography

Figliolini, G. and Ceccarelli, M. (1997). Mechanical design of an anthropomorphic electropneumatic walking robot. *ROMANSY 11: robot design, dynamics, and control*. Eds. A. Morecki, C. Rzmkowski, G. Bianchi, Springer, Vienna. 189–196.

Figliolini, G. and Ceccarelli, M. (1999). Walking programming for an electropneumatic biped robot, *Mechatronics*, 9 (8). 941–964.

Figliolini, G. and Ceccarelli, M. (2004). EP-WAR3 biped robot for climbing and descending stairs, *Robotica*, 22 (4). 405–417.

Figliolini, G. and Rea, P. (2007). Mechanics and simulation of six-legged walking robots. *Climbing & Walking Robots, Towards New Applications*, Ed. H. Zhang, I-Tech Education and Publishing, Vienna. 1–22.

Figliolini, G., Rea, P. and Conte, M. (2009). Mechanical design of a six-legged walking robot with Sarrus-2-(3-RPS) leg mechanism. *Mobile Robotics: Solutions and Challenges*. Eds. O. Tosun and H. L. Akin, World Scientific Company, Singapore. 487–494.

Nishi, A., (1992). A biped walking robot capable of moving on a vertical wall, *Mechatronics*, 2 (6). 543−554.

Hirose, S. and Kawabe, K. (1998). Ceiling walk of quadruped wall climbing robot NINJA-II. 1st *Int. Symp. on Mobile, Climbing and Walking Robots*, Brussels. 143−147.

Bahr, B., Li, Y. and Najafi, M. (1996). Design and suction cup analysis of a wall climbing robot, *Computers & Electrical Engineering*, 22 (3). 193–209.

Minor, M.A. and Mukherjee, R., (2003). Under-actuated kinematic structures for miniature climbing robots, *ASME J. of Mechanical Design*, 125 (2). 281−291.

Balaguer, C., Gimenez, A. and Jardon, A. (2005). Climbing robots' mobility for inspection and maintenance of 3D complex environments, *Autonomous Robots*, 18 (2). 157−169.

Kim, H. S. and Tsai, L. W. (2003). Kinematic synthesis of a spatial 3-RPS parallel manipulator, *ASME J. of Mechanical Design*, 125 (2). 92–97.

Mattiazzo, G., Pastorelli, S. and Sorli, M. (2005). Motion simulator with 3 d.o.f.s pneumatically actuated, *Bath Workshop on Power Transmission & Motion Control*. Eds. D.N. Johnston, C.R. Burrows and K. Edge, John Wiley & Sons, London. 395–406.

Lukanin, V. (2005). Inverse kinematics, forward kinematics and working space determination of 3 d.o.f. parallel manipulator with S-P-R joint structure, *Periodica Polytechnica*, Ser. Mech. Eng., 49 (1). 39–61.

Di Gregorio, R. and Parenti-Castelli, V. (2006). A new approach for the evaluation of kinematic and static performances of a family of 3-UPU translational manipulators. *ROMANSY 16: robot design, dynamics, and control*. Springer, Vienna. 47–54.

Chapter III

Humanoid Robots, Bio-Robotics, Multi-Robot, Multi-Agent Systems

Development of the Anthropomorphic Waseda Saxophonist Robot

Jorge Solis[1,2] Klaus Petersen[3] Tetsuro Yamamoto[3] Maasaki Takeuchi[3]
Shimpei Ishikawa[3] Atsuo Takanishi[1,2] and Kunimatsu Hashimoto[4]

[1] Faculty of Science and Engineering, Waseda University, Tokyo, Japan
[2] Humanoid Robotics Institute, Waseda University, Tokyo, Japan
[3] Graduate School of Advanced Sci. and Eng., Waseda University, Tokyo, Japan
[4] Partner Robot Division, Toyota Motor Corporation, Toyota, Japan
E-mail: solis@ieee.org

Abstract Our research is related to the development of an anthropomorphic saxophonist robot, which it has been designed to mechanically reproduce the organs involved during the saxophone playing. Our research aims in understanding the motor control from an engineering point of view and enabling the communication between humans and robots in musical terms. In this paper, we present the Waseda Saxophone Robot No. 2 (WAS-2) which is composed by 22-DOFs. In particular, the lip mechanism of WAS-2 has been designed with 3-DOFs to control the motion of the lower, upper and sideways lips to increase the sound range and to reproduce the dynamic effect of the sound (i.e. crescendo and decrescendo). In addition, a human-like hand (16-DOFs) has been designed to enable to play all the keys of the instrument. A set of experiments were carried out to verify the effectiveness of the mechanical design and the control system improvements.

1 Introduction

The development of anthropomorphic robots is inspired by the ancient dream of humans replicating themselves. In fact, the research on musical performance robots seems like a particularly promising path toward helping to overcome this limitation (Solis et al., 2008). Furthermore, research into robotic musical performance can shed light on aspects of expression that traditionally have been hidden behind the rubric of "musical intuition". In 1984, at Waseda University, the WABOT-2 was the first attempt of developing an anthropomorphic musical robot, it was able to play a concert organ (Kato et al., 1973). At that time, the late Prof. Ichiro Kato argued that

the artistic activity such as playing a keyboard instrument would require human-like intelligence and dexterity.

Nowadays, different kinds of musical performance robots (MPRs) have been developed. In particular, Takashima has been developing different music performance robots that are able of playing wind instruments such as (Takashima and Miyawaki, 2006): saxophone, trumpet, trombone, etc. In particular, the saxophone playing robot has been developed under the condition that the musical instrument played by robots should not be change or remodeled at all. This robot is composed of an artificial mouth, fingering mechanisms and air supplying system. Due to the complexity of replicating the motion of human fingers, the fingering mechanism is composed by twenty-three fingers so that each finger can press each key of the saxophone.

At Waseda University, since 2007, we have proposed the development of an anthropomorphic saxophone robot. Our research aims, as a long-term research goal, to enable the interaction between two human-like robots (by developing two different robots able of performing different wind instruments), and to enable a single human-like robot to play different kind of wind instruments (our ability to enable a single human-like robot to play different kind of wind instruments can be studied in detail). As a result of our research, in (Solis et al., 2009), we have presented the Waseda Saxophonist Robot No.1 (WAS-1), which was composed by 15-DOFs required to play an alto saxophone. In particular, the mouth (1-DOF lower lip), tongue (1-DOF), oral cavity, artificial lungs (1-DOF air pump and 1-DOF air flow valve) and fingers (11-DOFs) were developed. Even that the lip mechanism of WAS-1 was useful in order to adjust the pitch of the saxophone sound, the range of sound pressure was too short. Moreover, the finger mechanism was designed only to play from C3 to C♯5.

Therefore, the mechanical design of the lip and finger mechanisms were improved to increase the range of sound pressure and to enable the saxophone robot to play all the keys of the alto saxophone (A♯2 to F♯5). From the control system point of view, a considerable delay in the attack time to reach the desired air pressure was detected when playing musical scores at fast tempo. Thus, we describe the implementation of a feed-forward air pressure control system with dead-time compensation.

2 Waseda Saxophonist Robot No.2 (WAS-2)

In this year, we have developed the Waseda Saxophonist Robot No. 2 (WAS-2) which has been designed to increase the range of sound by improving the design of the artificial lips and to increase the range of playable notes by designing a human-like hand. In particular, the WAS-2 is com-

posed by 22-DOFs that mechanically emulate the organs involved during the saxophone playing as follows (Figure 1): 3-DOFs (from which 1-DOF is passively controlled) to control the shape of the artificial lips, 16-DOFs for the human-like hand, 1-DOF for the tonguing mechanism and 2-DOFs for the lung system (1-DOF for the air pump and 1-DOF for the valve mechanism).

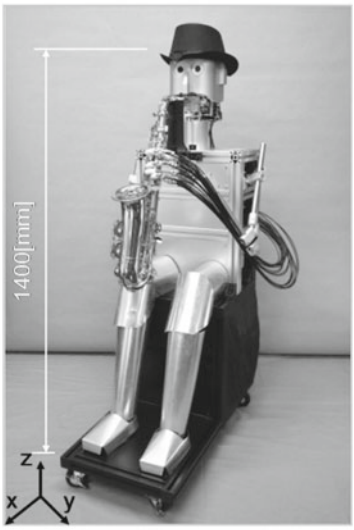

Figure 1. The Waseda Saxophonist Robot No.2 has been developed with 22-DOFs which has improved the design of the mouth and hand mechanisms.

2.1 Mechanical System

The artificial lip of the mouth mechanism of the WAS-1 was designed with 1-DOF in order to control the vertical motion of the lower lip (Solis et al., 2009). Based on the up/down motion of the lower lip, it became possible to control the pitch of the saxophone sound. However, it is difficult to control the sound pressure by means on 1-DOF. For this purpose, the improved version of the mouth mechanism has been designed to expand the range of sound. The new artificial lip of the WAS-2 is shown in Fig. 2. As we may observe, the lip mechanism consists of 2-DOFs designed to control the up/down motion of both lower and upper lips. In addition, a passive 1-DOF has been implemented to modify the shape of the side-way lips. The

material of the artificial lips is thermoplastic elastometer (Septon), which reproduces the elasticity and stiffness of human lips.

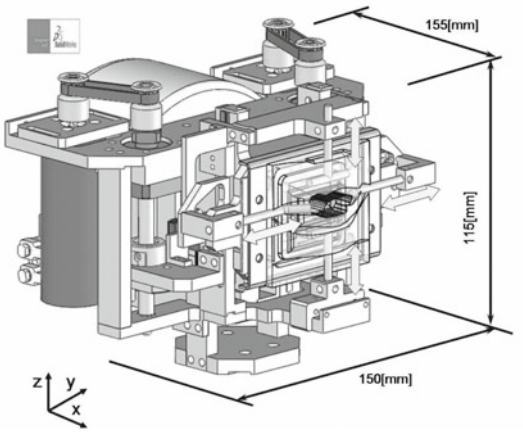

Figure 2. New mouth mechanism designed for the WAS-2; where the motion of upper and sideways lip, as well the lower lips were implemented.

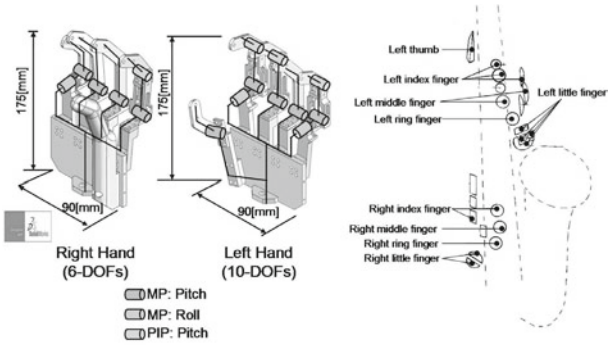

Figure 3. Arrangement of DOFs for the human-like hand of the WAS-2

The upper lip has been designed to avoid any possible leak of the air flow coming from the artificial lungs. The actuation system of the upper lips is composed by a timing belt and ball screw in order to convert the rotation of the motor axis into vertical motion. The lower lip is used to apply the pressure to the reed of the instrument to produce the required vibration for blowing each note. The actuation system is composed by a

timing belt and ball screw so that the rotational movement of the motor axis is converted into vertical motion. Finally, the sideways lip has been designed for avoiding the rolling of the artificial lips. A passive 1-DOF coupled to the motion of the upper lip has been implemented to close/open the lips when the instrument is held by the robot's mouth. The upper lip is attached to a roller with a limited range of motion. When the range of motion is exceeded, the guide is horizontally moved along the sliding guide. From this, it becomes possible to implement the extension motion of the lips. On the other way, the contraction motion depends on the stiffness properties of the artificial lips.

On the other hand, in order to produce the saxophone sound, it is required to control the motion of each of the fingers to push the correspondent keys. The finger mechanism of the WAS-1 was composed by a link connected directly to the RC motor axis. In particular, eleven motors were used to play from the notes from C3 to C♯5. However, with the alto saxophone is possible to play from A♯2 to F♯5. For this purpose, a human-like hand has been designed, which it is composed by 16-DOFs (Figure 3). In order to reduce the weight on the hand part, the actuation mechanism is composed by a wire and pulley connected to the RC motor axis. The RS-485 communication protocol has been used to control the motion of the finger system.

2.2 Control System

In our previous research, a cascade feedback control system was implemented to assure the accuracy of the air pressure during a musical performance (Solis et al., 2009). Basically, based on the measurements of the pressure sensed at the output of the air pump and the position of the lower lips, the air pressure has been controlled. However, during the attack time the target air pressure is reached around 100ms later during a musical performance. Mainly, this effect is related to the way the musical performance control is implemented. Basically, the signal of the note to be played is sent to the control system through a MIDI message. As soon as message of a note change is received, the air pressure as well as the position of the lower lips areadjusted. Thus, a delay on the control of the air pressure is observed.

For this purpose; in this paper, a modified version of the feedback error learning has been used. The feedback error learning is a computational theory of supervised motor learning proposed by Kawato (Kawato and Gomi, 1992); which is inspired by the way the central nervous system theory. In addition, Kawato extended that the cerebellum, by learning, acquires an

internal model of inverse dynamics of the controlled object. From this extension, the feedback error learning can be also used as training signal to acquire the inverse dynamics model of the controlled system based on Neural Networks. On the other hand, the dead-time compensation is used to control devices that take a long time to show any change to a change in input. A dead-time compensation control uses an element to predict how changes made now by the controller will affect the controlled variable in the future (Kim et al., 2003).

In particular, we have proposed the implementation of a feed-forward error learning control system with dead-time compensation as it is shown in Fig. 4. The inputs of the ANN are defined as follows (the input is based on the difference with the previous played note): pressure reference, note, and lower/upper lips position. In this case, a total of six hidden units were used (experimentally determined while varying the number of hidden units). As an output, the position of the air valve is controller to assure the accurate control of the required air pressure to blow a sound. In addition, a dead-time factor (referred as e^{sL}) is introduced to compensate the delay during the attack time.

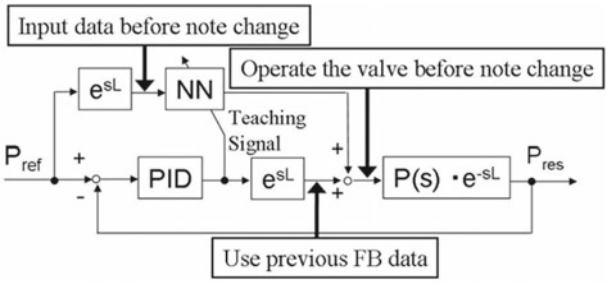

Figure 4. Block diagram of the proposed feed-forward control system with dead-time compensation implemented to assure the accuracy of the air pressure control during a performance

2.3 Experiments and Results

In order to verify if the designed new mouth mechanism enables to extend the range of sound pressure; we have compared the previous mechanism with the new one while playing the notes from C3 to C♯5. The experiment results are shown in Fig. 5a. As we may observe, the new mechanism has effectively increased the range of sound pressure (an average increment of 33%). Even though the range of sound pressure was expanded (even though, there are

still differences with the one measure by an intermediate level saxophonist). Thanks to this improvement, we could perform experiments with the WAS-2 in order to vary the dynamic properties of the sound such as decrescendo.

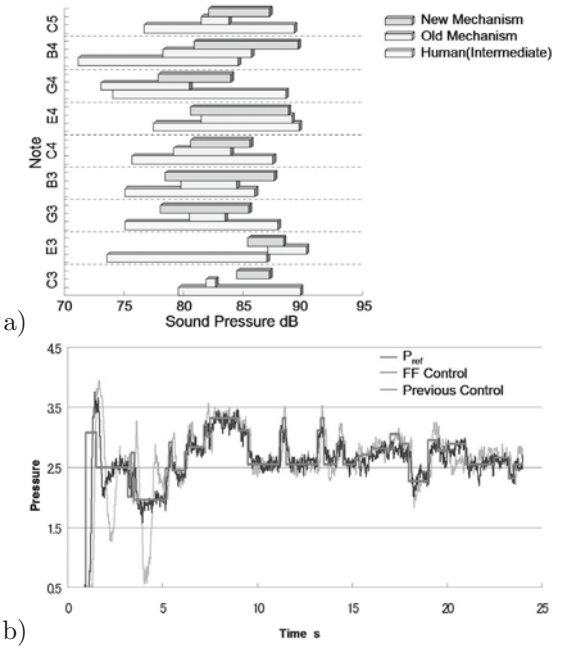

Figure 5. a) Comparison of the range of air pressure between the previous mouth mechanism of WAS-1 and the new one of WAS-2; b) Experimental results with the Feed-Forward Control System with Dead Time Compensation.

In order to determine the effectiveness of the proposed control system implemented on the WAS-2, we have programmed the robot to perform the "Moonlight Serenade" composed by Glenn Miller. In order to train the ANN, a total of 523 learning steps were done. The experimental results are shown in Fig. 5b. As we may observe, we can clearly observe that the proposed feed-forward control system with dead-time compensation presented a more stable dynamic response to the air pressure reference. In order to compare both dynamic responses, we have computed the correlation coefficient respect to the target signal (P_{ref}). The correlation coefficient is a quantity that gives the quality of a least squares fitting to the original data. As a result, we found that the resulted air pressure with the feed-

forward control system with dead-time compensation became closer to the target one (correlation coefficient of 0.636) than the previous control system (correlation coefficient of 0.459). With these results, we could confirm the improvements achieved respect to the previous control system (cascade feedback control).

2.4 Conclusion and Future Work

In this paper, the details of the mechanical improvements on the WAS-2 have been detailed. Moreover, an air pressure feed-forward control system with dead-time compensation has been implemented to improve the dynamic response of the air pressure control. From the experimental results, we could confirm the effectiveness of the mechanical and control improvements. As a future work, the proposed feed-forward control system will include as well the pitch information (acoustic feedback) as there is still deviation of the pitch during the performance.

Bibliography

I. Kato, S. Ohteru, H. Kobayashi, K. Shirai, and A. Uchiyama. Information-power machine with senses and limbs. In *Proceedings of the CISM-IFToMM Symposium on Theory and Practice of Robots and Manipulators*, pages 12–24, 1973.

M. Kawato and H. Gomi. A computational model of four regions of the cerebellum based on feedback-error-learning. *Biological Cybernetics*, 68: 95–103, 1992.

H. Kim, K. Kim, and M Young. On-line dead-time compensation method based on time delay control. *IEEE Transactions on Control Systems Technology*, 11(2):279–286, 2003.

J. Solis, K. Taniguchi, T. Ninomiya, and A. Takanishi. Understanding the mechanisms of the human motor control by imitating flute playing with the waseda flutist robot wf-4riv. *Mechanism and Machine Theory*, pages 527–540, 2008.

J. Solis, K. Petersen, T. Ninomiya, M. Takeuchi, and A. Takanishi. Development of anthropomorphic musical performance robots: From understanding the nature of music performance to its application to entertainment robotics. In *Proceedings of the IEEE/RSJ International Conference on Intelligent Robots and Systems*, pages 2309–2314, 2009.

S. Takashima and T. Miyawaki. Control of an automatic performance robot of saxophone: Performance control using standard midi files. In *Proceedings of the IROS Workshop on Musical Performance Robots and Its Applications*, pages 30–35, 2006.

Design and Simulation of a Waist-Trunk System for a Humanoid Robot

Conghui Liang[‡*] and Marco Ceccarelli[‡]

[‡]Laboratory of Robotics and Mechatronics, DiMSAT, University of Cassino, Cassino (Fr), Italy

Abstract In this paper, a new waist-trunk system has been proposed for a humanoid robot by using parallel architectures. The structure of human torso and its function have been used as inspirations for design purposes. The proposed waist-trunk system consists of a 3 legged UPS orientation parallel platform and a 6 legged UPS parallel platform which are connected together in a serial architecture. A 3D model of the proposed system has been elaborated in SolidWorks® both for design and simulation purposes. Kinematic equations have been formulated for characterization and evaluation of performances. Simulation results show that the proposed system is able to imitate the movements of human torso with suitable motion capability, flexibility, and operation performances.

1 Introduction

Nowadays, the available humanoid robots are capable of performing basic human movements like different patterns of walking, running, ascending and descending stairs (Carbone and Ceccarelli, 2005). Research activities have been focused on the upper and lower limbs of humanoid robots like for example on dynamic walking control, biped walking pattern generation, and dual-arm dexterous manipulation (Kemp et al., 2008). Nevertheless, due to the mechanical design difficulties and complex control of multi-body systems, the torso is somehow a neglected or simplified design part. The torsos of the existing humanoid robots like ASIMO, HRP, and HUBO have almost a box shaped body with only 2 to 3 d.o.f.s.

Actually, human torso is a complex system with many d.o.f. and plays an important role during human locomotion such as in walking, turning, and running. Therefore, an advanced torso system is needed for humanoid

[*]The first author is supported by the Chinese Scholarship Council (CSC) for his PhD study and research at LARM in the University of Cassino, Italy for the years 2008-2011.

robots so that they can be better accommodated in our daily life environment with suitable motion capability, flexibility, operation performances, and anthropomorphic characteristics. Few works have been addressed on design and control issues of torso system for humanoid robots. WABIAN-2R has 2-d.o.f. waist and 2-d.o.f. trunk in a serial architecture (Omer et al., 2005). A musculoskeletal flexible-spine humanoid robot named as "Kotaro" has an anthropomorphic trunk system with several d.o.f.s and it is actuated by using artificial muscle actuators (Or, 2008). A 3-d.o.f. parallel manipulator named as CaPaMan2 bis at LARM has been proposed as the trunk module for a low-cost easy-operation humanoid robot CaLuMa in (Nava Rodriguez et al., 2006). These torso systems are fundamentally different from the waist-trunk system that is proposed in this paper.

In this paper, a new waist-trunk system has been proposed by using two parallel architectures with a high d.o.f., high payload capacity, suitable dynamic performance, and simple-to-control features (Carbone et al., 2009). Kinematic equations of the system have been formulated for characterization and evaluation of performances. Finally, simulation results are reported and discussed.

2 Human Torso and Proposed Waist-Trunk System

Figure 1(a) shows a scheme of the skeleton of human torso. It consists of three parts: pelvis, waist, and thorax. The rib cages and spine column of the upper part contribute to thorax which contains important human organs like heart, lung, liver, and stomach. The lumbar spine, which is the waist segment, is the most important and largest part of human spine. The spine is connected with the pelvis by sacrum and the pelvis is connected with two femurs in the lower part (Virginia, 1999).

The torso plays an important role during human locomotion as it can be well understood. The "spine engine", (Gracovetsky, 1988), is a theory for studying the human locomotion. He proposed that the spine can be considered as the predominant machinery involved with gait. He proved that the legs do not move the body, and they are not the motor behind the movement, but it is the spine and its local musculature that are the driving engine for human movement. Figure 1(b) shows a conceptual model of the spine engine. In the presence of normal lumbar lordosis, side bending produced an axial torque (coupled motion) for actuating the pelvis rotation. The thorax and upper extremities counter rotate with respect to the pelvis and lower limbs in order to maintain angular momentum.

In Figure 2 the proposed waist-trunk system is illustrated in a 3D model and a kinematic scheme with design parameters. The proposed waist-trunk

system consists of two classical parallel architectures which are connected together in a serial chain architecture. The combination of the two systems is a novel design as a complex system with easy operation performance because of their well understood single behaviour.

The upper part of waist-trunk system is the trunk module, which consists of a thorax platform, a waist platform, and six identical leg mechanisms to obtain a 6 d.o.f.s parallel manipulator structure. Each leg mechanism is composed of a universal joint, a spherical joint, and an actuated prismatic translation joint. The trunk module has six d.o.f.s with the aims to imitate the movements of human lumbar spine and thorax.

The lower part in Figure 2(a) is the waist module, which consists of a pelvis platform, a waist platform, and three identical leg mechanisms to obtain a 3 d.o.f.s parallel manipulator structure. The waist module shares waist platform with the trunk module but the leg mechanisms are installed on the counter side in a down-ward architecture. The pelvis platform is connected to the waist platform with three leg mechanisms and a passive spherical joint. There are six bars connected with the passive spherical joint with the waist platform and pelvis platform. The waist module is an orientation platform with three rotation d.o.f.s. that are aimed to imitate the movements of human pelvis.

3 An Inverse Kinematics Study

Figure 2(b) shows a kinematic scheme with design parameters for the proposed waist-trunk system. Coordinate systems $TX_TY_TZ_T$, $WX_WY_WZ_W$, and $PX_PY_PZ_P$ have been attached on the trunk platform TP, waist platform WP, and pelvis platform PP, respectively.

Supposing that the waist platform WP is the fixed base, position and orientation of the waist platform WP can be prescribed for different walking patterns according to ZMP criterion. $TX_TY_TZ_T$ has been fixed with Z_T axis orthogonal to the TP plane, X_T axis with the line joining T to T_1, and Y_T axis to give a Cartesian frame according to the right-hand rule. δ_i is the structure angle between TT_1 and TT_i. Z_W axis is orthogonal to the WP plane, X_W axis coincides with the line joining W to W_1 and Z_P axis is orthogonal to the PP plane. σ_i is the structure angle between WW_1 and WW_i. ξ_k is the angle between MM_1 and MM_k; γ_k is the angle between PP_1 and PP_k. Each leg mechanism W_iT_i is connected to the waist platform by using a 2-d.o.f. universal joint and to the thorax platform TP with a spherical joint S_i (i=1,...,6). Particularly, joints T_1 and T_2 are installed on the trunk platform TP at the same point, and similar by joints T_3 and T_4, as well as joints T_5 and T_6. In Figure 2(b) spherical joints are marked with

T_i (i=1,...,6), universal joints with W_i (i=1,...,6), and prismatic joints with L_i (i=1,...,6).

The position of the thorax platform TP is represented by three Cartesian coordinates x_T, y_T, and z_T. The orientation of TP with respect to the fixed base WP can be represented with the three Euler angles θ_T, φ_T, and ψ_T as indicated in Figure 2(b), where φ_T is a rotation about the Z_W axis; θ_T is a tilting rotation about the Y_T axis, which is the Y_W axis after a θ_T rotation; and ψ_T is a rotation about the Z_T axis. The pelvis platform PP is connected to the waist platform WP by means of three UPS leg mechanisms. Particularly, the universal joints P_k (k=1,2,3) are installed on the platform PP with axes perpendicular to each other intersecting at the passive spherical point O. Three spherical joints M_k (k=1,2,3) are installed on the downward side of the waist platform WP with a equivalent triangle configuration. The pelvis platform PP is actuated by three prismatic joints S_k.

By properly formulating the constraint equations for each leg mechanism, the solution of the inverse kinematics problem for the trunk module can be obtained as

$$\mathbf{W_i T_i} = \mathbf{WT} + \mathrm{r_T R_T u_{\delta i}} - \mathrm{r_W u_{\sigma i}} \tag{1}$$

where $\mathbf{u}_{\delta i}$ (i=1,...,6) is the unit vector for TT_i, which is described with respect to $TX_TY_TZ_T$; $\mathbf{u}_{\sigma i}$ is the unit vector of WW_i. R_T is the rotation matrix from the moving thorax platform TP to the fixed waist platform WP. By substituting the design parameters and prescribed position and orientation angles into Equation (1), the required length for each leg mechanism can be computed. Similarly, the required length for each leg mechanism of the waist module can be by using the following equation.

$$\mathbf{M_k P_k} = \mathbf{OP} - \mathbf{OM} + \mathrm{r_P R_W u_{\lambda k}} - \mathrm{r_M u_{\xi k}} \tag{2}$$

where $\mathbf{u}_{\xi k}$ (k=1,2,3) is the unit vector for MM_k. $\mathbf{u}_{\lambda k}$ is the unit vector of PP_k which are described with respect to $PX_PY_PZ_P$. R_W is the rotation matrix from the pelvis platform PP to the waist platform WP.

4 Simulation Results

Simulation time has been prescribed in 1.5s to simulate the function of the waist-trunk system in a full cycle of humanoid robot normal walking. In general, the range of motion of human pelvis is between 5 degrees and 15 degrees (Lingyan et al., 2005), and the orientation capability of the waist module has been designed to be within a range of 20 degrees. Prescribed orientation angles of the trunk module and waist module are shown in Figure 3 for an example.

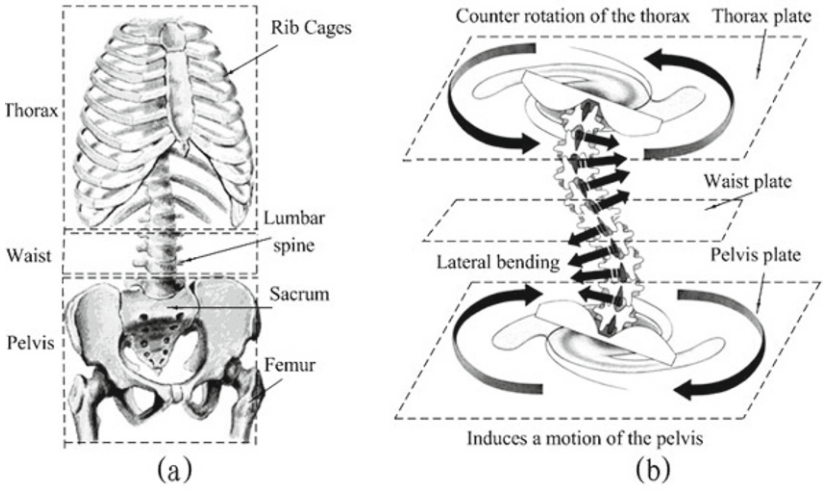

Figure 1. Schemes for human torso: (a) skeleton structure; (b) spine engine.

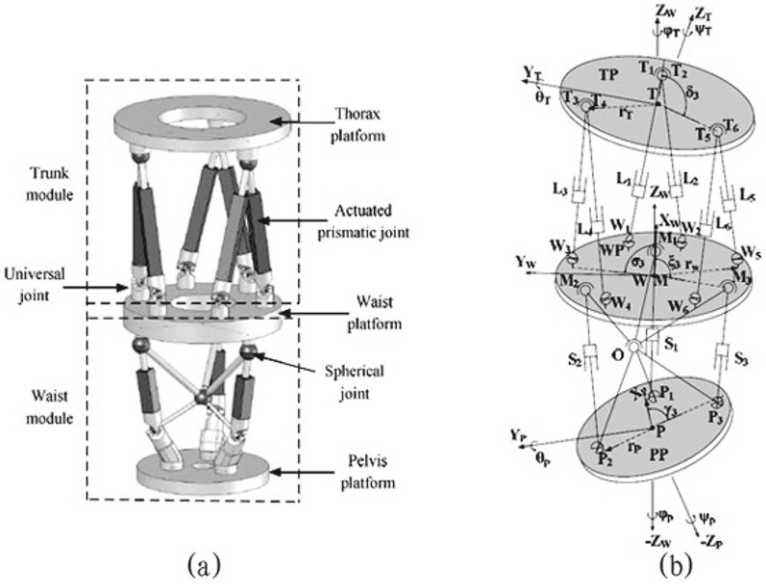

Figure 2. The proposed waist-trunk system for a humanoid robot: (a) a 3D model; (b) a kinematic scheme with design parameters.

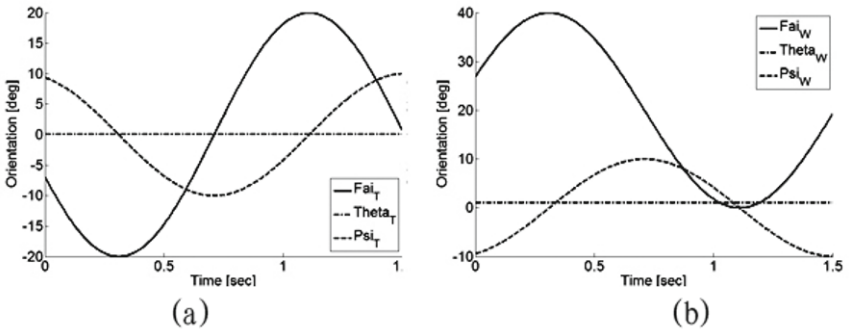

Figure 3. Prescribed angles: (a) thorax platform; (b) pelvis platform.

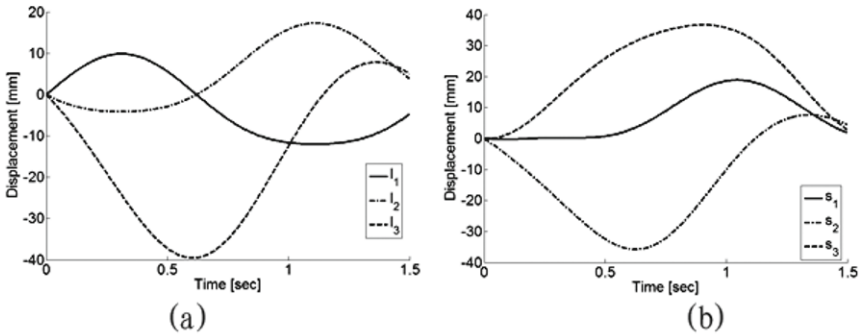

Figure 4. Computed leg displacemets: (a) trunk module; (b) waist module.

Figures 4 to 6 show results of simulation. The maximum velocity has been computed as 58 mm/s along Y axis for the trunk module and 120 mm/s for the waist module. The maximum acceleration has been computed as 240 mm/s^2 along Y axis for the trunk module and 460 mm/s^2 for the waist module. These values are feasible for the operation of the parallel manipulators and they properly simulate the operation of human torso.

Figure 7(a) shows the snapshots of the movements of the waist-trunk system for a walking task. The thorax platform and pelvis platform have counter-rotation movements so that the angular moment can be maintained during a humanoid robot walking. Figure 7(b) shows the corresponding motion of the 3D model with smooth behaviour, which well imitates the movements of human thorax and pelvis during a walking task as outlined by the plots of numerical results in Figure 3 to Figure 6.

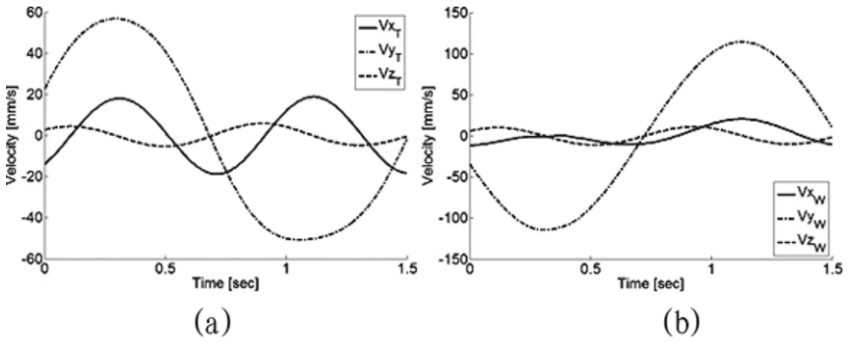

Figure 5. Computed velocities: (a) trunk module; (b) waist platform.

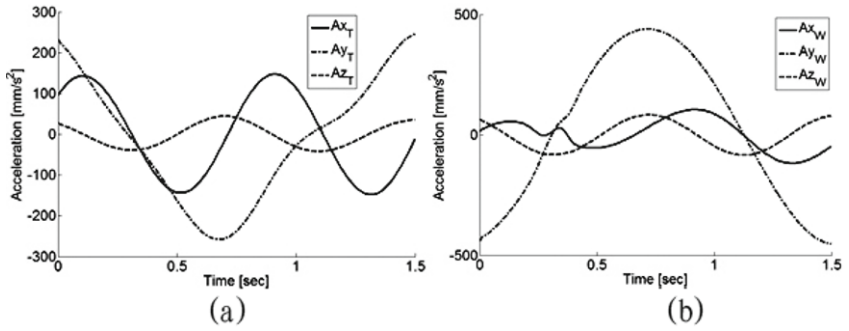

Figure 6. Computed accelerations: (a) trunk module; (b) waist platform.

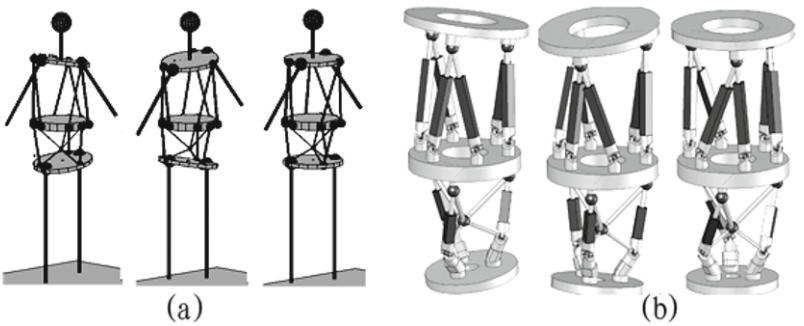

Figure 7. Snapshots of movements of the proposed waist-trunk system: (a) simulating a humanoid robot in a walking task; (b) the motion sequences of the 3D model.

5 Conclusions

A novel waist-trunk system for a humanoid robot has been proposed by using suitable parallel architectures. The proposed system shows an anthropomorphic design and operation with several d.o.f.s, flexibility, and high payload capacity. Inverse kinematic equations have been formulated and closed form solutions have been obtained for operation characterization and evaluation of performances. A 3D model has been elaborated and simulated for checking the operation feasibility and design sizes. Simulation results show that the proposed waist-trunk system can well imitate movements of human torso during a normal human walking and has practical feasible operation performances for a humanoid robot design solution.

Bibliography

G. Carbone and M. Ceccarelli. *Legged Robotic Systems, Cutting Edge Robotics ARS Scientific Book*. Springer Verlag, 2005.

CC. Kemp, P. Fitzpatrick, H. Hirukawa, K. Yokoi, K. Harada, and Y. Motosumoto. *Springer Handbook of Robotics, Part G. Humanoid Robots*. Springer-Verlag, 2008.

A.M.M. Omer, Y. Ogura H. Kondo, A. Morishima, G. Carbone, M. Ceccarelli, L. Hun-ok, and A. Takanishi. Proceedings of 2005 5th ieee-ras international conference on humanoid robots. In *2nd IEEE International Conference on Robotics, Automation and Mechatronics*, pages 333–338, 2005.

J. Or. *The development of emotional flexible spine humanoid robots,Affective Computing, Emotion Expression, Synthesis and Recognition (Advanced Robotics Systems)*. InTech Education and Publishing, 2008.

N.E. Nava Rodriguez, G. Carbone, and M. Ceccarelli. Capaman 2bis as trunk module in caluma (cassino low-cost humanoid robot). In *2nd IEEE International Conference on Robotics, Automation and Mechatronics*, pages 347–352, 2006.

G. Carbone, C. Liang, and M. Ceccarelli. Using parallel architectures for humanoid robots. In *Kolloquium Getriebetechnik, Aachen 2009*, pages 177–188, 2009.

C. Virginia. *Bones and Muscles: An Illustrated Anatomy*. Wolf Fly Press, 1999.

S. Gracovetsky. *The Spinal Engine*. Springer Verlag, 1988.

Z. Lingyan, Z. Lixun, W. Lan, and W. Jian. Three-dimensional motion of the pelvis during human walking. In *IEEE International Conference on Mechatronics and Automation, ICMA2005*, pages 335–339, 2005.

Safe Navigation in Dynamic Environments

Zvi Shiller * Oren Gal**, and Elon Rimon **
* Leo Paslin Robotics Research Laboratory
Department of Mechanical Engineering and Mechatronics
Ariel University Center, Israel
** Department of Mechanical Engineering, Technion, Israel

Abstract.
This paper addresses the issue of motion safety for on-line navigation in dynamic environments. Using velocity obstacles to represent the dynamic environment, we propose to truncate the velocity obstacle by the minimum time horizon, computed to ensure that the velocity obstacle is truncated close to the boundary of the set of inevitable collision states. Thus, using the velocity obstacle to select potential avoidance maneuvers would ensure that only safe maneuvers are being selected. The concept of velocity obstacles was known for some time, but the issue of how to truncate it without compromising safety was not addressed until recently. The computation of the minimum time horizon is formulated as a minimum time problem, which is solved numerically for each static or moving obstacle. The "safe" velocity obstacles are used in an on-line planner that generates near-time optimal trajectories to the goal. The planner is demonstrated for on-line motion planning in very crowded static and dynamic environments.

1 Introduction

Motion planning in dynamic environments is challenging since it requires the selection of safe maneuvers, hopefully on-line, that reach the goal while avoiding any number of static and moving obstacles. While reaching the goal with an on-line planner cannot be guaranteed, one can reduce the search to only safe states, i.e. states from which at least one other safe state is reachable. Most current local (reactive) planners (Fox et al. (1997); Minguez and Montano (2000)) do not guarantee safety as they are too slow and hence their ability to look-ahead and avoid states of inevitable collision (Fraichard and Asama (2004)) is very limited. A promising approach to safe motion planning in dynamic environment is the consideration of "regions

of inevitable collision" (Petti and Fraichard (2005); Fraichard and Asama (2004); Chan and M. Zucker (2008)). The computation of the "regions of inevitable collision" in those planners is however cumbersome.

We address the issue of safety for an on-line local planner in dynamic environments using velocity obstacles (Fiorini and Shiller (1998)). Safety is guaranteed by ensuring that the robot's velocity does not penetrate the velocity obstacle, which is generated for a carefully selected time horizon. This time horizon ensures that the velocity obstacle contains the set of inevitable collision states. Repelling the robot's velocity from entering the inevitable collision states ensures (if a solution exists) that the robot does not crash into any static or moving obstacle. The computation of the safe time horizon, which is obstacle specific, is formulated as a minimum time problem that minimizes the time for the robot velocity to exit the velocity obstacle. The solution is along an extremal, generated on the boundary of the control constraints. Determining the safe time horizon is computationally efficient and it does not require a prior mapping of inevitable collision states. Since the time horizon is obstacle specific, motion safety is guaranteed if obstacles can be avoided individually or if the state-space between the current position and the goal state stays connected. The velocity obstacles, truncated at the minimum time horizon, are used for an on-line planner that generates near-time optimal trajectories by minimizing at each time step the time-to-go to the goal. The planner is demonstrated for on-line motion planning in crowded static and dynamic environments. It is also used for collision-free multi-robot navigation in the plane and in 3D spaces.

2 The Velocity Obstacle

The velocity obstacle represents the set of all colliding velocities of the robot with each of the neighboring obstacles (Fiorini and Shiller (1993); Shiller et al. (2001)). It maps static and moving obstacles into the robot's velocity space. The velocity obstacle of a planar obstacle, B, that is moving along a general known trajectory, $c(t)$, is a warped cone in the velocity space of the point robot A. It is called a nonlinear velocity obstacle ($NLVO$) since it accounts for a general (nonlinear) trajectory of the obstacle. Selecting a single velocity at time $t = t_0$ outside the $NLVO$ guarantees no collision at all times, as long as the obstacle stays on its current trajectory.

The non-linear v-obstacle is constructed as a union of its temporal elements, $NLVO(t)$, which is the set of all absolute velocities of A, v_a, that would result in collision at a specific time t. Referring to the left side of Figure 1, v_a that would result in collision with point $p \in B(t)$ at time $t > t_0$,

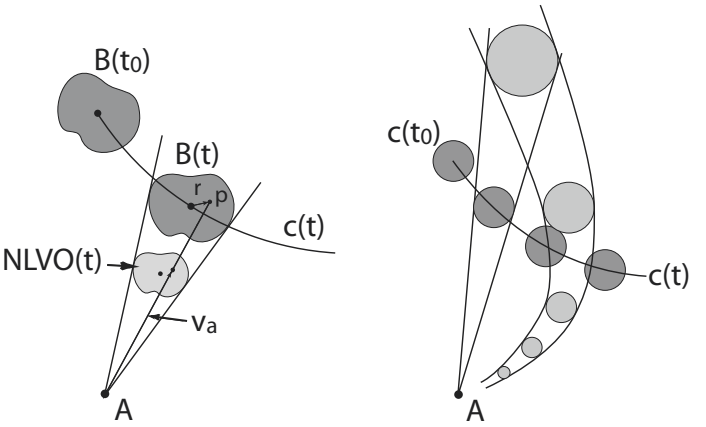

Figure 1. A non-linear velocity obstacle

expressed in a frame centered at $A(t_0)$, is simply

$$v_a = \frac{c(t) + r}{t - t_0}, \tag{1}$$

where r is the vector to point p in the obstacle's fixed frame. It is a homothety transformation (Dodge (2004)), centered at $A(t_0)$ and scaled by $k = \frac{1}{t-t_0}$:

$$v_a = H_{A,k}(c(t) + r); k = \frac{1}{t - t_0}. \tag{2}$$

The set, $NLVO(t)$ of all absolute velocities of A that would result in collision with any point in $B(t)$ at time $t > t_0$ is thus:

$$NLVO(t) = H_{A,k}(B(t)); k = \frac{1}{t - t_0}. \tag{3}$$

Integrating (3) over $t = [t_0, \infty)$ yields the non-linear v-obstacle, $NLVO^{\infty}_{t_0}$, representing the set of all linear velocities of A that would collide with $B(t)$ at time $t = (t_0, \infty)$:

$$NLVO^{\infty}_{t_0} = \bigcup_t H_{A,k}(B(t)); k = \frac{1}{t - t_0}; t = (t_0, \infty). \tag{4}$$

The non-linear v-obstacle is a warped cone, as shown schematically on the right side of Figure 1. If $c(t)$ is bounded over $t = (t_0, \infty)$, then the apex

of this cone is at $A(t_0)$. The boundaries of the $NLVO$ represent velocities that would result in A grazing B. The smallest safe time horizon is the one that allows sufficient time to avoid or escape collision as discussed next.

3 Time Horizon

The nonlinear velocity obstacle consists of the union of temporal velocity obstacles from time t_0 to infinity. It thus accounts for colliding velocities that would result in collisions at all times.

We wish to select the smallest time horizon that would mark as dangerous only those velocities at which the obstacle is unavoidable given robot dynamics and its dynamic and kinematic constraints. The smallest safe time horizon should allow sufficient time for the robot to avoid the obstacle, or equivalently, bring its velocity vector outside the velocity obstacle. We thus define the smallest safe time horizon as the minimum time to exit the velocity obstacle from a given state, subject to robot dynamics and actuator constraints, which is the solution of the minimization problem:

$$min \int_{t_0}^{t_h} 1dt, \tag{5}$$

with the initial condition

$$x(t_0), \dot{x}(t_0) \tag{6}$$

the final condition

$$\dot{x}(t_h) \notin NLVO_{t_h}^{\infty} \tag{7}$$

satisfying system dynamics

$$\ddot{x} = f(x, \dot{x}, u) \tag{8}$$

and control constraints

$$u \in U, \tag{9}$$

where $NLVO_{t_h}^{\infty}$ denotes a velocity obstacle generated at $t = t_h$ for an infinite time horizon.

It is easy to show that the solution, t_h, to problem (5) is obtained by an extremal trajectory that is generated on the boundary of the control constraints. For a point mass model, there are four such trajectories, generated by the four corners of the set of admissible control U. Figure 2 shows a point robot A, a static obstacle B, and the initial velocity $v_a(t_0)$ that is pointing towards B. Obviously, $v_a(t_0)$ is inside the velocity obstacle of B, or $v_a(t_0) \in NLVO_{t_0}^{\infty}$. Applying the controls associated with the four corners of the set of admissible control U results in four extremal trajectory denoted

$x_1 - x_4$. We wish to compute the minimum time at which the velocity along at least one of the extremals points outside of the current velocity obstacle, or equivalently, the velocity $v_a(t_h)$ is tangent to B.

Three cases are shown in Figure 2. The one on the right represents a case when collision is unavoidable (A is inside the ICS); the one in the center represents a case when only one maneuver can avoid collision (A is on the boundary of the ICS); and on the left, only three of the four extremals penetrate the obstacle. The minimum time t_h that is the solution to problem (5) is the time where the tangent line at $x_1(t_h)$ is tangent to B, as shown in Figure 2. The smallest time horizon t_h is obstacle specific, and it depends on the size of the obstacle, its velocity, the robot's velocity and its dynamic constraints. It can be easily computed by expressing all four extremal trajectories analytically and searching for the nearest (in time) tangency point of the common tangent between B and every extremal. The case shown in Figure 2 is for a static obstacle. The analysis for a moving obstacle is similar except that v_a is replaced with the relative velocity $v_{a/b}$ and v_b is subtracted from the extremals.

Using the smallest time horizon computed by solving problem (5) to truncate the velocity obstacle produces a conservative approximation of the set of inevitable collisions (ICS). This is so because the extremal along which the time horizon was determined is usually a curved and decelerating trajectory, whereas the velocity obstacle assumes that the robot (not the obstacle) moves at a constant velocity. Truncating the velocity obstacle by the minimum time horizon alerts the robot of a potential collision earlier than necessary had it been decelerating towards the obstacle.

It is possible to account for the robot's actual trajectory, using the *self motion velocity obstacle* (SMVO) (Shiller et al. (2008)), however this would require generating a larger velocity obstacle that accounts for all possible robot trajectories–in itself a conservative representation. For simplicity, we prefer the original $NLVO$ that assumes constant robot velocities, while accounting for the error introduced by the curved trajectory (Shiller et al. (2010)).

It is important to note that by integrating the extremals to compute t_h, one determines if the current state is safe or not without resorting to the velocity obstacles. However, knowing that a specific state may lead to a collision does not help in selecting a safe maneuver. This is where the velocity obstacles, generated for the smallest time horizon, become most useful.

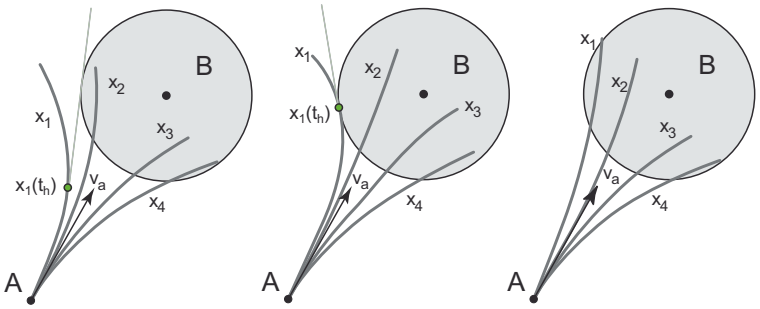

Figure 2. The robot and obstacle on a collision course

4 The Planner

The efficient representation of static and moving obstacles by velocity obstacles allows us to efficiently plan safe trajectories in dynamic environments. We assume knowledge of the positions and velocities of the neighboring obstacles. Our planner is local as it generates one move at every time step. The proper choice of the time horizon ensures survival of the robot, i.e. not entering inevitable collision states (ICS). For one obstacle, this guarantees convergence to the goal. For many obstacles, a solution cannot be guaranteed due to the changing nature of the environment: it is possible that during the local search, the state space around the robot becomes disconnected from the goal even though the global search might escape such a trap.

5 Examples

The on-line planner was implemented and tested for crowded static and dynamic environments. Figure 3, shows four snapshots of the robot avoiding 70 moving obstacles. Despite the very challenging environment, the robot succeeds in reaching the goal while planning only one step at a time. This is largely due to the use of the minimum time horizon to truncate the velocity obstacles. This in turn drastically reduced the number of open nodes compared to the global search. Typical reductions have been between 0.1 to 0.2 of the number of nodes for the global search, a significant reduction that does not compromise safety. More simulations of this planner to navigate through busy traffic, and to coordinate the motions of multi-robots in the plane and in 3D can be viewed at www.ariel.ac.il/me/pf/shiller/vo.

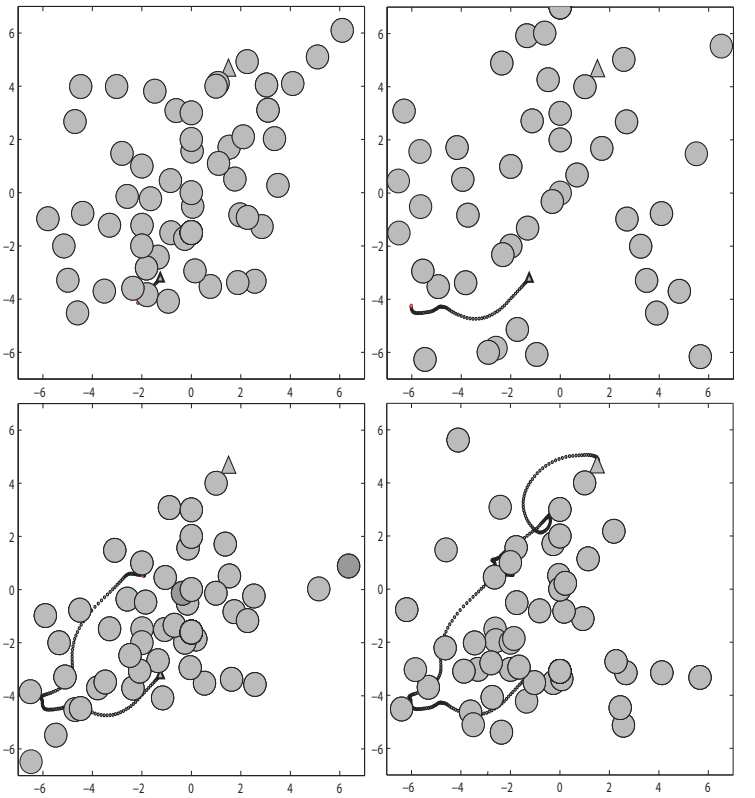

Figure 3. Avoiding 70 moving obstacles

6 Conclusion

A new time horizon for on-line planning in dynamic environments using velocity obstacles was presented. This time horizon is selected for each obstacle, static or moving, as the minimum time required to bring the robot velocity outside the velocity obstacle from the current state. Keeping the robot's velocity vector out of the velocity obstacle ensures that the robot does not enter unsafe states from which avoidance cannot be guaranteed. Recognizing unsafe states using the velocity obstacles is not only safe but also very efficient as it drastically reduces the search tree. The planner generates near time-optimal trajectories, using the minimum time-to-go to guide the tree search. The planner was demonstrated for a point mass dynamic model. Other robot models can be used with minor modifications.

The planner was successfully tested for crowded static and dynamic environments. It is suitable for real time generation of high speed trajectories in crowded static and dynamic environments.

Bibliography

N. Chan and J. Kuffner M. Zucker. Improved motion planning speed and safety using region of inevitable collision. In *ROMANSY*, pages 103–114, July 2008.

C. W. Dodge. *Euclidean Geometry and Transformations*. Dover Publications, 2004.

P. Fiorini and Z. Shiller. Motion planning in dynamic environments using the relative velocity paradigm. In *IEEE International Conference of Automation and Robotics*, volume 1, pages 560–566, May 1993.

P. Fiorini and Z. Shiller. Motion planning in dynamic environments using velocity obstacles. *International Journal of Robotics Research*, 17(7): 760–772, July 1998.

D. Fox, W. Burgard, and S. Thrun. The dynamic window approach to collision avoidance. *IEEE Robotics and Automation Magazine*, 4:23–33, 1997.

T. Fraichard and H. Asama. Inevitable collision state-a step towards safer robots? *Advanced Robotics*, 18:1001–1024, 2004.

J. Minguez and L. Montano. Nearest diagram navigation. a new real-time collision avoidance approach. In *International Conference on Intelligence Robots and Systems*, 2000.

S. Petti and T. Fraichard. Safe motion planning in dynamic environment. In *International Conference on Intelligence Robots and Systems*, 2005.

Z. Shiller, F. Large, and S. Sekhavat. Motion planning in dynamic environments: Obstacle moving along arbitrary trajectories. In *Proc. of the IEEE International Conference on Robotics and Automation*, 2001.

Z. Shiller, R. Prasanna, and J. Salinger. A unified approach to forward and lane-change collision warning for driver assistance and situational awareness. In *SAE 2008 World Congress*, volume SAE 2008-01-0204, Detroit, Michigan, April 2008.

Z. Shiller, O. Gal, and T. Fraichard. Motion planning in dynamic environments: the nonlinear velocity obstacle and safe time horizon. *In preparation*, March 2010.

Development of a Visual Interface for Sound Parameter Calibration of the Waseda Flutist Robot WF-4RIV

Klaus Petersen [1], Jorge Solis [2,3] and Atsuo Takanishi [2,3]

[1] Graduate School of Advanced Sci. and Eng., Waseda University, Tokyo, Japan
[2] Faculty of Science and Engineering, Waseda University, Tokyo, Japan
[2] Humanoid Robotics Institute, Waseda University, Tokyo, Japan
E-mail: klaus@moegi.waseda.jp, solis@ieee.org,
contact@takanishi.mech.waseda.ac.jp

Abstract The Waseda Flutist Robot WF-4RIV is a humanoid robot that is able to imitate a human flute performance. In the recent years the mechanical construction of the robot has been improved, so that the robot's playing capabilities have reached the level of an intermediate human instrument player. To make the robot able to play at this performance level, careful calibration of its musical parameters is necessary. Using the flutist robot's core control software, this procedure is very complicated to perform. In this paper we present the implementation of a visual control interface that allows also non-technical users to calibrate the sound settings. The newly developed control interface enables a musician to adjust certain parameters of the robot performance while the robot is playing. Experiments in which we verify the functionality of this sound calibration system are presented. We examine the visual processing system's perception of the instrument movements of a human performer and analyze their effect on the performance of the robot.

1 Introduction

Thanks to recent advances in computer science, electronics, sound processing and artificial intelligence, musical performance robot research has not been limited to only developing sound-making devices that automatically play musical instruments. In fact, several researchers have been interested in developing musical robots that are able to display human-like dexterity as well as an amount of intelligence required for playing musical instruments. From this point of view, the development of musical performance

robots provides opportunity to study human physiology and behavior from different approaches such as: Human-Robot Interaction (Solis et al., 2007); Human Motor Control (Solis et al., 2006b); Art/Entertainment (Weinberg and Driscoll, 2007) and Education (Solis et al., 2004).

The authors have been developing an anthropomorphic flutist robot to study the methodology of human motor control, to introduce novel ways of man-machine interaction and to propose interesting applications for humanoid robots (i.e. musical tutor, etc.). After initial stages of research the flutist robot has been capable of basic playing techniques, the sound production quality (fingering, breath control etc.) being similar to a flutist beginner's. After further developments, extended technical skills (Solis et al., 2006c), which are typically practiced by intermediate level flutists (i.e. vibrato, etc.), have been successfully implemented. More recently, in (Solis et al., 2006a), the authors have presented the Waseda Flutist Robot No.4 Refined III (WF-4RIII).

In this paper we present results on the development of a visual tracking system that enhances the possibility to calibrate performance parameters of the robot. The purpose of this interface is to allow a human without special technical skills to influence sound parameters of the robot (e.g. vibrato amplitude) in an intuitive fashion. As most skilled musicians that might use the flutist robot as a musical tool do not have the necessary technical skills to operate the core control software of the robot, improvement of the procedure of adjusting these settings is necessary to give more users the possibility to operate robot.

2 Waseda Flutist Robot No.4 Refined IV

The Waseda Flutist Robot No.4 Refined IV (WF-4RIV) has a total of 41-DOFs (Figure 1a), which mechanically emulate the human organs involved in flute playing (Solis et al., 2008).

The robot has humanoid arms and fingers that strike the keys of the flute. The air pressure to produce the flute sound is generated using a lung mechanism. The lung compressor has two (right and left) parts similar to the human lung shape. The air is transferred into the oral cavity of the robot through a tube system. There is an artificial vocal cord that is used to regulate the strength of the air stream coming from the lung. During a performance, periodic (opening / closing) movement of the vocal cord applies a vibrato effect the sound of the flute play. The oral cavity contains a tonguing mechanism to make more precise note-to-note transitions possible. When the air stream leaves the oral cavity it is shaped using an artificial lips mechanism that generates the characteristic beam to produce the flute

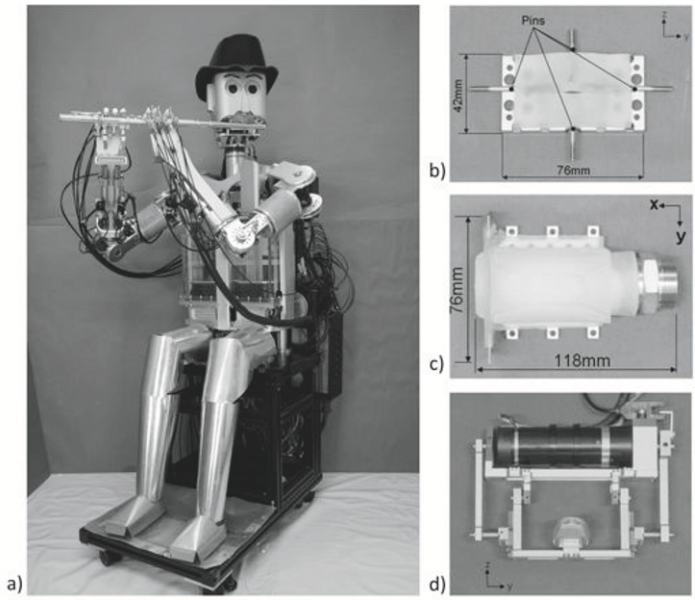

Figure 1. The Waseda Flutist No.4 Refined IV (WF-4RIV) and its newly developed lips, tonguing and oral cavity mechanisms.

sound.

In recent research the design of the lips and the tonguing mechanism (2-DOFs) has been improved: Due to the use of a new material with very realistic shape and elasticity properties for the lips, a more natural sound can be generated. The improved tonguing mechanism allows accurate control of note attack times and enhances the double tonguing (extended technical skill) capabilities of the robot. In addition, the implementation of an auditory feedback control system to enable the robot to improve its own performance has been proposed.

Building upon this achievement, we focused our latest research on improving the capabilities to control the robot's sound calibration parameters more comfortably. Up to now the procedure of setting these parameters could only be achieved by an expert in controlling the robot, as understanding of the usage of the robot's control-software was necessary. Using the visual control system, a musician without technical skills can adjust the robot's performance parameters with instrument gestures. In this case the movements of the musician's interface are translated into values that adjust

the robot's sound setting. In the experimental section we show how a musician can control the vibrato amplitude of the robot's flute performance. The vibrato is generated by movement of the artificial vocal chord of the robot. By moving the instrument the user of the robot can effectively control the amplitude of the opening-and-closing motion of the vocal chord.

3 Instrument Position Mapping

In the first stages of our research, we have concentrated on creating a visual interface, that enables a human to control the robot through gestures with his musical instrument. Our emphasis here is to create an interface, that allows to control the sound parameters of the robot accurately, but also robustly and computationally efficiently (at a later stage we would like among other things to perform audio processing on the same hardware). In order to satisfy those requirements, we propose to implement color histogram matching (Saxe and Foulds, 1996) and particle tracking (Arulampalam et al., 2002) to follow the movement of a musical instrument, while satisfying the previously introduced requirements.

We model the shape of the saxophone as a line. The hands of the player are located on two spots on that line. The average of the position of the hands is recorded as the center position of the saxophone. Similarly we deal with the orientation: We consider a line drawn from the center of one hand to the center of the other. The inclination of the line is the orientation of the instrument.

¿From the 2D coordinates of the four hand particles we calculate the relative position, inclination and rotational angle of the instrument. To compute the depth values of both hands we use a z-transformation:

$$\Delta x_p = abs(x_{pl} - x_{pr}), z = \frac{1}{\Delta x_p}\alpha \tag{1}$$

Δx_p is the distance between the X-coordinate of the patch in the left camera image (x_{pl}) and the right camera image (x_{pr}). Accordingly z denominates the Z-coordinate of the patch. We use α as a constant to adjust the value of Δz for further calculations.

We use a Cartesian coordinate system parallel to the view plane of the robot to calculate roll (ϕ), pitch (θ) and yaw (ρ) inclination of the instrument.

$$\phi = arctan(\frac{\Delta y}{\Delta x}), \theta = arctan(\frac{\Delta y}{\Delta z}), \rho = arctan(\frac{\Delta x}{\Delta z}) \tag{2}$$

A particle filter is a Bayesian filter method that uses randomly generated samples to approximate an unknown state configuration. Similar to a

Kalman filter it works in prediction-update cycles. It is considered to be superior to other filtering schemes used in object tracking (Hess and Fern, 2007).

A Bayesian filter represents the PDF (Probability Density Function) $p(\underline{x}_k|\underline{z}_{k-1})$ of state $\underline{x}_k$ given observation $\underline{z}_{k-1}$ were k is the discretized time. Specifically for the particle filter this PDF is defined through a set of N_s random measurements $\underline{s}_k^i$ with weights π_k^i. In this case, the current observation $\underline{X}_k$ is given by

$$\underline{X}_k = \sum_{i=1}^{N_s} \pi_k^i \underline{s}_k^i \tag{3}$$

and the PDF $p(\underline{x}_k|\underline{z}_{k-1})$ can be approximated as (Arulampalam et al., 2002)

$$p(\underline{x}_k|\underline{z}_{k-1}) \approx \sum_{i=1}^{N_s} \pi_k^i \delta(\underline{x}_k - \underline{s}_k^i) \tag{4}$$

with

$$\sum_{i=1}^{N_s} \pi_k^i = 1 \tag{5}$$

δ denotes the Dirac delta function. $\delta(\underline{x}_k - \underline{x}_k^i)$ represents the deterministic relationship between the random samples and the actual state. Both of the above equations show, how we gather random samples, assign them with weights and construct an approximation of our actual state. The random samples (or particles) are our sensor input, that we use to predict a new location of the object of interest. We restrict the algorithm to a limited set of samples N_s to keep the computational effort manageable / real-time.

4 Experiments and Results

We performed two types of experiments: In each of the experiments the vibrato amplitude of the flute player is manipulated by changing the saxophone orientation. We considered that the absolute positioning of the saxophone relative to the robot does not have to be evaluated: the orientation of the saxophone is calculated from the absolute position values of the hands. Thus, is the absolute position of the instrument calculated as the mean of the hand positions. The saxophone can be rotated by the player, in terminology changing *pitch*, *roll* and *yaw*. We did not assign any function to the yaw, as normally a saxophone player will not move the instrument in this way. Modes of individual experiments as follows:

1. Variation of the *roll* changes the vibrato amplitude of one tone, that the robot is playing.

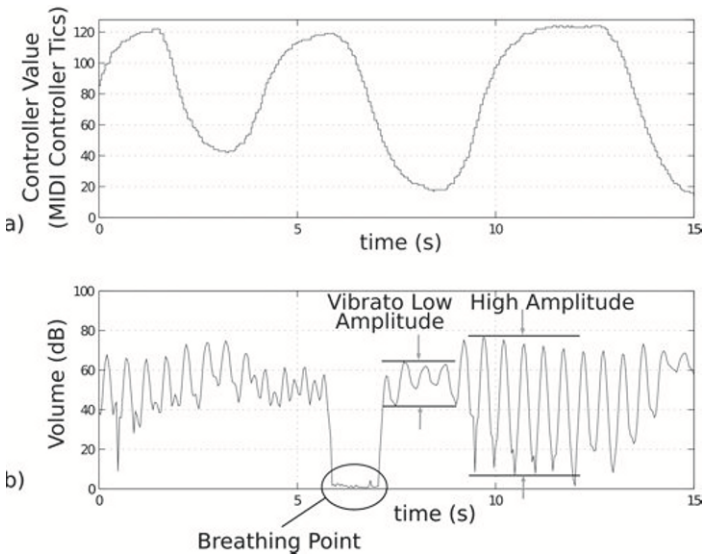

Figure 2. a) The recorded roll inclination data of the musical instrument. In the experiment, a musician performed a continuous regular up-and-down motion. b) The volume plot of the tone played by the flutist robot. Representative areas for strong Vibrato and Vibrato with low amplitude are indicated. We notice a significant volume drop (at 6s), when the artificial lung of the robot is deflated and needs to be refilled with air.

2. Changing the *pitch* (orientation) manipulates the vibrato amplitude of the tone, that the robot is playing.

As described in the previous section, we have requirements for our method to fulfill certain standards in recognition quality and ease of use. In our experiments we tried to give rather a qualitative than quantitative examination of the characteristics of our method. As performance environments may strongly vary, we tested our system with different backgrounds and varying lighting conditions.

Fig. 2 and Fig. 3 show that the visual input to our system does closely relate to its acoustic output. In the graphs areas of high and low vibrato amplitudes are marked. These areas match with the controller data peaks and troughs, respectively.

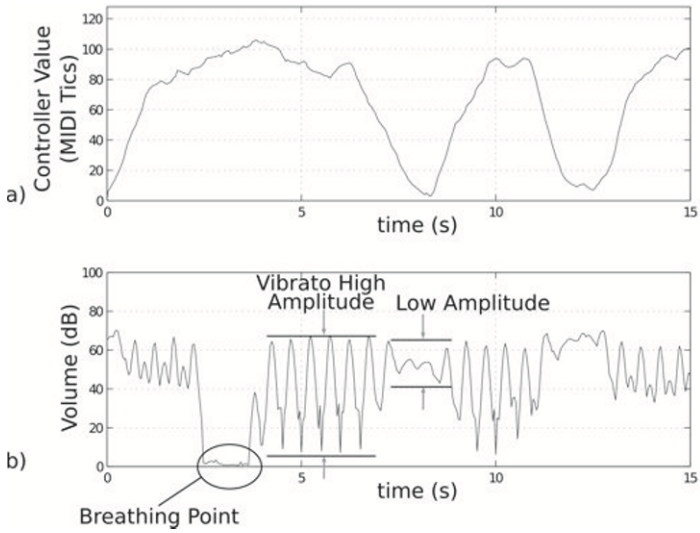

Figure 3. a) The recorded pitch inclination data of the musical instrument. Again, the musician performed a continuous regular up-and-down motion. The recorded information is notably more noisy than in the case of the previous experiment (Figure 2). b) Again, the volume plot is shown, with indicators for strong and weak vibrato. The breathing point occurs at 2.5s.

5 Conclusion and Future Works

In this paper, we have displayed our current research on the development of the Waseda Flutist Robot No.4 Refined IV (WF-4RIV). Besides presenting significant improvements of the actual sound production mechanisms, we have shown our preliminary results in enhancing the calibration system of the WF-4RIV. Performance sound parameters can be manipulated visually in real-time by instrument gestures of the musician partner of the robot. Through this a part of the calibration procedure necessary for the operation of the robot can be facilitated by non-technical users.

We plan to integrate the pressure sensors built into the lip mechanism of the robot with the overall motor control system. The goal is to dynamically readjust the flute position during a performance in order to provide consistent sound results. To achieve this we currently perform experiments to determine the relation between sensor output, flute position and sound quality. In future works we will feed the sensor output to the robot's motor control software to adjust the position parameters of the arms and hands.

Bibliography

M. Arulampalam, S. Maskell, N. Gordon, and T. Clapp. A tutorial on particle filters for online nonlinear / non-gaussianbayesian tracking. In *IEEE Transactions on Signal Processing*, pages 174–188, 2002.

R. Hess and A. Fern. Improved video registration using non-distinctive local image features. In *Proceedings IEEE Conference on Computer Vision and Pattern Recognition (CVPR)*, pages 127–151, 2007.

D. Saxe and R. Foulds. Toward robust skin identification in video images. In *2nd International Conference on Automatic Face and Gesture Recognition*, pages 379–384, 1996.

J. Solis, S. Isoda, K. Chida, A. Takanishi, and K. Wakamatsu. An anthropomorphic flutist robot for teaching flute playing to beginning students. In *Proceedings of the IEEE International Conference on Robotics and Automation*, pages 146–150, 2004.

J. Solis, K. Chida, K. Suefuji, and A. Takanishi. The development of the anthropomorphic flutist robot at waseda university. *International Journal of Humanoid Robots*, 3:127–151, 2006a.

J. Solis, K. Suefuji, K. Chida, K. Taniguchi, and A. Takanishi. The mechanical improvements of the anthropomorphic flutist robot wf-4rii to increase the sound clarity and to enhance the interactivity with humans. In *Proceedings of the Sixteenth CISM-IFToMM Symposium on Robot Design, Dynamics, and Control*, pages 247–254, 2006b.

J. Solis, K. Suefuji, K. Taniguchi, T. Ninomiya, M. Maeda, and A. Takanishi. Implementation of expressive performance rules on the wf-4riii by modeling a professional flutist performance using nn. In *Proceedings of the IEEE International Conference on Automation and Robotics*, pages 312–317, 2006c.

J. Solis, K. Suefuji, K. Taniguchi, T. Ninomiya, M. Maeda, and A. Takanishi. Implementation of expressive performance rules on the wf-4riii by modeling a professional flutist performance using nn. In *Proceedings of the IEEE International Conference on Robotics and Automation*, pages 2552–2557, 2007.

J. Solis, K. Taniguchi, T. Ninomiya, and A. Takanishi. Understanding the mechanisms of the human motor control by imitating flute playing with the waseda flutist robot wf-4riv. *Mechanism and Machine Theory*, 44(3): 527–540, 2008.

G. Weinberg and S. Driscoll. The perceptual robotic percussionist: New developments in form, mechanics, perception and interaction design. In *Proceedings of the ACM/IEEE International Conference on Human-Robot Interaction*, pages 97–104, 2007.

Simulation of a Humanoid Robot walking gait on Moon Surface

Aiman Musa M. Omer[1], Hun-ok Lim[2], and Atsuo Takanishi[3]

[1] Graduate School of Science and Engineering, Waseda University, Tokyo, Japan
[2] Department of Mechanical Engineering, Kanagawa University, Yokohama, Japan
[3] Department of Mechanical Engineering / Humanoid Robotics Institute, Waseda University, Tokyo, Japan

Abstract. Humanoid robots are developed to be used in many areas in the human environment, especially area where it is highly dangerous for human to work or live in. Outer space or even the moon surface is one of the areas where are people trying to explore, but it is highly risky and costly. Sending humanoid robot to the moon could one of the solution to explore the moon surface and research on the real effect of the moon gravity on human walking motion. Using dynamic simulation we can have an approach to imitate human walking gait and analyze the effect of the low gravity which could result on the walking velocity.

1. Introduction

The explosion of the outer space has been a great interest for human begins since centuries ago. Physical exploration of space began in the mid of the 20th century by robotics spacecraft before human could successfully go to space in a Human spaceflight in late fifties. Successful exploration of the space had extended the human interests to exit the Earth orbit and reach fare planets. The challenge of exploring the moon and land on it surface has driven the research and development for the technology to reach the goal. The first robotics spacecraft to reach the surface of the moon with an impact was Luna 2 in 1959. Further attempts had been made to make a soft landing on the surface until it was successfully made in 1966 by Luna 9. Human spacecrafts were not developed to operate out of the Earth orbit until the 1968 when Apollo 8 carrying three astronauts flew around the moon and returned safely to earth. This had lead the first human walk on the moon by Neil Armstrong in 1969, a part of Apollo 11 mission which was the first manned spacecraft to the moon. The NASA`s Apollo program had made nine missions to the moon all occurred between 1968 and 1972. The high cost of sending human to the moon had stopped the any planned mission after 1972. Moreover, great risk of the mission could be also considered.

After more 30 years from the last manned mission to the moon, many countries

are now developing projects and research to send human beings back to the moon. Currently, EU, India, China, Japan, USA, and even Russia are under developing manned missions to the moon by 2020 to 2030. Recently, there are several robotics spacecrafts impacted on moon surface or flying around the moon orbit. The future planes are to construct bases on the moon surface for several purposes including scientific research. However, this will required many aspects concerning the payload work, safety, and energy. Therefore, the use of space robotics could reduce the load work on astronauts by providing assistance, and reduce cost for sending large number in a group or life support system.

The Japan Aerospace Exploration Agency (JAXA) has proposed a plane to explore the moon using bipedal walking robots. The proposal is being considered as a part of Japan's new space strategy. Sending bipedal robot to the moon to on its surface has never been achieved. Success in operating a bipedal walking robot could extend for further robotics mission in the moon. Japan advanced robotics technology could be used to develop and build a moon base and work with astronauts in many operates needed be conducted during moon exploration.

In Japan many bipedal walking robots had been developed by different research groups and institutes. For examples, ASIMO a humanoid robot that is developed by HONDA. The Japanese National Institute of Advanced Industrial Science and Technology (AIST) and Kawada Industries, Inc. have developed HRP-2P. These robots are highly advanced and can perform bipedal walking motion. In Waseda University a long research has been going in developing a bipedal walking robot. The latest achievement made is the development of WABIAN-2R (Waseda Bipedal Humanoid), which is capable of simulating human walking motion. The major difference that was achieved by WABIAN-2R is the ability to perform a human like walking motion with stretched knees where other bipedal robots walk with bend knees stable walking motion. The use of WABIAN-2R on the moon surface could help for the research and understanding the effect of moon gravity on human walking motion.

The concern about walking on the moon is the low gravity. It may case a high velocity of movements which will make the walking motion unstable. Therefore, the astronauts whom had landed on the moon were in fact jumping or even running. In order to perform a walking gait motion, the velocity should decrease to have a stable walking. Simulating walking gait using WABIAN-2R, which can walking much similar to human than other robots, could be tested and checked through a dynamic simulation. The performance in the dynamic simulation could give an approach to word the real walking robot on the moon.

2. Walking Behavior on Moon Gravity

The ability of walking on moon surface could face many difficulties due to the low

gravity which is one sixth of the earth gravity. This will have a great impact in the dynamical behavior due reduction in the potential energy store in each step. Therefore, the amount of kinetic energy that is transform from potential energy will be decrease. Less amount of kinetic energy will result in low velocity for a walking gait. The increase of the mechanical energy will either be by increasing the vertical displacement which will result in switching to running gait instead of walking gait, or increase the mass of the body which is not probably accepted.

2.1. Human body modeling

The human body could be modeled as a spring damper system. The leg could act as a spring that store potential energy and released it during walking, as shown in figure 1. A low stiffness elastic leg model is the form of running gait simulation where the higher stiffness will result in a walking gait. In the running gait the vertical displacement with respect to the step is slightly high compare to the walking gait. In the case of low gravity, the vertical displacement increases which could decrease the stability of movement. Therefore, high stiff leg could increase the motion stability in a walking gait.

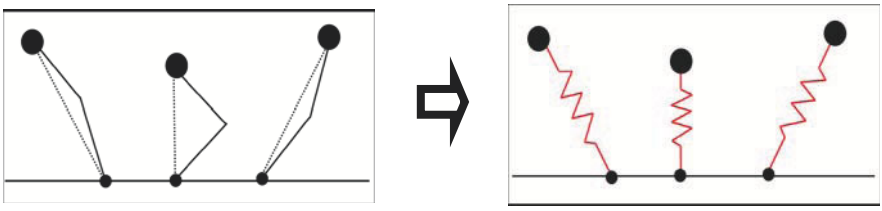

Figure 1. Modeling of the leg in terms of spring system

The walking gait for locomotion could be simulated in terms of an inverse pendulum. The body is supported by the leg and rotating around the ankle joint, as shown in figure 2. In order to perform the walking gait properly the rotational velocity has to be quite enough to complete the step cycle. Moreover, the velocity must be too large otherwise the normal acceleration will be larger than the gravitational acceleration which is in the opposite direction.

The period of the step cycle which is defined by the law of the pendulum:

$$P = 2\pi \sqrt{(l / g)}$$

Where l is the leg length and g is the gravity. Since the moon gravity is lower than the earth gravity, the step cycle period will increase which means long time to complete one step on the moon surface than on earth.

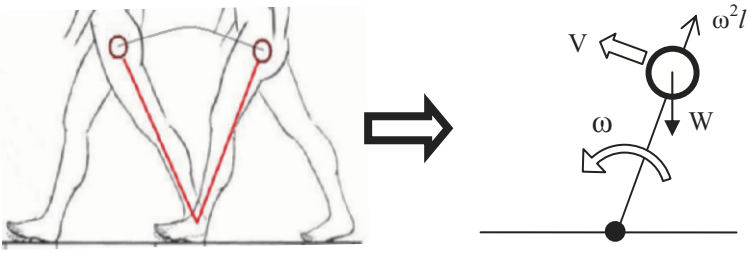

Figure 2. Human Walking gait as Inverse Pendulum system

2.2. Froude number

Froude number is a dimensionless ratio of centripetal force to gravitational force. It could set as:

$$Fr = v^2/gl$$

where v is the forward velocity of the body, g is the gravitational acceleration, and l is the length of the leg. Froude number is used to determine the walking velocity according to the gravity.

Walking gait for locomotion is defined as a movement with keeping a least one foot connected to the ground. On the other hand, running gait could make by lifting both feet for ground at some point, it could for a long or a short period of time depending on leg length or velocity. The maximum walking velocity is approached when the double phase, both feet are touching the ground, is equally zero. This is classified as walk-run transition where it is transfer from walking gait to running gait. Scientific researches found that the Froude number for maximum velocity is closely to 0.5. The walking velocity could be a function of gravity for a walking style by setting the Froude number as a constant value. However, since the leg length is constant value as the Froude number, the velocity is the square root of the gravitational acceleration.

$$v = \sqrt{(g\, l\, Fr)}$$

For compression between the velocity on earth and the velocity on the moon both could be divided as

$$v_{Earth} / v_{Moon} = \sqrt{(g_{Earth}\, l\, Fr)} / \sqrt{(g_{Moon}\, l\, Fr)}$$

by solving the above equation, the velocity on the moon will be

$$v_{Moon} = v_{Earth} \sqrt{(g_{Moon} / g_{Earth})}$$

since the moon gravity is one sixth of the earth gravity, the velocity on the moon surface with respect to velocity on earth is as follow

$$v_{Moon} \approx 0.4\, v_{Earth}$$

If the same walking gait performed on the earth and is needed to be performed on the moon, the velocity should be reduced to almost 40 per cent. Some researches and studies show that the maximum possible walking velocity for a 0.9 m leg long is close to 3 m/s. Therefore, the maximum velocity on the moon could be about 1.2 m/s.

3. Control Method of the Robot

WABIAN-2R control system is trajectory positioning control base. It reads the trajectory planning for waist, foot, and hand from a pattern file previously generated. And through inverse kinematics method the controller calculate the each joint position. The walking pattern is generated base on ZMP (Zero Moment Point) method which is a general theory for bipedal walking robot. WABIAN-2R control loop is run every 30 ms. The low level control of the system control the actuator velocity by checking the difference between the current and target position with respect to the control loop timing.

When the simulation of the walking on low gravity the forward velocity must be decreased in order to have a stable walking gait. The velocity of the robot on the moon surface will have to be reduced to about 40%. The waist and feet of the robot has a trajectory planned based on position and each phase has to be operated each 30 ms. However, since the positions will not change if the same pattern of walking gait is used on the moon, the control loop timing has to be increase in order to slow the motion of legs. Therefore, the step time will be increase to about 250% to have the reduction on the velocity. The controller of the robot run with 75 ms for one control step to perform the slow motion need on the moon.

4. Simulation Result of Walking Motion

To simulation a real physical environment of the moon is highly difficult due to low gravity simulation on the earth. Therefore, computer simulation could give an easy approach for simulating robot walking in low gravity. In our research we use Webots which is a highly advanced and fast prototyping and Simulation used for mobile robots. We modeled the structure of our robot WABIAN-2R and the simulation environment of the moon. The simulation can show the behavior of the robot walking in such a low gravity.

We run the simulation of the robot by setting the control step to 30 ms which is the same that is used for the real walking simulation. The robot slipped of the ground due to the high velocity of the leg motion and fell down. However, when the control step is increased to 75 ms, the walking motion was going smoothly and stable (see

figure 3). The walking motion with high control step (75 ms or higher) could result on better stability of walking motion but it requires a longer time due to the slow motion and high time to complete one step. The walking pattern took 38.4 second to have a stable walking on the moon gravity where it takes 15.36 second to complete the same walking pattern when it is on earth gravity. The velocity data shows a little bite of disturbance due to the angular momentum which could increase in low gravity satiation (see figure 4).

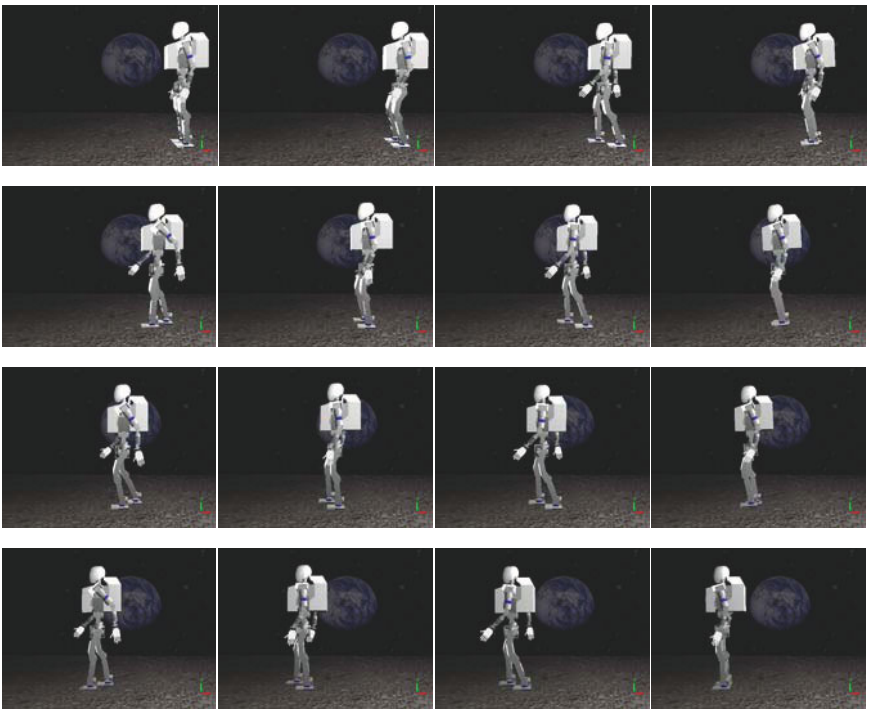

Figure 3. Simulation of walking gait on Moon Surface

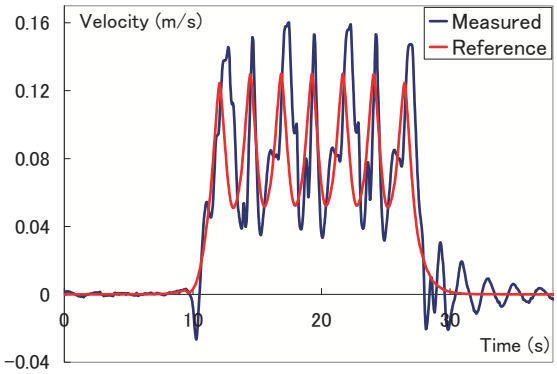

Figure 4. Forward Velocity (X axis) Data

5. Conclusion & Future Work

The walking of a bipedal humanoid robot is be tested and checked through dynamic simulation. For achieving high stability for walking gait on moon gravity, long time is needed to complete one step cycle. If higher velocity of forward movement on the moon surface is needed, transferring to running gait could be the only solution for stable motion.

The future work in this research involves development of walking and running method on low gravity. Successful achievement in this filed will help to design a real prototype the can be send to the moon in future mission for moon exploration.

References

Alexander, R. M. (1996). Walking and running. *The Mathematical Gazette,* Vol. 80, No. 488, pp. 262-266.

Breniere, Y. (2001). Simulation of gait and gait initiation associated with body oscillating behavior in the gravity environment on the Moon, Mars and Phobos. *Biological Cybernetics,* Vol. 84, No. 4, pp. 261-267.

Donelan, JM., Kram, R. (1997). The effect of reduced gravity on the kinematics of human walking: a test of the dynamic similarity hypothesis for locomotion. *Journal of Experimental Biology,* Vol 200, Issue 24, pp. 3193-3201.

Donelan, JM., Kram, R. (2000). Exploring dynamic similarity in human running using simulated reduced gravity. *Journal of Experimental Biology*, Vol 203, Issue 16, pp. 2405-2415.

Kram, R., Domingo, A., Ferris, DP. (1997). Effect of reduced gravity on the preferred walk-run transition speed. *Journal of Experimental Biology*, Vol 200, Issue 4, pp. 821-826.

Margaria, R. (1976). Biomechanics and energetics of muscular exercise, Oxford University Press.

Oda, M. (2008). JAXA's Space Robotics Road Map. In *Proceedings of International Symposium on Artificial Intelligence, Robotics and Automation in Space.* Hollywood, USA, February 26 - 29, 2008.

Vaughan, C., O`Malley, M. (2005). Froude and the contribution of naval architecture to our understanding of bipedal locomotion. *Gait & Posture*, Vol. 21, Issue 3, pp. 350-362.

Development of New Biped Foot Mechanism Mimicking Human's Foot Arch Structure

Kenji Hashimoto[*], Yuki Takezaki[†], Kentaro Hattori[†], Hideki Kondo[†], Takamichi Takashima[‡], Hun-ok Lim[¶, §] and Atsuo Takanishi[*, §]

[*] Department of Modern Mechanical Engineering, Waseda University, Japan
[†] Graduate School of Science and Engineering, Waseda University, Japan
[‡] College, National Rehabilitation Center for Persons with Disabilities, Japan
[¶] School of Engineering, Kanagawa University, Japan
[§] Humanoid Robotics Institute, Waseda University, Japan
E-mail: k-hashimoto@takanishi.mech.waseda.ac.jp

Abstract. The humanoid robot, WABIAN-2R, has achieved human-like walking with heel contact and toe off motions with a foot mechanism with a passive toe joint. However, the foot structure is different from a human's. In this paper, we describe a new foot mechanism mimicking the human's foot arch structure to figure out its function. Especially, the developed foot mimics the elastic properties of the arch and the change of the arch height during walking. We conducted several walking experiments by using WABIAN-2R, and we confirmed that the arch elasticity could absorb a foot-landing impact force at the plantar contact phase and the change of the arch height contributed to a strong thrust at the push-off phase.

1 Introduction

A human foot is anatomically composed of 26 bones excluding sesamoid bone. Considering that an adult human body has 206 bones, a quarter of the bones concentrate in the feet. A human foot has a complex structure, and few mammals, including humans, have a foot arch structure.

There are several theories about the reasons for the existence of the human's foot arch structure. The development of the medial longitudinal arch was a primary step in the evolution of bipedal human gait (Day and Napier, 1965; Morton, 1924). This terrestrial modification to the arboreal foot had two major effects. First, it provided the plantarflexors enough mechanical advantage to lift the weight of the body during the stance phase (Morton, 1924; Schultz, 1963). Second, it provided the foot with the capacity to absorb some of the increased shock caused by upright striding (Ker et al., 1987). The transformation of the grasping function of the medial rays of our primate ancestors into the plantigrade propulsive feet of modern human was clearly a seminal event in prehuman evolution (Harris, 1990). But few theories verified the

significance of arch structure quantitatively. The reasons for the existence of the arch structure are still remain to be clarified.

Meanwhile, we have developed a biped humanoid robot named WABIAN-2R (Waseda Bipedal humanoid - No.2 Refined) to simulate human motion (Ogura et al., 2006) (see Figure 1). WABIAN-2R has a foot with a passive toe joint and achieves a human-like walk with the knees stretched, heel-contact and toe-off motion. However, the foot of WABIAN-2R is different from the human's on the point that the foot sole is flat and the foot breadth is wide. In this paper, we aim to clarify the function of human foot in gait. We develop a new biped foot mechanism mimicking a human's foot arch structure and verify the significance of arch structure quantitatively through walking experiments by WABIAN-2R mounted on the new feet.

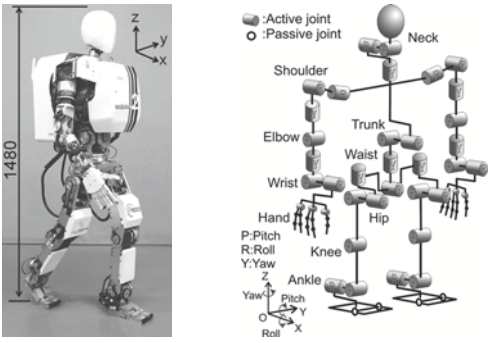

(a) (b)

Figure 1. WABIAN-2R: (a) Overview; (b) DOF Configuration.

2 Development of Human-like Foot Mechanism

2.1. Modeling of Human's Foot Arch Structure

The human foot has three arches; the medial longitudinal arch, the lateral longitudinal arch, and the transversal arch (Kapandji, 1988). The chief characteristic of the medial longitudinal arch is its elasticity, due to its height and to the number of small joints between its component parts. The lateral longitudinal arch allows only a limited movement. The most marked features of this arch are its solidity and its slight elevation compared with the medial longitudinal arch. The transversal arch is elastic to follow the unevenness on a ground and cannot keep the arch structure when a large load is applied during walking. The stiffness of the arch was identified at the following four phases in a gait cycle (see Figure 2);

I. Heel contact phase
II. Plantar contact phase
III. Push-off phase
IV. Swing phase

In the phase I, the medial longitudinal arch is elastic because a load isn't applied. In the phase II, it provided that the foot can absorb a foot-landing impact force (Ker et al., 1987). In the phase III, the toes are extended, and they pull the plantar pads and hence the aponeurosis forward around the heads of the metatarsals, like a cable being wound on to a windlass (Hicks, 1954) (see Figure 3 (a)). As a result, the arch is caused to rise because the distance between the metatarsal heads and the calcaneum is thereby shortened. The arch becomes the stiffest in a gait cycle. In the phase IV, the arch becomes elastic again because a foot is unloaded. The characteristics of the human's foot are the changes of the elasticity of the medial longitudinal arch with the change of the arch height during walking.

In this research, we approximate the arch structure by a rotational spring and damper as shown in Figure 3 (b), referring to the Takashima's method (Takashima et al., 2002). The identified viscoelasticities of k Nm/rad and c Nm/rad^2 show different values in a gait cycle as shown in Table 1. In this paper, we focus on only the medial longitudinal arch because the change of its elasticity is much larger than the lateral longitudinal arch and the transversal arch. The foot is classified into the following four parts; the medial toe, the lateral toe, the medial plantar and the ankle-lateral plantar (see Figure 4 (a) and (b)).

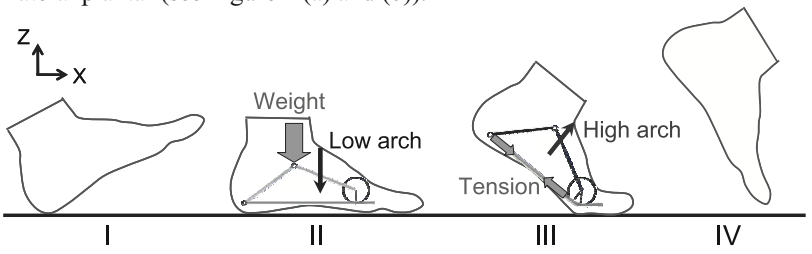

Figure 2. Transformation of medial longitudinal arch in a gait cycle.

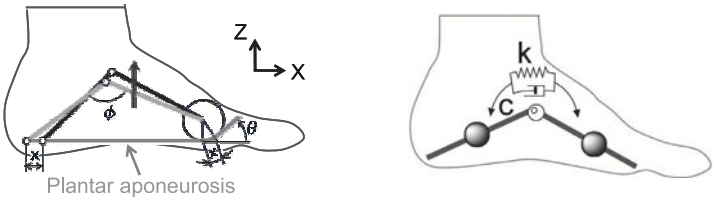

Figure 3. Modeling of human's foot arch structure: (a) Windlass mechanism (Hicks, 1954); (b) Foot model with a rotational spring-damper.

We set the targets of arch viscoelasticity to the elasticity in the phase II and the phase III. We designed a new foot mechanism as shown in Figure 5 to mimic the change of the elasticity with the change of the arch height. It consists of a toe axis, an arch axis and a wire that mimics the plantar aponeurosis to realize the windlass mechanism. It has two soft materials to limit the arch movement, and it can realize the change of the arch elasticity during walking.

Table 1. Viscoelasticity at each phase (Takashima et al., 2003).

	I	II	III	IV
Elasticity k Nm/rad	19	386	488	-19
Viscosity c Nm/rad^2	17	24	8	3

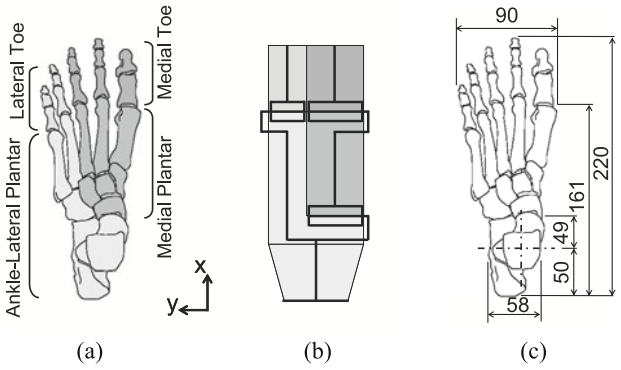

Figure 4. Foot skeleton model (left foot): (a) Parts; (b) 3-DOF model; (c) Dimension of human-like foot mechanism.

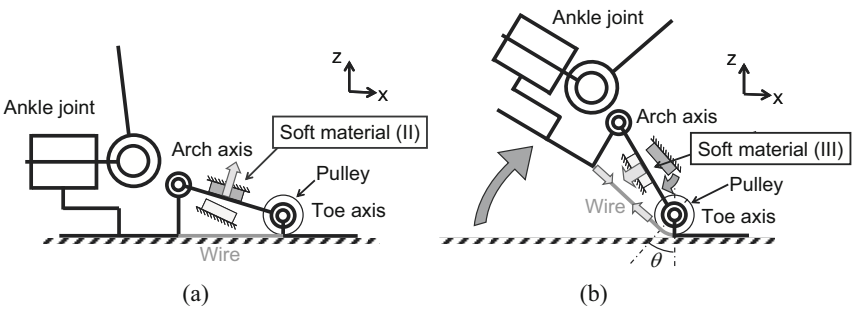

Figure 5. Joint configuration: (a) Phase II; (b) Phase III.

2.2. Human-like Foot Mechanism Design

Fugure 6 shows the human-like foot mechanism developed. Its weight is 1.1 kg equal to a human's foot, and its size and the position of each joint axis are determined based on the converted size by the mean size of adult women's feet (Kouchi and Mochimaru, 2005) using the WABIAN-2R's height (see Figure 4 (c)). It has a medial toe axis, a lateral toe axis and an arch axis. A medial toe axis and an arch axis are connected by a wire which mimics the plantar aponeurosis, and we selected a stainless wire which has a high mechanical strength and a high stiffness. The toes are passive joint as the previous research (Ogura et al., 2006). The developed foot also mimics the change of the arch height in the phase II and the phase III.

The developed foot mechanism mimics the rotational spring constant by attaching a soft material between the foot frame and the stopper. The soft material is selected through compression tests using a universal testing machine as shown in Figure 7. A compressive load is applied to the developed foot with the universal testing machine, and a rotational spring constant is calculated from the moment about the arch axis.

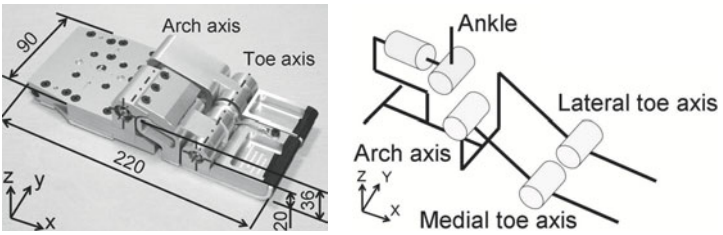

(a) (b)

Figure 6. Human-like foot mechanism (left foot): (a) Photograph; (b) DOF configuration.

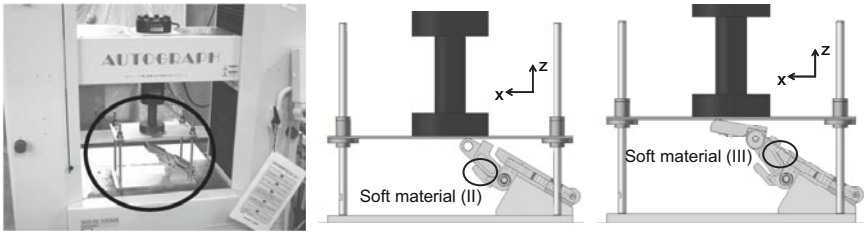

(a) (b) (c)

Figure 7. Experimental system testing the foot: (a) Experimental setup; (b) Configuration for the phase II; (c) Configuration for the phase III.

After conducting experiments repeatedly by changing kinds and thickness of soft material, we selected a polyurethane rubber whose Shore hardness is Shore A 30 with 10 mm thickness as the soft material in the phase II.

On the other hand, the rotational spring constants had a constant value as 60 Nm/rad even if we changed kinds and thickness of soft material, and we could not find significant differences of rotational spring constants among soft materials. This is because a stainless wire mimicking the plantar aponeurosis is "a stranded wire" and it can be stretched at a low-load condition. The soft material for the phase III cannot be compressed enough due to the stretch of the stainless wire. To mimic the rotational spring constant k_{III}, a wire which is hard to be stretched should be selected, or the foot mechanism itself should be reconsidered.

However, the developed foot mimics the rotational spring constant at the phase II and the change of the arch height during walking. It is possible to verify the shock absorbing function at the phase II which is explained as a hypothesis about the reason for the existence of the arch structure in ergonomics field (Ker et al., 1987). It is also possible to verify the function of the windlass mechanism related to the change of the arch height. So we conducted some experiments described in the next chapter.

3 Experimental Tests and Consideration

3.1. Verification of Walking with Human-like Foot Mechanism

Because the breadth of the developed foot is as narrow as 90 mm, we must confirm whether a humanoid biped robot, WABIAN-2R can walk with the knees stretched, heel-contact and toe-off motion. The human-like foot mechanism was attached to WABIAN-2R, and forward walking experiments were conducted with a step length of 450 mm/step and a walking cycle of 1.0 s/step. Although we applied a polyurethane rubber with the hardness of Shore A 30 and the thickness of 10 mm to the soft material in the phase II, we tentatively applied a polyurethane rubber with the hardness of Shore A 70 and the thickness of 5 mm to the soft material in the phase III, and the medial longitudinal arch is transformed by the stainless wire. Then the rotational spring constant in the phase III is 60 Nm/rad. As shown in Figure 8 (a), WABIAN-2R mounted on the human-like foot mechanism realized a stable walk with the knees stretched, heel-contact and toe-off motion.

3.2. Consideration of Function of Foot Arch Structure

We compared the vertical ground reaction forces when a polyurethane rubber (Shore A 30 and 10 mm thickness) is attached to the arch and when a fixation part is attached to the arch.

Figure 8 (b) shows the ground reaction force in a gait cycle. At the beginning of the phase II, the foot-landing force with fixed-arch condition was larger than that with movable-arch condition. So, we confirmed that the foot can absorb a foot-landing impact force by the elasticity of the medial longitudinal arch.

We can also find that the ground reaction force with movable-arch is larger than that with fixed-arch at the end of the phase II. It is considered that the windlass mechanism which causes the change of the arch height contributes to this strong thrust at the push-off phase. If the heel point is fixed in Figure 3, the toe position moves to the left with elevation of the arch height, and this movement contributes to the strong thrust at the push-off phase.

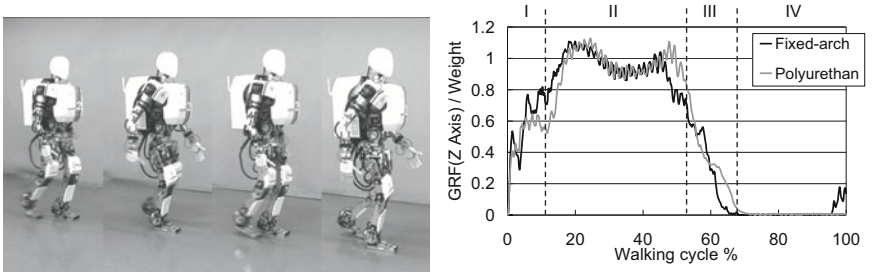

(a) (b)

Figure 8. Walking experiment with human-like foot mechanism developed. The walking cycle is 1.0 s/step and the step length is 450 mm/step: (a) Sequential photographs; (b) Vertical ground reaction force in a gait cycle. GRF with movable-arch is smaller than GRF with fixed-arch at the beginning of the phase II. GRF with movable-arch is larger than that with fixed-arch at the end of the phase II.

4 Conclusions and Future Work

To clarify the function of the foot arch structure, we developed a new human-like foot mechanism that mimics the changes of the elasticity of the medial longitudinal arch with the change of the arch height during walking. As experimental results using a biped humanoid robot, WABIAN-2R mounted on the new human-like foot mechanism, we confirmed that the arch elasticity could absorb a foot-landing impact force at the plantar contact phase and the windlass mechanism which caused change of the arch height contributed to a strong thrust at the push-off phase.

At the present stage, the mimesis of the elasticity at the phase III has not realized. Therefore, we will improve the human-like foot mechanism and continue to research to clarify the function of the arch structure quantitatively.

Acknowledgment

This study was conducted as part of the Advanced Research Institute for Science and Engineering, Waseda University, and as part of the humanoid project at the Humanoid Robotics Institute, Waseda University. It was also supported in part by Global COE Program "Global Robot Academia" from the Ministry of Education, Culture, Sports, Science and Technology of Japan, Grant-in-Aid for Scientific Research (B) (18360126), SolidWorks Japan K.K., QNX Software Systems, and DYDEN Corporation, whom we thank for their financial and technical support.

Bibliography

M. H. Day and J. R. Napier. Fossil foot bones. *Current Anthropology*, 6(4): 419-420, 1965.

M. Harris. *Our Kind: Who We Are, Where We Came From, Where We Are Going*. Herper Perennial, 1990.

J. H. Hicks. The mechanics of the foot: II. The plantar aponeurosis and the arch. *Journal of Anatomy*, 88:25-30, 1954.

I. A. Kapandji. *The Physiology of the joints: Lower limb, Volume 2*. Churchill Livingstone, 1988.

R. F. Ker, M. B. Bennett, S. R. Bibby, R. C. Kester, and R. McN. Alexander. The spring in the arch of the human foot. *Nature*, 325:147–149, 1987.

M. Kouchi and M. Mochimaru. AIST Research Information Database (http://riodb.ibase.aist.go.jp/riohomee.html). H16PRO287, 2005.

D.J. Morton. Evolution of the longitudinal arch of the human foot. *Journal of Bone Joint Surgery*, 6:56-90, 1924.

Y. Ogura, K. Shimomura, H. Kondo, A. Morishima, T. Okubo, and S. Momoki. Human-like walking with knee stretched, heel-contact and toe-off motion by a humanoid robot. In *Proceedings of the 2006 IEEE/RSJ International Conference on Intelligent Robots and Systems*, pages 3976-3981, 2006.

A. H. Schultz. Relatives between the lengths of the main parts of the foot skeleton in primates. *International Journal of Primatology*, 1:150–171, 1963.

T. Takashima, H. Fujimoto, and A. Takanishi. Determination of the longitudinal arch moment of the human foot complex during gait: inverse dynamics model analysis. *Transactions of the Japan Society of Mechanical Engineers*. C, 68(672): 2425-2430, 2002. (in Japanese)

T. Takashima, H. Fujimoto, and A. Takanishi. Analysis of the human foot arch viscoelasticity using the simple model of the arch support elements. *Transactions of the Japan Society of Mechanical Engineers*. C, 69(685), 2003. (in Japanese)

Design and Development of Bio-mimetic Quadruped Robot

Hiroyuki ISHII, Qing SHI, Yuichi MASUDA, Syunsuke MIYAGISHIMA, Syogo FUJINO, Atsuo TAKANISHI
Faculty of Science and Engineering, Waseda University
Satoshi OKABAYAHI, Naritoshi IIDA, Hiroshi KIMURA
Faculty of Letters, Arts and Science, Waseda University

Abstract

Robot Technology should contribute to the progress of other research fields. We'd like to propose one example of it. In psychology, basic medicine and biological science, several experiments on animal behavior have been performed to clarify brain functions or mechanisms of learning. These experiments have been playing very important role to understand human mind. Rats and mice have been well used in these experiments. Therefore, we have been developing quadruped robots that reproduce animal behavior as new experimental tools. We developed a quadruped robot that has 4 legs and reproduces some social behaviors. Each leg has 3 DOFs. The robot also has 2 DOF at the neck and 2 DOF at the waist.

Introduction

Robot Technology (RT) should contribute to the progress of other research fields. The application of RT to other fields is also very important for the progress of itself. Based on this idea, we'd like to propose an example.

In psychology, brain science and basic medicine, several experiments on animal behavior have been performed to clarify brain functions or mechanisms of learning. These experiments have been playing very important role to understand human mind. In these experiments, rats and mice have been well used [1][2], and several experiments on social interactions have been performed to study mental disorders or social learning of human beings [3][4]. However, some researchers mention lack of reproducibility in these experiments. We consider it's very difficult to improve reproducibility of these experiments because the social interactions of animals are not reproducible. On the other hand, some computer scientists and psychologists have been developing intelligence models of rodents, such as navigation or sensory-motor coordination [5]-[7]. Some researchers developed rodent-like robots to verify their intelligence model [8][9]. However, none of them has legs hence some researchers require new robots that have fore legs like a real rat.

In robotics, several quadruped robots have been developed. One of the most

famous quadruped robots is AIBO [10]. Big Dog and Little Dog are also well known [11][12]. We then considered that reproducibility of the experiments on social interactions can be improved by using a biomimetic quadruped robot as an agent that interacts with an animal subject. In addition, a quadruped robot can be used as a platform to verily the intelligence model developed by computer-scientist. We had developed two different quadruped robots. The first one had four 2-DOFs legs [13]. However, this robot doesn't reproduce rat's social behavior such as rearing, sniffing or mounting. The second one had four 2-DOFs legs, and a 1-DOF waist yaw joint [14]. However, this robot doesn't reproduce rat's social behavior either.

Thus, we developed a new biomimetic quadruped robot WR-2 (Waseda Rat No. 2). WR-2 is original in respect of reproducing not only walking behavior but also other behaviors such as rearing, grooming and mounting of a rat. Because of this characteristic, WR-2 can be used as an agent that interacts with a rat in the experiments on social interactions and also as a robotic platform for computer-scientists. Before designing its hardware, we analyzed rat's proportion and motion. We then determined DOF arrangement and proportion of WR-2. DOF arrangement of WR-2 is unique in respect of having 2 DOF at the waist. This robot also has 1-DOF at the neck. It also has a microcontroller, a wireless communication module and a battery. In this paper, we describe mechanical design, control system and specification of WR-2.

Fig. 1 Real rat (left) and WR-2 (right)

Analysis of Rat's Motion and Proportion

To determine the specification and DOF configuration of the new quadruped robot, we analyzed rat's motion and muscle skeleton.

Size and Proportion. An x-ray picture of a mature rat and the proportion of each part are shown in figure 2. Comparing to other quadruped animals such as dogs or horses, the proportion of rat's spine to its front and hind legs is longer. As shown in the figure, the lower hind leg is longer than the upper hind leg while the upper

fore leg and the lower fore leg is almost same.

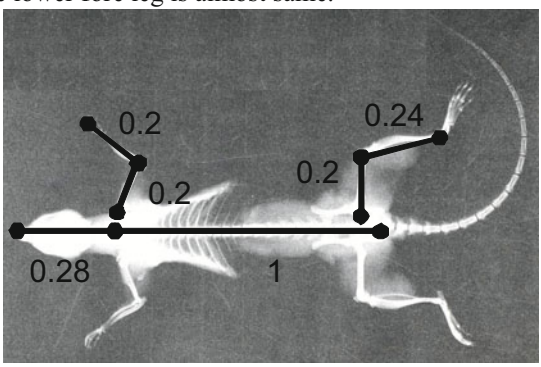

Fig. 2 Proportion of a rat obtained from X-ray picture

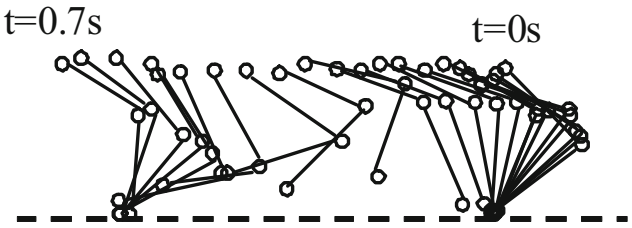

Fig. 3 Stick diagram of walking rat, drawn in ever 0.03 [ms]

DOF arrangement. The DOF arrangement model of a mature rat is experimentally obtained by a motion analysis. Walking motion of a mature rat is recorded by a video camera, and a stick diagram is obtained by observation as shown in figure 3. We analyzed the motion of both the fore and hind legs in not only x-z plane but also y-z plane. From the result of this analysis, we consider that each fore/hind legs can be represented as a 3-DOF manipulator, a roll and pitch at the shoulder/hip, a pitch at the elbow/knee. In addition, rats have a flexible spine, and they can bend their body when they rear or groom. We consider these kinds of motions can be reproduced by a 2-DOF waist joint, a pitch and a yaw. Through this kind of motion and kinematical analysis, we consider that the muscle skeleton structure of the mature rat can be represented by the DOF arrangement model as shown in figure 4.

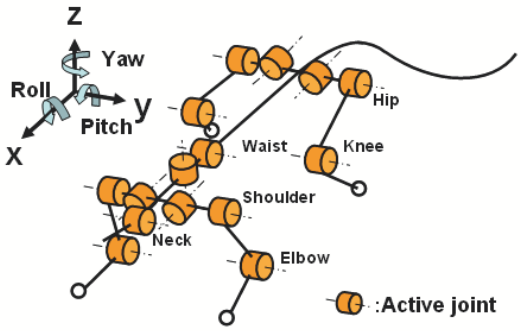

Fig. 4 DOF arrangement model of rats

Hardware Design

Hardware of WR-2 was designed based on the model as shown in figure 4 and the studies in anatomy [15]. Dimensions and weight are shown in table 2.

Table 2 Dimensions and weight of WR-2

Width	mm	70
Height	mm	90
Length	mm	240
Weight	g	850

Fore legs. Each fore leg consists of 3 DOF, a roll and pitch at the shoulder and a pitch at the elbow. The proportion between the upper and the lower leg is determined based on the model as shown in figure 2. As shown in figure 2, the legs of a rat are very short and small. Therefore, we consider that actuators should be implemented in the body, not in the legs. Each joint is actuated by a DC motor with a rotary encoder. Specifications of the motors are shown in table 1.

Table 1 Specifications of the motors on WR-2

Joint	Power W	Encoder resolution deg/pulse
Shoulder/Hip roll	2.5	8.8×10^{-2}
Shoulder/Hip pitch	0.75	3.5×10^{-1}
Elbow/Knee pitch	0.75	3.5×10^{-1}

As shown in figure 5, only the shoulder roll is directly driven by the DC motor. The shoulder pitch and the elbow pitch are driven by the DC motors via the wire and outer-tube connection mechanisms. The motors to drive these joint are implemented in the body. The problems of this kind of wire and outer-tube mechanisms are buckling of the tube and friction between the wire and the tube. To solve these problems, the outer-tubes are made from fluorine resin.

Hind legs. Design of each hind leg is almost same as that of the fore leg except for position of the motor to drive the knee pitch joint as shown in figure 5.

Waist. The waist consists of 2-DOF joint, a yaw and pitch. Each axis is actuated by a servo motor for hobby use.

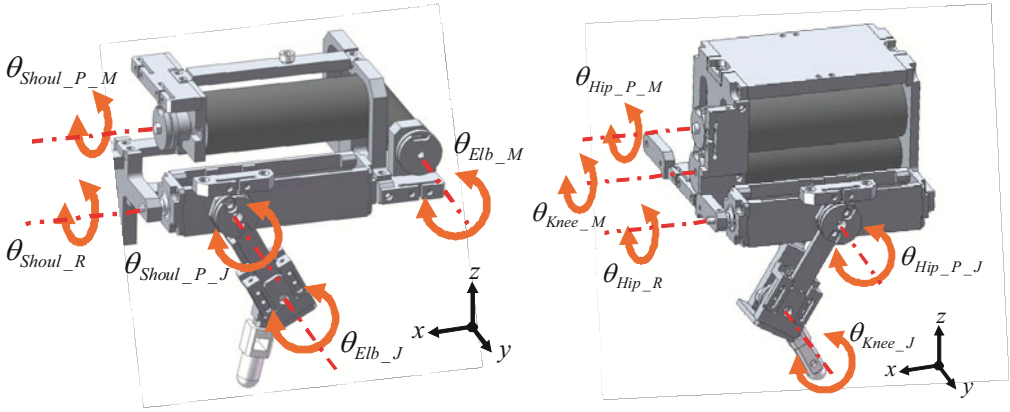

(a) Fore leg (left) (b) Hind leg (left)

Fig. 5 Design of legs

Control of WR-2

A microcontroller, wireless communication module are implemented in WR-2. This robot is controlled by the PC via wireless connection.

Controller circuit. A controller circuit that is originally designed for WR-2 is implemented. A microcontroller and 6 motor drivers (each drives two motors) are implemented in it. All the motors, not only the DC motors but also the servo motors are connected with this circuit and controlled. Some motion patterns are implemented in the microcontroller as time-line data of each joint angle. The microcontroller controls the angle of each joint according to the pattern when it receives the instruction from the PC.

Walking pattern generator. Walking motion patterns are computed using the walking pattern generator as shown in figure 6 and recorded in the controller. This generator was developed for WR-2 based on the theory of ZMP stability criterion

[16]. Kinematic model with mass distribution as shown in figure 6 (b) is implemented in this generator. It computes time-line data of each joint angle based on the procedure as shown in figure 6 (a).

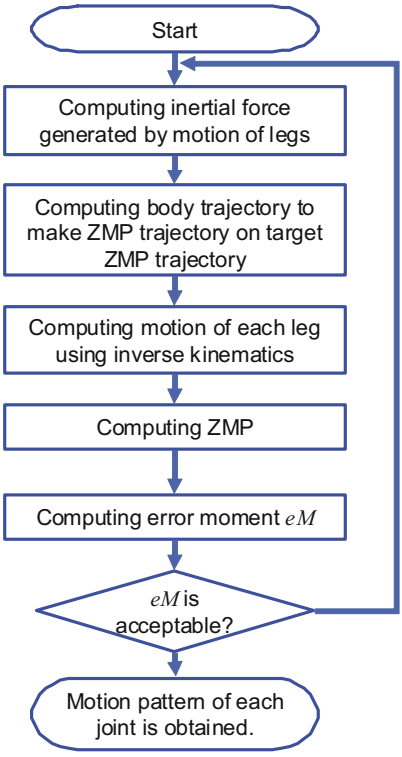

(a) Algorithm

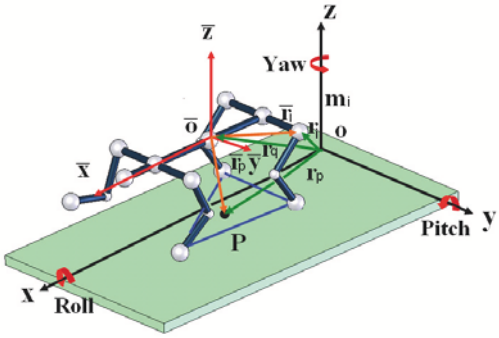

m_i : mass of particle i
r_i : position vector of particle i
r_p : position vector of P
O-XYZ : absolute coordinate system
O-X'Y'Z' : moving coordinate system

(b) Kinematics model

Fig. 6 Walking pattern generator for WR-2

Performance Verification

We performed a performance verification test of WR-2. In this test, WR-2 walked 5 trials and we measured the walking speed. The result of the test, average of the speed and its standard deviation of 5 trials are shown in table 3 and the sequence photographs of a trial are shown in figure 7.

Table 3 Result of performance verification test

	Average of 5 trials	SD
Walking speed mm/s	20.7	5.9

Summary and Future works

We developed a new quadruped robot WR-2. This robot was designed to reproduce not only walking but also other behaviors of a rat. Its DOF arrangement and proportion were determined based on the motion and proportion analysis of a mature rat. In verification test, we confirmed walking performance of WR-2. It walks like rat. However, the walking speed was slower than that of a real rat. We are now tuning some mechanical parameters such as tension of each wire and material of the feet. After tuning, we believe the walking speed of WR-2 become faster. We are also now, making motion pattern generator for social behaviors such as rearing, grooming and mounting.

Fig. 7 Sequence photographs of walking of WR-2

References

[1] DS. Woodruff-Pak, “Animal models of Alzheimer's disease: therapeutic implications,” Journal of Alzheimer’s disease, Vol. 15(4), pp. 507-521, 2008.

[2] N. Hiroi, et al., “A 200-kb region of human chromo-some 22q11.2 confers antipsychotic-responsive be-havioral abnormalities in mice,” Proceedings of the National Academy of Science of U.S.A., 102(52), 19132-7, 2005.

[3] M. Tonissaar, L. Herm, M. Eller, K. Koiv, A. Rinken, J. Harro, “Rats with high or low sociability are differently affected by chronic variable stress,” Neuroscience. Vol. 152(4), pp.867-76. 2008.

[4] L. Jans, G. Korte-Bouws, S. Korte, A. Blokland. “The effects of acute tryptophan depletion on affective behaviour and cognition in Brown Norway and Sprague Dawley rats,” Journal of Psychopharmacology. 2008.
[5] A. Barrera and A. Weitzenfeld, Biologically-inspired robot spatial cognition based on rat neurophysiological studies, Autonomous Robot Vol. 25(1-2), pp. 147-169, 2008.
[6] M.D. Humphries, Is There an Integrative Center in the Vertebrate Brain-Stem? A Robotic Evaluation of a Model of the Reticular Formation Viewed as an Action Selection Device, Journal of Adaptive Behavior, Vol. 13(2), 2005.
[7] V. Hafner, Cognitive Maps in Rats and Robots, Journal of Adaptive Behavior, Vol. 13(2), 2005.
[8] JA. Meyer, et al., The Psikharpax project : towards building an artifical rat, Robotics and Autonomous Systems, Vol 50. 2005.
[9] S. Elfwing, E. Uchibe, K. Doya, and H. I. Christensen. Evolutionary Development of Hierarchical Learning Structures. IEEE Transactions on Evolutionary Computations, Vol. 11, Issue 2, pages 249--264, 2007.
[10] Sony AIBO Europe; http://support.sony-europe.com/aibo/
[11] R. Playter, M. Buehler, M. Raibert, “BigDog,” Proceedings of SPIE, Vol. 6230, 2006.
[12] L.D. Jackel, et al., “How DARPA structures its robotics programs to improve locomotion and navigation,” Communications of the ACM, Volume 50 (11), 2007.
[13] C. Laschi, B. Mazzolai, F. Patane, V. Mattoli, P. Dario, H. Ishii, M. Ogura, S, Kurisu, A. Komura, A. Takanishi, “Design and Development of a Legged Rat Robot for Studying Animal-Robot Interaction,” Proceedings of BioRob2006, 2006.
[14] F. Patane, V. Mattoli, C. Laschi, B. Mazzolai, P. Dario, H. Ishii, S. Kurisu, A. Koumura, A. Takanishi, “Biomechatronic Design and Development of a Legged Rat Robot,” Proceedings of ROBIO 2007, 2007.
[15] F.W. Warren, G. H. Dominique, “Anatomy and Dissection of the Rat,” W. H. Freeman, 1997.
[16] H. Nishizawa, A. Takanishi., H. Lin, “Realization of Quadruped Walk with ZMP stable (*in Japanese*),” Proceedings of RSJ2003, 2003.

Static and Dynamic Maneuvers With a Tendon-Coupled Biped Robot

Paul J Csonka [*] and Kenneth J Waldron [*†]

[*] Robotic Locomotion Laboratory Stanford University, USA
[†] Center for Automated Systems University of Technology, Sydney, AUS

Abstract Bipedal robots have generally either been designed for static motions or dynamic maneuvers, but the ability for operation in the real world in both realms is becoming increasingly relevant. In this work we explain the abilities of a human scale bipedal robot with tendon-coupled knee and ankle joints that is able to balance, step, hop and run several steps in a two dimensional plane.

1 Introduction

1.1 Motivation

As part of ongoing research into legged robot dynamics, the articulated bipedal robot TRIP (Tendonized Running Inspired Platform) of human proportions is being developed at the Robotic Locomotion Laboratory at Stanford University. The goal is for the robot to be capable of dynamic gaits such as running, and static gaits such as stepping.

Static motions are useful for tasks requiring fine motor control, such as taking steps through delicate environments, while dynamic maneuvers are useful for clearing larger obstacles or traveling long distances in short time periods. TRIP was optimized for running through the use of inelastic tendons coupling the ankle and knee joints, in a fashion similar to the *GAS* coupling observed in larger mammals.

The robot has a small moment of inertia in the torso about the hip compared to the legs. This mass distribution allows more careful study of leg behavior during dynamic maneuvers, as opposed to robots where torso to leg moment of inertia ratio is maximized.

1.2 Prior Work

Numerous successful walking robots exist in the repertoire, with the most advanced including Honda's HRP2 (Kajita et al. (2002)). Prismatic-

legged robots have successfully maintained dynamic running, with one example being Raibert's 3D Biped (Playter and Raibert (1992)); limited articulated-legged dynamic running has been achieved by a few others such as Chevallereau's Rabbit (Chevallereau et al. (2005)). However, the use of inelastic coupling tendons is still relatively unexplored despite research into elastic tendons (Hyon and Mita (2002)).

2 Design

2.1 Mechanical Design

The robotic system used in this work consists of a small torso and two articulated legs (0.95 m when extended). The torso is constrained to move in a vertical plane with a 3.5 m boom, and to pitch about an axis common to the hip joints. The robot and boom arm mass is 17 kg, with approximately 60% of the system mass in the legs.

The actuation system consists of a pneumatic cylinder (Bimba 704-DXP for the knee, and 505-DXPBF for the hip) and a proportional valve (Festo Corporation MPYE-5-1/4-010-B) for each hip and knee joint, running on 0.83 MPa compressed air.

To more closely mimic a human's muscular system, a tendon connects the thigh and foot together. The tendon is 788 mm in length, 1.5 mm diameter, 200 kg test pull Kevlar. Figure 1 shows one of the legs.

2.2 Electrical Design

A microcontroller (Elba Corp. zx-1280n) controls the robot, while a gyroscope (Analog Devices ADXRS300) measures torso angular pitch velocity, and rotary encoders measure joint angles (US Digital MAE3-P12-250). A potentiometer (Bourns 6639-2-102) is mounted to the horizontal sweep axis of the boom, and a 100 mm linear potentiometer (Midori Precisions LP-100 Greenpot) measures torso pitch. Ground contact is detected with an accelerometer (Analog Devices ADXL202) fixed to the ground platform.

3 Control Results

In this tendon-coupled system, the toe points during extension, similar to the natural motion observed in humans. For this work, Extension of a given leg is defined as rotation of its knee joint such that the distance from hip to ankle increases, and Contraction the opposite rotation. Similarly, a Swing Forward is rotation of a leg about its hip joint such that the ankle moves forward, and a Swing Backward is caused by opposite rotation. The Swing

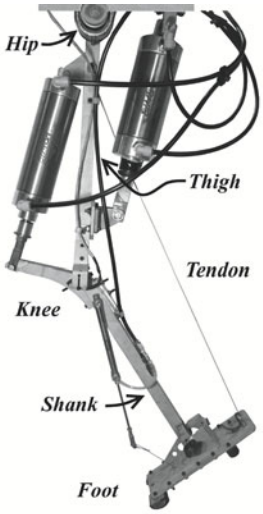

Figure 1. Photograph of the Left leg, with principal components labeled.

Leg is the leg currently positioning for ground contact, and the Contact Leg is the leg contacting the ground.

Compared to a prismatic leg, one of the differences between thrusting with an articulated leg is that large horizontal impulses are generated while thrusting as the leg's center of mass moves backwards. The use of a fixed-length tendon simplifies the control of dynamic motions such as hopping by partially canceling out this undesired impulse through coupled ankle thrust.

A properly selected tendon length allows the control algorithm to drive only the knee joint, while the ankle automatically creates the necessary horizontal impulses that essentially turn the leg into a prismatically behaving one. This also allows for a certain degree of self-stabilizing behavior of the leg. Should the toe land forward of the hip, the tendon engages (undergoes tension) later in the Contact phase and disengages (slackens) earlier in the Thrust phase; this reduces the impulse compensation, and the leg naturally swings backwards. The opposite effect occurs for a toe behind the hip.

The torso angular velocity ω_t is positive when the top of the torso rotates towards the front of the robot. The horizontal angular velocity of the boom arm ω_a is positive when the robot moves forward.

3.1 Balancing

For simplicity, when balancing on a single leg, the swing leg's knee is disabled, and the two hip joints mirror hip position commands. All sensing for balancing is kinematic via joint angles.

Balancing is accomplished through a continuous loop as the system calculates the CoM position relative contact leg's toe. The hip and knee angles are adjusted through inverse kinematics.

Experimental Result Figure 2 portrays one example of the robot's reaction to disturbances. The robot cannot recover from disturbances in either direction beyond 70 mm or 60 $\frac{mm}{s}$.

3.2 Stepping

For stepping with low velocities, the CoM always remains inside at least one of the contact feet. We also succeeded with quasi-static stepping, where the CoM falls outside the single contact foot, and the pivoting robot is caught by the swing foot.

In both cases, walking is a delicate maneuver since the legs are underactuated. Since walking is generally accepted as a well-explored maneuver in the research community, the algorithm will not be elaborated upon here, and extensive walking was not attempted.

Experimental Result Steps were completed at CoM velocities of 30 $\frac{mm}{s}$.

3.3 Hopping

Basic stable hopping is defined in this work as repeating jump cycles, where the steady-state landing positions are close to one another. Additionally, a somewhat vertical torso angle should be maintained, and a significant portion of the gait should be in flight.

In a bipedal robot with freely pitching torso, stable hopping on one tendon-driven leg is more complex than that of a monopod (which is simple to achieve) due to the swing leg affecting torso motion as well. Compliant cylinders further complicate matters.

All joints of the robot were velocity controlled during hopping. The algorithm which which governs single leg hopping is as follows.

Flight Phase
Action 1 The robot disables all joints.
Phase switch criteria Ground contact.

Contact Phase
Action 1 The swing leg's hip cylinder retracts slightly.

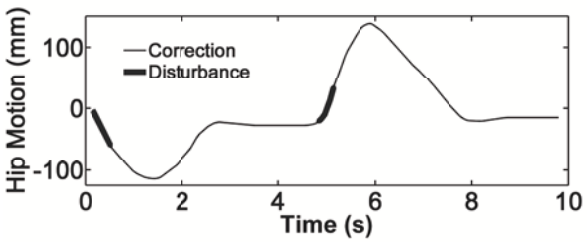

Figure 2. Horizontal torso displacement in response to a push and pull disturbance while balancing .

Elaboration This is not necessary with large torso to leg moment of inertia ratios or stiff hip actuators. This retraction is important in this algorithm, and reduces unwanted energy storage in the hip cylinder while swinging backwards upon contact; this energy otherwise causes the leg to swing forward later, destabilizing the torso.

Action 2 The contact leg's hip cylinder extends an equivalent amount.

Elaboration Maintains an upright torso due to compliant cylinders.

Phase switch criteria The contact leg's knee angle is minimized.

Thrust Phase

Action 1 A maximum knee thrust occurs on the contact leg.

Action 2 The swing leg's hip cylinder extends slightly.

Elaboration Similar to Contact, this reduces unwanted energy storage.

Action 3 The hip cylinder of the contact leg retracts as the leg thrusts.

Elaboration Maintains an upright torso. Retraction is faster if $\omega_t > 0$, and *vice versa*.

Phase switch criteria The contact leg reaches its maximum extension.

Experimental Result The biped can achieve ten consecutive hops on one leg, with a hop height of 150 mm, and with the last five hops landing within 50 mm of each other. The torso angle remains within 10^o of vertical.

3.4 Running

Basic stable running is defined in this work as consecutive hops where the CoM moves forward with each hop, terminated only when desired. Additionally, a significant portion of the gait is in flight, and the torso angle is maintained inside a specified range. Attempts are being made to achieve running without precise knowledge of the robotic system, i.e. without ex-

tensive calibration or matching of valve or cylinder characteristics, instead relying on the self-correcting nature of the algorithm and tendon-coupled legs. The current algorithm follows.

Flight Phase

Action 1 Contract the swing leg with a high torque.

Elaboration When either ω_t or ω_a are positive, the torque increases to keep the torso upright. Contracting the leg reduces its moment of inertia about the hip during a swing forward. See *Elaboration* on *Action 4* .

Action 2 Extend the swing leg with medium torque.

Elaboration Prepares the swing leg for contact. See *Elaboration* on *Action 4* .

Action 3 The swing leg swings forward with medium torque.

Elaboration See *Elaboration* on *Action 4* .

Action 4 The contact leg swings backwards with high torque.

Elaboration When $\omega_t > 0$, the torque increases to keep the torso upright, and *vice versa*.

Phase switch criteria Ground contact.

Contact Phase

Action 1 The swing leg's hip cylinder retracts on contact.

Elaboration See *Elaboration* on *Action 1* for the Contact phase of 3.3.

Action 2 The contact leg's hip cylinder extends an equivalent amount.

Elaboration Maintains an upright torso due to compliant cylinders. To keep the torso upright, torque increases when $\omega_t > 0$, and *vice versa*.

Phase switch criteria The contact leg's knee angle reaches a local minimum value.

Thrust Phase

Action 1 A maximum knee thrust occurs on the contact leg.

Action 2 The swing leg's hip cylinder extends slightly.

Elaboration This reduces unwanted energy storage that arises from acceleration while thrusting.

Action 3 The thrusting contact leg swings backwards during extension.

Elaboration This keeps the torso upright. Retraction is faster if $omega_t >$ 0, and *vice versa*.

Phase switch criteria The contact leg reaches maximum extension.

Experimental Result With the hip and knee valves uncalibrated, and the cylinders uncharacterized, the biped achieved five running steps thus far, in the forward direction at an average 1 $\frac{m}{s}$, a maximum 14 cm hop height

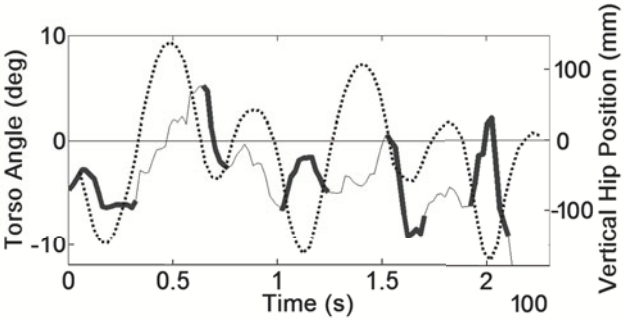

Figure 3. Results for a five-step run. Torso angles are solid lines, while ground contact is denoted by a thick section. Hip position is shown with a dashed line, with positive values corresponding to flight heights.

(the height beyond an extended stance), a flight phase duty factor of 51%, and a torso pitch angle within 6^o about vertical during most of the strides (see Figure fig:run). It has also achieved four running steps backwards at an average of 0.75 $\frac{m}{s}$, 10 cm hop height, and a flight phase duty factor of 49%. These results are obviously not considered stable running, given the asymmetric hop height and limited number of gait cycles. The research into planar running is ongoing.

4 Discussion

Balancing and stepping are achievable with tendon-coupled knee and ankle joints. However, one limitation of the tendon-leg linkage is that only specific postures can be commanded. A generally strategy is to use adjustable tendons to improve the applicability of tendon coupling. For example, stepping could benefit from a tendon longer than those used in dynamic maneuvers. This is not unlike biological systems, where muscles can contract and reposition tendons based on the motion of the host system.

This separate tendon actuator need not be fast nor powerful, but it cannot be back drivable: our own findings, and separate research shows that compliant tendons are difficult to control (Hyon and Mita (2002)). The advantages of an actuated tendon system, then, compared to an actuator directly controlling the ankle, are due to the automatic impulse compensation, the tendon actuator needing to only occasionally vary length, and a tendon actuator can be located near the hip.

Due to its self-correcting nature, a tendon simplifies the control required

for running and stable hopping on one leg. Indeed, the algorithms used have been almost open-loop. The difficulty in maintaining hopping beyond ten hops arises primarily from the nonrepeatable nature of the uncalibrated hardware used, gradually leading to excessive torso pitch. This is also the failure mode that so far has limited attempts to run, and led to the asymmetry and small number of running strides. Stronger state feedback is being implemented to assist in remedying this situation, and calibration is being added back to the system to match the behavior of the legs.

5 Conclusion

Using a tendon to couple joints in an articulated bipedal robot, the potential for both static and dynamic motions has been shown. The configuration described here is particularly suited for dynamic maneuvers, given that it allows a certain degree of automatic motion correction. While a fixed-length tendon is suboptimal for both dynamic and static motions, both are achievable; a variable-length tendon is an ideal biologically-inspired mechanism.

Acknowledgment

Support for this work was provided by grant number CMMI 0825364 from the National Science Foundation to Stanford University.

Bibliography

C. Chevallereau, E. R. Westervelt, and J. W. Grizzle. Asymptotically Stable Running for a Five-Link, Four-Actuator, Planar Bipedal Robot. *The International Journal of Robotics Research*, 24(6):431–464, 2005.

S.H. Hyon and T. Mita. Development of a biologically inspired hopping robot-"kenken". In *Robotics and Automation, 2002. Proceedings. ICRA '02. IEEE International Conference on*, volume 4, pages 3984–3991 vol.4, 2002.

S. Kajita, F. Kanehiro, K. Kaneko, K. Fujiwara, K. Yokoi, and H. Hirukawa. A realtime pattern generator for biped walking. In *Robotics and Automation, 2002. Proceedings. ICRA '02. IEEE International Conference on*, volume 1, pages 31–37 vol.1, 2002.

R.R. Playter and M.H. Raibert. Control of a biped somersault in 3d. In *Intelligent Robots and Systems, 1992., Proceedings of the 1992 lEEE/RSJ International Conference on*, volume 1, pages 582–589, Jul 1992.

Chapter IV

Control, Modelling, and Analysis of Robotic Systems

Kinematic Calibration of Small Robotic Work Spaces Using Fringe Projection

Dipl.-Ing. Klaus Haskamp [*‡] and Prof. Dr.-Ing. E. Reithmeier [†‡]

[*] Research Associate in the work group Production Measurement and Technology

[†] Head of the Institute and head of the working group Control Engineering

[‡] Institute of Measurement and Control Engineering, Leibinz Universität Hannover, Hannover, Germany

Abstract In recent years a number of medical therapy concepts have taken hold in the field of microsurgery. These concepts require measurement accuracies below 0.3 mm. The positioning accuracy needed in surgical applications is higher than what surgeons usually are able to achieve. In this case robot manipulators can be employed to support surgical skills. The robotic movement has to be sufficiently reliable and has to incorporate safety procedures like fast collision detection and avoidance. Furthermore, important premisses to the technical system were given by the absolute and the relative accuracy.

In industrial applications the absolute accuracy is enhanced by calibrating the kinematic parameters and compensating manufacturing errors. The achieved accuracies are less than 0.7 mm and do not comply with the actual medical standard. In this article a new method for modeling and calibrating the kinematics of robots with the aim of achieving precisions less than 0.1 mm respectively 0.1° in a 1000 mm^3 work space is presented. The used mathematical description of the kinematics and the calibration strategy is explained in detail.

1 Introduction

Robots are applied in industrial applications as manipulator systems for tasks like pick and place, path-welding, bonding or milling. Medical engineering is a new application field. For example a robot can be equipped with a milling cutter or a burr and be used in the precision engineering from hard tissue like bones or tooth enamel. Thereby, new problems that refer to positioning- and the motion-behavior have to be solved. For example, a very high absolute positioning accuracy and an excellent tracking accuracy

have to be realized to remove only material, which is planned to carry off. Furthermore, the whole system has to be insensitive with respect to exterior disturbances, which are induced through the material removal.

Recent research works deal with the calibration of industrial robots, which is described in Wiest (2001), Atkinson (1996), Everett (1988). The kinematics is usually described using the modified Denavit-Hartenberg- Parameters to consider geometric errors like home position errors. Thereby, absolute accuracies of less than 1 mm were achieved. Medical applications have higher requirements relating to the absolute positioning accuracy and due to this the kinematic model have to be extended to include additional parameters. The problem is that the parameters are correlated and therewith cannot be identified seperately.

In this work, a new calibration strategy for identifying the whole kinematics is presented. The kinematic is described using polynomial functions and due to this each geometrical and non-geometical error, like offset angles and elasticities, are regarded. Additionall to the description of the kinematics the measurement procedure of the pose of the endeffector is explained in detail. The paper is concluded presenting a validation of the determined forward and inverse kinematic functions.

2 Methods for the Modeling of the Kinematics

2.1 Conventional Modeling

Generally, the forward kinematics ${}_{\mathbf{0}}\mathbf{x} = \mathbf{f}(\mathbf{q})$ is described using the Denavit-Hartenberg-Notation or the modified Denavit-Hartenberg-Notation, as specified in Wiest (2001). ${}_{\mathbf{0}}\mathbf{x}$ denotes the pose of the robot endeffector (TCP) with respect to an inertial world coordinate system CS_0 and $\mathbf{q}$ represents the joint angles of the robot.

The inverse kinematics can be obtained from the solution $\mathbf{q} = \mathbf{f}^{-\mathbf{1}}(\mathbf{x})$. Usually, this cannot be done analytically due to the fact that $\mathbf{f}$ has a nonlinear character. Normally, nonlinear optimization algorithms like the Nelder-Mead-Method or the Rosenbrock-Method have to be implemented in order to calculate the joint angles $\mathbf{q}$ for a given pose $\mathbf{x}$, as written in Logt (1998).

This modeling method implicates some advantages and disadvantages. The main benefit is given by the fast setup of the forward kinematic functions through easy geometrical relationships. On the other hand, the description is not clear if consecutive axis are parallel. Furthermore, singularities appear if the robot is in an inappropriate angle configuration. Another disadvantage is that mechanical components like elasticity and friction cannot be considered in this model so that an error remains between the virtual and the real kinematics.

2.2 Kinematic Modeling with respect to Polynomial Functions

In our application a 6-axis-robot as shown in figure 1 is moved in a small work space of about 1000 mm^3. Due to the assumption that the joint movements are small the behavior of the forward and the inverse kinematics is approximately linear and both can be described using polygons:

$$x_i = \sum_{k=0}^{N_1-1} a_{1ik} \cdot q_1^k + \sum_{k=0}^{N_2-1} a_{2ik} \cdot q_2^k + \cdots + \sum_{k=0}^{N_6-1} a_{6ik} \cdot q_6^k \quad (1)$$

$$q_i = \sum_{k=0}^{M_1-1} b_{1ik} \cdot x_1^k + \sum_{k=0}^{M_2-1} b_{2ik} \cdot x_2^k + \cdots + \sum_{k=0}^{M_6-1} b_{6ik} \cdot x_6^k \quad (2)$$

$$1 \leq i \leq 6 \quad (3)$$

with a_{jik} and b_{jik} as the polynomial coefficients. The polynomial functions present a black-box-method. Because of this, each physical effect like deflection of the axis or home position errors are considered which is an advantage compared to the conventional model. However, the dimension of the working area restricts the applicability from describing the kinematics through polynomials. In the case that the work space is too large the kinematics and the polynomials become nonlinear and the functions g_i and h_i oscillate in the boundary area.

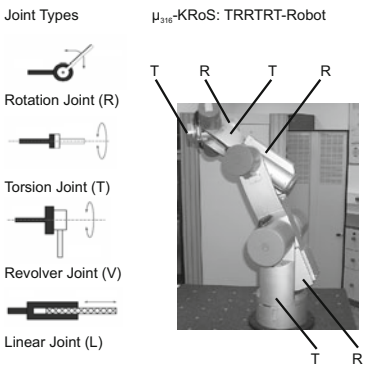

Figure 1. μ_{316}-KRoS-Robot

3 Identification of the Kinematics

3.1 Calibration Functional

The mathematical model of the kinematics deviates from the real kinematic structure of the robot with the consequence that positioning errors appear when a pose is approached. The errors can be divided in pure geometrical errors and non-geometrical errors. Examples for geometrical errors are home position errors or deviations from the orthogonality of the axis. Gear elasticities, friction or temperature influence are examples for non-geometrical errors. In order to enhance the absolute accuracy the geometric and non-geometric effects have to be taken into account within the model and to be identified through a calibration process.

In Wiest (2001) null position errors for example can be considered in the Denavit Hartenberg Matrix as an offset $\Delta\theta_{\mathrm{i}}$ to the joint angle $\mathrm{q_i}$. In order to identify the model parameter, a functional ε has to be defined which combines a set of measured poses $\mathbf{x}_{measure}$ with the modeled poses $\mathbf{x}_{model}$, as written in Wiest (2001):

$$\varepsilon = \sum_{i=1}^{N} \|\mathbf{x}_{measure,i} - \mathbf{x}_{model,i}\|^2 = f(\mathbf{p}) \tag{4}$$

with $\mathbf{p}$ as the parameter vector. Usually, $\mathbf{x}_{model}$ is expressed through the forward kinematics and the joint angles $\mathbf{q}$ are given by the angle encoders. In this case we use the polynomial functions described in chapter 2.2. To estimate capable values for the parameters, the minimum of ε has to be determined using numerical methods.

Wiest (2001) points out that the measured pose should have 6 dimensions to get a high information content. Using laser tracker, a 3D-position can be captured with a very high accuracy of about $5\mu m \pm 10\frac{\mu m}{m}$, as described in Illemann (2007). By measuring different targets, which are fixed at the robot endeffector, a 6D-position measurement can be realized. Another opportunity for 6D-position measurement is given by fringe projection systems. This will be explained in detail in chapter 3.2.

3.2 Experimental Setup

Figure 2 shows the experimental setup. The measurement is accomplished by three spheres which are fixed at the endeffector and positioned in the working area.

As the result of the measurement using fringe projection, data points are fitted to spheres and the center points $\mathbf{x_{M1}}$, $\mathbf{x_{M2}}$ and $\mathbf{x_{M3}}$ are available for further analysis. A fringe projection system, as shown in figure 2, consists

of a beamer and one or more cameras. Common fringe projection systems use straight fringe patterns which are projected from the beamer onto an object, as specified in Valkenburg, Mc Ivor (1998). Afterwards the deformed patterns on the surface of the measurement object are recorded by the camera. The relationship between a camera pixel and the beamer phase is calculated using image processing and is used to reconstruct the object surface with triangulation. Furthermore, in figure 2 the principle of the construction of the endeffector coordinate system is illustrated. To start with the analysis the distances between the center points of the three spheres l_1, l_2 and l_3 have to be calculated, whereas all lengths are different. The center of the coordinate system is given by the center point $\mathbf{x_{M1}}$. The **z**-axis is created from the difference vector of $\mathbf{x_{M1}}$ and $\mathbf{x_{M3}}$: The **x**-axis is

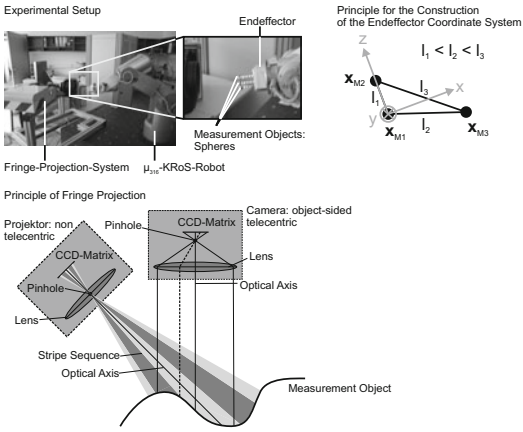

Figure 2. Experimental Rig and Principle for the Construction of the Endeffector Coordinate System

perpendicular to the **z**-axis and the normal vector of the plane, build up from $\mathbf{x_{M1}}$, $\mathbf{x_{M2}}$ and $\mathbf{x_{M3}}$, and points in the direction of $\mathbf{x_{M3}}$. The **y**-axis can be constructed assuming that the coordinate system is a right hand system. Each coordinate system CS can be fully described using a position vector **r** and the **x**-, **y**- and **z**-axis, which were combined in the matrix **X**:

$$\mathbf{X} = [\ \mathbf{x} \quad \mathbf{y} \quad \mathbf{z}\ ] \wedge CS = \{\ \mathbf{r} \quad \mathbf{X}\ \} \tag{5}$$

Furthermore, the coordinate system is defined in the coordinate system of the fringe projection system. To get the measured pose $\mathbf{x}_{measure,i}$ a basis

coordinate system CS_{Basis} has to be determined:

$$CS_{Basis} = \{ \ \mathbf{r_{Basis}} \quad \mathbf{X_{Basis}} \ \} \tag{6}$$

This coordinate system is the new inertial coordinate system and is given by the joint angle configuration $\mathbf{q}^*$, which is absolute with respect to the home position of the robot. Through a movement of the robot endeffector the coordinate system, represented by the spheres, is displaced and tilted with respect to the coordinate system of the fringe projection system and CS_{Basis}. This coordinate system is named CS_{New}:

$$CS_{New} = \{ \ \mathbf{r_{New}} \quad \mathbf{X_{New}} \ \} \tag{7}$$

The displacement and the tilting of CS_{New} with respect to CS_{Basis} result in the pose $\mathbf{x}_{measure,i}$. Thereby, the difference vector $\mathbf{r_{diff}}$

$$\mathbf{r_{diff}} = \mathbf{r_{New}} - \mathbf{r_{Basis}} \tag{8}$$

is the positioning part of the pose. The rotation part can be estimated using the following equation:

$$\mathbf{X_{Basis}} = \mathbf{R} \cdot \mathbf{X_{New}} \tag{9}$$

$$\mathbf{R} = \mathbf{X_{Basis}} \cdot \mathbf{X_{New}^{-1}} \tag{10}$$

$$\tag{11}$$

whereas $\mathbf{R}$ is the 3x3 rotation matrix defined by the roll-pitch-yaw-angles (RPY).

4 Determination of the Kinematics

For the calculation of the polynomial coefficients the relative positioning accuracy from the movement to the joint angle configuration $\mathbf{q}^*$ has to be estimated. Therefore, multiple measurements of the basis coordinate system have to be accomplished whereas the following standard deviations could be specified:

Table 1. Standard deviation of the pose

Position	$[\mu m]$	Rotation	$[^\circ]$
s_x	8	s_θ	0.01
s_y	8	s_ψ	0.009
s_z	11	s_ϕ	0.007

To determine the polynomial coefficients a_{jik} and b_{jik}, 500 measurements were done to get a high resolution of the work space. Each measurement consists of the measurement of the joint angles through the angle encoders and the measurement of the spheres with the fringe projection system. After that the coordinate systems $\{ \mathbf{r_i} \quad \mathbf{X_i} \}$ and the measured pose $\mathbf{x}_{measure,i}$ were calculated whereby corresponding pairs of values are available for the estimation of a_{jik} and b_{jik}. Finally, a_{jik} and b_{jik} were calculated using non-linear optimization algorithms. For convenience the values of the calculated polynomial coefficients are not shown.

5 Validation of the Determined Kinematic Functions

To specify the quality of the estimated kinematic polynoms the forward and the inverse kinematics have to be tested. To test the forward kinematics the robot was moved to a position and the pose $\mathbf{x_{estimate}}$ was calculated with the forward kinematic functions and the joint angles from the angle encoders. Furthermore, the three spheres, which are fixed at the robot endeffector, were measured through the method described in chapter 3.2 with the result $\mathbf{x_{measure}}$. Comparing $\mathbf{x_{estimate}}$ and $\mathbf{x_{measure}}$ shows that the deviation is quite small:

$$\Delta\mathbf{x} = \|\mathbf{x_{estimate}} - \mathbf{x_{measure}}\| \tag{12}$$

The values showed above are the maximum measured values from 20 dif-

Table 2. Deviation between $\mathbf{x_{estimate}}$ and $\mathbf{x_{measure}}$

Position	$[\mu m]$	Rotation	$[°]$
Δx	87	$\Delta\theta$	0.08
Δy	40	$\Delta\psi$	0.05
Δz	56	$\Delta\phi$	0.09

ferent poses in the new working room of the robot.

This implies that the forward kinematic functions coincide with the real kinematics of the robot.

To test the inverse kinematics the joint angles $\mathbf{q_{demand}}$ for a given pose $\mathbf{x_{demand}}$ were calculated and the robot was moved to the configuration $\mathbf{q_{demand}}$. After that, the fringe projection system was used to measure the pose of the endeffector $\mathbf{x_{measure}}$. The comparison of $\mathbf{x_{demand}}$ and $\mathbf{x_{measure}}$ shows that there is just a small difference:

$$\Delta\mathbf{x} = \|\mathbf{x_{demand}} - \mathbf{x_{measure}}\| \tag{13}$$

Table 3. Deviation between $\mathbf{x_{demand}}$ and $\mathbf{x_{measure}}$

Position	$[\mu m]$	Rotation	$[^\circ]$
Δx	87	$\Delta\theta$	0.06
Δy	39	$\Delta\psi$	0.08
Δz	55	$\Delta\phi$	0.06

The values shown above are the maximum measured values from 20 different poses in the new working room of the robot.

This implies that the inverse kinematic functions projects the real kinematics of the robot.

6 Conclusion

In this paper a new method for the identification of the kinematics was described. Beside the description of the kinematic functions the measurement procedure was explained in detail. To verify the forward and inverse kinematic functions the deviation for given poses were determined and the maximum occured deviation is less than 0.1 mm respectively 0.1°.

Bibliography

U. Wiest, *Kinematische Kalibrierung von Industrierobotern*, Dissertation Technische Universität Karlsruhe, 2001.

G. van de Logt, *Entwicklung von numerischen Verfahren zur Planung von Trajektorien fuer Roboter*, Dissertation Universität des Saarlandes, 1998.

L.J. Everett, T.W. Hsu, *The Theory of Kinematic Parameter Identification for Industrial Robots*, Trans. ASME, Journal of Dynamic Systems, Measurement and Control 110, pp. 96-100, 1988.

K.B. Atkinson, *Close Range Photogrammetry and Machine Vision*, Whittles Publishing, UK, 1996.

J. Illemann, *Aufbau, Funktionsweise Lasertracker und Produktübersicht*, in: Schriftenreihe des Geodätischen Instituts, Heft 4. Dresdner Ingenieurgeodäsietag - Industriemesstechnik", Geodätisches Institut der Technischen Universität Dresden, 2007.

R.J. Valkenburg, A.M. Mc Ivor, *Accurare 3D Measurement using a structured light system*, in: Image and Vision Computing, pp. 99 - 110, 1998.

Forward Dynamics of 3-DOF Parallel Robots: a Comparison Among Different Models

Miguel Díaz Rodríguez [*] , Vicente Mata [†] , Ángel Valera [‡] , Álvaro Page [§]

[*]Departamento de Tecnología y Diseño, Facultad de Ingeniería, Universidad de Los Andes, Mérida, Venezuela, dmiguel@ula.ve

[†]Centro de Investigación de Tecnología de Vehículos , Universidad Politecnica de Valencia, Spain, vmata@mcm.upv.es

[‡]Departamento de Ingeniería de Sistemas y Automática, Universidad Politécnica de Valencia, Valencia, Spain

[§]Departamento de Física Aplicada,Universidad Politécnica de Valencia, Valencia, Spain

Abstract In this paper, an approach for solving the forward dynamic problem by using identified parameters is presented. A comparison between the identified models; the so-called reduced model and the complete model, and a model with dynamic parameters obtained by a CAD approach is carried out. The results show that the reduced model, obtained based on a set of so-called relevant parameters, is closely related to the actual system response when compared with the other two models.

1 Introduction

Parallel robots perform better in terms of high accuracy, high-load capacity, high rigidity and speed compared to serial robots. Therefore, it is an object of study in academic circles and nowadays their application is being transferred into industry (Pierrot et al., 2009). Thus, the improvement and the development of accurate dynamic models for this class of robots, particularly for those with less than 6-DOF, are of current interest.

Realistic dynamic simulations of mechanical systems require an accurate knowledge of the underlying dynamic parameters. The dynamic parameters are usually determined by parameter identification techniques (Khalil and Dombre, 2002). However, when dynamic parameter identification is applied, only a subset of so-called base parameters can be identified. These parameters are a linear combination of the link inertial parameters which

are defined with respect to a non-centroidal coordinated system attached to the link. Generally in the solution of the forward dynamic problem, the inherent dynamic parameters are defined with respect to the link gravity center or to a non-centroidal reference system. Thus, the use of identified parameters for the resolution of the forward dynamic problem is not a straightforward task. Indeed, papers dealing with the dynamic parameter identification of robots barely focus on this matter.

It is worth noting that an important amount of research has been focused on applying advanced numerical methods for integrating the equations of motion, for instance Negrut et al. (2003). However, if the set of dynamic parameters does not correspond to the actual system response, even with advanced numerical methods, the simulation can lead to inaccurate results. Thus, extending the use of identified parameters for dynamic simulation is necessary and is the aim of this paper. Moreover, a comparison among identified models is carried out: 1) a model obtained by the identification, herein called: the Complete Model. 2) an identified model, herein called : the Reduced Model and 3) a model in which their rigid body parameters were obtained through a CAD model. The Reduced Model refers to a model obtained by way of a methodological strategy based on statistical considerations and the feasibility of its dynamic parameters (Díaz-Rodríguez, 2009).

The paper has the following structure. Section II contains the derivation of the forward dynamic problem in terms of identified parameters. In Section III the case studies are described. Section IV shows the results for the case studies. Finally, in Section V the main conclusions are summarized.

2 Forward Dynamics in Terms of Identified Dynamic Parameters

In robotics, when dealing with dynamic parameter identification the rigid body dynamic model can be written in linear form with respect to the dynamic parameters (Khalil and Dombre, 2002). For parallel robots (Farhat et al., 2008) the linear parameter model form can be written as,

$$\vec{\tau}_i = \left(\mathbf{K}_i + \mathbf{X}^T \mathbf{K}_d\right) \vec{\Phi} \tag{1}$$

In Eq. 1, $\mathbf{K}_i$ is a matrix of size $n \times np$, where n is the number of DOF and np is the number of parameters, $\mathbf{K}_d$ is a matrix of size $(m-n) \times np$, where m is the number of generalized coordinates. Matrix $\mathbf{X}^T$ of $n \times (m-n)$ is related to the Jacobian matrix.

Eq. 1 allows us to identify the dynamic parameters by identification techniques. In order to solve the forward dynamic problem, Eq. 1 has to

be written as follows,

$$\vec{\tau}_i = \mathbf{M}\ \ddot{\vec{q}}_i + \vec{C} + \vec{G} + \vec{F}_f + \mathbf{J}_m\ \ddot{\vec{q}}_i \tag{2}$$

where $\vec{F}_f$ is the vector corresponding to the friction of the system presented in the joints and matrix $\mathbf{J}_m$ is a diagonal matrix including the inertial effect of actuators. Starting from Eq. 1 in the sections below, the mass matrix $\mathbf{M}$, the vector corresponding to the centrifugal and Coriolis forces $\vec{C}$ and the gravity vector $\vec{G}$, are written in terms of the identified parameters.

2.1 Mass Matrix

The mass matrix is built based on its properties. If the vector of velocity and gravity is set to zero, the resulting equation contains the components of the mass matrix. Let us start by separating the mass matrix into independent and dependent coordinates,

$$\mathbf{M}_{i_{n\times n}}\ddot{\vec{q}}_i + \mathbf{M}_{d_{n\times m-n}}\ddot{\vec{q}}_d \tag{3}$$

The part of the matrix in independent and dependent coordinates can be obtained as follows,

Input: $\dot{\vec{q}} = 0$, $\vec{g} = 0$, $\ddot{\vec{q}}_d = 0$
for *i=1:n* **do**
$\ddot{\vec{q}}_i(1:n) = 0$;
$\ddot{\vec{q}}_i(i) = 1$;
$\mathbf{M}_i(1:3, i) =$
$\left(\mathbf{K}_i + \mathbf{X}^T\,\mathbf{K}_d\right)\ \vec{\Phi}$;
end

Input: $\dot{\vec{q}} = 0$, $\vec{g} = 0$, $\ddot{\vec{q}}_i = 0$;
for *i=1:m-n* **do**
$\ddot{\vec{q}}_d(1:m-n) = 0$;
$\ddot{\vec{q}}_d(i) = 1$;
$\mathbf{M}_d(1:3, i) =$
$\left(\mathbf{K}_i + \mathbf{X}^T\,\mathbf{K}_d\right)\ \vec{\Phi}$;
end

In order to build the forward dynamic model in independent generalized coordinates, the component of dependent accelerations has to be written with respect to independent accelerations,

$$\ddot{\vec{q}}_d = \mathbf{A}_d^{-1}\vec{b} - \mathbf{X}\cdot\ddot{\vec{q}}_i \tag{4}$$

By substituting Eq. 4 into Eq. 3 the following equation can be obtained,

$$\mathbf{M}_{i_{n\times n}}\ddot{\vec{q}}_i + \mathbf{M}_{d_{n\times m-n}}\ddot{\vec{q}}_d = \mathbf{M}_i\ddot{\vec{q}}_i + \mathbf{M}_d\left[\mathbf{A}_d^{-1}\vec{b} - \mathbf{X}\cdot\ddot{\vec{q}}_i\right] \tag{5}$$

As can be seen, when replacing the dependent accelerations, a vector depending on the vector of velocity appears, thus this term has to be included

in the vector of centrifugal and Coriolis forces $\vec{C}$. Finally, The mass matrix is built as follows,

$$\mathbf{M} = \mathbf{M}_i - \mathbf{M}_d\mathbf{X} \tag{6}$$

2.2 Vector of Velocity components

The vector corresponding to the centrifugal and Coriolis forces ($\vec{C}$) is found thanks to it only includes the components of generalized coordinates and velocities,

Input: $\vec{g} = 0$, $\ddot{\vec{q}} = 0$
$\vec{C}_d(1:n,1) = \mathbf{M}_d\mathbf{A}_d^{-1}\vec{b}$;
$\vec{C}_i(1:n,1) = \left(\mathbf{K}_i + \mathbf{X}^T\,\mathbf{K}_d\right)\,\vec{\Phi}$;
$\vec{C} = \vec{C}_i + \vec{C}_d$;

2.3 Vector of Gravity components

The vector of gravity includes only contains the generalized coordinates and the vector of gravity. Thus,

Input: $\dot{\vec{q}} = 0$, $\ddot{\vec{q}} = 0$
$\vec{G}(1:n,1) = \left(\mathbf{K}_i + \mathbf{X}^T\,\mathbf{K}_d\right)\,\vec{\Phi}$;

3 Case Studies

The proposed approach was applied to actual 3-DOF parallel robots, namely, a 3-RPS and a 3-PRS robot. Both 3-DOF robots are actuated by a ball-screw driving system. As mentioned before, 3 sets of parameters were used for simulation. The Complete Model refers to a model obtained by applying Eq. 1 to the parallel robot and then the base parameter model is found. Thus, the model includes all the rigid body parameters that contribute to the dynamic response of the system.

The number of parameters in the models used for identification and hence for simulations for the 3-PRS robot is listed in Table 1. For the 3-RPS they are listed in Table 2. In addition, in both cases the model includes 6 parameters for modeling friction in actuated joints. The Coulomb friction

Table 1. Identified models used for simulations of the 3-PRS robot.

Identified Model	Rigid Body	Friction	Actives Elements
Complete Model	19	6	3
Reduced Model	4	6	3

Table 2. Identified models used for simulations of the 3-RPS robot.

Identified Model	Rigid Body	Friction	Actives Elements
Complete Model	25	6	3
Reduced Model	3	6	3

and viscous friction model was used. The inertia of the actuators adds 3 parameters to the model. The base parameters model and the numerical values considered for simulations of the 3-PRS robot are listed in Table 3 where lm is the length between the spherical joints located in the moving platform and lr is the length of the connecting rod.

The friction parameters for the model based on CAD parameters for the 3-PRS were found by a direct identification conducted on each actuator. The inertia of the actuators was estimated as if they were cylinders with their diameters equal to the screw of the actuator. A similar approach was used for estimating the parameters based on CAD for the 3-RPS robots, but in this case the final parameter values were obtaining after adjusting the response of the CAD model to the actual one by hand. Several attempts were needed in order to adjust the model (Díaz-Rodríguez et al., 2008).

To evaluate the response of the identified models with respect to the actual experiments the Relative Absolute Error is used,

$$\varepsilon_{ra} = \frac{\sum_i |x_{iden_i} - x_i^*|}{\sum_i |x_i^* - \overline{x}^*|} \tag{7}$$

The simulations are carried out in the Matlab environment using the *ode45* function, which is based on an explicit Runge-Kutta 45 formula. It is important to mention that the identified friction model introduces a discontinuity into the equation of motions. Thus, a procedure for solving the discontinuity problem was implemented (Farhat et al., 2010).

4 Results

Table 4 shows the results for the mean values of the relative absolute error between the measured position of the actual robot and the position obtained through simulation for the 3-PRS robot. The mean values were obtained

Table 3. Dynamic parameters of the 3-PRS parallel robot.

Φ [SI Unit]	CAD + Friction	Model 1	Reduced
$Izz_2 - lr^2 \sum_{i=1}^{2} m_i$	-1.9780	-2.34	
$mx_2 - lr^2 \sum_{i=1}^{2} m_i$	-4.7000	165.55	
my_2	0.0000	183.85	
$Ixx_3 - (3/2\ lm^2 \sum_{i=1}^{5} m_i$	-5.3018	9.00	
$Ixy_3 + (3/4) lm^2 \sum_{i=1}^{5} m_i$	2.8794	-181.77	3.51
Ixz_3	0.0000	-2.34	
$Iyy_3 - (lm/2)^2 \sum_{i=1}^{3} m_i + lm \sum_{i=4}^{5} m_i$	1.3480	-1.29	
Iyz_3	0.0000	3.65	
$Izz_3 - lm \sum_{i=1}^{3} m_i$	-3.9549	4.98	
$mx_3 - (lm/2) \sum_{i=1}^{5} m_i + lm \sum_{i=1}^{5} m_i$	0.0000	7.18	
$my_3 - (\sqrt{3}/2\ lm) \sum_{i=1}^{5} m_i$	-13.7116	61.90	-19.29
mz_3	0.0000	-2.70	
$Izz_5 - lr^2 \sum_{i=4}^{5} m_i$	-1.9780	-1.81	
$mx_5 - lr \sum_{i=4}^{5} m_i$	-4.7000	20.03	
my_5	0.0000	-298.52	
$Izz_7 + lr^2 \sum_{i=1}^{5} m_i$	7.0693	8.55	
$\sum_{i=1}^{7} m_i$	56.5457	327.84	62.17
$mx_7 + lr \sum_{i=1}^{5} m_i$	17.9183	-25.34	51.2
my_7	0.0000	-271.24	
F_{v_1}	3267.45	2922.85	3278.96
F_{v_2}	2127.48	194.54	150.79
F_{v_3}	2120.09	2207.71	2167.74
F_{c_1}	152.70	108.32	118.59
F_{c_2}	118.32	2349.38	1999.54
F_{c_3}	247.97	223.00	255.90
J_{r_1}	2.257e-003	2.100e-3	1.485e-3
J_{r_2}	2.257e-003	1.675e-3	2.037e-3
J_{r_3}	2.257e-003	2.178e-3	1.7821e-3

for 10 trajectories, which were different from the ones considered for identification. The results indicate that the predicted error of the independent generalized coordinates at position level and velocity for the reduced model are lower than those obtained for the Complete Model and the CAD model. In terms of the generalized coordinates, values for the Reduced Model are far below the ones obtained by means of the CAD parameters. In addition, the prediction error in terms of the inverse dynamics, $\varepsilon(\vec{\tau})$, for the Reduced Model is lower than the two previously mentioned models.

Table 4. Relative Absolute Errors ε (3-PRS parallel robot).

	$\varepsilon(\vec{q})$	$\varepsilon(\dot{\vec{q}})$	$\varepsilon(\vec{\tau})$
CAD + Friction	53.37	25.49	20.20
Complete Model	24.99	18.30	16.72
Reduced Model	21.41	17.20	14.94

Figure 1 shows the evolution of the generalized independent coordinates for the Complete Model, the Reduced Model and the measured actuator

position. As can be seen, the Reduced Model follows the measured actuator positions more closely than the Complete Model. Moreover, for some validation trajectories the Complete Model was not able to accomplish the simulation.

On the other hand, the results for the 3-RPS, listed in Table 5, indicate that the Reduced Model predicts the response of the system with more accuracy than the Complete Model and the CAD model, not only with respect to the generalized coordinates, but also with respect to the generalized forces.

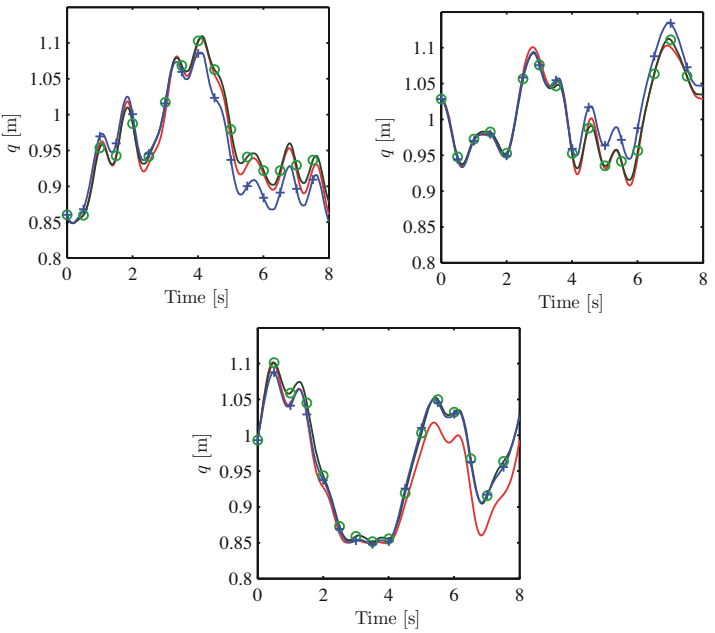

Figure 1. Actual displacement —, simulated reduced model (o—) and simulated complete model (+—), for the 3-PRS robot.

Table 5. Relative Absolute Error ε (3-RPS parallel robot).

	$\varepsilon(\vec{q})$	$\varepsilon(\dot{\vec{q}})$	$\varepsilon(\vec{\tau})$
CAD + Friction	19.54	10.37	12.61
Complete Model	23.08	11.991	14.28
Reduced Model	17.33	9.44	11.31

In this case the CAD model performs more closely to the system response. However,, as mentioned before, the parameters were obtained after several attempts which is a time-consuming approach.

5 Conclusions

In this paper, an approach for solving the forward dynamic problem in terms of identified parameters was proposed. The approach has allowed us to establish a comparison among identified models, and with a model in which its dynamic parameters were obtained by the CAD model. The results indicated that the identified model, obtained based on relevant parameters, is closely related to the actual system response when compared with the response of a Complete Model and the CAD model. In addition, for some of the several trajectories used for validation, the Complete Model failed to achieve the simulation time, indicating that the reduced model whose parameters are identified properly has advantages over the use of Complete identified Model.

Bibliography

M. Díaz-Rodríguez. *Identificación de parámetros dinámicos de robots paralelos basada en un conjunto de parámetros significativos.* PhD thesis, Universidad Politécnica de Valencia, 2009. URL `http://hdl.handle.net/10251/6344`.

M. Díaz-Rodríguez, V. Mata, N. Farhat, and S. Provenzano. Identifiability of the dynamic parameters of a class of parallel robots in the presence of measurement noise and modeling discrepancy. *Mechanics Based Design of Structures and Machines*, 36(4):478–498, 2008.

N. Farhat, V. Mata, A. Page, and F. Valero. Identification of dynamic parameters of a 3-DOF RPS parallel manipulator. *Mechanism and Machine Theory*, 43(1):1–17, 2008.

N. Farhat, V. Mata, A. Page, and M. Díaz-Rodríguez. Dynamic simulation of a parallel robot: Coulomb friction and stick-slip in robot joints. *Robotica*, 28(1):35–45, 2010.

W Khalil and E Dombre. *Modeling Identification and Control of Robots.* Hermes Penton Ltd, London, 2002.

D. Negrut, E. J. Haug, and H. C. German. An implicit Runge-Kutta method for integration of differential algebraic equations of multibody dynamics. *Multibody System Dynamics*, 9(2):121–143, 2003.

F. Pierrot, V. Nabat, O. Company, S. Krut, and P. Poignet. Optimal design of a 4-DOF parallel manipulator: From academia to industry. *IEEE Transactions on Robotics*, 25(2):213–224, 2009.

Workspace Generation of Planar Wire-Actuated Parallel Manipulators with Antipodal Method

Derek McColl and Leila Notash[1]
Department of Mechanical and Materials Engineering, Queen's University, Kingston, ON, Canada

This article presents an analytical solution to workspace generation of planar wire-actuated parallel manipulators based on the planar antipodal theorem from multi-fingered grasping. Using the geometry of the wires, equations describing the borders of the workspace are formulated. The external force is modeled as a wire, and the workspace of manipulators with more than four wires is obtained by the union of the workspace contributions of each set of four wires. The workspaces of a manipulator, with and without external force, are generated with this method.

1. Introduction

This article concentrates on the workspace formulation of planar wire-actuated parallel manipulators. An example planar wire-actuated parallel manipulator can be seen in Figure 1(a). The position and orientation of the mobile platform is controlled by changing the length of the wires. These manipulators have light weight and long wires which allow for high speed motion and a large workspace.

Wire-actuated parallel manipulators require redundancy because wires can only apply force in the form of tension. For example, gravity or at least $n + 1$ wires are needed to maintain positive tension in all the wires of a manipulator with n degrees of freedom (Kawamura and Ito, 1993). For this reason, manipulators with $n + 1$ wires will be referred to as non-redundant and those with more than $n + 1$ wires will be referred to as redundant manipulators.

A wire-actuated parallel manipulator that can withstand any external force/moment (wrench) applied to the mobile platform has wrench closure, i.e., when all the wires have positive tension the manipulator can withstand any external wrench. The collection of manipulator poses at which the manipulator has wrench closure is called the wrench-closure workspace. The wrench-closure workspace of planar wire-actuated parallel manipulators has been studied, e.g., Williams and Gallina (2002) and Gouttefarde and Gosselin (2006). Wrench-closure workspaces do not take into account wire tensions of the manipulator.

---

[1] The encouragement of Dr. Jean-Pierre Merlet in extending the antipodal theorem-based approach of McColl and Notash (2009b) for analytical workspace identification is highly appreciated.

McColl and Notash (2009a) investigated an analytical wrench-closure workspace generation with external wrench (modeled as a wire).

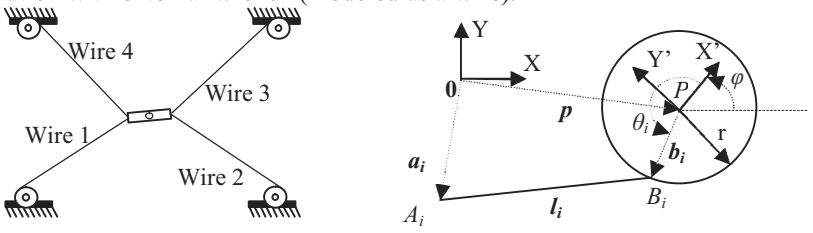

Figure 1. (a) Example planar wire-actuated parallel manipulator, and (b) coordinate systems.

To investigate the workspace of a manipulator, fixed and moving coordinate systems are assigned. The coordinates and parameters for a planar wire-actuated parallel manipulator are shown in Figure 1(b). The base has the fixed coordinate system Ψ(X, Y) located at **0**, while the mobile platform has a coordinate system, Γ(X', Y'), fixed to the center of mass, point P; P has coordinates (x, y) in Ψ(X, Y). The mobile platform is connected to the base by n wires each with length l_i. The attachment points of the wires to the base frame, anchors, are denoted A_i, while the attachment points on the mobile platform are denoted B_i. The angle at which the mobile platform is oriented with respect to Ψ(X, Y) is given as φ and the orientation of lines $\overline{PB}_i$ with respect to the mobile platform frame are given by angles θ_i.

The position vector of point A_i with respect to the fixed frame is ${}^{\Psi}\mathbf{a}_{i,} = [\, a_{ix} \quad a_{iy} \,]^T$, and the position vector of point B_i with respect to Γ(X', Y') is given as ${}^{\Gamma}\mathbf{b}_{i,} = [\, b_i \cos\theta_i \quad b_i \sin\theta_i \,]^T$, $i = 1, \ldots, n$, where b_i is the length of the line segment $\overline{PB}_i$. Then, the position of B_i relative to the base frame is calculated as

$$ {}^{\Psi}\mathbf{b}_i = \begin{bmatrix} x + b_i \cos\theta_i \cos\varphi - b_i \sin\theta_i \sin\varphi \\ y + b_i \cos\theta_i \sin\varphi + b_i \sin\theta_i \cos\varphi \end{bmatrix}, \quad i = 1, \ldots, n \qquad (1) $$

This article investigates the analytical workspace formulation of planar wire-actuated parallel manipulators based on the geometry of the wires. The theory is presented in Section 2 and the simulation is discussed in Section 3. The conclusions of the article are stated in Section 4.

2. Theory

The wires of wire-actuated parallel manipulators can only exert a force pulling the mobile platform. This is similar to the fingers of the grasping manipulators which may only exert a force inwards on the object being grasped, when friction is ignored.

If each finger of a multi-fingered manipulator is modelled with friction, between the finger and the object being grasped, then the force that each finger applies on the object can be modelled as a friction cone. The vertex of the friction cone is located at the point of contact. The height and base radius of the cone are respectively equal to the magnitude of the normal and friction forces applied by the finger. For a planar grasp, two friction cones are required to completely restrain the object (Murray et al, 1994). When a grasping manipulator uses frictionless fingers the "friction cones" are created by finding the intersection of the lines of contact force no matter where the fingers contact the surface of the object (Nguyen, 1988).

For planar grasping manipulators, an object is fully constrained if the following theorem is satisfied.

Planar Antipodal Grasp Theorem – Two contact points with friction

A planar grasp with two point contacts with friction is force closed if and only if the line connecting the contact points lies inside both friction cones (Murray *et al*., 1994).

Extending the antipodal grasp theorem to four separate contact points, the following theorem is proposed.

Planar Antipodal Grasp Theorem – Four frictionless contact points

Taking the intersection point of two adjacent forces and then the intersection point of the two remaining forces, a planar grasp with four frictionless contact points is wrench closed if and only if the line connecting these two points lies inside both "friction cones".

Comparing the wire-actuated manipulators to the grasping manipulators, if two wires are connected to the same point on the mobile platform (or base), like the manipulator in Figure 1(a), then the forces applied by these two wires on the mobile platform can be modelled as a "friction cone" (Ebert-Uphoff and Voglewede, 2004). By extending the wire axes, "friction cones" can be formed for manipulators with distinct wire attachments. The manipulator has wrench closure if the "friction cones" created by the wire axes satisfy the planar antipodal grasp theorem.

For wire-actuated manipulators, the axes of the tension force created by the wires, i.e., the lines coincident with the wires, are used to create the "friction cones" or reversed "friction cones" as shown in Figure 2. If the line connecting the vertices of "friction cones" is contained in both of the reversed "friction cones" then the current pose satisfies the planar antipodal grasp theorem and is realizable and part of the workspace.

When the line connecting the vertices of the reversed "friction cones" is collinear with one of the edges of the corresponding "friction cones" the manipulator is at the border of the workspace. A non-redundant manipulator reaches a singularity when two of the wire axes are collinear. The borders of the

workspace are found by formulating the curves which describe the collinearity of each wire axis with every other wire axis and the curves which describe the collinearity of each wire axis with the line that connects the vertices of the "friction cones". The area inside the curves that satisfies the antipodal grasp theorem is the workspace of the manipulator.

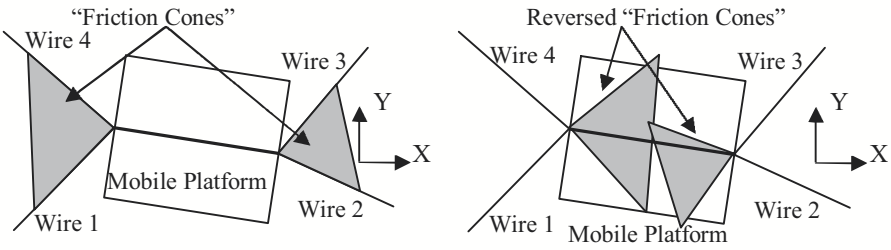

(a) "Friction cones" (b) Reversed "friction cones"

Figure 2. "Friction cones" for manipulator in Figure 1(a).

The expressions of the curves that define the borders of the workspace are functions of the anchor positions, ${}^{\Psi}\mathbf{a}_i$, which are constant, and the wire attachment points on the mobile platform, ${}^{\Psi}\mathbf{b}_i$, which are written in terms of the mobile platform pose.

For a planar manipulator with 3 degrees of freedom, two "friction cones" (four wires) are required to check for wrench closure. For a given orientation of mobile platform, the vertices of two "friction cones", $(x_{\text{int1}}, y_{\text{int1}})$ and $(x_{\text{int2}}, y_{\text{int2}})$, are identified in terms of the mobile platform position (x, y). The curves which comprise the borders of the constant orientation workspace, set of locations reachable for a given mobile platform orientation, are formulated using the collinearity of the line connecting the vertices of the "friction cones" with each wire and the collinearity of each wire with every other wire. To test the collinearity of the line that connects the vertices of the two "friction cones" and the edge of a "friction cone", the two vertices of the "friction cones", $(x_{\text{int1}}, y_{\text{int1}})$ and $(x_{\text{int2}}, y_{\text{int2}})$, and the anchor position of the wire, corresponding to the edge of the "friction cone" being investigated, (a_{ix}, a_{iy}), are utilized. If these three points are collinear then the edge of the "friction cone" is collinear to the line connecting the vertices of the "friction cones". To formulate the expression of collinearity, the following equation is used.

$$\det\begin{bmatrix} a_{ix} & a_{iy} & 1 \\ x_{\text{int}1} & y_{\text{int}1} & 1 \\ x_{\text{int}2} & y_{\text{int}2} & 1 \end{bmatrix} = 0 \tag{2}$$

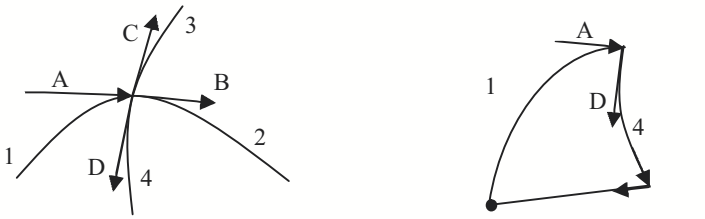

(a) Example curve segments (b) Simple closed curve

Figure 3. Example formation of closed curve

The expressions for the collinearity are quadratic or linear equations in terms of the mobile platform position, x and y for a constant orientation workspace. These equations are plotted as curves to identify the constant orientation workspace. The areas, created by the intersecting curves that contain manipulator poses which satisfy the planar antipodal grasp theorem, comprise the constant orientation workspace. To find these areas, the curves are discretized to define the border of an area as a set of points by substituting the x (or y) coordinate of the mobile platform position in equation (2) to calculate values of y (or x).

Each curve is split into segments between intersection points, identified using a certain number of points along the curves and the end points. These segments are numbered sequentially along the curves. Figure 3(a) shows two curves intersecting and the numbering of each curve segment. Since the curve segments are represented as arrays with a finite number of points, there is an uncertainty between an intersection point and the closest point in the array to that intersection point. This uncertainty can be decreased by increasing the resolution of points per curve.

Each area is bordered by a collection of curve segments that create a simple closed curve, a curve that does not intersect itself (Saff and Snider, 2003). Starting at the first curve segment, one of the end points of the curve is chosen arbitrarily and all the curve segments which share that endpoint (within the uncertainty) are identified. For each one of these curve segments that share the endpoint $\mathbf{x}_{ep}$, the point in the curve segment array closest to the endpoint, $\mathbf{x}_{cep}$ is used to form the vector $\mathbf{x}_{ep} - \mathbf{x}_{cep}$, referred to as tangent vector. An example of this procedure is shown in Figure 3(a).

The curve segment whose tangent vector has the smallest angle and a clockwise orientation with respect to the tangent vector of the first curve segment (vector A in Figure 3(a)), is retained to start forming the simple closed curve, tangent vector D in Figure 3(a). This curve segment now replaces the first curve segment and the process is repeated until a simple closed curve is formed. Figure 3(b) shows the identification of the next curve segment to form a simple closed curve. The arrays for all the curve segments that create a simple closed curve are compiled into a single array that defines the simple closed curve.

By defining a small circle around an end point of one of the corresponding curve segments on the simple closed curve, a point on the circle and inside the simple closed curve is identified and tested with the planar antipodal grasp theorem. If that point satisfies the planar antipodal grasp theorem, the area surrounded by the simple closed curve is part of the workspace.

For planar manipulators with more than four wires, the union of workspace contributions of each combination of four wires is the workspace of the manipulator. If an external force is applied to the mobile platform, the external force is modelled as a wire. To model the external force as a wire, an arbitrary point along the force axis well away from the mobile platform is taken as a point in the collinearity formulation. This workspace formulation method will be referred to as the analytical antipodal method. The analytical antipodal method reported here is the extension of the antipodal method for the discrete workspace analysis of McColl and Notash (2009b).

3.Simulation

The workspace of the example manipulator in Figure 1(a) is investigated using the analytical antipodal method proposed in this article. For all the simulations in this work, each distinct curve is formulated as an array of 200 data points, resulting in a maximum error in the calculation of intersection points of less than 0.01 units. Since this method only investigates the configuration of the wire axes, the workspace plots would be the same for any unit of length, e.g., millimetres, meters, etc. The constant orientation workspace plots of the manipulator in Figure 1(a) with no external force are formulated with the analytical antipodal method and shown in Figure 4. Figures 4(a)-4(c) show the workspaces formulated at $\varphi = 0^o$, 5^o, and 20^o respectively. The curves which describe the configuration of the "friction cones" and wires, formulated using collinearity, are the lines drawn on each plot and the small circles represent anchor positions. The workspace of manipulator, represented by the black area in each figure, corresponds to the positions reachable by the centre of the mobile platform for the given mobile platform orientation.

The workspace of the manipulator in Figure 1(a) is also investigated with external force acting in the negative Y-direction at the centre of mass of the mobile platform. Similar to the wire tensions, the magnitude of external force is not considered. The analytical antipodal method investigates the workspaces of each set of four wires/forces at a time. The workspace contributions are shown in Figures 5(a)-(e) and the manipulator workspace is shown in Figure 5(f) for the manipulator in Figure 1(a) at $\varphi = 15^o$ with an external force in the negative Y-direction. For the external force in negative Y-direction, since some contributions to the workspace taper to infinity in the negative Y-direction, only a part of the area is formulated for the workspaces. Figures 6(a)-6(c) show the workspaces of this manipulator with the external force at $\varphi = 0^o$, 5^o, and 20^o. It

should be noted that this manipulator was investigated in McColl and Notash (2009a) employing the workspace envelope characterization method (based on the null space of the Jacobian matrix, characterized by the 3x3 minors of this matrix) and the workspace results presented in these two articles are identical within uncertainty.

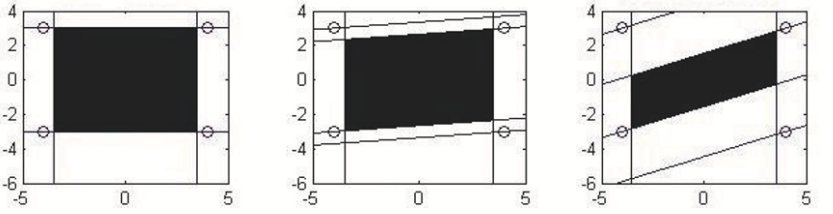

(a) $\varphi = 0^o$ (b) $\varphi = 5^o$ (c) $\varphi = 20^o$

Figure 4. Workspaces of the manipulator in Figure 1(a).

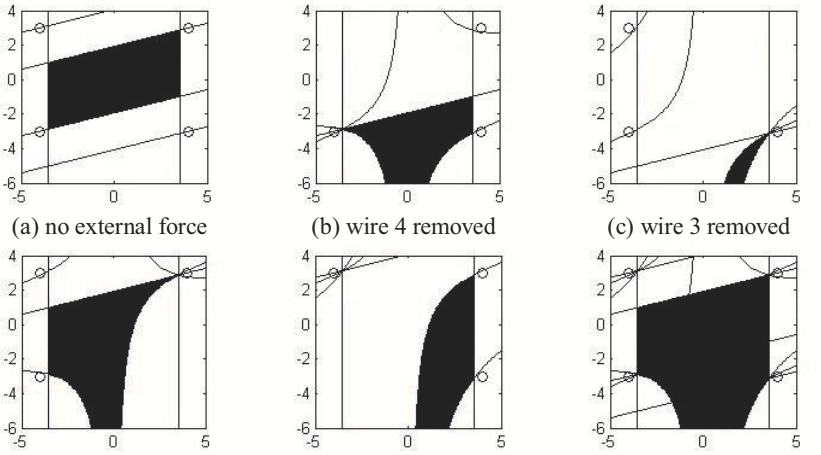

(a) no external force (b) wire 4 removed (c) wire 3 removed

(d) wire 2 removed (e) wire 1 removed (f) manipulator workspace

Figure 5. Workspace contributions of the manipulator at $\varphi = 15^o$ with an external force.

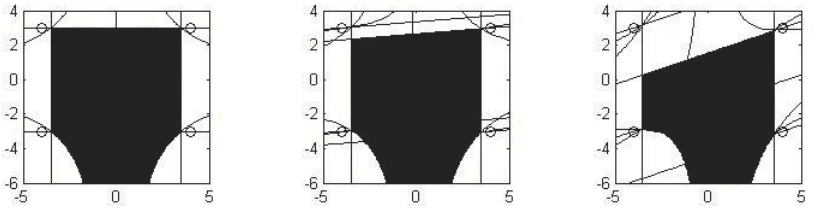

(a) $\varphi = 0^o$ (b) $\varphi = 5^o$ (c) $\varphi = 20^o$

Figure 6. Workspaces of the manipulator with an external force.

4. Conclusion

In this article, the analytical antipodal method, based on the planar antipodal theorem from multi-fingered grasping, was presented to generate an analytical solution to the workspace of planar wire-actuated parallel manipulators. The external force applied to the mobile platform was modelled as a wire. The borders of workspaces, formulated with the analytical antipodal method, were investigated by the workspace contribution of each set of four wires/forces. The borders of each contribution to the workspace were identified by considering the collinearity of the line connecting the vertices of the "friction cones" with each line that represents a wire/force, as well as collinearity of two wire axes. Since the antipodal method investigates the direction of the wires/force acting on the mobile platform, there is no limit on the wire tension and the magnitude of external force. This results in the largest possible workspace. The proposed procedure has been applied to a wide range of planar wire-actuated parallel manipulators with shared/distinct wire attachment points on the base and/or mobile platform, non-redundant and redundant manipulators with or without external force. Due to space limitation, the results for a four-wire manipulator with two wire attachment points on the mobile platform were reported here.

References

Ebert-Uphoff, I., and Voglewede, P. A. (2004). On the connections between cable-driven robots, parallel manipulators and grasping. *Proceedings of the IEEE Conference on Robotics & Automation.* 5:4521-4526.

Gouttefarde, M., and Gosselin, C.M. (2006). Analysis of the wrench–closure workspace of planar Parallel cable-driven mechanisms. *IEEE Transactions on Robotics* 22(3):434-445.

Kawamura, S., and Ito, K. (1993). A new type of master robot for teleopertaion using a radial wire drive system. *Proceedings of the IEEE/RSJ International Conference on Intelligent Robots and Systems*. 55-60.

McColl, D., and Notash, L. (2009a). Workspace envelope formulation of planar wire-actuated parallel manipulators. *Proceedings of the CCToMM M³ Symposium*.

McColl, D., and Notash, L. (2009b). Extension of Antipodal Theorem to Workspace Analysis of Planar Wire-Actuated Manipulators, *Proceedings of the 5th IFToMM International Workshop on Computational Kinematics*.

Murray, R., Li, Z., and Sastry, S. (1994). *A Mathematical Introduction to Robotic Manipulation*. New York. CRC Press.

Nguyen, V.D. (1988). Constructing force-closure grasps. *International Journal of Robotics Research* 7(3):3-16.

Saff, E.B., and Snider, A.D. (2003). *Fundamentals of Complex Analysis with Applications to Engineering and Science Third Edition*. New Jersey. Pearson Education, Inc.

Williams, R.L. II, and Gallina, P. (2002). Planar cable-direct-driven robots: design for wrench exertion. *Journal of Intelligent and Robotics Systems* 35(2):203-219.

Trajectory Following and Vibration Control for Flexible-link Manipulators

P. Boscariol, A. Gasparetto and V. Zanotto
Dipartimento di Ingegneria Elettrica, Gestionale e Meccanica
Università di Udine, Italy

Abstract This paper is aimed at showing the capabilities of the Model-based Predictive Control for simultaneous vibration suppression and trajectory following for a class of flexible-link multi-actuated manipulators. For this class the requirements for the control system are very strict, since any error on the end-effector trajectory can be amplified by the time-varying kinematic configuration of the manipulator. Moreover, an optimal synchronization between the movement of the two axes must be settled. The tests provided here have been developed through exhaustive numerical simulations, the results of which show the capabilities of the MPC controller even for multi-actuated compliant mechanisms.

1 Introduction

The modeling and control of flexible-link mechanisms are key issues in robotics engineering. Critical vibration due to inertial components of the motion arise in manipulators when they are exposed to large acceleration. These dynamic effects can lead to considerable worsening of accuracy, to mechanical failures, as well as instability. An accurate description of the dynamics of multi-link flexible mechanism requires complex and nonlinear models. The problem is even more challenging when trajectory tracking in the operative space is the main concern, since the accuracy requirements are much stricter. The purpose of this paper is to show the capabilities of the Model-based Predictive Control (MPC) strategy for trajectory control and vibration reduction for with regard of a class of multi-actuated flexible-link mechanisms. The use of MPC as a vibration controller has been investigated in a limited number of scientific papers. For example, in [1] the MPC has been applied as a vibration controller in a constrained beam, by means of piezo-electric actuators. In [2] the MPC has been used to control torsional vibration in a milling machine, while in [3] it has been

used to control a flexible-joint mechanism. Moreover, as far as the use of MPC for flexible-links mechanism is concerned, the literature is even less significant: to the authors' knowledge the only papers focusing on this field are [4–7]. In [4, 6, 7] predictive control strategies have been used to control position and the vibration of a single-link mechanism, while in [5] a constrained MPC has been applied as the position-regulator for a four-link closed-chain compliant mechanism. The present work is, therefore, an evolution of previously published studies [4, 5]. In particular, a 5-R planar mechanism will be employed to verify the performance of the MPC strategy for a class of multi-actuated flexible-link mechanisms. The 5-R mechanism has two rigid degrees of freedom and requires two actuators. The control problems increase with respect to the previous works, since the movement of the controlled axes must be more precise and synchronized. This causes the major constraints on the accuracy in each axis. The MPC controller has been implemented in software simulation using Matlab/ Simulink ®. Exhaustive simulations have been conducted to prove the effectiveness of this control approach.

This paper is arranged as follows: Section 2 will briefly illustrate the MPC control strategy. The dynamic model of the 5-R flexible-link mechanism will be constructed in Section 3, while Section 4 will describe the overall control system. Finally, Section 5 will show and discuss the results of a suitable simulation.

2 Model-based Predictive Control

MPC control is based on the following basic ideas: receding-horizon strategy, the internal prediction model, and constraints on control action and manipulated variables. Owing to the length constraints of this paper, in this section only a brief explanation of the concepts mentioned above will be given. Therefore, for more details the reader should refer to [4, 5, 9–11]. The term MPC control refers to a class of optimal controllers. In the MPC controller, the cost-function depends on the instantaneous feedback signals, on the prediction of the future behavior of the plant and, finally, on the ideal trajectory (Figure 1.a).

The evaluation of the future behavior of the plant is obtained from an internal model of the plant, which is computed over a time interval called *prediction horizon* (H_p). The term *control horizon* (H_c) refers, on the other hand, to the length of the control sequence. By defining $\mathbf{z}(k)$ as the vector of the manipulated variables and $\mathbf{r}(k)$ as the vector of the instantaneous reference, the optimal control sequence $\mathbf{w}(k)$ is computed at every step by minimizing this cost-function:

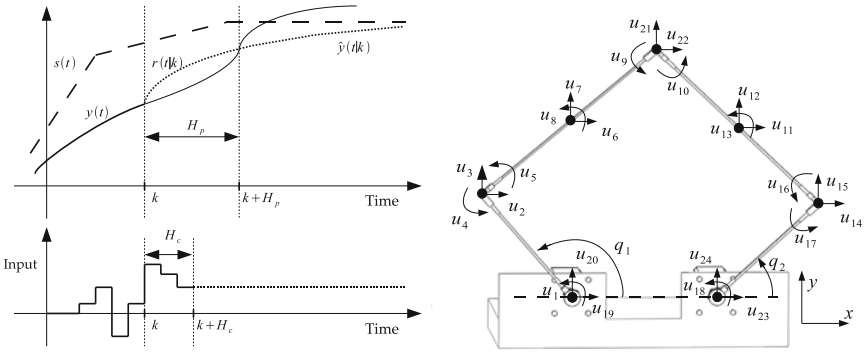

(a) (b)

Figure 1. (a) Receding horizon strategy; (b) 5-R mechanism: elastic and rigid displacements

$$\mathcal{V}(k) = \sum_{i=1}^{H_p} \|\mathbf{z}(k+i|k) - \mathbf{r}(k+i)\|^2_{\mathbf{Q}} + \sum_{i=0}^{H_c-1} \|\Delta\mathbf{w}(k+i|k)\|^2_{\mathbf{R}} \qquad (1)$$

It must be pointed out that the optimal control sequence is computed at every time step k. However, only the first element of this sequence is eventually fed back to the plant. $\mathbf{Q}$ and $\mathbf{R}$ are weighting matrices for the quadratic norm of the tracking error and control effort. A more detailed description of the use of MPC for flexible-link mechanisms can be found in [5].

3 Dynamic model

In this section the dynamic model of the flexible-link mechanism proposed by Giovagnoni [8] will be briefly explained. The choice of this formulation among the several proposed in the last 40 years has been motivated mainly by the high level of accuracy allowed by this model. Each flexible link belonging to the mechanism is subdivided into finite elements. The mechanism's motion can be thought as the superposition of the motion of an equivalent rigid-link system (ERLS) and the elastic motion of the nodes of the finite elements. Therefore, the independent coordinates of the system correspond to the angular position of the two cranks and the vector of the nodal displacement $\mathbf{u}$. The dynamic equation of motion is:

$$\begin{bmatrix} \mathbf{M} & \mathbf{MS} & \mathbf{0} & \mathbf{0} \\ \mathbf{S}^T\mathbf{M} & \mathbf{S}^T\mathbf{M}S & \mathbf{0} & \mathbf{0} \\ \mathbf{0} & \mathbf{0} & \mathbf{I} & \mathbf{0} \\ \mathbf{0} & \mathbf{0} & \mathbf{0} & \mathbf{I} \end{bmatrix} \begin{bmatrix} \ddot{\mathbf{u}} \\ \ddot{\mathbf{q}} \\ \dot{\mathbf{u}} \\ \dot{\mathbf{q}} \end{bmatrix} = \begin{bmatrix} \mathbf{M} & \mathbf{I} \\ \mathbf{S}^T\mathbf{M} & \mathbf{S}^T \\ \mathbf{0} & \mathbf{0} \\ \mathbf{0} & \mathbf{0} \end{bmatrix} \begin{bmatrix} \mathbf{g} \\ \tau \end{bmatrix}$$
$$+ \begin{bmatrix} -2\mathbf{M}_G - \alpha\mathbf{M} - \beta\mathbf{K} & -\mathbf{M}\dot{\mathbf{S}} & -\mathbf{K} & \mathbf{0} \\ \mathbf{S}^T(-2\mathbf{M}_G - \alpha\mathbf{M}) & \text{-}S^T\mathbf{M}\dot{\mathbf{S}} & \mathbf{0} & \mathbf{0} \\ \mathbf{I} & \mathbf{0} & \mathbf{0} & \mathbf{0} \\ \mathbf{0} & \mathbf{I} & \mathbf{0} & \mathbf{0} \end{bmatrix} \begin{bmatrix} \dot{\mathbf{u}} \\ \dot{\mathbf{q}} \\ \mathbf{u} \\ \mathbf{q} \end{bmatrix} \tag{2}$$

A detailed description of this model can be found in [8].

The 5-R mechanism is the 2DoFs manipulator shown in Figure 1.b. It is comprised of four steel rods connected in a closed-loop chain by using five revolute joints. The motion of the cranks is governed by two torque-controlled actuators. The fifth link (i.e., the chassis) can be considered to be perfectly rigid without affecting the accuracy of the model. The mechanical characteristics of the mechanism are shown in Table 1. The links are very thin and the whole mechanism is quite prone to vibration.

The overall FEM model is characterized by 24 nodal displacements, as it can be seen in Figure 1.b.

Table 1. The kinematic and dynamic characteristics of the flexible-link mechanism

	symbol	value
Young's modulus	E	200×10^9 [Pa]
Flexural inertia moment	J	1.08×10^{-10} $[m^4]$
Beam width	a	6×10^{-3} [m]
Beam thickness	b	6×10^{-3} [m]
Mass/unit of length of links	m	0.282 $[kg/m]$
Length of links 1-4	L_i	0.3 [m], 0.6 [m], 0.6 [m], 0.3 [m]
Ground length	L_5	0.3 [m]
Rayleigh damping constants	α	8.72×10^{-2} $[s^{-1}]$
	β	2.1×10^{-5} [s]

4 Control System

Figure 2 shows the control scheme. Since only a set of the state vector's components can be measured (i.e., the cranks' angular position and the corresponding elastic displacements), an Extended Kalman Filter is used to estimate the whole state from a subset of it. The estimated current state, as well as the previously generated inputs, are used to predict the future behavior of the mechanism and to optimize it. Eventually, the optimal sequence is computed and its first component input into the actuators.

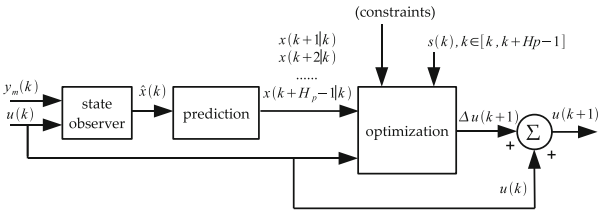

Figure 2. Control scheme

5 Simulation results: trajectory tracking

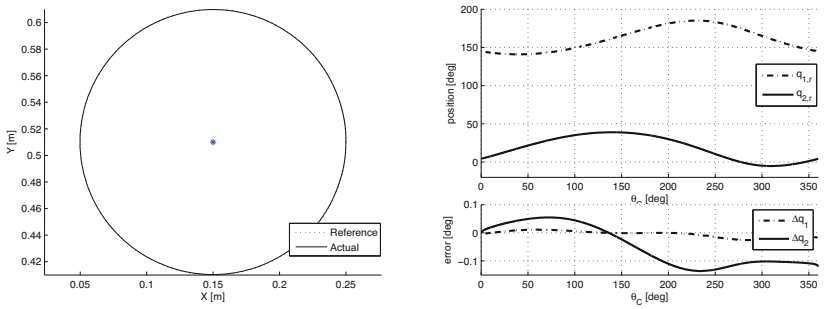

(*a*) (*b*)

Figure 3. (a) Trajectory in the Cartesian space; (b) Trajectory and position errors of the joints

In this section, the effectiveness of the MPC as a suitable controller for multi-actuated flexible-link manipulators will be proven and discussed by investigating the behavior of the 5-R mechanism. The task consists of tracking the circumference with the center in $\mathbf{C}_c = [0.150m, 0.510m]^T$ and radius $r_c = 0.10m$: $C : \mathbf{X}(\theta_c) = \mathbf{C}_c + r_c \begin{bmatrix} \cos\theta_c & \sin\theta_c \end{bmatrix}^T$, $\theta_c \in [0, 2\pi]$

The trajectory has been planned as in [12]. This procedure, indeed, allows for the computation of the optimal trajectory depending on jerk and execution time. Figure 3.(a) shows the trajectory in the Cartesian space, while Figure 3.(b) shows the trajectories of the related joints. The MPC controller has been tuned with the following values: $H_p = 5$, $H_c = 5$,$w_{u_1} = w_{u_{18}} = 2 \times 10^3$, $w_{q_1} = w_{q_2} = 4 \times 10^4$.

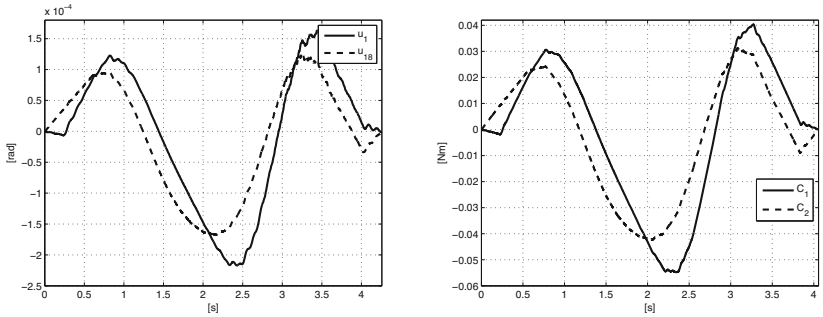

(*a*) (*b*)

Figure 4. (a) Nodal displacements u_1, u_{18}; (b) Input torques

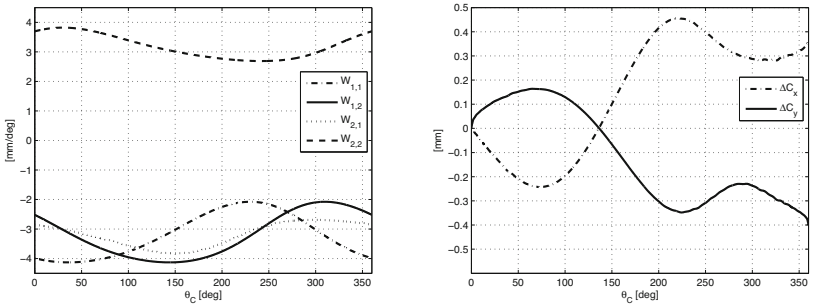

(*a*) (*b*)

Figure 5. (a) Sensibility's coefficients; (b) Position error

The main simulation results are shown in Figures 3 through 5. In particular, Figure 3.b shows the angular positions of cranks q_1 and q_2 and their corresponding errors. It should be pointed out that the joint errors are never more than 1.2 tenths of degree, which proves the considerable performance of the controller. At the same time, the elastic displacements u_1 and u_{18} are shown in Figure 4.a. By comparing Figure 4.a with Figure 4.b (where the input torques are shown); it is possible to evaluate the capabilities of such a controller much more clearly. The vibration affecting the nodal displacements is, indeed, kept very minimal and the main displacements can be attributed largely to the accelerating torques input; therefore, the MPC controller is able to reduce vibration as well. As far as the position errors in

the Cartesian space are concerned, the MPC seems to be a little less high-performance (Figure 5.b). This can be imputed to the kinematic structure of the mechanism, as well as to the physiological behavior of the proposed controller. The kinematics of the manipulator, indeed, amplifies the joint errors as follows: $\Delta\mathbf{C} = \mathbf{S}_C(\mathbf{q})\Delta\mathbf{q} = [w_{ij}]\,\Delta\mathbf{q}$, where $\mathbf{S}_C(\mathbf{q})$ is the sensibility coefficients' matrix of the end-effector. It should be noted that this matrix depends on the current manipulator configuration. As such, the amplification of the joint errors varies as the manipulator changes configuration. Figure 5.a shows the values of the four elements of $\mathbf{S}_C$. By considering the joint errors of Figure 3.b and the coefficients of Figure 5.a, it is possible to infer the error of the end-effector shown in Figure 5.b. As a result, in order to reduce the position error in the Cartesian space, a high-performance control action must be settled on the joints. This issue is dependent on the physiological behavior of the controller, which can only handle the end-effector position through the kinematic structure of the manipulator. Neither does a position's feedback exist nor does the MPC controller have an internal kinematic model of the structure. The kinematic model would enormously complicate the controller and would require a much higher computational effort. A better solution for MPC control is currently being investigated by the authors. It will permit forcing the axes to behave in a more synchronized way. Although the resulting trajectory will be slightly slowed down , the position performance appears to be very promising.

6 Conclusion

In this paper a predictive control strategy has been proposed as an effective solution to the problem of simultaneous trajectory tracking and vibration suppression for compliant mechanisms with multiple actuation. The control system is based on receding horizon strategy, reference lookahead and an accurate prediction model. The mechanism chosen to validate, trough extensive sets of numerical simulations, the effectiveness of the controller is a flexible five-link planar mechanism. The control system proved to be very effective in both trajectory tracking and vibration suppression, even in tasks encompassing high speed and extensive movement.

Bibliography

[1] A.G. Willis, D. Bates, A.J. Fleming, B. Ninness, S.O. Moheimani, Model Predictive Control Applied to Constraints Handling in Active Noise and Vibration Control, *IEEE Transaction on Control Systems Technology* 16, 1, 3-12 (2008)

[2] J. Wang, Y. Zhang, L. Xu, Y. Jing, S. Zhang, Torsional Vibration Suppression of Rolling Mill with Constrained Model Predictive Control, *proc. 6th World Congress on Intelligent Control and Automation*, Dalian, China, (21-23 June 2006)

[3] N.O. Ghahramania, F. Towhidkhah, Constrained Incremental Predictive Controller Design for a Flexible Joint Robot, *ISA Transactions*, 48, 3, 321-326 (2009)

[4] P. Boscariol, A. Gasparetto, V. Zanotto, Vibration Reduction in a Single-Link Flexible Mechanism Through the Synthesis of an MPC Controller, *proc. of IEEE International Conference on Mechatronics*, Malaga, Spain (14-17 April 2009)

[5] P. Boscariol, A. Gasparetto, V. Zanotto, Model Predictive Control of a Flexible Links Mechanism, *Journal of Intelligent and Robotic Systems*, Published Online (2009)

[6] M. Hassan, R. Dubay, C. Li, R. Wang, Active Vibration Control of a Flexible One-link Manipulator Using a Multivariable Predictive Controller, *Mechatronics* 17, 311-323 (2007)

[7] T. Fan, C.W. de Silva, Dynamic Modelling and Model Predictive Control of Flexible-Link Manipulators, *International Journal of Robotics and Automation* 23, 4 (2008)

[8] M. Giovagnoni, A Numerical and Experimental Analysis of a Chain of Flexible Bodies, *Journal of Dynamic Systems, Measurement, and Control* 113, 73-80 (1994)

[9] J. M. Maciejowski, Predictive Control with Constraints, *Prentice Hall* (2002)

[10] L. Wang, Model Predictive Control System Design and Implementation using Matlab, *Spinger-Verlag*, London (2009)

[11] E.F. Camacho, C. Bordons, *Model Predictive Control*, Springer, New York (2004)

[12] A.Gasparetto, V.Zanotto, A Technique for Time-Jerk Optimal Planning of Robot Trajectories, *Robotics and Computer-Integrated Manufacturing*, 24, 3, 415-426 (June 2008)

Shaking Forces Minimization of High-Speed Robots via an Optimal Motion Planning

S. Briot[1], V. Arakelian[2], N. Sauvestre[2] and J.-P. Le Baron[2]

[1]Institut de Recherches en Communications et Cybernétique
de Nantes (IRCCyN), Nantes, FRANCE
Sebastien.Briot@irccyn.ec-nantes.fr

[2]Institut National des Sciences Appliquées (INSA), Rennes, FRANCE
vigen.arakelyan@insa-rennes.fr
nayelli_sauvestre@hotmail.com
jean-paul.le-baron@insa-rennes.fr

Abstract. This paper deals with the problem of shaking force balancing of high-speed robots based on a new optimal trajectory planning approach. The aim of the new approach is the optimal path planning of the robot links centre of masses, which allows a considerable reduction of the variable inertia forces transmitted to the robot frame. The efficiency of the suggested method is illustrated by a numerical simulation of a planar two links 2*R* serial robot, in which reductions in the shaking force of 63 % and in input torque of 84 % are achieved.

1 Introduction

A primary objective of linkage balancing is to cancel or reduce the variable dynamic loads transmitted to the frame and surrounding structures. Different approaches and solutions devoted to this problem have been developed and documented for one degree of freedom mechanisms (Lowen et al., 1983), (Arakelian et al., 2000), (Arakelian and Smith, 2005). A new field for their applications is the design of mechanical systems for fast manipulation, which is a topical problem in advanced robotics.

The balancing of a mechanism is generally carried out by two steps: (i) the cancellation (or reduction) of the shaking force and (ii) the cancellation (or reduction) of the shaking moment. Traditionally, the cancellation of the shaking force transmitted to the robot frame can be achieved via adding counterweights in order to keep the total centre of mass of moving links stationary (Lowen et al., 1983), (Arakelian et

al., 2000). However, this approach leads to the increase in the total mass of the mechanical systems and consequently the increase in input torques.

With regard to the shaking moment balancing of robots, the following approaches were developed: (i) balancing by counter-rotations (Berkof, 1973), (Dresig et al., 1994), (Arakelian and Smith, 1999), (Herder and Gosselin, 2004), (ii) balancing by adding four-bar linkages (Gosselin et al., 2004), (Ricard and Gosselin, 2000), (iii) balancing by optimal trajectory planning (Papadopoulos and Abu-Abed, 1994), (Fattah and Agrawal, 2006), (Arakelian and Briot, 2008) and (iv) balancing by adding an inertia flywheel rotating with a prescribed angular velocity (Arakelian and Smith, 2008).

It should be noted that the complete dynamic balancing can only be reached by a considerably complicated design of initial robot mechanisms and by unavoidable increase in the total mass. This is the raison why we focused our research studies on the development of robot balancing methods via optimal motion planning approaches, i.e. without modification of the initial mechanical structure and without any adding masses.

The paper is organized as follows. In the next part, the suggested optimal motion planning is described. Then, for illustration of the efficiency of this approach, simulations carried out using ADAMS software for a planar two links 2*R* serial robot are presented. Finally, conclusions are drawn in the last section.

2 Minimization of the Shaking Forces via an Optimal Motion Planning of the Total Mass Centre of Moving Links

The shaking forces $\mathbf{f}^{sh}$ of a robot can written in the form:

$$\mathbf{f}^{sh} = m_{tot}\ddot{\mathbf{x}}_S \tag{1}$$

where m_{tot} is the total mass of the moving links of a robot and $\ddot{\mathbf{x}}_S$ the acceleration of the total mass centre. The classical balancing approach consists in adding counterweights in order to keep the total mass centre of moving links stationary. In this case, $\ddot{\mathbf{x}}_S = 0$ for any configuration of the mechanical system. But, as a consequence, the total mass of the robot is considerably increased. Thus, in order to avoid this drawback, in the present study, a new approach is proposed, which consists of the optimal control of the total mass centre of moving links. Such an optimal motion planning allows the reduction of the total mass centre acceleration and, consequently, the reduction of the shaking force.

Classically, robot displacements are defined considering either articular coordinates $\mathbf{q}$ or Cartesian variables $\mathbf{x}$. Knowing the initial and final robot configurations at time t_0 and t_f, denoted as $\mathbf{q_0} = \mathbf{q}(t_0)$ and $\mathbf{q_f} = \mathbf{q}(t_f)$, or $\mathbf{x_0} = \mathbf{x}(t_0)$ and $\mathbf{x_f} = \mathbf{x}(t_f)$, in the

case of the control of the Cartesian variables, the classical displacement law may be written in the form:

$$\mathbf{q}(t) = s_q(t)\left(\mathbf{q_f} - \mathbf{q_0}\right) + \mathbf{q_0} \tag{2a}$$

or

$$\mathbf{x}(t) = s_x(t)\left(\mathbf{x_f} - \mathbf{x_0}\right) + \mathbf{x_0} \tag{2b}$$

where $s_q(t)$ and $s_x(t)$ may be polynomial (of orders 3, 5 and higher), sinusoidal, bang-bang, etc. laws (Khalil and Dombre, 2002).

From expression (1), we can see that the shaking force, in terms of norm, is minimized if the norm $\left\|\ddot{\mathbf{x}}_S\right\|$ of the masses centre acceleration is minimized along the trajectory. This means that if the displacement $\mathbf{x}_S$ of the robot centre of masses is optimally controlled, the shaking force will be minimized.

Let us consider a robot composed of n links. The mass of the link i is denoted as m_i (i = 1, …, n) and the position of its centre of masses as $\mathbf{x}_{Si}$. Once the articular coordinates $\mathbf{q}$ or Cartesian variables $\mathbf{x}$ are known, the values of $\mathbf{x}_{Si}$ may easily be obtained using the robot kinematics relationships. As a result, the position of the robot centre of masses, defined as

$$\mathbf{x}_S = \frac{1}{m_{tot}} \sum_{i=1}^{n} m_i \mathbf{x}_{Si} \tag{3}$$

may be expressed as a function of $\mathbf{x}$ or $\mathbf{q}$. It may also be shown that, if dim($\mathbf{x}_S$) = dim($\mathbf{q}$) (= dim($\mathbf{x}$) in the case of non redundant robots), $\mathbf{x}$ and $\mathbf{q}$ may be expressed as a function of $\mathbf{x}_S$. We would like to mention that the case where dim($\mathbf{x}_S$) < dim($\mathbf{q}$) will not be considered in this paper. It will be the topic of our further research works.

Thus, taking into account that $\mathbf{q} = \mathbf{f}(\mathbf{x}_S)$ (and as a consequence $\mathbf{x} = \mathbf{g}(\mathbf{x}_S)$), the problem remains to optimally define the trajectory $\mathbf{x}_S(t)$. For this reason, let us consider the displacement $\mathbf{x}_S$ of a point S in the Cartesian space. We assume that, at any moment during the displacement, the norm of the maximal admissible acceleration the point S can reach is constant and denoted as $\ddot{x}_S^{\max}$. Taking that into consideration, the displacement law that minimize the time interval (t_0, t_f) for going from position $\mathbf{x_{S0}} = \mathbf{x_S}(t_0)$ to position $\mathbf{x_{Sf}} = \mathbf{x_S}(t_f)$ is the "bang-bang" law (Khalil and Dombre, 2002), given by (Fig. 1)

$$\begin{cases} \mathbf{x}_S(t) = s(t)\left(\mathbf{x}_{Sf} - \mathbf{x}_{S0}\right) + \mathbf{x}_{S0} \\ \dot{\mathbf{x}}_S(t) = \dot{s}(t)\left(\mathbf{x}_{Sf} - \mathbf{x}_{S0}\right) \\ \ddot{\mathbf{x}}_S(t) = \ddot{s}(t)\left(\mathbf{x}_{Sf} - \mathbf{x}_{S0}\right) \end{cases} \tag{4}$$

with

$$\ddot{s}(t) = \frac{1}{\left\|\mathbf{x}_{Sf} - \mathbf{x}_{S0}\right\|} \begin{cases} \ddot{x}_S^{\max} & for\ t \le (t_f - t_0)/2 \\ -\ddot{x}_S^{\max} & for\ t \ge (t_f - t_0)/2 \end{cases} \tag{5}$$

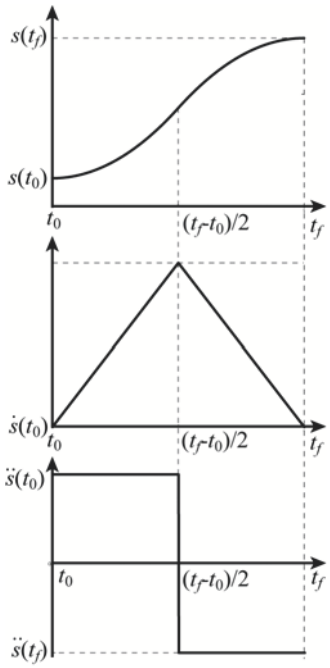

Figure 1. "Bang-bang" displacement law.

Consequently, if the time interval (t_0, t_f) for the displacement between positions $\mathbf{x}_{S0}$ and $\mathbf{x}_{Sf}$ is fixed, the "bang-bang" law is the trajectory that minimizes the value of the maximal acceleration $\ddot{x}_S^{\max}$ (Khalil and Dombre, 2002). Thus, in order to minimize $\|\ddot{\mathbf{x}}_S\|$ for a displacement during the fixed time interval (t_0, t_f), the "bang-bang" law has to be applied on the displacement $\mathbf{x}_S$ on the robot total mass centre.

3 Illustrative Example

For illustration of the efficiency of the suggested solution, let us consider a planar 2*R* serial robot (Fig. 2b) with following parameters:

- $l_{OA} = 0.5$ m, $l_{AB} = 0.3$ m, where l_{OA} and l_{AB} are the lengths of segments OA and AB, respectively;
- $r_1 = 0.289$, where $l_{OS1} = r_1\, l_{OA}$ and $r_2 = 0.098$, where $l_{AS2} = r_2\, l_{AB}$, l_{OS1} and l_{AS2} being the lengths of segments OS_1 and AS_2, respectively.

Its mass and inertia parameters are:

- $m_1 = 24.4$ kg and $m_2 = 8.3$ kg, where m_i is the mass of element i ($i = 1, 2$);
- $m_{tool} = 5$ kg, where m_{tool} is the payload;
- $I_1 = 1.246$ kg.m² and $I_2 = 0.057$ kg.m², where I_i is the axial moment of inertia of element i.

We would like to note that the mentioned parameters correspond to the IRCCyN's robot parameters (Fig. 2), which will be used in future for experimental tests and validation of the force minimization approach developed in the present work.

In order to have the possibility to control the robot, let us express the articulated joint positions $\mathbf{q} = [q_1, q_2]^T$ as a function of the position $\mathbf{x}_S$ of the robot centre of masses. From (3), we obtain:

$$\mathbf{x}_S = \begin{bmatrix} x_S \\ y_S \end{bmatrix} = \frac{m_1 r_1 l_{OA}}{m_{tot}} \begin{bmatrix} \cos q_1 \\ \sin q_1 \end{bmatrix} + \frac{m_2}{m_{tot}} \left(l_{OA} \begin{bmatrix} \cos q_1 \\ \sin q_1 \end{bmatrix} + r_2 l_{AB} \begin{bmatrix} \cos(q_1 + q_2) \\ \sin(q_1 + q_2) \end{bmatrix} \right) \quad (6)$$

This expression leads to:

$$(x_S - l_{eq1} \cos q_1)^2 + (y_S - l_{eq1} \sin q_1)^2 - l_{eq2}^2 = 0 \quad (7)$$

where $l_{eq1} = (m_1 r_1 + m_2) l_{OA} / m_{tot}$ and $l_{eq2} = m_2 r_2 l_{AB} / m_{tot}$.

Replacing $\cos q_1$ and $\sin q_1$ by $(1 - t_1^2)/(1 + t_1^2)$ and $2t_1/(1 + t_1^2)$ ($t_1 = \tan(q_1/2)$), respectively, and developing (7), we obtain:

$$q_1 = 2 \tan^{-1} \left(\frac{-b \pm \sqrt{b^2 - c^2 + a^2}}{c - a} \right) \quad (8)$$

where

$$a = -2 l_{eq1} x_S, \; b = -2 l_{eq1} y_S \text{ and } c = x_S^2 + y_S^2 + l_{eq1}^2 - l_{eq2}^2. \quad (9)$$

In expression (8), the sign ± stands for the two possible working modes of the robot (for simulations, the working mode with the "+" sign is used). Once q_1 is known, q_2 may easily be found from (6):

$$q_2 = \tan^{-1} \left(\frac{y_S - l_{eq1} \sin q_1}{x_S - l_{eq1} \cos q_1} \right) - q_1. \quad (10)$$

Now, let us consider a pick-and-place displacement between two positions of the end-effector $\mathbf{x_0} = [0.3 \text{ m}, 0.7 \text{ m}]^T$ and $\mathbf{x_f} = [0.3 \text{ m}, 0.4 \text{ m}]^T$, beginning at $t_0 = 0$ s and finishing at $t_f = 0.25$ s. Two cases will be simulated:

1. a fifth order polynomial law is applied on the displacement of the robot's end-effector (Eq. (2b));

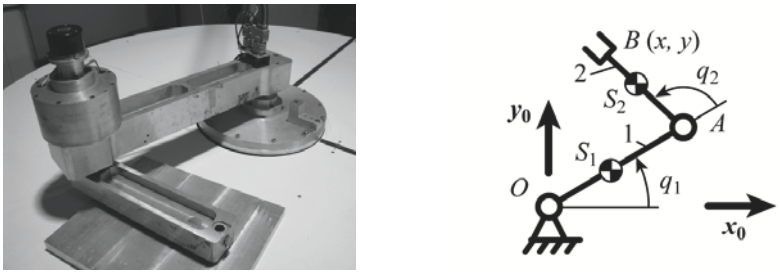

(a) (b)

Figure 2. The 2*R* serial robot: (a) prototype; (b) schematics.

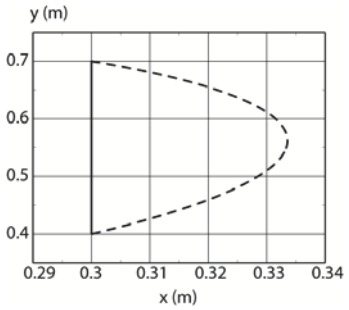

Figure 3. Displacement of the end-effector for two examined cases:

1) fifth order polynomial law applied on the displacement of the end-effector (full line)
2) "bang-bang" law applied on the displacement of the robot centre of masses (dotted line).

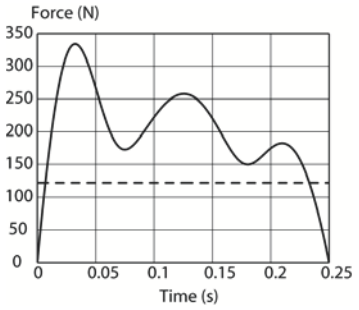

Figure 4. Shaking forces for two examined cases:

1) fifth order polynomial law applied on the displacement of the end-effector (full line)
2) "bang-bang" law applied on the displacement of the robot centre of masses (dotted line).

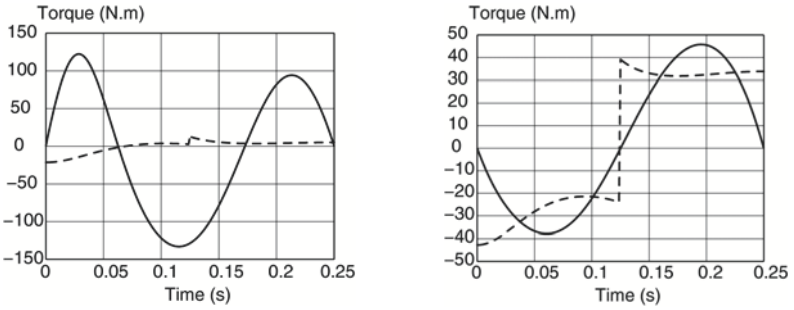

(a) actuator q_1 (b) actuator q_2

Figure 5. Input torques for two examined cases:

1) fifth order polynomial law applied on the displacement of the end-effector (full line)
2) "bang-bang" law applied on the displacement of the robot centre of masses (dotted line).

2. a "bang-bang" law is applied on the displacement of the robot centre of masses (Eq. (5));

The resulting displacements of the end-effector are shown in Fig. 3. These trajectory parameters are implemented into ADAMS software and we obtain the variations of shaking forces (Fig. 4). The obtained results shown that the optimal trajectory planning (case 2) allows the reduction of the shaking forces up to 63 %.

It should be noted that the optimal trajectory planning (case 2) has a good influence also on the input torque reduction (Fig.5). For example, in the case of the first actuator, the reduction in the input torque is 84 %.

4 Conclusions

In this paper, we have presented a new approach, based on an optimal trajectory planning, which allows the considerable reduction of the shaking forces transmitted to the robot frame. The aim of the suggested method is to optimally control the acceleration of the robot centre of masses using "bang-bang" displacement law. In other words, in the suggested approach, the robot is controlled not by applying end-effector trajectories but by planning the displacements of the total mass centre of moving links. The trajectory of the total mass centre of moving links is defined as straight line and it is parameterized with "bang-bang" displacement law. Such a control approach allows the reduction of the acceleration of the total mass centre of moving links and, consequently, the reduction in the shaking forces. It should be noted that such a solution is also very favourable for reduction of input torques. Numerical simulations carried out using ADAMS software for a planar 2*R* serial

manipulator have shown that reductions in the shaking force of 63 % and in input torque of 84 % have been achieved.

References

Arakelian, V., and Briot, S. (2008). Dynamic balancing of the SCARA robot. In *Proceedings of the 17th CISM-IFToMM Symposium on Robot Design, Dynamics, and Control (Romansy 2008), Tokyo, Japan, July 5-9.*

Arakelian, V, Dahan, M., and Smith, M.R. (2000). A historical review of the evolution of the theory on balancing of mechanisms. In *Proceedings of the International symposium on history of machines and mechanisms*. Dordrecht: Kluwer Academic Publishers. 291-300.

Arakelian, V, and Smith, M.R. (1999). Complete shaking force and shaking moment balancing of linkages. *Mechanism and Machine Theory.* 34(8). 1141-1153.

Arakelian, V, and Smith, M.R. (2005). Shaking force and shaking moment balancing of mechanisms: a historical review with new examples. *Transactions of the ASME, Journal of Mechanical Design.* 127. 334-339.

Arakelian, V. and Smith, M.R. (2008). Design of planar 3-DOF 3-*RRR* reactionless parallel manipulators. *Mechatronics,* 18, 601-606.

Berkof, R.S. (1973). Complete fore and moment balancing of inline four-bar linkages. *Mechanism and Machine Theory.* 8(3). 397-410.

Dresig, H., Naake, S., and Rockausen L. (1994). Vollständiger und harmonischer Ausgleich ebener Mechanismen.VDI Verlag, Düsseldorf, 73p.

Fattah, A., and Agrawal, S.K. (2006). On the design of reactionless 3-DOF planar parallel mechanisms. *Mechanism and Machine Theory.* 41(1). 70-82.

Gosselin, C.M., Cote, G., and Wu, Y. (2004). Synthesis and design of reactionless tree-degree-of-freedom parallel mechanisms. *IEEE Transactions on Robotics and Automation*. 20(2). 191-199.

Herder, J.L., and Gosselin, C.M. (2004). A counter-rotary counterweight for light-weight dynamic balancing. In *Proceedings of ASME 2004 DETC/CIEC Conference, September 28 – October 2, Salt Lake City, Utah, USA.* 659-667.

Khalil, W., and Dombre, E. (2002). Modeling, identification and control of robots. Hermes Sciences Europe.

Lowen, G.G., Tepper, F.R., and Berkof, R.S. (1983). Balancing of linkages – an Update. *Mechanism and Machine Theory*. 18(3). 213-230.

Papadopoulos, E., and Abu-Abed, A. (1994). Design and motion planning for a zero-reaction manipulator. In *Proceedings of the IEEE International Conference on Robotics and Automation, San Diego, CA*. 1554-1559.

Ricard, R., and Gosselin, C.M. (2000). On the design of reactionless parallel manipulators. In *Proceedings of the ASME 2000 DETC/CIEC Conference, Baltimore, Maryland, September 10-13.* 1-12.

Passivity Based Backstepping Control of an Elastic Robot

Peter Staufer[†*], Hubert Gattringer[†*], Wolfgang Höbarth[†*] and Hartmut Bremer[† *]

[†] Institute for Robotics, Johannes Kepler University Linz, Austria

Abstract In industry plants, a trade off between the requirements of speed and cost efficiency often results in lightweight constructions. However, this introduces elastic deflections causing vibrations and a loss in tracking precision. Hence, investigations in suitable models and control laws are necessary. By using the Projection Equation with a Ritz expansion, a set of nonlinear ordinary differential equations which describes the motion of the system is developed. The utilized control law is a combination of a feedforward and a feedback scheme. The latter is based on backstepping methods, with respect to passivity ports. Finally experimental results are shown to verify the proposed control strategy.

1 Overview

The considered flexible structure, illustrated in Figure 1.1, is an elastic laboratory robot consisting of 6 joints with DC motors combined with Harmonic Drive gears and 2 flexible links, see Höbarth et al. (München, Germany, 2008) for a detailed description of the setup. The mechanical system allows to measure the deflections (two bending directions and torsion) with strain gauges, attached to the flexible links. For this work we limit the task to the tracking of a desired planar motion, using only two joints. The first part of this paper discusses the theory of modeling elastic multibody systems, see Bremer and Pfeiffer (1992), and the second part the designing of an appropriate controller, respectively. In the literature solutions of different control types are developed only for single elastic links, see Staudecker et al. (2008); Arteaga and Siciliano (2003); Lee and Prevost (2005), or several concepts without considering elastic deformations. Important improvements in controlling flexible-link robots are worked out in Kleemann (1989).

[*]Support of the present work in the framework of the peer-reviewed Austrian Center of Competence in Mechatronics (ACCM) is gratefully acknowledged.

It has been pointed out, that control schemes of elastic robots require suitable feedforward and feedback control using deflection measurements to eliminate tracking errors. Flatness-based concepts introduced by Fliess et al. (1995) are often proposed for solving tracking problems. However, the method of flatness is not feasible for elastic multibody systems. Therefore a feedforward scheme, as suggested in Höbarth et al. (München, Germany, 2008) is used, and a closed loop controller based on the backstepping theory (Khalil, 2002) is introduced. In the 4th section experimental results are presented to prove the feasibility of this approach and the last section closes with a brief conclusion.

Figure 1.1. Elastic robot

2 Mathematical Model

The mechanical structure of the elastic robot, Figure 1.1, leads to a subsystem based model, because the robot consists of two nearly identical links. The Projection Equation in subsystem formulation assigns each subsystem n a vector of describing velocities $\dot{\mathbf{y}}_n$. Specifically the mechanical system $n = [1, 2]$, a subsystem consists of a motor-gear unit, an elastic arm and the tip body, see Figure 2.1. The chosen vector of describing velocities of this subsystem is

$$\dot{\mathbf{y}}_n^T = (v_{0x}\ v_{0y}\ \omega_{Fz}\ \Omega_M\ \Omega_A\ \dot{\mathbf{q}}_R^T) \tag{2.1}$$

with v_{0x}, v_{0y}, ω_{Fz} as guidance velocities, which represent the velocities of the selected reference frame, and relative angular velocities Ω_A, Ω_M, which represent the arm and motor rotations relative to the moving frame.

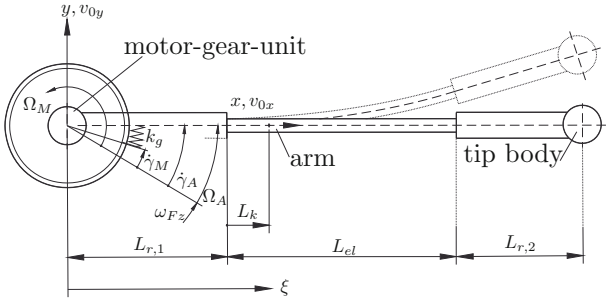

Figure 2.1. n-th Subsystem

The motor angle γ_M is measured directly, while the according angular velocity $\dot{\gamma}_M$ is obtained through a filter approximating time differentiation. The bending moments M_B at $\xi = L_{r,1} + L_K$ are measured through strain gauges, which are mounted at the links (index n is omitted). The beam is characterized by a cross section area A, an elastic beam length L_{el}, a bending stiffness $E\,I_z$ and a mass density ρ. For calculation of the system kinematics, the mass center vector of an infinitesimal element dm is written as $\mathbf{r}_c^T = (\xi \;\; v(\xi,t) \;\; 0)$. To receive a finite dimensional system, the deflection $v(\xi,t)$ in y-direction is approximated with a Ritz expansion $v(\xi,t) = \mathbf{v}(\xi)^T\mathbf{q}_R$, where $\mathbf{q}_R$ denotes the Ritz coordinates. Shape functions $\mathbf{v}(\xi)$ are defined piecewise, to include the rigid parts of the link. The fully elastic section ($L_{r,1} \leq \xi < L_{r,1} + L_{el}$) is chosen as

$$\mathbf{v}(x)^T = (\frac{x^2}{L_{el}^2} - \frac{x^3}{L_{el}^3},\; 3\frac{x^2}{L_{el}^2} - 2\frac{x^3}{L_{el}^3})$$

with $x = \xi - L_{r,1}$. In this formulation all geometric boundary conditions (clamped-free) are satisfied and a total description of the deflection is obtained. A tip body at $\xi = L_{r,1} + L_{el} + L_{r,2} = L_{total}$ is taken into account by $dm = \rho A dx + m_{tip}\delta(\xi - L_{total})$ and the moments of inertia by $d\mathbf{J} = d\mathbf{J}_{arm} + \mathbf{J}_{tip}\delta(\xi - L_{total})$, with the Dirac distribution δ. The interconnection between motor and arm unit is achieved by a Harmonic Drive gear with high transmission ratio i_G and gear elasticity k_g. The gear torque depends on the difference of arm and motor angle $(\gamma_A - \gamma_M)$.

Kinematic Model The kinematic model of an articulated robot can be schematized. This formulation is called the kinematic chain, see Bremer (2008) and reads as

$$\dot{\mathbf{y}}_i = \mathbf{T}_{ip}\dot{\mathbf{y}}_p + \mathbf{F}_i\dot{\mathbf{s}}_i.$$

The equation connects a subsystem i with its predecessor p. The describing velocity $\dot{\mathbf{y}}_i$ is linked with the velocity of the predecessor system $\dot{\mathbf{y}}_p$ via $\mathbf{T}_{ip}$ and the local minimal velocity vector $\dot{\mathbf{s}}_i$ via the Jacobian matrix $\mathbf{F}_i$. For a correct linearization a second order expansion of the elastic deflections, is included in $\mathbf{T}_{ip}$.

Equations of Motion The equations of motion are derived with the Projection Equation in Subsystem representation

$$\sum_{n=1}^{N_{sub}} \left(\frac{\partial\dot{\mathbf{y}}_n}{\partial\dot{\mathbf{s}}}\right)^T \{\mathbf{M}_n\ddot{\mathbf{y}}_n + \mathbf{G}_n\dot{\mathbf{y}}_n - \mathbf{Q}_n^e - \mathbf{Q}_n^c\} = 0, \tag{2.2}$$

see Bremer (2008) for details. Each subsystem n is associated with describing velocities $\dot{\mathbf{y}}_n$, mass matrix $\mathbf{M}_n$, matrix of Coriolis and centrifugal terms $\mathbf{G}_n$, generalized active $\mathbf{Q}_n^e$ and constraint forces $\mathbf{Q}_n^c$. However $\dot{\mathbf{y}}_n$ contains spatial derivations of the non-holonomic minimal velocities $\dot{\mathbf{s}}$ and therefore a Ritz expansion is used in this expression. A summation over all subsystems and evaluation of the kinematic chain leads to

$$\mathbf{M}\ddot{\mathbf{s}} + \mathbf{g}(\mathbf{q}, \dot{\mathbf{s}}) = \mathbf{Q}.$$

Applied to the elastic laboratory robot the equation of motion is calculated with[1] $\dot{\mathbf{q}} = \dot{\mathbf{s}}$ and $\mathbf{Q} = \mathbf{B}_1 M_{M,1} + \mathbf{B}_2 M_{M,2}$, where $M_{M,n}$ are the motor torques.

3 Controller Design

As mentioned briefly, the control strategy is a combination of a feedforward and a feedback scheme. As suggested in Höbarth et al. (München, Germany, 2008), an open loop control has to respect the elastic deflections. To meet this requirement, quasi-static elastic deflections, depending on the default motor angle (reference track), are calculated. With these results, the desired tracks of the motor angles are altered in the sense of a minimization of the static TCP errors. The stabilization of the error dynamics is done by a passivity based backstepping theory. This control strategy is built on the energy flows in the system. Therefore, energy functionals of each subsystem, kinetic energy $T_{dm,n}$ and potential energy $V_{dm,n}$ of the elastic bodies, as well the kinetic energy of the motor unit $T_{M,n}$, with $n = 1, 2$, are required. For the controller design, it is sufficient to neglect gear elasticity ($q_A = \gamma_A = \gamma_M$). Another simplification concerns $L_k = L_{r,1} = L_{r,2} = 0$ and only terms with $C_M i_G^2$ are considered[2]. In a first step the control concept is developed for stabilization around $\mathbf{q} = 0$. The energy functional of the total system is calculated as

$$H = \sum_{n=1}^{2} H_n = \sum_{n=1}^{2} (T_{dm,n} + V_{dm,n} + T_{M,n}). \tag{3.3}$$

Time derivation of this functional leads to

$$\dot{H} = \dot{\mathbf{q}}^T \mathbf{Q} = \sum_{n=1}^{2} (M_{M,n}\, i_{G,n}\, \dot{q}_{A,n}), \tag{3.4}$$

and a simple control law, according to Lyapunov theory, with $M_{M,n} = -\lambda_n \dot{q}_{A,n}$ and $\lambda_n > 0$ is accomplished. Stability is guaranteed by $\dot{H} =$

[1] Only a holonomic system is considered.

[2] All other terms associated to the motor inertia C_M are neglected.

$-\sum_{n=1}^{2} \lambda_n i_{G,n} \dot{q}_{A,n}^2$. The controller based on the use of the energy function of eq. (3.3) allows to achieve a good damping behavior. However, the results are not satisfactory, because only motor velocities are included. In a next step the Lyapunov function may be rewritten as

$$\overline{H} = \sum_{n=1}^{2} \overline{H}_n = \sum_{n=1}^{2} (T_{dm,n} + V_{dm,n}). \tag{3.5}$$

In terms of eq. (3.5) the mentioned subsystem (elastic beam with a motor-gear unit) is split, and a new arrangement of subsystems is built. Therefore eq. (2.2) is divided into

$$\sum_{n=1}^{2} \left(\frac{\partial \dot{\mathbf{y}}_n}{\partial \dot{\mathbf{q}}} \right)^T \left[\mathbf{M}_{B,n} \ddot{\mathbf{y}}_n + \mathbf{G}_{B,n} \dot{\mathbf{y}}_n - \mathbf{Q}_{B,n}^e \right] = \sum_{n=1}^{2} \left(\frac{\partial \dot{\mathbf{y}}_n}{\partial \dot{\mathbf{q}}} \right)^T \mathbf{Q}_{B,n}^c, \tag{3.6}$$

a motion equation of the elastic bodies (Index: B), and

$$\sum_{n=1}^{2} \left(\frac{\partial \dot{\mathbf{y}}_n}{\partial \dot{\mathbf{q}}} \right)^T \mathbf{Q}_{B,n}^c = -\sum_{n=1}^{2} \left(\frac{\partial \dot{\mathbf{y}}_n}{\partial \dot{\mathbf{q}}} \right)^T \left[\mathbf{M}_{M,n} \ddot{\mathbf{y}}_n - \mathbf{Q}_{M,n}^e \right], \tag{3.7}$$

an equation for the drive units (Index: M), connected by $\mathbf{Q}_{B,n}^c$, the generalized forces at $\xi = 0$. If eq. (3.6) is multiplied by $\dot{\mathbf{q}}^T$ it is obvious that

$$\dot{\overline{H}} = \dot{\mathbf{q}}^T \sum_{n=1}^{2} \left(\frac{\partial \dot{\mathbf{y}}_n}{\partial \dot{\mathbf{q}}} \right)^T \left[\mathbf{M}_{B,n} \ddot{\mathbf{y}}_n + \mathbf{G}_{B,n} \dot{\mathbf{y}}_n - \mathbf{Q}_{B,n}^e \right] = \sum_{n=1}^{2} M_{B,n} \dot{q}_{A,n}. \tag{3.8}$$

According to the new energy function, an 'elastic body' subsystem (including beam 1 and 2) is formed. The remaining subsystems are motor 1 and 2. To take the position error of the motor angle into account, the energy functional eq. (3.5) is extended as follows

$$\overline{\overline{H}} = \sum_{n=1}^{2} \Big(\overline{H}_n + \alpha_{2,n} \int_0^{q_{A,n}} c_n(\delta) d\delta \Big) \tag{3.9}$$

with $\alpha_{2,n} > 0$ and the conditions $c_n(\delta)\delta > 0$ for $\delta \neq 0$ and $c_n(0) = 0$. Time derivation of eq. (3.9) returns

$$\dot{\overline{\overline{H}}} = \sum_{n=1}^{2} \big(M_{B,n} + \alpha_{2,n} c_n(q_{A,n}) \big) \dot{q}_{A,n}. \tag{3.10}$$

Now, with the help of backstepping methods, a closed-loop controller is designed. For the next steps it is essential, that the bending moments

$M_{B,n}$ contain the coupling between the considered arms and present inner moments. Therefore, a 'quasi' -decoupled controller can be realized. If $\dot{q}_A$ (index n is omitted[3]) is a virtual control input k_A of the arm-unit, in analogy to the backstepping algorithm, a control law $k_A = \dot{q}_A = -\frac{1}{\alpha_1} M_B - \frac{\alpha_2}{\alpha_1} c(q_A)$ is found with $\dot{\overline{\overline{H}}} = -\alpha_1 \dot{q}_A^2 < 0$. Indeed $\dot{q}_A$ is not the real control input, an error $e = \dot{q}_A - k_A$ is defined and leads to

$$\dot{H}^* = \big(M_B + c(q_A)\big)(e + k_A) + \alpha_3 e\, \dot{e}. \tag{3.11}$$

Inserting the bending moment $M_B = i_G\, M_M - C_M i_G^2\, \ddot{q}_A$, see eq. (3.7) into eq. (3.11) yields

$$\dot{H}^* = -\tfrac{1}{\alpha_1}\big(M_B + \alpha_2 c(q_A)\big)^2 + \alpha_3\big(\dot{q}_A + \tfrac{1}{\alpha_1} M_B + \tfrac{\alpha_2}{\alpha_1} c(q_A)\big)$$
$$\Big(\tfrac{1}{\alpha_3}\big(M_B + \alpha_2 c(q_A)\big) + \tfrac{1}{C_M\, i_G}\big(M_M - \tfrac{1}{i_G} M_B\big) + \tfrac{1}{\alpha_1}\dot{M}_B + \tfrac{\alpha_2}{\alpha_1}\tfrac{\partial c(q_A)}{\partial q_A}\dot{q}_A\Big).$$

Thus a control input

$$M_M = \frac{1}{i_G} M_B + C_M i_G\Big(\quad -\tfrac{1}{\alpha_1}\dot{M}_B - \tfrac{\alpha_2}{\alpha_1}\tfrac{\partial c(q_A)}{\partial q_A}\dot{q}_A - \tfrac{1}{\alpha_3}\big(M_B + \alpha_2 c(q_A)\big)$$
$$-\alpha_4\big(\dot{q}_A + \tfrac{1}{\alpha_1} M_B + \tfrac{\alpha_2}{\alpha_1} c(q_A)\big)\Big)$$

is found, leading to

$$\dot{H}^* = -\frac{1}{\alpha_1}\big(M_B + \alpha_2 c(q_A)\big)^2 - \alpha_3\alpha_4\big(\dot{q}_A + \frac{1}{\alpha_1} M_B + \frac{\alpha_2}{\alpha_1} c(q_A)\big)^2,$$

while $\alpha_1, \alpha_2, \alpha_3, \alpha_4 > 0$ ensure stability[4]. With the transformation $\mathbf{e} = \mathbf{q} - \mathbf{q}_d$ and $M_{Mn,e} = M_{Mn} - M_{Mn,d}$ the error system is obtained. This system is nonlinear and time variant. More investigations are necessary to show the tracking stability by using the suggested feedforward in combination with the feedback controller.

4 Experimental Results

To verify the suggested solution, some experimental results are presented. Thus a circle (Figure 4.1) and a straight line (Figure 4.2) in a planar space were tracked. The desired tool center point is $\mathbf{r}_{TCP,d}$. The illustrated figures compare the concept of a simple Joint-PD controller in combination

[3] For each arm a similar control design is possible.

[4] The design of the backstepping controller is not limited to a planar motion. The concept can be expanded to control a motion in space.

with a reduced (stiff gears and arms) open loop (FB1) and the scheme with deflection measurements and an altering of the motor angle (FB2), suggested by Höbarth et al. (München, Germany, 2008), and the proposed backstepping method (B.S.M.), with $c(c_{q_A}) = c_2 \tanh(c_3 e_{q_A})$.

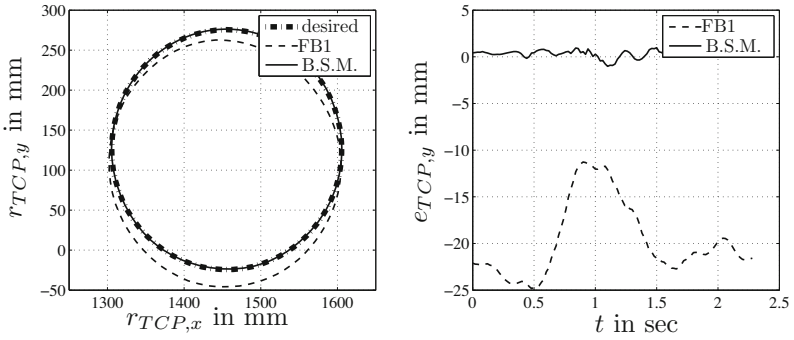

Figure 4.1. Comparison between different controllers, tracking a circle in space

Figure 4.1 illustrates the results of tracking a circle (radius $r = 150$mm) in the $x-y$ plane on the left side, and on the right side the $y(t)$ component of the TCP error ($\mathbf{e}_{TCP} = \mathbf{r}_{TCP,d} - \mathbf{r}_{TCP}$), where gravity is acting. In the other experiment (Figure 4.2) the TCP error in x and y directions are plotted. The analysis shows a significant improvement in the TCP error. A reduction of the peaks during the default track is attained. The main goal, vibration damping in combination with a good tracking precision, is met.

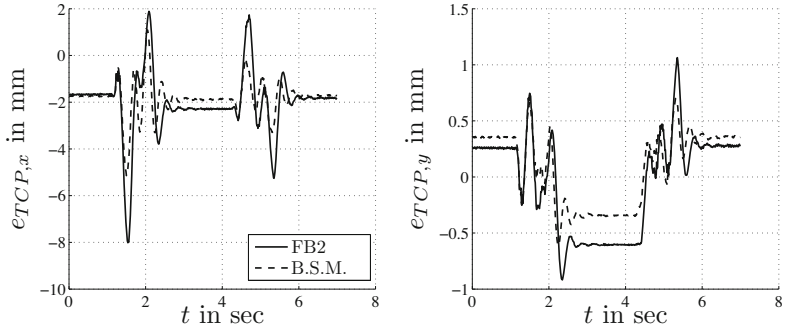

Figure 4.2. Comparison between different controllers, tracking a straight line in space

5 Conclusion

The example emphasizes the feasibility of this approach. To overcome the tracking deviations and oscillations, the backstepping approach leads to a sufficient control strategy. These tools result in an active vibration damping and the TCP errors are kept down.

Bibliography

M. A. Arteaga and B. Siciliano. *Flexible-link Manipulators: Modeling, Nonlinear Control and Observer, In: Advanced Studies of Flexible Robotic Manipulators Modeling, Design, Control and Application, Series in Intelligent Control and Intelligent Automation, Editors: Wang F., Gao Y.*, volume 4. World Scientific, 2003.

H. Bremer. *Elastic Multibody Dynamics, A Direct Ritz Approach*. Springer Verlag, 2008.

H. Bremer and F. Pfeiffer. *Elastische Mehrkörpersysteme*. Verlag B. G. Teubner, Stuttgart, 1992.

M. Fliess, J. Lévine, P. Martin, and P. Rouchon. Flatness and defect of nonlinear systems: introductory theory and examples. *International Journal of Control*, 61(6):pp. 1327–1361, 1995.

W. Höbarth, H. Gattringer, and H. Bremer. Modeling and control of an articulated robot with flexible links/joints. In *Proceedings of the Ninth conference on Motion and Vibration Control*, München, Germany, 2008.

H. K. Khalil. *Nonlinear Systems*. Prentice-Hall, Upper Saddle River, New Jersey, 3-rd edition, 2002.

U. Kleemann. *Regelung elastischer Roboter*. Fortschrittsberichte, Reihe 8, Nr. 191, VDI Verlag, Düsseldorf, 1989.

H.-H. Lee and J. Prevost. A coupled sliding-surface approach for the trajectory control of a flexible-link robot based on a distributed dynamic model. *International Journal of Control*, 78(9):pp. 629–637, 2005.

M. Staudecker, K. Schlacher, and R. Hansl. Passivity based control and time optimal trajectory planning of a single mast stacker crane. In *Proceedings of the 17th IFAC World Congress, The International Federation of Automatic Control, Seoul, Korea*, 2008.

Economical Control of Robot Systems Using Potential Energy

Werner Schiehlen* and Makoto Iwamura†

* Institute of Engineering and Computational Mechanics, University of Stuttgart, Stuttgart, Germany

† Department of Mechanical Engineering, Fukuoka University, Fukuoka, Japan

Abstract This paper considers the problem to minimize the energy consumption of horizontal robot systems utilizing passive storage elements. We propose a simultaneous optimization method for trajectory planning and power saving based on the optimal control theory. The effectiveness of the design method is demonstrated for a 2DOF planar manipulator.

1 Introduction

The energy problem has captured the attention of people worldwide in recent years. In the manufacturing industry, a lot of robot systems controlled by actuators are utilized and these actuators are consuming a great amount of energy. Therefore, saving the energy of such systems is a very important problem.

As a fundamental study toward the energy conservation for mechanical systems, Schiehlen and Guse (2001) analyze the power aspects of an actively controlled oscillator and point out that a large amount of energy can be saved by using the proper linear and nonlinear springs. Furthermore, Schiehlen and Guse (2005) discuss the energy conservation problem for mechanical systems with prescribed trajectories. They show that adapting the periodic trajectories as closely as possible to the limit cycle of the underlying mechanical system and combining with the inverse dynamics control can reduce the energy consumption dramatically.

On the other hand, the problem to find the minimum energy trajectories between two given points is also actively studied mainly for manipulators, see e.g. Izumi et al. (1997). However, in the area of trajectory planning, utilization of storage elements for energy conservation is not discussed yet.

In this paper, we consider the simultaneous optimization problem of storage elements and trajectories with respect to the energy consumption for horizontal robot systems as proposed by Schiehlen and Iwamura (2009). Firstly, based on the linearized equations of motion, we analyze the relationship between the consumed energy and the operating time, and the optimal trajectory using optimal control

theory. Then, we verify the analytical solution by comparing with the numerical one computed considering the full nonlinear dynamics. After that we derive a condition for the operating time to be optimal, and propose the optimal design method for springs. Finally, we show the effectiveness of the method by applying it to a robot arm modeled as a 2DOF planar manipulator.

2 Optimal Control of Robot Systems

The equations of motion for a robot system in the horizontal plane with N degrees of freedom and N_p parameters read as

$$\boldsymbol{M}(\boldsymbol{y})\ddot{\boldsymbol{y}} + \boldsymbol{h}(\boldsymbol{y}, \dot{\boldsymbol{y}}) = \boldsymbol{f}(\boldsymbol{y}, \boldsymbol{p}) + \boldsymbol{u}, \tag{1}$$

where $\boldsymbol{y} \in R^N$ is the vector of generalized coordinates, $\boldsymbol{M} \in R^{N\times N}$ is the inertia matrix, $\boldsymbol{h} \in R^N$ is the vector of centrifugal and Coriolis forces, $\boldsymbol{f} \in R^N$ is the vector of applied forces/torques, $\boldsymbol{p} \in R^{N_p}$ is the vector of parameters, and $\boldsymbol{u} \in R^N$ is the vector of actuator driving forces/torques. In this paper, we consider only the applied forces/torques by passive storage elements that can be expressed in the form $\boldsymbol{f}(\boldsymbol{y}, \boldsymbol{p}) = -\boldsymbol{K}(\boldsymbol{y} - \boldsymbol{y}_n)$ where $\boldsymbol{K} \in R^{N\times N}$ is the stiffness matrix, $\boldsymbol{y}_n \in R^N$ is the vector of spring mounting positions. We define $\boldsymbol{k} = [k_1\ k_2\ \cdots\ k_{N_k}] \in R^{N_k}$ as the vector of independent spring stiffnesses that form $\boldsymbol{K}$. Then, the vector of design variables can be expressed as $\boldsymbol{p} = [\boldsymbol{k}^T\ \boldsymbol{y}_n^T]^T$.

Here, we consider motions that move between two points and rest at both ends, i.e., $\boldsymbol{y}(0) = \boldsymbol{y}_0, \boldsymbol{y}(t_f) = \boldsymbol{y}_f, \dot{\boldsymbol{y}}(0) = \dot{\boldsymbol{y}}(t_f) = \boldsymbol{0}$. The energy consumed by this motion can be estimated by the following cost function

$$J = \frac{1}{2}\int_0^{t_f} \boldsymbol{u}^T \boldsymbol{W} \boldsymbol{u} dt, \tag{2}$$

where $\boldsymbol{W} \in R^{N\times N}$ is a positive definite symmetric matrix.

The problem considered in this paper can be formulated as follows: Find $\boldsymbol{u}(t)$, $\boldsymbol{y}(t)$, t_f and $\boldsymbol{p} = [\boldsymbol{k}^T\ \boldsymbol{y}_n^T]^T$ by minimizing the energy consumption (2) subject to the initial and final conditions for the system (1).

3 Linear Analysis of Optimal Solution

3.1 Linearization of the Equations of Motion

We analyze the optimization problem approximately using the linearized equations of motion based on the optimal control theory. Firstly, to make the later calculations easy, we shift the reference point to the middle point of the initial and final points. To this end, we define $\boldsymbol{y_m}$ and $\boldsymbol{y_e}$ as $\boldsymbol{y}_m = (\boldsymbol{y}_f + \boldsymbol{y}_0)/2, \boldsymbol{y}_e = (\boldsymbol{y}_f - \boldsymbol{y}_0)/2$ and shift the coordinates as $\tilde{\boldsymbol{y}}(t) = \boldsymbol{y}(t) - \boldsymbol{y}_m$, $\tilde{\boldsymbol{y}}_n = \boldsymbol{y}_n - \boldsymbol{y}_m$. This transforms the initial and final conditions to the symmetric form $\tilde{\boldsymbol{y}}(0) = -\boldsymbol{y}_e, \tilde{\boldsymbol{y}}(t_f) = \boldsymbol{y}_e, \dot{\tilde{\boldsymbol{y}}}(0) = \dot{\tilde{\boldsymbol{y}}}(t_f) = \boldsymbol{0}$. And the equations of motion (1) can be rewritten as

$$\tilde{\boldsymbol{M}}(\tilde{\boldsymbol{y}})\ddot{\tilde{\boldsymbol{y}}} + \tilde{\boldsymbol{h}}(\tilde{\boldsymbol{y}}, \dot{\tilde{\boldsymbol{y}}}) + \boldsymbol{K}\tilde{\boldsymbol{y}} = \boldsymbol{u} + \boldsymbol{K}\tilde{\boldsymbol{y}}_n. \tag{3}$$

Here we assume that the centrifugal and Coriolis forces are negligible $\tilde{\boldsymbol{h}}(\tilde{\boldsymbol{y}}, \dot{\tilde{\boldsymbol{y}}}) \backsimeq \boldsymbol{0}$. In addition, we approximate the inertia matrix as $\hat{\boldsymbol{M}} = \tilde{\boldsymbol{M}}(\boldsymbol{0}) = \boldsymbol{M}(\boldsymbol{y_m}) = \text{const}$. The validity of these approximations will be examined numerically in Section 3.3. These assumptions lead the following linearized equations

$$\hat{\boldsymbol{M}}\ddot{\tilde{\boldsymbol{y}}} + \boldsymbol{K}\tilde{\boldsymbol{y}} = \boldsymbol{u} + \boldsymbol{K}\tilde{\boldsymbol{y}}_n. \tag{4}$$

Let us consider the free vibration system corresponding to (4) and compute the modal matrix $\boldsymbol{\Phi} \in R^{N\times N}$ that satisfies $\boldsymbol{\Phi}^T\hat{\boldsymbol{M}}\boldsymbol{\Phi} = \boldsymbol{I}$ and $\boldsymbol{\Phi}^T\boldsymbol{K}\boldsymbol{\Phi} = \boldsymbol{\Omega}^2$, where $\boldsymbol{I}$ is the identity matrix, $\boldsymbol{\Omega} = \text{diag}[\omega_1, \omega_2, \cdots, \omega_N]$, ω_i is the i-th natural frequency arranged as $\omega_1 < \omega_2 < \cdots < \omega_N$ where some of the lowest may vanish. We make the coordinate transformation $\tilde{\boldsymbol{y}} = \boldsymbol{\Phi}\boldsymbol{q}$ substituted into (4). Premultiplying the equation by $\boldsymbol{\Phi}^T$ yields

$$\ddot{\boldsymbol{q}} + \boldsymbol{\Omega}^2\boldsymbol{q} = \boldsymbol{\Phi}^T\boldsymbol{u} + \boldsymbol{\Omega}^2\boldsymbol{q}_n, \tag{5}$$

where $\boldsymbol{q}_n = \boldsymbol{\Phi}^{-1}\tilde{\boldsymbol{y}}_n$. We define the state vectors $\boldsymbol{x} = [\boldsymbol{x}_1^T\ \boldsymbol{x}_2^T]^T$ as $\boldsymbol{x}_1 = \boldsymbol{q}, \boldsymbol{x}_2 = \dot{\boldsymbol{q}}$. Then, the state equations are written as

$$\dot{\boldsymbol{x}}_1 = \boldsymbol{x}_2, \tag{6}$$

$$\dot{\boldsymbol{x}}_2 = -\boldsymbol{\Omega}^2\boldsymbol{x}_1 + \boldsymbol{\Phi}^T\boldsymbol{u} + \boldsymbol{\Omega}^2\boldsymbol{q}_n. \tag{7}$$

The initial and final conditions are expressed as $\boldsymbol{x}_1(0) = -\boldsymbol{q}_e, \boldsymbol{x}_1(t_f) = \boldsymbol{q}_e, \boldsymbol{x}_2(0) = \boldsymbol{x}_2(t_f) = \boldsymbol{0}$, where $\boldsymbol{q}_e = \boldsymbol{\Phi}^{-1}\boldsymbol{y}_e$.

3.2 Analysis Using Optimal Control Theory

We introduce an adjoint vector $\boldsymbol{\psi} = [\boldsymbol{\psi}_1^T\ \boldsymbol{\psi}_2^T]^T$ and define the Hamiltonian as

$$H = \frac{1}{2}\boldsymbol{u}^T\boldsymbol{W}\boldsymbol{u} + \boldsymbol{\psi}_1^T\boldsymbol{x}_2 + \boldsymbol{\psi}_2^T(-\boldsymbol{\Omega}^2\boldsymbol{x}_1 + \boldsymbol{\Phi}^T\boldsymbol{u} + \boldsymbol{\Omega}^2\boldsymbol{q}_n). \tag{8}$$

Then, the optimal control can be derived from $\partial H/\partial \boldsymbol{u} = \boldsymbol{0}$ as

$$\boldsymbol{u} = -\boldsymbol{W}^{-1}\boldsymbol{\Phi}\boldsymbol{\psi}_2. \tag{9}$$

Substituting (9) into (8) yields

$$H = \boldsymbol{\psi}_1^T\boldsymbol{x}_2 - \boldsymbol{\psi}_2^T\boldsymbol{\Omega}^2\boldsymbol{x}_1 - \frac{1}{2}\boldsymbol{\psi}_2^T\boldsymbol{\Phi}^T\boldsymbol{W}^{-1}\boldsymbol{\Phi}\boldsymbol{\psi}_2 + \boldsymbol{\psi}_2^T\boldsymbol{\Omega}^2\boldsymbol{q}_n. \tag{10}$$

From (10), the canonical equations of Hamilton are derived as follows.

$$\dot{\boldsymbol{x}} = \frac{\partial H}{\partial \boldsymbol{\psi}} = \boldsymbol{A}\boldsymbol{x} + \boldsymbol{B}\boldsymbol{\psi} + \boldsymbol{c}_n, \tag{11}$$

$$\dot{\boldsymbol{\psi}} = -\frac{\partial H}{\partial \boldsymbol{x}} = -\boldsymbol{A}^T\boldsymbol{\psi}, \tag{12}$$

$$\boldsymbol{A} = \begin{bmatrix} \boldsymbol{0} & \boldsymbol{I} \\ -\boldsymbol{\Omega}^2 & \boldsymbol{0} \end{bmatrix},\ \boldsymbol{B} = \begin{bmatrix} \boldsymbol{0} & \boldsymbol{0} \\ \boldsymbol{0} & -\boldsymbol{\Phi}^T\boldsymbol{W}^{-1}\boldsymbol{\Phi} \end{bmatrix},\ \boldsymbol{c}_n = \begin{bmatrix} \boldsymbol{0} \\ \boldsymbol{\Omega}^2\boldsymbol{q}_n \end{bmatrix}. \tag{13}$$

By solving these differential equations under the two-point boundary conditions, we can obtain the optimal solution that minimizes the energy consumption. However, it is difficult to obtain the closed-form solution of these equations since they are coupled due to the term $\boldsymbol{\Phi}^T\boldsymbol{W}^{-1}\boldsymbol{\Phi}$ in $\boldsymbol{B}$. On the other hand, selecting the weighting matrix as $\boldsymbol{W} = \hat{\boldsymbol{M}}^{-1}$ results in the cost function of mechanical power and allows to decouple these equations by $\boldsymbol{\Phi}^T\hat{\boldsymbol{M}}\boldsymbol{\Phi} = \boldsymbol{I}$. Hence, in the following, we analyze this case. In this case, we can get the closed-form solution of $\boldsymbol{\psi}_2(t)$ as

$$\boldsymbol{\psi}_2(t) = [\psi_{21}(t)\ \psi_{22}(t)\ \cdots\ \psi_{2N}(t)]^T, \tag{14}$$

$$\psi_{2i}(t) = \frac{2\omega_i^2\{\sin\omega_i(t_f - t) - \sin\omega_i t\}}{\sin\omega_i t_f - \omega_i t_f} q_{ei} + \frac{2\omega_i^2\{\sin\omega_i(t_f - t) + \sin\omega_i t\}}{\sin\omega_i t_f + \omega_i t_f} q_{ni},$$

where q_{ei} and q_{ni} is the i-th element of $\boldsymbol{q}_e$ and $\boldsymbol{q}_n$ respectively. The optimal control $\boldsymbol{u}(t)$ is obtained by substituting (14) and $\boldsymbol{W} = \hat{\boldsymbol{M}}^{-1}$ into (9). The cost function (2) can be derived by considering (9) and $\boldsymbol{W} = \hat{\boldsymbol{M}}^{-1}$ as

$$J = \frac{1}{2}\int_0^{t_f} \boldsymbol{\psi}_2^T\boldsymbol{\psi}_2 dt = \sum_{i=1}^{N} \frac{2\omega_i^3(1 + \cos\omega_i t_f)}{\omega_i t_f - \sin\omega_i t_f} q_{ei}^2 + \sum_{i=1}^{N} \frac{2\omega_i^3(1 - \cos\omega_i t_f)}{\omega_i t_f + \sin\omega_i t_f} q_{ni}^2. \tag{15}$$

In the above equation, it is easily confirmed that $\frac{2\omega_i^3(1-\cos\omega_i t_f)}{\omega_i t_f + \sin\omega_i t_f} \geq 0$. Therefore, it is understood that the optimal spring mounting position that minimizes J is always $\boldsymbol{q}_n = \boldsymbol{0}$, i.e., $\boldsymbol{y}_n = \boldsymbol{y}_m$. Hence, in the following, we analyze the problem by setting $\boldsymbol{q}_n = \boldsymbol{0}$. In this case, the relationship between the minimum value of the consumed energy J and the operating time t_f can be expressed as

$$J(t_f) = \sum_{i=1}^{N} J_i(t_f), \tag{16}$$

$$J_i(t_f) = \begin{cases} \dfrac{2\omega_i^3(1 + \cos\omega_i t_f)}{\omega_i t_f - \sin\omega_i t_f} q_{ei}^2 & (\text{ if } \omega_i \neq 0\ ) \\ \dfrac{24}{t_f^3} q_{ei}^2 & (\text{ if } \omega_i = 0\ ) \end{cases}, \tag{17}$$

where we use L'Hospital's theorem to derive the equation for the singular point $\omega_i = 0$ that is $\lim_{\omega_i \to 0} \frac{2\omega_i^3(1+\cos\omega_i t_f)}{\omega_i t_f - \sin\omega_i t_f} = \frac{24}{t_f^3}$. Equations (16) and (17) show that we can reasonably understand the consumed energy of robot systems with storage elements as the sum of energy corresponding to the mode.

3.3 Comparison with Simulation Results

The analytical solution obtained in the previous section is derived based on the linearized equations of motion (4). Therefore, we should check the influence of the nonlinearity ignored in the analysis. Hence, in this section we compare the analytical solution with the numerical one considering the full nonlinear dynamics (1) by a general purpose optimal trajectory planning algorithm for multibody

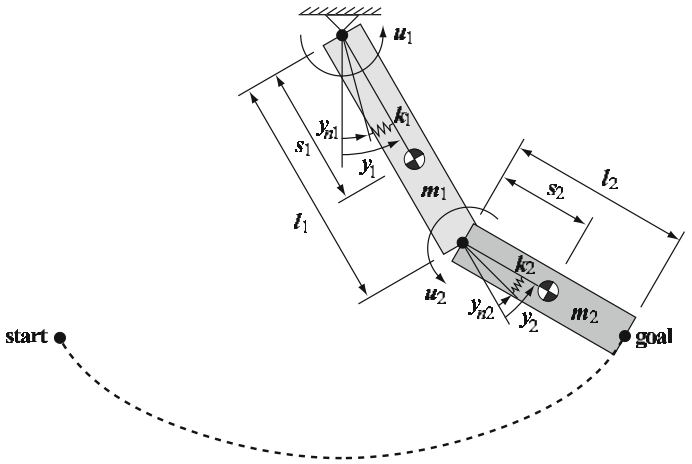

Figure 1. 2-DOF manipulator.

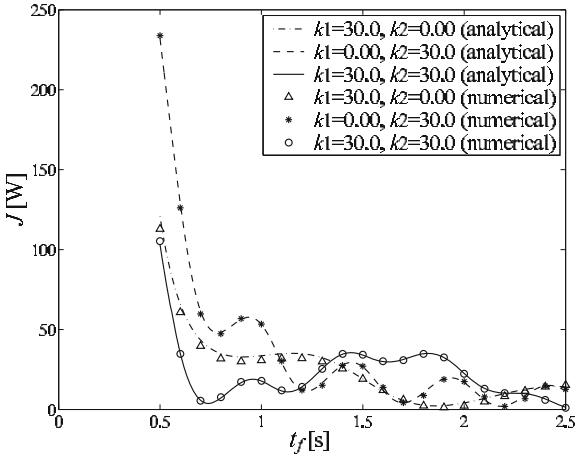

Figure 2. Power J of 2-DOF manipulator with spring.

systems (Iwamura et al., 2009). Here we consider the horizontal robot manipulator shown in Fig. 1. In this figure, y_i is the angle, u_i is the torque, k_i is the spring stiffness, l_i is length of the link, s_i is the distance between the joint and the center of mass, m_i is the mass, and I_i is the moment of inertia about the center of mass. The parameters used for the simulation are $l_1 = 0.25$m, $l_2 = 0.16$m, $s_1 = 0.125$m, $s_2 = 0.08$m, $m_1 = 14.25$kg, $m_2 = 10.0$kg, $I_1 = 0.43$kgm^2, $I_2 = 0.244$kgm^2.

As an example, we consider the motion under the initial and final conditions $\boldsymbol{y}_0 = [-30 \ \ -30]^T$deg and $\boldsymbol{y}_f = [30 \ 30]^T$deg. Figure 2 shows the comparison between the analytical solution (16) and the numerical one of J for the cases of $\boldsymbol{k} = [k_1 \ k_2]^T = [30 \ 0]^T, [0 \ 30]^T, [30 \ 30]^T$. We can observe that both results are well coinciding everywhere. Since the analytical solution is well approximating the characteristics of the exact one, it is proposed that the analytical solution can be used for analysis and design of robot systems with potential energy.

4 Optimal Design Method

4.1 Optimal Operating Time

We first derive a condition for t_f to be optimal. Let us consider the case that all ω_i are non-zero. If we consider t_f as the free quantity that takes any value, the transversality condition $H(t_f) = 0$ should be satisfied. Since (10) does not contain t explicitly, $\partial H/\partial t = 0$, i.e., $H =$ const. is hold. Hence, the condition $H(0) = 0$ should be satisfied. By substituting initial and final conditions, $\boldsymbol{q}_n = \boldsymbol{0}$ and $\boldsymbol{\psi}(0)$ into (10), we get

$$H(0) = \boldsymbol{\psi}_2^T(0)\boldsymbol{\Omega}^2\boldsymbol{q}_e - \frac{1}{2}\boldsymbol{\psi}_2^T(0)\boldsymbol{\psi}_2(0) = \sum_{i=1}^{N} \frac{-2\omega_i^5 t_f \sin\omega_i t_f}{(\omega_i t_f - \sin\omega_i t_f)^2} q_{ei}^2. \tag{18}$$

From (18), it is understood that $H(0) = 0$ is satisfied if $\sin\omega_i t_f = 0$ $(i = 1, 2, \cdots, N)$, or equivalently $\omega_i t_f = r_i\pi$ $(i = 1, 2, \cdots, N)$ where r_i is an integer. By substituting this into (16), the cost function can be expressed as

$$J = \sum_{i=1}^{N} \frac{2\omega_i^3(1 + \cos r_i\pi)}{r_i\pi} q_{ei}^2. \tag{19}$$

From (19), we can understand that J_i takes the maximum $4\omega_i^3 q_{ei}^2/r_i\pi$ if r_i is an even number and vanishes if r_i is an odd number. Therefore, J takes the global minimum if all r_i are odd number resulting in the minimum value of zero.

4.2 Optimal Design of Springs

In this section, we consider the problem to design the spring parameters $\boldsymbol{p} = [\boldsymbol{k}^T \ \boldsymbol{y}_n^T]^T$ to make the consumed energy minimum at the specified time t_f^*. As for $\boldsymbol{y}_n$, it is already proven that $\boldsymbol{y}_n = \boldsymbol{y}_m$ is always the best choice, hence in the following we explain the optimal design method for $\boldsymbol{k}$. We assume that the number of independent springs N_k is $N_k \geq N$.

Firstly, from the optimal condition $\omega_i t_f = r_i\pi$, we can determine ω_i as $\omega_i = r_i\pi/t_f^*(i = 1, 2, \cdots, N)$. All r_i should select to be odd number so that all J_i takes the minimum. Moreover, r_i should satisfy $r_1 < r_2 < \cdots < r_N$ since we assumed that $\omega_1 < \omega_2 < \cdots < \omega_N$. It is noted that as ω_i becomes larger, the mode shape becomes more complicated. Therefore, in the practical sense, it is reasonable to choose r_i as $r_i = 2i - 1$ so that it becomes the smallest possible integer.

The spring stiffnesses $\boldsymbol{k} = [k_1\ k_2\ \cdots\ k_{N_k}]^T$ contained in the stiffness matrix $\boldsymbol{K}$ should be determined as they satisfy the characteristic equation $\det[\boldsymbol{K} - \omega_i^2 \hat{\boldsymbol{M}}] = 0$ $(i = 1, 2, \cdots, N)$. Let us define the error function $e_i = \det[\boldsymbol{K} - \omega_i^2 \hat{\boldsymbol{M}}]$ and the error vector $\boldsymbol{e} = [e_1\ e_2\ \cdots e_N]^T$. Then, the problem here is to find $\boldsymbol{k}$ that satisfies $\boldsymbol{e}(\boldsymbol{k}) = \boldsymbol{0}$. By solving this nonlinear equation, we can obtain the optimal spring stiffness $\boldsymbol{k}$. For more details see Schiehlen and Iwamura (2009).

4.3 Application Example

The optimal design method is demonstrated for the 2DOF manipulator shown in Fig. 1. As in the previous chapter, we consider the motion under the initial and final conditions $\boldsymbol{y}_0 = [-30\ -30]^T$deg and $\boldsymbol{y}_f = [30\ 30]^T$deg. Here we assume that the operating time is specified as $t_f^* = 1$ s. Firstly, we choose r_i as $r_1 = 1, r_2 = 3$, then the natural frequencies become $\omega_1 = \pi$, $\omega_2 = 3\pi$. We set the initial guess of the spring stiffnesses as $\boldsymbol{k}^{(0)} = [k_1\ k_2]^T = [30\ 30]^T$. Though the consumed energy J corresponding to this spring stiffnesses was already shown in Fig. 2, we show it again on a different scale with J_1 and J_2 in Fig. 3. Since the minimum of J_1 and J_2 do not coincide, J is not vanishing. Hence, we optimize the spring stiffnesses. By solving $\boldsymbol{e}(\boldsymbol{k}) = \boldsymbol{0}$, we obtain $\boldsymbol{k} = [k_1\ k_2]^T = [21.854\ \ 14.182]^T$. The consumed energy J corresponding to this spring stiffnesses is shown in Fig. 4. We can observe that the minimum of J_1 and J_2 coincides at $t_f^* = 1$ s and therefore J also becomes zero at $t_f^* = 1$ s. In Fig. 4, the minimal value of J corresponding to the case without spring, i.e. a conventional robot manipulator, is also shown by a dotted line. We can confirm that the consumed energy is strongly reduced at the design point $t_f^* = 1$ s. This proves the effectiveness of the proposed method.

5 Conclusion

In this paper, we considered the problem to minimize the energy consumption of robot systems in the horizontal plane utilizing storage elements and proposed a simultaneous optimization method for storage elements and trajectory. The effectiveness of the design method was shown by applying it to a 2DOF manipulator.

Bibliography

M. Iwamura, P. Eberhard, W. Schiehlen, and R. Seifried. A general purpose optimal trajectory planning algorithm for multibody systems. In *Proceedings of the 28th IASTED International Conference on Modeling, Identification, and Control, K.M., Hangos (ed.)*, pages 55–62, 2009.

T. Izumi, P. Boyagoda, and T. Satoh. Optimal trajectory for minimizing dissipative energy of a horizontal articulated manipulator with energy regeneration and the effect of operating time. *Journal of the Robotics Society of Japan*, 15(4):601–607, 1997.

W. Schiehlen and N. Guse. Power demand of actively controlled multibody systems. In *Proceedings of DETC, ASME paper DETC/VIB 21343*, 2001.

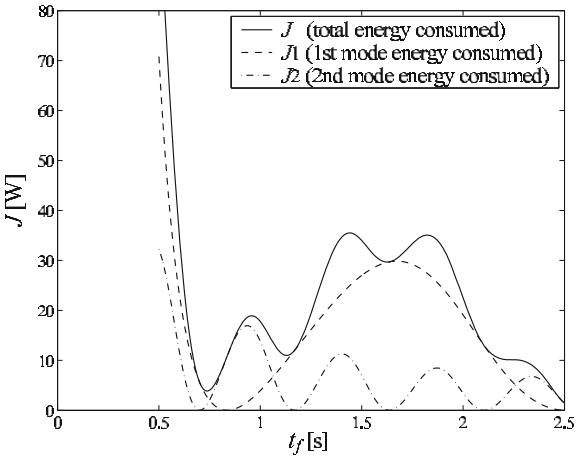

Figure 3. Power J before optimization.

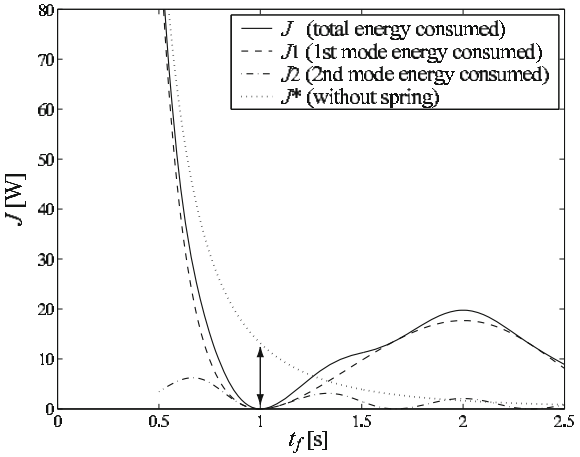

Figure 4. Power J after optimization.

W. Schiehlen and N. Guse. Control of limit cycle oscillations. In *Proceedings of the IUTAM Symposium on Chaotic Dynamics and Control of Systems and Processes in Mechanics, G. Rega, and F. Vestroni (eds.)*, pages 429–439, 2005.

W. Schiehlen and M. Iwamura. Minimum energy control of multibody systems utilizing storage elements. In *Proceedings of DETC, ASME paper DETC2009 86327*, 2009.

Motion Control of an Under-Actuated Service Robot Using Natural Coordinates

László L. Kovács [*‡], Ambrus Zelei [‡], László Bencsik [‡],
János Turi [†] and Gábor Stépán [‡]

[*] HAS-BME Research Group on Dynamics of Machines and Vehicles
[†] The University of Texas at Dallas, Department of Mathematical Sciences
[‡] Budapest University of Technology and Economics,
Department of Applied Mechanics

Abstract The recent work presents the motion control of a pendulum like under–actuated service robot ACROBOTER. This robot is designed to be applied in indoor environments, where it can perform pick and place tasks autonomously and/or with close cooperation with humans. It can also serve as a platform that carries other service robots with lower mobility. The cable suspended robot has a complex structure and its dynamics is difficult to model using conventional robotic approaches. Instead, in this paper natural (Cartesian) coordinates are used to describe the configuration of the robot, while its dynamics is modeled as a set of differential algebraic equations. The method of computed torque control with a PD controller is applied to the investigated under–actuated system. The inverse dynamics solution is obtained via direct discretization of the DAE system. Results for a real parameter case study are presented by numerical simulations.

1 Introduction

Obstacle avoidance is an important problem in service and mobile robotics, especially when the robots are operating in an everyday indoor environment. Static obstacles on the floor of a room include various objects such as stairs, doorsteps, chairs, tables and even the edges of carpets. Hence,

This work was supported in part by the Hungarian National Science Foundation under grant no. OTKA K068910, the ACROBOTER (IST-2006-045530) project, the Hungarian Academy of Sciences under grant no. MTA-NSF/103, the HAS-BME Research Group on Dynamics of Machines and Vehicles and by National Science Foundation DMS-0705247.

floor based domestic robots need to have strategies to overcome randomly placed objects.

A new direction in the development of indoor service robots is the use of robotic structures that can move on the, almost obstacle free, ceiling of a room. An application which addresses the need for a robot to climb on the walls and crawl on the ceiling inside a building is the MATS robot (*et al.*, 2006). Another examples include actuator mechanisms showing similarities with gantry cranes, e.g., the mobile robot platform described in (Sato et al., 2004) and the FLORA walking assisting system developed by FATEC Corporation (FATEC Co., 2004). These platform concepts solve the problem of avoiding obstacles on the floor, while they are able to roam over almost the whole inner space of a room, and compared to gantry cranes, they enable the use of co-operating multiple units.

The present paper describes a new indoor service robot platform developed within the ACROBOTER IST-2006-045530 project (*et al.*, 2009). The ceiling suspended robot (see Figure 1a) is equipped with windable cables and ducted fan actuators. Compared to (Sato et al., 2004; FATEC Co., 2004) the use of complementary actuators makes it possible to control and utilize the pendulum-like motion of the system, and provide larger workspace and better maneuverability. The ACROBOTER robot is able to move along a prescribed spatial trajectory while it performs various tasks like pick and place of objects and manipulating other service robots. Despite of the large number of actuators, the ACROBOTER robot is still under–actuated. The application of the method of computed torque control for this system leads to a set of differential algebraic equations adjoining to the geometric constraints which also appear as algebraic equations. The generalized coordinates that describe the configuration of the system are coupled and cannot be partitioned into passive and active coordinates in general. Instead, in this paper the direct solution of the DAE problem is presented for ACROBOTER system using the Backward-Euler discretization method as it is also proposed in (Blajer and Kolodziejczyk, 2008). The algorithm is formulated semi-analitically. Its applicability is demonstrated by numerical experiments.

2 Mechanical Model and Problem Formulation

The ACROBOTER system shown in Figure 1a consists of Anchor Points (AP) placed on the ceiling, a Climer Unit (CU) that can swap between these APs and a Swinging Unit (SU) which has a mechanical interface for connecting the payload. The CU is an RRT robot that moves parallel to the ceiling and provides the horizontal motion of the system. The windable

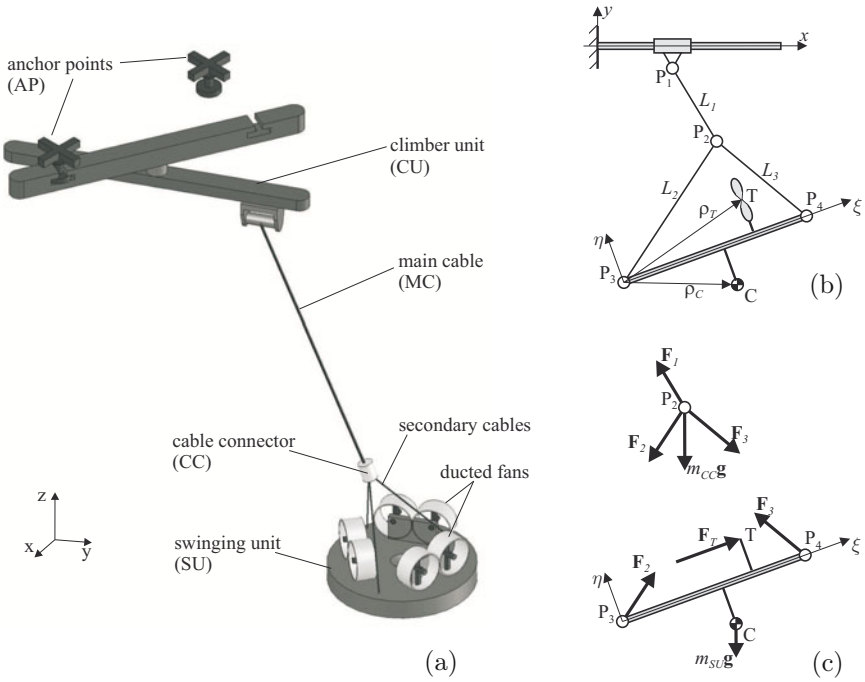

Figure 1. ACROBOTER (a), planar model (b), free body diagrams (c)

Main Cable (MC) connects the CU and the SU through the Cable Connector (CC) to which the secondary orienting cables are also attached. By using the mechanical interface the Swinging Unit (SU) can be equipped with grippers and various tools. In this concept the three secondary cables orient the SU, while the three pairs of ducted fans are used for performing and stabilizing the motion of the SU along its desired trajectory. The thrust forces provided by the ducted fans make it possible to move the payload even when the CU does not move at all.

For developing the control algorithm of this device we consider the planar model of the ACROBOTER (see Figure 1b). The free-body-diagrams corresponding to this model are shown in Figure 1c. We treat the robot as a multibody system described by natural (Cartesian) coordinates (de Jalón and Bayo, 1994). This formalism provides the equation of motion for both the planar and spatial cases in the same form. Modeling of the spatial ACROBOTER system does not require further complexity, only the number of descriptor coordinates and geometric constraints will be higher.

In Figure 1b the SU is modeled as a rod with length L_{34} and mass m_{SU}, which includes the mass of the payload as well. The CC is considered as a

point mass m_{CC}. The length of the MC is denoted by L_1 and the corresponding cable force is $\mathbf{F}_1$. The actuator forces acting upon the secondary cables are $\mathbf{F}_2$ and $\mathbf{F}_3$, respectively. The configuration of the system is described by the coordinates (x_i, z_i) of the points P_i. In addition, the center of mass of the SU is given by the vector $\boldsymbol{\rho}_C$ in the body frame, and the loading point of the resultant thrust force is represented by the vector $\boldsymbol{\rho}_T$.

By considering that the CU moves exactly on a prescribed trajectory and using the set of descriptor coordinates $\mathbf{q} = [x_2, z_2, x_3, z_3, x_4, z_4]^{\mathrm{T}}$, the equation of motion of the ACROBOTER system can be written as

$$\mathbf{M}\ddot{\mathbf{q}} + \boldsymbol{\Phi}_{\mathbf{q}}^{\mathrm{T}}(\mathbf{q})\boldsymbol{\lambda} = \mathbf{Q}_g + \mathbf{H}(\mathbf{q})\mathbf{u}\,, \tag{1}$$

$$\boldsymbol{\phi}(\mathbf{q}) = \mathbf{0}\,, \tag{2}$$

$$\boldsymbol{\phi}_s(\mathbf{q}, \mathbf{p}(t)) = \mathbf{0}\,. \tag{3}$$

Equation (1) is a Lagrangian equation of motion of the first kind, where $\mathbf{M}$ is the $n \times n$ sized constant mass matrix (de Jalón and Bayo, 1994) which may also depend on the payload. Symbol $\mathbf{Q}_g$ is the generalized gravity force. The m geometric constraints are represented by the vector $\boldsymbol{\phi}(\mathbf{q})$ in (2) and $\boldsymbol{\Phi}_{\mathbf{q}}$ is the Jacobian matrix of the constraints. The corresponding Lagrange multipliers are denoted by $\boldsymbol{\lambda}$. The l dimension input vector is $\mathbf{u}$ and $\mathbf{H}$ is the generalized input matrix.

The number of control inputs, l, is less than the $n - m$ DoFs of the system, thus it is under-actuated. The task of the robot can be formulated by the servo-constraints $\boldsymbol{\phi}_s(\mathbf{q}, \mathbf{p}(t))$ (Blajer and Kolodziejczyk, 2008) given in equation (3). The dimension of the $\boldsymbol{\phi}_s(\mathbf{q}, \mathbf{p}(t))$ vector is also l which means that the l dimensional control input can be determined uniquely.

The servo constraints depend on the function $\mathbf{p}(t)$ that can be handled as the desired system output and it may describe the desired trajectory of a certain point and/or the desired orientation of the SU. For example, if the position of the center of mass of the SU and its horizontal orientation is prescribed together with the elevation of the CC, the servo constraints can be expressed in the form

$$\boldsymbol{\phi}_s(\mathbf{q}, \mathbf{p}(t)) = \mathbf{h}(\mathbf{q}) - \mathbf{p}(t) \quad \text{with} \tag{4}$$

$$\mathbf{h}(\mathbf{q}) = [1/2(x_3 + x_4),\, 1/2(y_3 + y_4),\, y_3 - y_4,\, y_2]^{\mathrm{T}}\,, \tag{5}$$

$$\mathbf{p}(t) = \left[x_C^d(t),\, y_C^d(t),\, 0,\, y_2^d(t)\right]^{\mathrm{T}}\,, \tag{6}$$

where $\mathbf{h}(\mathbf{q})$ gives the prescribed system outputs as the function of the descriptor coordinates by assuming that $\boldsymbol{\rho}_C = [L_{34}/2,\, 0]^{\mathrm{T}}$.

We assume that the servo-constraints and a well chosen subset of geometric constraints can be solved for the controlled coordinates $\mathbf{q}_c$ in closed form.

Then the task can be defined by $\mathbf{q}_c = \mathbf{q}_c^d$, where the superscript d refers to the desired trajectory. In the case of the planar ACROBOTER model the vector of these desired coordinates is $\mathbf{q}_c^d = \left[y_2^d(t),\, x_3^d(t),\, y_3^d(t),\, y_4^d(t)\right]^{\mathrm{T}}$. For the partitioning of the descriptor coordinates we introduce the vector of controlled and uncontrolled coordinates with $\mathbf{q}_c = \mathbf{S}_c^{\mathrm{T}}\mathbf{q}$ and $\mathbf{q}_u = \mathbf{S}_u^{\mathrm{T}}\mathbf{q}$, respectively, where $\mathbf{S}_c$ and $\mathbf{S}_u$ are task dependent selector matrices.

3 Computed Torque Control

The computed torque method was generalized in (Lammerts, 1993) for the case of under-actuated systems. The generalized method is called Computed Desired Computed Torque Control method (CDCTC), where the expression "computed desired" refers to the fact that the uncontrolled coordinates cannot be prescribed arbitrarily, since they depend on the internal dynamics of the system. In case of the CDCTC method the equations of motion are ordinary differential equations (ODE) and the null space of the coefficient matrix of the input vector is used to project these equations into the space of uncontrolled motions. The projected set of differential equations can then be solved for the desired values of the uncontrolled coordinates and the control inputs can then be expressed.

To apply the CDCTC method to the ACROBOTER model described by equations (1–3) an additional projection is required. Since the equations of motion are given as a DAE system, first, the DAE system has to be reduced to an ODE. This can be accomplished by projecting the equations of motion to the subspace of admissible motions by the constraints (Kövecses et al., 2003). However, the repeated projections and the stabilization (configuration correction) of the numerical solution make the application of the method rather complex and computationally expensive.

Instead, we apply the Backward Euler discretization for the DAE system and the resulting set of implicit equations are solved by the Newton-Raphson method for the desired actuator forces. Considering a PD controller with gain matrices $\mathbf{K}_P$ and $\mathbf{K}_D$ the control law can be formulated as

$$\mathbf{M}\ddot{\mathbf{q}}^d + \boldsymbol{\Phi}_{\mathbf{q}}^{\mathrm{T}}(\mathbf{q}^d)\boldsymbol{\lambda} = \mathbf{Q}_g + \mathbf{H}(\mathbf{q}^d)\mathbf{u} - \mathbf{K}_P(\mathbf{q}^d - \mathbf{q}) - \mathbf{K}_D(\dot{\mathbf{q}}^d - \dot{\mathbf{q}})\,, \quad (7)$$

$$\boldsymbol{\phi}(\mathbf{q}^d) = \mathbf{0}\,, \quad (8)$$

where $\mathbf{q}$ and $\mathbf{q}^d$ are the measured and the desired descriptor coordinates, respectively. Introducing $\mathbf{y}^d = \dot{\mathbf{q}}^d$, equations (7) and (8) can be rewritten as

$$\dot{\mathbf{q}}^d = \mathbf{y}^d\,, \quad (9)$$

$$\dot{\mathbf{y}}^d = \mathbf{M}^{-1}\Big(\mathbf{Q}_g + \mathbf{H}(\mathbf{q}^d)\mathbf{u} - \boldsymbol{\Phi}_{\mathbf{q}}^{\mathrm{T}}(\mathbf{q}^d)\boldsymbol{\lambda} - \mathbf{K}_P(\mathbf{q}^d - \mathbf{q}) - \mathbf{K}_D(\dot{\mathbf{q}}^d - \dot{\mathbf{q}})\Big), \quad (10)$$

$$\mathbf{0} = \boldsymbol{\phi}(\mathbf{q}^d)\,. \quad (11)$$

The set of equations (9–11) can be partitioned into the prescribed controlled coordinates and the uncontrolled coordinates yielding the vector of unknowns

$$\mathbf{z} = \left[\, \mathbf{q}_u^d \,,\, \mathbf{y}_u^d \,,\, \mathbf{u} \,,\, \boldsymbol{\lambda} \,\right]^{\mathrm{T}} \,. \tag{12}$$

Using the Backward Euler method, the set of difference equations $\mathbf{F}(\mathbf{z}) = \mathbf{0}$ has to be solved for the (n+1)*th* value of $\mathbf{z}$, where

$$\mathbf{F}_{n+1} = \begin{bmatrix} \mathbf{q}_{u,n+1}^d - \mathbf{q}_{u,n}^d - h\mathbf{y}_{u,n+1}^d \\ \mathbf{y}_{u,n+1}^d - \mathbf{y}_{u,n}^d - h\mathbf{f}_{n+1} \\ \mathbf{g}_{n+1} \\ \boldsymbol{\phi}_{n+1} \end{bmatrix} \quad \text{with} \tag{13}$$

$$\mathbf{f}_{n+1} = \mathbf{S}_u^{\mathrm{T}}\mathbf{M}^{-1}\big(\mathbf{Q}_g + \mathbf{H}(\mathbf{q}^d)\mathbf{u} - \boldsymbol{\Phi}_{\mathbf{q}}^{\mathrm{T}}(\mathbf{q}^d)\boldsymbol{\lambda} - \mathbf{K}_P(\mathbf{q}^d - \mathbf{q}) - \mathbf{K}_D(\dot{\mathbf{q}}^d - \dot{\mathbf{q}})\big) \,, \tag{14}$$

$$\mathbf{g}_{n+1} = -\dot{\mathbf{y}}_c^d + \mathbf{S}_c^{\mathrm{T}}\mathbf{M}^{-1}\big(\mathbf{Q}_g + \mathbf{H}(\mathbf{q}^d)\mathbf{u} - \boldsymbol{\Phi}_{\mathbf{q}}^{\mathrm{T}}(\mathbf{q}^d)\boldsymbol{\lambda} - \mathbf{K}_P(\mathbf{q}^d - \mathbf{q}) - \mathbf{K}_D(\dot{\mathbf{q}}^d - \dot{\mathbf{q}})\big) \,. \tag{15}$$

The solution of the above system can be obtained for the consecutive time steps with sampling time h, by iterating to $\mathbf{z}_{n+1}$ via the repeated solution of the equation

$$\mathbf{J}_{n+1}(\mathbf{z}_{n+1} - \mathbf{z}_n) = -\mathbf{F}_{n+1} \,, \tag{16}$$

where $\mathbf{J}$ is the Jacobian matrix

$$\mathbf{J} = \left[\begin{array}{c|c|c|c} \mathbf{I} & -h\mathbf{I} & \mathbf{0} & \mathbf{0} \\ \hline h\mathbf{S}_u^{\mathrm{T}}\mathbf{M}^{-1}[\mathbf{K}_P\mathbf{S}_u + (\boldsymbol{\Phi}_{\mathbf{q}}^{\mathrm{T}}\boldsymbol{\lambda})_{\mathbf{q}_u^d} - (\mathbf{H}\mathbf{u})_{\mathbf{q}_u^d}] & \mathbf{I} + h\mathbf{S}_u^{\mathrm{T}}\mathbf{M}^{-1}\mathbf{K}_D\mathbf{S}_u & -h\mathbf{S}_u^{\mathrm{T}}\mathbf{M}^{-1}\mathbf{H} & h\mathbf{S}_u^{\mathrm{T}}\mathbf{M}^{-1}\boldsymbol{\Phi}_{\mathbf{q}}^{\mathrm{T}} \\ \hline \mathbf{S}_c^{\mathrm{T}}\mathbf{M}^{-1}[\mathbf{K}_P\mathbf{S}_u + (\boldsymbol{\Phi}_{\mathbf{q}}^{\mathrm{T}}\boldsymbol{\lambda})_{\mathbf{q}_u^d} - (\mathbf{H}\mathbf{u})_{\mathbf{q}_u^d}] & \mathbf{S}_c^{\mathrm{T}}\mathbf{M}^{-1}\mathbf{K}_D\mathbf{S}_u & -\mathbf{S}_c^{\mathrm{T}}\mathbf{M}^{-1}\mathbf{H} & \mathbf{S}_c^{\mathrm{T}}\mathbf{M}^{-1}\boldsymbol{\Phi}_{\mathbf{q}}^{\mathrm{T}} \\ \hline \boldsymbol{\Phi}_{\mathbf{q}}\mathbf{S}_u & \mathbf{0} & \mathbf{0} & \mathbf{0} \end{array}\right] \tag{17}$$

with

$$(\boldsymbol{\Phi}_{\mathbf{q}}^{\mathrm{T}}\boldsymbol{\lambda})_{\mathbf{q}_u^d} = \frac{\partial \boldsymbol{\Phi}_{\mathbf{q}}^{\mathrm{T}}\boldsymbol{\lambda}}{\partial \mathbf{q}_u^d} \quad \text{and} \quad (\mathbf{H}\mathbf{u})_{\mathbf{q}_u^d} = \frac{\partial \mathbf{H}\mathbf{u}}{\partial \mathbf{q}_u^d} \,. \tag{18}$$

4 Real parameter case study and simulation

The planar ACROBOTER model was simulated with realistic mechanical and control parameters. The mass of the swinging unit was set to

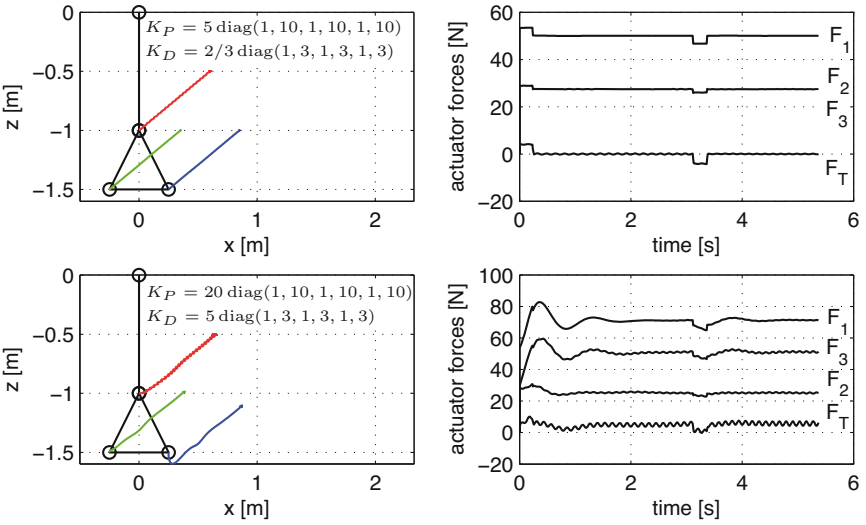

Figure 2. Simulation results

$m_{SU} = 5\text{kg}$, while the mass $m_{CC} = 0.1\text{kg}$ was set relatively small compared to it. In addition, the geometry of the SU was given by the length of the rod $L_{34} = 0.5\text{m}$. As an important control parameter the sampling time of the system was $h = 10\text{ms}$ during the simulation.

In the simulation the actuator forces were determined according to Section 3, while the equations of motion (1) and (2) were solved by using the method of Lagrange multipliers with Baumgarte stabilization (de Jalón and Bayo, 1994). This co-simulation made it possible to feed back the state of the system for the calculation of the actuator forces.

Figure 2 presents two sets of simulation results. In both cases the geometric center of the swinging unit was commanded to move along a straight line between the points (0, -1.5) and (0.6, -1). The trajectory had a trapezoidal velocity profile, characterized by the maximum acceleration and velocity $a_{max} = 1\text{m/s}^2$ and $v_{max} = 0.25\text{m/s}$, respectively. In the simulation presented in the top panels in Figure 2 the mass and inertia properties were considered as exactly known parameters of the system, i.e., the center of gravity and the geometric center were the same and the rod was considered to have homogeneous mass distribution. In contrast, the bottom panels show the simulation result when the effect of the payload were also considered. In this case, the mass of the SU was increased with a payload of 1kg. The payload was considered as a point mass causing the change of the common center of gravity expressed by $\rho_C = [0.3\text{m}\,, -0.05\text{m}]^{\mathrm{T}}$.

5 Conclusion

The computed torque control of an under-actuated service robot was presented. The calculation of the desired control inputs led to a DAE problem, which was solved via the Backward Euler discretization of the system and by using the Newton-Raphson method. The Jacobian matrix of the iteration algorithm was determined semi-analytically. The method is applicable for broad class of systems that can be modeled by natural coordinates.

The presented numerical results clearly show the applicability of the proposed control method. On the other hand, compensation is needed for modeling errors caused by unknown payloads. The tracking error can be decreased by increasing the values of the proportional gain matrix, while the stationary pose error at the final time may be eliminated by a PID controller. The limitations of the applied model based control may be improved by introducing an adaptation law for the control gains. Possible large disturbances are to be handled by the high level controller of the ACROBOTER, which may couple the separate controllers of the CU and SU.

Bibliography

W. Blajer and K. Kolodziejczyk. Modeling of underactuated mechanical systems in partly specified motion. *Journal of Theoretical and Applied Mechanics*, 46(2):383–394, 2008.

J.G. de Jalón and E. Bayo. *Kinematic and dynamic simulation of multibody systems: the real-time challenge*. Springer-Verlag, 1994.

C. Balaguer *et al. The* MATS *robot.* IEEE Robotics and Automation Magazine*, 13(1):51–58, 2006.*

G. Stépán et al. A ceiling based crawling, hoisting and swinging service robot platform. In *Proceedings of Beyond Gray Droids: Domestic Robot Design for the 21st Century Workshop at HCI 2009*, page in press, 2009.

J. Kövecses, J.-C. Piedoboeuf, and C. Lange. Dynamic modeling and simulation of constrained robotic systems. *IEEE/ASME Transactions on mechatronics*, 8(2):165–177, 2003.

I. M. M. Lammerts. *Adaptive Computed Reference Computed Torque Control*. PhD thesis, Eindhoven University of Technology, 1993.

FATEC Co. Walking assist system by supporting from ceiling (FLORA). `http://www.fa-tec.co.jp/FLORA-C/index.htm`, 2004. Last accessed: December 2009.

T. Sato, R. Fukui, H. Mofushita, and T. Mori. Construction of ceiling adsorbed mobile robots platform utilizing permanent magnet inductive traction method. In *Proceedings of 2004 IEEEiRSJ International Conference on Intelligent Robots and Systems*, pages 552–558, 2004.

Control Law Synthesis for Slip Reduction of Wheeled Robot

Teresa Zielinska and Andrzej Chmielniak
Warsaw University of Technology,
Institute of Aeronautics & Applied Mechanics (WUT–IAAM),
ul.Nowowiejska 24, 00–665 Warsaw, Poland,
teresaz@meil.pw.edu.pl

Abstract A new method of motion synthesis for wheeled mobile robots is presented. Dynamics model describing the slip phenomenon taking into account the wheel-ground interaction is derived. The pattern of wheel motion control reducing the slip is proposed. The presented results were obtained in the frame of PROTEUS project devoted to the autonomous robots for inspection and exploration.

1 Introduction

Many works focusing on wheel-ground interaction discusses the design of automated braking systems for slip avoidance in cars. Only few publications are devoted to mobile robots. The two main approaches are used for motion synthesis taking into account the ground properties. In the first approach – the slip avoiding motion patterns are derived (Siegward R. et al. (2003)), in the second – the slip is minimized over the time using the slip estimators and sliding mode control (Li Ya.P. et al. (2006)). The second approach results in chattering of the actuation torque. No information is provided how this control method will be realized in reality when due to the system inertia and time limits affecting the theoretically produced high frequency torque components the real motion differs than those expected. In the presented work we obtain the constraints for wheel acceleration, and constraints for actuating torque preventing longitudinal slip.

2 Slip Avoidance

In this paper we analyse the straight-line rolling. This neglects the lateral motion resistances. The wheel traction force F_n equilibrates: F_I – wheel inertia force, F_v – vehicle inertia force; $F_v = m\dot{v}_p$ (m – is the part of robot

mass ,,supported" by the wheel, v_p is the linear velocity of the robot (equal to the linear velocity of the wheel circumference v_c with no slip), F_r – rolling resistance force; F_r, is the force to has to be spent to passively stop (without any actuation or breaking) the wheel which is rolling on a horizontal surface. This means that $F_r = fQ/r$ (r – is the wheel radius). F_a – the cohesion force $F_a = \mu_0 Q$, where μ_0 is the wheel-ground cohesion coefficient (Muro T. and O'Brien J. (2004)), F_e – other internal and external resistive forces, non-dimensional factor $f_o = f/r$ is the rolling resistance coefficient – (Smieszek M. (2000)):

$$F_n = F_I + F_v + F_r + F_a + F_e = F_I + m\dot{v}_p + f_o Q + \mu_0 Q + F_e. \quad (1)$$

Q is the force acting on the wheel shaft. This vertical force results from the part of vehicle weight and inertial forces supported by the considered wheel being in contact with the ground. During horizontal motion of an n-wheeled robot with equally distributed total mass M, when the robot is not subjected to vertical acceleration (excluding gravity), we have $Q = mg = Mg/n$ ($m = M/n$, g – is the gravity constant). The distance f is the horizontal shift of the application point of the vertical component Q of the inertia force acting on the wheel-ground contact point, towards the application point of that force on the wheel shaft. The wheel inertia is J. The part of actuation torque compensating the wheel inertia moving with acceleration $\ddot{\phi}$ is equal to $J\ddot{\phi}$. The actuation torque M_k must overcome moment resulting from resistive forces (Smieszek M. (2000)) – that means it overcomes: $J\ddot{\phi}$ – the wheel inertia moment, $F_v\, r$ – the part of torque due to the vehicle inertia, $F_r\, r$ – the torque compensating to rolling resistance, $F_a\, p$ – the torque overcoming cohesion, M_e – torque due to the additional external factors. Taking into account rel.(1) we obtain:

$$M_k = J\ddot{\phi} + m\dot{v}_p r + f_o Q r + \mu_0 Q p + M_e. \quad (2)$$

p is the normalized radius of the wheel-ground contact. It should be noted that p is considered as the acting arm for F_r when evaluating the torque due to cohesion. It does not depends on the wheel radius. Slip is proportional to the difference between the linear velocity of the wheel $v_c = \dot{\phi} r$ and the vehicle velocity v_p. Slip ratio is defined as $\lambda = \frac{\dot{\phi} r - v_p}{max(v_p, \dot{\phi} r)}$. The torque not causing the slip fulfills $M_k \leq \mu_c Q r$. Hence:

$$J\ddot{\phi} + m\dot{v}_p r + f_o Q r + \mu_0 Q p + M_e \leq \mu_c Q r. \quad (3)$$

Without slip the wheel and vehicle velocities are equal $\dot{v}_p = \dot{v}_c = \ddot{\phi} r$, and the following relation is valid:

$$J\ddot{\phi} + m\ddot{\phi} r^2 + f_o Q r + \mu_0 Q p + M_e \leq \mu_c Q r, \quad (4)$$

This is transformed to the condition limiting wheel angular acceleration:

$$\ddot{\phi} \leq (\mu_c Qr - f_o Qr - \mu_0 Qp - M_e)/(J + mr^2) \tag{5}$$

3 Traction Force During the Slip

We introduced the term of critical friction coefficient interpreted in similar way as μ_c but for the slip. The critical friction coefficient results from the pessimistc slip estimation that means it assumes the wheel-ground resistance smaller than the real one. This critical coefficient is expressed by:

$$\mu_{cs}(\lambda) = \mu_c e^{-(\lambda^2)/b} \tag{6}$$

With $b = 0.26$ for $\mu_c \leq 0.9$ μ_{cs} it will be be smaller than $\mu(\lambda)$ (to safe the space the graphical illustration is not submitted). The following relation must be fulfilled:

$$M_k/r = (J\ddot{\phi} + m\dot{v}_p r + f_o Qr + \mu_0 Qp + M_e)/r \leq \mu_{cs} Q \tag{7}$$

Taking into account (6) the boundary condition for actuation torque not causing the slip greater than the existing one is following:

$$M_k = \mu_c e^{-(\lambda^2)/b} Qr, \tag{8}$$

Torque greater than that given by (8) will increase the already existing slip.

4 Slip Reduction

Assuming that the initial slip is equal to λ_0 we propose the wheel revolutions pattern resulting in slip reduction during the given time. For the sake of simplicity in (2) we will neglect the external moment M_e, and the moment resulting from cohesion. To express the wheel inertia we will consider it as a solid disc, thus $J = m_k r^2$ (m_k is the wheel mass). With the above we obtain:

$$\ddot{\phi} \leq (\mu_c Qr - f_o Qr)/(0.5 m_k r^2 + mr^2). \tag{9}$$

This is the simplified condition for acceleration limit not causing the slip. We assume that the slip will be decreasing according to:

$$\lambda(t) = \lambda_0 e^{-at} \tag{10}$$

t is the time measured from the start of slip reduction, the constant a is iteratively chosen to keep the wheel velocity and acceleration in acceptable

ranges thAt means it must be enough small to fulfill (7). Function (10) is the slip reduction envelope curve. Neglect the small component $f_o Qr$ we obtain the short formula for the acceleration initiating the slip: $\ddot{\phi} \geq \frac{(\mu_c Qr)}{(0.5 m_k r^2 + m r^2)}$. When the torque exceeds $\mu_c Qr$ by some amount the slip is bigger the the inial one. The torque cauing such slip is evaluated using the following logic – the amount of torque causing initial slip is equal to $\mu_c Qr$, during the slip increase the resistive forces decrease, hence after the wheel-ground contact is lost the traction force F_n causing the slip λ is approximated by $(\mu_c - \mu_c e^{-(\lambda^2)/b})Q$ (referring to (Shoop S.A. (2001))). This results in the overall torque $(2\mu_c - \mu_c e^{-(\lambda^2)/b})Qr$ giving the slip characterised by critical friction coefficient $\mu_c e^{-(\lambda^2)/b}$. Taking into account the actuation torque equal to $J\ddot{\phi} + m\dot{v}_p r$ (several terms are neglected as previously mentioned) we obtain a relation expressing the torque causing slip λ:

$$J\ddot{\phi} + m\dot{v}_p r = (2\mu_c - \mu_c e^{-(\lambda^2)/b})Qr \tag{11}$$

Slip ($\lambda = \lambda(t)$) changes in time, thus the velocity v_p conforms to the slip definition $v_p = \dot{\phi} r(1 - \lambda(t))$. Differentiating v_p: $\dot{v}_p = \ddot{\phi} r(1 - \lambda(t)) - \dot{\phi} r \dot{\lambda}(t)$. Taking into account that during slip reduction $J\ddot{\phi} + m\dot{v}_p r = \mu_c e^{-(\lambda^2)/b} Qr$ we obtain the equation:

$$J\ddot{\phi} + mr^2(\ddot{\phi}(1 - \lambda(t)) - \dot{\phi}\dot{\lambda}(t)) = \mu_c e^{-(\lambda(t)^2)/b} Qr \tag{12}$$

Trajectories $\phi(t)$, $\dot{\phi}(t)$ will be obtained with the example discussed bellow.

Implementation of Control Strategy

To evaluate the envelope curves for the wheel rotation pattern the discretized time was applied. For each t_i $\lambda(t_i) = \lambda_i$, and accordingly $\mu(\lambda(t_i) = \mu_i$, $\dot{\lambda}(t_i) = \dot{\lambda}_i$ – are constant ($\dot{\lambda}(t)$ is obtained easy as the time derivative of(10) for $t = t_i$), then (11) has the form:

$$J\ddot{\phi} + mr^2(\ddot{\phi}(1 - \lambda_i) - \dot{\phi}\dot{\lambda}_i) = \mu_c e^{-(\lambda_i^2)/b} Qr \tag{13}$$

Using the Laplace transform to the above linear differential equation we get:

$$\phi(t) = \frac{P_i}{B_i}(1 - exp^{(-B_i t/A_i)}) + \phi(0) exp^{(-B_i t/A_i)} \quad B_i \neq 0 \tag{14}$$

where $P = (\mu_c e^{-(\lambda_i^2)/b} Qr) + (J + mr^2(1 - \lambda_i))\dot{\phi}(0) - mr^2 \dot{\lambda}_i \phi(0)$, $B = -mr^2 \dot{\lambda}_i$, $A = J + mr^2(1 - \lambda_i)$. Implementing the slip control strategy we must take into account model inaccuracies. The low level control for mobile robots uses the encoder feedback delivering the information about wheel position and/or

velocity plus acceleration. We propose divided model-based controller, the control signal (control torque) is:

$$T_c = \alpha T_l + \beta \tag{15}$$

T_l is linear part of controller – $T_l = \ddot{\phi} + k_v\dot{\phi} + k_p\phi$, β is model-based remaining part. For our problem basis on (13) it is:

$$[J + mr^2(1 - \lambda_M)][\ddot{\phi} + k_v\dot{e} + k_p e] - mr^2\dot{\phi}\dot{\lambda}_M = T_c \tag{16}$$

where $e = e(t) = \phi_d(t) - \phi(t) = \phi_d - \phi$, ϕ_d is reference value, ϕ is real (given by encoder) value. λ_M is the slip got using the slip decrease model (10). For the real slip λ_R and the real position ϕ, the torque is:

$$[J + mr^2(1 - \lambda_R)]\ddot{\phi} - mr^2\dot{\phi}\dot{\lambda}_R = T_R \tag{17}$$

The difference between produced and real torque $T_R - T_c$ in the stable control must converge to zero (that means $T_R = T_C$). With this condition, and after proper grouping of the terms it is:

$$\ddot{e} + (k_v - \frac{mr^2\dot{\lambda}_M}{1 + mr^2(1 - \lambda_M)})\dot{e} + \frac{k_p}{1 + mr^2(1 - \lambda_M)}e = \frac{1}{1 + mr^2(1 - \lambda_M)}[(\lambda_M - \lambda_R)\ddot{\phi} + mr^2(\dot{\lambda}_M - \dot{\lambda}_M)\dot{\phi}] \tag{18}$$

Applying Laplace transform the error-to-wheel transfer function G_E is produced:

$$G_E(s) = \frac{E(s)}{\Phi(s)} = \frac{s(As + B)}{s^2 + k'_v s + k_p} \tag{19}$$

$k'_v = k_v - -\frac{mr^2\dot{\lambda}_M}{1+mr^2(1-\lambda_M)}$, $A = \frac{\lambda_M - \lambda_R}{1+mr^2(1-\lambda_M)}$, $B = \frac{\dot{\lambda}_M - \dot{\lambda}_R}{1+mr^2(1-\lambda_M)}$

From the above $E(s) = G_E(s)\Phi(s)$. In convergent control the steady state error is zero. This error ($e(t \to \inf)$) can be evaluated using the final value theorem.

$$e(t \to \inf) = (s \to 0)\ sG_E(s)\Phi(s) = \frac{s^2(As + B)}{s^2 + k'_v s + k_p}\Phi(s) \tag{20}$$

Error decreases to zero if the Laplace transform of ϕ is such that, after applying the final value theorem in Laplace domain, at least one free s in numerator remains. The simplest examples of such functions are 1 or $1/s$. The first one in time domain is delta Dirac function what is not possible to obtain in real control, second one is step function of wheel position.

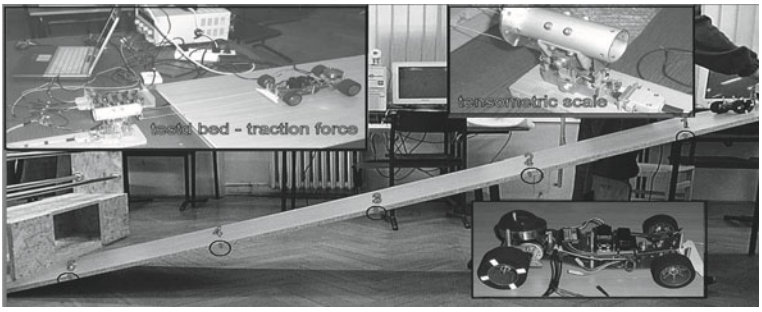

Figure 1. Test bed: the reference points S1-S4 are in distance 0.5m each

This will result in delta Dirac function for wheel velocity what again is not realistic. Therefore as the possible control signals for slip control more complex functions giving smooth velocity and acceleration profiles must be proposed. If the robot must transverse some distance the following function describing the reference position is here the good candidate $\Phi(s) = A\frac{\omega_n^2}{s(s^2+2\eta\omega_n s+\omega^2)}$), then $\dot{\Phi}(s) = A\frac{\omega_n^2}{s^2+2\eta\omega_n s+\omega^2}$ and $\ddot{\Phi}(s) = A\frac{s\omega_n^2}{s^2+2\eta\omega_n s+}\omega^2$, this gives in time domain: $\phi(t) = A[1-\frac{1}{\sqrt{1-\eta^2}}e^{-\eta\omega_n t}sin(\omega_n\sqrt{1-\eta^2}t)+\alpha)]$,

$\dot{\phi}(t) = A\frac{\omega_n}{\sqrt{1-\eta^2}}e^{-\eta\omega_n t}sin(\omega_n\sqrt{1-\eta^2}t)$,

$\ddot{\phi}(t) = -A\frac{1}{\sqrt{1-\eta^2}}e^{-\eta\omega_n t}sin(\omega_n\sqrt{1-\eta^2}t)-\alpha)]$,

where $\alpha = tan^{-1}(\sqrt{1-\eta^2})/\eta)$, and A is the reference value for wheel position. The physical experiment was performed. The small car model with wheel speed control was used. Two rear wheels with radius 0.027m were actuated by DC motors. The car weight, together with additional mass 0.5kg put over the back wheels shaft, was 0.7kG (6.897N). The aim was to test the efficiency of slip reduction using periodic signals with different frequencies and different magnitudes. To test the method of slip reduction the vehicle was placed on the inclined smooth surface, the inclination by $15^o45^{“}$ was chosen by continuous increase from horizontal level till the slop value when vehicle started sliding down with locked wheels. This inclination confirmed the evaluated friction coefficient – the inertia force along surface is $mg\ sin\alpha = 2.6N$, what is comparable to the value of force causing slip in horizontal plane. The setting of the test bed using this inclination created the situation as it is when the initial (critical) slip is caused. Moreover such arrangement created fixed and easier experiment conditions comparing to

horizontal level, where the change of motor control signal (from continuous one stimulating slip, to periodic one decreasing the slip) will be needed, evaluation of searched time factors will be also more troublesome. In the experiment vehicle was put in the top of inclination – the sinusoidal voltage signals with different frequency or different magnitude were applied to control the wheels speed. The speed of sliding was registered using high speed video camera. With the constant recording time, the position of the vehicle towards reference points (see Fig.1) in time instants allowed to detect the changes in sliding time. This method of sliup estimation is more accurate than the typical slip registration using sensors detecting the vehicle-ground relative velicity, but it needs the proper test rig and is limited to the range of the camera. In our experiment this limitation was not significant. Fig.2 and Fig.3 give the results. Each drawing represents the average result from several experiments (min 2 max 5). The longest duration of vehicle sliding (most effective slip prevention) was identified for 6Hz signal, and the magnitude 2.2V was the best from the range of tested. The sliding time for frequency 6Hz was about 25% shorter than the time obtained for locked wheels. The signal 2.2V reduced the slippage time by three comparing to non-controlled sliding (only due to inertia). It is expecting that the most ,,efficiemt" frequency in slip reduction for our car is between 6 and 10Hz (probably around 8Hz). Unfortunately we not tested it due to the limits of available equipment. The identified ,,best" magnitude is close to the magnitude registered during the tests on the horizontal surface for the moment of slip beginning (magnitude was in range 1.7-2.2V).

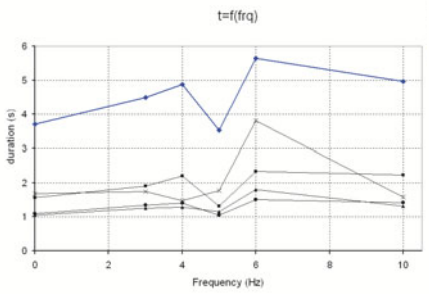

Figure 2. Duration of sliding depends on signal frequency; each drawing represents the average result for one reference point on the test path

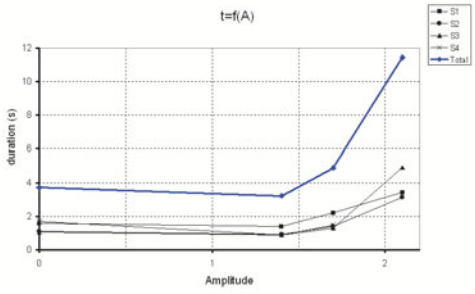

Figure 3. Duration of sliding depends on signal magnitude; each drawing represents the average result for one reference point on the test path

5 Conclusions

Taking into account small (but not too small) friction coefficient μ_c we will get in our theoretical models pessimistic (too big) slip ratio. It will result in longer time of slip reduction than the possible. The completed experiment confirmed the efficiency of proposed periodic wheel motion pattern during the slip reduction.

Our work is aiming the development of autonomous robots dedicated for search and inspection of dangerous zones in the outdoor and indoor environment. The slip reduction mechanism will increase its mobility and accuracy in self navigation.

Acknowledgments: The work is supported by European Regional Development Fund, Operational Program – Innovative Economy – grant PO IG.01.02.01-00-014/08-00.

Bibliography

Muro T., O'Brien J., *Terramechanics. Land Locomotion Mechanics.* A.A. Balkema Publishers Tokyo 2004.

Shoop S.A., *Finite element method modeling of tire-terrain interaction.* Engineers Research and Development Center, USA. Report ERDC/CRREL TR-01-16, Nov. 2001

Siegward R., Lamon P., Estier T., Lauria M., Piguet R., *Innovative design for wheeled locomotion in rough terrain.* J. of Robotics and Autonomous Systems. Vol. 40 2003, pp.151-162.

Smieszek M., *Motion description and energy requirements of automatically controlled transport vehicle – mobile robot* (in Polish). Oficyna Wydawnicza Politechniki Rzeszowskiej 2000.

Wong J.Y., *Theory of Ground Vehicles.* 3rd ed. New York, Wiley 2001

Li Ya.P., Zielinska T., Ang M.H., Liu W., *Vehicle Dynamics of Redundant Mobile Robots with Powered Caster Wheels.* RoManSy 16, no.487, Springer 2006, ISBN-3-211-36064-6, Eds. T.Zielinska, C.Zielinski, pp.221-228

A Kinematic Model of the Tibio-Talar Joint Using a Minimum Energy Principle

Michele Conconi[‡] * and Vincenzo Parenti Castelli[‡]

[‡] Dept. of Mechanical Engineering, University of Bologna, Italy

Abstract This work presents a 3D kinematic model for the passive flexion motion of the tibio-talar joint. With only knowledge of the articular surface shapes, the spatial trajectory of passive motion is obtained as the envelop of joint configurations that maximize the surfaces congruence. An increase in joint congruence corresponds to an improved capability of distributing an applied load, allowing the joint to attain better strength with less material. Thus, joint congruence maximization is a simple geometric way to capture the idea of joint energy minimization. The results obtained are compared with in vitro measured trajectories. Preliminary experimental data provide strong support for the predictions of the theoretical model.

1 Introduction

The modeling of human diarthrodial joints is a very wide and complex field of research. In order to be meaningful and of practical use, a model should be simple and general enough to make possible the comprehension of the functional anatomy of the joint under study. On the other hand, it should also be subject-specific which could aid in the pre-surgical planning. To circumvent this complexity, it is useful to adopt a sequential approach, which subdivides the analysis into different steps (Franci et al., 2008). Each step studies few anatomical structures under hypotheses that allow to neglect the influence of the others joint elements, making thus possible to isolate and better understand their role in the behavior of the joint. At each further step new features are added and the hypotheses are made less restrictive, increasing the complexity and the generality of the model.

*This study was supported by AER-TECH and MIUR founds. The authors wish to thank Dr. Alberto Leardini and his staff at Istituti Ortopedici Rizzoli for collection of experimental data, and Eng. Luca Tersi for providing the distance map code.

Many works in the literature exploit similar approaches. Blankevoort et al. (1991) developed a quasi static model for moderate loaded knee relaying on articular surfaces and ligaments. Wilson and O'Connor (1997) first proposed a parallel mechanism kinematically equivalent to the knee to separate the position form the static analysis. Later, Parenti-Castelli and Di Gregorio (2000) and Sancisi and Parenti-Castelli (2007) improved this model, also extending it to the ankle (Di Gregorio et al., 2007; Franci and Parenti-Castelli, 2007).

All these works start by modeling the motion under virtually unloaded conditions the so-called *passive motion*. This ideal motion can be obtained as a sequence of position of neutral equilibrium (Wilson and O'Connor, 1997; Wilson et al., 2000). Under this assumption it is possible to study the role played by passive biological structures, namely the articular surfaces and the ligaments that remain unextended in this motion. In the absence of external perturbations indeed, a joint should move along a path determined solely by the constraints imposed by these structures.

It is possible to go further on the sequential approach and isolate the role played by solely the articular surfaces. Passive structures may apply only mono-lateral constraint to the joint motion, the ligaments working only in traction while the articular surfaces only in compression. Their constraint act thus complementarly and independently to each other in governing the passive motion. It is therefore possible to consider these structures separately, providing an additional restrictions that restore the total constraint conditions of the passive motion.

This can be obtained by imposing that the model minimizes the energy in the joint. It is worth noticing that previous models built on unextended ligaments (e.g., Franci and Parenti-Castelli (2007, 2008) for recent contributions) already contain such a principle. Indeed, keeping the length of the ligaments constant minimizes the joint elastic potential.

A first attempt to extend this reasoning to articular surfaces has been developed by Sirkett et al. (2004) for the wrist. Their study builds on the work of the German anatomist Julius Wolff (Wolff, 1986; Frost, 2004), according to whom bones adapt optimally to change in stress, attaining maximum strength with minimum material. Sirkett et al. try to translate this concept into a wrist kinematic model, assuming that the wrist moves so as to maximize contact areas, therefore minimizing peak local loading. As pointed out by Marai (2007), however, this model is only able to correctly predict wrist kinematics in a very narrow range of motion. This may be due to various reasons. First of all, Sirkett et al. try to model a generic loaded motion. However, any applied load leads to deformations of the anatomical structures composing the joint, possibly guiding the relative motion of the

bones on a path that is not in accordance with the idea of energy minimization. Moreover, faraway from an unloaded motion, the deformations in the joints are no longer negligible and neither it is the contribution of the ligaments to determine the joint kinematic. Furthermore, they try to follow the energy minimization employing a purely geometric definition of contact area, while this measure is intrinsically related to the acting load. Finally, they apply their analysis to the wrist, which is a highly complex articulation.

The tibio-talar kinematic model developed in this work attempts to overcome these problems in the following way: *i*) modeling only the passive motion; *ii*) using the idea of joint congruence maximization to translate the minimum energy principle; *iii*) applying the model to a simpler joint, the ankle, comparable under the assumption of point i to one degree of freedom (dof) joint (Leardini et al., 1999).

2 Materials and Methods

2.1 Data Acquisition

Passive motion of the Talus with respect to the Tibia was recorded for three specimen as a sequence of neutral equilibrium configuration using a standard stereophotogrammetric system (Stryker Navigation System; precision: ± 0.5 degrees, ± 0.5 mm) during in vitro experimental sessions. In the same way the points of the articular surfaces were digitalized. Two anatomical reference systems were defined to follow the bones relative motion. Relative orientation was described with a sequence-independent joint coordinate system (Grood and Suntay, 1983). The whole procedure and the experimental setup are described in Franci and Parenti-Castelli (2007).

2.2 Bone Modeling

Triangular mesh models for the bones were found in the VAKHUM database (www.ulb.ac.be/project/vakhum). This models were then manually adapted to fit the experimental data for the articular surfaces. Similarly to Marai et al. (2004), the tibia was modeled with a double representation: a mesh and a distance field. The talus was instead simply represented with a mesh.

2.3 Trajectory Generation

The relative position between two bones is described by six spatial coordinate. Together they identify the relative pose between two bones. If the considered joint has n dof, its kinematics can be parameterized by means of

n coordinates. The remaining coordinates can be obtained by imposing the congruence maximization. The tibio-talar joint may be considered as a single dof joint (Leardini et al., 1999), therefore its motion can be parametrized with the dorsi-plantar flexion angle. The trajectory of the tibio-talar passive motion was obtained as the envelop of successive maximum congruence configuration (as defined in Section 3) by subsequent optimization with a customized genetic algorithm.

Starting from an initial guess, usually taken from experimental measures, a grid of poses was built representing a neighborhood around it. This contains all the possible combinations of coordinates variation of a small amount δ, keeping the flexion fixed. Further configurations were added to this neighborhood exploiting the genetic algorithm techniques.

A (objective) function of the joint configuration was then evaluated in each of these points, returning a measure of the joint congruence for the considered pose. Around the configuration with the maximum congruence a new neighborhood was built and the analysis was repeated. This procedure continued until a (local) maximum was reached. The best pose was added to the trajectory and then used as initial guess for the next optimization, after its flexion angle has been incremented. This procedure was repeated on the whole flexion range, resulting in a spatial trajectory. To increase the reliability of the algorithm, more than one neighborhood was usually taken, obtained by increasing the value of δ.

3 A Measure of Joint Congruence

A key point of this model is the definition of a measure for the joint energy. Joint congruence indicates how well mating surfaces fit together. An increase in it corresponds to a better mating between the articular surfaces and to an improved capability of distributing an applied load. This results in an optimum employ of the bone material. Thus, joint congruence maximization is a simple geometric way to capture the idea of energy minimization.

In the literature it is possible to find different measure for the congruence in a joint (see for instance Connolly et al. (2009) and Simon et al. (1973)), all essentially based on the relative curvature of surfaces at the contact point or region. To make joint congruence independent from the bones to be in contact, we adopted here a different measure. We define a control volume by offsetting of a prescribed threshold the articular surfaces of one bone. Then, in each configuration of the joint, we measure the congruence as the intersection of this volume with the second bone volume (Fig. 1.a), discarding pose leading to co-penetration. This volume is approximated as

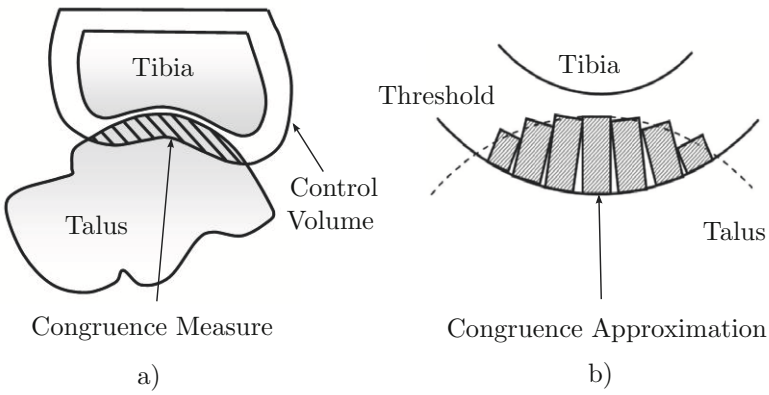

Figure 1. A 2D representation of a) the joint congruence measure and b) its approximation.

the sum of small discrete contributions. The area of each triangle of the talus mesh laying inside the control volume is multiplied by its distance from the control volume surface and add to the joint congruence measure (Fig. 1.b). The triangle distance is defined as the mean of its vertex distances from the same surface. All the distances are evaluated by means of the distance map representing the tibia. This procedure has proved to be up to six times faster than boolean computations among the same volumes, without affecting the results.

4 Result and Discussion

Figures 2.a, 2.b and 2.c show the computed and mean experimental trajectory for the passive motion of the three specimens. The first plot of each Figure shows the progression of the prono-supination and intra-extra rotation angles while the second shows the progression of the x, y and z displacements, all plotted versus the dorsi-plantar flexion angle.

Results for the first and the second specimens seemed to be affected by a constant error in the definition of the anatomical frame on the bones. To test this idea, the transformation bringing computed and experimental trajectories to coincide for a prescribed flexion angle has been calculated and than applied to the whole computed trajectory. The similarity between the two trajectories after this operation seems to validate the idea that the model predictions differ form experimental data only by a constant rototranslation, this being ascribable to a constant error in the measure.

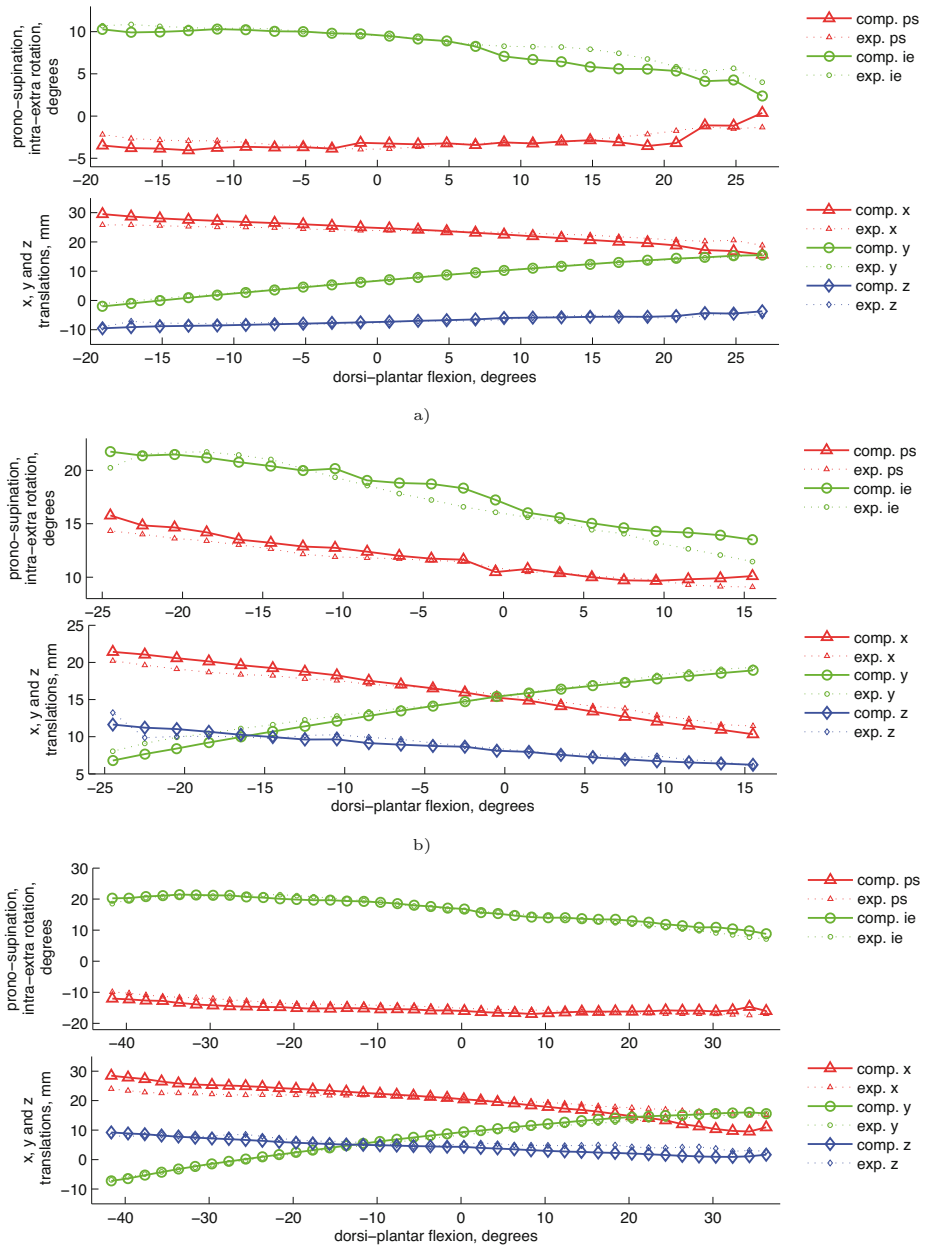

Figure 2. Computed (comp) and experimental (exp) prono-supination (ps), intra-extra rotation (ie) and x, y, and z displacements versus dorsi-plantar flexion for the a) first, b) second and c) third specimen, respectively.

Table 1. Mean Absolute Error (MAE) for prono-supination (PS), intra-extra rotation (IE), X, Y and Z displacement.

	PS (degrees)	**IE (degrees)**	**X (mm)**	**Y (mm)**	**Z (mm)**
1^{st} **leg**	0.60	0.74	1.75	0.30	0.59
2^{st} **leg**	0.54	0.90	0.81	0.60	0.51
3^{st} **leg**	1.25	0.75	2.49	0.73	1.38

Figures 2.a and 2.b show the results after this correction, not needed for the third specimen.

Table 1 shows the mean absolute error (MAE) between each coupled component of the computed and measured passive motion. Both inspection of the plots and numerical results shows a good agreement between predicted and measured motion.

5 Algorithm Sensitivity

The results of the algorithm may be influenced by the random component in the generation of new poses with genetic methods, by the threshold defining the control volume, by the distance map density and of course by the initial guess. To assess the sensitivity of the algorithm to these parameters, the third specimen has been chosen, being the one that shows less difference between computed and measured passive motion, even without corrections.

A preliminary analysis has shown that, despite the random component, the algorithm is highly repeatable. Multiple launches produced well grouped trajectories. Table 2.a shows the mean standard deviation (MSD) for each computed component of the passive motion, together with the MAE respect the measured one. The small MSD value underlines the repeatability of the algorithm, the discrepancy from experimental measure being consistent with the data of Table 1.

The threshold defining the control volume has been manually chosen equal to 7 mm so to maximize the portion of the articular surface laying into it. The analysis of the algorithm sensitivity to this parameter has shown that the congruence measure fails to drive the simulation for a value of 2mm, it produces noticeable discrepancy from the experimental path for a threshold of 3 mm but the MSD and MAE lay in the repeatability range from 4.5 to 11 mm (Tab. 2.b).

Table 2. Variation of the Mean Standard Deviation (MSD) and Mean Absolute Error (MAE) with different algorithm parameters for prono-supination (PS), intra-extra rotation (IE), X, Y and Z displacement.

	PS (degrees)	**IE (degrees)**	**X (mm)**	**Y (mm)**	**Z (mm)**
a) Multiple Launches (repeatability)					
MSD	0.51	0.85	0.19	0.11	0.27
MAE	1.86	0.72	2.60	0.67	1.63
b) Control Volume Threshold: 4.5÷11 mm					
MSD	0.37	0.60	0.19	0.09	0.19
MAE	1.78	0.55	2.57	0.71	1.54
c) Distance Map Smaller Cube Side: 0.5÷2.5 mm					
MSD	0.49	0.66	0.15	0.09	0.23
MAE	1.93	1.02	2.60	0.63	1.70
d) Initial Guess Variation: -5÷+4 mm					
MSD	0.92	1.50	0.67	0.21	0.40
MAE	2.18	3.08	2.61	0.40	2.24

To study the influence of the distance map refinement, the value of its smaller cube side was incremented from 0.5 to 2.5 mm, showing no significant variation among the computed trajectories (Tab. 2.c).

Different initial guesses were considered by varying of a same amount all the coordinate of the original one but the flexion angle (Tab. 2.d). In the range $-5 \div +1$ the trajectory variations are still ascribable to the algorithm repeatability, while in the range $+1 \div +4$ they become more sensible to the initial guess choice, especially for the intra-extra rotation, which in some point differs from experimental data up to 10 degrees. Anyway after a first assessment the trajectories still tend to converge to the experimental ones.

It is worth noting that the algorithm presents a non isotropic behavior.

Predictions obtained for the dorsi flexion differ from those for the plantar flexion and are in general less precise and stable. This can be due to the non symmetry into the talo articular surface, which at the beginning of the dorsi flexion offer a much smaller area, thus less suitable for the generation of motion guidance. This aspect surly deserves further studies.

6 Conclusion

The comparison between experimental and computed trajectories seems to validate the model for the tibio-talar joint on a range of more than 70 degrees of plantar flexion. A preliminarily analysis shows the algorithm to be repeatable and robust. It is worth to underline the predictive nature of the model: it does not rely on a measure of the trajectory it aims to match. Also, unless very general this approach make possible to generate subject-specific models, requiring relatively simple anatomical measures. Finally, the model provides a theoretical representation for passive motion as a minimum energy path and it shows the effectiveness of a sequential approach for the modeling of human diarthrodial joints.

Possible application of such a model may be found in pre-surgical planning, in the study of the effect of articular surface damages on the overall joint behavior and in the prosthesis design.

Future works will aim to further validate this model on the ankle with more experimental analysis and to test its applicability on other joints, such the knee and the wrist.

Bibliography

L. Blankevoort, J. H. Kuiper, R. Huiskes, and H. Grootenboert. Articular contact in a three-dimensional model of the knee. *Journal of Biomechanics*, 24(11):1019 – 1031, 1991.

K. D. Connolly, J. L. Ronsky, L. M. Westover, J. C. Kupper, and R. Frayne. Analysis techniques for congruence of the patellofemoral joint. *Journal of Biomechanical Engineering*, 131(12):124503, 2009.

R. Di Gregorio, V. Parenti-Castelli, J.J. O'Connor, and A. Leardini. Mathematical models of passive motion at the human ankle joint by equivalent spatial parallel mechanisms. *Medical and Biological Engineering and Computing*, 45(3):305 – 313, 2007.

R. Franci and V. Parenti-Castelli. A 5-5 one-degree-of-freedom fully parallel mechanism for the modeling of passive motion at the human ankle joint. In *DETC2007*, volume 8 PART A, pages 637 – 644, Las Vegas, NV, United states, 2007.

R. Franci and V. Parenti-Castelli. A one-degree-of-freedom spherical wrist for the modelling of passive motion of the human ankle joint. In *Proceedings of IAK 2008*, pages 1–13, Lima, Peru, January 2008.

R. Franci, N. Sancisi, and V. Parenti-Castelli. A three-step procedure for the modelling of human diarthrodial joints. In *Proceedings of the RAAD 2008*, pages 1–10, Ancona, Italy, September 2008.

H. M. Frost. A 2003 update of bone physiology and wolffs law for clinicians. *Angle Orthodontist*, 74:3–15, 2004.

E. S. Grood and W. J. Suntay. A joint coordinate systenf for the clinical description of three-dimensional motions: Application to the knee. *Journal of Biom.echilnlcal Engineering*, 135:136–144, May 1983.

A. Leardini, J.J. O'Connor, F. Catani, and S. Giannini. Kinematics of the human ankle complex in passive flexion; a single degree of freedom system. *Journal of Biomechanics*, 32(2):111 – 18, 1999.

G.E. Marai. *Data-Driven Predictive Modeling of Diarthrodial Joints*. PhD thesis, Brown University., 2007.

G.E. Marai, D.H. Laidlaw, C. Demiralp, S. Andrews, C.M. Grimm, and J.J. Crisco. Estimating joint contact areas and ligament lengths from bone kinematics and surfaces. *IEEE Transactions on Biomedical Engineering*, 51(5):790 – 9, 2004.

V. Parenti-Castelli and R. Di Gregorio. *Parallel mechanisms applied to the human knee passive motion simulation*, pages 333–344. Kluwer Academic Publishers, Pirano-Portoroz, Slovenia, June 2000.

N. Sancisi and V. Parenti-Castelli. A 1-dof parallel spherical wrist for the modelling of the knee passive motion. In *Proceedings of IFToMM 2007*, pages 1 1–6, Paper no. A94, Besançon, France, June 2007.

W. H. Simon, S. Friedensberg, and S. Richardson. Joint congruence: a correlation of joint congruence and thikness of articular cartilage in dogs. *Journal of Bone and Joint Surgery*, 55:1614–1620, 1973.

D.M. Sirkett, G. Mullineux, G.E.B. Giddins, and A.W. Miles. A kinematic model of the wrist based on maximization of joint contact area. *Proceedings of the Institution of Mechanical Engineers, Part H: Journal of Engineering in Medicine*, 218(5):349 – 359, 2004.

D.R. Wilson and J.J. O'Connor. A three-dimensional geometric model of the knee for the study of joint forces in gate. *Gait and Posture*, 5:108–115, 1997.

D.R. Wilson, J.D. Feikes, A.B. Zavatsky, and J.J. O'Connor. The components of passive knee movement are coupled to flexion angle. *Journal of Biomechanics*, 33(4):465 – 473, 2000.

J. Wolff. *The Law of Bone Remodelling*. (translated into English by P. Maquet and R. Furlong), 1986.

Chapter V

Innovations in Sensor Systems for Robots and Perception

Development of the Ultrasound Probe Holding Robot WTA-1RII and an Automated Scanning Algorithm based on Ultrasound Image Feedback

Ryu Nakadate[1] Jorge Solis[2,3] Atsuo Takanishi[2,3] Motoaki Sugawara[4] Kiyomi Niki[5] and Eiichi Minagawa[6]

[1] Graduate School of Advanced Science and Engineering, Waseda University, Tokyo, Japan
[2] Faculty of Science and Engineering, Waseda University, Tokyo, Japan
[3] Humanoid Robotics Institute, Waseda University, Tokyo, Japan
[4] Department of Medical Engineering, Himeji Dokkyo University, Himeji, Japan
[5] Department of Biomedical Engineering, Tokyo City University, Tokyo, Japan
[6] Aloka Co., Ltd., Tokyo, Japan
E-mail: r-nakadate@takanishi.mech.waseda.ac.jp; solis@ieee.org; contact@takanishi.mech.waseda.ac.jp

Abstract. In this paper, we present our research on the development of an automated medical ultrasound scanning system for the carotid artery using probe a supporting manipulator (parallel link mechanism). In particular, we detail the mechanism design of the manipulator and a real-time image processing algorithms to detect the carotid artery and tissue layer of its walls (in the B-mode of ultrasound image). Several sequential patterns of ultra-sound probe trajectory were implemented in order to enable the manipulator to scan the surface of neck effectively. A set of experiments has been carried out to verify the effectiveness of the proposed system.

1 Introduction

The preventive medicine to detect arteriosclerosis and myocardial dysfunction is highly important as they are the main and increasing causes of death in the recent world. One of the non-invasive methods to evaluate the cardiovascular function is the measurement of Wave Intensity (WI) (Jones et al., 1994). This hemodynamic index is calculated by measuring the blood pressure and velocity, and has demonstrated to be effective in detecting cardiovascular changes. The WI is measured at the common carotid artery (CCA) using an ultrasound diagnostic system (Harada et al., 2000).

The practical problem in the WI measurement is related to the positioning of the ultrasound probe. Sonographers are required to hold the probe at the patient neck and obtain a clear image of longitudinal section of the CCA. The ultrasound probe should be exactly placed at the center of the artery in order to measure the change in the artery diameter by heart beat. It is a difficult task for sonographer because the allowable error of probe position is 0.5mm. A robot-assisted system for the probe positioning may solve this problem. There are many past researches on visual feedback control of medical ultrasound image (Abolmaesumi et al., 2002)(Krupa et al., 2007). Most of them are for tracking the image feature, however there are few researches on automated scanning and detection of any organ by means of the robotic system.

In this paper, we firstly present a development of ultrasound probe manipulator WTA-1RII (the Waseda-Tokyo Women's Medical-Aloka Blood Flow Measurement Robot System No. 1 Refined II) which is composed by master-slave robotic system for assuring a precise positioning of the probe. And then we will introduce an automated scanning algorithm by the feedback control based on the ultrasound image processing in real-time.

2 Development of the Probe Holding Robot WTA-1RII

The details of the probe holding robot WTA-1RII is shown in Figure 1. It contains 6-DOF parallel link manipulator which holds the ultrasound probe, 6-DOF serial link passive arm which holds whole manipulator, and a master controller. The serial link passive arm is used to locate the manipulator close to the neck. All passive joints of the serial link arm include magnetic brakes which are used to lock/unlock the joints controlled by foot switch. The magnetic brakes unlock the joints when power supply is turned on so that any possible risk of injury caused by a power shutdown is eliminated.

Before we designed the manipulator of the WTA-1RII, the serial and parallel link mechanisms were compared. Regarding the serial link mechanism case, the actuator close to the base link should have enough power to hold the weight of other parts of the manipulator, so that the overall weight tends to be large. On the contrary, in the parallel link mechanism case, all actuators can be located at the base. Although the workspace can not be so large, the diagnosis of the carotid artery does not require large workspace, whereas the accuracy of positioning is rather important. In fact, parallel mechanism has smaller workspace compared with serial link mechanism because of interference of each link, on the other hand, has higher precision because the position errors of each link are not accumulated but averaged.

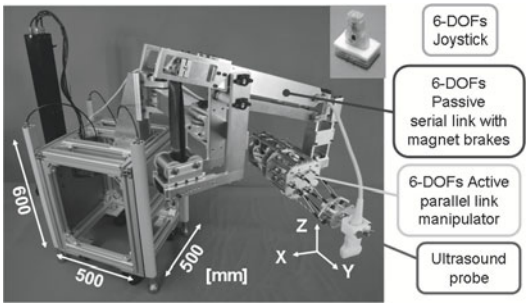

Figure 1. The Waseda-Tokyo Women's Medical-Aloka Blood Flow Measurement Robot System No.1 Refined II.

Therefore we have chosen the parallel link mechanism for manipulator.

Thus, the slave manipulator is composed by a linear type parallel link mechanism. The linear actuators are composed by DC servo motors and a ball screw. Each link is composed of 2 universal joints, 1 bearing and a rod. Each of those links has a total of 6-DOFs which are actuated by a linear actuator (1-DOF), two universal joints (4-DOFs) and a bearing (1-DOF). The cross section size of the slave manipulator is 100x120 mm, overall length is 340-400 mm, and weight is approximately 2.0 kg. The length of the rod is 70 mm, the movable angle of the universal joint is 45 degrees and the stroke of linear actuator is 60 mm.

Design parameters of the 6-DOFs parallel link manipulator are position of 6 link in base and end plates, and rod length. Initially we have designed the link position of our prototype WTA-1 by trial and error using simulator based on the point symmetrical design (Sadamitsu et al., 2006). In order to find the optimal link position which satisfies the required workspace, we have applied the Genetic Algorithm for the design of the WTA-1RII (Nakadate et al., 2009).

3 Automated Scanning Method

Even though the WTA-1RII can be used as master-slave robot by means of joystick type controller operated by sonographer, we have implemented full-automated positioning system by visual feedback of ultrasound image so that the sonographer can concentrate in the measurement itself rather than in the operation of the manipulator. The overall system is shown in Figure 2.

The principal requirement of the ultrasound image, in order to perform

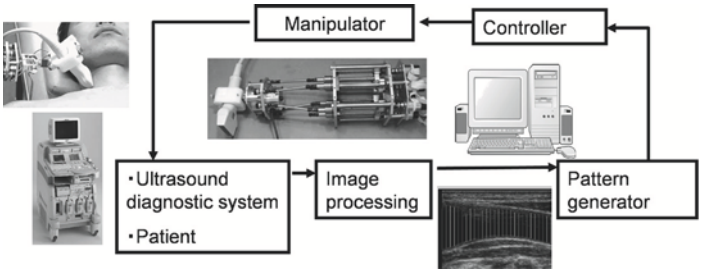

Figure 2. Block diagram of the proposed automated scanning system designed to automatically detect the carotid artery.

the WI measurement, is to obtain a clear longitudinal section of the CCA in which the intima can be observed. The intima is one of the tissue layers of the CCA walls, which can be observed as double white lines within the ultrasound image only when the probe is located exactly at the center of the vessel. Thus, this principle can be considered in order to confirm the correct positioning of the probe respect to the vessel.

Before starting automatic detection sequence, the manipulator should be placed by the operator approximately 10-20mm from the location of the CCA (the probe can either touch the surface of the neck or not).

3.1 Image processing

The algorithm to detect the CCA should be enough simple so that a real-time processing can be implemented. In particular, we have implemented the image processing based on the following two steps: detection of longitudinal section of CCA and detection of intima.

The first step consists of scanning vertical lines at a regular interval and dark zones are extracted by thresholding (vertical lines in Fig. 3a). Those extracted lines are connected each other in horizontal, and the group of the lines which has most smooth connection are chosen as CCA (transversal lines in Figure 3a). Secondly, the intima location is determined by computing the largest and second largest local maximum of the gradient observed near the detected CCA walls. In those 2 pixels, not all, but most of contour of intima (if appeared) is included. If intima is clearly shown in the image, those 2 pixels are defined by two smooth lines. If intima is not shown, those 2 pixels form one smooth line and scattered dots. Therefore, a threshold of length is applied for the continuity of the extracted pixels (Figure 3b). The number of the pixels of extracted intima is regarded as the Score. The

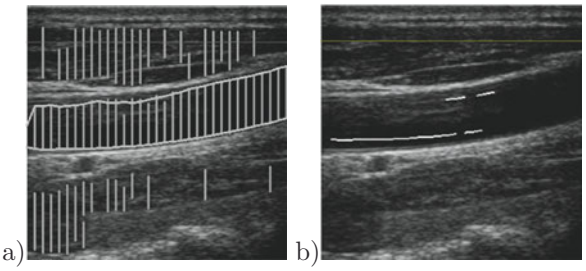

Figure 3. a) Extraction of the CCA.; b) Extraction of the intima.

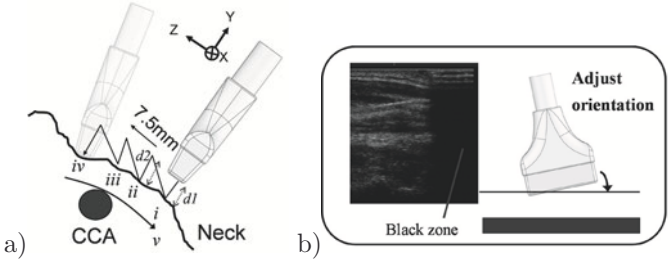

Figure 4. a) Scanning pattern to search the CCA.; b) Fitting the probe to the skin surface.

Score will drop periodically with movement of the vessel by heart beat. A sample holding filter is applied.

3.2 Probe Path Planning

In order to define the probe's trajectory, the following steps are done: detection of morphology of the patient's neck, scanning/detection CCA and finally the detection of intima. Regarding the detection of morphology of the patient's neck; at first, four points along the surface of the neck are defined at a regular interval of 7.5 mm (Figure 4a). This is done by detecting the contact of the probe with the neck surface, which is detected by calculating inter-frame differential of the ultrasound image. By comparing d1 and d2 in Fig. 4a, the probe angle against the skin around x axis can be determined. The manipulator adjusts the probe angle towards the normal vector of the skin. In order to obtain a clear ultrasound image, the probe should remain in contact with the subject's skin. If the vertical black zone is observed in the image, it means that there is a gap between probe and skin. Thus, the probe is rotated around z axis until the probe is effectively in contact with

the skin surface (Figure 4b). The six axes coordinates of those previously defined four points are linearly interpolated. The connecting lines between those four points represent the morphology of the patient's neck.

In the next step, scanning/detection of the CCA is performed. The manipulator scans the neck surface tracing those four points, and it will stop when the CCA is detected. In the case that the probe and the CCA are parallel, the clear longitudinal section of the CCA will appear in the image. Otherwise, if the probe and the CCA are not parallel, a partial image of the CCA (small black zone) is observed within the image. Therefore, any kind of black zones observed within the image are labeled and tracked, and if the length of a locus is more than a predetermined threshold, it will be regarded as the CCA. However; sometimes the internal jugular vein (IJV) is detected instead of the CCA as their appearance in the ultrasound image is quite similar. Here, the inner pressure of the IJV is lower than that of the CCA. After the detection of the vessel, the manipulator pushes the neck by the probe and the change in the diameter of the vessel is measured. If the diameter decreased, it will be defined as the IJV and the manipulator repeats the CCA searching sequence. Finally, the detection of the intima is done. The objective of this procedure is to locate the probe where the clearest image of the intima is observed. The observable length of intima (score) in the ultrasound image is measured by image processing. Here, the manipulator is programmed to scan within a small area (6mm forward and backward). During a forward scanning, the score of intima (number of pixels) is calculated and the maximum score is recoded. During the backward scanning, when the recorded maximum score is reproduced, the probe will stop.

4 Experiments and Results

4.1 Manipulator Positioning Accuracy

In order to verify the positioning accuracy of the parallel link manipulator, we have carried out an experiment using a phantom in which a needle is inserted. The needle appears in ultrasound image as bright dot. The operator tries to move this dot from the initial position to the target position (distance 5 mm) in the image by moving ultrasound probe by the manipulator using joystick controller, and by hand. After reached at the target position, the operator keeps the position on the target line for 30 seconds. During 30 seconds, the position error is recorded. The position of the needle in the image is automatically measured by image processing. The experiments have been carried out by 3 professional clinicians and 3 non-professionals for 3 times each. For each trial, maximum error during

the trial was recorded. The results are shown in Table 1. The average error of by hand is 0.27-0.29 mm while maximum error by manipulator is 0.06-0.07 mm. Comparing the clinicians group and the non-clinicians group, no significant difference of the average errors by hand has been observed. From the result of the experiment, it is observed that the manipulator can position the ultrasound probe with higher precision than by hand.

Table 1. Position error during the phantom positioning test.

	Error [mm]		
	max.	avg.	min.
Clinicians, by hand	0.36	0.29	0.21
Non-clinicians, by hand	0.77	0.27	0.10
Non-clinicians, by manipulator	0.10	0.07	0.05

4.2 Automated Scanning

The proposed automated scanning algorithm based on the WTA-1RII is implemented in the system shown in Figure 2. It is composed of the ultrasound diagnostic system (Pro Sound II SSD-6500SV commercialized by ALOKA Co., Ltd.), a PC, and a manipulator. By the ultra-sound diagnostic system, B-mode image (about 20 fps) is obtained and captured by PC (Pentium 4 3.2GHz) through NTSC format signal. The PC processes the ultrasound image in order to generate the target trajectory of the probe.

We have conducted an experiment with 11 healthy subjects (10 males and 1 female, age 20-30's) to verify the effectiveness of the proposed algorithms. Automatic scanning was tested 5 times for each subject. The subjects lay on the bed in supine posture. Then, the manipulator was at the position where the ultrasound probe is about 5mm above the neck surface by operator. After that, no human intervention was allowed. If the robot completed the whole sequences (detected the CCA, and obtained clear image of intima), the trial was counted as successful. The results are shown in Table 2. Among total of 55 trials, 50 trials (91%) have been successfully finished. The causes of failed trials are as follows: detected vein and could not find the CCA, the transversal dark zone other than vessel appeared in the ultrasound image.

Table 2. Experiment results of the automated scanning.

Succeeded	Failed	Total
50 (91%)	5 (9%)	55(100%)

5 Conclusion and Future Work

In this paper, we have presented the WTA-1RII, a robotic assisted ultrasound diagnostic system to measure the carotid blood flow. In particular mechanical design of parallel link manipulator was described. Moreover, an automated scanning method has been proposed to enable the WTA-1RII the searching and detection of the CCA and its tissue layers by using medical ultrasound. The positioning accuracy of the manipulator and the effectiveness of the proposed automated system were evaluated by clinical test.

As a future work, we will extend the usability of the proposed robotic system to measure other parts of the body. On the other hand, further improvements on the proposed algorithms will be proposed to enhance the effectiveness of the system.

Bibliography

P. Abolmaesumi, S. E. Salcudean, W.-H. Zhu, M. R. Sirouspour, and S. P. DiMaio. Image-guided control of a robot for medical ultrasound. *IEEE Transaction on Robotics and Automation*, 18(1):11–23, 2002.

A. Harada, T. Okada, M. Sugawara, and K. Niki. Development of a non-invasive real-time measurement system of wave intensity. pages 1517–1520, 2000.

C. J. H Jones, M. Sugawara, R. H. Davis, Y. Kondoh, K. Uchida, and K. H. Parker. Arterial wave intensity: physical meaning and physiological significance. In S. Hosoda, T. Yaginuma, M. Sugawara, M.G. Taylor, , and C.G. Caro (eds), editors, *Recent progress in cardiovascular mechanics*, pages 129–148. Hanvood Academic Publishers, Chur, Switzerland,, 1994.

A. Krupa, G. Fichtinger, and G. D. Hager. Full motion tracking in ultrasound using image speckle information and visual servoing. *Proceedings of 2007 IEEE International Conference on Robotics and Automation*, pages 2458–2464, 2007.

R. Nakadate, H. Uda, H. Hirano, J. Solis, A. Takanishi, E. Minagawa, M. Sugawara, and K. Niki. Development of assisted-robotic system designed to measure the wave intensity with an ultrasonic diagnostic device. *Proceedings of 2009 IEEE/RSJ International Conference on Intelligent Robots and Systems*, pages 510–515, 2009.

Y. Sadamitsu, A. Fujita, C. Arino, A. Takanishi, A. Harada, M. Sugawara, , and K. Niki. Development of a robotic carotid blood flow measurement system - a compact ultrasonic probe manipulator consisting of a parallel mechanism. *Proceedings of 2006 IEEE International Conference on Robotics, Automation, and Mechatronics*, pages 1–6, 2006.

RFID-Assisted Detection and Handling of Packages

Antonios Bouzakis, Ludger Overmeyer

Institute of Transport and Automation Technology, Leibniz Universität Hannover, Germany

Abstract. In the field of automated warehousing a method is described for product detection and handling with the aid of industrial robots and the radio frequency identification (RFID). While the detection of objects is of the essence, RFID labels (tag inlays) widely used in supply chain management for inventory tracking serve herein as beacons placed on predefined positions on the surface of product containers such as cardboard boxes, in such way as to describe sufficiently the geometry of the package, thus enabling its automated manipulation by an industrial robot. An arrangement of RFID systems fixed on the robot's end effector, serves as a sensor to detect and localize RFID tags fixed on the box surface.

1 Introduction

Automation of warehousing processes undergoes in the last years a vast increase. Shortly after arriving and entering the warehousing facilities, the incoming goods are recorded principally with the aid of RFID labels and the status of the warehouse inventory is updated. Subsequently products are transported on conveyors or with the aid of forklift trucks and treated by manipulators, such as depalletizers and other robotic arrangements. The objective is to alleviate as much as possible the human interference since the time of arrival until the time when the product has to leave the warehouse again; for which reason when products need be stored on shelves or diverted from one conveyor lane to another, robotic manipulators come into play.

The defining component of automated product handling, when no standard (de-)palletizers are used, is the detection of the volume and geometrical properties of the objects to be manipulated. To fulfill this purpose additional systems are required, to provide the necessary information for the collision-free handling of the goods (Scholz-Reiter et al., 2008). Apart from the nowadays dominant methods involving image processing and laser scanning which implicate costly algorithms in terms of time (Schmidt et al., 2005), a new approach is herein introduced with the aid of electronic marks on the packaging surface.

Our efforts focused on expanding the functionality of RFID labels from inventory tracking to precise localization, based on the major advantages of RFID

communication: high speed detection of the labels inside a limited space (interrogation zone), high speed data exchange and low-cost, easy-to-integrate electronics (Finkenzeller, 2003).

2 State of the art

Many papers have illustrated the use of RFID systems as sensors in robotic applications. An RFID-based robot navigation system with customized tag architecture is described by Suruz and Wail (2007). A mobile robot equipped with an RFID reader analyzes the signals' strength received from RFID tags located in its surroundings. Since the absolute position of the tags is stored in an onboard database, the robot position is calculated by the method of trilateration based on the acquired signals. Kämpke et al. (2008) described the integration of RFID labels in a 'smart floor' so that above passing robots can identify their position. Non-customized label transponders implanted in a floor at predefined locations reproducing a matrix of known positions on a 2 dimensional cartesian plane.

Baum et al. (2007) described a localization method of RFID tags for automated guided vehicle (AGV) applications. Tags are placed on the ground at pre- specified positions and the RFID system calculates the course offset, as the vehicle drives along a path above them.

3 Experimental Setup

This paper is focused on light logistic applications, where the maximum weight per transported package is limited to 30 Kg, an area in which a package includes light weighing goods, a small quantity of, or simply one product. Although package design is thought of as a special field of interest in the design of a new product, when big quantities are transported packaging falls under a more general category which includes drum containers, crates, wooden boxes, cardboard boxes, packaging films and palletizing. This paper is focused on standard cardboard box applications and product flow on conveyors after depalletizing.

The industrial robot KUKA KR-16 was selected as a manipulator to assist in the product handling and warehouse conditions were built around it. The roller conveyor type RC 27 (TRANSNORM) indicated for applications in the desired weight and size area was fixed next to the robot at a distance so that the end effector can sufficiently reach its upper surface. The three different box sizes 1, 2, 3 representing standard postal cardboard boxes with dimensions: 295 x 170 x 125, 355 x 300 x 150 and 495 x 325 x 205 respectively, were used to demonstrate the capability of the process to adapt to geometrical variety.

4 RFID Localization

The radio frequency identification is defined as the communication in form of data exchange between two radio wave modulating devices, which in the high frequency band is realized by means of inductive coupling. The one end is the reader module with its respective antenna and the other is the transponder or simply tag. Regarding passive tags, the change in current flow through the reader's antenna induces a voltage across the ends of the transponder's antenna. When the induced voltage surpasses the minimum amount needed, signal transmission is provoked. The two major factors that contribute to the amplitude of the induced voltage are the distance between the two coils and their relative orientation (Finkenzeller, 2003).

The distinction between detection and localization in such RFID applications is of the essence (Overmeyer et al. 2008). Normally the detection of tags within a finite region is sufficient and while antennas with bigger range can detect more remote tags they are commonly preferred. Since our objective was to interpret the event of a successful tag-reader communication as localization, it was rather chosen the use of antennas with relatively small extent of the interrogation zone, which eventually leads to a smaller space where the tag can be located in the event of detection. In this way, a small movement of the reader's antenna can reveal the position of the tag in space, thus interpreting detection as localization. Furthermore, a reader-tag antenna ratio close to 1/1 leads to a more uniform shape of the interrogation zone; note that typical label sizes do not exceed 70mm x70 mm.

The objective was to alleviate the orientation dependency and the interrogation zone inconsistency and at the same time to interpret the detection as localization. Therefore, a rectangular shaped antenna 40mm x 30mm was selected. An antenna array was created consisting of 9 antennas fixed on a plastic frame, each independently controlled by an ID CPR40.01-UCD (FEIG) reader. The re-created experimental setup along with the localization concept is illustrated in figure 1.

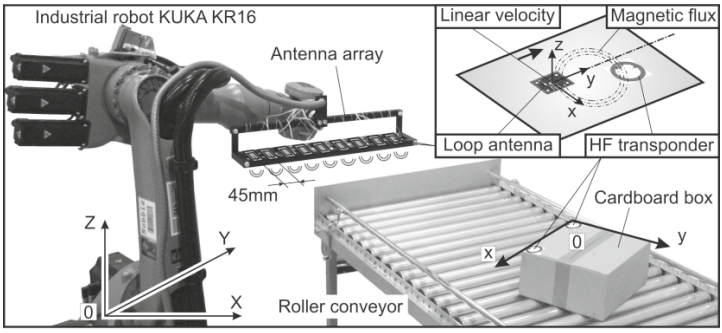

Figure 1. Experimental setup for RFID label localization.

The behavior of a single antenna was investigated, with the aid of 38 mm round shaped Mifare Classic 1K tags conforming to ISO 14443. The shape and uniformity of the interrogation zone were examined for the parallel reader-tag antenna alignment by means of scanning the space above tags fixed on cardboard and recording successful detections at the reader. A high uniformity is achieved for the investigated reader-tag antenna ratio with the shape resulting in a 3D ellipsoidal. A cross-section is illustrated in figure 2, where the range is clearly visible.

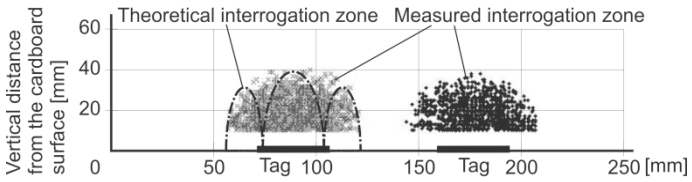

Figure 2. Antenna interrogation zone for 1/1 reader-tag antenna ratio.

It is clear that, while the antenna is linearly moving above the surface where the tag is located, the coordinate of the tag's center in the direction of scanning can be recorded, due to the symmetry of the interrogation zone. A subsequent scanning of a perpendicular direction provides 2D localization. The measurement deviation from the real position was examined relative to the linear scan velocity, to minimize localization time while maintaining high precision. The distance between the antenna array and the scanned surface was selected at 20 mm from the results depicted in figure 2. Ten measurements were conducted for each linear velocity starting from 0.1 m/s with a step of 0.01 m/s, scanning the surface of a cardboard box equipped with two transponders fixed at predefined positions. Since the principle of the measurement was the same, the four different coordinates serve as four different sets of data for the evaluation of the precision as illustrated in figure 3. The absolute consistency of the process in terms of successful detection is restricted by 0.43 m/s, above which at least one detection failure was observed.

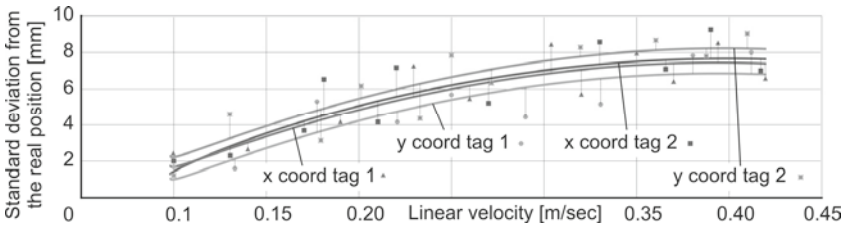

Figure 3. Precision versus velocity for the scanning process.

5 Package localization and handling

5.1 Selection of the Gripper

For the handling of the packages a gripping system operating under the vacuum principle has been assembled, since it provides the lightest option and it is less likely to cause damage to the boxes. Furthermore, the suction cup arrangement was assembled in such way as to coexist simultaneously with the 2D tracking system, without any additional complex mechanisms to separate them during the tracking and the gripping process. Fixed on an aluminum frame 8 suction cups are aligned in two rows at specific distances, so that the efficient handling of all box sizes is permitted. The whole construction weighs 5 Kg thus enabling the handling of additional 11 Kg. Each suction cup has a maximum lifting load of 33 N and in this way 4 cups can lift up to 132 N which lies safely above 110 N.

The tracking system is directly fixed underneath the gripper, with solely the possibility of a relative translational motion vertical to the direction of the suction cup shriveling as illustrated in figure 4. In this way the antenna array is suspended from the gripper 5 mm lower than the edge of the suction cups and when a package is gripped it simply shifts 15 mm higher to compensate the shriveling.

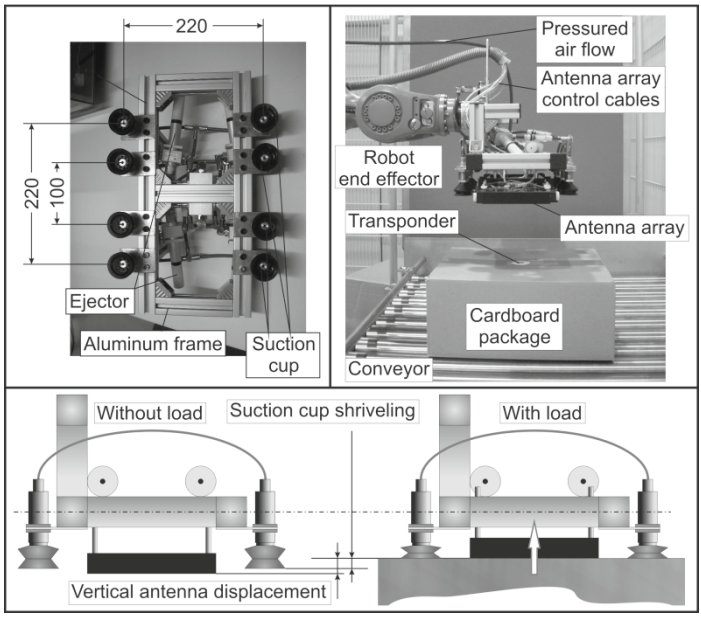

Figure 4. Gripping system with integrated 2D RFID tracking system.

5.2 Handling Process

The gripping system is operating under the vacuum principle reaching a package from above. Therefore, the upper surface needs to be defined in terms of position and orientation in space. Since the objects to be manipulated have cubic geometries their upper surfaces will always be parallel to the conveyor-ground. In this way 2 of the 6 degrees of freedom are known in advance, thereby leaving 4 more to be defined: Three coordinates of a reference point and the rotation around the z axis. A vector passing through the center of symmetry of the surface can serve this cause. Furthermore, if the middle points of two opposite sides are selected this rotation needs only to be defined within the first two quadrants of a 2D cartesian coordinate system. This leads to the definition of a senseless vector with its middle point coinciding with the surface's center of symmetry.

Though the 2D tracking ability is integrated in the gripper, the 3rd coordinate of the tags, in other words the height for the scanning process, will be acquired through the RFID communication. An ISO 15963 tag commonly used for inventory tracking can communicate at bigger distances with a respective antenna, but relatively slower compared to the ISO 14443 (Baum, 2009). The dimensions of each package, as well as the weight, the type of the content and the alignment of the ISO 14443 transponders on the cardboard surface (along the length or along the width) are stored in the memory of an ISO 15963 tag. Upon identification this data is collected and correlated with the data stored in the inventory database and become available to the process as illustrated in figure 5. When reaching the robot's close proximity the boxes are stopped with the aid of laser barrier that provides the robot enough time to scan and grab them. While time is of the essence the use of the barrier remains a disadvantage of the process.

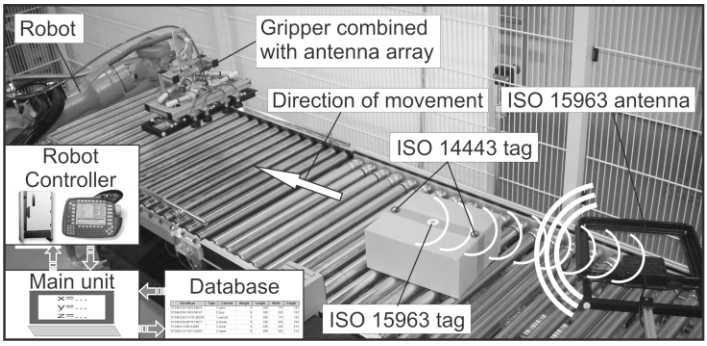

Figure 5. RFID localization for package handling.

It is a matter of detection and distribution of information. Geometrical properties of the packages along with properties regarding the content are transferred to the main control unit upon package identification and become verified by the data stored in the inventory database. Making use of the package height, the upper surface is scanned for the localization of the two marks and subsequently the 4 degrees of freedom in combination with the alignment of the tags on the surface are diverted to the control unit to enable a successful grabbing. Afterwards, the handling conditions are regulated by the weight of the content and a factor defining if the content is orientation-sensitive. Finally, the packages are stored on racks with the aid of the rest of their geometrical properties. The process is illustrated in figure 6.

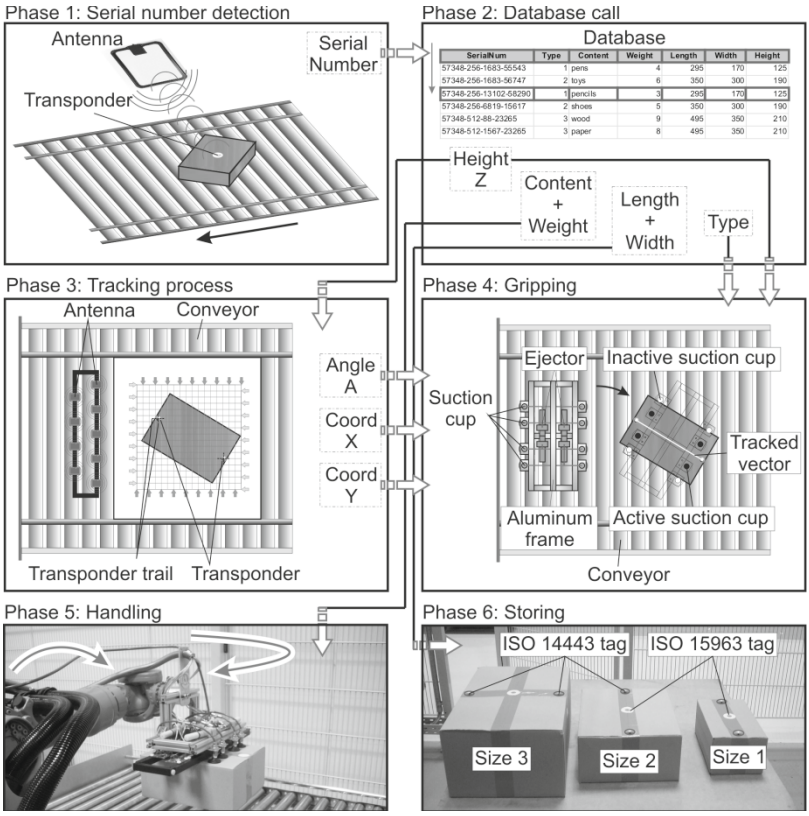

Figure 6. RFID-Assisted detection and handling of packages.

6 Conclusions

The demonstrated process for package detection and handling denotes a new method that can lead to new trends in automated manipulation of transported goods. While its integration can be a tough task, it can assist in real time tracking of products, with the aspect of minimizing time consumption of warehousing processes. Future objective is to achieve on the fly localization and manipulation of packages without the need to pause the product flow. Warehousing can be vastly accelerated with such applications in terms of inventory tracking, through the possibility of real time creation of inventory databases while the products are still being manipulated. Furthermore, a new horizon is opened for intelligent manipulators that can realize fully automated handling processes without human interference by means of RFID.

References

Baum, M., Niemann, B., Overmeyer, L., 2007. Passive 13.56 MHz RFID Transponders for Vehicle Navigation and Lane Guidance. Proceedings of the 1st International EURASIP Workshop on RFID Technology, S. 83-86. Wien, Österreich, 2007. – ISBN 978-3-902477-10-1

Baum, M., 2009. Transpondergestützte Fahrzeugleitsysteme. Dissertation, Berichte aus dem ITA Band 01/2009, Ed.; Overmeyer, L.

Finkenzeller, K., 2003. RFID-Handbook - Fundamentals and Applications in Contactless Smart Cards and Identification, 2nd edition, Wiley & Sons, 2003.

Kämpke, T., Kluge, B., Erwin Prassler, E., Strobel, M., 2008. Robot Position Estimation on a RFID-Tagged Smart Floor. Field and Service Robotics, Volume 42/ 2008, Springer Berlin Heidelberg. ISBN 978-3-540-75403-9

Md. Suruz, M., Wail, G., 2007. An RFID-Based Robot Navigation System with a Customized RFID Tag Architecture, Proceedings of the IEEE International Conference on Microelectronics, Cairo, Egypt, December 29-31 2007.

Overmeyer, L., Jungk, A., Eds.; Pfohl, H.C., Wimmer, T., 2008. Bewertung der Übertragungssicherheit von RFID-Systemen am Beispiel eines Flurförderzeuges. Wissenschaft und Praxis im Dialog; Robuste und sichere Logistiksysteme. Hamburg: Deutscher Verkehrs-Verlag, 2008. – ISBN 978-3-87154-381-4

Schmidt, T., Wohlfahrt, A., ten Hompel, M., 2005. Greifertechnologie im Materialfluss, Hebezeuge und Fördermittel, 2005. März, 2005, 45. Jahrgang, S. 82-85

Scholz-Reiter, B., Kirchheim, A., Burwinkel, M., Echelmeyer, W., Rhode, M., Schmidt, K., 2008. Automatische Entladung von Stückgütern durch ein kognitives Robotersystem. Industrie Management 24 (2008) 4.

Virtual Haptic Map Using Haptic Display Technology for Visually Impaired

Tsuneo Yoshikawa*, Takayuki Satoi* and Masanao Koeda†

* Department of Human and Computer Intelligence, Ritsumeikan University, Noji Higashi 1-1-1 Kusatsu, Shiga, 525-8577, JAPAN.

† Department of Computer Science, Osaka Electro-Communication University, Kiyotaki 1130-70, Shijyounawate, Osaka, 575-0063, JAPAN.

Abstract We propose a new virtual haptic map system for visually impaired persons that uses a force display device and a GPS receiver. This system can haptically display the roads, city blocks, and buildings which are automatically constructed from a numerical map in DXF format and the information of current location from a GPS receiver. To evaluate the usability of this system, recognition experiments using several simple maps were conducted by ten blindfolded subjects. In the experiments, recognition rates were compared between two representation methods of roads: concaved roads and convexed roads. As a result, high recognition rates were confirmed in both methods, and it shows that this system has reasonable usability. We have also developed a mobile robot system with our virtual haptic map system which is aimed to be a guide dog robot with the ability of providing near-by haptic maps. A preliminary experiment is conducted to examine the validity of this mobile robot system.

1 Introduction

Tactual maps that are fixed to the environment is the most common means for supporting visually impaired persons to recognize and walk around the current location. However, current tactual maps are difficult to change their contents quickly(1). Hence it is desirable to develop new tactile display devices which are easy to change the content.

One such direction is tactor-pin type display devices(2)-(4). Although they can change the content of display quickly, the display resolution is limited by the size of pins.

Another direction is to use haptic display devices developed in the field of haptic virtual reality technology(5). Haptic virtual reality technology has

various advantages compared to tactor pin devices. For example, it is much easier to construct virtual objects or spaces of various types and to combine with other modalities such as audio channel.

Two-dimensional map based on force feedback and vibration was developed by Colledge et al.(6), Feintuch et al.(7). These systems create haptic-aural virtual environments for way-finding by children with congenital blindness. Murai et al.(8) developed "Haptic Walk-Guide Simulator" which gives a simulator training of an indoor pathway finding. There are also researches about a framework of map image analysis and presentation of the semantic information to blind users using alternative modalities(9). However, these systems are mainly for displaying static information and display of dynamically changing information was not discussed.

On the other hand, there are various researches about guide-dog robot(10) and guide robot for walking outdoor(11). These robots, however, can only navigate the user to a specified destination. Therefore, it is difficult to walk in unknown area.

In this paper, we propose a dynamic haptic map using a force display device. We call this system as "Virtual Haptic Map". This system can haptically display the roads, city blocks, and buildings which are automatically constructed from a numerical map and the information on present location from a GPS receiver. Hence this system will be especially useful for supporting outdoor activities of visually impaired persons. This system can create maps by various representation methods. We compare two representation methods experimentally: One method is to make the road area concaved and the other is to make it convexed. We also conducted some experiments to evaluate the usability of this system. As an application of this haptic map, we have developed a mobile robot system with our virtual haptic map system which is aimed to be a guide dog robot with the ability of providing a haptic map of the near-by area in accordance with the need of the user. A preliminary experiment is conducted to show the validity of this mobile robot system.

2 Virtual Haptic Map

The Virtual Haptic Map system consists of a haptic device (SensAble Technologies, PHANToM OMNI), a laptop PC (Dell, Precision M6300) and a GPS receiver (GARMIN, eTrex Vista) as shown in Fig.1.

The system creates a virtual space which includes roads, city blocks and buildings in the area around the present location and it is automatically generated by OpenGL from a numerical map in DXF format and the GPS receiver output. The DXF format is a standard format used in CAD (Com-

Figure 1. Overview of Virtual Haptic Map

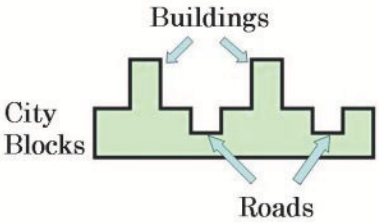

Figure 2. Representation of Virtual Haptic Map

puter Aided Design) and it holds vector data of two dimensional or three dimensional figures. This numerical map is produced by NTT-Neo-Mate, a Japanese company.

Haptic roads, city blocks and buildings shown in Fig.2 are constructed in the three-dimensional space paralleled to the horizontal plane between the user and the haptic device. The Virtual Haptic Map feeds back reaction force to the user by touching the map.

The features of this Virtual Haptic Map system are that various rendering characteristics such as concave-convex shapes or friction of surfaces is easy to change depending on the user's requirement. Hence the user will be able to walk in unknown area, recognizing around the present location by carrying the Virtual Haptic Map.

The software functions of the Virtual Haptic Map include the following.

(a) Displaying map in centering around the present location: In this system, longitude, latitude and direction of movement are acquired from the GPS receiver once a second and the map is constructed in centering around the present location.

(b) Checking present location: In the function of checking present location, the expanding factor is kept a constant value. When the blue button of the stylus is pushed, the user can feel a pulling sensation to the present location on the map.

(c) Scaling in centering around the present location: Scaling function is keeping viewpoint fixed and zooming in the map. User can zoom in five steps (2, 5, 10, 20, 30 times) by pushing blue button that is attached to the PHANToM OMNI's stylus.

(d) Support by Auditory Channel: Speech output is useful in supplying detailed information. For, example, "Zoom in" is announced in the scaling

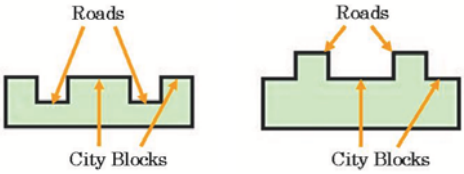

(a)Method A (b)Method B

Figure 3. Two representation method

Figure 4. Test overview

Figure 5. Eight maps in the experiment

function and "Here is the present location" is announced in the function of checking present location.

3 EXPERIMENT

In conventional tactual maps, objects are generally constructed by convex shapes. However, it is not clear if their representation method is good for every users. As the first step, we conducted experiments to compare the concave and convex representations of the roads (Fig.3).

Fig.4 shows the overview of this experiment. The subjects were ten sighted persons (eight males and two females) aged 21-24. The subject was wearing an eye mask and blindfolded. A randomly-selected map from the eight maps shown in Fig.5 was displayed to the subject. The size of the map is 120x120mm, the width of road is 3mm, the height of city block is 6mm. One trial takes two minutes and each subject was asked to do eight trials in each representation method. After each experiment, the following question was asked to the subjects showing eight maps.
(Q-a). "Which maps did you touch among these eight maps?"

Then after finishing all experiments, the following question was asked to the subjects.
(Q-b). "Which representation method did you feel easy to recognize roads or shape of map?"

Table 1. Result of experiment

[Note] SN: Subject Number, NT: Number of Trial, RR: Recognition Rate(%)

SN	NT	1	2	3	4	5	6	7	8	9	10	11	12	13	14	15	16	RR
A	Map Number	b	f	d	e	g	a	c	h	d	g	c	b	f	e	a	h	
	Map Recognition	○	○	○	○	○	×	○	○	○	○	○	○	○	○	○	○	91.7
B	Map Number	c	f	a	g	d	e	h	b	c	e	a	g	b	f	d	h	
	Map Recognition	○	○	○	×	○	○	○	○	○	○	○	○	○	○	○	○	91.7
C	Map Number	g	h	a	c	d	b	f	e	d	h	g	c	b	f	e	a	
	Map Recognition	○	○	○	○	○	○	○	○	○	○	○	○	○	○	○	○	100
D	Map Number	d	g	b	h	c	e	f	a	e	f	b	a	c	h	d	g	
	Map Recognition	○	○	○	○	○	○	○	○	○	○	○	○	○	○	○	○	100
E	Map Number	b	a	d	e	f	h	g	c	b	g	c	e	d	h	f	a	
	Map Recognition	○	○	○	○	○	○	○	○	○	○	○	○	○	○	○	○	100
F	Map Number	g	b	d	a	h	c	f	e	a	f	h	c	d	b	e	g	
	Map Recognition	×	×	×	○	○	○	○	○	○	○	○	○	○	○	○	○	75
G	Map Number	h	d	b	g	a	e	c	f	a	f	e	b	d	g	c	h	
	Map Recognition	○	○	○	○	○	○	○	○	○	○	×	○	○	○	○	○	91.7
H	Map Number	e	h	a	b	c	d	g	f	h	c	g	e	d	a	b	f	
	Map Recognition	×	○	○	○	○	○	○	×	○	×	○	○	○	○	○	○	75
I	Map Number	c	h	g	b	f	e	d	a	h	a	f	d	e	g	b	c	
	Map Recognition	○	○	○	○	○	○	○	○	○	○	○	○	○	×	○	○	91.7
J	Map Number	h	b	f	a	d	e	g	c	f	b	g	a	c	e	d	h	
	Map Recognition	○	○	○	○	○	○	○	○	○	○	○	○	○	○	○	○	100

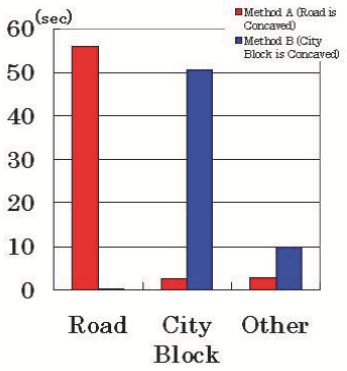

Figure 6. Contact time of each part of the Virtual Haptic Map

To accustom subjects to the system, the experiment was conducted after practice for two minutes. To reduce the effect of order, five subjects(A-E) conducted in the order of method A first and then method B. The other five subjects (F-J) conducted in the order of method B first and then method A. To investigate the difference of usability between two representation methods, time in contact with each part (road, city block, other) was measured.

Table 1 shows the result of experiment. Map number means the kind of displayed map in each trial. ◯ or × means whether the subject answered correctly or not to each question.

From Table 1 we can see that the recognition rate (the percentage of correct answers among all tests) is 93.8% for both representation methods A and B, showing that this system has reasonable usability. We also conducted preliminary experiments about recognizing buildings as shown in Fig.2, we obtained similar result to this experiment.

As for question (Q-b), all subjects felt easy to recognize roads in method A (concave representation method) and all subjects felt easy to recognize shape of maps in method B (concave representation method). Fig.6 shows times in contact with each part in experiment. In both methods A and B, subjects touched concave parts for a long time and didn't touch convex parts so much. From these results, we believe that the information represented by concave area will perform a crucial function for usability.

4 Mobile Robot System with Virtual Haptic Map

We have developed a mobile robot with our virtual haptic map system on it (Fig.7) which is aimed to be a guide dog robot with the ability of providing

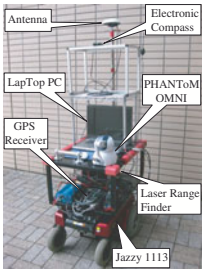

Figure 7. Mobile robot system with virtual haptic map

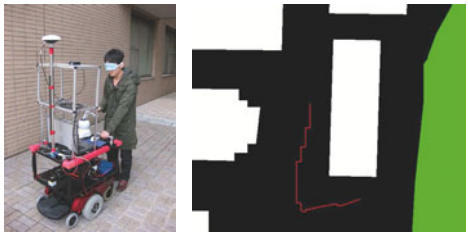

(a) (b)

Figure 8. Experiment: (a) Scene of experiment, (b) Trajectory of robot

near-by haptic maps. The mobile robot consists of a wheeled platform (Pride, Jazzy1113), a GPS receiver (GARMIN, eTrex Vista), an electronic compass, a lazer range finder, and a laptop PC (Dell, Precision M6300). In this system, the user can recognize the present location by Virtual Haptic Map and specifiy an intermediate point or a destination in the map, and the mobile robot moves to the point and waits for another command.

We conducted an outdoor experiment. Fig.8(a) shows a scene of experiment where a blindfolded subject is operating the robot. The mobile robot was ordered to go through the first destination from the start point and then to go to the final destination. A trajectory of the robot acquired from the GPS receiver is shown by red line in Fig.8(b). By this preliminary experiment it has been shown that the robot can be useful for outdoor activity of visually impaired persons.

5 CONCLUSION

We have proposed the Virtual Haptic Map. This system can haptically display the roads, city blocks, and buildings which are automatically constructed from a numerical map given in DXF format and the information on present location and orientation from a GPS receiver. This system aims to give map information to visually impaired persons for supporting outdoor activities. The usability of this system has been shown by experiments using simple virtual haptic maps by ten blindfolded subjects.

We have also developed a mobile robot with our virtual haptic map system. This system is expected to be a useful guide dog robot with the ability of providing local map information. A preliminary experiment was conducted to show the validity of this mobile robot system.

Bibliography

[1] M.G. Kwok, "Guideline for Tactile Figures and Maps", Guidelines On Tactile and Haptic Interactions(GOTHI'05), pp.43-47, 2005.

[2] S. Shimada, M. Shinohara, Y. Shimizu, and M. Shimojo, "An approach for direct manipulation by tactile modality for blind computer users:Development of the second trial production", In Proc. 10th International Conference on Computers Helping People with Special Needs (ICCHP2006), pp.1039-1046, 2006.

[3] R. Velazquez, E.E. Pissaloux, M. Wiertlewski, "A compact tactile display for the blind with shape memory alloys", IEEE International Conference on Robotics and Automation 2006 (ICRA2006), pp.3905-3910, 2006.

[4] G. Petit, A. Dufresne, V. Levesque, V. Hayward, N. Trudeau, "Refreshable Tactile Graphics Applied to Schoolbook Illustrations for Students with Visual Impairment", Proc. 10th International ACM SIGACCESS Conference on Computers and accessibility (ASSETS 2008), pp. 89-96, 2008.

[5] T. Yoshikawa and K. Yoshimoto, "Haptic Simulation of Assembly Operation in Virtual Environment," Proceedings of the ASME, Dynamic Systems and Control Division–2000, pp.1191–1198, 2000 (Orlando, FL, USA).

[6] R.G. Colledge, M. Rice, R.D. Jacobson, "A Commentary on the Use of Touch for Accessing On-Screen Spatial Representations: The Process of Experiencing Haptic Maps and Graphics", The Professional Geographer, vol.57, issue3, pp.339-349, 2005.

[7] U. Feintuch, J. Haj, and P.L.(Tamar) Weiss, "Low-cost haptic-aural virtual environments for way-finding by children with congenital blindness: feasibility study", 2006 International Workshop on Virtual Rehabilitation, pp.78-81, 2006.

[8] Y. Murai, H. Tatsumi, and M. Miyakawa, "A Haptic Walk-Guide Simulator for the Visually Impaired -A Prototype-", IEEE International Conference on Systems, Man and Cybernetics 2007, pp.3731-3736, 2007.

[9] K. Moustakas, G. Nikolakis, K. Kostopoulos, D. Tzovaras, M.G. Strintzis, "Haptic Rendering of Visual Data for the Visually Impaired", Multimedia IEEE vol.14, pp.62-72, 2007.

[10] S. Tachi, K. Komoriya, "GUIDE DOG ROBOT", The Second International Symposium of The Robotics Research, pp.333-340, 1985.

[11] S. Yafang, S. Kotani, H. Mori, "A pre-journey system of the Robotic Travel Aid", IEEE International Conference on Robotics and Automation, 2002.

EXTRACTION OF SEMANTIC INFORMATION FROM THE 3D LASER RANGE FINDER

Michal Gnatowski[‡] and Barbara Siemiątkowska[‡] and Jacek Szklarski[‡]

[‡] Institute of Fundamental Technological Research, Polish Academy of Sciences, Warsaw, Poland

Abstract In this paper a system for extracting semantic information in indoor and outdoor environment from 3D laser scanner is presented. The largest objects (like walls, floor, ceiling, etc.) are recognized by constructing an RGB image based on normal vectors and applying a simple rule-based system. More sophisticated techniques are used to detect the remaining ones: Haar-like features – to classify small and irregular objects, and Cellular Neural Networks – to distinguish between different types of ground on which the robot is able to operate.

1 Introduction

Classical navigation system consists of the following parts: mapping, localization and collision-free path-planning. A comprehensive overview of the existing navigation techniques can be found in (Thrun et al., 2005). Many environment representations have been proposed. One of the most popular is 2D representation (Elfes, 1987; Thrun et al., 2005) which has many limitations, for example the height of obstacles is not taken into account. In the last decade 3D sensors are being more popular which makes possible 3D map building. The following representations are used most often:

- point clouds (Triebel et al., 2006), (Vosselman et al., 2004)
- grid-based representation (Sakas and Hartig, 1992), (Siemiątkowska et al., 2007), (Gnatowski et al., 2008) which can be divided into: elevation maps (standard or extended) and multi-level surface maps.

In case of human-robot interaction the map has to contain not only metric but also semantic information (Rusu et al., 2008; Mozos et al., 2007). The main goal of our current project is to build a semantic map of unknown environment based on data obtained from a 3D laser scanner. In this paper we presented that semantic information can be extracted from

the data obtained by a laser range sensor. This extraction is performed by a combination of image analysis techniques and background knowledge.

2 Data Acquisition

The experiments have been done on a mobile robot equipped with a head module comprising a 3-dimensional scanning laser rangefinder used for navigation and creating 3-dimensional representation of the environment. The module consists of a SICK LMS 200 scanning laser rangefinder installed on a rotating support, which can rotate the scanner around the horizontal axis within the angular range from -15 to +90. The scanning laser enables to measure the distance to the obstacle within 180 with resolution of 0.5. The data is subsequently transmitted to the control unit by means of an RS 422 bus. The module is powered by a DC planetary gear motor. The power is then transferred by means of a toothed belt transmission. Two rotational encoders measure the scanning velocity and angle. The first encoder installed on the motor shaft is used for regulating the position whereas the other is responsible for measuring the rotation angle directly on the rotation axis of the scanner. The two measuring systems allow precise steering and positioning of the sensor. The unit controlling the head enables both continuous as well as step-by-step modes of the head. PID control algorithms were used for positioning and controlling the drive unit. Communication with the main control unit is achieved by means of an RS 422 bus. Figure 1 (left) presents pure data obtained from the described device.

3 Texture-based object detection

In our approach polar coordinates obtained from the laser range finder are transformed into Cartesian coordinates and then they are represented as a set of normal vectors n. A color RGB image is constructed by assigning values of the coordinates n_x, n_y, n_z as colors red, green and blue accordingly. The normal vectors give very important information about surfaces which are observed - when two points belong to the same plane the normal vectors computed in this points are equal. This allows us to perform segmentation of data obtained from the laser range finder in office-like environment. The purpose of the first step is to perform a fast segmentation of the gathered data into areas, each one representing a flat polygon in the real scene. The most important areas are, of course, ceiling, floor, walls, doors, etc. Besides the list of polygons, some numbers characterizing physical properties of a polygon can be extracted as well, which can be used later for better object classification. Simple rule-based system allows to classify the surfaces like:

walls, ceiling, floors, doors, etc.(Siemiątkowska et al., 2009). The ramaing objects have to be classified using different methods. We performed the classification based on Haar-like features, which is described in the next section. Figure 1 presents the point cloud obtained from the laser range finder in the corridor and the result of classification. Gray area represents walls, dark blue - the floor and bright blue - the ceiling. The yellow area represents objects which are not classified.

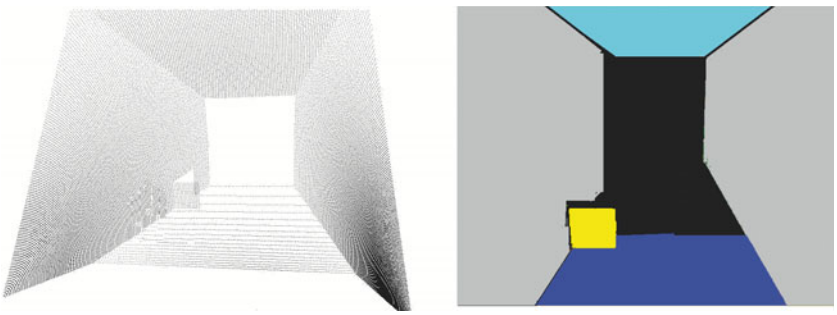

Figure 1. *Left:* Point cloud; *Right:* Detected walls, the ceiling and the floor. Yellow area represents unrecognized objects.

We performed the similar experiments in outdoor environment (Figure 2). We classify the ground into three classes: flat surface (pavement), grass and obstacles. The ground is recognized based on metric information and Cartesian coordinates, but in order to distinguished pavement from the grass the Cellular Neural Network (CNN) is used.

4 Haar-like features

Detecting regular and large areas like floor or ceiling in indoor environment in the way described above is a fairly easy task. However, for more complex objects the approach for the detection process should be different. Treating laser scanner data as an image makes it possible to apply well known methods for recognition from image analysis. Here we propose a simple classifier based on Haar features and rules related to geometrical features of objects. Algorithms which are applied here are available in OpenCV library and they implement methods proposed by (Viola and Michael, 2001) for basic set of Haar-like features and by (Lienhart and Maydt, 2002) for rotated features which enhance the basic set. Similar work, however, based on reflectance images and depth images has been proposed by, e.g., (Nüchter et al., 2005,

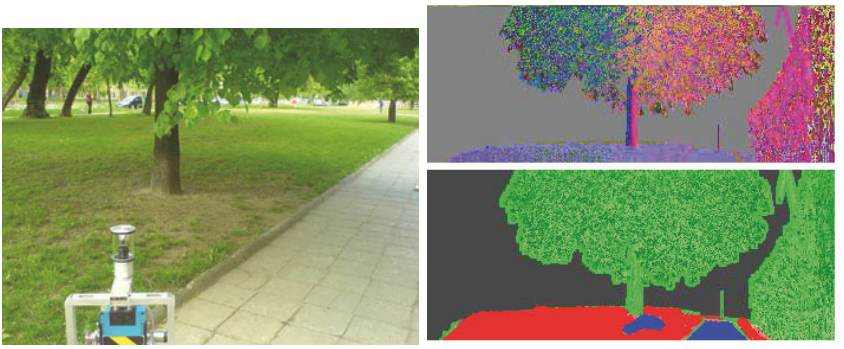

Figure 2. *Left:* The scene where the experiment was performed; *Right upper:* Normal vectors on RGB image; *Right lower:* Recognized objects: grass(red), pavement(blue) and unrecognized (green);

2004).

In the first step we define set of classes $\mathcal{C}$ of objects, like stairs, windows, doors, wastebaskets, and any objects which a mobile robot should be able to recognize. Then for each class a specific Haar-like classifier is created. This is done by training the classifier with use of a large set of positive and negative sample images representing objects for the given class and part of background respectively. All of the images should be scaled to the same size, we use 20x20. As the set of negative examples we use large number of arbitrary images representing a scene without any object from the class of interest.

The first stage of the classification process is to search an image constructed from laser data for objects belonging to any class $\mathcal{C}$. The classifier can be applied to any region of an image giving *true* if the region is likely to contain pattern similar to one of those from the positive samples set, *false* otherwise. Analysis is very fast so one can try many different regions with varied sizes from all parts of the image. By doing this in a loop one can search entire image for any object belonging to any class from set $\mathcal{C}$. Figure 3 shows a result of such analysis when searching with classifier trained for detection of a wastebasket.

In the next step false-positives are removed. This is done under assumption that any object from class $\mathcal{C}$ represents a ,,continuous structure" in the real space 3D. First, a gray-scale image representing distance to obstacles is divided into N areas A_i. A flood fill algorithm is run on the image representing distance with pixel (0,0) as the seed point. The threshold for the

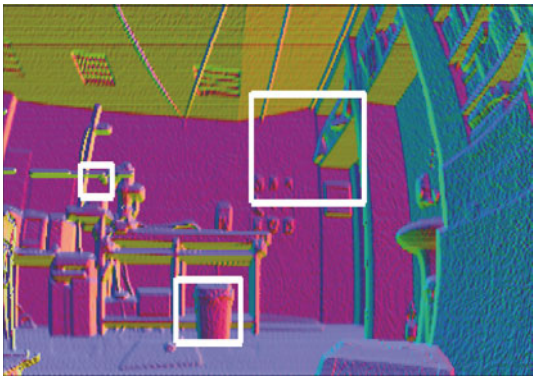

Figure 3. An RGB image constructed from laser measurements. White rectangles represent results of a Haar classifier trained for detection objects like a wastebasket. Note, that besides the wastebasket, there are two recognized regions which clearly should not be labeled as ,,wastebasket" (false-positives).

algorithm is constant and it corresponds to about 5 cm (difference between neighbor pixels is considered when flooding). If the resulting area is large enough, i.e., has total size grater than 15 pixels is marked with number 1 and then the same procedure is applied for a next pixel which has not been assigned to the area. In this way we obtain area number 2, and the procedure is repeated until all the pixels are assigned to one of the n areas. All areas which are to small to be classified are marked with number 0 and are not considered in any later stage of the process.

In order to check if any area H_i detected by the Haar classifier represents indeed a ,,continuous" object, it is checked if there exists i, so that $(A_\mathrm{H} \cap A_i)/A_i > 0.9$, where $A_\mathrm{H} \cap A_i$ is size of the common area between area detected by the classifier and the area A_i. In other words there should exist a continuous area A_i which covers most of the region recognized by the Haar-classifier (and A_i can not be much larger than this region). In this way all false-positives are rejected. Figure 4 shows 30 largest areas A_i together with rectangle which denotes the region recognized by the Haar classifier.

Naturally, each pixel of an image constructed from laser measurements corresponds to a 3D point from the associated point cloud. Therefore immediately there is available information about real size of any considered area A_i. For example, for the area labeled with white rectangle from Fig. 4

Figure 4. Areas A_i resembling continuous objects in real space (for each area, the real distance between neighbouring pixels is smaller than 5cm). The white rectangle denotes the region which has been recognized by the Haar classifier as a wastebasket.

all points can be placed into a box with size 27cm x 12cm x 31cm (width, depth, height). This information serves as an input for another rule-based classification scheme which filters out potentially bad recognized objects. For example, for the wastebasket we assume that its height must be between 20cm and 60cm and width between 20cm and 40cm.

5 Conclusions

In the article we discussed methods of extracting semantic information from 3D laser range finder. In contrary to visual cameras, using such 3D scanners gives data which are independent of lightening. Moreover, there is geometrical information available which can be used in the rule-based classification procedure. The goal of the research is to give the mobile robot an ability to recognise objects of certain classes. This will make possible to give commands like, *"Go to the* ***kitchen*** *and bring* ***a bottle of milk*** *from the* ***refrigerator****"*.

In order to make use of some classical approaches from computer vision, we construct RGB images based on vectors normal to surface at each point provided by the range finder. These images are then used in a simple rule-based classification system, detection process based on Haar-like features, and Cellular Neural Networks which distinguish between different types of ground. Experiments indoor as well as outdoor were performed and the

Figure 5. Another example of recognition using Haar-like features and geometrical information. Here the recognized areas are marked as ,,stairs" (for creating the image from normal vectors to RGB, absolute values $|\vec{n}_x|, |\vec{n}_y|, |\vec{n}_z|$ instead of $\vec{n}_x, \vec{n}_y, \vec{n}_z$ were used).

results are promising. In the future we will enlarge the list of identified objects.

6 Acknowledgment

This work was supported by the Polish Ministry of Science and Higher Education (grant 4311/B/T02/2007/33)

Bibliography

A. Elfes. Sonar-based real-world mapping and navigation. *IEEE Transactions on Robotics and Automation*, pages 249–265, 1987.

M. Gnatowski, B. Siemiątkowska, and R. Chojecki. Cellular neural networks in 3d laser data segmentation. In *9th WSEAS International Conference on NEURAL NETWORKS*, pages 84–88, 2008.

R. Lienhart and J. Maydt. An extended set of haar-like features for rapid object detection. *IEEE ICIP 2002*, 1:900–903, 2002.

O. M. Mozos, R. Triebel, P. Jensfelt, A. Rottman, and W. Burgard. Supervised semantic labeling of places using information extracted from sensor data. *Internationl Journal of Advanced Robotics Systems*, 2007.

Andreas Nüchter, Hartmut Surmann, and Joachim Hertzberg. Automatic classification of objects in 3d laser range scans. In *In Proc. 8th Conf. on Intelligent Autonomous Systems*, pages 963–970. IOS Press, 2004.

Andreas Nüchter, Kai Lingemann, Joachim Hertzberg, and Hartmut Surmann. Accurate object localization in 3d laser range scans. In *In Proceedings of the 12th IEEE International Conference on Advanced Robotics (ICAR '05)*, 2005.

R. Rusu, Z. Marton, N. Blodow, M. Dolha, and M. Beetz. Towords 3d point cloud based object maps for household environment. *Journal of Robotics and Autonomous Systems*, 56:927–941, 2008.

G. Sakas and J. Hartig. Interactive visualization of large scalar voxel fields. In *Vizualization*, pages 29–36, 1992.

B. Siemiątkowska, M. Gnatowski, and A. Zychewicz. Fast method of 3d map building based on laser range data. *Journal of Automation, Mobile Robotics and Intelligent systems*, 1(2):35–39, 2007.

B. Siemiątkowska, J. Szklarski, M. Gnatowski, and A. Borkowski. *Towards Semantic Navigation System, Recent Advances in Intelligent Information Systems*. Academic Publishing House EXIT, 2009.

S. Thrun, W. Burgard, and D. Fox. *Probabilistic Robotics*. MIT-Press, Cambridge, Masachussets, USA, 2005.

R. Triebel, P. Pfaff, and W. Burgard. Multi-level surface maps for outdoor terrain mapping and loop closing. In *In Proc. of IROS*, pages 1–2, 2006.

P. Viola and J. Michael. Rapid object detection using a boosted cascade of simple features. *IEEE CVPR*, 2001.

G. Vosselman, B. Gorte, G. Sithole, and T. Rabbani. Recognizing structure in laser scanner point clouds. In *Proceedings of Conference on Laser scanners for Forest and Landscape assessment and instruments*, Freiburg, Germany, 2004.

THE APPLICATION OF ICP AND SIFT ALGORITHMS FOR MOBILE ROBOT LOCALIZATION

Barbara Siemiątkowska[‡1] and Arkadiusz Zychewicz[‡]

[‡1] Warsaw University of Technology, Warsaw, Poland [‡] Institute of Fundamental Technological Research, Polish Academy of Sciences, Warsaw, Poland

Abstract

In this paper the algorithm of mobile robot localization in an unknown unstructured environment is presented. In the approach the combination of ICP (Iterative Closest Point) algorithm with SIFT algorithm is used. It is assumed that the robot is equipped with 3D laser range scanner and it acts in 3D space. Classical ICP method is time consuming but using SIFT methods for features detection makes the process of localization more effective. Before the process of localization starts the 3D data are transformed into 2D image. In the paper a few methods of data transformation are presented. They were tested in a real indoor and outdoor environments. The main advantages of the approach is that it can be used in the outdoor unstructured environment and the computation can be performed in real time.

1 Introduction

Localization can be performed using internal sensors (dead reckoning) , external sensors or both kind of sensors. A typical example of dead reckoning is odometry. It is cheap but the errors cumulate in time. Odometry errors can be both systematic or non-systematic. In series of papers (J. Borenstein and Wehe (1997); Weiss and Puttkamer (1995); S. Thrun and Fox (2005)) possible sources of both kind of errors are described. In the work (Jensfelt and Christensen (1998)), a calibration technique called UMBmark test has been presented.

The main advantage of using external sensor for localization is that they allow to reduce accumulated error. It is possible to localize the current position of a robot using map matching or scan matching techniques. Scan matching techniques compute the relative motion of a vehicle between two

points by maximizing the overlap between the range of measurements obtained at each point. Almost all conventional methods use geometric features of environments for instance one of the most popular methods of scans matching in 2D space is to create angular histograms (Weiss and Puttkamer (1995)). In this method the existence of polygonal structures like walls is assumed so this approach fails in outdoor unstructured environment. In unstructured 3D environment the ICP (Iterative Closest Point) algorithm is used (Zinsser et al. (2003); Rusinkiewicz and Levoy (2001)). When the approach is applied into large amount of the data the method is time consuming. In this paper we propose using the combination of two kind of techniques ICP algorithm and SIFT algorithm. The method consists of three basic steps:

- the characteristic features of the environment detection using SIFT method,
- points matching, comparing feature vectors,
- the position of the robot determination using ICP algorithm.

The main advantages of the approach is that it can be used in an outdoor unstructured environment and the computation can be performed in real time.

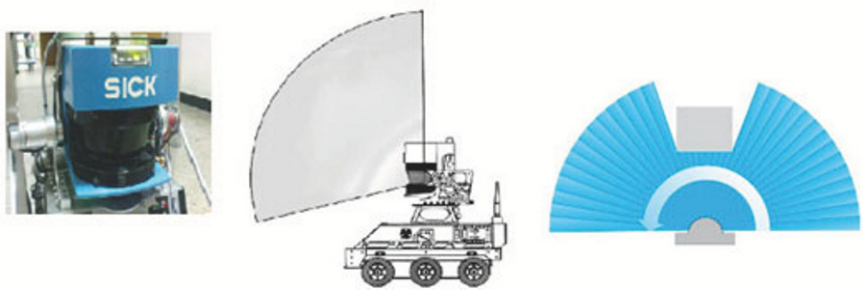

a) b) c)

Figure 1. Robot Elektron: a) Sick laser, b) vertical scanning, c) horizontal scanning method

2 Hardware

The experiments have been performed on a mobile robot Elektron which has been made at the Institute of Automatic Control and Robotics of Warsaw University of Technology. The robot is equipped with the 3D laser range finder which consists of Sick LMS 200 2D laser range scanner mounted on a

rotating support. The scanner is rotated around the horizontal axis within the angular range from -15^o to $+90^o$. $SICK$ laser enables to measure the distance to obstacles within 180^o with resolution of 1^o, 0.5^o or 0.25^o. There is a possibility of continuous measurement mode (scanner and the platform act independently) and stepping (rotational platform is stopped during the scan). Figure 1 shows an idea behind the scanning approach.

The data are obtained in pseudo-polar coordinate system: (r, ϕ, θ), where r is a distance to an obstacle, θ - is an angle of rotation around horizontal axis, and ϕ is the horizontal angle of the laser ray. Usually the first step of data analysis is to transform data into a point cloud which is a set of 3D points in a Cartesian coordinate system. The transformation can be performed using following equations:

$$\begin{aligned} x &= r \sin\phi \cos\theta \\ y &= r \cos\phi \\ z &= r \sin\phi \sin\theta \end{aligned} \tag{1}$$

The cloud of points is very useful in the case of map building but we propose to convert the measurements into a 2D image and then apply SIFT method for feature detection. We tested three different methods of 3D data transformation into an image:

- *depth map* - values (ϕ, θ) are used as the pixel coordinates and its gray-level is assigned according to the measured distance,
- *RGB map* - three coordinates associated with normal vector are represented as RGB values,
- *cosine map* - values of cosine between normals are transformed to gray-level value.

Fig.2 presents the environment, depth map and the image created based on normal vectors.

a) b) c)

Figure 2. Representation of the environment a) the environment, b) depth map, c) RGB map

3 SIFT-ICP Algorithm

3.1 SIFT Algorithm

SIFT (Scale-invariant feature transform) algorithm computes the set of vectors (feature vectors) which describe the characteristic points of the image (Ke and Sukthankar (2004); Zhou et al. (2009); Moradi and Abolmaesumi (2005)). The features have to be invariant to shift, scaling and image rotation. They are usually partially invariant to changes in the local geometric distortion. In order to find potential characteristic points the cascade of filtration is performed. The algorithm consists of the following steps:

- scale-space extrema detection - it is implemented by using a difference-of-Gaussian functions in order to find potential interest points,
- keypoint localization,
- orientation assignment - each feature is transformed relatively to the assigned orientation, scale, and location in order to provide invariance to these transformations,
- keypoint description - the gradients are measured in the area around each keypoint for selecting scales.

3.2 ICP Algorithm

In the classical ICP algorithm it is assumed that two point clouds (A,B) are obtained from two different position of the robot, $A = \{a_i\}$, $B = \{b_j\}$, $0 < i \leq n_A$ and $0 < j \leq n_B$. The goal is to find correct transformation R which aligns A and B. The algorithm consists of the following steps:

- the initial transformation $R_k = R_o$ is chosen and the algorithm transforms an input scan B using transformation matrix,
- for each point in $b_j \in B$ a corresponding point m_i in a reference scan A is found. It is assumed that $m_j \in A$ is the closest to $R_k b_j$,
- new transformation matrix R_{k+1} which minimizes evaluation value is computed.

After the third step, the method returns to the first step. The algorithm is continued until $R_k = R_{k+1}$.

Unfortunately ICP in its original form is time consuming so it cannot be used in robotics applications. One of the methods to speed up the algorithm is to reduce the number of points. In the article Rusinkiewicz (2001) a review of known methods of achieving this goal is presented. All of them assume the existence of the grid of points at the entry. In many applications obtaining a grid of points is not possible, measurements usually contain Gaussian noise and noise salt-pepper, and some of the measurements are rejected. In Ho and Jarvis (2007) the k-dtree are proposed, the approach makes the process of localization more effective but for large amount of

data obtained from 3D scanner this algorithm needs a relatively long time (about 1-2 s.). In the article Rusu et al. (2008) instead of a point to point alignment method the plane to point alignment approach is presented. We tested a plane to plane method. It is an extension of angular histograms Weiss and Puttkamer (1995) into 6D space. Unfortunately, this method cannot be used in unstructured environment. In our approach we proposed to use SIFT algorithm to find characteristic points in both scans.

3.3 SIFT algorithm in ICP

The amount of the 3D input data can be reduced by:

- selecting every n-th point (eg, n = 10),
- selecting a random subset of points.

However, this may lead to an incorrect result, because selected points may not necessarily be characteristic points of the environment. To improve the method the Sift algorithm is used but first a cloud of points should be converted into an image. Algorithm consists of the following steps:

- two point clouds are converted into a gray-scale images,
- the features of the images are calculated using SIFT,
- pixels are transformed into 3D points,
- IPC algorithm is applied in order to find correct transformation R which aligns two sets of points.

4 Experiments

The experiments were carried out both in indoor and outdoor environments. The point cloud consisted of 360×300 points. The tests were performed for three different transformation: converting the depth map into gray scale image, calculating the normals and mapped the coordinates into the RGB image and transformation the cosines into gray scale image.

For different types of transformation different characteristic points are chosen (Fig. 4). In the case of transformation into RGB one point in the first image was assigned to more than one point in the second image. In all cases the method is very fragile to small (one point error) of corresponding point assignment. Therefore, in order to minimize the impact of such effects the set of points (input to ICP algorithm) consists not only of the characteristic points but also of theirs neighbors. Table 1 presents the time and errors of computation for classical ICP algorithm and SIFT-ICP algorithm for depth image. The robot position is described in 6D space. The maximal error of x,y,z coordinates and rotation around each axis is determined. The results of the algorithm depends on the scan overlapping ratio, the kind of the environment and the error of determining initial robot position computed

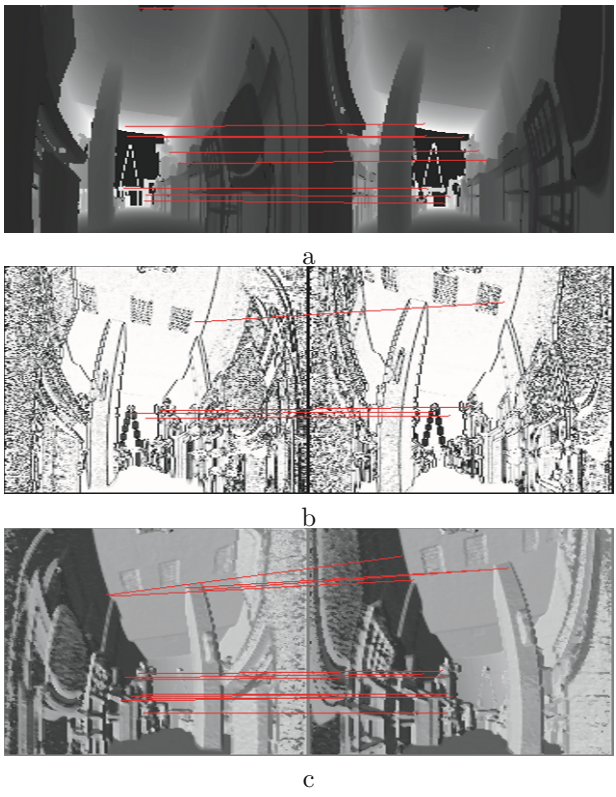

Figure 3. Points detected by Sift algorithm (indoor environment): a) depth map, b) cosines map, c) normal vectors

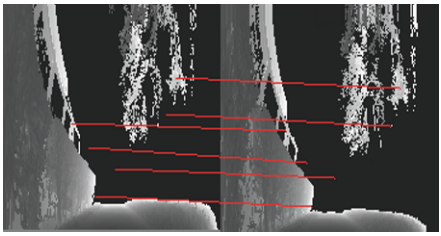

Figure 4. Points detected by Sift algorithm (outdoor environment)

Table 1. Running times and errors of the algorithms

algorithm	time [s]	overlapping ratio %	odometry error [cm]	error [cm]	error deg
ICP	3.5	90	10	0.2	0.05
SIFT-ICP	0.01	90	10	0.1	0.05
ICP	32	90	200	lm.	lm.
SIFT-ICP	0.01	90	200	lm.	lm.
ICP	6.6	70	10	6.1	1.2
SIFT-ICP	0.01	70	10	7.2	1.1

based on odometry. If the error of odometry is large (more than 1 meter or more than 15^o) then ICP and ICP-Shift algorithms tend to fall into local minima. In indoor structured environment like corridor the best result are obtained using plane to plane method. The error of localization does not increase 0.5cm (for coordinates x,y,z). The results of application SIFT-ICP for RGB or cosine images are poor the errors are about 0.3m and time of computation is about 5s for transformation cosines into gray image and 1.2s for transformation normals into image. The error of application of SIFT-ICP for depth image and overlapping ratio about 75% is about 0.12m the same result is obtained when ICP algorithm is applied. ICP is more fragile to initial position of the robot than SIFT-ICP algorithm.

5 Conclusions

This paper presents a novel rejection technique. Conducted experiments showed that the combination of ICP and the Sift algorithm enables the location of the robot in outdoor environment in real time, it can also solve the SLAM problem for a robot moving in 3D space. The experiments shows that best results of localization in outdoor environment are achieved when the depth maps are analyzed. In structured indoor environment the best results are obtained when plane to plane method is used. In future work, we plan to use this approach in a complete SLAM algorithm in a dynamic environment.

This work was supported by the Polish Ministry of Science and Higher Education (grant 4311/B/T02/2007/33)

Bibliography

N. Ho and R. Jarvis. Large scale 3d environmental modelling for stereoscopic walkthrough visualisation. In *3DTV Conference*, pages 1–4, 2007.

L. Feng J. Borenstein, H. Everett and D. Wehe. A cognitive load application in tutoring. *Mobile robot positioning: Sensors and techniques*, 14:231–249, 1997.

P. Jensfelt and H. Christensen. Laser based position acquisition and tracking in an indoor environment. In *Proceedings of the IEEE International Symposium on Robotics and Automation*, pages 331–338, 1998.

Y. Ke and R. Sukthankar. Pca-sift: A more distinctive representation for local image descriptors. *IEEE CVPR*, 2:506–513, 2004.

M. Moradi and P. Abolmaesumi. Medical image registration based on distinctive image features from scaleinvariant (sift) keypoints. *CARS*, pages 1292–1292, 2005.

S. Rusinkiewicz. *Real Time Acquisition and Rendering of Large 3D Models*. Ph.D. Dissertation, 2001.

S. Rusinkiewicz and M. Levoy. Efficient variants of the icp algorithm. In *Proceedings of International Conference 3DIM*, 2001.

R. Rusu, Z. Marton, N. Blodow, M. Dolha, and Beetz M. Towords 3d point cloud based object maps for household environment. *Journal of Robotics and Autonomous Systems*, 56:927–941, 2008.

W. Burgard S. Thrun and D. Fox. *Probabilistic Robotics*. MIT Press, Cambridge, 2005.

G. Weiss and E. Puttkamer. A map based on laserscans without geometric interpretation. In *Proceedings of Intelligent Autonomous Systems*, pages 403–407, 1995.

H. Zhou, Y. Yuan, and C. Shi. Object tracking using sift features and mean shift. *Computer Vision and Image Understanding*, 113:345352, 2009.

T. Zinsser, J. Schmidt, and H. Niemann. A refined icp algorithm for robust 3-d correspondence estimation. In *Proceedings of International Conference on Image Processing (ICIP)*, 2003.

Estimation of Complex Anatomical Joint Motions Using a Spatial Goniometer

V. A. Dung Cai*, Philippe Bidaud*,
Vincent Hayward*, and Florian Gosselin†
*UPMC Univ Paris 06, Institut des Systèmes Intelligents et de Robotique,
4 place Jussieu, 75005, Paris, France
Email: cai,bidaud,hayward@isir.upmc.fr
†CEA, LIST, Laboratoire de Robotique Interactive,
18 route du Panorama, BP6, 92265, Fontenay Aux Roses, France
Email: florian.gosselin@cea.fr

Abstract The determination of the instantaneous axis of rotation of human joints has numerous applications. The screw axis can be determined using optical motion capture systems or electromechanical goniometers. In this paper, we introduce a new method for the localization of the instantaneous screw axis in human anatomical joints from the data given by a spatial mechanical goniometer.

1 Introduction

The knowledge of the kinematics of human joints is needed in numerous instances, such as in prostheses or orthoses design, or to help the treatment of diseased and injured joints. The knee joint kinematics is known as having a complex motion resulting from a combination of rolling and sliding movements of the femur onto the tibia. The complex, spatial motion of the knee joint varies from one individual to another. It also changes with load conditions and, of course, as the the result of certain pathologies (Markolf et al., 1984; Winsman et al., 1980).

To date, the kinematics of a human anatomical joint is identified by functional methods employing standardized movements of extension-flexion, adduction-abduction, and of circumduction. The movement data are acquired with various measurement devices including motion capture systems with cameras and optical markers, or medical imaging modalities to measure the movement of bones. Different kinematic analysis methods have been developed for these different categories of devices (Woltring et al., 1985; Ehrig et al., 2006; Blankevoort et al., 1990). Simple goniometers are

also used for the measurement of rotational amplitude, but this technique has several restrictions such as attachment problems or the lack of device mobility.

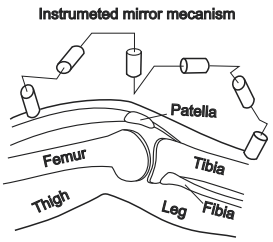

Figure 1. Spatial linkage as a goniometer for an anatomical knee joint.

Another approach for the identification of a six degrees-of-freedom motion is to employ an instrumented spatial linkage, i.e. a goniometer, attached to the skeletal segments of interest and to measure the motion between adjacent fixations, viz. the femur and the tibia, that primarily define the movement of the joint. Please see Fig. 1 for a diagram of the concept. Several of these systems have been designed by the past that have at least six degrees-of-freedom (Townsend et al., 1977). Indeed six degrees of freedom are required to track limbs motions without any constraint, as the knee joint and mechanism can be misaligned. Numerous goniometers have been so far developed for use in clinical joint tests, or for the measure of knee kinematics. They were used to analyze continuously the joint motion based on different models, essentially finite transformation models (Kinzel et al., 1972).

In this paper, the use of a spatial linkage goniometer with integrated angle sensors to estimate the anatomical joint motion in real time is investigated. Since the total relative motion between the upper and the lower parts of a human leg belong to the group of rigid motions $SE(3)$, the notion of screw axis can be used along with methods for the identification of the infinitesimal screw axis and others kinematic parameters. An example of design of a knee goniometer is shown and validated by simulations.

2 Estimation of the Anatomical Joint Screw Axis

2.1 Approach Using the Velocities of Points

In this method, the positions and velocities of different points on the moving segment are measured. The localization of the instantaneous screw axis can be then described by the orthogonal projections A_i' of the points A_i, belonging to the moving segment, onto the screw axis (Bru and Pasqui, 2009). These projections are defined to be

$$\overrightarrow{A_i A_i'} = (\boldsymbol{v}_{A_i} \wedge \boldsymbol{\omega})/(|\boldsymbol{\omega}|^2), \tag{1}$$

where $\boldsymbol{\omega}$ and $\boldsymbol{v}_{A_i}$ are respectively the angular and linear velocities of the second segment at the point A_i. For systems using optical markers, these values can be measured and determined by using different transformation methods. The relative linear velocity of the two body segments can be estimated from the expression

$$\boldsymbol{v}_{A_i'} = \boldsymbol{v}_{A_i} - \boldsymbol{\omega} \wedge \overrightarrow{A_i A_i'}. \tag{2}$$

In the case of a spatial goniometer, the sum of the velocities, $\boldsymbol{\omega}_{i,i+1}$, provides the relative angular velocity between the two segments, that is,

$$\boldsymbol{\omega}_{06} = \sum_{i=0}^{5} \boldsymbol{\omega}_{i,i+1}. \tag{3}$$

If $\boldsymbol{q}$ is the known vector of joint angles, from the forward kinematic model, the twist expressed at points A_i of the moving segment is

$$\begin{pmatrix} \boldsymbol{\omega}_{06} \\ \boldsymbol{v}_{A_i} \end{pmatrix} = J_{A_i}(\boldsymbol{q})\dot{\boldsymbol{q}}, \tag{4}$$

where J_{A_i} are the Jacobian matrices of the spatial linkage written at points A_i of the second limb.

2.2 Approach by Loop Closure

It is also possible to compute the coordinates of points of the instantaneous screw axis by solving a linear system of equations obtained from loop closure at these points (Cai et al., 2009). If the segments of an anatomical joint are considered to be part of a linkage, then the loop-closure equation gives

$$J_P(\boldsymbol{q})\dot{\boldsymbol{q}} - \begin{pmatrix} \boldsymbol{\omega}_{06} \\ \boldsymbol{v}_P \end{pmatrix} = 0, \tag{5}$$

where P is a point on the instantaneous screw axis and the twist at this point is

$$\begin{pmatrix} \boldsymbol{\omega}_{06} \\ \boldsymbol{v}_P \end{pmatrix} = \begin{pmatrix} \omega_x & \omega_y & \omega_z & v_x & v_y & v_z \end{pmatrix}^\top. \tag{6}$$

Let the position of the point P relative to the reference body be

$$\overrightarrow{PO}_0 = \begin{pmatrix} a & b & c \end{pmatrix}^\top. \tag{7}$$

From (5)–(7), the loop-closure equations give a system of equations

$$\begin{cases} K_1 b + K_2 c + K_3 = v_x, \\ K_4 a + K_5 c + K_6 = v_y, \\ K_7 a + K_8 b + K_9 = v_z, \end{cases} \tag{8}$$

where the K_i's depend on the configuration variables (joint angles, θ_i's, and joint positions, r_i's, for revolute and prismatic joints respectively), as well as design parameters, l_i's and d_i's. Moreover, it can be verified that several relationships exist between the K_i's, including

$$K_1 = -K_4 = \omega_z, \quad K_7 = -K_2 = \omega_y, \text{ and } K_5 = -K_8 = \omega_x. \tag{9}$$

When the anatomical joint motion comprises a rotation, at least one of the twist components, ω_x, ω_y, ω_z, must differ from zero. Let us suppose that it happens that ω_x is different from zero. Since there is an infinity of choices for the point P, one of its coordinates, a, b, or c, can be selected arbitrarily in order to compute the two others. Since $\omega_x \neq 0$, a is selected and the coordinates b , c of the vector $\overrightarrow{PO_0}$ may be computed as follows,

$$b = \frac{\omega_y a + K_9 - v_z}{\omega_x}, \qquad c = \frac{\omega_z a - K_6 + v_y}{\omega_x}. \tag{10}$$

Since an anatomical joint is modeled by a screw joint, all the points on the instantaneous screw axis have a common velocity that is aligned with the axis. Given ϵ, a non-zero constant, and another point P' on the screw axis with coordinates (a', b', c'), the common velocity property gives

$$\boldsymbol{v}_P = \boldsymbol{v}_{P'} = \epsilon \overrightarrow{PP'} = \epsilon \begin{pmatrix} a' - a \\ b' - b \\ c' - c \end{pmatrix}. \tag{11}$$

Two systems of equations are obtained by rewriting (8) for two different points P and P'. From (11), subtracting the two systems gives a new one:

$$\begin{cases} K_1(b - b') + K_2(c - c') = 0, \\ K_4(a - a') + K_5(c - c') = 0, \\ K_7(a - a') + K_8(c - c') = 0. \end{cases} \tag{12}$$

The later system, (12), can be rewritten in terms of v_x, v_y, v_z,

$$\begin{cases} K_1 v_y + K_2 v_z = 0, \\ K_4 v_x + K_5 v_z = 0, \\ K_7 v_x + K_8 v_y = 0. \end{cases} \tag{13}$$

From (9), if $\omega_x \neq 0$, K_5 and K_8 are also different from zero. The quantities v_y and v_z can then be computed as a function of v_x,

$$v_y = -\frac{K_7 v_x}{K_8} = \frac{\omega_y v_x}{\omega_x}, \qquad v_z = -\frac{K_4 v_x}{K_5} = \frac{\omega_z v_x}{\omega_x}. \tag{14}$$

From (8), (10), (14), the velocity coordinate v_x can be computed as a function of $(\theta_i,d_i,\dot{\theta}_i,\dot{r}_i,l_i)$. All calculations done,

$$v_x = \frac{\omega_x^2 K_3 + \omega_x\omega_y K_6 + \omega_x\omega_z K_9}{\omega_x^2 + \omega_y^2 + \omega_z^2}. \tag{15}$$

Similar results are obtained when ω_y or ω_z are different from zero and b or c are chosen arbitrarily. In the case of a pure translation of the joint, according to (8) and (9), the linear velocity is expressed as

$$\boldsymbol{v}_P = \begin{pmatrix} v_x & v_y & v_z \end{pmatrix}^\top = \begin{pmatrix} K_3 & K_6 & K_9 \end{pmatrix}^\top. \tag{16}$$

3 Application to a Goniometer for The Knee Joint

3.1 System description

Figure 2. The knee goniometer.

Figure 2 shows the overall architecture for a spatial goniometer designed for the knee joint. This mechanism has three intersecting revolute joints, a sliding joint and two others intersecting revolute joints. Like for robot manipulators, intersecting revolute joints simplify the kinematic analysis.

The slider gives to the mechanism the ability to accommodate different limb sizes. The design meets several specifications such as large workspace, no collision with limbs in the operating range and minimum slider displacement during motion. Sensors give the displacements of the six different joints of the mechanism. A computer model, which is illustrated in Fig. 3, is used for the simulation. For testing purposes, the anatomical joint is represented by orthogonal, non-intersecting axes that produce complex motions in three dimensions.

3.2 Simulation results

A simulation was set up to validate these methods. The instantaneous angular and linear velocities are computed by a second-order derivation method from predetermined position input data. The time step was set to be 3ms. The knee joint was modelized as a moving screw joint. Knee amplitude

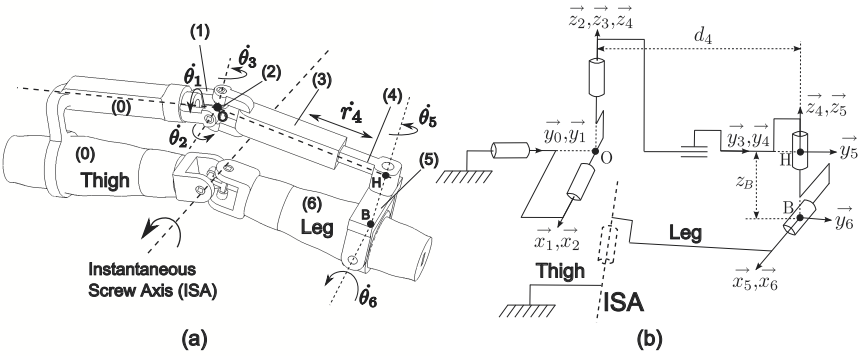

Figure 3. The computer model for the simulation of the knee electrogoniometer (a) and its frame assignment (b).

is set to 90 degree for flexion and 0 degree for extension. The maximum knee internal/external rotation is 9 degree. The simulations lasted for 3 seconds (for a total of 1000 samples). Offset errors were set to 2 degree for revolute joints and to 2 mm for the slider joint. Errors of 0.001 degree (for smooth angular value) or 0.01 degree (for discontinuous angular values) were added to each sample. For the slider, this error was set to 0.001 mm or to 0.01 mm. When there was no simulated measurement error, the localization of the instantaneous screw axis was exact. Then measurement errors were added in order to test the sensibility of the system to inaccuracies. All results are computed in the frame $R_0 = (O, \mathbf{x_0}, \mathbf{y_0}, \mathbf{z_0})$.

The first simulation was carried out with a fixed instantaneous screw axis. The angular velocity was set to 30 deg/s and the linear velocity was set to 2 mm/s. Figures 4–5 show the results of the simulation with measurement and offset errors due to calibration. In spite of important offset errors, the estimated axis is still located near to the real screw axis with a small angular deviation of 6 degree), see Fig. 5.b. Figure 5.c shows the estimated instantaneous linear velocity of the knee joint. The estimated values are also near to the real velocity in spite of large offset errors. Angular values, however, could differ significantly from the real values due to calibration errors. According to Fig. 5.d, the estimated absolute angular error of the second segment can reach 5 degree for offset errors of 2 degree. Hence, the use of high-performance calibration procedures is required for applications in which the estimation of angles is needed.

A second simulation was run to simulate a moving instantaneous screw axis. The knee motion was a compound motion of two simultaneous rota-

tions, the first at angular velocity of 3 degrees/s, and the second to 30 degree/s. Figure 4.b shows the evolution of the moving screw axis during the knee movement.

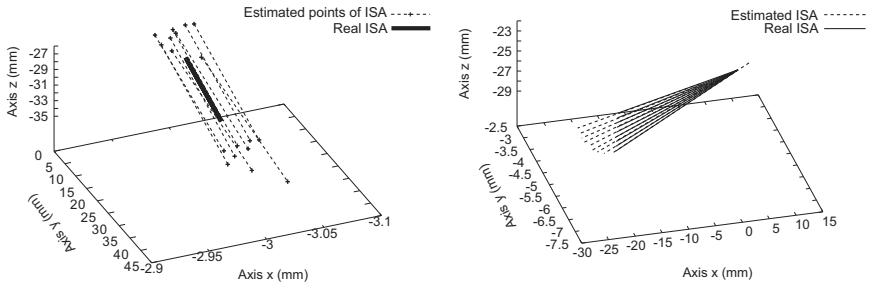

Figure 4. (a) First simulation: Localization of a fixed ISA. (b) Second simulation: Localization of a mobile ISA - Real and estimated ISA fall graphically on top of each other.

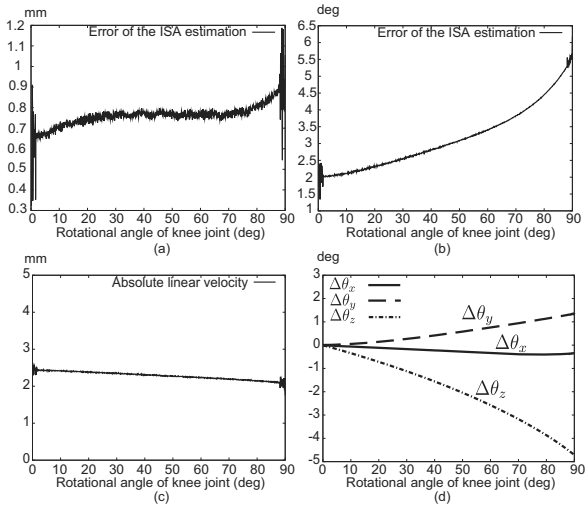

Figure 5. Result of the first simulation.(a) ISA estimation error: Distance beetween the two axes. (b) ISA estimation error: Angular deviation error. (c) Estimated linear velocity. (d) Estimated errors of the rotational angles of the knee joint.

4 Conclusion

In this paper, we proposed a new method for the estimation of the instantaneous human joint kinematics based on the use of a mechanical goniometer. This method allows the system to estimate all kinematic parameters of the user's joint, including the angular and linear displacements, angular and linear velocities of the second limb, and the localization of the instantaneous screw axis. The knowledge of the screw axis and of the velocities of the anatomical joint is the most interesting result because it makes it possible to design rehabilitation devices that could conform to the physiological movements of patients.

In future works, this technique will be validated by comparison with other methods using motion capture systems.

Bibliography

L. Blankevoort, R. Huiskes, and A. De Lange. Helical axes of passive knee joint motions. In *Journal of Biomechanics*, pages 1219–1229, 1990.

B. Bru and V. Pasqui. A new method for determining the location of the instantaneous axis of rotation during human movements. In *Computer Methods in Biomechanics and Medical Engineering*, pages 65–67, 2009.

V.A.D. Cai, P. Bidaud, V. Hayward, and F. Gosselin. Design of self-adjusting orthoses for rehabilitation. In *Proceedings of the 14th IASTED International Conference Robotics and Applications*, 2009.

R.M. Ehrig, W.R. Taylor, G.N. Duda, and M.O. Heller. A survey of formal methods for determining the centre of rotation of ball joints. In *Journal of Biomechanics*, pages 2798–2809, 2006.

G.L. Kinzel, A.S. Hall, and B.M. Hillberry. Measurement of the total motion between two body segments - i. analytical development. In *Journal of Biomechanics*, pages 93–105, 1972.

K.L. Markolf, A. Kochan, and H.C. Amstutz. Measurement of knee stiffness and laxity in patients with documented absence of the anterior cruciate ligament. In *The Journal of Bone and Joint Surgery*, 1984.

M.A. Townsend, M. Izak, and R.W. Jackson. Total motion knee goniometry. In *Journal of Biomechanics*, pages 183–193, 1977.

J. Winsman, F. Veldpaus, J. Janssen, A. Huson, and P. Struben. A three-dimensional mathematical model of the knee-joint. In *Journal of Biomechanics*, pages 677–685, 1980.

H.J. Woltring, R. Huiskes, and A. De Lange. Finite centroide and helical axis estimation from noisy landmark measurements in the study of human joint kinematics. In *Journal of Biomechanics*, pages 379–389, 1985.

Chapter VI

Recent Advances in Robotics

Modeling and Motion Planning for a Population of Mobile Robots

Qirong Tang and Peter Eberhard
Institute of Engineering and Computational Mechanics,
University of Stuttgart, Stuttgart, Germany
[tang, eberhard]@itm.uni-stuttgart.de

Abstract This paper investigates modeling and motion planing for a population of mobile robots. A mechanical model is built for the robot motion planning which is inspired by particle swarm optimization and combined with multibody system dynamics. It uses the augmented Lagrangian multiplier method to treat the constraints and an independent module to handle obstacle avoidance. Simulations show that the robots moving in the environment display the desired behavior well, and so this model and related algorithms will next be transfered to a large scale mobile robotic system.

1 Introduction

Nowadays, controlling of a multi-robot or so called swarm robots is still a challenge in the robotics area despite of its fast development. Thus, several researchers worked on finding methods of modeling and motion planning for such swarm robotic systems.

In recent years, the comparatively new stochastic particle swarm optimization (PSO) algorithms have been applied to many engineering areas, among them also the robotics area. (Doctor et al., 2004) discussed using PSO for multi-robot searching. Their focus was on optimizing the parameters and they did not consider the scalability of the standard PSO for a large numbers of robots. (Hereford and Siebold, 2008) developed a distributed PSO but with shortcomings of non-consideration of obstacles or restriction to just static simple obstacles in the environment and the real robots could only rotate at a specified angle range. (Pugh et al., 2006) contributed a simple PSO version in multi-robot searching and they mainly focused on how to model the biological algorithm.

In contrast to the mentioned publications this paper builds a model and does the motion planning for a population of mobile robots based on PSO combined with multibody systems. It is expected that after some adaption, such models and methods can be adjusted for real mobile robots.

2 Modeling for a Population of Mobile Robots

A population of robots is not simply a group of individuals. The behavior shown by a population of robots should be collective, coordinated and requires information exchange. So far, many algorithms and methods are used in this area, among them traditional and recursive biology inspired methods, see (Tang and Eberhard, 2009). The PSO algorithm is very appealing due to its clear ideas, simple iteration equations, and the possibility to be mapped onto several robots or even swarm robots.

2.1 Basic Particle Swarm Optimization

The original model of PSO, see (Kennedy and Eberhart, 1995), uses the vectors $\Delta \boldsymbol{x}$ and $\boldsymbol{x}$ to denote the particle's 'velocity' and actual position, respectively. The so called 'velocity' of the i-th particle at the $(k+1)$-th iteration can be described with the equation

$$\Delta \boldsymbol{x}_i^{k+1} = \omega \Delta \boldsymbol{x}_i^k + c_1 r_{i,1}^k (\boldsymbol{x}_{i,self}^{best,k} - \boldsymbol{x}_i^k) + c_2 r_{i,2}^k (\boldsymbol{x}_{swarm}^{best,k} - \boldsymbol{x}_i^k) \tag{1}$$

and the position update is done in the traditional PSO algorithm by

$$\boldsymbol{x}_i^{k+1} = \boldsymbol{x}_i^k + \Delta \boldsymbol{x}_i^{k+1}. \tag{2}$$

If consider in a general way and for all n particles, the basic PSO model can be foumulated by

$$\begin{bmatrix} \boldsymbol{x}^{k+1} \\ \dot{\boldsymbol{x}}^{k+1} \end{bmatrix} = \begin{bmatrix} \boldsymbol{x}^k \\ \omega \dot{\boldsymbol{x}}^k \end{bmatrix} + \begin{bmatrix} \dot{\boldsymbol{x}}^{k+1} \\ c_1 \boldsymbol{r}_1^k (\boldsymbol{x}_{self}^{best,k} - \boldsymbol{x}^k) + c_2 \boldsymbol{r}_2^k (\hat{\boldsymbol{x}}_{swarm}^{best,k} - \boldsymbol{x}^k) \end{bmatrix}. \tag{3}$$

Detailed interpretation for this structure and related parameters please see (Tang and Eberhard, 2009).

2.2 Build Mechanical Model for Practical Use in a Population of Mobile Robots

This study wants to interpret the PSO algorithm as providing the required forces in the view of multibody system dynamics rather than a mathematical optimization tool as usual since the application purpose is swarm mobile robots motion planning. Each particle (robot) is considered as one body in a multibody system which is influenced by forces and torques from other bodies in the system but without direct mechanical constraints between them. The forces are artificially created by corresponding drive controllers. From another point of view, based on the Newton-Euler equations, the general form of equation of motion for swarm

mobile robots can be formulated as

$$\boldsymbol{M}\ddot{\boldsymbol{x}}+\boldsymbol{k}=\boldsymbol{q} \qquad \text{or} \qquad \ddot{\boldsymbol{x}}=\boldsymbol{M}^{-1}(\boldsymbol{q}-\boldsymbol{k})=\boldsymbol{M}^{-1}\boldsymbol{F}. \tag{4}$$

For a free system without joints, $\boldsymbol{M}=\boldsymbol{diag}(m_1\boldsymbol{I}_3,m_2\boldsymbol{I}_3,\cdots,m_n\boldsymbol{I}_3,\boldsymbol{J}_1,\boldsymbol{J}_2,\cdots,\boldsymbol{J}_n)=\boldsymbol{M}^T\geq 0$ is the inertia matrix collecting the masses and moments of inertias of the particles, $\ddot{\boldsymbol{x}}=[\boldsymbol{a}\ \ \boldsymbol{\alpha}]^T$ is the generalized acceleration, $\boldsymbol{k}$ is a term which comes from the Euler equation, and $\boldsymbol{q}$ contains forces and torques acting on the robots. The force $\boldsymbol{F}$ is determined from three PSO-related parts which are defined as

$$\boldsymbol{f}_1^k=-\boldsymbol{h}_{f_1}^k\left(\boldsymbol{x}^k-\boldsymbol{x}_{self}^{best,k}\right),\ \ \boldsymbol{f}_2^k=-\boldsymbol{h}_{f_2}^k\left(\boldsymbol{x}^k-\hat{\boldsymbol{x}}_{swarm}^{best,k}\right),\ \ \boldsymbol{f}_3^k=-\boldsymbol{h}_{f_3}^k\dot{\boldsymbol{x}}^k, \tag{5}$$

with the matrices

$$\boldsymbol{h}_{f_i}^k=\boldsymbol{diag}(h_{1,f_i}^k\boldsymbol{I}_3,h_{2,f_i}^k\boldsymbol{I}_3,\cdots,h_{n,f_i}^k\boldsymbol{I}_3,\boldsymbol{0}_{3n}), \qquad i=1,2,3. \tag{6}$$

Here $\boldsymbol{I}_3$ is a 3×3 unit matrix, $\boldsymbol{0}_{3n}$ is a $3n\times 3n$ zero matrix. The forces $\boldsymbol{f}_1^k$ and $\boldsymbol{f}_2^k$ are attraction forces from the last best position of the robot itself and the last swarm best robot position and are proportional to their distances. The vector $\boldsymbol{f}_3^k$ represents the force which is proportional to the last velocity and is a kind of inertia which counteracts a change in direction. One can also write Eq. (4) as a state equation with the state vector $\boldsymbol{y}=[\boldsymbol{x}\ \ \dot{\boldsymbol{x}}]^T$, where $\boldsymbol{x}$ and $\dot{\boldsymbol{x}}$ are the translational and rotational position and velocity of the robots. Together with the initial conditions, first order of differential equation, the motion of the swarm robots over time can be computed, e.g., by the simple Euler forward integration formula, which yields the mechanical PSO model

$$\begin{aligned}\begin{bmatrix}\boldsymbol{x}^{k+1}\\ \dot{\boldsymbol{x}}^{k+1}\end{bmatrix}&=\begin{bmatrix}\boldsymbol{x}^k\\ \left(\boldsymbol{I}_{6n}-\Delta t\boldsymbol{M}^{-1}\boldsymbol{h}_{f_3}^k\right)\dot{\boldsymbol{x}}^k\end{bmatrix}\\ &\quad+\Delta t\begin{bmatrix}\dot{\boldsymbol{x}}^k\\ \boldsymbol{M}^{-1}\boldsymbol{h}_{f_1}^k\left(\boldsymbol{x}_{self}^{best,k}-\boldsymbol{x}^k\right)+\boldsymbol{M}^{-1}\boldsymbol{h}_{f_2}^k\left(\hat{\boldsymbol{x}}_{swarm}^{best,k}-\boldsymbol{x}^k\right)\end{bmatrix}.\end{aligned} \tag{7}$$

Comparing Eq. (7) to Eq. (3), one can see that they are quite similar and the corresponding relationships are introduced in (8), in (Tang and Eberhard, 2009) we give a very sound and useful interpretation, please see the related reference for details.

$$\Delta t\boldsymbol{M}^{-1}\boldsymbol{h}_{f_1}^k\ \longleftrightarrow\ c_1\boldsymbol{r}_1^k,\ \ \Delta t\boldsymbol{M}^{-1}\boldsymbol{h}_{f_2}^k\ \longleftrightarrow\ c_2\boldsymbol{r}_2^k,\ \ \boldsymbol{I}_{6n}-\Delta t\boldsymbol{M}^{-1}\boldsymbol{h}_{f_3}^k\ \longleftrightarrow\ \omega. \tag{8}$$

3 Design a Control Scheme for a ROBOTINO

3.1 Constraint Handling

Engineering optimization problems usually have constraints, e.g., if the particles (robots) are searching in the environment with some limitations, like inter-

ference districts or several obstacles. In this study, we also take into account the treatment of constraints. So, here the general optimization problem with an objective function and constraints is

$$\begin{aligned} &\text{minimize} \quad \Psi(\boldsymbol{x}) \\ &\text{subject to} \quad \begin{cases} \boldsymbol{g}(\boldsymbol{x}) = \boldsymbol{0}, & m_e \text{ equality constraints,} \\ \boldsymbol{h}(\boldsymbol{x}) \le \boldsymbol{0}, & m_i \text{ inequality constraints,} \end{cases} \end{aligned} \tag{9}$$

where $\boldsymbol{x}$ is the position of the particle bounded additionally by $\boldsymbol{x}_{min} \le \boldsymbol{x} \le \boldsymbol{x}_{max}$.

For such an optimization problem, the augmented Lagrangian multiplier method can be used where each constraint violation is penalized separately by using finite penalty factors $\boldsymbol{r}_p$. Thus, the minimization problem with constraints in Eq. (9) can be transformed into an unconstrained minimization problem

$$\text{minimize} \quad L_A(\boldsymbol{x}, \boldsymbol{\lambda}, \boldsymbol{r}_p) \tag{10}$$

$$\text{with} \quad L_A(\boldsymbol{x}, \boldsymbol{\lambda}, \boldsymbol{r}_p) = \Psi(\boldsymbol{x}) + \sum_{i=1}^{m_e+m_i} \lambda_i P_i(\boldsymbol{x}) + \sum_{i=1}^{m_e+m_i} r_{p,i} P_i^2(\boldsymbol{x}), \quad \text{and}$$

$$P_i(\boldsymbol{x}) = \begin{cases} g_i(\boldsymbol{x}), & i = 1(1)m_e, \\ \max\left(h_{i-m_e}(\boldsymbol{x}), \frac{-\lambda_i}{2r_{p,i}}\right), & i = (m_e+1)(1)(m_e+m_i). \end{cases}$$

Please refer to (Sedlaczek and Eberhard, 2006) and (Tang and Eberhard, 2009) for details of this method.

3.2 Control Scheme

This work proposes to use a PSO based model for a swarm of mobile robots to search a target in the environment. Such a target can be specified by an objective function and several constrains, e.g., in our example

$$\text{minimize } \Psi(\boldsymbol{x}) \quad \text{with } \Psi(\boldsymbol{x}) = \frac{1}{f(\boldsymbol{x})} - \varepsilon = (x_1 - x_{m_1})^2 + (x_2 - x_{m_2})^2 \tag{11}$$

$$\text{subject to} \quad \begin{cases} h_1(\boldsymbol{x}) = 3 - x_1 \le 0, \\ h_2(\boldsymbol{x}) = 2 - x_2 \le 0, \\ h_3(\boldsymbol{x}) = 1 + x_1^2 - x_2^2 \le 0. \end{cases}$$

If the center of the source $\boldsymbol{x}_m$ is infeasible, then the robots should at least get as close as possible. In this example, we choose $\boldsymbol{x}_m = (3, \sqrt{10})$ and the constrained minimum is $\boldsymbol{x}_{opt} = \boldsymbol{x}_m$ with $\Psi(\boldsymbol{x}_{opt}) = 0$.

We try to use our model and related algorithms in the autonomous robot ROBOTINO (see Festo Home Website, 2009) for future work, so here we extract some main components of ROBOTINO and present the control scheme for simulation and also later for practical use, see Figs. 1 and 2.

Figure 1. Components of the Festo ROBOTINO

4 Simulation and Results

Some assumptions for the simulation experiments must be made:

1. the static obstacles are represented by polygons,
2. all simulations treat only the planar case, and
3. during the avoidance of obstacles, the robots can rotate full 360 degrees.

This study classifies the simulation experiments as shown in Table 1. The symbol of a circle ' ○ ' is used for a volume robot, and a '∗' for the target. The objective function and constraints are as same as described in (11).

The trajectories of five searching robots of experiment no. 1 are shown in Fig. 3, where obstacle avoidance and target searching can be seen clearly. Experiment no. 2 uses external forces to steer a robot in a specified direction, see Fig. 4. The red robot e.g. will turn left when it meets the first obstacle, see Fig. 3, but with influence from an external guiding force which is in right direction it turns to the opposite side. Compared to experiment no. 1 and no. 2, in experiment no. 3 we use more robots and try to show the ability of mutual avoidance, see Fig. 5. In experiment no. 4, the target is within an obstacle, see Fig. 6. The initial and final status are shown. As the algorithm and model are designed, the 50 robots get as close as they can to the target and siege it.

In summary, all above four experiments are obtaining the correct results from our swarm model and the designed algorithms, strategies, and methods.

5 Conclusion and Future Work

The application of PSO to our swarm model requires some extensions for the use of this scheme for the motion planning and control of large scale mobile robots. The results show that the algorithm and model used in our experiment are simple,

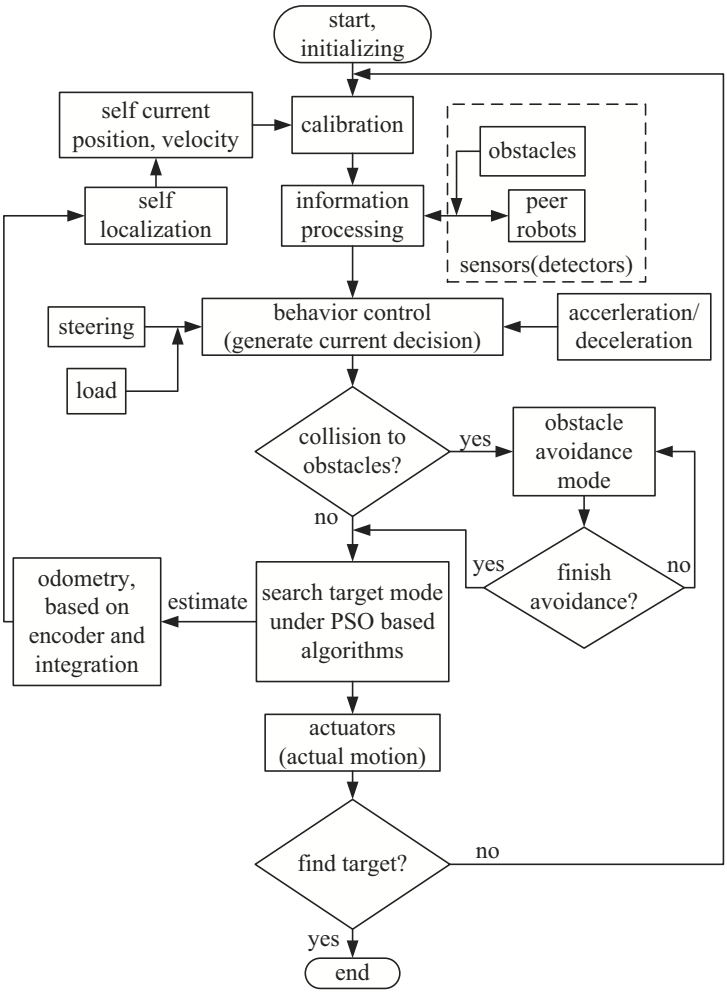

Figure 2. Control scheme

reliable, and transferable to a population of many mobile robots. It has the ability of effectively treating constraints with acceptable computational cost and it is able to avoid obstacles and other robots in the environment. The proposed model has no need of a central processor and it uses the information of each single robot's neighborhood and so it can be implemented decentralized on a large scale mobile robotic system and makes the robots move well coordinated.

Table 1. Type of experiment.

no.	robots	experiment description
1	n=5	robots coordinated movement under constraints and obstacles, target locates outside of obstacle, show trajectories
2	n=5	as experiment one, add external force to steer a robot in a specified direction
3	n=50	as experiment one, more robots, show stages
4	n=50	as experiment three, but the target is within an obstacle

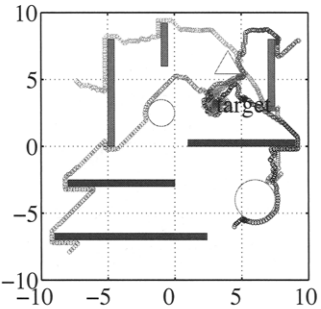

Figure 3. Result of experiment one.

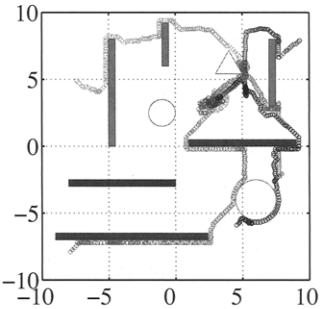

Figure 4. Result of experiment two.

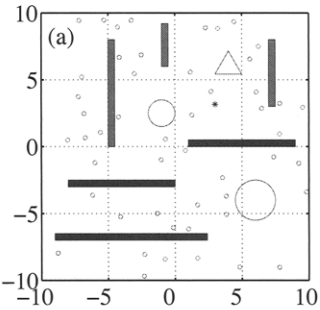

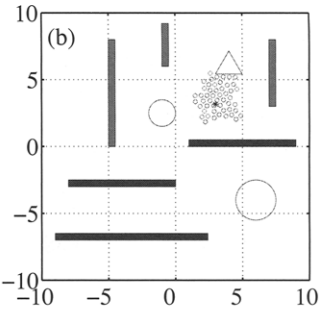

Figure 5. Experiment three, (a) t=0 s, (b) t=371.95 s.

The natural next step after the simulations are finished will be to use it for the ROBOTINO, to identify clearly the mechanical properties of a single robot and then to run everything for a population of real mobile robots.

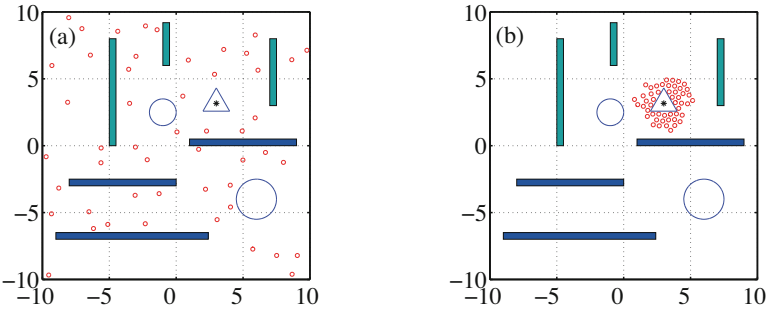

Figure 6. Experiment four, (a) t=0 s, (b) t=350.48 s.

Acknowledgements

The authors want to thank Prof. W. Schiehlen for his encouragement and detail discussion, as well as the China Scholarship Council for providing a Ph.D. fellowship to Qirong Tang to study in Germany. Parts of this research are done in the framework of SimTech, the Stuttgart Research Center for Simulation Technology. All this support is highly appreciated.

Bibliography

S. Doctor, G. K. Venayagamoorthy, and V. G. Gudise. Optimal PSO for collective robotic search applications. In *IEEE Congress on Evolutionary Computation*, pages 1390–1395, 2004.

Festo Home Website. http://www.festo-didactic.com, 2009.

J. M. Hereford and M. Siebold. Multi-robot search using a physically-embedded particle swarm optimization. *International Journal of Computational Intelligence Research*, 4(2):197–209, 2008.

J. Kennedy and R. C. Eberhart. Particle swarm optimization. In *Proceedings of the international conference on neural networks*, volume 4, pages 1942–1948, Perth, Australia, November 1995.

J. Pugh, L. Segapelli, and A. Martinoli. Applying aspects of multi-robot search to particle swarm optimization. In *Proceedings of the 5th International Workshop on Ant Colony Optimization and Swarm Intelligence*, pages 506–507, Brussels, Belgium, 2006.

K. Sedlaczek and P. Eberhard. Using augmented Lagrangian particle swarm optimization for constrained problems in engineering. *Structural and Multidisciplinary Optimization*, 32(4):277–286, 2006.

Q. R. Tang and P. Eberhard. A PSO-based algorithm designed for a swarm of mobile robots. *Structural and Multidisciplinary Optimization*, 2009. (submitted).

Reconfigurable Planar Three-Legged Parallel Manipulators

M. John D. Hayes

Department of Mechanical and Aerospace Engineering, Carleton University, Ottawa, ON K1S 5B6, Canada

Abstract A new class of reconfigurable planar three legged platforms is introduced. Kinematic mapping techniques are applied to solve the forward and inverse kinematic problems, and to visualize the reachable workspace of the platform. The results show that the new class of manipulator is viable from a kinematic modelling point of view.

1 Introduction

There has been great interest in reconfigurable mechanisms in recent years (see Yim et al., March 2007, and Shen et al., 2003). Of particular interest is their application to manufacturing and assembly. This is partly due to the observation that such devices can change their topology (Fisher et al., 2004), which enables obstacle avoidance and the ability to move in crowded workspaces, et c.. What appears to be missing in the body of literature is a planar three-legged parallel manipulator kinematic architecture capable of changing the configuration of its moving platform, thereby enabling the reshaping of its reachable workspace. Such a platform could have applications to terrestrial and space telescope lens polishing and reshaping (Klimas, 2009).

In this paper, a novel architecture for reconfigurable three legged planar platforms with three degrees of freedom (DOF) is presented for the first time. The architecture comprises three revolute-prismatic-revolute (RPR) legs where the distal end of each kinematic chain is connected to a distinct point on the moving platform, while the other end is connected to ground. The moving platform is manipulated by changing the lengths of each of the three active prismatic joints. Such a topologically symmetric platform is abbreviated as a 3-$R\underline{P}R$ platform. Reconfigurability is provided by three redundant active prismatic joints joining every adjacent pair of the distal ends of the three $R\underline{P}R$ chains, see Figure 1. These three connecting $R\underline{P}R$

chains essentially comprise the moving platform. When the length of one of the connecting $R\underline{P}R$ chains is varied, the configuration of the platform changes.

The change in the relative location of the platform attachment points changes the platform forward and inverse kinematics, as well as the shape of the reachable workspace. The three DOF provided by changing the relative locations of the platform attachments points are redundant, and are reserved exclusively for reconfiguring the platform. For the kinematic analysis presented in this paper, it is assumed that all prismatic pairs (P-pairs) are active, and can change length in a controlled manner. All remaining revolute pairs (R-pairs) are passive.

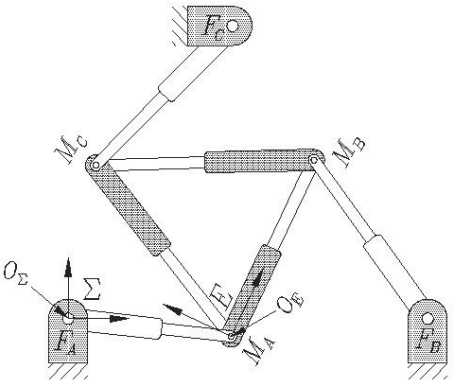

Figure 1. A reconfigurable planar three-legged platform.

The goals of this paper are to solve the forward and inverse position-level kinematic problems for such a platform, thereby demonstrating the viability of this class of platform from the perspective of kinematic modelling. The kinematic model developed by Hayes et al. (2004) will be adapted for this architecture. In addition, the reachable workspace envelope will be examined. This will be done by considering the limits of travel of each of the active P-pairs, and generating the workspace envelopes, adapting the techniques from Husty (1996) and Hayes (Oct. 2002).

2 The Forward And Inverse Kinematics Problem

Kinematic mapping may be used to compute the forward and inverse kinematics of reconfigurable 3-$R\underline{P}R$ planar platforms. While a very thorough discussion may be found in Bottema and Roth (1990), the essential idea is to

map the three homogeneous coordinates of the pole of a planar displacement to the points of a three dimensional projective image space.

Consider the reference frame E which can undergo general planar displacements relative to reference frame Σ, as illustrated in Figure 1. Let the homogeneous coordinates of points in the moving frame E be the ratios $(x : y : z)$, and homogeneous coordinates of the same point, but expressed in the fixed frame Σ, be the ratios $(X : Y : Z)$. The kinematic mapping image space coordinates are defined as:

$$\begin{aligned} X_1 &= a\sin(\varphi/2) - b\cos(\varphi/2); \quad X_2 = a\cos(\varphi/2) + b\sin(\varphi/2); \\ X_3 &= 2\sin(\varphi/2); \quad X_4 = 2\cos(\varphi/2); \end{aligned} \tag{1}$$

where a and b are the $(X/Z, Y/Z)$ Cartesian coordinates of the origin of E expressed in Σ, and φ is the orientation of E relative to Σ, respectively.

By virtue of the relationships expressed by Equations (1), the linear transformation that represents the basic group of planar Euclidean displacements of E with respect to Σ in terms of the image point is (Bottema and Roth, 1990)

$$\lambda \begin{bmatrix} X \\ Y \\ Z \end{bmatrix} = \begin{bmatrix} X_4^2 - X_3^2 & -2X_3X_4 & 2(X_1X_3 + X_2X_4) \\ 2X_3X_4 & X_4^2 - X_3^2 & 2(X_2X_3 - X_1X_4) \\ 0 & 0 & X_3^2 + X_4^2 \end{bmatrix} \begin{bmatrix} x \\ y \\ z \end{bmatrix}, \tag{2}$$

where λ is some non-zero constant arising from the use of homogeneous coordinates.

It has been shown (Hayes et al., 2004) that displacements of E relative to Σ in a planar 3-$R\underline{P}R$ platform map to the points of intersection of three quartics in X_i, each of which factors into two quadrics. The geometry of each $R\underline{P}R$ leg defines one of the quartics, having the following form:

$$\begin{aligned} &\big(K_0z^2(X_1^2 + X_2^2) + (-K_0x + K_1z)zX_1X_3 + (-K_0y + K_2z)zX_2X_3 \\ &-(K_0y + K_2z)zX_1X_4 + (K_0x + K_1z)zX_2X_4 - (K_1y - K_2x)zX_3X_4 \\ &\qquad + \tfrac{1}{4}[K_0(x^2 + y^2) - 2z(K_1x + K_2y) + K_3z^2]X_3^2 \\ &+ \tfrac{1}{4}[K_0(x^2 + y^2) + 2z(K_1x + K_2y) + K_3z^2]X_4^2\big)\left(\tfrac{1}{4}(X_3^2 + X_4^2)\right) = 0. \end{aligned} \tag{3}$$

The *circle coordinates* (Hayes et al., 2004) which constrain the surface are $\mathbf{K} = [K_0 : K_1 : K_2 : K_3]$, and are artifacts of the geometry of each leg. The coordinate K_0 is an arbitrary homogenising constant, while $K_1 = -X_c$, $K_2 = -Y_c$, $K_3 = X_c^2 + Y_c^2 - r^2$, X_c and Y_c being the Cartesian coordinates of the centre of the ground fixed R-pair, and r is the length of the P-pair. The parameters X_c, Y_c, and r define a circle on which the centre of the distal R-pair must move.

The factor $1/4(X_3^2 + X_4^2)$ is exactly the non-zero condition of the planar kinematic mapping (Bottema and Roth, 1990), which must be satisfied for a point to be the image of a real displacement. Hence, this factor must be non-zero and may be safely divided out of the equation, leaving only the one quadric.

The set of three quadric constraint equations can always be simplified by setting $K_0 = X_4 = z = 1$ (Hayes and Husty, 2003) whereby the three quadrics take the form of three hyperboloids of one sheet when projected into the hyperplane $X_4 = 1$. These generally skew hyperboloids have the special property that they always have circular traces in planes parallel to $X_3 = 0$.

Moreover, the moving platform has a geometry defined by the locations of the vertices of the triangle determined by the three moving platform reference points, which in turn is defined by the lengths of the 3-$R\underline{P}R$ platform P-pairs. The forward kinematic problem can be stated as *given the lengths of the active P-pairs in each ground-fixed leg, and the lengths of the active P-pairs comprising the moving platform, what is the resulting position and orientation of the moving platform*? Solutions, if they exist, are the mutual intersections of the three constraint hyperboloids.

The inverse kinematic problem can be similarly stated as *given the position and orientation of the moving platform, together with its geometry, what are the lengths of the active P-pairs in each ground-fixed leg required to attain the specified pose*? Each leg can be considered separately because the solutions are decoupled from leg-to-leg. For any of the three legs, the distance between the fixed base point, F, and the moving platform point, M for that leg is the radius r of the constraint circle (the length of the P-pair, all other quantities being constants, see Figure 1. After setting $K_0 = X_4 = z = 1$, then substituting the coordinates of the image space point, $[X_1 : X_2 : X_3 : X_4]$, together with specified values for x, y, K_1, K_2, and K_3 into Equation (3), then expanding and collecting in terms of r yields a quadratic having the form:

$$Sr^2 + T = 0; \tag{4}$$

where

$$\begin{aligned} S &= -(X_3^4 + 1); \\ T &= 4(X_1^2 + X_2^2) + ((K_1^2 + K_2^2) - 2(K_1x + K_2y) + x^2 + y^2)X_3^2 + \\ &\quad (K_1^2 + K_2^2) + 2(K_1x + K_2y) + x^2 + y^2 + 4(K_1 - x)X_1X_3 - \\ &\quad (K_2 + y)X_1 + (K_2 - y)X_2X_3 + (K_1 + x)X_2 + (K_2x - K_1y)X_3. \end{aligned}$$

While this result means that there are two real solutions, only one is acceptable since the quantity represents the radius of a circle, which is, by convention, a positive non-zero number:

$$r = \left| \frac{\sqrt{-ST}}{S} \right|. \tag{5}$$

3 Workspace Boundary Visualization

The individual $R\underline{P}R$ leg lengths, r_i, must be within the joint limits $r_{i_{min}} \leq r_i \leq r_{i_{max}}$, where i denotes one of the legs in the set $\{A, B, C\}$. This condition means that for each leg there correspond two coaxial constraint hyperboloids. They bound the region of all possible positions and orientations of the platform, assuming the platform attachment points of the other two legs have been disconnected. Performing the same procedure for each leg in turn yields three solid regions bounded by six hyperboloids, each pair coaxial. The volume common to the six surfaces is the image of the reachable workspace for a particular set of platform edge lengths.

The active P-pairs on the moving platform change the relative locations of the platform attachment points in the moving frame E. This has the effect of translating the respective locations of the hyperboloid axes in the image space. Because the origin of E is on the platform attachment point of Leg A, the constraint hyperboloid axis of Leg A is invariant, whereas the axis locations for the other two legs can be manipulated. Regardless, the reachable workspace bounds are reshaped by changing the lengths of the active platform P-pairs.

4 Example

The following example illustrates: the forward and inverse kinematic solution procedures for arbitrary P-pair lengths within the ranges of travel of the three legs, and three platform edges; the effects of altering the geometry of the moving platform on the boundaries of the reachable workspace.

The goal in this first part is to solve the forward kinematic problem given arbitrary lengths of the three P-pair legs and three P-pair moving platform edges within finite bounds. Table 1 lists the ground-fixed R-pair centres expressed in Σ, the moving platform attachments expressed in E, the limits on the lengths of the base P-pairs, and the limits on the associated circle coordinates. An arbitrary set of leg lengths and platform edge lengths are listed in Table 2. These are the inputs to the forward kinematics problem.

Applying the algorithm described in Section 2 reveals that the three

constraint surfaces intersect in two real points. The two corresponding Cartesian poses of the platform, relative to Σ, are listed in Table 3, and illustrated in Figure 2.

Table 1. Manipulator kinematic geometry: fixed, minimum and maximum leg lengths and circle coordinates.

i	$F_{i/\Sigma}$	$M_{i/E}$ min	$M_{i/E}$ max	r_i min	r_i max	$\mathbf{K}_i$ min	$\mathbf{K}_i$ max
A	(0:0:1)	(0:0:1)	(0:0:1)	2	3	[1:0:0:-4]	[1:0:0:-9]
B	(4:0:1)	(2:0:1)	(3:0:1)	2	3	[1:-4:0:12]	[1:-4:0:7]
C	(2:4:1)	(1:$\sqrt{3}$:1)	($\frac{3}{2}$:$\frac{3}{2}\sqrt{3}$:1)	2	3	[1:-2:-4:16]	[1:-2:-4:11]

Table 2. Arbitrary kinematic geometry.

i	r_i	$M_{i/E}$
A	9/4	(0:0:1)
B	5/2	(9/4:0:1)
C	11/4	(1:7/4:1)

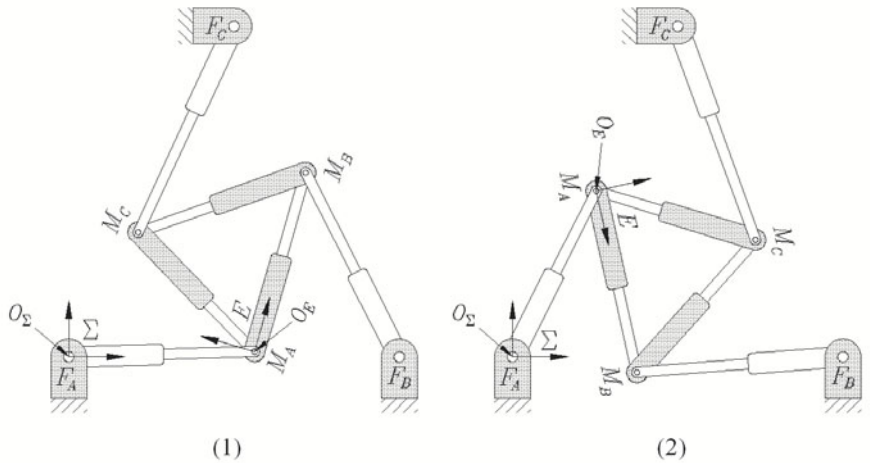

Figure 2. Two real solutions for the arbitrary geometry forward kinematic problem.

Next, the inverse kinematics problem is solved by determining the joint input value from the image point satisfying the associated constraint surface

Table 3. The two real solutions.

Solution	a	b	φ (deg.)
1	2.249073252	0.06457102532	74.07534341
2	1.014270872	2.008420726	-77.35021607

equation for each leg of the platform. When the two poses, the solutions to the forward kinematics problem, defined by a, b, and φ listed in Table 3 are mapped to X_1, X_2, and X_3, together with the appropriate fixed kinematic geometry listed in Table 1 are substituted into Equation (4), the result is exactly the inputs to the forward kinematics problem: the leg lengths listed in Table 2.

Finally, the effects of altering the geometry of the moving platform on the boundaries of the reachable workspace is addressed. The shape of the workspace is modified by changing the lengths of the three prismatic joints comprising the moving platform. For the kinematic geometry limits listed in Table 1, the corresponding bounding minimum and maximum hyperboloids are ilustrated in Figure 3.

Figure 3(a) illustrates the effects of changing the location of the platform attachment point for Leg C between it's minimum and maximum location in E. The axes of the two coaxial families of constraint hyperboloids are seen to be displaced. The total volume in common to the five sets of constraint hyperboloids is the kinematic mapping image of the reachable workspace. Cross-sections in the planes planes $X_3 = t$, where t is an arbitrary constant, reveal the reachable workspace at a particular orientation corresponding to $X_3 = t$.

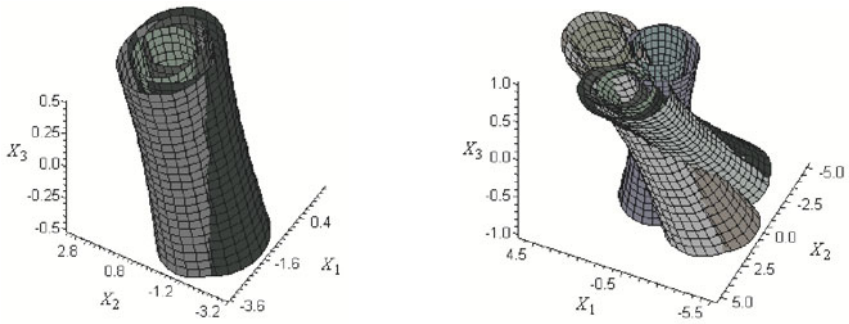

(a) Image of Leg C workspace.

(b) Image of platform workspace.

Figure 3. Kinematic image of the reachable workspace.

5 Conclusions

In this paper, a novel architecture for reconfigurable three legged planar platforms with three DOF has been presented for the first time. Reconfigurability is provided by three redundant active prismatic joints connecting every adjacent pair of distal ends of the three ground fixed $R\underline{P}R$ chains. The platform forward and inverse kinematics, as well as the effects of change in the relative location of the platform attachment points on the area of the reachable workspace have been illustrated with an example. These results demonstrate the kinematic feasibility of this class of reconfigurable three legged planar platform.

Bibliography

O. Bottema and B. Roth. *Theoretical Kinematics.* Dover Publications, Inc., New York, N.Y., U.S.A., 1990.

R. Fisher, R. P. Podhorodeski, and S. B. Nokleby. "Design of a Reconfigurable Planar Parallel Manipulator". *Journal of Robotic Systems*, vol. 21, no. 12: pages 665–675, 2004.

M.J.D. Hayes. "Architecture Independent Workspace Analysis of Planar Three-Legged Manipulators". *Proceedings of the WORKSHOP on Fundamental Issues and Future Research Directions for Parallel Mechanisms and Manipulators,* Québec, QC, Canada, pages 57–66, Oct. 2002.

M.J.D. Hayes and M.L. Husty. "On the Kinematic Constraint Surfaces of General Three-Legged Planar Robot Platforms". *Mechanism and Machine Theory*, vol. 38, no. 5: pages 379–394, 2003.

M.J.D. Hayes, P.J. Zsombor-Murray, and C. Chen. "Kinematic Analyais of General Planar Parallel Manipulators". *ASME, Journal of Mechanical Design*, 2004.

M.L. Husty. "On the Workspace of Planar Three-legged Platforms". *Proc. World Automation Conf., 6th Int. Symposium on Rob. and Manuf.* (ISRAM 1996), Montpellier, France, vol. 3: pages 339–344, 1996.

P. Klimas. "Research Possibilities into Mirror Polishing". *private communication,* (COM DEV Ottawa), 2009.

W.-M. Shen, P. Will, and B. Khoshnevis. "Self-Assembly in Space via Self-Reconfigurable Robots". *Multi-robot systems: from swarms to intelligent automata: proceedings from the 2003 International Workshop on Multi-Robot Systems edited by Alan C. Schultz, Lynne E. Parker, Frank E. Schneider*, pages 165–177, 2003.

M. Yim, W.-M. Shen, B. Salemi, D. Rus, M. Moll, H. Lipson, E. Klavins, and G.S. Chirikjian. "Modular Self-Reconfigurable Robot Systems: Challenges and Opportunities for the Future". *IEEE Robotics & Automation Magazine*, pages 43–52, March 2007.

Multi-Objective Trajectory Planning in Wire-Actuated Parallel Manipulators

Maryam Agahi and Leila Notash
Department of Mechanical and Materials Engineering, Queen's University, Kingston, ON, Canada

In the work presented, the redundancy resolution of planar wire-actuated parallel manipulators is investigated at the torque level in order to perform desirable tasks while maintaining positive tension in each wire. A local optimization routine is used in order to minimize the norm of actuator torques, maintain positive tension in each wire, reduce the effect of impact and avoid collision while modifying the trajectory of the mobile platform. The effectiveness of the presented approach is studied through a simulation of an example planar wire-actuated manipulator.

1. Introduction

In closed-loop manipulators, if the number of actuators is greater than the degrees of freedom of the manipulator, the manipulator is redundantly actuated and for a given end effector trajectory and external forces/moments, an infinite number of actuator torques/forces exists. Redundant manipulators can use their degree(s) of redundancy to satisfy additional desirable task(s), e.g., to reduce actuators forces/torques. In wire-actuated parallel manipulators, wires connect the mobile platform to the base and have the advantage of being light weight, reconfigurable and transportable, and allowing high speed motion and a larger workspace compared to conventional manipulators. Wires can only apply force in the form of tension. Therefore, to design a fully controllable wire-actuated parallel manipulator, the manipulator has to be redundantly actuated. Thus, to keep positive tension in all wires, at least $n+1$ wires are required for a manipulator with n degrees of freedom (DOF) (Kawamura et al. 2000).

When resolving redundancy at the torque level, the null term of actuator forces/torques is interpreted as portions of actuator forces/torques that result in zero forces/moments at the end effector. Because of the existence of infinite solutions for the actuator forces/torques, the proper use of the null term is of great importance in redundancy resolution.

The kinematic, dynamic and stiffness analyses, as well as, the design of wire-actuated manipulators have been investigated, e.g., (Kawamura et al. 2000, Williams and Gallina 2003, Oh and Agrawal 2005, Notash and Kamalzadeh 2007, McColl and Notash 2009, Agahi and Notash 2009). Oh and Agrawal (2005), and Agahi and Notash (2009) investigated how to design positive tension controllers for wire-actuated manipulators with redundant wires to follow prescribed

trajectories. For kinematically redundant manipulators, obstacle avoidance approaches have been proposed, e.g., (Maciejewski and Klein 1985).

In the presented work, redundancy resolution of wire-actuated parallel manipulators during collision is investigated. The collision is detected considering the minimum distance between the mobile platform and a specified obstacle. Some of the challenges associated with the redundancy resolution of wire-actuated parallel manipulators, including positive tension in each wire and infinite inverse dynamic solutions, are addressed. The effect of impact during collision is reduced and the error in the trajectory of the mobile platform after collision is minimized. The kinematic and dynamic modelling of an example planar wire-actuated parallel manipulator is presented in Section 2. The collision detection method is explained in Section 3. The multi-objective redundancy resolution scheme is given in Section 4. Simulation results are discussed in Section 5 in order to verify the effectiveness of the redundancy resolution technique. The conclusion of the article is in Section 6.

2. Modelling

The kinematics and dynamics of a planar wire-actuated parallel manipulator shown in Figure 1(a) are investigated for redundancy resolution. Moreover, the dynamical problem of collision with stationary obstacles is discussed. Figure 1 shows the coordinates and parameters used for the analysis of a planar wire-actuated parallel manipulator. The fixed coordinate system $\Psi(X, Y)$, located at O, is attached to the base, while the moving coordinate system, $\Gamma(X', Y')$, is attached to the mobile platform at its centre of mass P with position vector of $\mathbf{x} = [x, y]^T$ in $\Psi(X, Y)$. All vector expressions will be in the base reference frame unless otherwise stated. The position of base attachment point of each wire (anchor) A_i is $\mathbf{a}_i = [a_{ix}, a_{iy}]^T$, the position of attachment point on the mobile platform B_i is $\mathbf{r}_{Bi/P} = [r_{Bi/P}\cos\theta_i, r_{Bi/P}\sin\theta_i]^T$ in $\Gamma(X', Y')$, and $\mathbf{l}_i = [l_i\cos\alpha_i, l_i\sin\alpha_i]^T$ is the vector of the magnitude and direction of each wire length. When collision occurs, the mobile platform becomes in contact with the obstacle at point C, as shown in Figure 1(a). The position vector of contact point C is $\mathbf{r}_{C/P} = [r_{C/P}\cos\theta_{nc}, r_{C/P}\sin\theta_{nc}]^T$ in $\Gamma(X', Y')$. As shown in Figure 1(a), the position of the centre of the circular obstacle Q with respect to O and P are $\mathbf{r}_{Q/O} = [r_{Q/Ox}, r_{Q/Oy}]^T$ and $\mathbf{r}_{Q/P} = [r_{Q/Px}, r_{Q/Py}]^T$, respectively. $\mathbf{F}_{nc}$ is the normal contact force acting towards the center of the mobile platform (due to the circular shape of the mobile platform) and $\mathbf{F}_f$ is the friction force acting on the mobile platform in the opposite direction of the motion of the mobile platform.

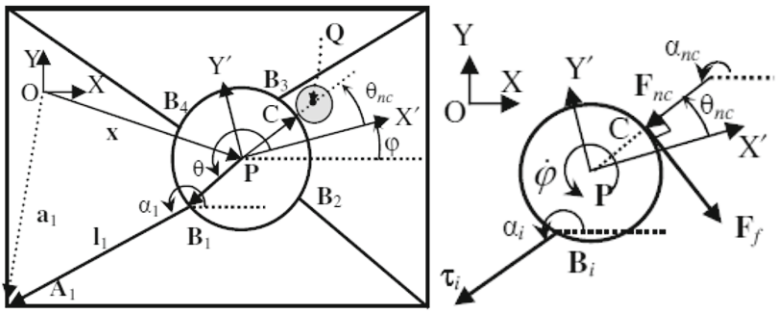

Figure 1. (a) Coordinates and variables for planar parallel manipulators during collision, (b) free-body diagram of the mobile platform during collision.

The inverse velocity solution that relates the mobile platform velocity $\dot{\mathbf{x}} = [\dot{x}, \dot{y}, \dot{\varphi}]^T$ to the wire length rates $\dot{\mathbf{l}} = [\dot{l}_1, \ldots, \dot{l}_n]^T$ is given by

$$\begin{bmatrix} \dot{l}_1 \\ \vdots \\ \dot{l}_n \end{bmatrix} = -\begin{bmatrix} c_1 & s_1 & -r_{B_1/P}\, s(\varphi + \theta_1 - \alpha_1) \\ \vdots & \vdots & \vdots \\ c_n & s_n & -r_{B_n/P}\, s(\varphi + \theta_n - \alpha_n) \end{bmatrix} \begin{bmatrix} \dot{x} \\ \dot{y} \\ \dot{\varphi} \end{bmatrix} = -\mathbf{J} \begin{bmatrix} \dot{x} \\ \dot{y} \\ \dot{\varphi} \end{bmatrix} \tag{1}$$

where c_i, s_i and $s(\varphi + \theta_i - \alpha_i)$ stand for $\cos\alpha_i$, $\sin\alpha_i$ and $\sin(\varphi + \theta_i - \alpha_i)$, respectively, φ is the orientation of the mobile platform and n ($n \geq 4$) is the number of wires. From dynamic force and moment balances

$$\mathbf{J}^T \begin{bmatrix} \tau_1 \\ \vdots \\ \tau_n \end{bmatrix} = \begin{bmatrix} m & 0 & 0 \\ 0 & m & 0 \\ 0 & 0 & I_z \end{bmatrix} \begin{bmatrix} \ddot{x} \\ \ddot{y} \\ \ddot{\varphi} \end{bmatrix} - \begin{bmatrix} 0 \\ -mg \\ 0 \end{bmatrix} - \begin{bmatrix} F_{ext_x} \\ F_{ext_y} \\ M_{ext_z} \end{bmatrix} = \mathbf{M} \begin{bmatrix} \ddot{x} \\ \ddot{y} \\ \ddot{\varphi} \end{bmatrix} - \mathbf{g} - \begin{bmatrix} F_{ext_x} \\ F_{ext_y} \\ M_{ext_z} \end{bmatrix} \tag{2}$$

where m and I_z are the mass and moment of inertia of the mobile platform respectively, $\ddot{x}$ and $\ddot{y}$ are the components of linear accelerations and $\ddot{\varphi}$ is the angular acceleration of the mobile platform, $[\tau_1, \ldots, \tau_n]^T$ is the vector of dynamic wire forces, F_{ext_x} and F_{ext_y} are the components of the external force, M_{ext_z} is the external moment acting on the mobile platform, $\mathbf{M}$ is the inertia matrix, and $\mathbf{g}$ is the vector of gravitational force with $g = 9.81$ m/s^2. Considering Figure 1(b), in the absence of any other external force/moment, $\mathbf{F}_{ext}$ and M_{ext_z} can be written as

$$\begin{aligned} \mathbf{F}_{ext} &= \mathbf{F}_{nc} + \mathbf{F}_f \\ M_{ext_z} &= -F_{nc} r_{C/P} \sin(\varphi + \theta_{nc} - \alpha_{nc}) + F_f r_{C/P} \cos(\varphi + \theta_{nc} - \alpha_{nc}) \operatorname{sgn}(\dot{\varphi}) \end{aligned} \tag{3}$$

where $\operatorname{sgn}(\dot{\varphi}) = 1$ if $\dot{\varphi} > 0$, $\operatorname{sgn}(\dot{\varphi}) = 0$ if $\dot{\varphi} = 0$, and $\operatorname{sgn}(\dot{\varphi}) = -1$ if $\dot{\varphi} < 0$, and α_{nc} defines the orientation of the normal contact force $\mathbf{F}_{nc}$. Considering $F_f = \mu_k F_{nc}$, where μ_k is the coefficient of kinetic friction, equation (2) is simplified as

$$\mathbf{J}^T\begin{bmatrix}\tau_1\\ \vdots\\ \tau_n\end{bmatrix}=\mathbf{M}\begin{bmatrix}\ddot{x}\\ \ddot{y}\\ \ddot{\varphi}\end{bmatrix}-\mathbf{g}-F_{nc}\begin{bmatrix}\cos\alpha_{nc}+\mu\cos(\alpha_{nc}+\frac{\pi}{2}\mathrm{sgn}(\dot{\varphi}))\\ \sin\alpha_{nc}+\mu\sin(\alpha_{nc}+\frac{\pi}{2}\mathrm{sgn}(\dot{\varphi}))\\ -r_{C/P}\sin(\varphi+\theta_{nc}-\alpha_{nc})+\mu r_{C/P}\cos(\varphi+\theta_{nc}-\alpha_{nc})\mathrm{sgn}(\dot{\varphi})\end{bmatrix} \tag{4}$$

The solution of equation (4) is given by

$$\begin{bmatrix}\tau_1 & \dots & \tau_n\end{bmatrix}^T=\mathbf{J}^{T\#}\left(\mathbf{M}\begin{bmatrix}\ddot{x} & \ddot{y} & \ddot{\varphi}\end{bmatrix}^T-\mathbf{g}-F_{nc}\mathbf{c}\right)+(\mathbf{I}-\mathbf{J}^{T\#}\mathbf{J}^T)\mathbf{k}=\boldsymbol{\tau}_p+\boldsymbol{\tau}_h \tag{5}$$

where $\mathbf{c}$ is the vector of coefficients of the normal contact force F_{nc} in equation (4). $\boldsymbol{\tau}_p=\mathbf{J}^{T\#}(\mathbf{M}[\,\ddot{x}\;\ddot{y}\;\ddot{\varphi}\,]^T-\mathbf{g}-F_{nc}\mathbf{c})$ is the minimum norm (particular) solution of equation (4) and $\mathbf{J}^{T\#}=\mathbf{J}(\mathbf{J}^T\mathbf{J})^{-1}$ is the generalized inverse of matrix $\mathbf{J}^T$, and $\boldsymbol{\tau}_h=(\mathbf{I}-\mathbf{J}^{T\#}\mathbf{J}^T)\mathbf{k}$ is the homogeneous solution that maps the free vector $\mathbf{k}$ to the null space of $\mathbf{J}^T$. The homogeneous solution could be written as $\boldsymbol{\tau}_h=\mathbf{N}\boldsymbol{\lambda}$, where $\mathbf{N}$ is a matrix that its columns correspond to the orthonormal basis for the null space of $\mathbf{J}^T$ and may be determined using the singular value decomposition, and $\boldsymbol{\lambda}$ is an arbitrary vector. To resolve the redundancy at the torque level, for given trajectories of the platform, a $\boldsymbol{\lambda}$ is identified (if it exists) at each instant such that a desirable task is achieved avoiding negative tension in each wire. It should be noted that throughout this paper, the term "norm" stands for the 2-norm, and all minimizations correspond to the 2-norm of the relevant vector. The constraint tension function, which is the solution to equation (2), is

$$\boldsymbol{\tau}=\boldsymbol{\tau}_p+\mathbf{N}\boldsymbol{\lambda}\geq\boldsymbol{\tau}_{\min} \tag{6}$$

If $\mathbf{J}^T$ in equation (4) has full row-rank, then $\mathbf{J}^{T\#}$ is invariant to the choice of weighing metric, e.g., Doty et al. (1995). Thus, using a weighing metric is not required.

3. Collision Detection

To detect collision, the minimum distance between the mobile platform and the obstacle is monitored at each time instant. When collision occurs, the given trajectory of the mobile platform is modified such that the minimum distance between the mobile platform and the obstacle is greater than a threshold. When the mobile platform and the obstacle are circular, the minimum distance d is calculated as $d=\overline{PQ}-(r_{C/P}+r_{ob})$, where r_{ob} is the radius of the obstacle. Given the position of the centre of obstacle $\mathbf{r}_{Q/O}$, and pose (position and orientation) of the platform, the position of Q relative to P is $\mathbf{r}_{Q/P}=[\,r_{Q/O_x}-x,\ r_{Q/O_y}-y\,]^T$. Using the orientation of $\mathbf{r}_{Q/P}$, i.e., $\theta_{nc}=\tan^{-1}(r_{Q/Py}/r_{Q/Px})-\varphi$, the orientation of the normal contact force F_{nc} is $\alpha_{nc}=\pi+(\theta_{nc}+\varphi)$. Then, α_{nc} is substituted into equation (4) to construct the solution of wire tensions as given by equation (5).

4. Trajectory Planning and Impact Reduction

When collision occurs, the given trajectory of the mobile platform has to be modified while keeping positive tension in each wire and satisfying additional desirable criteria, i.e., minimizing the norm of tension in the wires for a given normal contact force $\mathbf{F}_{nc}$ and minimizing the trajectory deviation from the desired trajectory of the mobile platform. In the work presented, before collision occurs, redundancy will be resolved at the torque level while tracing the given trajectory of the mobile platform. Therefore, the optimization problem before collision is formulated as follows:

$$\begin{aligned} &\text{minimize } \boldsymbol{\tau}^T\boldsymbol{\tau} = \tau_1^2 + \cdots + \tau_n^2 \\ &\text{subject to } \boldsymbol{\tau} = \boldsymbol{\tau}_p + \mathbf{N}\boldsymbol{\lambda}_\tau \geq \boldsymbol{\tau}_{\min} \end{aligned} \tag{7}$$

For each pose of the mobile platform, the value of $\boldsymbol{\lambda}_\tau$ is calculated such that minimum wire tensions are maintained subject to positive tension in each wire. When there is no external force/moment, $[F_{ext_x}, F_{ext_y}, M_{ext_z}] = [0, 0, 0]$. When collision occurs, the minimum positive tension in the wires is determined for each time instant such that the normal contact force F_{nc} does not exceed a certain value. For the subsequent instants, the trajectory of the mobile platform is modified while collision is avoided and the modified trajectory traces the given mobile platform trajectory as close as possible. Then, using the redundancy of the manipulator, the minimum tension in the wires is calculated such that the tension of each wire is positive. If the positive tension in each wire is not achieved, the trajectory is modified again and the tension minimization procedure is repeated. For this purpose, the trajectory of the mobile platform is

$$\mathbf{x}(t) = \begin{bmatrix} x & y & \varphi \end{bmatrix}^T = \begin{cases} \mathbf{x}_o(t) & t \leq t_c \\ \mathbf{x}_o(t) + \mathbf{x}_{\text{var}}(t) & t_c < t \leq t_{oc} \end{cases} \tag{8}$$

where t_c is the instant at which the minimum distance d becomes zero and collision occurs, t_{oc} is the time instant to clear the obstacle. The given trajectory of the mobile platform $\mathbf{x}_o(t)$ is chosen to be a fifth order polynomial, and $\mathbf{x}_{\text{var}}(t) = [x_{\text{var}}(t), y_{\text{var}}(t), \varphi_{\text{var}}(t)]^T$ is referred to as the variable portion of the mobile platform trajectory and is calculated at each time instant after collision. Once the mobile platform clears the obstacle, $\mathbf{x}_{\text{var}}(t) = 0$. The fifth order trajectories for x_o, y_o and φ_o are chosen to satisfy eighteen initial and final boundary conditions of the trajectory, $\mathbf{x}$, and its derivatives.

In order to have continuous x_{var} and y_{var} for $t > t_c$, when collision occurs, the original trajectory of the mobile platform is changed in a way that x_{var} and y_{var} are modified dependently considering the slope of the line $\overline{PQ}$, as shown in Figure 1(a). The trajectory is modified at $t = t_c + \Delta t$ using $y_{\text{var}} = -x_{\text{var}} \tan(\varphi + \theta_{nc})$, where Δt is the time step. For $t > (t_c + \Delta t)$, similar to the collision instant, the modified trajectory is along the line that is perpendicular to $\overline{PQ}$ and tangential to

both circular objects, and is such that $\overline{PQ} \geq r_{Bi/P} + r_{ob} + \delta_{th}$, where δ_{th} is the minimum distance threshold. Using $\mathbf{x}_{\text{var}}$, the constraint function represented in equation (7) will become a function of x_{var}, y_{var} and φ_{var}. The goals after collision are to trace the given trajectory as close as possible and minimize the tension in the wires, so the objective functions are to minimize $\mathbf{x}_{\text{var}}^T \mathbf{x}_{\text{var}} = x_{\text{var}}^2 + y_{\text{var}}^2 + \varphi_{\text{var}}^2$ and $\boldsymbol{\tau}^T \boldsymbol{\tau} = \tau_1^2 + \cdots + \tau_n^2$, one at a time, subject to $\boldsymbol{\tau}(t, x_{\text{var}}, y_{\text{var}}, \varphi_{\text{var}}) \geq \boldsymbol{\tau}_{\min}$.

In the simulation, the wires are allowed to cross over the obstacle which could occur when the obstacle and the wires are on different planes. After calculating x_{var}, y_{var} and φ_{var}, at each time instant ($t > t_c$), the minimum $\boldsymbol{\lambda}$ is calculated that maintains positive tension in each wire. The velocity and acceleration of the platform are then approximated using backward difference method as $\dot{\mathbf{x}}(t_i) = (\mathbf{x}(t_i) - \mathbf{x}(t_{i-1}))/(t_{i-1} - t_i)$ and $\ddot{\mathbf{x}}(t_i) = (\dot{\mathbf{x}}(t_i) - \dot{\mathbf{x}}(t_{i-1}))/(t_{i-1} - t_i)$, where i corresponds to the iteration number for the time step. The results are then substituted into equation (5) for tension optimization purposes.

5. Simulation

For the simulation, the anchor positions are $\{\mathbf{a}_1, \mathbf{a}_2, \mathbf{a}_3, \mathbf{a}_4\} = \{(-1, -0.75), (1, -0.75), (1, 0.75), (-1, 0.75)\}$ (units in meters), and the connection points of wires on the mobile platform are $\{\theta_1, \theta_2, \theta_3, \theta_4\} = \{225, 315, 45, 135\}$ (units in degree). The mass m, moment of inertia I_z, and radius $r_{Bi/P}$ of the mobile platform are respectively 2 kg, 0.0144 kg.m^2, and 0.125 m. The radius and position of the obstacle are $r_{ob} = 0.05$ m and $(r_{Q/Ox}, r_{Q/Oy}) = (0.25$ m, 0.1 m). The initial and final boundary conditions $(x, \dot{x}, \ddot{x}, y, \dot{y}, \ddot{y}, \varphi, \dot{\varphi}, \ddot{\varphi})$ are $(0, 0, 0, 0, 0, 0, 0, 0, 0)_0$ and $(0.25$ m, 0, 0, 0.25 m, 0, 0, 2 deg, 0, $0)_f$, respectively, with $t \in [0, 10]$ s and time step of $\Delta t = 0.01$ s. The minimum allowable tension of each wire is $\tau_{\min} = 2$ N. The upper limit on the actuator torques is calculated based on the maximum allowable wire tension of 525 N (McColl and Notash 2009).

With four wires, the constraint function in equation (7) is reduced to four linear inequalities in terms of $\boldsymbol{\lambda}_\tau$, where $\boldsymbol{\lambda}_\tau$ is reduced to a scalar. At the instant of collision, the maximum allowable normal contact force F_{nc} is 5 N. The termination tolerances placed on constraint violations are chosen as 0.001 N, on the objective function as 0.001 N^2, and on the estimated parameter values (i.e., λ_τ) as 0.0001 N. The simulation results are obtained using the *fmincon* function in MATLAB. Figure 2 shows the trajectories $\mathbf{x}$ and $\mathbf{x}_o$, and $\mathbf{x}_{\text{var}} = \mathbf{x} - \mathbf{x}_o$. Figure 2(b) shows how close $\mathbf{x}$ is to $\mathbf{x}_o$. Collision has occurred at instant $t_c = 3.92$ s. For $t > 3.92$ s, the minimization of $\mathbf{x}_{\text{var}}$ has resulted in the x component of the trajectory with lower magnitude compared to x_o. Therefore, due to location of the obstacle, the collision has delayed tracing the x component of the trajectory. The displacement of the platform in Y direction is not affected by the location of the obstacle noticeably.

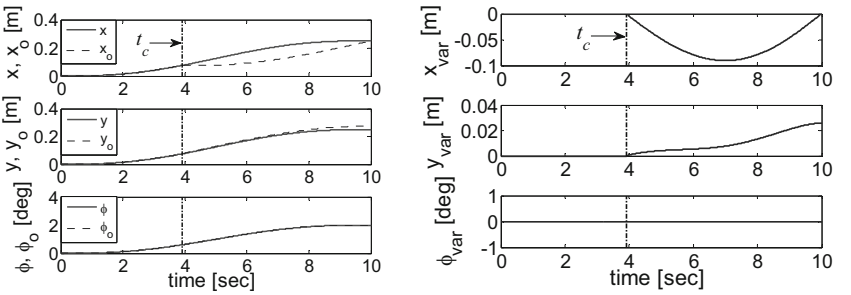

Figure 2. (a) Original and modified poses, (b) variable portion of the trajectory.

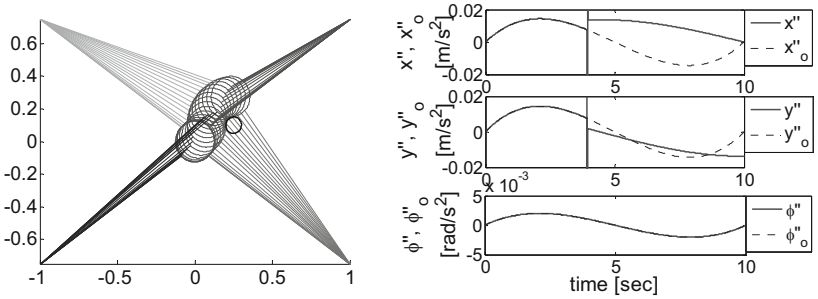

Figure 3. (a) Change in the configuration, (b) original and modified accelerations.

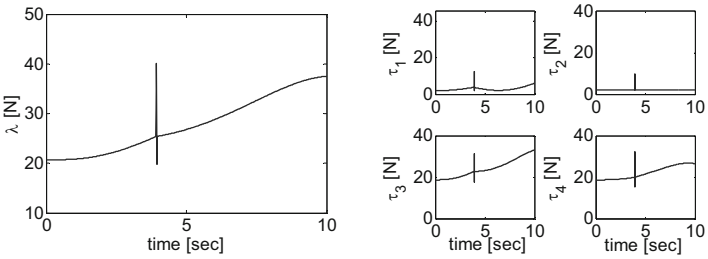

Figure 4. (a) Minimum λ, (b) wire tensions.

Figure 3(a) shows how the mobile platform moves around the obstacle until it clears the obstacle and then continues the original trajectory. Figure 3(b) depicts the actual acceleration of the platform. Collision results in jumps in the velocity and acceleration of the platform at $t_c = 3.92$ s. For $t > 3.92$ s, the trajectory of the platform is modified such that the magnitude of the acceleration should not exceed 3g m/s^2. The magnitude of the maximum linear acceleration is less than 0.5g m/s^2. Due to the redundancy of the manipulator, the orientation of the platform φ is remained unchanged and so are its derivatives. Figure 4(a) shows the minimum λ

that guarantees positive tension in each wire. Figure 4(b) illustrates the tension histories. It can be seen that the second wire is not critical (except for the collision instant) for maintaining the configurations shown in Figure 3(a). The peaks in the acceleration components of Figure 3(b) have resulted in discontinuous wire tensions at corresponding time instants.

6. Discussion and Conclusions

An approach to resolve the actuation redundancy of planar wire-actuated parallel manipulators was investigated to minimize the wire tensions and deviation in the trajectory while clearing an obstacle with positive tension in each wire. Before collision, a prescribed trajectory of the mobile platform was followed and the norm of wire tensions was minimized. The infinite solutions for wire tensions were utilized to identify a vector of wire tensions such that the contact force was kept below an assigned value while the wire tensions were minimized. After collision, the desired trajectory was modified at each time instant such that the platform traced its predefined trajectory as close as possible. Then, using the redundancy of the manipulator, the minimum norm tension in the wires was determined. The simulation of a 3-DOF planar wire-actuated parallel manipulator was developed satisfying objective functions and constraints. Based on the optimization criteria, the tolerances used in the optimization routine, the optimization scheme, and the desired continuous trajectories, continuous wire tensions were produced before and after collision.

References

Agahi, M. & Notash, L. (2009). Redundancy Resolution of Wire-Actuated Parallel Manipulators. *special edition of the Transactions of the Canadian Society of Mechanical Engineers*. 33(4):561-575.

Doty, K.I., Melchiorri, C. & Bonivento, C. (1995). A Theory of Generalized Inverses Applied to Robotics. *International Journal of Robotics Research*. 12(1):1-19.

Kawamura, S., Hitoshi, K. & Choe, W. (2000). High-speed manipulation by using parallel wire-driven robots. *Robotica*. 18:13-21.

McColl, D. & Notash, L. (2009). Extension of Antipodal Theorem to Workspace Analysis of Planar Wire-Actuated Manipulators. *Proc. of 5th IFToMM Int. Workshop on Computational* Kinematics. 9-16.

Notash, L. & Kamalzadeh, A. (2007). Inverse dynamics of wire-actuated parallel manipulators with a constraining linkage. *Mechanism and Machine Theory*. 42(9):1103-1118.

Oh, S. R. & Agrawal, S.K. (2005). Cable Suspended Planar Robots with Redundant Cables: Controllers with Positive Tensions. *IEEE Transactions on Robotics*. 22(3):457-465.

Williams II, R.L. & Gallina, P. (2003). Translational Planar Cable-Direct-Driven Robots. *Journal of Intelligent and Robotic Systems*. 37(1):69-96.

Design of the Facial Expression Mechanism for Humanoid Robots

Junyao Gao*, Qiang Huang*, Zhangguo Yu*, Xuechao Chen*, Wei Xu*, Weimin Zhang*, Qian Xu*, Ping Song*, Kejie Li*, Lin Xie*, Wenjuan Guo†, Renti Zou‡, Ziting Zou‡, and Yong Zhang‡ *

*Intelligent Robotics Institute, School of Mechatronical Engineering, Beijing Institute of Technology Beijing, China

†Beijing Huakaihui Information Technology, Co., Ltd, Beijing, China

‡Xi'an Chaoren Robot Technology Company, Xi'an, China

Abstract This paper introduces a new humanoid robot capable of facial expression modifications. Since the face and its expressions play a significant role for natural communication, the robotic face was developed using highly vivid facial expressions. After having outlined the development of the humanoid robot, we describe the distributed control system. Then, the design of the robotic face is presented. Finally, the typical facial expressions and walking patterns are demonstrated via experiments.

1 Introduction

A humanoid robot (HR) features human appearance and behaviors. HRs are capable to adapt to human life environments and coexist with human beings. HRs can perform a variety of tasks without introducing any modification to the standard tools and environment used by humans. The application of the HRs is limitless. HRs are the backbone of future generation home service robots, social entertainment robots and hazardous operation robots. During the last decade, many successful humanoid projects have been developed, such as ASIMO, WABIAN, HRP-2, H6, KHR-2, and JOHNNIE. Recently, Boston Dynamics demonstrated a hydraulically-powered biped walking at

*This work was supported by the National Natural Science Foundation of China under Grant 60874048, National Science Foundation for Distinguished Young Scholar under Grant 60925014, National High Technology Research and Development Program (863 Project) under Grant 2007AA04Z241, 2007AA041603 and 2008AA042601, and "111 Project" under Grant B08043. Corresponding Author: Junyao Gao, Email: gaojunyao@bit.edu.cn

a 3.2 *mph* speed. The progress in dynamic stability adjustments achieved by this prototype opens a new way to develop humanoid robots.

We launched the research on the humanoid robot in 2000. BHR-1 and BHR-2 humanoid robot prototypes were developed in 2002 and 2006.We also designed the BHR-3M series humanoid robots for serval science and technology museums in China. During the last decade, our main research effort was on humanoid robot mobility. As of recently, our focus has shifted to human-machine interaction, environment adaptability and safety aspects of humanoid robotics.

So far, many researchers have worked on robotic faces. Fukuda et al. studied human-robot mutual communication based on robotic faces (Fukuda et al., 2001). Tojo et al. developed a conversational robot using facial and body expressions (Tojo et al., 2000). Takanishi et al. developed an anthropomorphic robot head capable of expressing an autonomous facial expression using three independent parameters of a psychological model (Takanishi, 1999). Hara et al. developed a robotic face actuated by shape memory alloy (SMA) featuring six different facial expressions (Hara et al., 2001). Hashimoto et al.developed a face robot SAYA for rich facial expressions. Ge et al. studied active affective facial expressions (Ge et al., 2008). Itoh et al. developed a face robot that can express many types of human face by solving some problems of unsuitable wrinkle, low torque and low accuracy (Itoh et al., 2008). Hashimoto et al. developed a face robot reproducing dynamic facial expressions and face features successfully (Hashimoto et al., 2008). Most of the abovementioned works focused mainly on facial robotics. Works combing facial robotics and the mobility aspects of humanoid robotics have only started recently. The objective of this study is to develop a new humanoid robot to study facial expressions.

2 Architecture of the Humanoid Robot Prototype

The newly-built humanoid robot prototype for human-machine interaction has 51 active degrees of freedom (DOFs). The configuration of the DOFs of this prototype are as follows: 13 DOFs in face, 2 DOFs in neck, 6 DOFs in each arm (3 DOFs in shoulder, 1 DOFs in elbow, 2 DOFs in wrist), 5 DOFs in each hand, 2 DOFs in waist, and 6 DOFs in each leg (3 DOFs in each Hip, 1 DOFs in Knee, 2 DOFs in ankle). Its height and weight are $1.6m$ and $60kg$, respectively. Maximum walking speed is $2.0km/h$. The head is integrated with stereo CCD cameras, while wrists/feet feature torque/force sensors. Acceleration sensors and gyro sensors are embedded in the torso. The robot features also joint angle detection sensors. All in all the robot features vision, hearing, force and equilibrium sensing capability. The prototype can

walk straight and sideways, go around, negotiate stairs, perform Taiji and martial art, and some other complex motion, without resorting to external cables.

Both the face and the hands of the robot are made of silicone in order to improve the human-machine interaction. On the other hand, in order to enhance the environment adaptability of the robot, we added two waist joints (pitch and yaw DOFs) to adjust posture more conveniently. The hand design was also improved; it is now based on a designed a five-DOF mechanism. Each finger is implemented using a one-DOF mechanism.

The control system of the humanoid robot at hand includes *i*) the tele-operation system, *ii*) the audio-visual perception and planning (AVPP) system, and *iii*) the motion control system, as shown in Figure 1. The AVPP system is used to process vision and hearing sensor readouts. The operating system (OS) of each of the control sub-systems is Windows XP, except for the motion control system, while the communication interface is 802.11G wireless LAN. The OS of the main motion control computer is RT-Linux endowed with hard real-time capability.

Data communications between the AVPP system and the motion control system is implemented using Memolink boards from Interface Co. A controlled area network (CAN)-bus is used to support communication between the motion control system and the distributed joint actuators and sensors. However, the bit rate is limited (1Mbps). To cope with this, four CAN channels were adopted.

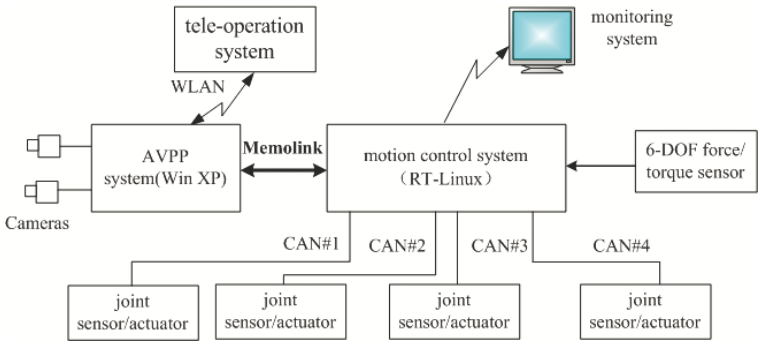

Figure 1. Architecture of the distributed control system.

3 Robot Face Design

3.1 Design Methodology

The procedure adopted to design the robotic face entails (see Figure 2):
(i) Acquisition of data associated to human facial expressions;
(ii) Data analysis aimed at identifying the active drive points (ADPs);
(iii) Design of the mechanism and of the controller;
(iv) Experiments.

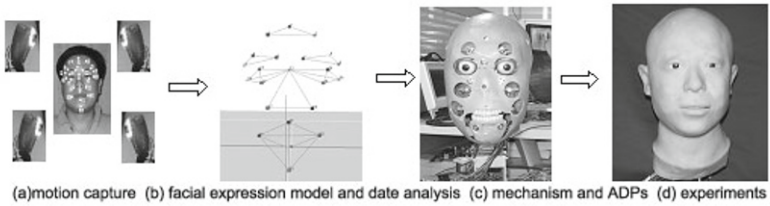

Figure 2. Procedure for designing the robot face.

3.2 Data Acquisition

In order to obtain the characteristics of human facial expression, we built an elementary face expression model. We define the key points of facial expression as the points by which most of the facial movement can be gotten. In this model, 23 key points are used to describe the facial expression (Figure 3): points at elbow middle(5,8), elbow head(6,7),elbow tail(4,9), eye tail(10,16), up eyelid(11,14), lower eyelid(12,15), nose corner(17,18), upper mouth lip(19), lower mouth lip(20), mouth corner(21,22), lower jaw (23). Note that in order to establish a base coordinate, other four points, at forehead (1,2,3), middle of eyes(13), is used as the base reference, since these points (1,2,3,13) are hardly move when human makes facial expression.

In order to acquire the data, a vision-based technique was adopted. The vision system consists of 12 optical cameras and 23 markers fixed on the actor's face. The system records three dimension data, namely the position (x, y, z) and velocity (V_x, V_y, V_z) of all markers at the rate of 100 frames per second with a position accuracy of 0.01mm. Data associated to the different facial expressions, such as smile, laugh, cry, anger, pain, astonishment, dissatisfaction and disgust, were collected. Figure 4 gives an example of the data acquired for the astonishment expression.

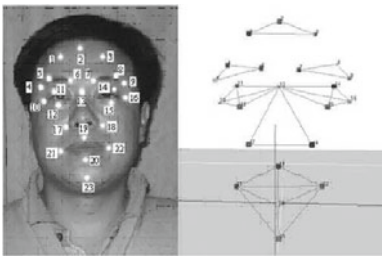

Figure 3. Key points and model of facial expression.

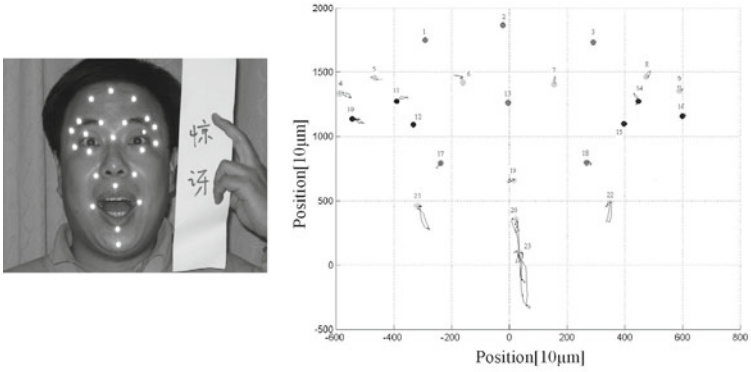

Figure 4. Data acquisition for the astonishment expression.

3.3 Active Drive Points

Based on both data analysis and experiments, we concluded that some of the key points, such as those located at the canthi, are indeed not needed to describe the facial expression. These points are not actively driving, but pulled passively by other parts of the face. Therefore, the irrelevant points were removed and new key points were added at the cheeks (9, 10 of Figure 5). Hence, 13 active drive points were selected. The design requirements for the facial skin are small thickness, high flexibility and strength. After a number of silicone rubber material experiments, a material with optimum ratio of components was developed. Its tensile strength, pulling strength, flexibility, and fatigue satisfy requirements of robot face skin. Through plastic injection process, the skin of the robot face was made. At each ADP, the skin is secured to the linkage using threaded fasteners. A stepper motor is used to drive the rigid links. The ATmega128 from ATMEL is

adopted to control the drive points synchronically. The motion control system described in Section 2, transmits the high level command to the ATmega128 to generate the desired facial expression. A prototype of the designed robotic head is illustrated in Figure 6.

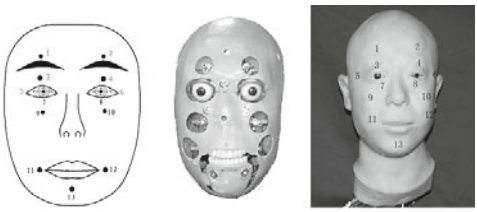

Figure 5. Active drive points on robot face.

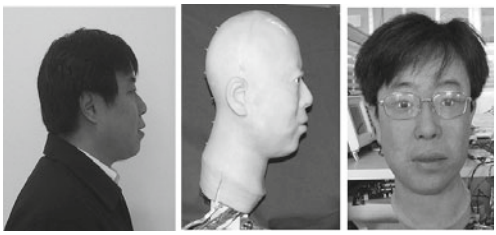

Figure 6. Experimental prototype of the robot head.

4 Experiment Results

4.1 Robotic Face Testing

The experimental prototype of the robot face features 13 DOFs. As shown in Figure 7, some complex facial expressions, such as smile, astonishment and pain, have been attempted using the robotic face. The weight of the prototype of the robot head is $3.5kg$.

4.2 Testing the Mobility of the Humanoid Robot

First, the walking gait data featuring the largest stability margin for dynamic locomotion on floor are calculated. The step length is $0.35m$, while the step cycle is $1.2s$. The zero moment point (ZMP) trajectories are shown in Figure 8. This Figure suggest that the walking gait is stable since the actual ZMP lines are within the stable boundary.

The experimental results of the humanoid robot walking test are illustrated in Figure 9. The humanoid robot could walk forward stably with a speed of $1km/h$. In our experiments, when this prototype of the robot head adds on the humanoid robot, the walking is still stable.

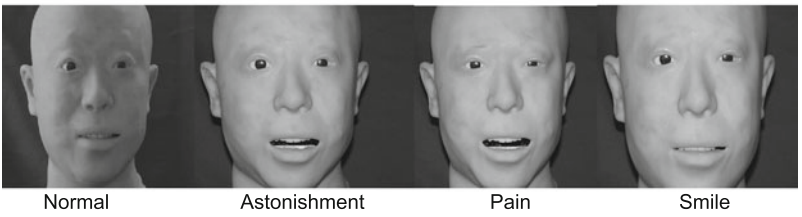

Figure 7. Testing different facial expression using the robotic face.

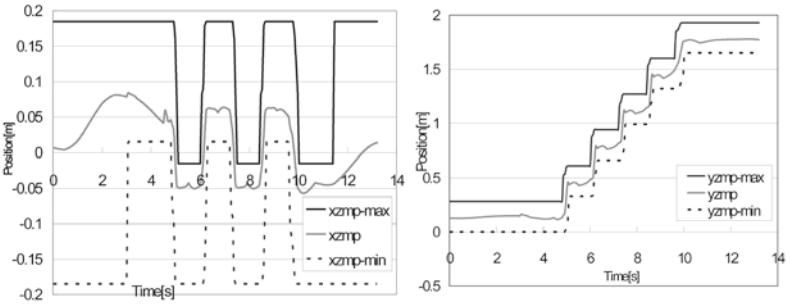

Figure 8. ZMP trajectories of the humanoid Robot.

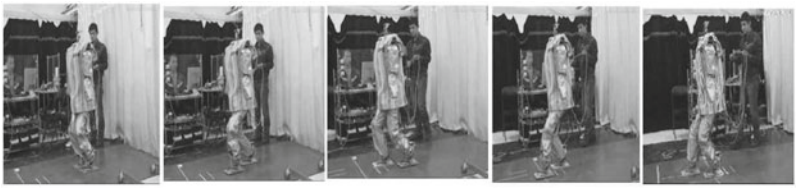

Figure 9. Experimental results of the humanoid robot walking test.

5 Conclusion

In this paper, we presented a new humanoid robot capable of performing different facial expressions. New mechanisms are embedded in the robot. Additionally, the design of the robotic face is also presented. The main results are summarized as follows: (1) A facial expression model including 13 active drive points is obtained. A robotic face with 13 DOFs is designed. Facial expressions include smile, laugh, cry, anger, pain, astonishment, and dissatisfaction. (2) The distributed control system of the humanoid robot is presented. (3) The performance of both the robotic face and of the mobility of the humanoid robot was demonstrated via experiments.

Bibliography

T. Fukuda, D. Tachibana, F. Arai, J. Taguri, M. Nakashima, and Y. Hasegawa. Human-robot mutual communication system. In *Proceedings of the IEEE International Workshop on Robot and Human Interactive Communication, Paris, France*, pages 14–19, 2001.

S.S. Ge, H.A. Samani, Y.H.J. Ong, and C.C. Hang. Active affective facial analysis for human-robot interaction. In *17th IEEE International Symposium on Robot and Human Interactive Communication, Munich, Germany*, pages 83–88, 2008.

F. Hara, H. Akazawa, and H. Kobayashi. Realistic facial expressions by sma driven face robot. In *Proceedings of the IEEE International Workshop on Robot and Human Communication, Paris, France*, pages 504–511, 2001.

T. Hashimoto, S. Hiramatsu, and H. Kobayashi. Dynamic display of facial expressions on the face robot made by using a life mask. In *8th IEEE-RAS International Conference on Humanoid Robots (HUMANOIDS 2008), Daejeon, South Korea*, pages 521–526, 2008.

K. Itoh, Y. Onishi, S. Takahashi, T. Aoki, K. Hayashi, and A. Takanishi. Development of face robot to express various face shapes by moving the parts and outline. In *2nd IEEE RAS and EMBS International Conference on Biomedical Robotics and Biomechatronics (BIOROB 2008), Scottsdale, AZ*, pages 439–444, 2008.

A. Takanishi. An anthropomorphic robot head having autonomous facial expression function for natural communication with humans. In *9th International Symposium of Robotics Research (ISRR99), London: Springer-Verlag*, pages 297–303, 1999.

T. Tojo, Y. Matsusaka, T. Ishii, and T. Kobayashi. A conversational robot utilizing facial and body expressions. In *Proceedings of the IEEE International Conference on Systems, Man, and Cybernetics, Nashville, TN*, pages 858–863, 2000.

A Method for Comparing Human Postures from Motion Capture Data

Wei-Ting Yang, Zhiqiang Luo, I-Ming Chen, and Song Huat Yeo
School of Mechanical and Aerospace Engineering, Nanyang Technological University, Singapore 637098, Singapore
E-mail: michen@ntu.edu.sg

Abstract With the advancement of information technology and motion capture (MoCap) technology, a new concept—Motion Replication (MoRep)—hereby the learning of spatial body motions from a virtual teacher becomes possible. Posture comparison is the first step towards a complete MoRep system. This paper propose a simple and accurate method for evaluating the similarity between human postures from motion capture data.

1 Introduction

Current development in the motion sensing technology enables 3-D body motion of a real human to be captured, processed, and rendered in digital form for computer animation, biomedical, entertainment, and sports applications (Gleicher, 2001; Sok et al., 2007; Suleiman et al., 2008; Brouwer et al., 2009). However, such technology allows only one-way interaction from the physical space to the virtual space (see Figure 1(a)). The notion of MoRep is to further advancing the MoCap technology to provide multi-modal feedback in real time to the person for duplicating the accurate motion or postures (see Figure 1(b)).

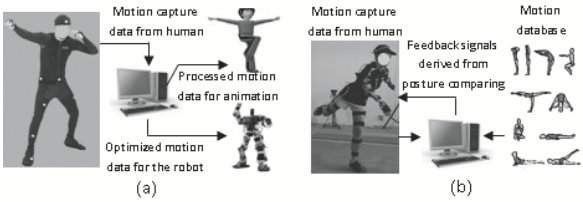

Figure 1. (a) MoCap for robot and animation. (b) MoRep system.

In this paper, we investigate the first step towards human MoRep—the comparison of human postures. Baek et al. (2003) developed a virtual-reality based training system which contained an avatar motion-guiding interface, motion retargeting , and simple audio and image feedback. J.Foody et al. (2006) presented a prototype kinematic and audio feedback based video game. The system used inertial and magnetic field transducers for capturing and comparing the Yoga motion. Lieberman and Breazeal (2007) developed a wearable vibrotactile feedback suit for motor training of the right arm. In the system, a optical MoCap system was used, and the feedback signals for driving vibrotactile actuators were calculated from differences between corresponding joint angles.

This paper presents a human posture comparison method which can determine the similarity of two postures. Each joint attaches an imaginary Cartesian coordinate system (frame) which is calculated from MoCap data. We could quantify the difference between two joints by calculating the difference between the axes of the two frames. This comparison method is simple and retains the basic information of the differences between the two postures, which could subsequently be used to determine feedback signals. While many statistical methods are available for posture comparison (Jain et al., 2000), these algorithm are in general more complex and time-consuming than the proposed method.

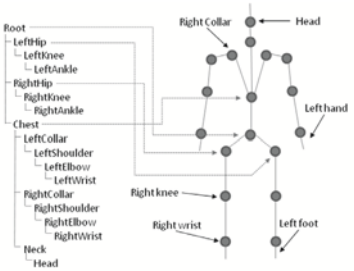

Figure 2. Hierarchical structure of BVH file.

2 Instrument and Data Format

A commercial MoCap system, IGS-190-M (Animazoo UK Ltd.), is chosen for our experiments. The system can output BVH format. BVH format is originally developed by BioVision Company. It is an ASCII format that can be used for importing and storing motion data. The BVH data is a joint-based format and it consists of the hierarchy and the motion section.

The hierarchy section details the structure and initial pose of the skeleton (see Figure 2). The motion section describes the channel data for each timeframe. The channel data record the Euler angles of every segment in the hierarchical structure. The rotation matrix of each joint could be calculated by using Euler angles. Eighteen local frames (see Figure 2) could be calculated from the BVH data captured by the IGS-190-M.

3 Posture Comparison Method

3.1 Comparison of Frames

In this method, the representations of all local frames are with respect to their parent frames. It is called relative representation or relative rotation matrix. The relative representations of frames have advantages over the absolute representations. The compute of relative rotation matrixes from the BVH data is simpler than that for absolute rotation matrixes. In addition, the relative representation is more suited to posture comparison. For example, if two persons perform the same posture but facing in different directions, the relative representations of the shoulder-frames are the same but their absolute ones are very different (see Figure 3(a)).

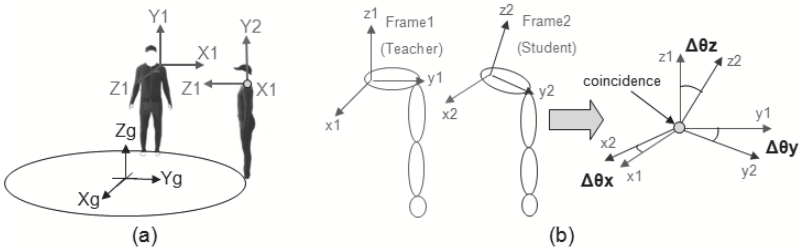

Figure 3. (a) Perform the same posture but facing different directions. (b) Comparison of two left collar-frames.

Image that every joint is attached with a frame which rotates together with the joint. Therefore, the similarity of postures of two corresponding segments could be determined by comparing the orientations of the two frames. Figure 3(b) shows two left upper limbs with their collar-frames. By coinciding the origins of the two collar-frames, three included angles ($\Delta\theta_x$, $\Delta\theta_y$, $\Delta\theta_z$) could be calculated from the six directional vectors of the axes ($x1, x2, y1, y2, z1, z2$) using (1).

$$\Delta\theta = \cos^{-1}\left(\frac{\vec{V}_1 \cdot \vec{V}_2}{|\vec{V}_1||\vec{V}_2|}\right) \tag{1}$$

The three included angles are integrated into a score that ranges between -1 and 1 by the following equation:

$$S_{segment} = \left[\sum_{i=x}^{z}(1 - \frac{\Delta\theta_i}{90})\right]/3 \tag{2}$$

$S_{segment}$ represents a score of a segment, and a larger score means a better similarity. The probability of obtaining negative $S_{segment}$ is small because of human physiological limitation (Oatis, 2009).

3.2 Plummet Method for Root-Frame Comparison

Different from the frames at other joints, the root-frame (on the waist) is defined with respect to the global frame. Referring to Figure 4(a), ambiguity will occur when two persons perform the same posture but facing different directions. Hence, the plummet method is proposed.

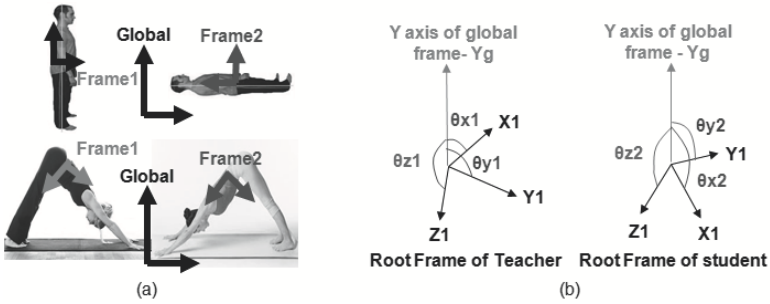

Figure 4. (a) Ambiguity in root-frame comparison. (b) The six included angles.

Using the BVH format, the direction of a plumb line is parallel with the Y-axis of the global frame. Referring to Figure 4(b), the six angles between the axes of the two root frames and the plumb line are calculated by (1). This is followed by the computation of $\Delta\vec{\theta}$:

$$\Delta\vec{\theta} = (|\theta_{x1} - \theta_{x2}|, |\theta_{y1} - \theta_{y2}|, |\theta_{z1} - \theta_{z2}|) = (\Delta\theta_x, \Delta\theta_y, \Delta\theta_z) \tag{3}$$

The similarity score of the root frames can be obtained by substituting $\Delta\theta_x$, $\Delta\theta_y$, and $\Delta\theta_z$ into (2). If the score is larger, the difference between the two root frames is smaller.

3.3 Total Score and Proportion

Excluding the root-frame, seventeen similarity scores for the segments (see Figure 2) could be obtained by (1) and (2). These scores can be consolidated into a local score, S_{local}, by:

$$S_{local} = \left(\sum_{i=1}^{17} S^i_{segment} \right) /17 \tag{4}$$

$S^i_{segment}$ means the $i-th$ score of segment.The local score and the root score are then integrated into a total score, S_{total}, by:

$$S_{total} = (S_{root} + S_{local})/2 \tag{5}$$

The total score represents the similarity index for two postures. Based on (4) and (5), the proportion of score for each segment could be determined as listed in Table 1.

Table 1. The proportion of score of each segment

Segments	Percentage	Segments	Percentage
Root	50.00	Right Lower Limbs	8.83
Right Upper Limbs	11.76	Left Lower Limbs	8.83
Left Upper Limbs	11.76	Chest,Neck,Head	8.82

4 Experiments and Results

Four normal male subjects, without past history of neurological or musculoskeletal disease, whose ages are between 25 and 31 (mean age = 27.25) are selected for the experiments. They are asked to perform the postures as shown in Figure 5. The 23 quasi-static postures are captured using the IGS-190-M. The sampling rate is 60 Hz and the format of the output file is in BVH. Since the postures are captured under quasi-static condition, the variance of values in each channel of the BVH data is small. Thus, the mean value of each channel is computed and considered as the angles of the posture. Based on the angles, the orientation of each local frame can be determined.

Two types of comparison are conducted. In Comparison-1, the similarity score between the stand postures and the other postures of the same

subject are computed. In Comparison-2, postures of the three subjects are compared against the corresponding postures of the selected subject.

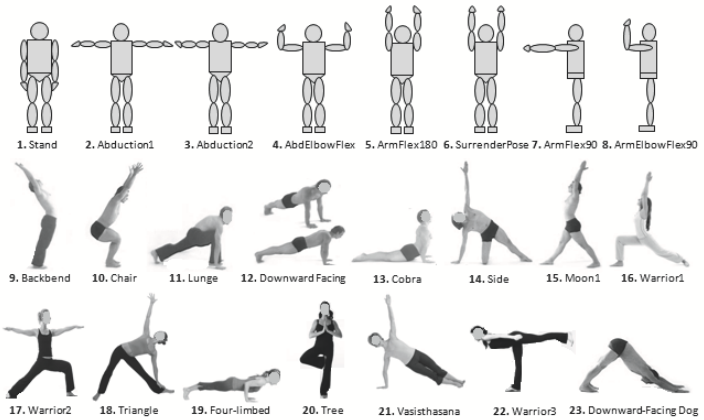

Figure 5. 8 basic upper limbs postures and 15 selected Yoga postures.

We name the four subjects A, B, C and D. Figure 6(a) shows results of comparison-1. The x-axis represents the posture index, and the y-axis represents the similarity score. The scores can be regarded as a similarity between the stand posture and others. Postures $2 \sim 8$ have higher scores because they only involve changes of upper limbs. The waist (root-frame) accounts for 50% of the total score. Thus, postures who have lower scores are because of the large changes of waist. In addition, it is noted that all the scores are positive as it is unlikely to get a negative score for any segment due to human physiological limitation. The standard deviation (SD) of scores for each posture is below 0.040 except the SD for posture 20 (tree posture). This is due to the extreme score of subject D for this tree posture. The results of Figure 6(a) proved that the proposed method is suitable in comparing the similarity of postures.

Figure 6(b) shows results of comparison-2. The x-axis represents index of the posture, and the y-axis represents the similarity score. Subject D is chosen as the teacher for the others to compare with. The score can be regarded as similarity of postures between the teacher and the students. In Figure 6(b), three extreme scores at posture 20 are computed due to a extreme data—tree posture of subject D. Therefore, the results of tree posture are rejected. The SD of score for all postures are under 0.048. This shows that our comparison method is suitable for different skeleton

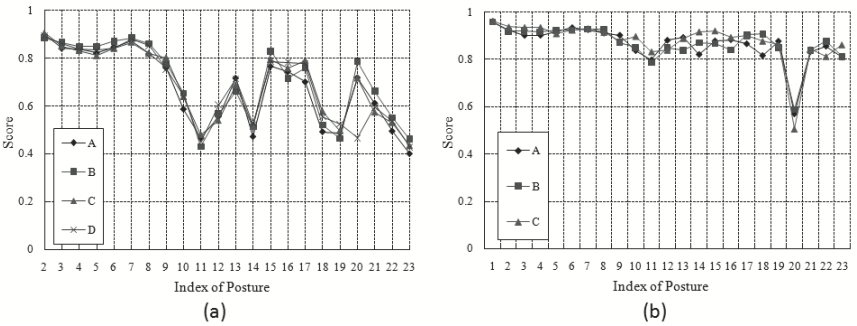

Figure 6. Results of (a) Comparison-1: comparing with stand posture, and (b) Comparison-2: comparing with teacher's posture.

proportion within the range of normal human. All scores are above 0.8 except that of posture 11 of subject B. Hence, it is reasonable to regard two postures as similar to each other when the score is above 0.8.

From the results of Comparison-1 and Comparison-2, we propose a scale of similarity based on the scores as listed in Table 2. Four grades of similarity (marginal, acceptable, good, excellent) are defined for the range between 0.8 and 1.0. This is necessary because as seen from Figure 6(a), the scores for postures $2 \sim 8$ fall within $0.8 \sim 0.9$ even though the placement of the upper limbs are different.

Table 2. The scale of similarity

Score interval	Appraisal of similarity
$0.950 \sim 1.000$	Excellent
$0.900 \sim 0.949$	Good
$0.850 \sim 0.899$	Acceptable
$0.800 \sim 0.849$	Marginal
$0.700 \sim 0.799$	Poor
$Below 0.699$	None

5 Conclusions and Future Works

A simple and accurate method for posture comparison is proposed. A similarity score between 0 and 1 is used to quantify the level of similarity between postures. The results of comparison show that the proposed com-

parison method is suitable for different skeleton proportion within the range of normal human. A look-up table of similarity is proposed and can be used to provide objective evaluation of similarity of postures.

The posture comparison method will be incorporated into a human MoRep system for slow speed sports, such as Yoga and Tai-Chi. The system will be capable of comparing a user's posture with a teacher's on-line, and providing the user feedback through sounds, images or tactual devices in time.

Acknowledgements: The project is supported by Media Development Authority, Singapore under NRF IDM004-005 Grant. We would like to thank Dr. Zhong Qiang Ding, Dr. Chee Kian Lim, Wei Ni, Chao Gu and Ke Yeng Tee for their assistance and doing user test.

Bibliography

S. Baek, S. Lee, and G. J. Kim. Motion retargeting and evaluation for vr-based training of free motion. *The Visual Computer*, 19:222–242, 2003.

B. Brouwer, K. Parvataneni, and S. J. Olney. A comparison of gait biomechanics and metabolic requirements of overground and treadmill walking in people with stroke. *Clinical Biomechanics*, 24:729–734, 2009.

M. Gleicher. Comparing constraint-based motion editing methods. *Graphical Model*, 63:107–134, 2001.

A. K. Jain, P.W. Duin, and J. Mao. Statistical pattern recognition: A review. *IEEE Transactions on Pattern Analysis and Machine Intelligence*, 22(1):4–37, 2000.

J.Foody, D. Kelly, D.Kumar, D. Fitzgerald, T. Ward, B. Caulfield, and C. Markham. A prototype sourceless kinematic-feedback based video game for movement based exercise. In *In Proceedings of IEEE International Conference on Engineering in Medicine and Biology Society*, pages 5366–5369, 2006.

J. Lieberman and C. Breazeal. Tikl: Development of a wearable vibrotactile feedback suit for improved human motor learning. *IEEE Transactions on Robotics*, 23(5):919–926, 2007.

C. A. Oatis. *Kinesiology: the mechanics and pathomechanics of human movement, 2nd ed.* Lippincott Williams and Wilkins, 2009.

K. Sok, M. Kim, and J. Lee. Simulating biped behaviors from human motion data. *ACM Transactions on Graphics*, 26(3):Article 107, 2007.

W. Suleiman, E. Yoshida, F. Kanehiro, J. P. Laumond, and A. Monin. On human motion imitation by humanoid robot. In *In Proceedings of IEEE International Conference on Robotics and Automation*, pages 2697–2704, 2008.

Evaluation of the KOBIAN and HABIAN Emotion Expression Humanoid Robots with European Elderly People[1]

Massimiliano Zecca[1,2,3,4], Giovanna Macrì[5], Yu Mizoguchi[6], Vito Monaco[5], Nobutsuna Endo[4,6], Kazuko Itoh[3,7], Paolo Dario[3,5], Atsuo Takanishi[1,2,3,4,7,8]

[1] *Institute for Biomedical Engineering, ASMeW, Waseda University, Tokyo, Japan*

[2] *Humanoid Robotics Institute (HRI), Waseda University, Tokyo, Japan*

[3] *Italy-Japan Joint Laboratory on Humanoid and Personal Robotics, Tokyo, Japan*

[4] *Global Robot Academia, Waseda University, Tokyo, Japan*

[5] *ARTS Lab, Scuola Superiore Sant'Anna, Pisa, Italy*

[6] *Graduate School of Science and Engineering, Waseda University, Tokyo, Japan*

[7] *Advanced Research Institute for Science and Engineering, Waseda Univ., Tokyo, Japan*

[8] *Department of Modern Mechanical Engineering, Waseda University, Tokyo, Japan*

1. Introduction

Our world is getting older and older (OECD 2009), and therefore there is considerable expectation for more widespread home, medical, and nursing care services to assist not self-sufficient elderly people, both from the physical and psychological points of view. In this context, robots are expected to perform human tasks such as operating equipment designed for humans in dangerous environments, providing personal assistance, social care, cognitive therapy, entertainment, and education (Kozima, Nakagawa et al. 2007). These robots should be capable of a smooth and natural adaptation and interaction with their human partners as well as with the environment. They should also be able to communicate naturally with humans, especially in home and personal assistance applications for elderly and/or handicapped persons. Moreover, these devices should be safe and, more in general, should never have a negative effect on their human partners, neither physical nor emotional.

[1] Research commissioned by The New Energy and Industrial Technology Development Organization (NEDO) and conducted at Humanoid Robotics Institute, Waseda University. Part of the research supported by a Grant-in-Aid for the WABOT-HOUSE Project by Gifu Prefecture. Partial support by: ASMeW Priority Research C Grant #11; JSPS Grant-in-aid for Scientific Research #19700389; Waseda University Grant for Special Research Projects (No. 266740). KOBIAN and HABIAN designed by 3D CAD software "SolidWorks". Special thanks to: SolidWorks Japan K.K. KURARAY Co., Ltd.; the Italian Ministry of Foreign Affairs; Okino Industries LTD; STMicroelectronics; Japan ROBOTECH LTD. A special thank also to Mr. Kimura of GADPA and Mr. Okubo for their help in the realization of the emotional patterns. Eventually, the authors would also like the Università della Terza Età of Pontedera, PI, Italy and its members who kindly accepted to be part of this experiment.

In recent years, several robots have been developed to investigate the socio-emotional aspects of human-robot interactions, in particular in Asian countries. Among them, we can find: animaloid robots such as the therapeutic robot PARO or SONY AIBO to interact with human beings and make them feel emotional attachment; humanoid robots like Honda ASIMO or Kawada HRP-2 to cooperate effectively with humans; humanoid robots like SONY QRIO, Waseda WE series and KOBIAN, Albert HUBO, android robots like Kokoro Actroid, SAYA, and Ishiguro's Geminoid, and even other kinds of robot like NEC's PaPeRo or MIT's Kismet to explore socio-emotive face-to-face interactions with people; and so on.

Our group has been investigating the fundamental technologies of RT service system that shares the living environment with elderly people with the aim to make them more comfortable during the normal activities of daily living (Itoh, Miwa et al. 2006; Zecca, Roccella et al. 2006; Endo, Momoki et al. 2008). To achieve this important goal, the robot appearance should be as human like as possible. We propose that humanoids should be designed to balance *human*-ness, to facilitate social interaction, and *robot*-ness, to avoid false expectations about the robots' abilities (Mori 1970; DiSalvo, Gemperle et al. 2002).

For this purpose, in the last years we have developed the whole body emotion expression humanoid robot KOBIAN (Fig. 1, left). The preliminary evaluation of its emotional expressions showed that the whole-body posture clearly improves the emotion recognition (Zecca, Endo et al. 2008). However, since the obtained results were not entirely satisfactory, we asked a professional photographer and a professional cartoonist to help us in the creation of new emotional poses.

Specific objective of this paper was the evaluation of the effectiveness of the emotional expressions and the acceptability of the two emotional robots with European Elderly people. Unlike Japan and Asia, in fact, in Europe humanoid robots are not usually well accepted, and European people do not like human-like artificial beings (Dario, Guglielmelli et al. 1999; Nisbett 2003).

This paper is organized as follows. Section 2 presents the development of an emotional wheeled robot, named HABIAN, with the main aim to compare its acceptability with respect to that of a biped emotional robot (2.A). The new emotional poses for KOBIAN and HABIAN were also realized in collaboration with one photographer and one cartoonist (2.B). A professional Japanese actor has also been asked to replicate the 14 emotional patterns (2.C). Section 3 presents the experimental evaluation, in particular, the recognition ratio of each emotional pattern (3.A) and the impression elicited by the two robots (3.B). Eventually, Section 4 presents the discussion and the conclusions.

2. Materials and Methods

A. Wheeled-type emotion expression humanoid robot HABIAN

The wheeled-type emotional humanoid robot HABIAN (Fig. 1, right) has been

developed based on the whole-body humanoid robot KOBIAN with a Blackship mobile base (SGI Japan 2008) instead of the two legs. A summary of the DOFs of KOBIAN and HABIAN is presented in Table 1.

Table 1: Main characteristics of KOBIAN and HABIAN.

	KOBIAN	HABIAN
Height	1400 mm	1400 mm
Width	520 mm	520 mm
Weight	62 kg	59 kg
DOFs	48:	37:
	Head 7	Head 7
	Neck 4	Neck 4
	Arm 7x2	Arm 7x2
	Hand 4x2	Hand 4x2
	Trunk 1	Trunk 1
	Waist 2	Waist 1
	Leg 6x2	Leg 2

B. Creation of the new emotional patterns

To improve the recognition ratio of the emotional patterns, we asked one professional cartoonist and one professional photographer to design their original emotional poses for the 7 selected emotions (Anger, Disgust, Fear, Happiness, Perplexity, Sadness, and Surprise). Each artist spent one day each playing with the robot in order to find the best possible posture for each given emotion. The results are presented in Fig. 2. As can be clearly seen from the pictures, some of the poses realized by the two artists were very similar, while others were completely different. In any case most of the poses were completely different from the ones prepared by the students in our lab (Zecca, Endo et al. 2008).

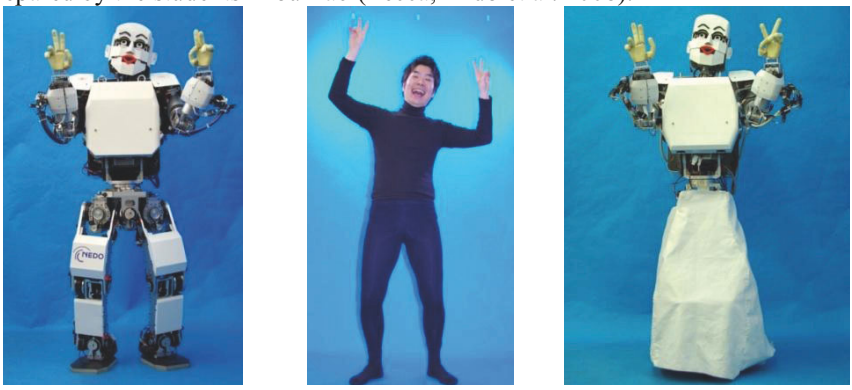

Fig. 1: KOBIAN (left), Japanese professional actor (center) and HABIAN (right) showing the same emotional pattern.

C. Human actor

A professional Japanese actor (Fig. 1, center) was asked to replicate the emotional expressions of the two robots. The 14 different expressions (7 for the Cartoonist, 7 for the Photographer) were repeated several times. The best matching videoclips were then selected and used for the evaluation phase.

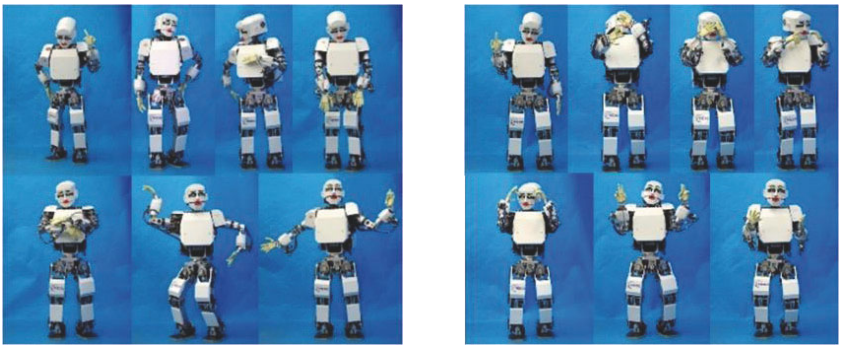

Fig. 2: Emotional postures realized by the cartoonist (left) and by the photographer (right).

3. Experimental evaluation

A group of 19 people (male:8; female: 11; age 70.6±8.9), all members of the "Università della Terza Età" of Pontedera, Pisa, Italy, with absolutely no previous experience with humanoid robots and/or emotional robots agreed to participate to the evaluation after giving their informed consent to the experiment.

42 short videoclips of 7 emotions (Anger, Disgust, Fear, Happiness, Perplexity, Sadness, and Surprise) x 3 performers (human actor, HABIAN, KOBIAN) x 2 types (Cartoonist, Photographer) were shown to the subjects. The order of these videos was randomly selected before the experiment but was not disclosed to the participants. Each videoclip was consecutively shown 3 to 6 times, depending on the reaction time of the subjects, before moving to the next one. In particular the first videos were shown for a longer time, to make the users better understand the experimental protocol. The subjects were asked to choose the emotion that they thought the video robot was expressing among a predetermined list.

A. Evaluation of the Emotion Recognition Ratio

The recognition ratio for each video was calculated as $r(v_i, e_j) = N_{i,j} / N$ where v_i = video #i (i =1...42), e_j = emotion #j (j = 1...7) (6 emotions + perplexity); $N_{i,j}$: number of right responses (v_i, e_j); N: total number of people. The collected data were transcripted in Excel (Microsoft) and saved for further processing, which was done in Matlab® (The Mathworks, Inc., MA, USA).

The results of the experiment are presented in Fig. 3, Fig. 4, and Table 2. In them, the following abbreviations are used: ANG: Anger; DIS: Disgust; FEA: Fear; HAP: Happiness; PER: Perplexity; SAD: Sadness; SUR: Surprise.

Overall, the recognition ratio of emotional patterns was quite low. In total, only 57.1% of the videos were correctly labelled; however, the average recognition ratio for these videos was only 50.2%. On average 14.7% of the responses were

"other" (i.e. 6 videos out of 42). 17 videos (40%) received very low recognition ratio, less than 22%: 4 for the actor, 7 for HABIAN, and 6 for KOBIAN.

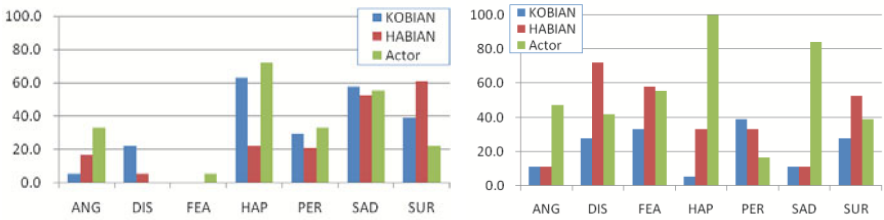

Fig. 3: Recognition ratio for the patterns prepared by the cartoonist (left) and by the photographer (right).

The recognition ratio for KOBIAN, HABIAN and Actor was 31.0 %, 25.6%, and 31.7% respectively for the patterns prepared by the cartoonist; 22.2%, 38.8% and 55.0% for the patterns prepared by the photographer. The combined recognition ratio – i.e. obtained by combining the best emotional expressions – was 38.7%, 46.7%, and 57.4%, respectively. Among the different emotions, Anger and Perplexity were the most difficult to recognize.

It is worth noticing, however, that the emotions expressed by the actors weren't always recognized well either. This could possibly indicate a negative effect due to the different culture and different age of the subjects (Nisbett 2003). Further experiments in this sense are therefore necessary.

B. Evaluation of the robot impression

28 semantic differential questions (Kanda, Ishiguro et al. 2001) were used to evaluate the impression of the two robots and of the human actor: (translated from Japanese) Gentle, Scary; Positive sensation, Negative sensation; Friendly, Hostile; Safe, Dangerous; Warm, Cold; Lovely, Hateful; Outgoing, Formal; Easy to understand, Difficult to understand; Easy to approach, Difficult to approach; Bright, Dark; Considerate, Selfishness; Human, Mechanical; Substantial, Empty; Interesting, Uninteresting; Pleasant, Unpleasant; Like, Dislike; Interesting, Boring; Good, Wrong; Complicated, Simple; Quick, Slow; Agile, Slow; Violent, Calm; Positive, Negative; Strong, Weak; Showy, Simple; Cheerful, Gloomy; Sensitive, Insensitive; Wise, Silly. The questionnaire was presented in Italian after a translation from the original Japanese. A 7-point Likert scale ranging from -3 to +3 was used for the evaluation, with 0 meaning the neutral response.

A Kruscal-Wallis one-way analysis of variance showed that there are significant differences between the human actor and the two robots in several parameters (see Fig. 4), while the two robots are evaluated almost the same except for the pair Considerate/Selfish, in which HABIAN was perceived as more considerate than KOBIAN ($p<0.05$) and as considerate as the actor. As expected, the human actor is always perceived as more "positive" than the two robots.

Table 2: Summary of the results of the evaluation. In the "Artist" column, Ca: Cartoonist; Ph: Photographer. In the "Performer" column: A: Actor; H: HABIAN: K: KOBIAN.

Emotion	Artist	Performer	ANGER	DISGUST	FEAR	HAPPINESS	PERPLEXITY	SADNESS	SURPRISE
Anger	Ca	A	33.3	5.6	0.0	11.1	16.7	5.6	5.6
		H	16.7	5.6	0.0	5.6	16.7	27.8	5.6
		K	5.6	11.1	5.6	0.0	22.2	16.7	5.6
	Ph	A	47.4	5.3	5.3	5.3	5.3	0.0	10.5
		H	11.1	0.0	0.0	11.1	5.6	33.3	5.6
		K	11.1	0.0	0.0	0.0	33.3	16.7	16.7
Disgust	Ca	A	5.9	0.0	0.0	17.6	29.4	0.0	5.9
		H	0.0	5.3	0.0	0.0	63.2	21.1	5.3
		K	0.0	22.2	16.7	0.0	11.1	16.7	11.1
	Ph	A	0.0	42.1	36.8	0.0	10.5	0.0	10.5
		H	0.0	72.2	11.1	0.0	0.0	0.0	11.1
		K	0.0	27.8	44.4	11.1	0.0	0.0	11.1
Fear	Ca	A	0.0	38.9	5.6	0.0	11.1	0.0	27.8
		H	5.6	33.3	0.0	5.6	16.7	5.6	16.7
		K	5.6	33.3	0.0	0.0	33.3	5.6	5.6
	Ph	A	5.6	5.6	55.6	0.0	5.6	27.8	0.0
		H	5.3	15.8	57.9	5.3	0.0	10.5	0.0
		K	0.0	27.8	33.3	0.0	0.0	38.9	0.0

Em	Art	Per	ANG	DIS	FEA	HAP	PER	SAD	SUR
Happiness	Ca	A	5.6	0.0	5.6	72.2	5.6	5.6	5.6
		H	11.1	0.0	0.0	22.2	11.1	0.0	44.4
		K	5.3	0.0	5.3	63.2	10.5	0.0	5.3
	Ph	A	0.0	0.0	0.0	100	0.0	0.0	0.0
		H	16.7	0.0	0.0	33.3	5.6	0.0	27.8
		K	15.8	0.0	10.5	5.3	15.8	0.0	36.8
Perplexity	Ca	A	5.6	5.6	0.0	11.1	33.3	16.7	11.1
		H	0.0	5.3	10.5	10.5	21.1	5.3	5.3
		K	5.9	5.9	0.0	0.0	29.4	11.8	17.6
	Ph	A	11.1	16.7	5.6	0.0	16.7	22.2	5.6
		H	16.7	0.0	11.1	0.0	33.3	5.6	22.2
		K	0.0	5.6	11.1	5.6	38.9	11.1	22.2
Sadness	Ca	A	0.0	22.2	5.6	0.0	5.6	55.6	0.0
		H	0.0	5.3	0.0	5.3	10.5	52.6	0.0
		K	5.3	0.0	10.5	0.0	10.5	57.9	5.3
	Ph	A	0.0	5.3	5.3	0.0	0.0	84.2	0.0
		H	5.6	33.3	0.0	5.6	22.2	11.1	5.6
		K	0.0	22.2	11.1	0.0	22.2	11.1	11.1
Surprise	Ca	A	5.6	0.0	16.7	38.9	5.6	5.6	22.2
		H	0.0	0.0	0.0	22.2	11.1	0.0	61.1
		K	0.0	0.0	5.6	38.9	5.6	0.0	38.9
	Ph	A	27.8	11.1	5.6	5.6	0.0	5.6	38.9
		H	5.3	0.0	5.3	5.3	5.3	5.3	52.6
		K	22.2	0.0	11.1	22.2	11.1	0.0	27.8

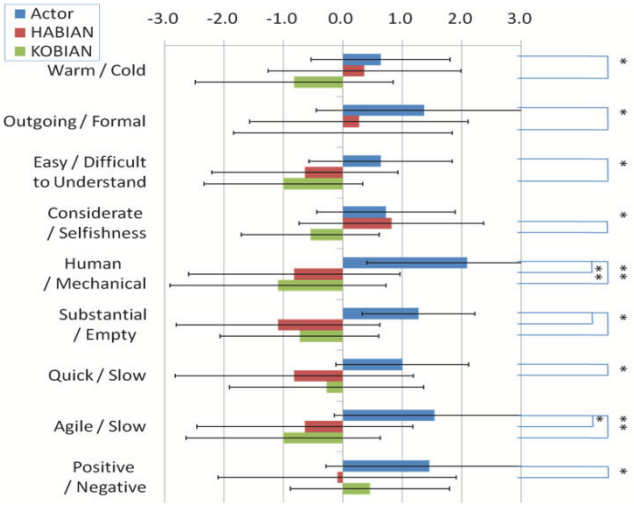

Fig. 4: Significative parameters. Significance level is indicated by *: $p < 0.05$; **: $p<0.01$.

C. Free comments

The users were also asked to provide some personal opinion on the robots. Most of the comments were definitely negative, such as "why do we need a biped robot in our house? There is no reason for it!", "I'm scared1", "I do not want a human being-like object in my house!", "why do you need to give it emotions? It frightens me!", and so on. These comments clearly show that the negative results are mostly due to the different cultural background, as in previous experiments with Japanese senior citizens we always got positive feedbacks (Zecca, Endo et al. 2008).

4. Conclusions

In this elderly-dominated society, Personal Robots and Robot Technology (RT)-based assistive devices are expected to play a major role, both for joint activities with their human partners and for participation in community life. So far, several different personal robots have been developed. However, it is not yet clear what kind of ability is necessary for personal robot. We think that emotional expression of robot is effective for joint activities of humans and robots. The robot should express in particular happiness and perplexity, which we are considered to be fundamental emotional expressions for a smooth and natural interaction with humans.

To this purpose we developed a whole body bipedal humanoid robot, named KOBIAN, which is also capable to express human-like emotions. This novel robot is based on the previously developed Biped Humanoid Robot WABIAN-2 for the lower body, and on the Emotion Expression Humanoid Robot WE-4R for the head. We also developed a new wheeled type emotion expressing humanoid robot named HABIAN, which is based on KOBIAN for the upper body, with a Blackship mobile base instead of the legs. We asked two professional artists (a cartoonist and a photographer) to help us in the realization of new emotional patterns; we also asked a professional actor to perform the same patterns.

In this paper we presented the preliminary evaluation of the new emotional expressions with a group of European elderly people. The preliminary results showed that – as expected – the emotions are not always correctly recognized. The two robots, nonetheless, are capable of expressing these emotions, and most of their expressions were correctly labeled as "emotional" and not neutral. It is worth noticing that the emotions expressed by the actors weren't always recognized well either. This could possibly indicate a negative effect due to the different culture and different age of the subjects, as Western people are not familiar with Japanese expressions (Dario, Guglielmelli et al. 1999; Nisbett 2003).

We also received several negative comments; which clearly show that the negative results are mostly due to the different cultural background, as in previous experiments with Japanese senior citizens we always got positive feedbacks.

For sure the expressiveness of the robots must be increased in their next

versions. We would also like to evaluate the new emotional expressions with more people from different countries and of different ages. In addition, we will investigate the influence of outer covering and the effects of sound, movement, arms, and whole body. Furthermore, we will investigate what kind of robot is effective in human living environment by human-robot interaction experiment.

References

Dario, P., E. Guglielmelli, et al. (1999). "MOVAID: a personal robot in everyday life of disabled and elderly people " Technology and Disability 10(2): 77-93.

DiSalvo, C., F. Gemperle, et al. (2002). "All robots are not created equal: the design and perception of humanoid robot heads." Proceedings of the conference on Designing interactive systems: processes, practices, methods, and techniques.

Endo, N., S. Momoki, et al. (2008). Development of Whole-Body Emotion Expression Humanoid Robot. 2008 IEEE International Conference on Robotics and Automation (ICRA). Pasadena, CA, USA: 2140-2145.

Itoh, K., H. Miwa, et al. (2006). Mechanisms and Functions for a Humanoid Robot to Express Human-like Emotions. IEEE International Conference on Robotics and Automation - ICRA 2006.

Kanda, T., H. Ishiguro, et al. (2001). Psychological Evaluation on Interactions between People and Robot. 19th Annual Conference of the Robotics Society of Japan (RSJ2001), Tokyo, Japan.

Kozima, H., C. Nakagawa, et al. (2007). "Children-robot interaction: a pilot study in autism therapy." Prog Brain Res 164: 385-400.

Mori, M. (1970). "Bukimi no tani [The Uncanny Valley]." Energy 7(4): 33-35 (Originally in Japanese).

Nisbett, R. (2003). The Geography of Thought : How Asians and Westerners Think Differently...and Why Nicholas Brealey Publishing.

OECD (2009). Population statistics. http://www.oecd.org, Organisation for Economic Co-operation and Development.

SGI Japan. (2008). "Blackship, http://www.sgi.co.jp/solutions/robot/blackship/."

Zecca, M., K. Endo, et al. (2008). Design and Evaluation of The Soft Hand WSH-1 For The Emotion Expression Humanoid Robot KOBIAN. 6th International Conference of the International Society for Gerontechnology (Gerontechnology2008). Pisa, Italy.

Zecca, M., N. Endo, et al. (2008). Design of the humanoid robot KOBIAN –preliminary analysis of facial and whole body emotion expression capabilities–. IEEE-RAS International Conference on Humanoid Robots HUMANOIDS2008. Daejeon, South Korea. 1: 487-492.

Zecca, M., S. Roccella, et al. (2006). From the Human Hand to a Humanoid Hand: Biologically-Inspired Approach for the Development of RoboCasa Hand #1. ROMANSY 16 - Robot Design, Dynamics and Control, CISM Lecture Note #487. T. Zielinska and C. Zielinski, Springer Wien: 287-294.

An Approach to the Dynamics and Kinematical Control of Motion Systems Consisting of a Chain of Bodies

Klaus Zimmermann , Igor Zeidis and Carsten Behn
Faculty of Mechanical Engineering, Ilmenau University of Technology, Germany

Abstract. Theoretical investigations concerning the motion of a straight chain of mass points interconnected with kinematical constraints are considered. The ground contact can be described by dry (discontinuous) friction. The controls are assumed in the form of periodic functions with zero average, shifted in phase to each other. There arises a spreading wave along the chain of mass points. In the case of small friction we derive a condition for the locomotion of the center of mass by means of an average method. Motion of the system can be generated both in case of isotropic and non-isotropic friction using specified controls, moreover the movement in the latter case in direction of the larger friction force. The obtained theoretical results give hints for the development of mobile robots applying the described principles of the motion.

1 Introduction

The rectilinear motion on a rough plane of bodies (mass points) connected by elastic elements is considered in a series papers. The system is moved by forces that changed harmonically and acting between the bodies (Miller, 1988). The force of normal pressure is not changed and the asymmetry of the friction force, required for a motion in a given direction, is provided by the dependence of the friction coefficient on the sign of the velocity of the bodies which make up the system (Blekhman, 2000). This effect can be achieved if the contact surfaces of the bodies are equipped with a special form of scales (needle-shaped plate with a required orientation of scales).

In the book, Zimmermann, Zeidis and Behn (2009), the dynamics of a system of two bodies moving along a rough plane joined by an elastic element are considered. The motion is excited by a harmonic force acting between the bodies. In the article, Zimmermann et al. (2004), a magnetizable polymer was employed as an elastic element and the motion was excited by a magnetic field. In the case of small friction, the analytical

expression for the average velocity of steady motion of the whole system was found and it is shown, that the motion with this velocity is stable. A similar investigation for a system of two bodies joined by a spring with a nonlinear (cubic) characteristic was shown in the article, Zimmermann et al. (2007). Algebraic equations were obtained for average velocities of the steady motion. It was shown that there exist up to three different motion modes, one or two of them are stable. Steigenberger (1999) presented a numerical solution of the motion equations of a chain of bodies joined by viscoelastic elements for the case, when each body can move only in one direction. In the article Bolotnik et al. (2006), the rectilinear motion of a vibration-driven system on a horizontal rough plane consisting of a carrying body, which interacts with the plane directly, and of internal masses that perform harmonic oscillations relative to the carrying body, is considered. The vertical and horizontal oscillations of the internal masses have the same frequency, but they are shifted in phase. It is shown, that by controlling the phase shift of the horizontal and vertical oscillations, it is possible to change the velocity of the steady motion of the carrying body, and it is not necessary to use scales in order to provide friction asymmetry.

Zimmermann et al. (2009) considered the motion of two mass points connected by a linear spring, when the coefficient of friction does not depend on the direction of motion. Due to the change of the normal force in dependence on time asymmetry of friction is present. The change of normal force is realized by the rotation of two unbalanced rotors with various angular velocities. Chernousko (2005) investigated the rectilinear motion of a body with a movable internal mass moving along a straight line parallel to the line of the body motion on a rough plane. A periodic control mode was constructed for the relative motion of the internal mass for which the main body moves with a periodically changing velocity passing the same distance in a given direction. It is supposed that, at the beginning and the end of each period, the velocity of the main body is zero. The internal mass can move within fixed limits. The control modes relative to the velocity and acceleration of the internal mass were considered. The optimal parameters of both modes which lead to a maximum of the average velocity of motion of the main body for a period were found.

In the present paper[1] we consider the motion of a straight chain of three equal mass points interconnected with kinematical constraints. The ground contact can be described by dry (discontinuous) friction. The controls are assumed in the form of periodic functions with zero average, shifted on a

[1]This study was partly supported by the German Research Society (DFG) (projects Zi 540-12/1 and the SFB 622).

phase one concerning each other. Thus, there is a travelling wave along the chain of mass points. It is shown that, using special control algorithms motion is also possible by isotropic friction and by constant normal force. In the case of non-isotropic friction the motion is possible even in the direction of the greater friction.

2 Equations of Motion

We consider the motion of a system of three mass points with the coordinates x_i $(i = 1\,, 2\,, 3)$ and with the masses m, connected by kinematical constraints along an axis Ox (see Figure 1). The motion of the system is excited by the kinematical constraints setting the distances $l_1(t)$ and $l_2(t)$ between mass points.

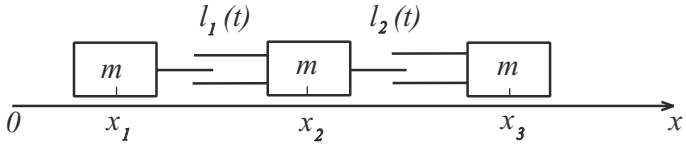

Figure 1. The schematic of the system of three mass points.

$$l_1(t) = l_0 + a_1(t), \quad l_2(t) = l_0 + a_2(t), \quad a_1(0) = a_2(0) = 0\,. \tag{1}$$

Let us consider the functions $l_1(t)$ and $l_2(t)$ (hence as well $a_1(t)$ and $a_2(t)$) that are periodic in time t with period T. The kind of functions $a_1(t)$ and $a_2(t)$ will be discussed below.

There is the force of friction $F(V_i)$ acting on each mass point from the surface, directed against motion and depending on the velocity $V_i = \dot{x}_i$ $(i = 1\,, 2\,, 3)$.

The velocity of the center of mass of system can be represented as $V = \frac{1}{3}(\dot{x}_1 + \dot{x}_2 + \dot{x}_3)$. The equation of the motion of the center of mass is:

$$3\,m\,\dot{V} = F(\dot{x}_1) + F(\dot{x}_2) + F(\dot{x}_3)\,. \tag{2}$$

Using $x_2(t) - x_1(t) = l_1(t)\,, \quad x_3(t) - x_2(t) = l_2(t)$ and substituting expressions (1) in (2) the equation of the motion (2) takes the form

$$3\,m\,\dot{V} = F\left(V - \frac{2}{3}\,\dot{a}_1 - \frac{1}{3}\,\dot{a}_2\right) + F\left(V + \frac{1}{3}\,\dot{a}_1 - \frac{1}{3}\,\dot{a}_2\right) + F\left(V + \frac{1}{3}\,\dot{a}_1 + \frac{2}{3}\,\dot{a}_2\right). \tag{3}$$

We assume, that in the initial moment $t = 0$ the velocity of the center of mass $V(0) = 0$.

Let us introduce dimensionless variables in according to the following formulas (the asterisk * is a symbol of dimensionless variables):

$$\begin{aligned} x_i^* &= \frac{x_i}{L}\ (i=1\,,2\,,3)\,, \quad V^* = V\,\frac{T}{L}\,, \quad t^* = \frac{t}{T}\,, \\ a_i^* &= \frac{a_i}{L}\,, \quad l_i^* = \frac{l_i}{L}\ (i=1\,,2)\,, \quad F^*(V^*) = \frac{F(V)}{F_s} = \frac{F(V^*\cdot L/T)}{F_s}\,. \end{aligned} \tag{4}$$

Here L is a characteristic linear dimension (for example the greatest value $a_1(t)$ or $a_2(t)$ in period T), F_s is a characteristic value of the friction force.

Hereafter, we use dimensionless variables. Introducing the dimensionless variables in equation (4) and denoting $u_1(t) = \dot{a}_1(t)$, $u_2(t) = \dot{a}_2(t)$, we rewrite equation (3) in dimensionless variables (the old symbols are hold)

$$\frac{dV}{dt} = \frac{\varepsilon}{3}\left[F\left(V-\frac{2}{3}\,u_1-\frac{1}{3}\,u_2\right)+F\left(V+\frac{1}{3}\,u_1-\frac{1}{3}\,u_2\right)+F\left(V+\frac{1}{3}\,u_1+\frac{2}{3}\,u_2\right)\right], \tag{5}$$

where $\varepsilon = F_s T^2/mL$.

Let us notice, that since $a_1(t)$ and $a_2(t)$ are periodic functions with period T, therefore $u_1(t) = \dot{a}_1(t)$ and also $u_2(t) = \dot{a}_2(t)$ are periodic functions with period T and have zero average.

Further we assume everywhere, that $\varepsilon \ll 1$. The smallness of the parameter ε shows that the value of the friction force F_s is small compared to the amplitude of the "driving" force mL/T^2. The equation (5) has a so called "standard" form (Bogolyubov and Mitropolslki, 1961). Averaging the right side of the equation (5) relative to the variable t in the period 1, we obtain

$$\frac{dV}{dt} = \frac{\varepsilon}{3}\,G(V)\,, \tag{6}$$

$$G(V) = \int\limits_0^1 \left[F\left(V-\frac{2}{3}u_1-\frac{1}{3}u_2\right)+F\left(V+\frac{1}{3}u_1-\frac{1}{3}u_2\right)+F\left(V+\frac{1}{3}u_1+\frac{2}{3}u_2\right)\right]dt\,.$$

Now it is necessary to define the functions $u_1(t)$, $u_2(t)$ and the law of friction.

3 Smooth Control

Let us consider the functions $a_1(t)$ and $a_2(t)$, composed from the parabolas. These functions have continuous derivatives $u_1(t)$ and $u_2(t)$, shown in Figure 2 accordingly marked as a solid and as a dotted line and have the form:

$$u_1(t) = \begin{cases} 0, & 0 \le t \le \dfrac{1}{3}, \\ 2\,(3\,t-1), & \dfrac{1}{3} < t \le \dfrac{1}{2}, \\ -2\,(3\,t-2), & \dfrac{1}{2} < t \le \dfrac{5}{6}, \\ 6\,(t-1), & \dfrac{5}{6} < t \le 1\,. \end{cases} \quad u_2(t) = \begin{cases} 6\,t, & 0 \le t \le \dfrac{1}{6}, \\ -2\,(3\,t-1), & \dfrac{1}{6} < t \le \dfrac{1}{2}, \\ 2\,(3\,t-2), & \dfrac{1}{2} < t \le \dfrac{2}{3}, \\ 0, & \dfrac{2}{3} < t \le 1. \end{cases} \tag{7}$$

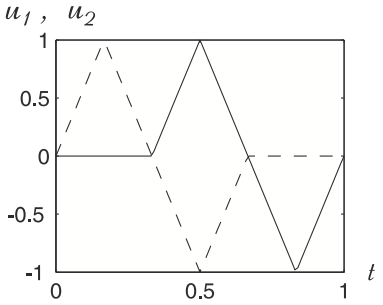

Figure 2. The function $u_1(t)$ (sol. line), $u_2(t)$ (dott. line).

They are equal to zero on an interval of length 1/3 and are shifted on time for this magnitude one relatively to another.

4 Dry (Discontinuous) Friction

We assume that Coulomb dry friction acts on the mass points. The dimension force of dry friction $F(V)$ satisfies the Coulomb law

$$F(V) = \begin{cases} F_- = k_- N\,, & \text{if } V < 0\,, \\ -F_0\,, & \text{if } V = 0\,, \\ -F_+ = -k_+ N\,, & \text{if } V > 0\,. \end{cases}$$

Here N is the force of normal pressure (in this case $N = mg$, where g is the free fall acceleration), k_- and k_+ are the coefficients of dry friction at the motion in a negative and in a positive direction respectively, $F_- \le F_+$ ($k_- \le k_+$), the value $F_0 \in [-F_-\,, F_+]$.

The expression for dimensionless friction force takes the form ($i = 1\,,2\,,3$):

$$F^*(\dot{x}_i^*) = \begin{cases} 1\,, & \dot{x}_i^* < 0\,, \\ -\mu_0\,, & \dot{x}_i^* = 0\,, \\ -\mu\,, & \dot{x}_i^* > 0\,. \end{cases} \tag{8}$$

Here, the value F_s in formulas (4) is $F_s = F_-$ (F_- is the magnitude of the friction force at the motion in a negative direction), $\mu = F_+/F_- = k_+/k_- \geq 0$, $\mu_0 \in [-1\,,\mu]$.

Let us prove this, assuming that $\dot{x}_i(t)$ is a piecewise continuous function of time. This assumption is quite sufficient for simulating feasible motion. The second condition (8) is connected with sticking ("stick-slip" motions). This effect is characteristic for systems with dry friction. Let us notice, that for the given control the velocity of each mass point could not be equal to zero on a finite time interval. Hence, the "stick-slip" effect is absent.

After substituting expressions (7) and (8) into equation (6), we receive

$$\frac{dV}{dt} = \frac{\varepsilon}{3} \begin{cases} 3\,, & V \leq -2/3\,, \\ 2 - \mu - 3\,V\,1 + \mu/2\,, & -2/3 < V \leq 0\,, \\ 2 - \mu - 6\,V\,(1+\mu)\,, & 0 < V \leq 1/3\,, \\ -3\,\mu\,, & V > 1/3\,. \end{cases} \tag{9}$$

We consider the solution of equation (9) with the initial condition $V(0) = 0$. If $\mu = 2$ (friction in the positive direction is double the friction in the negative direction), the system remains in rest.

If $\mu < 2$ the chain of mass points moves to the right with the velocity

$$V = \frac{2-\mu}{6\,(1+\mu)} \left[1 - e^{-2\,\varepsilon\,(1+\mu)\,t}\right]$$

and tends to stationary value $V_s = \dfrac{2-\mu}{6\,(1+\mu)}$. In the case of isotropic friction, we find $V_s = 1/12$.

Thus, under this control algorithms, motion is possible in the case of isotropic friction as well as in the direction of the greater friction in the case of non-isotropic friction. If $\mu > 2$ the chain moves to the left with the velocity

$$V = \frac{2\,(2-\mu)}{3\,(1+\mu)} \left[1 - e^{-\frac{\varepsilon}{2}\,(1+\mu)\,t}\right]$$

and tends to stationary value $V_s = \dfrac{2\,(2-\mu)}{3\,(1+\mu)}$.

In Figure 3 the results of the numerical integration of the exact and averaged equations in the case of symmetric friction ($\mu = 1$) and for parameter $\varepsilon = 0.3$ are shown.

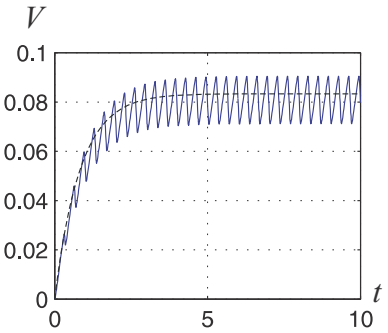

Figure 3. Solutions of the exact and the averaged equations for dry friction.

5 Conclusions

It is shown that, using periodical control algorithms, the motion of a chain of mass points is possible in the case of isotropic friction and in the case of non-isotropic friction in the direction of the greater friction. The locomotion is impossible without a shift of the phases in the control law.

In the case of small friction we derived a condition for the locomotion of the center of the mass with the help of an average method. In the case of smooth control we received explicit expressions for the average velocity of the motion of the center of mass. A prototype of this system was created (see Figure 4). Experiments with this system coincide with the qualitative predictions of the theory.

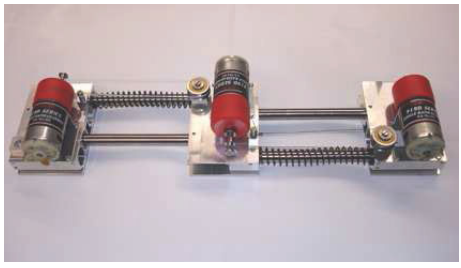

Figure 4. A first prototype of the motion system, Keil (2009).

Bibliography

I. Blekhman, *Vibrational Mechanics*, *W*orld Scientific, 2000.

N. Bogolyubov, and Yu.A. Mitropolski, *Asymptotic Methods in the Theory of Nonlinear Oscillations*, *G*ordon and Breach Scuence Publischers, 1961.

N. Bolotnik, I. Zeidis, K. Zimmermann, and S. Yatsun, *Dynamics of controlled motion of vibration-driven systems*, *J*ournal of Computer and Systems Sciences International, **45**, pages 831-840, 2006.

F. Chernousko, *On a motion of a body containing a movable internal mass*, *D*okl Akad Nauk, **405**, pages 1-5, 2005.

D. Keil, *Entwurf, Konstruktion und Inbetriebnahme eines wurmartigen Bewegungssystems bestehend aus drei Massepunkten*, *P*rojektarbeit, TU Ilmenau, 2009.

G. Miller, *The motion dynamics of snakes and worms*, *C*omputer Graphics, **22**, pages 169-173, 1988.

J. Steigenberger, *On a class of biomorphic motion systems*, In *P*reprint 12, 1999. Faculty of Mathematics and Natural Sciences, TU Ilmenau.

K. Zimmermann, I. Zeidis, V. Naletova, and V. Turkov, *Modelling of worm-like motion systems with magneto-elastic elements*, *P*hysica Status Solidi, (c), **1**, pages 3706-3709, 2004.

K. Zimmermann, and I. Zeidis, *Worm-like locomotion as a problem of nonlinear dynamics*, *J*ournal of Theoretical and Applied Mechanics, **45**, pages 179-187, 2007.

K. Zimmermann, I. Zeidis, M. Pivovarov, and K. Abaza, *Forced nonlinear oscil-lator with nonsymmetric dry friction*, *A*rchive of Applied Mechanics, **77**, pages 353-362, 2007.

K. Zimmermann, I. Zeidis, N. Bolotnik, and M. Pivovarov, *Dynamics of a two-module vibration-driven system moving along a rough horizontal plane*, *M*ultibody System Dynamics, **22**, pages 199 - 219, 2009.

K. Zimmermann, I. Zeidis, and C. Behn, *Mechanics of terrestrial locomotion*, *S*pringer, 2009.

Modular Design of Emotion Expression Humanoid Robot KOBIAN

Nobutsuna Endo[1], Keita Endo[1], Massimiliano Zecca[2,3], and Atsuo Takanishi[2,3,4,5]

[1] Graduate School of Science and Engineering, Waseda University, Tokyo, Japan
[2] Institute for Biomedical Engineering, ASMeW, Waseda University, Tokyo, Japan
[3] Italy-Japan joint laboratory on Humanoid and Personal Robotics "RoboCasa", Tokyo, Japan
[4] Humanoid Robotics Institute (HRI), Waseda University, Tokyo, Japan
[5] Advanced Research Institute for Science and Engineering, Waseda University, Tokyo, Japan

Abstract. Personal robots and Robot Technology (RT)-based assistive devices are expected to play a substantial role in our society, largely populated by elders; they will play an active role in joint works and community life with humans. In particular, these robots are expected to play an important role for the assistance of elderly and disabled people during normal activities of daily living (ADLs). To achieve this result, personal robots should be also capable of human-like emotion expressions. In this perspective we developed a whole body bipedal humanoid robot, named KOBIAN, which is also capable to express human-like emotions. In this paper we present the mechanical and modular design of KOBAIN.

Introduction

In our society getting older and older, there is considerable expectation for more widespread home, medical and nursing care services to assist not self-sufficient elderly people, both from the physical and psychological points of view. In this context, robots are expected to perform human tasks such as: 1) operating equipment designed for humans in dangerous environments, 2) providing personal assistance, social care, cognitive therapy, entertainment, and education. These robots should be capable of a smooth and natural adaptation and interaction with their human partners as well as with the environment. They should also be able to communicate naturally with humans, especially in home and personal assistance applications for elderly and/or handicapped persons. Moreover, these devices should be safe and, more in general, should never have a negative effect on their human partners, neither physical nor emotional.

Our group is investigating the fundamental technologies of RT service system that shares the living environment with elderly people with the aim to make them more comfortable during the normal activities of daily living. To achieve this important goal, the robot appearance should be as human like as possible. We propose that humanoids should be designed to balance human-ness, to facilitate

social interaction, and robot-ness, to avoid false expectations about the robots' abilities (DiSalvo et al., 2002, Mori, 1970).

For this purpose, in the last years we have developed the whole body emotion expression humanoid robot KOBIAN (Endo et al., 2008) based on the bipedal humanoid robot WABIAN-2 (Ogura et al., 2006) and emotion expression humanoid robot WE-4RII. KOBIAN is 1400 mm tall and 520 mm wide. Its weight is 62 kg. The preliminary evaluation of the whole body emotion expressions showed that the body of the robot clearly improves the emotion recognition.

KOBIAN's head was designed based on WE-4RII's one. WE-4RII's head has 22 degrees of freedom, but it is too bulky and heavy to mount on KOBIAN's body which was developed based on WABIAN-2's one, so we reduced the DOFs of KOBIAN's head by 7-DOFs, downsized, and trim weight. In order to evaluate the effect of DOF reduction, we designed the appearance of KOBIAN's face about the same as WE-4RII's. However, we can not predicate that the current appearance of KOBIAN's face is best suited to KOBIAN because people either like this appearance design or don't like it. For this reason, KOBIAN's head is designed as driving mechanism of facial expression and outer covering are separated, and it is easy to adapt to various outer covering. And, the driving parts are modularized and it is easy to change trajectories of each facial parts.

In this paper, we describe the modular designs of KOBIAN.

Design

Design Concept. As mentioned above, it is fundamental for the robot which is active in human living environment to be capable of biped walking. In addition, this kind of robot needs also the capability of moving in natural ways, as they share the living environment with human. Therefore, we developed the whole body emotion expression humanoid robot KOBIAN, based on the biped humanoid robot WABIAN-2 and WE-4RII (see Figure 1).

Concerning the interaction at emotional level, a mechanism to tell the user whether the robot understand human words or not is important for a smooth communication and interaction. In addition, it is necessary to transmit emotion for the emotional communication. Therefore the robot should be capable of facial expression for promotion of interaction, communication of meaning of the sensitivity, and indication of internal states. In particular, smile that indicates the robot feel pleasant and perplexity that indicates the robot cannot understand human words are essential.

As mentioned above, there are existing various types of humanoid robots and their appearance designs are varied. This is caused by variety of designers and developers, and in future, much more variety of robot's appearance will be required when humanoid robots come to be more imminent for a human being.

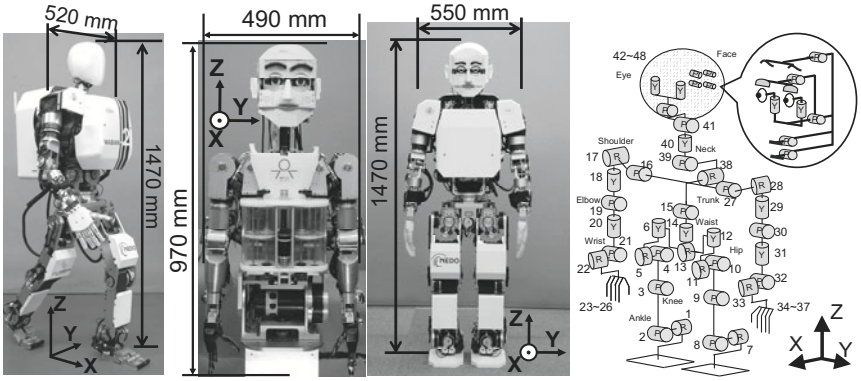

Figure 1. WABIAN-2R, WE-4RII, KOBIAN, and DOF configuration

With most of facial expression robots, the driving mechanism of facial parts and the appearance are tied closely because the facial expressions are made by each facial part such as eyebrows, eyelid, and mouth driven mechanically. In this way, however, developers have to design the driving mechanism from the beginning in order to adapt to various types of appearance, and we think of it as inefficient.

Likewise in WE-4RII, driving wires of eyebrow pass through the forehead and it is difficult to change the appearance and it is also difficult to maintain. So, with KOBIAN's head, we decided to separate the driving mechanism of facial parts and outer covering and also decided to conduct modular design in order to make the one head easier to adapt to various types of outer covering.

Mechanical configuration. Human's eyebrow grows on the surface of skin and move with skin. But, we focused on the change of the eyebrow shape, and decide to move KOBIAN's eyebrows independently from forehead. The eyebrow is molded with thermoplastic resin SEPTON (KURARAY Co. Ltd.). The both ends of the eyebrow are free turns, and an arbitrary point between the ends is assumed a control point. A neodymium magnet is mounted on the back of control point. The outer covering for forehead is molded with hard resin, and a neodymium magnet and a mechanism which drive the magnet are mounted on the corresponding position of control point of eyebrow. The magnet of mechanism side is vertically driven by wires, and the control point of eyebrow is driven in the same direction. The driving mechanism is shown in Figure 2, and the exploded view is shown in Figure 3. The basement of eyebrow driving mechanism can be fixed with moved in longitudinal direction and pitch direction, and easily adapt to change of the position of the control point of the eyebrow and the change of the inclination of the forehead. So, we can easily change to various types of the shapes of eyebrow and outer covering.

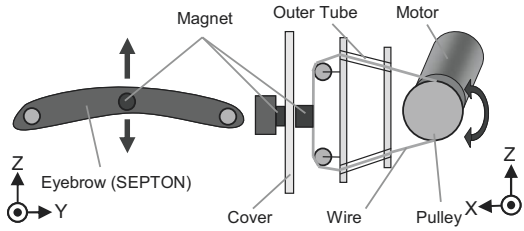

Figure 2. Mechanism of eyebrow

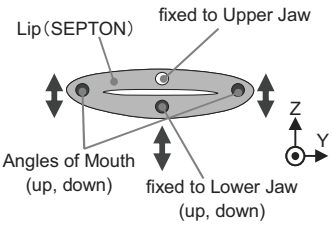

Figure 4. Mechanism of mouth

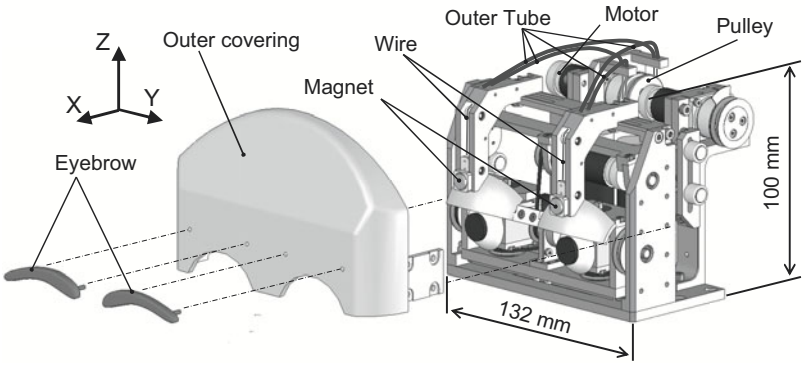

Figure 3 Exploded view of the driving parts and the outer covering of the eyebrows

WE-4RII has 5-DOFs at the mouth (open and close of the jaw, extending, up and down of the angles of mouth). The lip is made by using springs of spindle type and actuated by wires, and has high expression performance. However, assembly and maintenance are hard. KOBIAN has 2 -DOFs at the mouth (open and close of the jaw, up and down of the angles of mouth). The lip is molded with SEPTON. The mechanism of the mouth is shown in Figure 4. This mechanism is much easier to assembly and maintain than WE-4RII's one.

In addition, motor drivers (Tokushu Denso Co., Ltd) for the head's 7-DOFs can be stored into the back of the head. The lines for rotation speed command to motor driver and the lines for encoder pulses are collected at a junction circuit on the back of the head, and connect to a control PC on KOBIAN's back through one harness. All of electric interface are power line for the motor drivers (48V), power line for the encoders (5V), and the harness to junction circuit. By modularizing the entire head, it is easy to mount the head on other robot systems. The head is mounted on its body via neck. The neck is developed based on WE-4RII's neck (Miwa, et al., 2004) and has 4-DOFs. Figure 5 shows a CAD design of the head and Figure 6 shows an exploded view of the head and neck.

Figure 7 shows examples of KOBIAN's facial expressions. KOBIAN expresses them by using 4-DOFs at eyebrows, upper eyelids, and mouth.

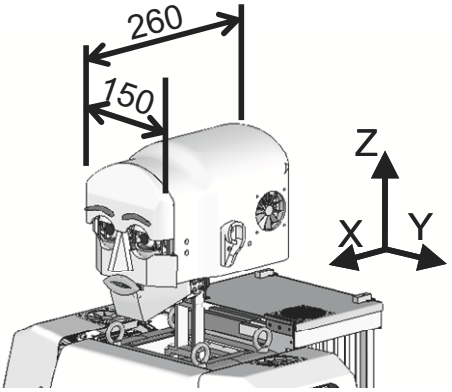

Figure 5. Overview of the head

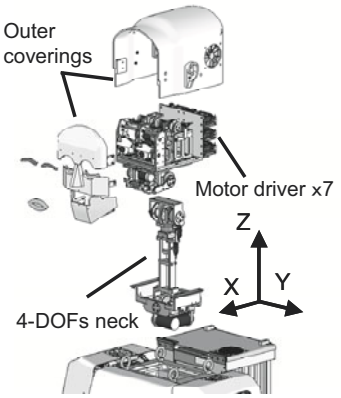

Figure 6. Exploded view of head and neck

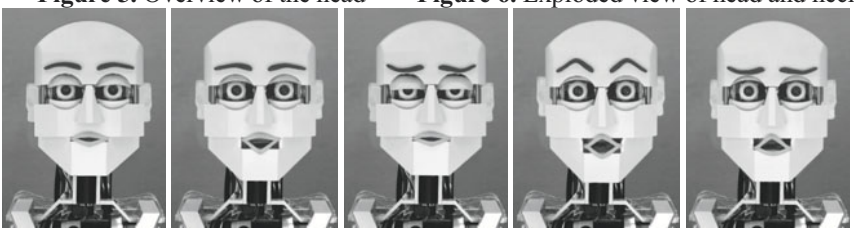

Figure 7. Examples of the facial expressions of the head

We have also developed a new anthropomorphic robotic hand WSH-1 (Waseda Soft Hand-No.1) for KOBIAN's hand (Zecca et al., 2008). WSH-1's palm consists of a framework structure and soft material (Hitohada gel, Exseal Co., Ltd.). WSH-1's finger is molded by silicone (ELASTOSIL M8520, Wacker Asahikasei Silicone Co., Ltd.) , wears a skin molded by Hitohada gel, and performs bending and stretching by a wire. Figure 8 and Figure 9 show the structure and picture.

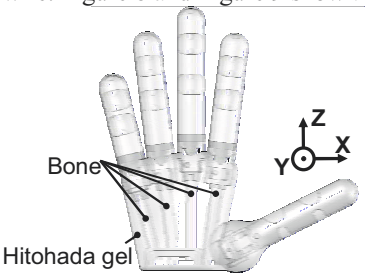

Figure 8. Structure of WSH-1

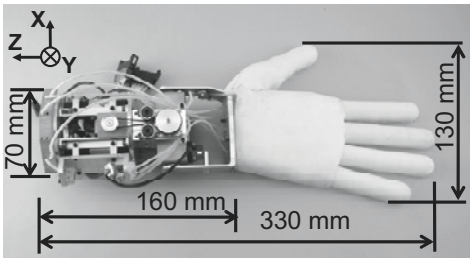

Figure 9. Picture of WSH-1

System configuration. The system configuration of KOBIAN is shown in Figure 10. The control PC (Pentium M 1.6GHz, RAM 2GB) is mounted on KOBIAN's back.

Storage is a Compact Flash memory 2GB, and an operating system (QNX Neutrino 6.3.0) is installed in it. The CPU communicates to HRP Interface Board (Zuco, Co., Ltd.) via PCI Back Plain Board. The control program give speed commands to motor drivers via D/A convertor on HRP Interface Board and get encoders' pulses via pulse counter on HRP Interface Board. Nitta 6-axis Force/Torque Sensors mounted on both feet send data via PCI Receiver Board. The control PC is operated by using remote desktop via Ethernet or Wireless LAN IEEE 802.11g. Figure 11 shows examples of the whole-body emotion expressions.

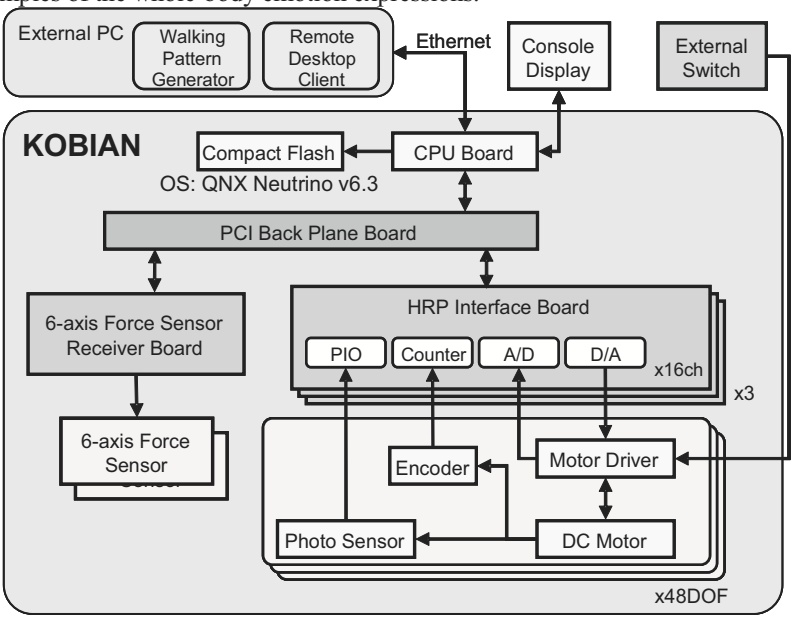

Figure 10. Control system configurations of KOBIAN

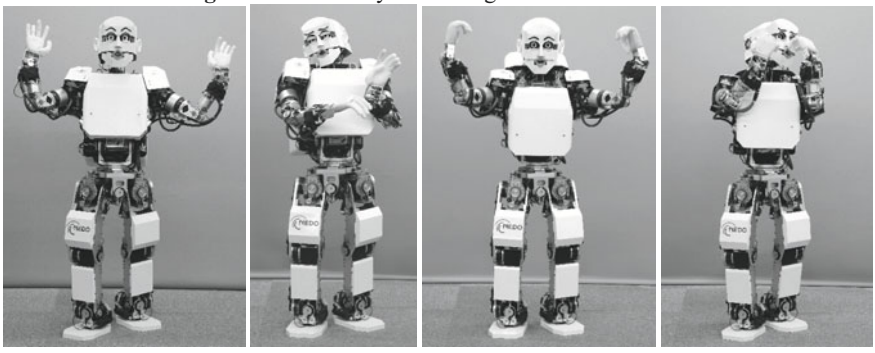

Figure 11. Examples of the whole-body emotion expression

Discussion

A modular design is a guidance to reduce costs for various product line developments. Naturally, module granularity depends on a desired product lineup.

The modular design guidance of KOBIAN's head is to adapt to various outer covering and easy to maintenance. At present, unfortunately, it has not been confirmed yet about the adaptation. We think this will be confirmed by collaborating with many appearance designers and making various types of outer covering. About the maintainability, it becomes easier rather than WE-4RII. In order to evaluate quantitatively, it is necessary to measure maintenance time.

KOBIAN's head is a module that provides a electric interface consist of motor speed commands and encoder pulses of 7-DOFs. However, we cannot assume it as the best modular design because it requires PID control of each motor to PC.

A module that connection interface is completely free does not exist. A module is a thing comprising some kind of limited connection interface. In this sense, the performance of the modularization depends on availability and compatibility of the connection interface.

On KOBIAN's head, it can be assumed as more-modularized by using communication interface used well such as RS-232C, RS-485, Ethernet and USB instead of the interface that requires many lines such as motor speed commands and encoder pulses. Furthermore, availability will be improved by using not only speed commands but also commands for angles and angular accelerations in the protocol. So, we think it is better way to mount a processor which executes PID control in each module.

Conclusion and Future Works

In this elderly-dominated society, Personal Robots and Robot Technology (RT)-based assistive devices are expected to play a major role, both for joint activities with their human partners and for participation in community life. So far, several different personal robots have been developed. However, it is not yet clear what kind of ability is necessary for personal robot. We think that emotional expression of robot is effective for joint activities of humans and robots.

To this purpose we developed a whole body bipedal humanoid robot, named KOBIAN, which is also capable to express human-like emotions. This novel robot is based on the previously developed WABIAN-2 for the lower body, and on WE-4RII for the head.

We consider an appearance of humanoid robot, particularly face, is that people either like it or don't like it. It is inefficient to design a driving mechanism of robot head from the beginning in order to adapt to various preferences. Therefore, we conduct modular design of driving part and outer covering. And, modular design

contributes to maintainability. In addition, we described the system configurations of KOBIAN, and discussed about modularizing and interface.

In the future, we would like to collaborate with appearance designers, develop varies types of outer covering, compare the difference of the impressions on humans, and approach to clarification of designer’ s sense. In addition, we will improve the modular design of the humanoid robots in order to make them easier to adapt to various requirements and designs.

Acknowledgement

This research was commissioned by the New Energy and Industrial Technology Development Organization (NEDO) and conducted at Humanoid Robotics Institute, Waseda University. Special thanks to SolidWorks Japan K.K. for the software contribution, and KURARAY Co., Ltd. for the SEPTON contribution. This work was supported in part by Global COE Program "Global Robot Academia" from the Ministry of Education, Culture, Sports, Science and Technology of Japan.

References

Miwa, H., Okuchi, T., Takanobu, H. and Takanishi, A. (2002). Development of a new human-like head robot WE-4. Proceedinds of the IEEE/RSJ International Conference on Intelligent Robots and System, 2002, 2443-2448.

Miwa, H., Itoh, K., Matsumoto, M., Zecca, M., Takanobu, H., Roccella, S., Carrozza, M. C., Dario, P., Takanishi, A. (2004). Effective Emotional Expressions with Emotion Expression Humanoid Robot WE-4RII. Proceedings of 2004 IEEE/RSJ International Conference on Intelligent Robots and Systems, September 28 - October 2, 2004, Sendai, Japan, 2203-2208.

Endo, N., Momoki, S., Zecca, M., Saito, M., Mizoguchi, Y., Itoh, K., and Takanishi, A. (2008). Development of Whole-Body Emotion Expression Humanoid Robot. Proceedings of the 2008 IEEE International Conference on Robotics and Automation, Pasadena, CA, USA, 2008, 2140-2145.

DiSalvo, C., Gemperle, F., Forlizzi, J., and Kiesler, S. (2002). All robots are not created equal: the design and perception of humanoid robot heads. Proceedings of the conference on Designing interactive systems: processes, practices, methods, and techniques, 2002.

Mori, M. (1970). Bukimi no tani [The Uncanny Valley]. Energy, vol. 7 (Originally in Japanese), 1970, 33-35.

Zecca, M., Endo, K., Endo, N.,Mizoguchi, Y., Kusano, T., Itoh, K., and Takanishi, A. (2008). Design and Evaluation of The Soft Hand WSH-1 For The Emotion Expression Humanoid Robot KOBIAN. Proceedings of the 6th International Conference of the International Society for Gerontechnology, Pisa, Italy, June, 2008.

A Random-Profile Approach for Trajectory Planning of Wheeled Mobile Robots With non-Slipping Constraint

M. Haddad and H.E. Lehtihet.

Laboratory of Structure Mechanics
EMP, BP 17 Bordj El-Bahri 16111, Algiers, Algeria.
haddadmoussa2003@yahoo.fr he.lehtihet@gmail.com

1. Introduction

Due to increased needs to improve the productivity in various industries, several methods have been proposed to solve the minimum-time trajectory-planning problem for a nonholonomic multi-body Wheeled Mobile Robot (WMR), subjected to move in a structured workspace under kinematics constraints (see, e.g., Jacobs et al., 1991, Reister and Pin, 1994, Renaud and Fourquet, 1997, Aydin and Temeltas, 2002, Balkcom and Mason, 2002). However, dynamics is also important, particularly if velocities are high or if it is needed to compute correctly inputs of the system control.

For instance, most trajectory planners for WMR suppose that the friction coefficient (wheels /ground) is sufficiently high. In other words, it is assumed that the tangential contact force always remains inside the friction cone. However, typically in the case of minimum-time trajectories undertaken on a slippery floor, dynamic states may exist where such a hypothesis would not hold. When that happens, the wheel concerned by the violation will slip and the robot will subsequently deviate from its reference trajectory. Of course, such an undesirable behavior cannot be avoided adequately just by using kinematics. This can be properly handled only by incorporating an additional dynamics constraint in the trajectory-planning problem.

Methods that handle dynamics without using any simplified model are quite few. Of interest here, is the Random-Profile Approach (RPA) that considers full dynamics and that is able to account for constraints on:

- *Geometry* (obstacle avoidance, bounded path curvature / joint positions);
- *Kinematics* (nonholonomic constraints, bounded velocities / accelerations);
- *Dynamics* (bounded torques, stability issue).

RPA is a flexible off-line planner that involves inverse dynamics only. Initially proposed for fixed-base manipulators (Chettibi and Lehtihet, 2002), it was later extended to WMRs (Haddad et al., 2005, 2007a) and to wheeled mobile manipulators (Haddad et al., 2006, 2007b, 2009).

Our goal is to show that RPA is versatile enough to handle non-slipping restriction. Thus, we will be concerned mainly by this newly introduced constraint, as the main development of this method is already available in the above-cited 2007a reference.

2. Description of the problem

Let $\Re = (O, \boldsymbol{x}, \boldsymbol{y}, \mathbf{z})$ be the fixed frame of the world coordinates. The robot considered here is a wheeled platform constituted of a rigid chassis supported by non deformable wheels. The platform type may belong to any of the nonholonomic WMRs discussed in Campion et al. (1996). We assume that the motion is confined to the $(O, \boldsymbol{x}, \boldsymbol{y})$ plan. We note $\Re' = (O', \boldsymbol{x}', \boldsymbol{y}', \mathbf{z}')$ the moving frame associated to the platform, such as $\mathbf{z}' // \mathbf{z}$. The platform state in $\Re$ can be described by a vector $\boldsymbol{X} = [x, y, \theta]^T$, where x, y are the coordinates of O' in $\Re$ while θ is the orientation of the platform in $\Re$. The generalized coordinates of the system are given by the n-vector $\boldsymbol{q} = [\boldsymbol{X}^T, \boldsymbol{q}_w{}^T]^T$, where $\boldsymbol{q}_w$ is the $(n-3)$-vector of independent coordinates related to the rotation/orientation of the wheels in $\Re'$.

The WMR is to move from $\mathbf{X}^{START} = [x^S, y^S, \theta^S]^T$ to $\mathbf{X}^{GOAL} = [x^G, y^G, \theta^G]^T$. The general trajectory problem consist of finding the trajectory $\boldsymbol{q}(t)$, the time history of vector $\boldsymbol{\Gamma}(t)$ of actuator efforts and the travel time T so that boundary conditions are matched, all constraints are respected and a given cost function J is minimized (here, we consider only the minimum-time problem, so that: $J \equiv T$).

The set of feasible trajectories may be restricted by numerous constraints that must be satisfied during the travel from $\mathbf{X}^{START}$ to $\mathbf{X}^{GOAL}$.

Boundary conditions

– *Position/Orientation* $\mathbf{X}(t=0) = \mathbf{X}^{START}$ and $\mathbf{X}(t=T) = \mathbf{X}^{GOAL}$ (1a)

– *Velocity* $\dot{\boldsymbol{q}}(t=0) = \vec{0}$ and $\dot{\boldsymbol{q}}(t=T) = \vec{0}$ (1b)

Physical limitations

The following constraints on active-joint torques must be verified for $t \in [0, T]$:

$$\left|\Gamma_i(t)\right| \le \Gamma_i^{max} \qquad i = 1, \ldots n \tag{1c}$$

All of the above restrictions (1), including nonholonomic constraints and collision issues, are already handled by the basic RPA scheme (see Haddad et al., 2007a).

Non-slipping constraint

Such a constraint is defined according to Coulomb's law as follows:

$$\frac{F_{ti}}{F_{zi}} \le \eta \qquad i = 1, \ldots n_w \quad \text{with} \quad F_{ti} = \sqrt{F_{xi}^2 + F_{yi}^2} \tag{2}$$

Here F_{xi}, F_{yi} and F_{zi} are the components of the contact force of the i^{th} wheel with the ground. These efforts can be easily calculated by Newton-Euler formalism. n_w is the number of wheels. η is the friction coefficient of the wheels/ground contact.

3. Proposed method

3.1. Overview of the basic RPA scheme

First, RPA treats the problem without integrating the set of differential equations governing the behavior of the robot. Indeed, RPA considers that T and $\boldsymbol{q}(t)$ are the only unknowns of the problem. Once these unknowns are found, the vector $\boldsymbol{\Gamma}(t)$ of generalized efforts is easily deduced via inverse dynamics.

Second, RPA builds time-scaled trajectory profiles to map real trajectories over the unit interval. Indeed, any given trajectory $\boldsymbol{q}(t)$ can be uniquely characterized by its travel time T and its time-evolution shape $\mathbf{Q}$:

$$\boldsymbol{q}(t) = \mathbf{Q}(\xi(t)) = \mathbf{Q}(\xi) \text{ o } \xi(t) \quad \text{with} \quad \xi(t) \equiv t / T \tag{3}$$

The trajectory profile $\mathbf{Q}(\xi)$ gives the shape of the time history of $\boldsymbol{q}$ from the start of the motion ($\xi = 0$) to its end ($\xi = 1$). Hereafter, the *prime* symbol will be reserved to indicate derivatives with respect to ξ. We note that any given profile $\mathbf{Q}$ uniquely defines a whole class of trajectories. All member $\boldsymbol{q}$ of a given class $\mathbf{Q}$ will share the same time-evolution shape but will have distinctive travel times T.

Third, all constraints of the problem can be grouped into two categories: class-related and member-related constraints. The former depend solely on the profile $\mathbf{Q}$ whereas the later further depend on the travel time T. For example, obstacle-avoidance constraints and other geometric constraints never depend on the travel time. They belong therefore to the first category. It can be shown that, for a given $\mathbf{Q}$, (in other words, within a given class), all member-related constraints, such as those on kinematics and dynamics, can be converted to bounds on admissible values of T.

Fourth, given a class $\mathbf{Q}$, we can easily extract the specific travel time $T_{\mathbf{Q}}$ that will distinguish the best member $\boldsymbol{q}$ within this selected class while taking into account all constraints. Hence, the problem of finding the overall best trajectory is converted to finding the class to which belongs this desired trajectory. In other words, RPA is a method that probes the solution space directly at the class level.

This problem is solved via a nested master/optimization whose final output is the best member of the best class, among those classes that would have been tested. The slave routine is a simple deterministic optimizer that actually plays the role of a workhorse fitness function evaluating any input class and extracting its best member. The master routine is a stochastic optimizer that plays the role of a class selector. It is based on a simulated-annealing strategy (Hajek, 1985) that randomly probes the class space to propose candidate profile for evaluation. Its build-in Metropolis algorithm gradually targets those promising candidate that would most likely hold the optimal trajectory.

Naturally, this difficult functional optimization is converted to a more tractable parametric problem via a discrete representation of trajectory profiles. Namely, each random profile is built from a finite set of free control nodes; continuity to a sufficient order is achieved by fitting a smooth model that accounts for boundary conditions and nonholonomic constraints. These free control nodes being the only unknowns, the whole problem boils down to finding their optimal setting.

Since a trajectory may be written in terms of a geometric path and a motion on this path, it is then convenient to express a trajectory profile as follows:

$$\mathbf{Q}(\xi) = \mathbf{P}(\lambda(\xi)) = \mathbf{P}(\lambda) \circ \lambda(\xi) \tag{4}$$

$\mathbf{P}(\lambda)$ is a time-independent vector with same dimension as that of $\mathbf{Q}$. It describes the geometric path pursued by the robot in the generalized-coordinate space when λ varies continuously from 0 (start) to 1 (end). The other form, $\lambda(\xi)$, is the motion profile. It is a monotonically increasing scalar function that describes how the robot actually moves on its path $\mathbf{P}$.

This partition path/motion of a trajectory profile $\mathbf{Q}$ greatly increases the flexibility of RPA. A random $\mathbf{Q}$ now can be built using two distinct sets of control nodes on two tailored fitting models: a cubic-spline model for $\lambda(\xi)$ and an 4th-order B-spline model for $\mathbf{P}(\lambda)$ (to insure afterward the continuity of torques). Moreover, geometric constraints and boundary conditions now can be distributed conveniently. For instance, $\lambda(\xi)$ will be concerned by boundary conditions on velocity; whereas $\mathbf{P}(\lambda)$ will be concerned by boundary conditions position/orientation, obstacle-avoidance and nonholonomic constraints. These constraints are handled either, *a posteriori*, by rejection or, *a priori*, by inclusion (Haddad et al., 2007a). The rejection is used exclusively for obstacle avoidance whereas the inclusion is used to handle nonholonomic constraints and boundary conditions.

3.2. Treatment of the non-slipping constraint

In the RPA framework, given a profile $\mathbf{Q}$, all kinodynamic constraints such as (1c) simply translate to bounds on admissible values of T (Haddad et al., 2007a).

$$T \in [T_L, T_R] \tag{5}$$

The non-slipping constraint (2) is converted also into a set of subintervals of admissible values for T. Indeed, components F_{xi}, F_{yi} and F_{zi} can be written as follows:

$$\begin{cases} F_{xi} = D_{xi}(\mathbf{Q}, \mathbf{Q}', \mathbf{Q}'')T^{-2} + H_{xi}(\mathbf{Q}) \\ F_{y_i} = D_{yi}(\mathbf{Q}, \mathbf{Q}', \mathbf{Q}'')T^{-2} + H_{yi}(\mathbf{Q}) \\ F_{zi} = D_{zi}(\mathbf{Q}, \mathbf{Q}', \mathbf{Q}'')T^{-2} + H_{zi}(\mathbf{Q}) \end{cases} \tag{6}$$

In the above expressions, the first terms (D) represent the effect of inertial, Coriolis and centrifugal forces while the second (H) regroups the effect of gravitational forces. Using (6), the constraint (2) may be rewritten under the following form:

$$A_{0i} + A_{2i}\,T^{-2} + A_{4i}\,T^{-4} \le 0 \qquad i = 1 \ldots n_w \tag{7}$$

$$A_{0i} = H_{xi}^2 + H_{yi}^2 - \eta^2 H_{zi}^2, \quad A_{2i} = 2\left(D_{xi}H_{xi} + D_{yi}H_{yi} - \eta D_{zi}H_{zi}\right), \quad A_{4i} = D_{xi}^2 + D_{yi}^2 - \eta^2 D_{zi}^2$$

Hence, each inequality in (7) may lead to, at most, two distinct intervals of admissible values of T:

$$T \in [T_{\mathrm{L}1i},\, T_{\mathrm{R}1i}] \cup [T_{\mathrm{L}2i},\, T_{\mathrm{R}2i}] \tag{8}$$

However, intersecting (5) and (8) for ξ in [0, 1] may yield to a set of k distinct windows: $\prod = [T_1, T_2] \cup [T_3, T_4] \cup \ldots [T_{2k-1}, T_{2k}]$. Consequently, for any trial $\mathbf{Q}$, the optimal travel $T_{\mathbf{Q}}$ must minimize J within $\prod$.

Let T_m be the travel time minimizing the cost function $J_{\mathbf{Q}}(T)$, for a given $\mathbf{Q}(\xi)$, without considering kinodynamic constraints. The value of T_m can be calculated easily via the minimization of a one-dimensional function (Haddad et al., 2007a). Therefore, the optimal $T_{\mathbf{Q}}$ minimizing $J_{\mathbf{Q}}(T)$ under kinodynamic constraints is deduced according to the position of T_m in the admissible interval $\prod$:

$$T_{\mathbf{Q}} = \begin{cases} T_m & \text{if} \quad T_m \in \prod \\ T_j \,/ \quad J_{\mathbf{Q}}(T_j) = \min\left(J_{\mathbf{Q}}(T_i) \;\; for \;\; i = 1 \cdots 2k\right) & \text{if} \quad T_m \notin \prod \end{cases} \tag{9}$$

4. Numerical example

We consider the WMR described in Table 1 and in Figure 1. This robot has two independent driving wheels and two free caster wheels. Contact forces of the driving wheels with the ground are given by the following:

$$\begin{cases} F_{x1} = \dfrac{1}{2T^2}\left(m_r v'(\xi) + \dfrac{Iz_r}{L_w}\theta''(\xi)\right) \\ F_{y_1} = \dfrac{m_r v(\xi)\theta'(\xi)}{2T^2} \\ F_{z1} = \dfrac{-r_w}{2L_w T^2}\left(m_r + \dfrac{2Iy_w}{r_w^2}\right)v(\xi)\theta'(\xi) + \dfrac{m_r g}{4} \end{cases}, \quad \begin{cases} F_{x2} = \dfrac{1}{2T^2}\left(m_r v'(\xi) - \dfrac{Iz_r}{L_w}\theta''(\xi)\right) \\ F_{y_2} = \dfrac{m_r v(\xi)\theta'(\xi)}{2T^2} \\ F_{z2} = \dfrac{r_w}{2L_w T^2}\left(m_r + \dfrac{2Iy_w}{r_w^2}\right)v(\xi)\theta'(\xi) + \dfrac{m_r g}{4} \end{cases}$$

with $m_r = m_p + 2m_w$, $\quad v(\xi) = x'(\xi)\cos(\theta(\xi)) + y'(\xi)\sin(\theta(\xi))$,

$Iz_r = Iz_p + 2(Iz_w + m_w L_w^2)$, $\quad v'(\xi) = x''(\xi)\cos(\theta(\xi)) + y''(\xi)\sin(\theta(\xi))$.

The workspace is a ($24m \times 21m$) flat floor with three obstacles (Figure 2*a*). Boundary conditions are as follows: $\mathbf{X}^{\mathrm{START}} = (3, 3, 0)$ and $\mathbf{X}^{\mathrm{GOAL}} = (22, 12, 0)$. The following results have been obtained using our RPA code running on a 1.6 GHz

Intel Centrino Duo PC. First, we solve the minimum-time trajectory problem under maximum-torque constraints but without considering non-slipping constraints. The solution is shown in Figure 2 with a score $T = 8.79\ s$ and a runtime of 63 *s*. The final path is given in Figure 2a. The time history of velocities, active-joint torques and ratio of contact forces is given, respectively, in Figure 2b, 2c and 2d. This result clearly indicates that such a solution is actually not feasible as the ratio of contact forces well exceeds the threshold value $\eta = 0.7$.

Table 1. Parameters of the WMR.

$L_w = 0.75\ m$	$m_p = 50.0\ kg$	$I_{zp} = 26.04\ kg.m^2$	$\Gamma_1^{\max} = 5Nm$
$L_v = 2.00\ m$	$m_w = 1.0\ kg$	$I_{zw} = 0.0025\ kg.m^2$	$\Gamma_2^{\max} = 5Nm$
$r_w = 0.10\ m$		$I_{yw} = 0.005\ kg.m^2$	$\eta = 0.7$

The platform is a $(2L_w \times L_v)$ *rectangle. The center of gravity is in the middle of the wheel axis. The inertia moment of the platform is considered only around the* $\mathbf{z}'$*-axis.* r_w *is the wheel radius.* m_p *and* m_w *are, respectively, the mass of the platform and that of the wheels.* I_{zp} *is the inertia moment of the platform about the* $\mathbf{z}'$*–axis.* I_{zw} *and* I_{yw} *are the inertia moment of the wheels about the* $\mathbf{z}'$*–axis and the* $\mathbf{y}'$*–axis (passing through the wheel center). The friction coefficient* η *is the same for the two driving wheels. Inertia parameters of the free caster wheels are negligible.*

We solve again the same problem including now the non-slipping constraint. The new solution is given in Figure 3 with a score T = 9.36 s and a runtime of 88 s. As shown in Figures 3c and 3d, both types of constraints are fully respected during the motion. As expected, the robot is compelled to decrease its speed significantly around the corner. However, RPA is a sufficiently flexible optimization technique that is able to compensate for this drawback by finding a new shorter path, now accessible to the robot due to its lower speed

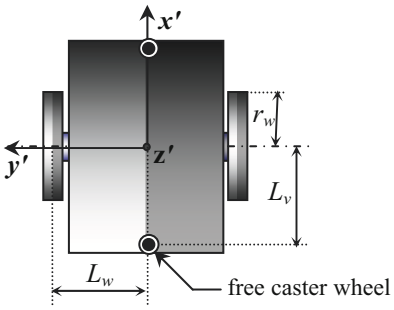

Figure 1. Wheeled mobile robot

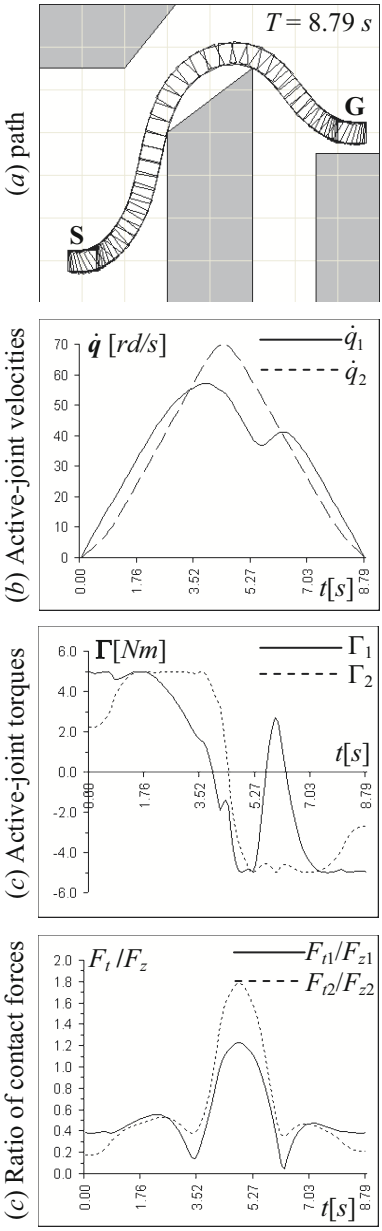

Figure 2. Results obtained without considering non-slipping constraints

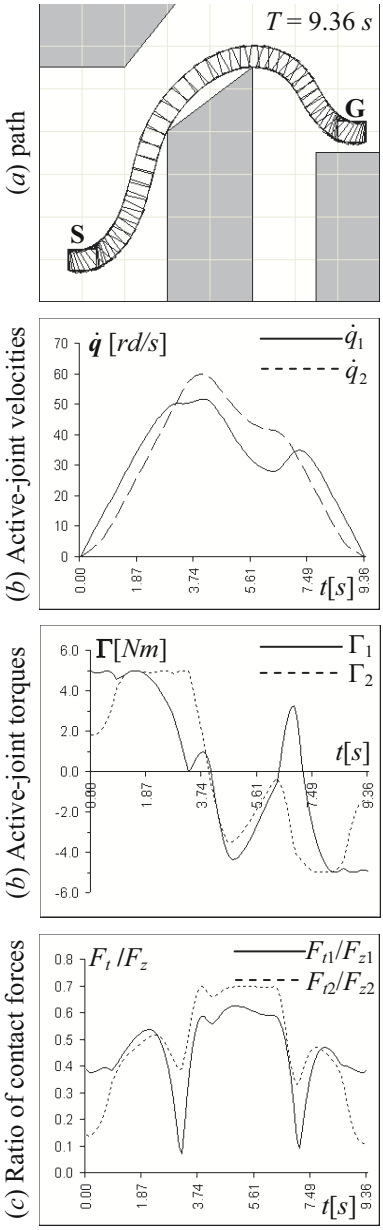

Figure 3. Results obtained while considering non-slipping constraints

5. Conclusion

We have proposed an extension of the random-profile approach to handle a trajectory-planning problem for a wheeled mobile robot while considering a non-slipping constraint. This constraint complicates the problem due to the non-linearity of the forces at the wheels/ground contact. Our approach is based on the simultaneous search for the robot path and for the time history on this path. In this approach, the issue of non-slipping has been treated by transforming this constraint to a set of admissible subintervals for the travel time.

6. References

Aydin, S., and Temeltas, H. (2002). A novel approach to smooth trajectory planning of a mobile robot. *IEEE Int. Workshop on Advanced Motion Control,* 472–477.

Balkcom, D. J., and Mason, M. T. (2002). Extremal trajectories for bounded velocity mobile robots. *In Proc. of IEEE Int. Conf. on Robotics & Automation.*

Campion, G., Bastin, G., and d'Andrea-Novel, B. (1996). Structural properties and classification of kinematic and dynamic Models of wheeled mobile robots. *IEEE Transactions on Robotics and Automation*, Vol. 12, No.1, 47–62.

Chettibi, T., and Lehtihet, H.E. (2002). A new approach for point-to-point optimal motion planning problems of robotic manipulators. *In Proc.* 6th *Biennial Conf. on Engineering Systems Design and Analysis,* APM10.

Haddad, M., Chettibi, T., Lehtihet, H. E., and Hanchi, S. (2005). A new approach for minimum-time motion planning problem of wheeled mobile robots. 16th *IFAC World Congress,* Prague.

Haddad, M., Chettibi, T., Saidouni, T., Hanchi, S., and Lehtihet, H. E. (2006). Sub-optimal motion planner of mobile manipulators in generalized point-to-point task with stability constraint. *In Romansy 16 Robot Design, Dynamics and Control,* edited by Teresa Zielinska and Cezary Zielinski, Springer Wien New York, 171–178.

Haddad, M., Chettibi, T., Hanchi, S., and Lehtihet, H. E. (2007a). A random-profile approach for trajectory planning of wheeled mobile robots. *European J. of Mechanics A/Solids,* Vol. 26, 519–540.

Haddad, M., Hanchi, S., and Lehtihet, H. E. (2007b). Sub-optimal motion planner of a mobile manipulator with end-effector's specified path. *IFToMM World Congress*.

Haddad, M., Hanchi, S., and Lehtihet, H. E. (2009). Point-to-point trajectory planning of wheeled mobile manipulators with stability constraint. Extension of the random-profile approach. *European J. of Mechanics, A/Solid,* Vol. 28, 477–493.

Hajek, B. (1985). A tutorial survey of theory and application of simulated annealing. *In Proceeding of* 24th *Conference on Decision and Control,* 755–760.

Reister, D. B., and Pin, F. G. (1994). Time-optimal trajectories for mobile robots with two independently driven wheels. *Int. J. of Robotic Research*, Vol.13, No.1, 38–54.

Renaud, M., and Fourquet, J. Y. (1997). Minimum-time motion of a mobile robot with two independent acceleration-driven wheels. *IEEE Int. Conf. on Rob. Aut.* NM, 2608–2613.

The Second Type of Singularity Analysis of the New Parallel Manipulator with 6 Degree-of-Freedom

Zh. Baigunchekov, M. Izmambetov

Kazakh-British Technical University, Almaty, Republic of Kazakhstan

Abstract - The analytical method of the second type of singularity analysis of the new parallel manipulator with 6 degrees-of-freedom is worked out on the bases of Jacoby matrix connecting output and input generalized velocities.

Introduction

As Merlet (2000) has noted, parallel manipulators (PM) in comparison with serial manipulators possess have big carrying capacity, high velocities and positioning accuracy. These advantages motivated the development of the new six-legged PM with six degree of freedom (DOF) by Baigunchekov et al. (2007, 2009).

However, PM have many singularity configurations in which they cannot carry out their functional tasks. Gosselin and Angeles (1990), Tsai (1999) describe three types of singularity of PM. The Jacobian of a PM can be divided into two matrix: one matrix **A** associated with the direct kinematics and the other matrix **B** associated with the inverse kinematics. In *the first type* of singularity, when det **B**=0, a manipulator loses 1 or more DOF. In *the second type* of singularity, when det **A**=0, a manipulator gains 1 or more DOF. In *the third type* of singularity the inverse and direct kinematic singularities are presented simultaneously.

We (2010) obtained some results for identification of the first type of singularities, and also one of conditions of occurrence of the second type of singularities of the new PM with 6 DOF. In this paper we have presented results of more full and detailed analysis of the second type of singularities of this PM based on research of degeneration of Jacobian matrix **A** because of a linear dependence of its columns.

Geometry of the PM with 6 DOF

The PM with 6 DOF contains a moving platform, connected with a fixed base by six legs of kind RSS, where R - a revolute active-joint, S - a spherical joint (Figure 1). This PM is intended for reproduction of movement of a mobile platform or the frame $Px_Py_Pz_P$ attached to it, with respect to base frame $OXYZ$

$$\left.\begin{array}{l} X_P = X_P(\mathbf{q}(t)),\ \ Y_P = Y_P(\mathbf{q}(t)),\ \ Z_P = Z_P(\mathbf{q}(t)) \\ \gamma_P = \gamma_P(\mathbf{q}(t)),\ \ \alpha_P = \alpha_P(\mathbf{q}(t)),\ \ \beta_P = \beta_P(\mathbf{q}(t)) \end{array}\right\} \qquad (1)$$

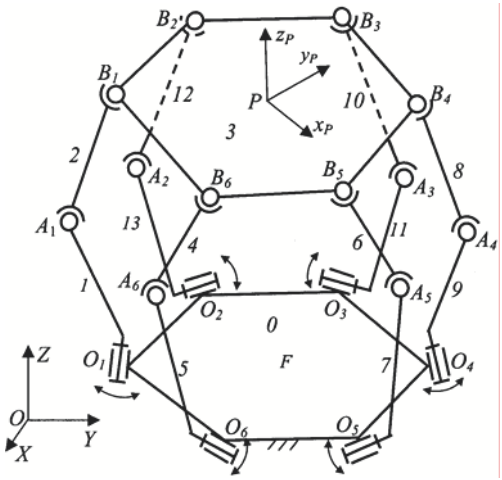

Figure 1. Six-legged parallel manipulator with 6 DOF.

where $\mathbf{q}(t)=[\theta_1(t),\ \theta_2(t),\ldots,\ \theta_6(t)]^{\mathrm{T}}$ - a vector of the input generalized coordinates; $\mathbf{x}(t)=[X_P,\ Y_P,\ Z_P,\ \gamma_P,\ \alpha_P,\ \beta_P]^{\mathrm{T}}$ - a vector of the output coordinates; γ_P, α_P и β_P - the components of relative orientation of coordinates systems $Px_Py_Pz_P$ and $OXYZ$.

Taking into structure symmetry of the PM with 6 DOF, all geometrical parameters are shown on the i-th leg $OO_iA_iB_iP$ (Figure 2). These geometrical parameters are determined on basis of the Denavit-Hartenberg Homogeneous Transformation Matrix: $l_{O_iA_i}=f_i$, $l_{A_iB_i}=g_i$ - lengths of actuated and passive links, respectively; $a_{0,i},b_{0,i},c_{0,i},\alpha_{0,i},\beta_{0,i},\gamma_{0,i}$ - parameters determining frame $O_ix_iy_iz_i$ attached to a motionless element of revolute active-joint O_i with respect to frame $OXYZ$; $l_{PB_i}=h_i$, φ_i - polar coordinates of spherical joints B_i with respect to local frame $Px_Py_Pz_P$. ψ_i, - a constant angle between link O_iA_i and an axis O_iz_i.

Let the relative positioning of local frame $Px_Py_Pz_P$ with respect to base frame $OXYZ$ is defined by a set of parameters $a_{0,P},b_{0,P},c_{0,P},\alpha_{0,P},\beta_{0,P},\gamma_{0,P}$, and the vector $\mathbf{g}_i=\overline{A_iB_i}$ is defined by the spherical coordinates g_i, θ_i', θ_i''. Then for PM the following equation is fair

$$\mathbf{A}(\mathbf{x},\mathbf{q})\dot{\mathbf{x}}=\mathbf{B}(\mathbf{x},\mathbf{q})\dot{\mathbf{q}}\ , \tag{2}$$

where $\mathbf{A}$ and $\mathbf{B}$ - 6×6 Jacobian matrices depending only from a configuration of PM; $\dot{\mathbf{x}}=\left[\dot{\mathbf{r}}_P^T,\boldsymbol{\omega}_P^T\right]^T$ - a vector of output velocities; $\dot{\mathbf{q}}=\left[\dot{\theta}_1,\dot{\theta}_2,...,\dot{\theta}_6\right]^T$ - a vector of the generalized velocities; $\dot{\mathbf{r}}_P=\left[\dot{X}_P,\dot{Y}_P,\dot{Z}_P\right]^T$ - a vector of velocity of the point P;

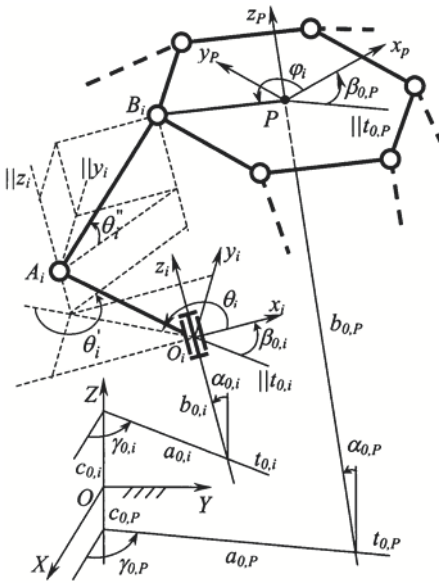

Figure 2. Geometry of the *i*-th leg of the PM.

$\boldsymbol{\omega}_P = \left[\omega_{P_X}, \omega_{P_Y}, \omega_{P_Z}\right]^T$ - a vector of angular velocities of a moving platform. Elements a_{ij} and b_{ij} of matrices **A** and **B** are determined through constant geometrical and variable kinematic parameters of PM by the following equations

$$
\begin{aligned}
a_{i1} &= \mathbf{g}_i \cdot \mathbf{e}_X = g_{iX} = g_i \{ c\theta_i'' c(\theta_i + \theta_i')(c\gamma_{0i} c\beta_{0i} - s\gamma_{0i} c\alpha_{0i} s\beta_{0i}) - \\
&\quad - c\theta_i'' s(\theta_i + \theta_i')(c\gamma_{0i} s\beta_{0i} + s\gamma_{0i} c\alpha_{0i} c\beta_{0i}) + s\theta_i'' s\gamma_{0i} s\alpha_{0i} \}, \\
a_{i2} &= \mathbf{g}_i \cdot \mathbf{e}_Y = g_{iY} = g_i \{ c\theta_i'' c(\theta_i + \theta_i')(s\gamma_{0i} c\beta_{0i} + c\gamma_{0i} c\alpha_{0i} s\beta_{0i}) + \\
&\quad + c\theta_i'' s(\theta_i + \theta_i')(c\gamma_{0i} c\alpha_{0i} c\beta_{0i} - s\gamma_{0i} s\beta_{0i}) - s\theta_i'' c\gamma_{0i} s\alpha_{0i} \}, \\
a_{i3} &= \mathbf{g}_i \cdot \mathbf{e}_Z = g_{iZ} = g_i \{ c\theta_i'' c(\theta_i + \theta_i') s\alpha_{0i} s\beta_{0i}) - \\
&\quad - c\theta_i'' s(\theta_i + \theta_i') s\alpha_{0i} c\beta_{0i} - s\theta_i'' c\alpha_{0i} \},
\end{aligned} \tag{3}
$$

$$
\begin{aligned}
a_{i4} &= (\mathbf{h}_i \times \mathbf{g}_i) \cdot \mathbf{e}_X = n_{iX} = h_{iY} g_{iZ} - h_{iZ} g_{iY} \\
a_{i5} &= (\mathbf{h}_i \times \mathbf{g}_i) \cdot \mathbf{e}_Y = n_{iY} = h_{iZ} g_{iX} - h_{iX} g_{iZ} \\
a_{i6} &= (\mathbf{h}_i \times \mathbf{g}_i) \cdot \mathbf{e}_Z = n_{iZ} = h_{iX} g_{iY} - h_{iY} g_{iX}
\end{aligned} \tag{4}
$$

$$
\begin{aligned}
b_{ii} &= \mathbf{e}_i^T \cdot (\mathbf{f}_i \times \mathbf{g}_i) = f_i \cdot g_i \cdot \sin\psi_i \cos\theta_i'' \sin\theta_i' \\
b_{ij} &= 0, \text{ for } i \neq j, \quad i = 1,2,...,6; \quad j = 1,2,...,6,
\end{aligned} \tag{5}
$$

where $\mathbf{e}_X$, $\mathbf{e}_Y$, $\mathbf{e}_Z$ - unit vectors indicating the direction of axes *OX*, *OY* and *OZ,* respectively; $\mathbf{f}_i = \overline{O_i A_i}$, $\mathbf{h}_i = \overline{PB}_i$; components of $\mathbf{h}_i$ are determined by equations

$$h_{iX} = h_i\{(c\gamma_{0P}c\beta_{0P} - s\gamma_{0P}c\alpha_{0P}s\beta_{0P})\cos\varphi_i - \\ -(c\gamma_{0P}s\alpha_{0P} + s\gamma_{0P}c\alpha_{0,P}c\beta_{0P})\sin\varphi_i\},$$

$$h_{iY} = h_i\{(s\gamma_{0P}c\beta_{0P} + c\gamma_{0P}c\alpha_{0P}s\beta_{0P})\cos\varphi_i + \\ +(c\gamma_{0P}c\alpha_{0P}c\beta_{0P} - s\gamma_{0P}s\beta_{0P})\sin\varphi_i\},$$

$$h_{iZ} = h_i\{s\alpha_{0P}s\beta_{0P}\cos\varphi_i + s\alpha_{0P}c\beta_{0P}\sin\varphi_i\} .$$

Singularity Analysis of the PM With 6 DOF

The first type of singularity of PM is associated with degeneration of matrix **B**, and the second type of singularity is associated with degeneration of a matrix **A**, and it is located in inside of working space. There are nonzero output velocities $\dot{\mathbf{x}}$ of the platform for a corresponding configuration of the PM, and they are transformed in zero vector by matrix **A.** These velocities of the platform are possible, even at immovable drives of input joints. We shall write matrix **A** in the following form

$$\mathbf{A} = \begin{bmatrix} g_{1X} & g_{1Y} & g_{1Z} & n_{1X} & n_{1Y} & n_{1Z} \\ g_{2X} & g_{2Y} & g_{2Z} & n_{2X} & n_{2Y} & n_{2Z} \\ \vdots & \vdots & \vdots & \vdots & \vdots & \vdots \\ g_{6X} & g_{6Y} & g_{6Z} & n_{6X} & n_{6Y} & n_{6Z} \end{bmatrix}, \tag{6}$$

where elements of first three columns are components of vectors $\mathbf{g}_i$, and elements of last three columns are components of vectors $\mathbf{n}_i = \mathbf{h}_i \times \mathbf{g}_i$.

Degeneracy of a matrix **A** in consequence of linear dependence of arbitrary two lines with numbers *j* and *k* have considered Baigunchekov et al. (2010). One of conditions of occurrence of the second type of singularity configuration is established. According to this condition passive links of PM corresponding to two linearly dependent lines of a Jacobian **A** attain layout along a direct line which passes through attachment points of these links with a mobile platform. In the given paper we shall consider linear dependence of columns of a matrix **A**. As against line vectors, each column vector is defined by a set separate coordinates of vectors of one group consisting either from vectors $\mathbf{g}_i$, or $\mathbf{n}_i = (\mathbf{h}_i \times \mathbf{g}_i)$ $i = 1,2,...,6$.

The following three cases of degeneration of matrix **A** are possible:

Case 1^0. three columns of one vectors group are linearly dependent.

Case 2^0. two columns of one vectors group are linearly dependent.

Case 3^0. all vectors of one vectors group are zero vectors.

Let's preliminary accept without the proof the following theorem.

The theorem. That two vectors laying in various and mutually crossed planes, were parallel, it is necessary and enough that each of these vectors was parallel to a straight line being intersection of their planes.

1^0. *Three columns of one vectors group are linearly dependent.* This case means that all vectors of this group are parallel.

Let's consider a case when all vectors $\mathbf{n}_i$ will be parallel, i.e., last three columns of matrix **A** will be linearly dependent. Fairly following statement.

The statement 1. Parallelism of all vectors $\mathbf{n}_i$ $i = 1,2,...,6$, is possible in that, and only in the event that each of these vectors is parallel to axis Pz_P of coordinates system $Px_Py_Pz_P$ connected to a mobile platform.

The proof of this statement is based on the above mentioned theorem.

In turn given statement means that in this case, according to definition of vector multiplication, vectors $\mathbf{g}_i$, $i = 1,2,...,6$ should lay in a plane of a mobile platform. Thus, we find one of conditions of degeneracy of **A**: z-components of vectors $\mathbf{g}_i$ with respect to local frame $Px_Py_Pz_P$ should have zero values, i.e.

$$g_{iz} = 0\,,\ i = 1,2,...,6 \tag{7}$$

We can obtain a kind of the equations (2) by transformation of coordinates it is possible concerning the coordinates system $Px_Py_Pz_P$ connected to a platform. Thus for a considered Case 1^0 the third, fourth and fifth columns of matrix **A** will be zero. Then the null-space of **A** is generated by a vector $[0, 0, 1, 1, 1, 0]^T$. This null-space corresponds to set of local rotations of a platform about an arbitrary axis of plane Px_Py_P and to its local linear moving in a direction of axis Pz_P at motionless drives. I.e. the PM gains the three transitory additional DOF. Moreover, a force applied at the platform in a direction of axis Pz_P, and also a forces couple applied at the platform in a arbitrary plane of parallel axis Pz_P do not influence drives, i.e. the PM is not capable to withstand these loadings.

2^0. *Two columns of one vectors group are linearly dependent.* This case means that all of a vector of this group lay in parallel planes or are simultaneously parallel to one common plane.

The statement 2. Vectors $\mathbf{n}_i = (\mathbf{h}_i \times \mathbf{g}_i)$ $i = 1,2,...,6$, can be simultaneously parallel to any plane.

Let's accept such statement without the proof. Not losing a generality of received results, we shall consider a special case when these vectors are parallel to a plane of platform Px_Py_P. As vectors $\mathbf{n}_i$ free, we admit, that $\mathbf{n}_i \in Px_Py_P$, $i = 1,2,...,6$. Then, for the sixth column of matrix **A** composed concerning frame $Px_Py_Pz_P$

$$n_{iz} = 0\,,\ i = 1,2,...,6 \tag{8}$$

Let's define a plane Γ_i, as a plane containing points P, A_i and B_i (Figure 3).

Then in view of that $\mathbf{n}_i \in Px_Py_P$, we shall obtain

$$\mathbf{g}_i \in \Gamma_i \Rightarrow \ \Gamma_i \perp Px_Py_P, \Rightarrow Pz_P \in \Gamma_i \quad i = 1,2,...,6 \tag{9}$$

whence follows

$$\mathbf{g}_i \in \Gamma_i, \quad Pz_P \in \Gamma_i \Rightarrow \begin{cases} 1) \ \ (\mathbf{g}_i) \cap Pz_P = P_i, \\ 2) \ \ (\mathbf{g}_i) \,||\, Pz_P, \end{cases} \quad i = 1,2,...,6 \tag{10}$$

where through ($\mathbf{g}_i$) the straight line containing a vector $\mathbf{g}_i$ is denoted.

Thus, at realization of a condition (8) links A_iB_i lay in the planes containing axis Pz_P. Moreover, cases when all lines of links A_iB_i either intersect axis Pz_P in corresponding points P_i or all these lines become parallel to axis Pz_P are possible.

In the first case (Figure 3a), local rotation of a platform about an axis Pz_P takes place. This is so because according to (8) the last column of the **A** is equal to zero, and hence, the null-space of matrix **A** is spanned by $[0, 0, 0, 0, 0, 1]^T$. This null-space corresponds to set of rotations of the platform about an axis Pz_P at motionless drives, i.e. PM gains the one additional DOF. This time the PM will not be able to withstand a torque applied at the platform in parallel to axis Pz_P.

In the second case (Figure 3b), from $(\mathbf{g}_i) \,||\, Pz_P, \ i = 1,2,...,6$ follows $g_{ix_P} = 0$, $g_{iy_P} = 0$, i.e. except for (8) we have also the first and second columns of **A** with zero elements. Then the null-space of **A** is spanned by $[1, 1, 0, 0, 0, 1]^T$ that corresponds here to set of rotations of a platform about an axis Pz_P and to local moving on plane Px_Py_P at motionless drives. Moreover, force and a forces couple applied at the platform in parallel to plane of a platform do not influence drives.

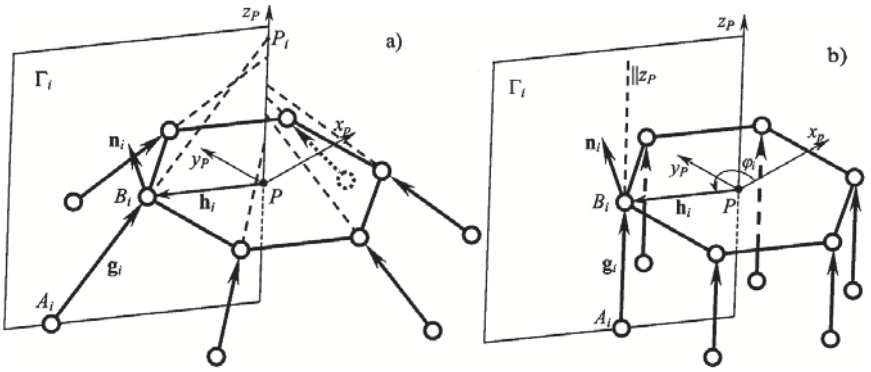

Figure 3. The second type of singularity of the PM.

As position of pole P of a platform is selected arbitrarily, and also vectors $\mathbf{n}_i$ can be parallel to any plane in space the considered case of singularity takes place every time when all lines of links A_iB_i of the PM simultaneously intersect arbitrary, but the same straight line in space, or become parallel to this straight line.

3^0. *All vectors of one group of vectors are zero.* Obviously, any of vectors $\mathbf{g}_i$ cannot be zero. And vectors $\mathbf{n}_i$, describing a relative positioning of a mobile platform and links A_iB_i, can be simultaneously zero, i.e.

$$\mathbf{n}_i = (\mathbf{h}_i \times \mathbf{g}_i) = \mathbf{0}\ ,\ i = 1,2,...,6 \tag{11}$$

Since $h_i \neq 0,\ \ g_i \neq 0$, from (11) it is obtained that $\mathbf{h}_i \,||\, \mathbf{g}_i$, i.e. lines of vectors $\mathbf{g}_i$ converge in pole P (Figure 4). However, as the position of pole P of a mobile platform is selected arbitrarily such singularity of a configuration occurs at any convergence of lines of passive links with lengths g_i .

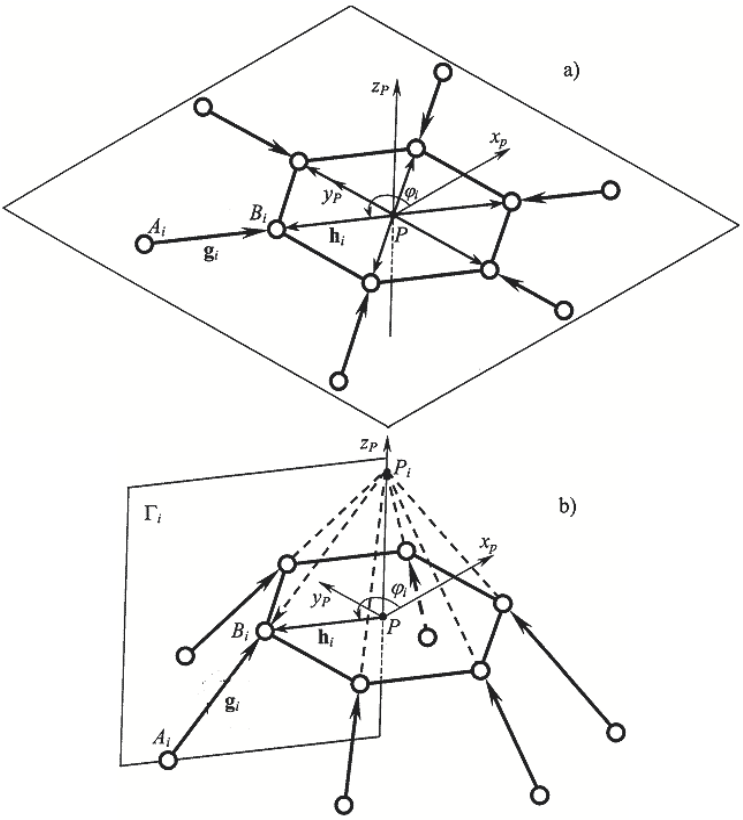

Figure 4. The second type of singularity of the PM.

In a case when all vectors $\mathbf{g}_i$, $i = 1,2,...,6$ lay in a platform plane (Figure 4a), using an invariant kind of the equations (2) with respect to frame $Px_Py_Pz_P$, it is possible to show, that the third column of matrix **A** also will be zero. Then the null-space of matrix **A** is generated by a vector $[0, 0, 1, 1, 1, 1]^T$. This null-space corresponds here to set of local rotations of a platform about its centroid and to local moving in a direction of axis Pz_P at motionless drives. Moreover, a force parallel to axis Pz_P, and also the any torque applied on a platform do not influence drives, i.e. the manipulator is not capable to counteract these loadings.

If all lines of passive links converge outside of a platform plane local spherical movability takes place (Figure 4b). This is so because pole P of a platform can be moved to a point of a convergence of lines of links A_iB_i on axis Pz_P. Then in the corresponding Jacobian **A** constructed concerning a local frame with a new pole only the last three columns will be zero. The null-space of matrix **A** is generated by a $[0, 0, 0, 1, 1, 1]^T$ that corresponds to local spherical movability about a pole P.

Conclusion

Research of degeneracy of Jacoby matrix **A** of the PM with six DOF in consequence of linear dependence of its columns - vectors is carried out. Corresponding conditions of the second type singularity of configurations of the PM are obtained; their geometrical and physical interpretations are given. The obtained analytical conditions of singularities of a configuration can be expressed through constants and variable parameters of the manipulator that is important for the control of such configurations. The further publication of results of research of singularity configurations of the third type of the manipulator is planned.

References

J.P. Merlet, 2000, *Parallel Robots*, Kluwer Academic Publishers, London.

Zh. Baigunchekov, M. Ceccarelli, B. Nurakhmetov, N. Baigunchekov, Parallel Manipulator, Patent No. 20727, Republic of Kazakhstan, Bulletin No. 2, 2009.

Zh. Baigunchekov, B. Nurakhmetov, B. Absadykov, K. Sartaev, M. Izmambetov, N. Baigunchekov "The New Parallel Manipulator with 6 Degree-of-Freedom", Proceedings of 12th IFToMM World Congress in Mechanism and Machine science, June 17-21, 2007, Besançon, France, Vol. 5, pp. 641-646.

L.W. Tsai, 1999, *Robot analysis: the mechanics of serial and parallel manipulators*, John Wiley & Sons, Inc., New York.

C. Gosselin and J. Angeles, 1990, "Singularity analysis of closed-loop kinematic chains," IEEE Trans. Robotics & Autom., Vol. 6, No. 3, pp. 281-290.

Zh. Baigunchekov, I. Beisembetov, M. Izmambetov, 2010, "Singularity Analysis of the New Parallel Manipulator with 6 Degrees-of-Freedom ", ICME 2010, 30 June – 2 July, London, it is presented.

Author Index